

THÈSE

En vue de l'obtention du

DOCTORAT DE L'UNIVERSITÉ DE TOULOUSE

Délivré par :

Institut National Polytechnique de Toulouse (Toulouse INP)

Discipline ou spécialité :

Science et Génie des Matériaux

Présentée et soutenue par :

Mme MARYLOU BOISSON

le jeudi 13 décembre 2018

Titre :

The effects of irradiation on the oxidation first stages of 316L austenitic stainless steel

---

Ecole doctorale :

Sciences de la Matière (SDM)

Unité de recherche :

Centre Interuniversitaire de Recherche et d'Ingénierie des Matériaux (C.I.R.I.M.A.T.)

Directeur(s) de Thèse :

M. ERIC ANDRIEU

MME LYDIA LAFFONT

Rapporteurs :

Mme M. GRACE BURKE, UNIVERSITY OF MANCHESTER

M. YVES WOUTERS, UNIVERSITE GRENOBLE ALPES

Membre(s) du jury :

M. PHILIPPE PAREIGE, UNIVERSITE DE ROUEN, Président

M. ERIC ANDRIEU, INP TOULOUSE, Membre

M. LAURENT LEGRAS, EDF R&D MORET SUR LOING, Invité

Mme FLORENCE CARRETTE, EDF R&D MORET SUR LOING, Invité

Mme LYDIA LAFFONT, INP TOULOUSE, Membre

Mme MURIEL HANTCHERLI, UNIVERSITE TOULOUSE 3, Membre

Table of Contents

Remerciements **v**

List of acronyms **vii**

Résumé **xi**

Introduction **1**

Chapter 1: Bibliographic study **7**

1.1 Austenitic stainless steels oxidation in Pressurized Water Reactors 9

1.1.1 Oxidation in primary water 9

1.1.1.1 Primary water environment 9

1.1.1.2 Oxide scales formed on austenitic stainless steels 10

1.1.1.3 Oxidation mechanisms 16

1.1.1.4 Effect of short oxidation times 22

1.1.2 Parameters affecting stainless steels oxidation 23

1.1.2.1 Surface state and cold-work 23

1.1.2.2 Chemistry of the medium and installation effect 26

1.1.2.3 Crystallographic orientation of the metal 28

1.1.2.4 Irradiation 30

1.1.3 Austenitic stainless steels oxidation in PWRs: Synthesis 34

1.2 Irradiation effect on austenitic stainless steels 35

1.2.1 Microstructural modifications 37

1.2.1.1 Frank loops 37

1.2.1.2 “Black dots” 38

1.2.1.3 Cavities and helium filled bubbles 38

1.2.1.4 Stacking Fault Tetrahedra 39

1.2.1.5 Modification of the dislocation network 40

1.2.2 Chemical modifications 40

1.2.2.1 Radiation Induced Segregation 40

1.2.2.2 Phase precipitation 43

1.2.3 Parameters affecting the changes induced by irradiation 44

1.2.3.1 Surface state and cold-work 44

1.2.3.2 Irradiation dose 45

1.2.3.3 Grain boundaries character 46

1.2.4 Synthetic irradiations 50

1.2.4.1 Generalities 51

1.2.4.2 Proton irradiation 52

1.2.5 Irradiation effect on austenitic stainless steels: Synthesis 53

1.3 Bibliographic summary and experimental approach 55

Chapter 2: Experimental techniques and studied materials **59**

2.1 Experimental techniques . . . 61
2.1.1 Optical microscopy . . . 61
2.1.2 Grazing Incidence X-Ray Diffraction . . . 61
2.1.3 Raman spectroscopy . . . 62
2.1.4 Scanning Electron Microscopy . . . 63
2.1.4.1 EBSD mapping before oxidation . . . 63
2.1.4.2 Surface observations after oxidation . . . 64
2.1.4.3 Oxide thickness measurements . . . 66
2.1.4.4 TEM lamellae preparation and optimisation . . . 66
2.1.5 Transmission Electron Microscopy . . . 69
2.1.5.1 Electron diffraction . . . 71
2.1.5.2 Bright Field images . . . 71
2.1.5.3 Dark Field images . . . 72
2.1.5.4 Scanning Transmission Electron Microscopy . . . 72
2.1.5.5 Energy Dispersive X-ray Spectroscopy . . . 73
2.1.5.6 Electron Energy Loss Spectroscopy . . . 74
2.1.6 Experimental techniques: Synthesis . . . 77
2.2 Materials and samples preparations . . . 78
2.2.1 Samples oxidised in simulated primary water . . . 78
2.2.1.1 Reference 316L alloy . . . 78
2.2.1.2 Cold-worked 316L alloy . . . 81
2.2.1.3 Proton pre-irradiated 316L alloy . . . 82
2.2.1.4 Oxidations in simulated PWR media . . . 84
2.2.2 Irradiation Assisted Corrosion . . . 86
2.2.3 Decommissioned bolt . . . 89
2.2.4 Materials and samples preparations: Synthesis . . . 91
2.3 Characterisation of the irradiated samples and proton irradiation representativeness . . . 91
2.3.1 Microstructural modifications characterisation . . . 92
2.3.1.1 Frank loops . . . 92
2.3.1.2 Cavities . . . 95
2.3.2 Chemical modifications characterisation . . . 99
2.3.2.1 Intragranular segregation and precipitation . . . 99
2.3.2.2 RIS at grain boundaries . . . 104
2.3.3 Proton irradiation representativeness . . . 107

Chapter 3: Characterisation of the oxides formed in simulated primary water 109
3.1 Description of the oxides formed on 316L exposed to simulated PWR medium 112
3.1.1 Morphological description of the oxide layers . . . 112
3.1.1.1 Optical microscopy study of the oxidised samples . . . 112
3.1.1.2 SEM characterisation of the outer oxide surface morphology . . . 112
3.1.1.3 Oxides morphology and thickness at nanoscopic scale . . . 113
3.1.1.4 Morphological description: Summary . . . 114
3.1.2 Analysis of the crystallographic structure of the oxide layers . . . 115
3.1.2.1 SEM description of the outer oxide morphology . . . 115
3.1.2.2 GIXRD analysis . . . 115
3.1.2.3 Raman spectroscopy . . . 117
3.1.2.4 TEM Dark Field and diffraction study . . . 118
3.1.2.5 Crystallographic structure: Summary . . . 121
3.1.3 Chemical analysis of the oxide layers . . . 122
3.1.3.1 Raman spectroscopy analysis . . . 122

3.1.3.2 EFTEM mapping . . . 123
3.1.3.3 EELS and EDXS quantitative analyses . . . 124
3.1.3.4 Chemical analysis: Summary . . . 126
3.1.4 Grain boundaries oxidation . . . 126
3.1.4.1 Morphological description . . . 126
3.1.4.2 Chemical analysis . . . 128
3.1.4.3 Grain boundaries oxidation: Summary . . . 130
3.1.5 Oxides formed on 316L exposed to simulated PWR medium: Synthesis, discussion and oxidation mechanism . . . 130
3.2 Crystallographic orientation effect on the oxide scales . . . 134
3.2.1 Morphological description of the oxide depending on the underlying grain orientation . . . 134
3.2.1.1 Optical microscopy study . . . 135
3.2.1.2 Description of the oxides using SEM . . . 135
3.2.1.3 TEM study of the inner oxides thickness . . . 137
3.2.1.4 Morphological description: Summary . . . 138
3.2.2 Chemical analysis of the oxide layers depending on the underlying grain orientation . . . 139
3.2.2.1 Raman spectroscopy analysis . . . 139
3.2.2.2 EDXS and EELS quantitative analyses . . . 140
3.2.2.3 Chemical analysis: Summary . . . 142
3.2.3 Crystallographic orientation: Synthesis, discussion and oxidation mechanism 142
3.3 Cold-work effect on the oxide scales . . . 145
3.3.1 Characterisation of the oxides morphology and thickness on cold-worked samples . . . 145
3.3.2 Chemistry of the oxides formed on cold-worked samples . . . 148
3.3.3 Cold-work effect: Synthesis, discussion and oxidation mechanism . . . 149
3.4 Effect of the presence of inclusions on the oxide scales . . . 151
3.4.1 Characterisation of the oxides morphology and thickness near inclusions . . 151
3.4.2 Chemistry of the oxides near inclusions . . . 154
3.4.3 Effect of the presence of inclusions: Synthesis, discussion and oxidation mechanism . . . 154
3.5 Oxide scales formed in simulated primary water: Synthesis . . . 156

Chapter 4: Irradiation effect on the oxide scales formed in primary water 159
4.1 Description of the oxides formed on proton pre-irradiated samples . . . 161
4.1.1 Morphological description of the oxides . . . 161
4.1.1.1 Optical microscopy study of the oxidised samples . . . 161
4.1.1.2 SEM characterisation of the outer oxide . . . 161
4.1.1.3 TEM study of the oxides at nanoscopic scale . . . 163
4.1.1.4 Effect of irradiation on the oxides morphology: Summary . . . 166
4.1.2 Crystallographic structure and epitaxy of the oxide layers . . . 167
4.1.2.1 Structure of the oxide scales . . . 167
4.1.2.2 Study of the epitaxial relationship . . . 168
4.1.2.3 Effect of irradiation on the oxides crystallographic structure and epitaxy: Summary . . . 170
4.1.3 Chemical analysis of the oxide layers . . . 171
4.1.3.1 Raman spectroscopy analyses . . . 171
4.1.3.2 EFTEM mapping . . . 172
4.1.3.3 EELS and EDXS quantitative analyses . . . 172
4.1.3.4 Effect of irradiation on the oxides chemical composition: Summary 175

4.1.4 Study of the intergranular oxidation on grain boundaries affected by RIS . 175
4.1.4.1 Morphological description 176
4.1.4.2 Chemical analysis 177
4.1.4.3 Irradiation effect on the grain boundaries oxidation: Summary . . 179
4.1.5 Oxides formed on proton pre-irradiated samples: Synthesis, discussion and oxidation mechanism 179
4.2 Study of the Irradiation Assisted Corrosion 183
4.2.1 Characterisation of the oxides formed on the IACUNIRR area 184
4.2.1.1 Description of the oxides morphology and thickness 184
4.2.1.2 Analysis of the oxides structure 186
4.2.1.3 Chemical analysis of the oxide layers 187
4.2.1.4 Grain boundary oxidation 190
4.2.1.5 Unirradiated area characterisation: Summary 190
4.2.2 Characterisation of the oxides formed on the IACIRR area 191
4.2.2.1 Description of the oxide scales 191
4.2.2.2 Proton pre-irradiated area characterisation: Summary 193
4.2.3 Characterisation of the oxides formed on the IACIAC area 193
4.2.3.1 Description of the oxide scales 194
4.2.3.2 Oxide formed under proton flux characterisation: Discussion and summary 199
4.2.4 Irradiation Assisted Corrosion experiment: Synthesis, discussion and oxidation mechanism 202
4.3 Oxides formed at the crack tips of a decommissioned bolt 203
4.3.1 Oxides description 204
4.3.2 Synthesis and discussion on the representativeness of short-time oxidations of proton pre-irradiated specimens 208
4.4 Oxide scales formed on irradiated materials: Synthesis 209

Conclusions and perspectives **211**

Appendix A: Rel-Rod Dark Field **217**

Appendix B: Raman spectroscopy applied to spinel oxides **219**

Appendix C: EELS and EDXS quantifications **225**

Appendix D: Sample polishing **229**

Appendix E: Additional characterisations on the irradiated samples **231**

Appendix F: Additional characterisations on the Michigan sample **243**

Bibliography **249**

Remerciements

Au moment ou j'écris ces lignes, un chapitre se clôt. Ce manuscrit représente l'aboutissement de trois années de travail intenses et enrichissantes. J'aimerais, à travers ces quelques mots, pouvoir exprimer la profonde gratitude que je ressens à l'égard de tous ceux qui ont croisé mon chemin et contribué de manière directe ou indirecte à cette aventure. Ce travail n'aurait pu aboutir sans la présence des personnes citées ci-dessous qui ont participé à cette formidable expérience scientifique et personnelle.

Ainsi je souhaite remercier chaleureusement M. Philipe Pareige du GPM de Rouen pour avoir présidé le jury de thèse. Je tiens à exprimer mes sincères remerciements à Mme. M. Grace Burke de l'Université de Manchester et M. Yves Wouters du SIMAP de Grenoble qui ont été les rapporteurs de ce travail. Mes remerciements vont également à Mme. Muriel Hantcherli du CEMES de Toulouse pour avoir intégré le jury de thèse en qualité d'examinatrice. Je souhaite témoigner ma reconnaissance à tous les membres du jury pour avoir accepté d'évaluer ce travail et pour les discussions enrichissantes qui ont eu lieu lors de la soutenance.

Je souhaite ensuite remercier les personnes ayant encadré cette thèse. Cette dernière n'aurait pu voir le jour ni se dérouler dans de bonnes conditions sans la présence, l'implication et la confiance d'Eric Andrieu, Lydia Laffont, Laurent Legras et Florence Carrette. Ils ont su guider avec efficacité mes recherches. Je tiens à adresser toute ma reconnaissance à mon directeur de thèse Eric Andieu et ma co-directrice de thèse Lydia Laffont qui ont su me transmettre leur passion pour les sciences des matériaux lors de cette thèse, mais également dans les années qui ont précédé durant mon cursus d'ingénieur au sein de l'ENSIACET. Je garderai un excellent souvenir de nos discussions scientifiques qui m'ont poussé à de belles découvertes et de nombreux questionnements et remises en question. Leur soutien, leur confiance et leurs compétences scientifiques m'ont permis de grandir à la fois scientifiquement et de manière personnelle. Mes sincères remerciements à Eric Andrieu avec qui j'ai eu un énorme plaisir à échanger sur ses multiples idées ou autour de ces remarques judicieuses et constructives. Malgré un emploi du temps encombré, sa gestion quasi surnaturelle de son temps et son souci de « l'humain » resteront longtemps gravés dans ma mémoire. Je suis de plus très reconnaissante à Lydia Laffont pour ses conseils, sa disponibilité, sa gentillesse et pour avoir géré toutes les démarches administratives à Toulouse lorsque je ne pouvais y être. J'adresse mes remerciements particulier à Laurent Legras, responsable de cette thèse à EDF R&D. Ayant passé le plus clair de mon temps à EDF, il a été celui avec lequel j'ai partagé les mauvaises nouvelles, mes déceptions et mes regrets. Il a toujours su me remotiver et me prodiguer des conseils avisés pour que j'avance malgré tout. Je garderai néanmoins en souvenir non pas les échecs, mais nos belles trouvailles et nos échanges enthousiastes autour des microscopes ou bien d'un café. Un immense merci de m'avoir transmis cette passion pour la microscopie. Je souhaiterais souligner la pédagogie dont il a fait preuve et l'apport scientifique, technique, mais aussi humain qu'il m'a apporté durant ces trois années. Ses critiques sur mes écrits et oraux ont toujours été constructives, ce qu'elles m'ont apporté dépasse largement le cadre de cette thèse. Il a été un pilier sur lequel je pouvais compter au quotidien. Je souhaite aussi remercier Florence Carrette d'EDF R&D pour sa gentillesse et pour avoir su me transmettre son goût pour la corrosion. Elle a su, malgré l'éloignement, se montrer présente et me soutenir.

Durant une thèse expérimentale, la partie technique est fondamentale. Ainsi je tiens à ex-

primer mes remerciements aux personnes ayant contribué à son bon déroulement. Mes vifs remerciements à Christian Cossange, Gilles Rolland, Gilles Espinasse et Emeric Brantus du laboratoire expertise d'EDF R&D pour leur aide et remarques avisées lors de la préparation des échantillons. Je salue également le travail d'Olivier Wendling, de Thierry Sauvage, d'Aurélien Bellamy et de Pierre Desgardin du CEMHTI pour les irradiations réalisées. Cette thèse n'aurait pu voir le jour sans la présence de Thomas Girard d'EDF R&D qui à réalisé d'une main de maître les oxydations. J'ai eu plaisir à échanger avec ce dernier sur les inhomogénéités observées. Je remercie sincèrement Gary Was et Rigel Hanbury de l'Université du Michigan qui m'ont accueilli afin de réaliser l'expérience d'oxydation sous flux de protons. Je tiens à exprimer ma gratitude à Yannick Fontaine d'EDF R&D pour sa réactivité lors de l'usinage des échantillons mais aussi de mes lubies pour réaliser un montage pour le polissage. J'ai énormément apprécié sa bonne humeur et son franc-parler. J'adresse aussi ma reconnaissance à Gilles Adjanor, Julien Vidal et Christophe Domain d'EDF R&D avec qui j'ai pu discuter sur la simulation numérique pour mieux comprendre les phénomènes se produisant à l'échelle atomique. Je tiens a remercier Philipe Le Bec, Pierre-Emile Lhuillier et Martin Bachet d'EDF R&D avec qui j'ai eu plaisir à échanger. Je souhaiterais également souligner l'implication de Bertrand Chassignole, Faiza Sefta, Marc Berveiller, Adrien Guery, Valérie Kervargant et Isabelle Pires d'EDF R&D qui ont contribué au bon déroulement de cette thèse. Je remercie sincèrement Julien Stodolna, Frédéric Delabrouille, Dominique Loisnard, Michel Mahé et Nicolas Brynaert et de manière plus générale le laboratoire microscopie d'EDF R&D. Vos conseils et votre bonne humeur quotidienne m'ont été précieux durant ces trois années. Les mots ne sauraient exprimer combien votre présence a contribué à mon arrivée souriante au travail chaque matin et combien votre aide m'a été précieuse. Je souhaiterais adresser des remerciements particuliers à Cédric Charvillat et Olivier Marsan du CIRIMAT de Toulouse avec qui j'ai eu un réel plaisir à travailler lors de mes passages à Toulouse. Un grand merci à Olivier Marsan qui a toujours accepté avec le sourire de pousser les caractérisations suite à mes nombreuses requêtes.

Cette aventure n'aurait pas été la même sans la présence de mes chers compagnons d'infortune thésards eux aussi: Camille Trottier, Benjamin Christiaen, Abel Rappeti, Baptiste Stephan, Baptiste Pannier, Jordan Baux et Julie Flambard. Je vous remercie tous chaleureusement, vous avez su insuffler une bonne humeur quotidienne, mais aussi me poser des questions pertinentes et contribuer à l'esthétique de ce manuscrit. Les mots me manquent, mais merci à vous, j'ai gagné de cette thèse des amis.

À ma famille, qui a su me soutenir durant ces trois années sans forcément tout comprendre de mes problèmes et questionnements, un immense merci. Mes parents, Laurent et Béatrice, ont été ma principale source de motivation afin d'atteindre mes objectifs. Je suis chanceuse de vous avoir à mes côtés et j'espère vous avoir rendus fiers. Parmi les personnes ayant contribué de manière indirecte à cette thèse par leur soutien et leur écoute, parfois quasi quotidienne, je souhaite remercier Lenaïg Molaret et Solène Guillet-Revol. Je ne saurais conclure ces remerciements sans évoquer Pierre-Loïc Neu. Je me souviendrai longtemps de nos soirées, pour moi d'écriture et pour lui de relecture sur un sujet qui était loin de lui être familier. Il a été d'un soutien sans faille ainsi que l'épaule sur laquelle j'ai pu pleurer et me reposer lors des moments difficiles. Il n'a cessé de m'impressionner par sa disponibilité, sa bienveillance et son envie de rendre mon quotidien plus facile. Son sourire et son habilité à me remonter le moral et me redonner confiance en moi ont été précieux.

En conclusion, collègues, amis, famille, par votre soutien technique et/ou moral vous avez contribué à la réalisation de cette thèse. Enfin, à celles et ceux qui n'auraient pas été cités, je vous prie de bien vouloir m'excuser pour cet oubli involontaire.

List of Acronyms

ADF Annular Dark Field

APT Atom Probe Tomography

BF Bright Field

BSE Back Scattered Electron

CCD Charge-Coupled Device

CDF Centered Dark Field

CDZ Cavity Denuded Zone

CFSE Crystal Field Stabilization Energy

CSL Coincident Site Lattice

DADF Displaced-Aperture Dark Field

DF Dark Field

DO Dissolved Oxygen

DOF Degree Of Freedom

dpa Displacement Per Atom

EBSD Electron Back Scattered Diffraction

ECP Electrochemical Corrosion Potential

EDM Electrical Discharge Machining

EDXS Energy Dispersive X-ray Spectroscopy

EELS Electron Energy Loss Spectroscopy

EFTEM Energy Filtered Transmission Electron Microscopy

ELNES Energy Loss Near Edge Structure

FCC Face Centered Cubic

FEG Field Emission Gun

FFT Fast Fourier Transform

FIB Focused Ion Beam

FP Frankel Pair

GDOES Glow Discharge Optical Emission Spectroscopy

GIF Gatan Imaging Filter

GIXRD Grazing Incidence X-Ray Diffraction

HAADF High Angle Annular Dark Field

HAGB High Angle Grain Boundary

HREELS High Resolution Electron Energy Loss Spectroscopy

HRTEM High Resolution Transmission Electron Microscopy

IAC Irradiation Assisted Corrosion

IAS Infrared Absorption Spectrometry

IASCC Irradiation Assisted Stress Corrosion Cracking

ICP Inductively Coupled Plasma

IFFT Inverse Fast Fourier Transform

LAGB Low Angle Grain Boundary

LTO Long Term Operation

MEB Microscopie Electronique à Balayage

MET Microscopie Électronique en Transmission

MIBL Michigan Ion Beam Laboratory

OP-S Oxide Polishing-Silica

PDM Point Defect Model

PECS Precision Etching and Coating System

PIPS Precision Ion Polishing System

PKA Primary Knock-on Atoms

PWR Pressurized Water Reactor

RCC-M Règles de Conception et de Construction des matériels Mécaniques des îlots nucléaires REP

REP Réacteur à Eau sous Pression

RHAGB Random High Angle Grain Boundary

RIS Radiation Induced Segregation

RPV Reactor Pressure Vessel

RRDF Rel-Rod Dark Field

SAED Selected Area Electron Diffraction

SCC Stress Corrosion Cracking

SDD Silicon Drift Detector

SE Secondary Electron

SEM Scanning Electron Microscopy

SFT Stacking Fault Tetrahedron

SIA Self Interstitial Atom

SIMS Secondary Ion Mass Spectrometry

SRIM Stopping and Range of Ions in Matter

STEM Scanning Transmission Electron Microscopy

STP Standard Temperature and Pressure

TEM Transmission Electron Microscopy

XFS X-ray Fluorescence Spectrometry

XPS X-ray Photoelectron Spectroscopy

XRD X-Ray Diffraction

Résumé

Les Réacteurs à Eau sous Pression (REPs) sont utilisés dans de nombreux pays depuis la fin des années 1960. Pour rester économiquement compétitive et constituer une source d'énergie sûre, l'industrie nucléaire doit continuellement améliorer et optimiser la durée de vie des centrales et leurs performances. L'allongement de la durée de vie des centrales nucléaires et la gestion de leur vieillissement constituent l'un des principaux problèmes énergétiques rencontrés au cours de ce siècle. Ces dernières années, des efforts importants ont été déployés pour allonger la durée du cycle d'exploitation des REPs, de 40 à 60 ans. Cela nécessite une bonne connaissance des matériaux et des structures en service, en conditions nominales et accidentelles, car leurs performances sont l'un des facteurs essentiels pour assurer un haut niveau de sécurité tout en maintenant des coûts d'exploitation concurrentiels. De plus, la dégradation des matériaux engendre une diminution du taux de disponibilité de l'installation et une augmentation des coûts de maintenance liés à la fois aux contrôles en service et aux interventions destinées à réparer les dommages. Ainsi, mieux comprendre les phénomènes régissant le vieillissement des matériaux est, de nos jours, l'un des enjeux majeurs. Les internes de cuve des REPs, en contact avec le milieu primaire, protègent la cuve de l'irradiation et supportent l'assemblage combustible. Ils sont fabriqués en acier inoxydable austénitique. Des vis de cloison-renfort en alliage 316L sont utilisées pour maintenir les plaques horizontales et verticales constituant les internes de cuves (Figure 1).

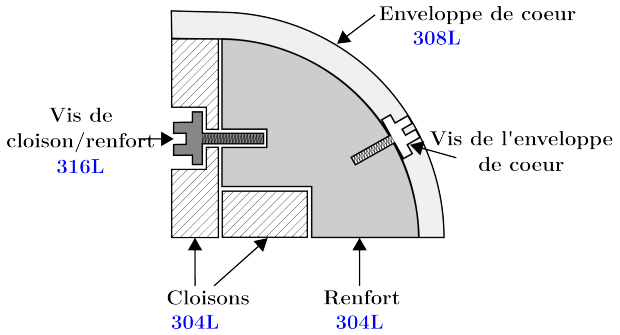

Figure 1: *Schéma de la configuration cloison/renfort avec les matériaux utilisés*

Ces vis sont exposées au milieu primaire sous irradiation et subissent des contraintes mécaniques. Dans ces conditions, une dégradation des vis par le phénomène de corrosion sous contrainte assistée par l'irradiation (IASCC) est susceptible de se produire. En effet, des fissures dues à l'IASCC ont été observées sur des vis extraites de centrales confirmant la susceptibilité des vis aux mécanismes de vieillissement. Les premières fissures ont été observées en 1989 lors d'inspections en service sur une vis extraite de Bugey 2 [1, 2]. Des fissures intergranulaires ont été mises en évidence à la jonction tête/fût d'une vis extraite de Fessenheim 2 comme présenté en Figure 2.

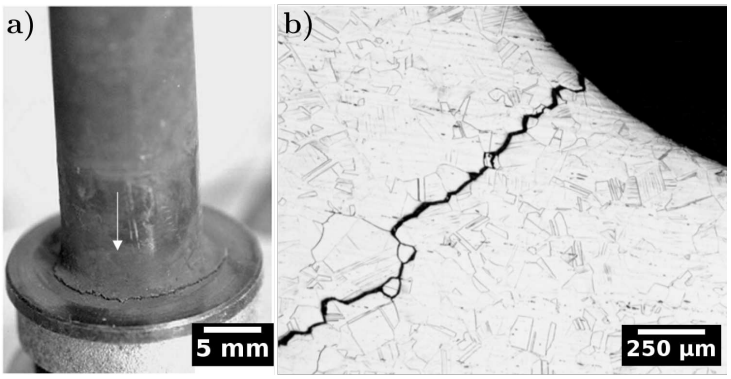

Figure 2: *Vis de cloison/renfort extraite de Fessenheim 2 irradiée à 11 dpa et fissurée à la jonction tête/fût a) examination visuelle de la fissure b) examination métallurgique de la fissure [1]*

Ce phénomène complexe peut avoir une influence significative sur le temps et le coût de maintenance des composants internes des REPs. La compréhension des mécanismes d'oxydation en pointe de fissure d'IASCC est donc essentielle pour mieux appréhender l'IASCC. D'un point de vue pratique, cela passe par la tenue de la couche passive lors des premières étapes de corrosion. En effet, les propriétés des films d'oxydes formés, notamment leur morphologie, leur épaisseur, leur structure et leur composition chimique, jouent un rôle important dans le processus d'oxydation, en particulier aux stades initiaux et en fonds de fissures. Au fur et à mesure que les fissures d'IASCC se propagent, elles présentent des zones oxydées correspondant aux premiers stades d'oxydation au niveau des fonds de fissures, car de nouvelles surfaces seront exposées au milieu primaire lors de la propagation de ces dernières. Ainsi, afin de mieux comprendre l'IASCC il est donc nécessaire d'étudier en détail les mécanismes de formation et de croissance des oxydes lors des premières étapes d'oxydation. De plus, les défauts d'irradiation et les modifications chimiques induites par l'irradiation sont susceptibles de modifier la cinétique d'oxydation et les couches d'oxydes formées.

La littérature atteste de la formation d'une couche d'oxyde duplex sur les aciers austénitiques inoxydables exposés en milieu primaire. Cet oxyde est constitué d'une couche externe discontinue riche en fer souvent décrite comme étant de la magnétite (Fe_3O_4) et d'une couche interne dense riche en chrome ($FeCr_2O_4$) (Figure 3). Un enrichissement en nickel est aussi présent à l'interface métal/oxyde. La plupart des auteurs reportent que les oxydes sont tous deux de structure spinelle mais une structure corindon (type Cr_2O_3) a parfois été observée. De plus, il existe des divergences sur la structure polycristalline ou monocristalline de l'oxyde interne. De nombreux paramètres peuvent affecter l'oxydation tels que l'état de surface du matériau et son écrouissage, la présence de précipités, l'orientation cristallographique du grain de métal sous-jacent, la nature des joints de grains, le milieu oxydant et l'irradiation. Ces derniers doivent être investigués plus en détail et pour de courtes durées d'oxydation afin de conclure sur leur effet sur les premiers stades d'oxydation. Ces informations permettront d'affiner au mieux les modèles de corrosion.

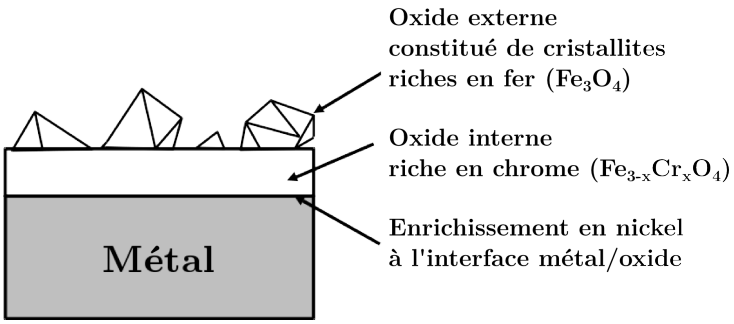

Figure 3: *Schéma de l'oxyde duplex formé sur les aciers austénitiques inoxydables exposés en milieu primaire*

L'irradiation neutronique est connue pour induire des défauts d'irradiation tels que des boucles de Frank, des cavités et bulles d'hélium, etc. ainsi que des modifications chimiques induites par l'irradiation (RIS) notamment aux joints de grains (Figure 4). Ces modifications sont dépendantes des conditions d'irradiation (dose, température, fluence, etc.) et sont susceptibles d'affecter l'oxydation. Certains auteurs ont reporté des oxydes plus épais ou plus minces sur échantillons irradiés, mais les oxydes internes sont souvent décrits comme plus riches en chrome que sur les échantillons non irradiés. Les modifications de la couche interne observées dans les échantillons irradiés sont probablement liées à la microstructure post-irradiation. De plus, la ségrégation sous irradiation étant susceptible d'influer le phénomène d'oxydation, il convient d'en étudier les effets. Le rôle de l'irradiation sur l'oxydation des aciers inoxydables dans le milieu REP est encore mal compris, il serait bénéfique de l'étudier à des temps d'oxydation courts afin de mettre en lumière les mécanismes impliqués dans les premières étapes de l'oxydation.

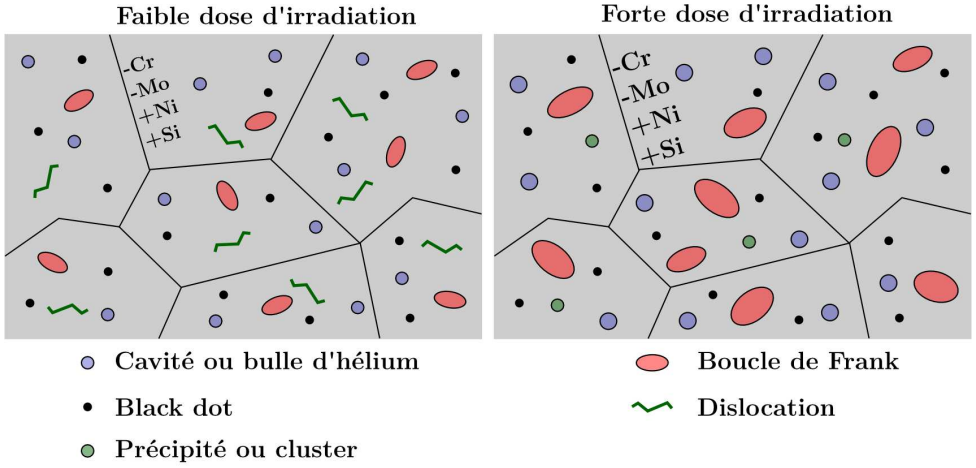

Figure 4: *Schéma récapitulatif des modifications induites par l'irradiation dans les aciers austénitiques inoxydables pour de faible et forte doses d'irradiation*

Dans ce travail, des échantillons de référence, des échantillons avec divers polissages ainsi que des échantillons pré-irradiés aux protons ont été étudiés et oxydés en milieu REP simulé. Dans un premier temps ces derniers ont été investigués avant oxydation pour confirmer la représentativité de la pré-irradiation protonique réalisée. Dans un second temps de courtes durées d'oxydation (entre 5 minutes et 96 heures) ont été réalisés pour étudier les premières étapes d'oxydation relatives à la formation d'oxydes et à leur croissance en pointe de fissures. Seuls quelques auteurs ont réalisé et étudié des oxydations aux temps courts et donc peu de données sont disponibles. Ainsi, des échantillons de références ont été oxydés durant de courtes durées afin de servir comme références lors des comparaisons avec les échantillons irradiés. L'orientation cristallographique du grain de métal sous-jacent influençant l'oxydation, l'examen des couches d'oxydes a été effectué de prime abord sur une unique orientation. Ensuite, une étude des couches d'oxyde plus

approfondie a été menée en tenant compte de l'orientation cristallographique du grain de métal sous-jacent. Une partie de cette étude vise à mieux comprendre comment des hétérogénéités de surface, telles que l'écrouissage induit par un polissage mal contrôlé et les inclusions, peuvent affecter l'oxydation. Ainsi, l'étude d'échantillons avec différents niveaux de déformation induits par le polissage a permis de mieux comprendre l'effet de la préparation des échantillons et plus généralement de l'écrouissage sur la cinétique d'oxydation. L'observation des oxydes formés proche des inclusions a aussi permis de révéler leur effet sur la cinétique d'oxydation. Des échantillons pré-irradiés aux protons ont été préparés et oxydés pour comprendre l'influence des défauts d'irradiation sur la cinétique d'oxydation. En outre, une oxydation sous flux de protons a été réalisée à l'Université du Michigan afin de déterminer la contribution du flux de protons au processus d'oxydation. Enfin, un fond de fissure oxydé d'une vis déclassée a été étudié et comparé à tous les autres échantillons avant de conclure sur la représentativité de cette étude. Les couches d'oxyde externe et interne ont été caractérisées à l'aide de techniques macroscopiques et nanoscopiques, allant de leur morphologie, épaisseur, structure à composition, tout en étudiant l'oxydation intergranulaire. Les mécanismes d'oxydation et paramètres étudiés ont été discutés en fonction des résultats obtenus.

Les techniques expérimentales choisies dans cette étude vont des techniques d'analyse macroscopique aux analyses microscopiques pour caractériser au mieux les couches d'oxydes formées. Ces dernières ont été choisies pour donner les informations nécessaires sur la morphologie, l'épaisseur, la chimie, la structure des oxydes à une échelle appropriée. Les résultats issus de l'utilisation de ces techniques ont permis de conclure sur la cinétique d'oxydation et les mécanismes impliqués. En ce qui concerne la préparation des échantillons, des cartographies EBSD ont été réalisées avant oxydation pour obtenir les orientations cristallographiques des grains de métal de base. Les lames FIB ont été réalisées sur les zones d'intérêt avant ou après oxydation en utilisant les cartographies EBSD. Les épaisseurs de lames ont été contrôlées en Microscopie Électronique en Transmission (MET) par microscopie électronique en énergie filtrée et les lames ont été amincies/nettoyées aux ions argon progressivement en utilisant un PIPS II. Les modifications induites par l'irradiation ont été analysées au MET. Les cavités ont été imagées en champ clair en sous et surfocus tandis que les boucles de Frank l'ont été en champ sombre en sélectionnant les tâches diffuses induites par ces boucles en deux ondes proche d'un axe de zone [101]. Enfin, les modifications chimiques ont été étudiées en spectroscopie X à dispersion d'énergie (EDXS) et spectroscopie de perte d'énergie des électrons transmis (EELS). Quant à eux, les oxydes formés ont premièrement été observés par microscopie optique et Microscopie Electronique à Balayage (MEB) en comparant ces images aux cartographies EBSD. Ensuite, la structure et la chimie des oxydes ont été étudiées par diffraction des rayons X par incidence rasante et spectroscopie Raman. Des analyses plus poussées au MET ont été réalisées sur des grains d'orientations choisies. Une grande variété de techniques a pour cela été utilisée tels que l'imagerie en champ clair (BF) et champ sombre (DF), la microscope électronique à balayage par transmission (STEM), la diffraction électronique par sélection d'aire (SAED) et enfin des analyses en microscopie électronique en transmission filtrée en énergie (EFTEM), EELS et EDXS.

L'alliage au coeur de cette étude est un acier austénitique inoxydable de type 316L comme utilisé pour les vis de cloison/renfort. Sa composition est présentée dans la Table 1. Néanmoins l'alliage étudié a été remis en solution afin de s'affranchir de l'effet de l'écrouissage. Des échantillons ont été découpés par électro-érosion aux dimensions suivantes : 10,85 mm x 11,85 mm x 1,7 mm. Les échantillons de référence ont été polis jusqu'à l'OP-S en utilisant un polissage de « référence » pour obtenir des surfaces sans écrouissage ou dislocations amenées par le polissage. Cet alliage est un alliage commercial et comprend donc des inclusions. Ces dernières sont principalement des inclusions de sulfure de manganèse (MnS) et des précipités d'oxydes. Les acquisitions EBSD ont révélé que les orientations cristallographiques des grains de métal de base

sont isotropiquement distribuées. Ensuite certains échantillons ont été repolis au papier SiC 4000 ou à la pâte diamantée 6 µm. Ces polissages ont induit des couches surfaciques déformées de 1,2 ± 0,2 et 0,4 ± 0,1 µm respectivement afin d'étudier l'effet du polissage réalisé sur l'oxydation. Des pré-irradiations aux protons ont aussi été réalisées sur des échantillons polis jusqu'à l'OP-S. Pour réaliser les irradiations ces échantillons devaient être fins (∼ 0,5 mm) et polis sur leur deux faces. Une dose d'irradiation de 1 dpa a été choisie afin d'être proche de la saturation des boucles de Frank et de la RIS. Une irradiation à 0,5 dpa, ainsi qu'une autre à 1,5 dpa ont également été effectuées afin d'étudier l'effet de la dose sur l'oxydation. Le diamètre de la zone irradiée est de 4 mm, de sorte que tous les échantillons possèdent des régions irradiées et non irradiées. Ceci a permis des études comparatives des oxydes formés sur les zones irradiées et non irradiées sur un même échantillon oxydé dans les exactes mêmes conditions. Ces irradiations ont été effectuées à 380 ± 7 °C et avec un débit de dose proche de 1,06 × 10^{-5} dpa/s pour des protons de 1,5 MeV. La température d'irradiation a été choisie afin de simuler l'irradiation neutronique se produisant dans les REPs et les modifications induites par l'irradiation. Les échantillons irradiés ont ensuite été polis avec de l'OP-S pour atteindre le plateau d'irradiation à la dose souhaitée à une profondeur d'environ 2 µm.

Table 1: *Composition de l'alliage 316L étudié comparé aux spécifications RCC-M [3]*

Element	C	Cr	Ni	Mo	Mn	Si	N	S	P	Cu	O	Fe
316L (% massique)	0,027	17,1	11,5	2,58	1,9	0,4	0,051	0,005	0,028	0,2	0,009	Bal.
316L (% atomique)	0,13	18,3	10,9	1,5	1,9	0,8	0,2	0,01	0,05	0,18	0,03	Bal.
Specifications RCC-M (% massique)	≤ 0,03	16-19	10-14	2,25-2,75	≤ 2	≤ 1	-	≤ 0,015	≤ 0,02	≤ 1	-	Bal.

Une fois poli jusqu'à l'OP-S des cartographies EBSD ont été réalisées au centre des échantillons pour obtenir l'orientation cristallographique des grains de métal sous-jacent. Juste avant l'oxydation les échantillons ont été nettoyés et polis aux ions argon pour retirer l'oxyde natif présent à la surface des échantillons et l'éventuelle contamination carbone apportée par les cartographies EBSD. Les oxydations ont été réalisées dans la boucle TITANE d'EDF R&D en milieu primaire simulé (T = 325 °C, P = 155 bar, [B] = 1000 ppm, [Li] = 2 ppm, $[H_2]$ = 30 cc/kg, $[O_2]_{\text{dissolved}} \leq 5$ ppb and $pH_{325\ °C} = 7.3$). Cette boucle, comme son nom l'indique est en titane afin d'éviter tout phénomène de dissolution/reprecipitation d'espèces provenant du matériau de l'installation.

Un échantillon a été oxydé sous flux de protons à l'Université du Michigan dans une cellule d'oxydation dédiée permettant de réaliser des irradiations et oxydations de façon simultanée (Figure 5). Cet échantillon est issu de la même nuance d'alliage 316L que précédemment et a été usiné par électro-érosion et poli jusqu'à l'OP-S. La moitié de cet échantillon a été pré-irradié aux protons avant l'oxydation sous flux à une dose proche de 1 dpa (0,94 dpa) et une température de 360 °C. L'échantillon a été aminci jusqu'à 46 µm et soudé à un disque d'alliage 17-4 PH de même diamètre et de 36 µm d'épaisseur afin d'apporter une résistance mécanique et réduire l'activité résiduelle de l'alliage 316L. Comme précédemment, la zone non irradiée et la zone pré-irradiée ont été oxydées simultanément durant 24 heures dans des conditions d'oxydation identiques. Ainsi, lors de l'oxydation, une petite zone (1 mm^2) de la zone pré-irradiée a été oxydée sous flux de protons à une dose de 0,064 dpa. Cela a ainsi permis une comparaison directe des trois domaines. La cellule d'oxydation est en acier inoxydable et le milieu consiste d'eau à 131 bar et 320 °C avec 3 ppm massique d'hydrogène dissous et un $pH_{320°C}$ de 6,2. La teneur en oxygène dissous a été maintenue sous 0,2 ppb et aucun bore ni lithium n'a été ajouté dans le milieu.

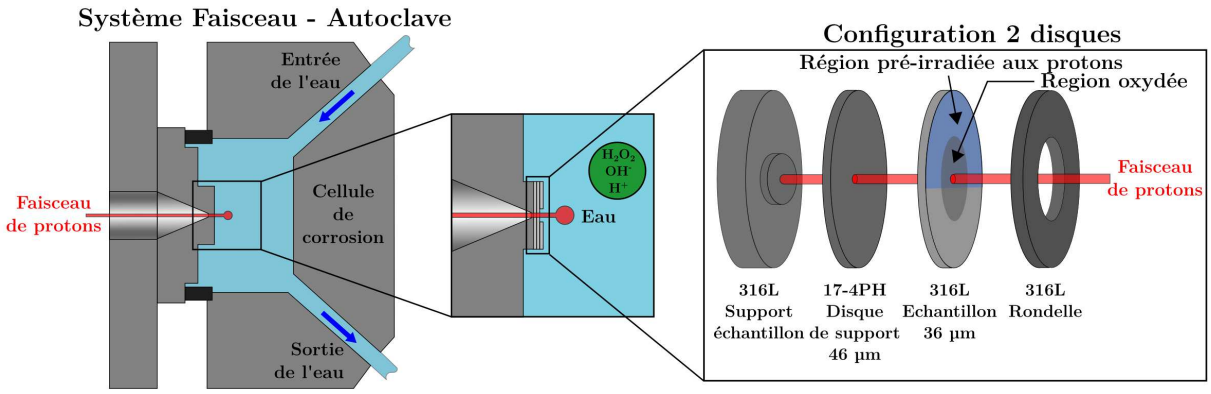

Figure 5: *Schéma du montage faisceau - autoclave et du montage de l'échantillon en configuration deux disques pour l'oxydation sous flux de proton*

En dernier lieu, une vis extraite de centrale a été étudiée. Cette vis a fissuré en service et permet donc d'étudier l'IASCC. Cette dernière a été extraite après environ 29 ans de service et est en acier austénitique inoxydable 316L écroui (Table 2). D'après les simulations numériques réalisées, à la tête/fût jonction la dose reçue a été estimée à 7 dpa et la température à 325 °C. Des lames FIB ont été extraites en pointe de fissure au laboratoire chaud de Chinon (LIDEC - EDF). Par la suite ces dernières ont été amincies et nettoyées en utilisant des ions argon jusqu'à l'épaisseur désirée.

Table 2: *Composition chimique de la vis extraite de centrale en alliage 316L comparé aux spécifications RCC-M (% massique) [2, 3]*

Element (% wt.)	C	Cr	Ni	Mo	Mn	Si	S	P	Cu	Co	Fe
Decommissioned bolt	0,042 ± 0,003	16,20 ± 0,8	12,90 ± 0,6	2,721 ± 0,092	1,82 ± 0,09	0,76 ± 0,06	0,038 ± 0,013	0,012 ± 0,003	0,061 ± 0,003	0,078 ± 0,004	Bal.
RCC-M specifications	≤ 0,03	16-19	10-14	2,25-2,75	≤ 2	≤ 1	≤ 0,015	≤ 0,02	≤ 1	≤ 0,20	Bal.

➤ Représentativité de l'irradiation protonique

Afin de confirmer la représentativité des irradiations protoniques, des analyses poussées au MET ont été réalisées sur les modifications induites par l'irradiation. Puisque des défauts (cavités et boucles de Frank) ont été observés en extrême surface, la préparation des échantillons réalisée a été validée. Sur tous les échantillons, des boucles de Frank et cavités ont été observées. La taille des boucles de Frank varie de 1 à 90 nm et leur densité varie entre ~ 2 et 16×10^{22} boucle/m^3. La taille des cavités varie de 1 à 20 nm et leur densité de 0,3 à 31×10^{21} cavité/m^3. Ces cavités sont facettées (facettes situées dans les plans {111} et {020}). De plus, sur la vis extraite de centrale et l'échantillon irradié aux protons à 1,5 dpa, des zones dénudées en cavités ont été observées aux joints de grains. Pour la première fois, la ségrégation sur les défauts d'irradiation a été analysée par MET et corrélée à la nature des défauts. Les cartographies chimiques réalisées ont révélé un enrichissement en Ni et Si ainsi qu'un appauvrissement en Fe, Cr et Mn autour des cavités et des boucles de Frank. Ces sites peuvent servir de précurseurs à la formation de phases γ' ou G. Cependant, toutes les boucles de Frank n'ont pas été trouvées ségrégées. De la ségrégation induite par l'irradiation a aussi été observée aux joints de grains. Ces derniers sont enrichis en Ni et en Si et déplétés en Cr, Fe et Mn. Des enrichissements et appauvrissements en phosphore et en molybdène respectivement ont été observés sur certains échantillons. L'enrichissement en nickel atteint jusqu'à ~ 30 % atomique et le maximum l'appauvrissement en chrome a été mesuré à environ 6 % atomique. La Figure 6 présente un résumé succinct des modifications induites par l'irradiation sur l'échantillon irradié aux protons à 1,5 dpa. En conclusion, l'irradiation des protons est un outil efficace pour simuler la microstructure et la ségrégation induite par l'irradiation aux neutrons.

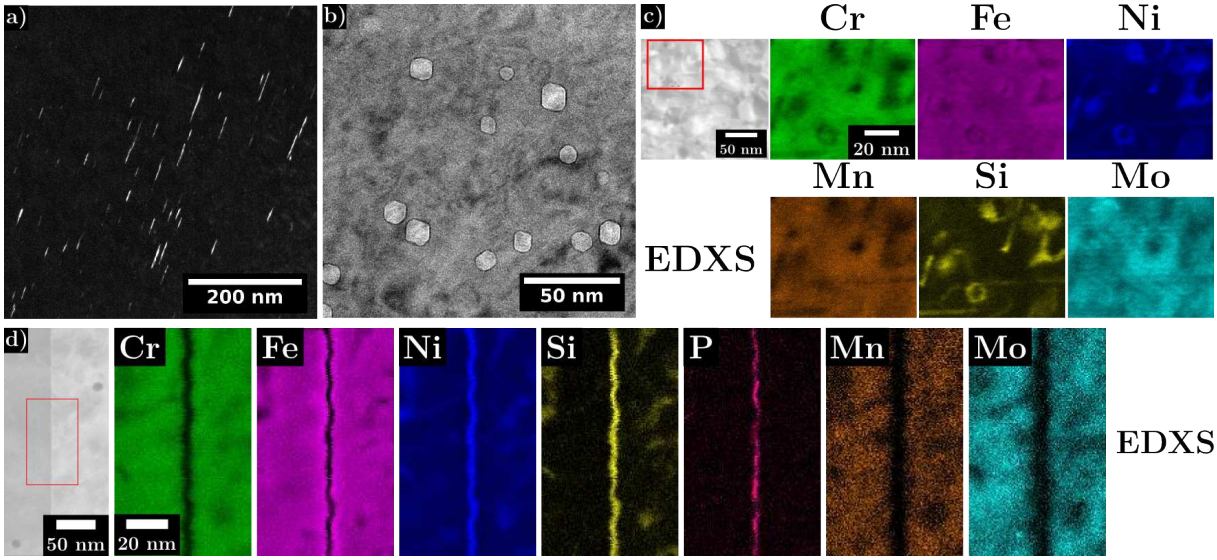

Figure 6: *Résultats MET sur l'échantillon irradié aux protons à 1,5 dpa a) boucles de Frank b) cavités c) ségrégation induite par l'irradiation sur les défauts d'irradiation et d) ségrégation induite par l'irradiation au joint de grains*

➤ Caractéristiques des oxydes formés en milieu REP

Les oxydes formés en milieu REP simulé ont été caractérisés sur des échantillons d'alliage 316L exposés au milieu entre 5 minutes et 96 heures. Les images de MEB ont mises en évidence qu'un oxyde externe est formé même après 5 minutes d'oxydation (Figure 7). Avant 24 heures d'oxydation, les cristallites sont globulaires. De plus le taux de couverture de l'oxyde est plus important après 1 heure d'oxydation et les cristallites sont plus grosses, mais moins nombreuses. Puisque moins de cristallites sont observées après 1 heure d'oxydation qu'après 5 minutes cela signifie que certaines cristallites se sont dissoutes dans le milieu. La dissolution des cristallites engendre certainement une saturation de la couche limite et les espèces en solution re-précipitent en participant à la croissance des cristallites adjacentes. Après 24 heures d'oxydation, des cristallites facettées sont visibles et se mélangent à des germes globulaires plus petits. Après 24 heures et 72 heures d'oxydation, le taux de couverture, la taille et le nombre de cristallites formées augmentent. Ainsi, la croissance des cristallites facettées est donc privilégiée par rapport à celle des cristallites globulaires. Les vues transversales des oxydes en MET ont révélées des oxydes duplex comme attendus avec des cristallites éparses formées sur un oxyde interne dense et sans porosités assez grosses pour être imagées. La spectroscopie Raman a confirmé que deux espèces sont présentes et donc le caractère duplex de l'oxyde même après 5 minutes d'oxydation. Après 1 heure d'oxydation, l'oxyde interne a une épaisseur inférieure à 5 nm tandis qu'après 24 heures d'oxydation il possède une épaisseur de 10 ± 2 nm.

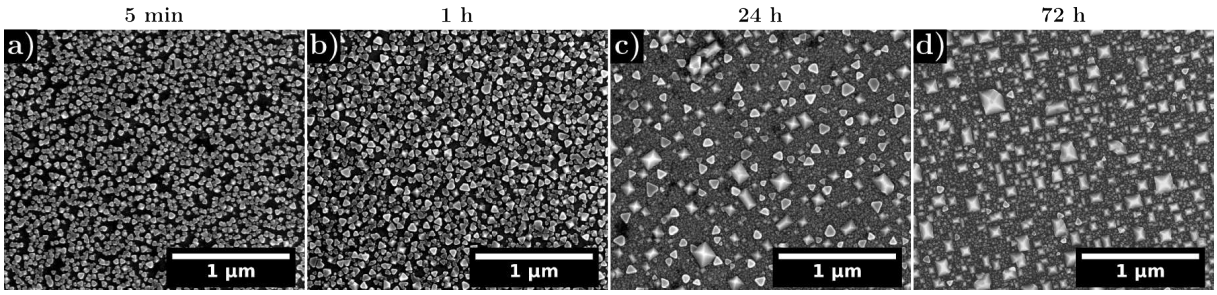

Figure 7: *Images MEB de l'oxyde externe formé sur l'orientation [100] sur un échantillon de référence oxydé a) 5 minutes, b) 1 heure, c) 24 heures and d) 96 heures*

La structure des oxydes a été étudiée de l'échelle macroscopique par MEB, diffraction des

rayons X par incidence rasante et spectroscopie Raman jusqu'à l'échelle nanométrique grâce à la diffraction électronique par sélection d'aire et à l'imagerie MET en champ sombre. Néanmoins, il est difficile, en raison de la faible épaisseur des couches d'oxyde, de différencier les deux oxydes. La diffraction par incidence rasante et la spectroscopie Raman ont mis en évidence la présence d'oxydes de type spinelle AB_2O_4 en accord avec la littérature. L'observation d'une morphologie de cristallite privilégiée a suggéré l'existence d'une relation épitaxiale entre certaines cristallites externes, la couche d'oxyde interne et le substrat. Ceci a été confirmé par des observations hautes résolutions au MET (Figure 8). Ces dernières ont révélé que la couche interne est un oxyde de type spinelle partageant une relation d'orientation épitaxiale cube/cube avec le grain de métal sous-jacent. Des contraintes dans l'oxyde interne ont aussi été mises en évidence expliquant pourquoi certaines zones ne sont pas correctement orientées avec la matrice. En ce qui concerne les cristallites externes, certaines d'entre elles partagent une orientation épitaxiale de type maclage avec la couche interne, tandis que quelques-unes sont en épitaxie cube/cube. La mise en place de telles relations d'épitaxie est responsable de l'observation d'une morphologie de cristallite préférentielle.

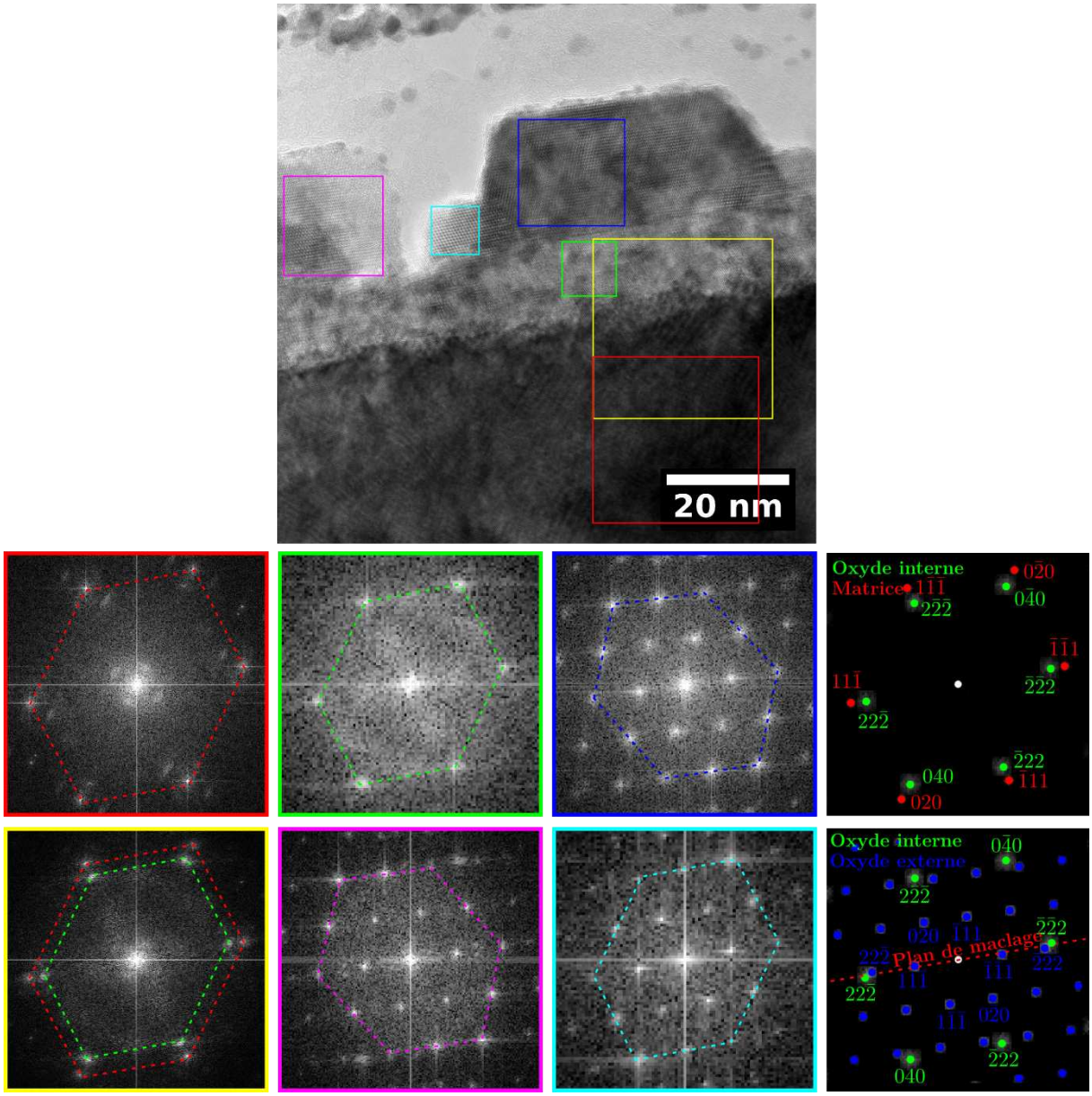

Figure 8: *Image MET haute résolution à l'interface métal/oxyde en axe de zone [101] et FFTs associées correspondant aux régions encadrées*

La chimie des couches d'oxydes a été investiguée en utilisant la spectroscopie Raman et différentes techniques de caractérisation au MET (analyses EFTEM, EDXS et EELS). Les cartographies EFTEM ont révélé que la couche d'oxyde externe est riche en fer alors que l'oxyde interne est riche en chrome. En combinant ces résultats à la spectroscopie Raman il apparaît que les cristallites externes sont proches de la magnétite et l'oxyde interne de la chromite. La composition des couches d'oxydes externe et interne a été étudiée via des analyses chimiques quantitatives au MET (EDXS et EELS). La couche externe peut être écrite comme $(Ni,Cr,Ti)_{3-x}Fe_xO_4$ avec $3 \geq x \geq 2{,}5$ alors que l'oxyde interne peut être écrite comme $(Ni_xFe_{1-x})(Cr_yFe_{1-y})_2O_4$ avec $0{,}6 \geq x \geq 0{,}4$ et $0{,}8 \geq y \geq 0{,}65$. Étant donné que les vitesses de diffusion des ions métalliques dans les oxydes sont classées dans l'ordre suivant: $Fe^{2+} > Ni^{2+} > Cr^{3+}$, les espèces diffusant le plus rapidement tel que le fer diffuseront principalement pour former la couche externe, tandis que ceux qui diffusent plus lentement comme chrome resteront dans la couche interne. Les analyses d'EELS ont montré que la couche interne s'enrichit progressivement en chrome au fur et à mesure de l'oxydation. Du titane a principalement été trouvé incorporé dans l'oxyde externe en faible concentration. Le titane de la boucle d'oxydation est supposé être dissous dans le milieu

et re-précipité dans l'oxyde externe. Les cartographies EFTEM ont mis en évidence la présence de nickel au niveau de l'interface métal/oxyde et la présence de cette région riche en nickel a été corroborée par les analyses EELS et EDXS. Aucune déplétion en nickel n'a été détectée dans le substrat sous-jacent suggérant que le nickel a été rejeté de l'oxyde vers le métal au cours de sa formation et de sa croissance. Cette zone aura probablement un paramètre de maille légèrement différent de celui du substrat et pourrait générer une contrainte à l'interface métal/oxyde. Il est plausible que le nickel proche du milieu soit dissous dans ce dernier puis re-précipite dans l'oxyde externe, tandis que celui proche de l'interface métal/oxyde s'accumule à cette interface et qu'une petite partie soit encore contenue dans l'oxyde interne.

L'étude des couches d'oxydes a aussi révélé qu'il ne s'agissait pas d'oxydes de type spinelle «purs», mais plutôt d'oxydes mixtes de structure spinelle non stœchiométriques, soumis à des contraintes. La couche d'oxyde interne contient un nombre important de défauts ioniques et leur présence offre des voies pour le transport des espèces ioniques à travers l'oxyde engendrant la dissolution du métal et son oxydation. La croissance de l'oxyde étant dépendante de la quantité de défauts dans ce dernier, plus l'oxyde contient de défauts et plus leur mobilité est importante, plus l'alliage sous-jacent est sensible à la corrosion. Ainsi, la présence de contraintes et de défauts dans la couche d'oxyde interne induira vraisemblablement une diminution de son pouvoir protecteur. De plus, la diffusion à travers cette couche d'oxyde interne limite la croissance de l'oxyde externe et le relâchement car la croissance des cristallites dépend de la diffusion cationique à travers la couche interne. Cette diffusion sera affectée par la quantité de contraintes et de défauts présents dans la couche et, par conséquent, par le caractère plus ou moins protecteur/barrière de la couche d'oxyde interne. L'ampleur de la précipitation étant régie par les solubilités du Fe et du Ni dans l'eau à haute température, il est probable que la précipitation soit proche de l'équilibre local, permettant la croissance des grosses cristallites observées. Le mécanisme d'oxydation d'un alliage 316L exposé en milieu primaire est présenté en Figure 9.

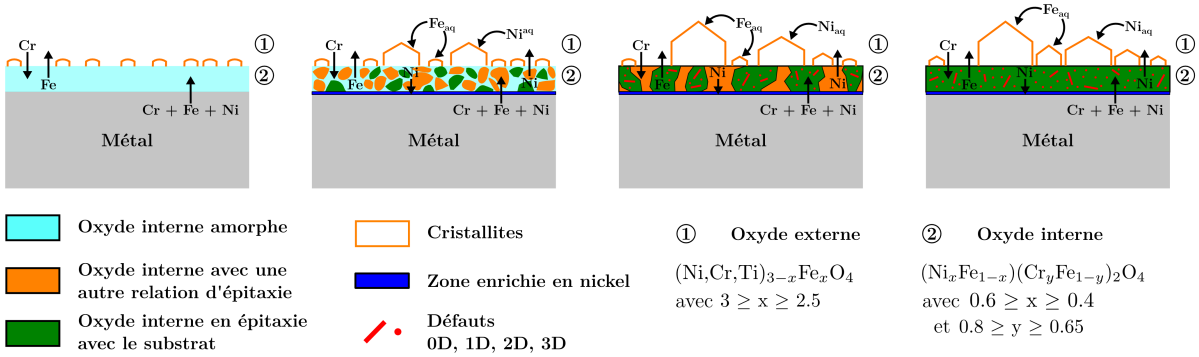

Figure 9: *Schéma du mécanisme d'oxydation d'un alliage 316L exposé en milieu primaire*

L'extraction de lames FIB au niveau de joints de grains a permis d'étudier l'oxydation intergranulaire. Ces sites d'oxydation sont particulièrement intéressants dans la mesure où la corrosion sous contrainte est susceptible de se produire au niveau des joints de grains. Par conséquent, l'oxydation aux joints de grains a été examinée et les oxydes intergranulaires formés ont été comparés à ceux formés à la surface des échantillons. Certains joints de grains semblaient préférentiellement oxydés et de grosses cristallites externes ont été observées au-dessus de ces derniers. Il est probable que les joints de grains, agissants comme des courts-circuits de diffusion, accélèrent la diffusion à la surface, favorisant ainsi la formation de cristallites externes au-dessus des joints de grains. Des images MET ont montrés que les pénétrations d'oxydes intergranulaires sont asymétriques et facettées sans porosités (Figure 10). L'oxydation aux joints de grains se déroule probablement en deux étapes. Tout d'abord, un oxyde superficiel protecteur se forme à la surface du joint de grains. Ensuite, le joint de grains faisant office de court-circuit

de diffusion sera oxydé préférentiellement le long du joint et dans le métal selon des directions préférentielles. Des profils EDXS et EELS ont montré qu'en dessous de cet oxyde intergranulaire, le joint de grain est légèrement enrichi en chrome et appauvri en fer. Une zone riche en nickel a été détectée sous le joint de grains oxydés et la concentration en nickel mesurée dans cette zone atteignait $\sim$ 40 % atomique (Figure 10). Au-dessus de cette région, la zone légèrement oxydée à la pointe de la pénétration d'oxyde s'est révélée être enrichie en nickel et résulte de l'oxydation de la zone riche en nickel. Un enrichissement en nickel a également été observé à l'interface métal/oxyde, comme précédemment observé sur les oxydes de surface. L'oxyde formé dans la pénétration est riche en chrome et le rapport $\frac{Cr}{Cr+Fe+Ni}$ est supérieur à 0,65. Cet oxyde peut être écrit comme de structure corindon avec $Cr_x(Fe,Ni)_{2-x}O_3$ et $2 \geq x \geq 1{,}3$. En comparant cet oxyde à celui formé à la surface, la présence d'un oxyde plus riche en chrome, mais appauvri en fer a été mise en évidence. Le mécanisme d'oxydation d'un alliage 316L exposé en milieu primaire au niveau du joint de grains est présenté en Figure 11.

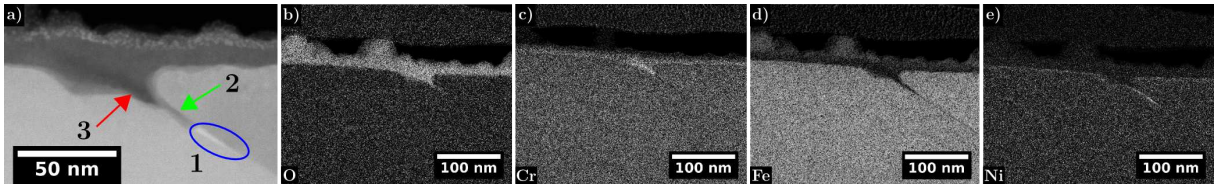

Figure 10: *Pénétration intergranulaire sur l'échantillon de référence oxydé 24 heures a) image STEM et cartographie EFTEM b) oxygène c) chrome d) fer et e) nickel*

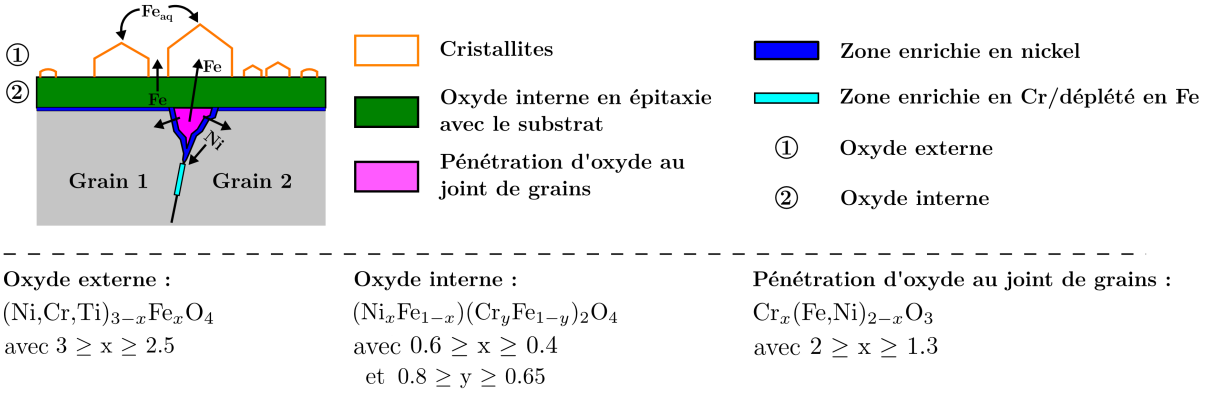

Figure 11: *Schéma du mécanisme d'oxydation d'un alliage 316L exposé en milieu primaire au joint de grains*

Ainsi, les couches d'oxydes formées sur l'alliage 316L oxydé en milieu primaire simulées dans cette étude sont en accord avec les données de la littérature.

➤ Influence de l'orientation cristallographique de grain de métal sous-jacent sur la cinétique d'oxydation

L'orientation cristallographique du métal de base affectant l'oxydation, son effet a été investigué. Aucun effet de l'orientation cristallographique n'a été observé avant 24 heures d'oxydation. Cependant, après 24 heures d'oxydation, les images de microscopie optique ont révélé que certains grains sont plus oxydés que d'autres. Notamment les grains d'orientation [100] semblent plus oxydés que les grains [111]. De plus, des morphologies de cristallites préférentielles sont observées et dépendent de l'orientation cristallographique du grain de métal sous-jacent comme visible en Figure 3.30. Cela suggère l'existence d'une relation d'épitaxie entre la couche d'oxyde et le substrat sur toutes les orientations étudiées comme mise en évidence précédemment. En

outre, le nombre de cristallites présent à la surface de chaque grain dépend de l'orientation cristallographique du métal de base et davantage de sites de nucléation sont disponibles sur les grains [111]. L'analyse « LayerProbe » a révélé que l'épaisseur totale de l'oxyde dépendait de l'orientation cristallographique. Une analyse MET supplémentaire a mis en évidence et confirmé que les oxydes internes sont plus épais au-dessus des grains d'orientation [100] que des grains d'orientation [111]. Cette dernière a aussi confirmé que la même relation d'orientation cube/cube est établie entre l'oxyde interne et le substrat après 24 heures d'oxydation. Comme précédemment observé l'oxyde interne est fortement déformé et contraint, et donc partiellement localement désorienté. Les spectres Raman acquis sur les différentes orientations à l'étude ont mis en évidence de légères différences entre les trois orientations étudiées. Celles-ci sont supposées être liées aux épaisseurs d'oxydes internes. Les analyses EDXS et EELS ont révélé que les oxydes externes ont une composition proche qui ne semble pas dépendre de l'orientation cristallographique du grain de métal sous-jacent. Cependant, l'oxyde interne est plus riche en chrome sur l'oxydation [111] que sur l'orientation [100].

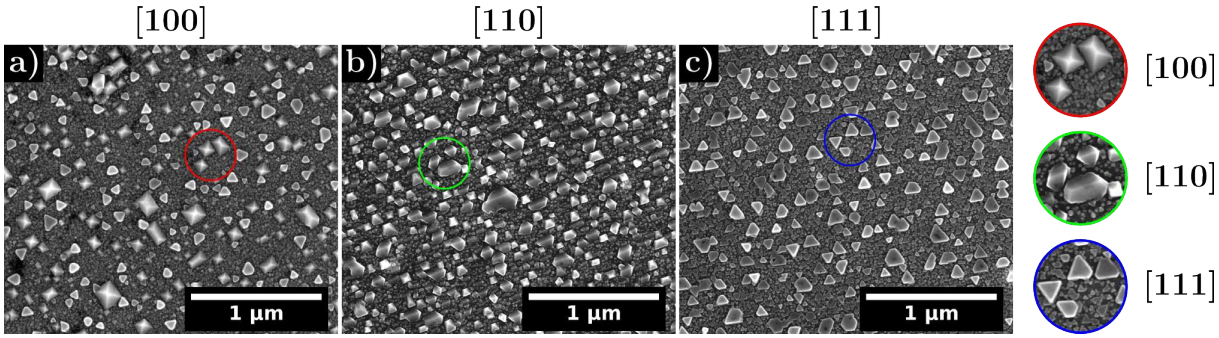

Figure 12: *Images MEB de l'oxyde externe formé sur un échantillon de référence oxydé 24 heures a) sur l'orientation [100], b) sur l'orientation [110] et c) sur l'orientation [111]*

L'établissement d'une telle relation épitaxiale est rendu possible grâce à une déformation élastique résiduelle du métal accommodant le désaccord paramétrique entre les deux réseaux. Le nombre de dislocations nécessaires pour accommoder le métal et oxyde interne diffère en fonction de l'orientation cristallographique des grains, modifiant l'énergie à apporter pour former la relation épitaxiale. Les grains [111] nécessitent moins de dislocations que les autres orientations pour accommoder le désaccord paramétrique et donc moins d'énergie pour être accommodés. Ces derniers possèdent ainsi la contrainte élastique résiduelle la plus faible des trois orientations étudiées. Étant donné que la croissance de l'oxyde dépend des réactions à l'interface métal/oxyde, il est probable que la vitesse d'oxydation soit influencée par la cohérence, les contraintes résiduelles ainsi que la vitesse d'établissement de la relation épitaxiale à l'interface métal/oxyde. Selon toute vraisemblance, les oxydes internes formés par croissance épitaxiale auront différents niveaux de contrainte de croissance en fonction de leur relation d'orientation avec le substrat et donc de l'orientation sous-jacente du grain de métal. En outre, la formation d'oxydes non stœchiométriques de paramètres de maille légèrement différents facilitera l'accommodation des contraintes internes. Cet écart de stœchiométrie sera compensé par un nombre plus élevé de défauts ponctuels au sein de la couche d'oxyde afin de préserver sa neutralité électrique. Par conséquent, plus la déformation de l'oxyde et de la stœchiométrie est élevée, plus la croissance de l'oxyde interne est rapide, car de nombreux défauts seront présents. Il est probable qu'une fois l'épitaxie établie, la diffusion à travers la couche interne sera ralentie par la formation d'une interface plus cohérente. Le réseau de dislocations relaxera la contrainte à l'interface, mais le nombre de dislocations nécessaires pour adapter l'interface, l'énergie nécessaire et la déformation résultante affecteront la cinétique d'oxydation globale.

Selon toute vraisemblance, à un temps d'oxydation court donné, un volume d'oxyde plus

important sera correctement établi et épitaxié sur l'orientation [111], car l'établissement de la relation épitaxiale est considéré comme la moins énergivore des trois orientations étudiées. Ainsi, la relation épitaxiale sera établie plus rapidement et induira moins de contraintes et de défauts sur cette orientation. Ceci explique l'observation d'un nombre plus élevé de cristallites facettées de morphologie privilégiée sur cette dernière, car davantage de régions ont servi de sites de germination préférentiels pour la croissance des cristallites. L'observation d'oxydes plus épais sur l'orientation [100] indique que la diffusion de l'oxygène est plus rapide sur cette orientation que sur l'orientation [111]. L'établissement de la relation épitaxiale étant plus difficile sur les grains [100] et consommant plus d'énergie, la couche interne développée par croissance épitaxiale sera plus contrainte et davantage de défauts seront présents en son sein expliquant sa croissance plus rapide. Comme la diffusion à travers la couche interne est plus lente pour les oxydes riches en chrome, cela contribuerait ainsi à la formation d'oxydes plus minces sur les grains [111]. Le mécanisme d'oxydation dépendant de l'orientation cristallographique du grain de métal sous-jacent est décrit en Figure 13.

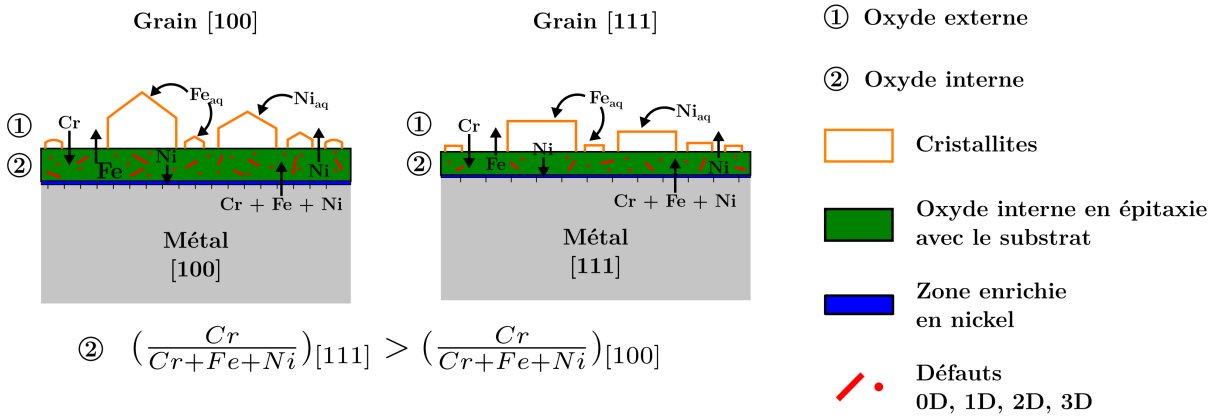

Figure 13: *Schéma du mécanisme d'oxydation d'un alliage 316L exposé en milieu primaire en fonction de l'orientation cristallographique du grain de métal sous-jacent*

➤ Effet de l'écrouissage induit par le polissage

L'étude d'échantillons ayant subi différents polissages avant oxydation a révélé que la réalisation d'un polissage mal contrôlé affecte la morphologie et l'épaisseur des oxydes. Les images optiques des échantillons polis avec le polissage de référence, la pâte diamantée 6 µm et le papier SiC P4000 indiquent que ce dernier est le plus oxydé des trois. Cet échantillon possède la zone impactée par le polissage la plus profonde (1,2 ± 0,2 µm) et certainement la plus écrouie. Ceci suggère que l'écrouissage accélère la cinétique d'oxydation. Après 24 et 72 heures d'oxydation, les échantillons polis avec le polissage de référence et la pâte diamantée 6 µm possèdent tous deux, sur les orientations étudiées, les morphologies de cristallites attendues révélant qu'une relation d'épitaxie est établie entre le métal et les couches d'oxyde. Ainsi, l'écrouissage induit par un polissage à la pâte diamantée 6 µm (0,4 ± 0,1 µm) n'est pas suffisant pour empêcher l'établissement de la relation d'épitaxie entre les couches d'oxyde et le grain de métal sous-jacent. Sur l'échantillon poli au papier SiC P4000 après 24 heures d'oxydation les cristallites sont globulaires tandis qu'après 72 heures d'oxydation plusieurs cristallites ayant différentes morphologies préférentielles sont présentes sur un unique grain. L'écrouissage (1,2 ± 0,2 µm) engendré par le polissage au papier SiC P4000 a vraisemblablement empêché ou retardé cette épitaxie. Il est probable que des cellules de dislocations soient formées et responsables de cette perte d'épitaxie locale dans l'oxyde interne engendrant l'établissement d'une autre relation d'épitaxie et la formation de cristallites de morphologies différentes sur un même grain. Cependant, si l'écrouissage induit par le polissage est trop important, il est probable qu'aucune relation épitaxiale ne sera établie, même à des temps d'oxydation plus longs, ce qui modifierait la cinétique d'oxydation

globale. Ceci sera vraisemblablement le cas pour les oxydes formés à la surface des composants de centrale qui sont brut de fabrication et écrouis. Néanmoins, une relation épitaxiale pourrait se former en fond de fissures d'IASCC sur les aciers inoxydables car il a été montré que le réseau de dislocations se restaure sous irradiation.

Un plus grand nombre de cristallites sont présentes sur l'échantillon poli à la pâte diamantée 6 µm que sur l'échantillon poli avec le polissage de référence et ces dernières sont plus grosses. Un polissage grossier induit des défauts dans le métal et ces derniers agissent probablement comme des sites de nucléation préférentiels pour les cristallites externes. L'observation de cristallites de taille plus importante indique que la diffusion dans la couche interne est plus rapide pour l'échantillon plus écroui. La présence de défauts induits par le polissage pourrait engendrer la formation d'oxydes internes encore plus contraints dans lesquels la diffusion serait accélérée. En effet de nombreux défauts seraient présent en leur sein et les défauts présents dans la couche déformée pourraient, eux aussi, agir comme court-circuit de diffusion. Ainsi l'écrouissage induit par le polissage favorise la nucléation et la croissance des cristallites externes. Les images MEB ont révélé que les rayures dues au polissage sont préférentiellement oxydées et que de plus grosses cristallites sont formées dans les rayures. Les phénomènes de dissolution/re-précipitation sont accentués dans les rayures en raison de la plus grande surface exposée localement au milieu. Ainsi, la croissance des cristallites est favorisée dans les rayures de polissage et les défauts induits par le polissage accélèrent la cinétique de croissance de l'oxyde. Le mécanisme d'oxydation en fonction du polissage réalisé est présenté en Figure 14.

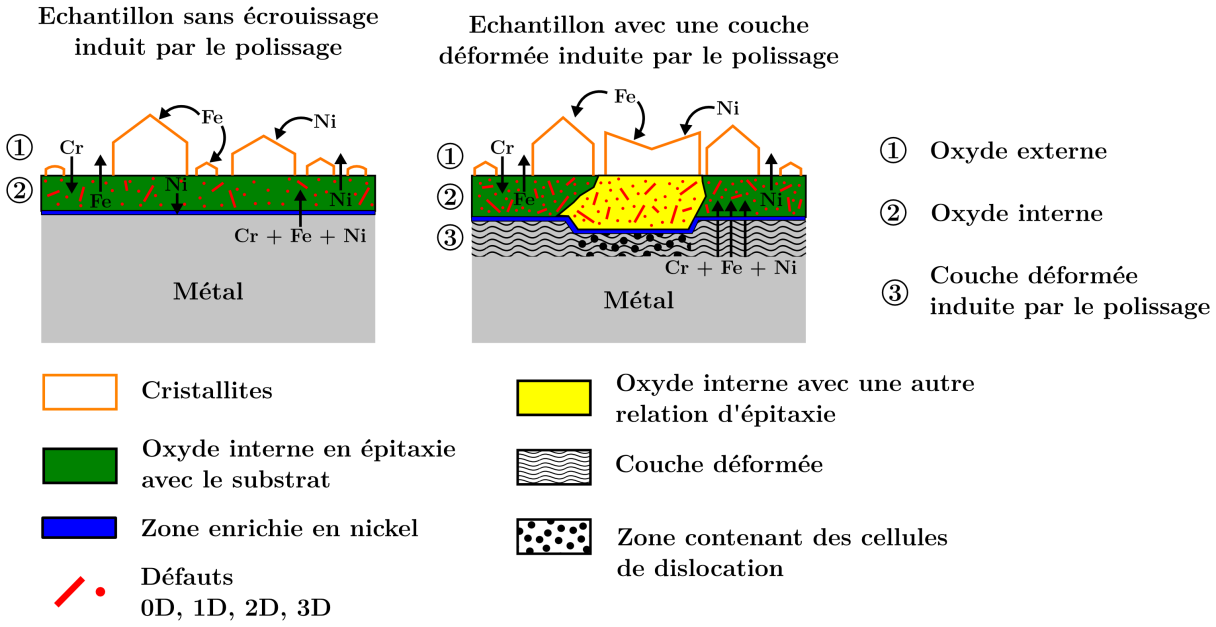

Figure 14: *Schéma du mécanisme d'oxydation d'un alliage 316L exposé en milieu primaire en fonction du polissage réalisé*

En conclusion, si le polissage de l'échantillon n'est pas bien contrôlé, cela affectera grandement la cinétique d'oxydation, en particulier pour des temps d'oxydation courts. De nombreux tests d'oxydation en laboratoire visent à mieux comprendre l'oxydation et la préparation des échantillons doit donc faire l'objet de prudence afin d'obtenir un polissage reproductible et représentatif.

➤ Effet de la présence d'inclusion sur l'oxydation

Les alliages de 316L industriels contenant des inclusions, l'oxydation proche de ces dernières a été étudiée pour obtenir des informations sur leur effet sur l'oxydation. Les images optiques

réalisées ont révélé que les précipités sont préférentiellement oxydés et que ces derniers accélèrent l'oxydation à leur périphérie. Les images MEB ont permis de voir que les inclusions de sulfure de manganèse sont dissoutes lors des premières étapes d'oxydation. Une oxydation préférentielle se produit autour des inclusions engendrant la formation de cristallites de plus grosse taille (Figure 15). Les cristallites autour des inclusions possèdent la morphologie préférentielle attendue indiquant que la relation d'épitaxie établie n'est pas modifiée par la présence de précipitée. Les images MEB en électrons rétrodiffusés, les analyses « Layerprobe » et la coupe FIB réalisée ont permis d'observer que l'oxyde interne est plus épais autour des inclusions (Figure 15). Les analyses Raman ont révélé que, proche des inclusions, la chimie des oxydes est modifiée. Les inclusions de MnS étant dissoutes, il est probable que des anions contenant du soufre et des cations de manganèse soient libérés dans le milieu. Le soufre relâché induira probablement des modifications locales de la chimie de l'eau et donc de l'oxydation. Les anions riches en soufre pourraient diminuer localement le pH de la couche limite, tandis que les ions manganèse pourraient saturer la couche limite et précipiter dans les oxydes expliquant les modifications chimiques des oxydes proches des inclusions. Le soufre pourrait également être incorporé dans l'oxyde ou à l'interface métal/oxyde. La couche limite proche des précipités, ayant un pH inférieur, est responsable de la formation d'oxydes plus épais. Près des inclusions les joints de grains sont aussi préférentiellement oxydés. En conclusion, la présence de précipités a favorisé la croissance des oxydes externes et internes (Figure 16).

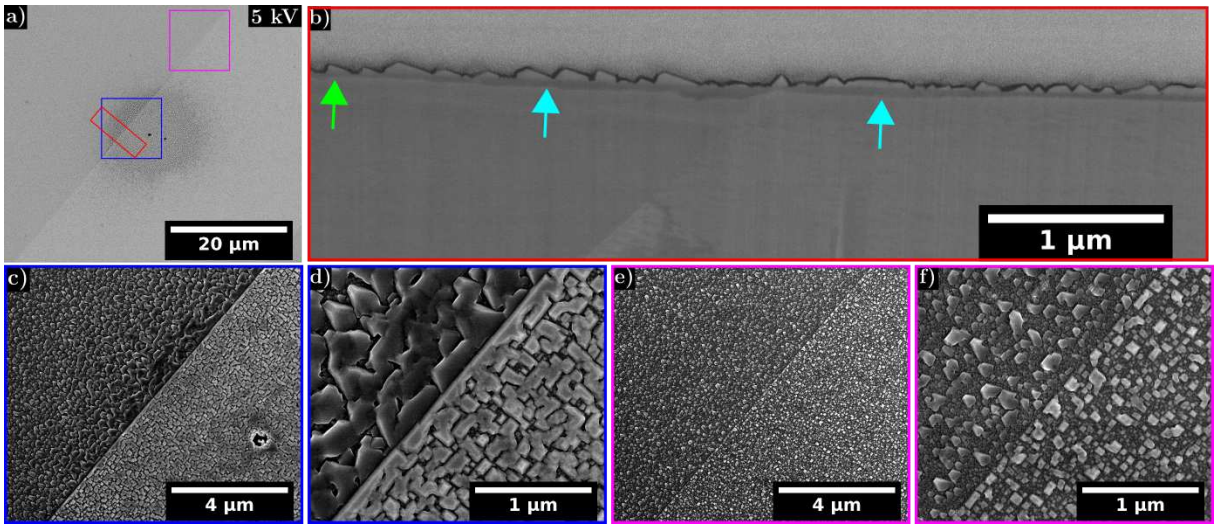

Figure 15: *Images MEB sur un échantillon de référence oxydé 24 heures proche d'une inclusion et loin de cette dernière a) région sur laquelle a été faite la coupe FIB et les images MEB, b) oxyde en vue transverse (flèche verte oxyde interne fin loin de l'inclusion, flèche bleu cyan oxyde interne plus épais proche de l'inclusion) c) et d) oxyde externe proche de l'inclusion et e) et f) oxyde externe loin de l'inclusion*

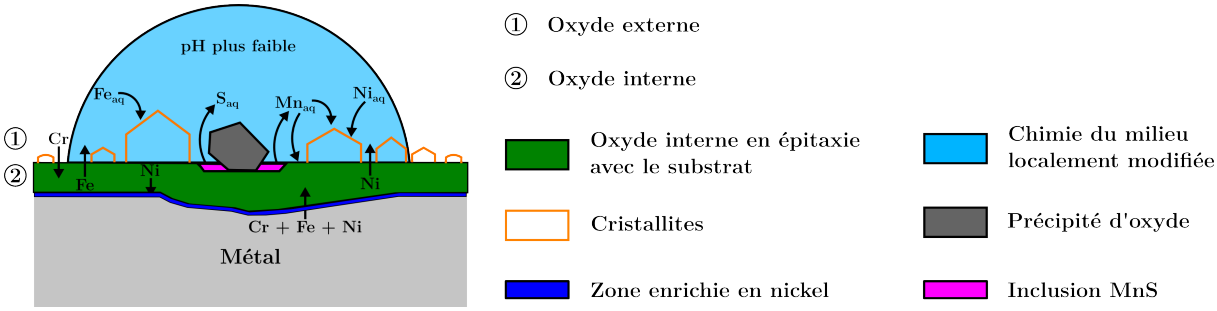

Figure 16: *Schéma du mécanisme d'oxydation d'un alliage 316L exposé en milieu primaire proche des inclusions*

➤ Influence de la chimie du milieu et de la boucle de corrosion utilisée

Certaines oxydations de 24 heures ont été réalisées dans une boucle d'oxydation en titane dans un milieu à un pH de 7,3 (contenant du bore et du lithium) alors qu'une autre a été effectuée dans une boucle en acier inoxydable sans bore ni lithium et donc à un pH de 6,2. Ainsi, il a été possible de comparer les oxydes formés et de conclure sur l'influence de la chimie du milieu et de la boucle de corrosion utilisée. En comparant les images MEB acquises sur les deux échantillons il apparaît clairement que l'oxyde externe formé dans la boucle en acier inoxydable est jusqu'à 20 fois plus gros (Figure 17). Le milieu est probablement saturé en cations métalliques dans la boucle en acier inoxydable ce qui engendre une forte re-déposition et croissance des oxydes externes. Les oxydes internes sont eux aussi beaucoup plus épais sur l'échantillon oxydé dans la boucle en acier inoxydable (jusqu'à 425 nm contre $\sim$ 10 nm sur l'échantillon oxydé dans la boucle en titane comme visible en Figure 17). Ces oxydes sont poreux alors que des oxydes internes denses ont été observés sur l'échantillon oxydé dans la boucle en titane. Ces porosités sont susceptibles d'agir comme court-circuit de diffusion, car ces porosités fournissent des interconnexions entre le métal et le milieu. Il est probable que le pH de ce milieu (6,2) soit responsable de la formation de ces porosités et donc cette forte épaisseur d'oxyde interne.

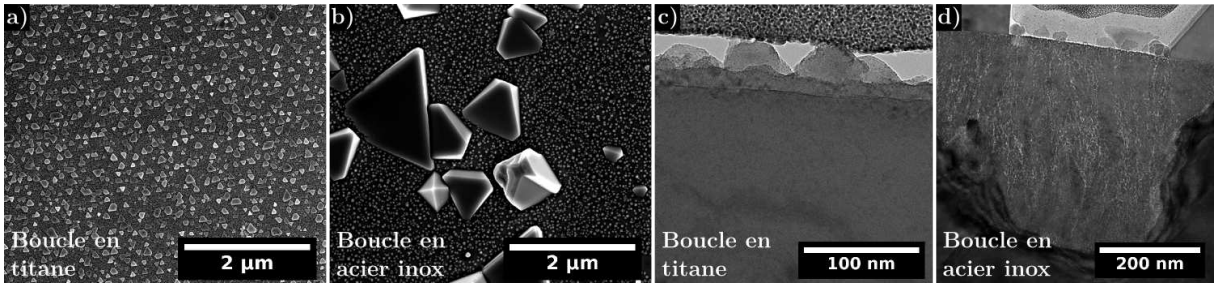

Figure 17: *a) et b) images MEB des oxydes formés respectivement sur les échantillons oxydés dans la boucle en titane et la boucle en acier inoxydable et c) et d) images MET des oxydes formés respectivement sur les échantillons oxydés dans la boucle en titane et la boucle en acier inoxydable*

➤ Effet de l'irradiation sur la cinétique d'oxydation et les mécanismes d'oxydation

Les échantillons ont été analysés dans les zones non irradiées et celles pré-irradiées aux protons pour mieux comprendre l'effet de l'irradiation sur l'oxydation. De nombreuses similitudes ont été observées entre les oxydes formés sur matériaux irradiés et non irradiés. Le caractère duplex de l'oxyde n'est pas affecté par l'irradiation ni sa structure de type spinelle comme observé au MET et par diffraction des rayons X en incidence rasante. Les mêmes morphologies préférentielles de cristallites ont été observées en zone irradiée et non irradiée. Cela suggère que la même relation d'épitaxie cube/cube est établie entre le substrat et les couches d'oxyde. Ceci a été confirmé au MET. L'orientation cristallographique contrôle toujours la cinétique d'oxydation. Néanmoins plus de cristallites possèdent la morphologie préférentielle attendue sur le matériau irradié relevant qu'une plus grande partie de l'oxyde interne est proprement épitaxiée à un temps d'oxydation donné. Cependant des différences ont été observées en termes de taille, de densité et de nombre de cristallites externes ainsi que concernant les épaisseurs d'oxyde interne. Un taux de couverture et un nombre de cristallites supérieur ont été observés indépendamment de la durée d'oxydation sur les échantillons irradiés, indiquant que la nucléation est favorisée sur ces échantillons. Les défauts d'irradiation jouent le rôle de sites de nucléation préférentiels induisant ce nombre plus élevé de cristallites au cours des premières étapes d'oxydation. Comme visible en Figure 18 des oxydes plus épais ont été observés sur les échantillons irradiés et leur épaisseur augmente avec l'augmentation de la dose d'irradiation ($\sim$ 10 nm vs 53 nm en zone non irradiée et irradiée à 1,5 dpa respectivement). L'irradiation accélère la croissance des oxydes. Les oxydes internes sont poreux dans ces zones, agissant comme court-circuit de diffusion et favorisant la

croissance des oxydes.

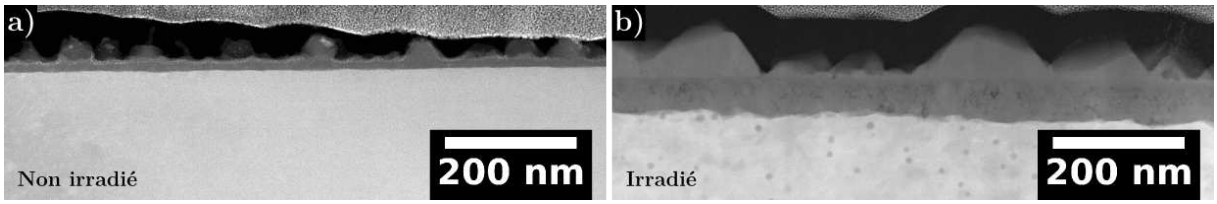

Figure 18: *Images STEM HAADF des oxydes formés après 24 heures d'oxydation sur un grain d'orientation [100] a) sur une zone non irradiée et b) sur une zone pré-irradiée à 1,5 dpa*

La chimie des oxydes est légèrement modifiée par l'irradiation. En effet, les analyses EDXS et EELS ont révélé que l'oxyde interne est légèrement enrichi en chrome. Ainsi les ratios $\frac{Cr}{Cr+Fe+Ni+Ti}$ dans l'oxyde interne sont de 0,50 et 0,56 respectivement pour la zone non irradiée et pré-irradiée à 1,5 dpa. Les analyses Raman réalisées dans la zone irradiée et dans la zone non-irradiée ont révélé que l'irradiation affectait l'oxydation et induisant un décalage des bandes vers les hauts nombres d'ondes. La formation d'oxydes internes plus épais et plus riches en chrome sur les régions irradiés est responsable de ces shifts observés. Une petite région duplex dans l'oxyde interne a de plus été observée sur l'échantillon irradié à 1,5 dpa. Cet oxyde interne duplex se compose d'une partie externe riche en chrome et d'une partie interne riche en fer dans laquelle le ratio $\frac{Cr}{Fe}$ est inversé. Il est possible que la présence de nombreux défauts ségrégés et donc d'une région localement déplétée en chrome soit responsable de la formation de cet oxyde duplex et déplété en chrome. Les défauts d'irradiation tels que les lacunes induites sont certainement responsables d'une diffusion de cations métalliques accélérée à l'interface métal/oxyde induisant la formation d'un oxyde plus riche en chrome. Même si ces oxydes internes sont plus riche en chrome, ce qui peut ralentir la diffusion au sein de cette couche, la présence de porosité est responsable de la formation d'oxydes internes plus épais. Ainsi, la nucléation et la croissance des oxydes internes et externes sont accélérées par la concentration de défauts d'irradiation à la surface durant les premières étapes d'oxydation.

Des défauts d'irradiation ont également été observés près de l'interface métal/oxyde, mais ces derniers ne sont pas préférentiellement oxydés. Les défauts ségrégés ont été analysés par EELS et EDXS proche du front d'oxydation (Figure 19). Ces analyses ont révélé que le silicium est déplété au front d'oxydation indiquant que le silicium se dissout probablement dans le milieu. Néanmoins ils affectent la cinétique d'oxydation en particulier sur l'orientation [111], car sur cette dernière une famille de boucles de Frank est parallèle à l'interface. L'inclinaison de ces boucles de Frank par rapport à la surface oxydée est supposée affecter la croissance de l'oxyde interne. Plus ces dernières sont parallèles à la surface oxydée, plus elles affectent la cinétique d'oxydation. En outre, lorsque le front d'oxydation atteint les défauts d'irradiation la croissance de l'oxyde progresse dans des directions préférentielles. Il est supposé que l'oxydation est ralentie au niveau de ces défauts et qu'une pénétration d'oxyde intragranulaire se produit autour de ces derniers selon des directions préférentielles. Ce comportement est similaire à celui observé en surface des échantillons en fonction de l'orientation cristallographique ainsi qu'à l'oxydation des joints de grains.

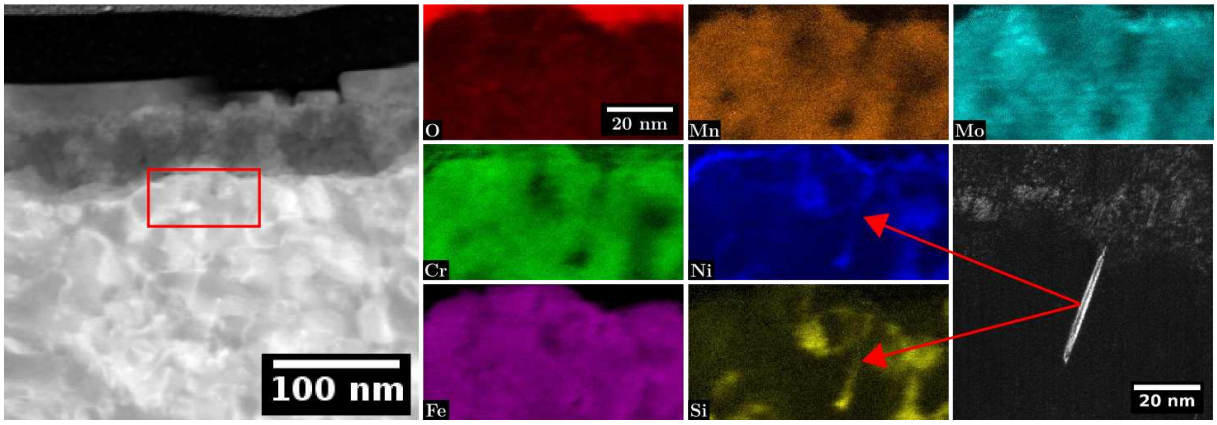

Figure 19: *Image STEM HAADF à l'interface métal/oxyde et cartographies EDXS associées sur l'échantillon irradié à 1,5 dpa et oxydé 24 heures et image en champ sombre d'une boucle à l'interface métal/oxyde*

Le schéma du mécanisme d'oxydation d'un alliage 316L pré-irradié et exposé en milieu primaire est introduit en Figure 20.

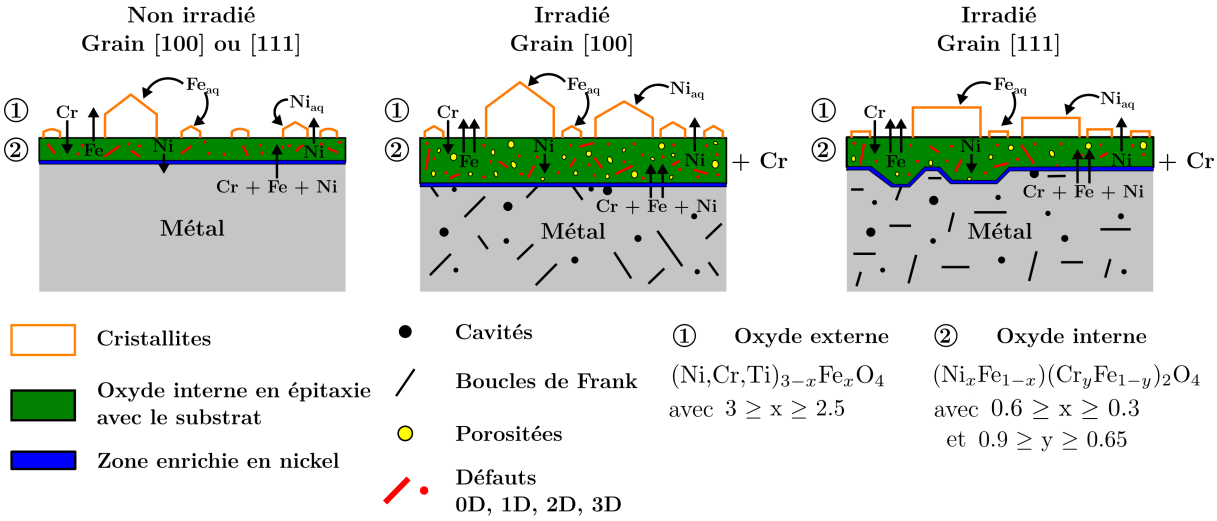

Figure 20: *Schéma du mécanisme d'oxydation d'un alliage 316L pré-irradié et exposé en milieu primaire*

Concernant l'oxydation aux joints de grains, les images MET acquises ont révélé que les pénétrations d'oxydes sont beaucoup plus profondes et larges dans les zones irradiées ($\sim$ 42 nm vs 141 nm après 24 heures d'oxydation dans la zone non irradiée et la zone irradiée à 1,5 dpa). Les joints de grains étant ségrégés et déplétés en chrome, cette déplétion est vraisemblablement responsable de cette oxydation préférentielle. Les oxydes intergranulaires sont poreux en zone irradiée et, comme en zone non irradiée, facettés. La pénétration d'oxyde est bien épitaxiée proche de la surface alors que la zone poreuse sous-jacente est désorientée et sa croissance s'est effectuée selon des directions préférentielles. La composition chimique de l'oxyde intergranulaire sur l'échantillon oxydé 24 heures dans la zone irradiée à 1,5 dpa a été étudiée en réalisant des cartographies EDXS (Figure 21). La pénétration d'oxyde est toujours plus riche en chrome que l'oxyde formé en surface, mais l'oxyde intergranulaire dans la zone irradiée est de structure spinelle et non corindon comme supposé dans la zone irradiée. Puisque le joint de grain est déplété en chrome dans la zone irradiée, la teneur en chrome résultante n'est certainement pas assez importante pour entrainer la formation d'un oxyde de chrome de type Cr_2O_3. Cette analyse EDXS a démontré que le phosphore et silicium ségrégés au joint de grains sous irradiation sont déplétés au front d'oxydation. Il est probable que ces derniers soient dissous dans le milieu. Un tel comportement a déjà été observé sur la boucle à l'interface métal/oxyde. Un enrichissement

en nickel prononcé a aussi été observé au front d'oxydation sur l'échantillon irradié confirmant qu'ici aussi le nickel est repoussé de l'oxyde vers le métal. Un enrichissement en soufre a été observé à l'interface métal/oxyde et confirmé en extrayant et comparant les spectres EDXS dans le métal et à l'interface métal/oxyde. Ce soufre provient probablement d'une inclusion de sulfure de manganèse proche. Le mécanisme d'oxydation d'un alliage 316L pré-irradié et oxydé en milieu primaire au joint de grains est présenté en Figure 22.

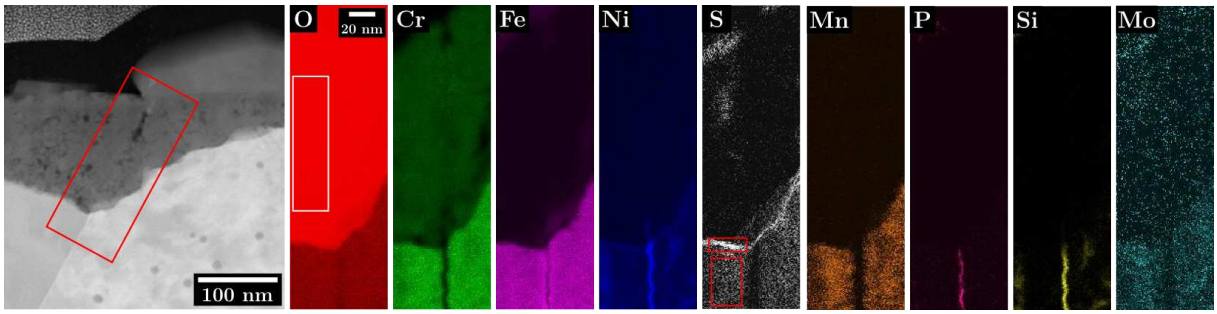

Figure 21: *Image STEM HAADF et cartographies EDXS associées de la pénétration d'oxyde intergranulaire sur l'échantillon oxydé 24 heures dans la zone irradiée à 1,5 dpa*

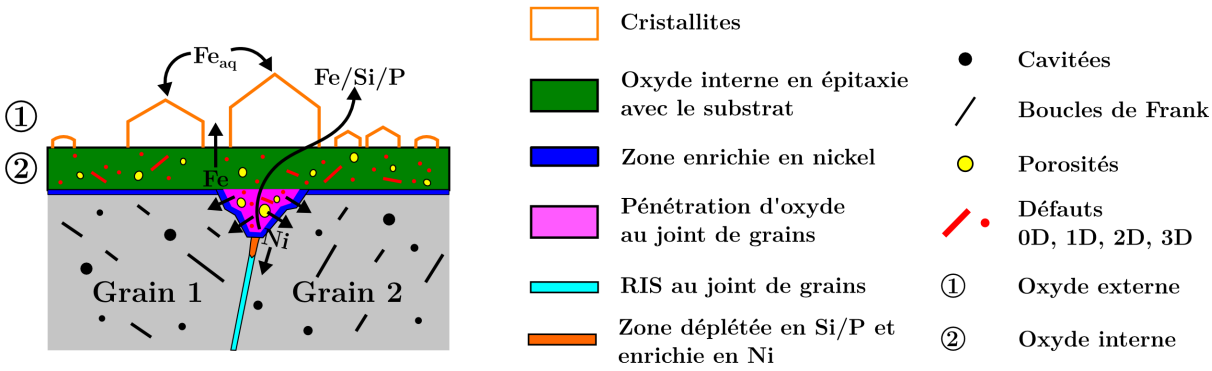

Figure 22: *Schéma du mécanisme d'oxydation d'un alliage 316L pré-irradié et exposé en milieu primaire au joint de grains*

➤ Oxydation sous flux de protons

Un échantillon a été oxydé sous flux de protons durant 24 heures à l'Université du Michigan afin de mieux appréhender l'effet simultané de l'oxydation et de l'irradiation. Dans la région oxydée sous flux de protons les images MEB ont révélé qu'une seconde morphologie de cristallite était présente et que de petites cristallites tapissent tout l'oxyde interne. Ces dernières ont été analysées par EELS et EDXS au MET et sont riches en chrome et nickel. L'analyse Raman de cette zone a confirmé que des oxydes de type spinelle étaient présents sur l'échantillon et a révélé la présence d'hématite. Cette hématite provient de la dissolution des gros cristaux de magnétite comme mis en évidence par les images MEB dans la région de flux. L'hématite n'est pas usuellement formée dans de telles conditions d'oxydation et son observation indique que le potentiel de corrosion a été suffisamment élevé dans cette région pour induire sa formation. Cette élévation du potentiel de corrosion est engendrée par la formation et forte concentration d'espèces radiolysantes formées sous irradiation. En réacteur, suffisamment d'hydrogène est ajouté afin de supprimer la radiolyse de l'eau, mais durant cette expérience la quantité d'hydrogène ajoutée n'a pas permis de supprimer la radiolyse de l'eau. En observant les oxydes en coupe transverse au MET il est apparu que l'oxyde interne formé est très mince ($\sim$ 15 nm contre plus de 100 en dehors de cette zone) et extrêmement poreux. Ces porosités résultent de la dissolution de l'oxyde interne, car le potentiel de corrosion est augmenté jusqu'à induire sa dissolution. Une

fois dissous, le chrome et le nickel se redéposent dans les petites cristallites externes denses. Le schéma du mécanisme d'oxydation sous flux de protons est présenté en Figure 23.

Région oxydée sous flux de protons

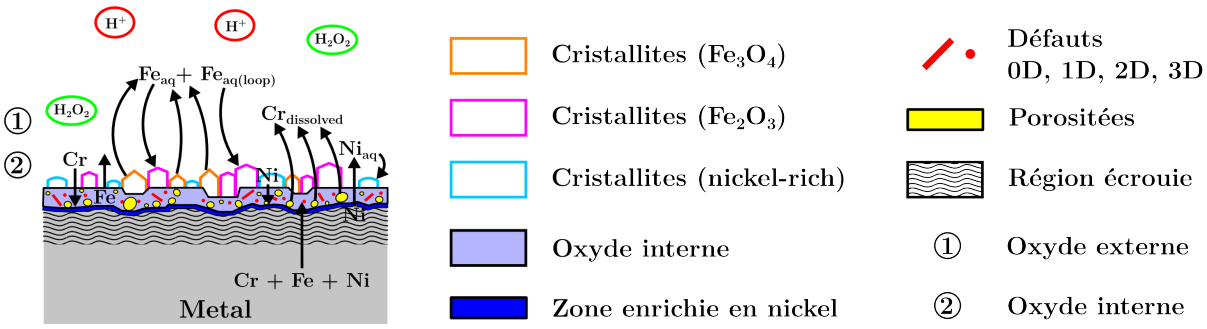

Figure 23: *Schéma du mécanisme d'oxydation d'un alliage 316L oxydé sous flux de protons*

➤ Représentativité de l'étude de l'oxydation de surface d'un alliage 316L aux temps courts pour simuler l'oxydation en pointe de fissure

Enfin, une vis extraite de centrale a été étudiée pour conclure sur la représentativité de cette étude. Comme observé sur les échantillons oxydés en milieu REP simulé, l'oxydation du joint de grains sur la vis extraite est asymétrique et facettée (Figure 24). L'affinité des plans de joints de grains à être oxydé peut se révéler préjudiciable pour la fissuration des vis et la propagation des fissures. Comme sur les échantillons pré-irradiés et oxydés, l'oxyde formé sur la vis est poreux. Les cartographies EFTEM, EELS et EDXS ont révélé que l'oxyde formé dans la fissure est riche en fer et un oxyde riche en chrome est formé le long des parois de la fissure (Figure 24). Un enrichissement en nickel à l'interface métal/oxyde a aussi été observé. Tout ceci est en accord avec les oxydes formés en milieu primaire simulé. En outre, des îlots de nickel non oxydés sont présents au centre de la fissure. Il est probable que, dans la fissure, le chrome et le fer s'oxydent préférentiellement alors que le nickel ségrégé au niveau du joint de grains se concentrera et formera ces îlots. Les cartographies réalisées ont démontré que la ségrégation induite par l'irradiation au joint de grains est affectée par l'oxydation. Un fort enrichissement en nickel a été noté sous la pointe de la fissure comme précédemment observé sur les échantillons oxydés en milieu primaire simulé. Du silicium oxydé est présent à la pointe de la fissure et couplé à sa déplétion en contrebas. Cela suggère que le silicium s'oxyde à la pointe de la fissure avant d'être dissous dans le milieu. Ce comportement est similaire à celui observé sur une boucle de Frank au front d'oxydation ainsi qu'à celui au joint de grains sur l'échantillon pré-irradié et oxydé en milieu REP simulé. Enfin, des clusters de soufre ont été révélés grâce aux cartographies EDXS en pointe de fissure couplée à un léger enrichissement en soufre à l'interface métal/oxyde comme précédemment observé au joint de grains sur l'échantillon pré-irradié et oxydé en milieu REP simulé. Ce soufre provient vraisemblablement d'une inclusion de sulfure de manganèse proche de la fissure. Sa dissolution dans le milieu est susceptible de modifier localement la chimie de ce dernier et donc l'oxydation comme observé en surface et proche des inclusions sur un échantillon oxydé en milieu REP simulé.

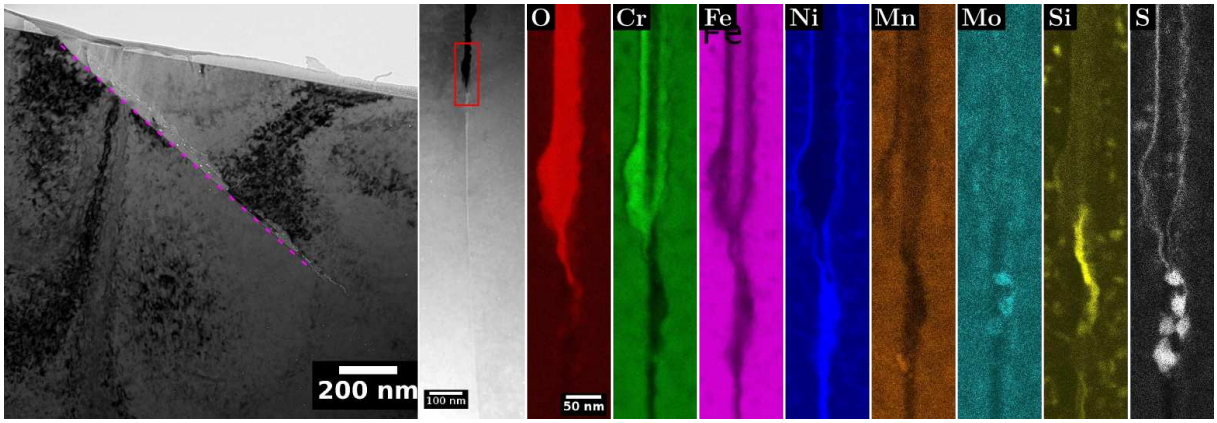

Figure 24: *Image MET en champ clair de la fissure sur la vis extraite et image STEM HAADF de la pointe de fissure avec les cartographies EDXS associées*

De nombreuses similitudes ont été observées entre les oxydes formés en fond de fissure et ceux formés en surface de matériaux pré-irradiés et oxydés en milieu REP simulé. Ainsi les résultats de cette étude confirment que réaliser des oxydations durant de courtes durées sur des échantillons pré-irradiés permet de simuler les oxydes formés en fond de fissure.

➤ Conclusion

Pour conclure, les irradiations protoniques permettent de simuler des modifications induites par l'irradiation (cavités, boucles de Frank, RIS sur les défauts et aux joints de grains). Pour la première fois, des analyses MET ont permis de relier la nature des défauts à la ségrégation induite par l'irradiation. Des études devraient être poursuivies pour mieux quantifier ces zones ségrégées. De plus, la température d'irradiation pour les irradiations synthétiques doit être ajustée au mieux pour induire des tailles et densités de défauts les plus proches possible de celles observées en réacteurs. L'étude des oxydes de surface formés lors d'oxydations aux temps courts sur des matériaux pré-irradiés permet de reproduire efficacement les oxydes formés en fond de fissure. Néanmoins de telles études devraient se dérouler sur des échantillons dont le polissage est parfaitement contrôlé et loin de potentielles inclusions. Le milieu doit de plus être le plus proche possible de celui en réacteur. Cette étude a fourni une meilleure compréhension des mécanismes d'oxydation et sur l'effet de l'irradiation sur l'oxydation. Une étude d'oxydation sous flux de proton en ajoutant suffisamment d'hydrogène afin de supprimer la radiolyse apparaît nécessaire afin de mieux comprendre l'effet du dommage d'irradiation. Dans le futur, réaliser des études se concentrant sur l'effet des défauts d'irradiation sur la cinétique d'oxydation ainsi que sur l'oxydation aux joints de grains en caractérisant entièrement ces derniers et investiguant l'effet de la nature du plan de joint de grains permettrait d'apporter des réponses complémentaires sur les mécanismes d'IASCC.

Introduction

Pressurized Water Reactors (PWRs) are used in numerous countries since the late 1960s. The nuclear industry, to stay economically competitive and a safe source of energy, must continuously improve and optimise the lifetime of the plants and their performance. Safe, economically profitable and reliable operations of PWRs will become more and more necessary. This implies the need to improve the reliability of technical solutions implemented along with a better understanding of the degradation mechanisms. Indeed, material degradation engenders a decrease in the plant availability rate and an increase of the maintenance costs associated both with the in-service checks and the interventions intended to repair any damage. The extension of the operating life of nuclear power plants (Long Term Operation (LTO) objective) and their ageing management is one of the main energetic issues encountered this century. In recent years, significant efforts were made to lengthen the operating cycle duration of PWRs from 40 to 60 years. It requires a good knowledge of the materials and structures in service both in nominal and accidental conditions since their performance is one of the key factors in ensuring a high level of safety, while maintaining a competitive operating cost. Thereby, better understanding the phenomena governing the materials ageing is one of the main focuses nowadays. To this end, researches are conducted in that field such as the present thesis.

The reactor core is constituted of a Reactor Pressure Vessel (RPV) which is the main component of the primary circuit. Inside this vessel, the core internals, in contact with the coolant, aim to protect the core barrel from the irradiation since the nuclear fuel proximity engenders a heavy neutron flux. The internals also support the fuel assembly properly aligned thanks to horizontal support plates called formers and vertical plates called baffles. The baffles and formers are maintained together using baffle-to-former bolts. The internals integrity must be maintained in all conditions hence the importance of the material choice. Austenitic stainless steels are used to manufacture internals structures due to their good mechanical properties and their corrosion resistance. Both the baffle and former plates are made of solutions annealed austenitic stainless steels 304 and/or 304L while bolts are made of cold-worked 316 (CW 316) and/or 316L (CW 316L) alloys (Figure 25). Bolts are also used between the core barrel and the formers (core barrel-to-former bolts) but only the baffle-to-former bolts will be described further on.

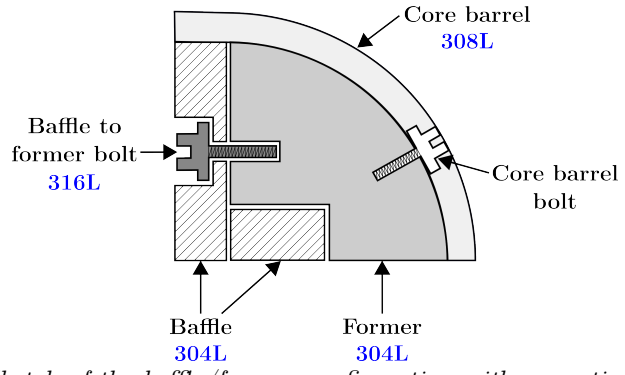

Figure 25: *Sketch of the baffle/former configuration with respective used materials*

The primary coolant is pure water containing boric acid, lithium and dissolved hydrogen maintained at the high temperature and pressure of the primary circuit. The materials in con-

tact with the coolant will thus oxidise. Combined with other stresses it may impair the material lifetime. In this context, it is primarily essential to understand the oxidation mechanisms of 316L austenitic stainless steel in-depth. In the open literature, work on the stainless steels corrosion in PWR medium mostly focuses on long durations and the oxide formation mechanism is still not yet well understood. In normal operating conditions, the materials used are submitted to an average temperature ranging from 300 to 330 °C but it can locally reach 360 to 380 °C due to gamma heating. Besides, being in the vicinity of the core, some of these components can experience doses as high as 80 dpa during their lifetime. Thereby, the corrosive medium in which are immersed the materials coupled with the mechanical stresses and the high irradiation dose is susceptible to alter the materials. These solicitations can lead to a decrease of the mechanical properties such as an increase of the yield strength inducing a higher material hardness but also a ductility decrease. Hence the materials lifetime will be shortened and must stain within requirements.

Among the altered components, cracks have been observed on a few baffle-to-former bolts during in-service inspections of the core internals in CP0 design (Bugey and Fessenheim nuclear power plants for example). It thus revealed the susceptibility of baffle-to-former bolts to ageing mechanisms. The first cracked bolts were observed in 1989 on decommissioned bolts from Bugey 2 [1, 2]. Intergranular cracks were highlighted on the shoulder between the head and the shank of the bolts as presented on an extracted bolt from Fessenheim 2 on Figure 26.

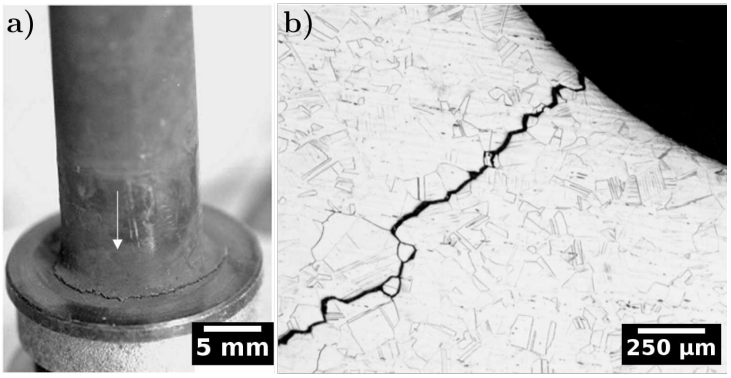

Figure 26: *Extracted baffle-to-former bolt from Fessenheim 2 irradiated at 11 dpa and cracked at the shoulder between the head and the tank a) visual examination of the bolt crack b) metallurgical examination of the crack [1]*

Such cracking was attributed to the Irradiation Assisted Stress Corrosion Cracking (IASCC) phenomenon (Figure 27). The detailed investigation revealed that all damaged bolts were located in high neutron irradiation fluence and high temperature regions and some of them were in high stressed region depending on their position. This degradation is highly problematic for the PWRs safety because it acts on the second containment barrier. It results from the superposition of mechanical damage, irradiation and high temperature corrosive environment. Since then, such incidents have occurred in a number of plants worldwide. To address this issue, the applied strategy is to replace the cracked bolts. In parallel, a new bolt design was implemented to reduce the stress concentration between the head and the shank. Moreover an "upflow" coolant configuration was adopted to reduce the pressure difference on both sides of the baffle plates, inducing a lower medium temperature and thus a better cooling of the bolts. Although only 1/3 of the internal baffle-to-former bolts are sufficient to assure the internals integrity, such cracking induces down times and increases of the plant maintenance costs. Those inspections and removals as well as replacements of the bolts had led plant manufacturers and operators to become interested in IASCC issues along with the underlying mechanisms. Furthermore, to extend the operating life of nuclear reactors it is important to anticipate if IASCC cracking

could occur for higher doses. Hence, IASCC in-depth study is essential to understand the involved mechanisms that could lead to the bolts cracking.

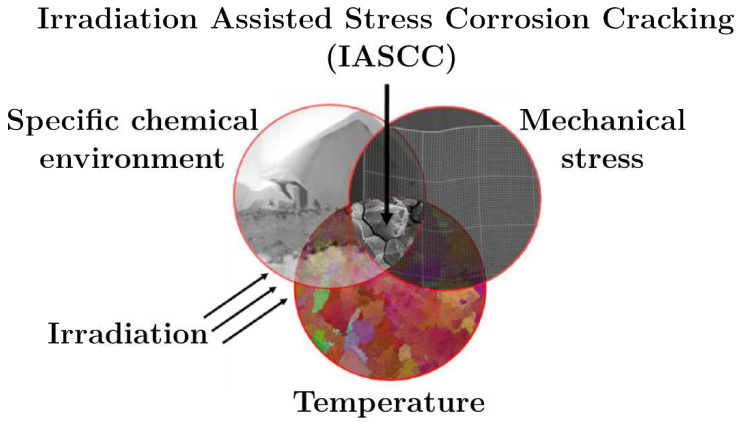

Figure 27: *IASCC phenomenon resulting from various stresses (mechanical stress, corrosive environment, high temperature and irradiation)*

Many models have been proposed to account for the cracking induced by IASCC. However, the multiplicity of parameters and their interactions create challenges and difficulties to implement a model able to take into consideration all the aspects of this cracking. To date, all the parameters influencing the IASCC and corrosion mechanisms are not well-known and therefore cannot anticipate sufficiently accurately the potential damages. Direct connection between radiation-induced changes and oxidation has not been well examined. Hence, the objective of this thesis is to investigate the oxidation mechanisms occurring on 316L alloy in PWR medium and the role of irradiation defects on these mechanisms. It aims to bring a better understanding of the coupling between irradiation and oxidation of a 316L austenitic stainless steel. Indeed, some recent studies [4–9], seem to indicate that irradiation modifies the kinetics and the nature of the oxides formed. From a practical point of view, the understanding of the cracking induced by the IASCC phenomenon therefore passes through that of the passive oxide layer, its evolution and the creation of defects in this layer.

The properties of oxide films formed, including morphology, thickness, structure and chemical composition, etc. are thought to play a crucial role in the oxidation process, especially at the initial stages and at crack tips. To study at best the IASCC mechanisms, one should focus on the investigation of the oxidation occurring at the crack tips. As cracks will further propagate, they will present at crack tips oxidised areas analogous to the oxidation first stages. Hence, to emulate the oxidation at crack tips, short times oxidations were carried out in simulated PWR environment. They allowed to investigate the oxidation first stages on surface oxides and especially the oxides formation and growth. Moreover, as sample preparation and its cold-work degree can greatly influence the oxide scales formed [7, 10, 11], it is necessary to understand better the effect of cold-work induced by the polishing steps. Therefore, samples with various polishing were investigated to help fathom the effect of sample preparation on the oxidation kinetic. These results will be extrapolated to give a more general conclusion on the cold-work effect. In addition, the influence of inclusions, always present in industrial 316L alloys, was taken into account. Oxides formed near these inclusions were studied to conclude on their effects on the oxidation kinetic. Given the few amount of data on short time oxidations, both unirradiated and irradiated 316L alloy were oxidised. The unirradiated ones acted as reference before further comparison with the irradiated ones. Moreover, since the crystallographic orientation of the underlying metal grain was demonstrated to play a role in the oxidation [12–14] and is susceptible to also affect the intergranular oxidation. Thereby its influence was taken into account in this work. Its role on the oxides morphology, thickness, chemistry and oxidation kinetic was investi-

gated for both unirradiated and irradiated specimens. The oxide layers were characterised using macroscopic and nanoscopic techniques from their morphology, thickness, structure to composition while investigating the intergranular oxidation. Indeed, since the main bolt cracks appear to be intergranular ones, attention was drawn on grain boundaries oxidation. A thorough study of the oxides formed at grain boundaries was performed from their morphology, the penetration depths to their compositions. The impact of grain boundaries Radiation Induced Segregation (RIS) on the oxide formed was considered with irradiated samples. These were compared to unirradiated samples to conclude if RIS modify the oxide formed at grain boundaries and the oxidation mechanisms. Such investigation will shed light on the intergranular crack initiation and propagation induced by the IASCC mechanism.

As neutron irradiation requires costly specialised facilities able to handle radioactive samples to investigate the materials, it is essential to emulate at best the PWR irradiation on laboratory samples. Synthetic irradiations can serve as an efficient tool to simulate neutron damage using correct temperature shifts [15–17]. Synthetic proton pre-irradiations were chosen to emulate neutronic irradiation and these samples could thus be characterised in usual laboratories. Proton irradiation also presents the advantage of being able to reach higher doses in a smaller amount of time than neutron irradiation but still inducing similar changes in the material (dislocation loops, Radiation Induced Segregation (RIS), etc.). The thorough characterisation of the changes induced by irradiation made will attempt to confirm the synthetic proton-irradiation representativeness to emulate neutron irradiation and highlight their limitations. Proton pre-irradiated as well as unirradiated oxidised samples were compared on same crystallographic orientations to conclude on the role of irradiation defects on the oxide scale and oxidation kinetics. Performing proton pre-irradiation and then short time oxidations of the samples was used to simulate the oxidation occurring in those crack tips. These experiments are more cost-efficient than oxidation under proton flux experiments that require specialised facilities. They moreover, permit to decorrelate the influence of the microstructure and chemistry induced by irradiation and displacement damage/creation of point defects into the oxides and alloy. All samples had both irradiated and unirradiated regions enabling comparative studies on a unique sample with the exacts same oxidation conditions in both areas. Hence, a thorough investigation of short time oxidation of irradiated 316L alloy will allow a better understanding of the oxide formation and growth and shed light on the interaction between irradiation and corrosion. To replicate even more closely phenomena occurring in PWR, an oxidation under proton flux experiment was conducted. It allowed to study the Irradiation Assisted Corrosion (IAC) phenomena. On a same sample oxidised during 24 hours, a region was only oxidised while a second one was proton pre-irradiated beforehand and the last one was proton irradiated and then oxidised under proton flux. Such experiment permitted to decorelate the effect of irradiation induced modifications on the oxide formed from the oxidation under proton flux process on a unique sample. Finally, an extracted cracked bolt from a French PWR was investigated at crack tips. Results on this crack tips were used to conclude at first on the representativeness of proton pre-irradiations and on the study of short time oxidations of surface oxides and secondly on IASCC mechanisms.

In a nutshell, to extend the literature and have better understanding of the underlying mechanism of IASCC, it is necessary to study oxidised irradiated materials in PWR medium. As the effect of irradiation on the oxidation is not yet clear, it should be investigated at short oxidation times to bring light on the involved mechanisms during the oxidation first stages at crack tips.

The first chapter will be devoted to a bibliographic overview of both austenitic stainless steels corrosion and the changes induced by the irradiation. Firstly, the nature of the oxide layers formed as well as their formation mechanism will be introduced. Details will be given on the main parameters affecting stainless steels oxidation. In a second step, a review of the knowledge

concerning irradiation effects on the microstructure and chemistry will be carried out as well as the main parameters altering those modifications. Synthetic irradiations as a way of emulating neutron irradiation will be presented along with their advantages and drawbacks. Ultimately, this bibliographic study will present the approach adopted in this work.

The second chapter will describe the studied materials, the irradiations performed, the corrosion tests and the characterisation techniques employed. Firstly, all the experimental techniques used in this work will be described from macroscopic investigations techniques (optical microscopy, Grazing Incidence X-Ray Diffraction (GIXRD), Raman spectroscopy) to microscopic ones (Scanning Electron Microscopy (SEM) and Transmission Electron Microscopy (TEM)). Then, the studied 316L alloy will be introduced along with the samples preparation method implemented. Details will be given on the 316L samples studied in this work from reference samples to the cold-worked and proton pre-irradiated ones. The synthetic pre-irradiations performed using protons will also be presented in this chapter. The corrosion loop used to oxidise the samples during short durations will be introduced. Then, further information will be given on the IAC experiment from the sample preparation to the experimental conditions and the device in which the oxidation under proton flux was carried out. The extracted bolt will be presented in this chapter. Finally, characterisations of the proton irradiated samples microstructure and chemistry will be laid out and compared to the decommissioned bolt. The representativeness of proton pre-irradiation will be discussed.

The characterisation of the oxide layers formed on unirradiated 316L stainless steel in simulated primary environment will be presented in the third chapter. Their nature, structure and morphology both on the surfaces and at grain boundaries were investigated and will help to conclude further on the effect of irradiation. The effect of crystallographic orientation of the underlying metal grain on the oxide scales and oxidation kinetic was thoroughly studied and will be presented. A study of the influence of sample preparation and the presence of inclusions on the 316L oxidation will also be carried out in this chapter.

The fourth chapter will be dedicated to the irradiation effect on the oxidation kinetics of austenitic stainless steels exposed to a primary environment. To do so focus will be made on the oxide morphology, thickness and composition both on the surface and at grain boundaries. Comparison with the ones formed on unirradiated samples will allow to conclude on the irradiation effect. Then, results on the IAC experiment of a sample oxidised under proton flux will be presented in the three areas investigated. Oxides from the proton flux area will be compared to the ones outside this area and to the proton pre-irradiated ones to provide information on the IAC mechanisms. Ultimately the oxides formed at the crack tips of the decommissioned bolt will be investigated and compared to the ones formed on samples surfaces synthetically irradiated. Such comparison will permit to conclude on the representativeness of this study.

Chapter 1

Bibliographic study

Contents

1.1 Austenitic stainless steels oxidation in Pressurized Water Reactors 9
1.1.1 Oxidation in primary water 9
1.1.1.1 Primary water environment 9
1.1.1.2 Oxide scales formed on austenitic stainless steels 10
1.1.1.3 Oxidation mechanisms 16
1.1.1.4 Effect of short oxidation times 22
1.1.2 Parameters affecting stainless steels oxidation 23
1.1.2.1 Surface state and cold-work 23
1.1.2.2 Chemistry of the medium and installation effect 26
1.1.2.3 Crystallographic orientation of the metal 28
1.1.2.4 Irradiation 30
1.1.3 Austenitic stainless steels oxidation in PWRs: Synthesis 34
1.2 Irradiation effect on austenitic stainless steels 35
1.2.1 Microstructural modifications 37
1.2.1.1 Frank loops 37
1.2.1.2 “Black dots” 38
1.2.1.3 Cavities and helium filled bubbles 38
1.2.1.4 Stacking Fault Tetrahedra 39
1.2.1.5 Modification of the dislocation network 40
1.2.2 Chemical modifications 40
1.2.2.1 Radiation Induced Segregation 40
1.2.2.2 Phase precipitation 43
1.2.3 Parameters affecting the changes induced by irradiation 44
1.2.3.1 Surface state and cold-work 44
1.2.3.2 Irradiation dose 45
1.2.3.3 Grain boundaries character 46
1.2.4 Synthetic irradiations 50
1.2.4.1 Generalities 51
1.2.4.2 Proton irradiation 52
1.2.5 Irradiation effect on austenitic stainless steels: Synthesis 53
1.3 Bibliographic summary and experimental approach 55

This chapter aims to present literature results on the oxidation in primary environment and irradiation mechanisms for stainless steel alloys. Based on the literature survey, the objective of this thesis will be defined as well as the set out of the followed approach with the characterisation techniques able to give the sought information.

The first part is dedicated to the description of the oxide formed in primary medium on austenitic stainless steels. The oxidation reactions and the Pressurized Water Reactor (PWR) medium will be described. An overview of the oxide layers formed in PWR medium will be given, depicting the duplex structure of the oxide as well its composition, structure and morphology. Several oxidation mechanisms proposed in the literature will be introduced and detailed. The effect of short oxidation times on the oxidation kinetic will also be presented. Finally, several parameters influencing oxidation will be set out. Details will be given on their influence on the overall oxidation kinetic and the oxide layers formed. The second part aims to present the effect of irradiation on the microstructure and microchemistry of austenitic stainless steels. The effect of neutron irradiation occurring in PWRs will be presented and details will be given on the defects induced by irradiation in austenitic stainless steels. Chemical modifications under irradiation will also be described from segregation to precipitation and mechanisms involved will be introduced. Several parameters influencing the irradiation induced changes will be detailed. Their repercussions on the microstructure and chemistry will be presented. Finally, we will focus on synthetic irradiation performed in order to simulate neutron irradiation. Their advantages and inconveniences will be laid out as well as the similarity between the proton and neutron irradiation induced changes. The last part of this chapter presents a summary of this bibliographic overview and an evaluation of the main points on which this study should focus. It also introduces a reflexion on the needed characterisation techniques to investigate irradiated materials oxidised in primary water.

1.1 Austenitic stainless steels oxidation in Pressurized Water Reactors

The primary water environment of PWRs is a reducing medium in which materials are submitted to oxidation phenomena. It results in an anionic reaction such as $M \rightarrow M^{x+} + xe^-$ coupled to the associated cathodic reaction $H^+ + e^- \rightarrow \frac{1}{2}H_2$. For austenitic stainless steels, these reactions lead to the formation of oxide layers and the dissolution of the material (or release). These oxides formed may be more or less adherent onto oxidised surfaces. The material longevity in a corrosive environment rests on the protective layer acting as a barrier between corrosive species and bare metal. The corrosion rate of the material is reduced to a negligible value if the passive film behaves like a protective barrier. This is the case of stainless steels. The oxidation processes and the oxide layer formed depend on numerous parameters associated, on the one hand, with the material (composition, microstructure, etc.) and, on the other hand, with the environment (composition of the medium, temperature, etc.). Its adhesion and protectiveness are primary characteristics for the corrosion resistance.

In the following paragraphs focus is primarily made on oxide layers resulting from corrosion in water at high temperature and high pressure, representative of the primary circuit of a PWR and the parameters influencing oxidation.

Shedding light on:

- Primary water environment,
- Nature of the oxides formed on austenitic stainless steels in Pressurized Water Reactor medium,
- Associated oxidation mechanisms and focus on short oxidation times oxidation mechanisms,
- Parameters affecting oxidation (alloy microstructure, medium chemistry, irradiation etc.).

1.1.1 Oxidation in primary water

The objective of this first paragraph is to synthesise the various studies relating to the characterisation of these oxide layers formed on stainless steels in primary environment and the associated mechanisms.

1.1.1.1 Primary water environment

Close to the reactor vessel, in the primary circuit, the water temperature is ranging from 293 °C to 328 °C with a pressure of 155 bar. This primary water serves as the heat transfer fluid. 1000 ppm of boric acid (H_3BO_3) are introduced in the water to control the neutron reaction taking place within the nuclear fuel. Boric acid is employed due to its ability to absorb neutrons. This water, demineralized and deoxygenated has a slightly alkaline pH thanks to the addition of 2 ppm of lithium hydroxide (LiOH) which counter the boron acidity thus decreasing the generalised corrosion that could happen. Dissolved hydrogen is introduced in the water allowing to suppress oxidising species induced by the water radiolysis and proving a reducing medium. Indeed, in pure water environment, irradiation can induce radiolysis. Water radiolysis engenders the decomposition of water (H_2O) molecules when irradiated by breaking the chemical bonds of H_2O and inducing the formation of several oxidising species [18]. H_2O molecules will form radiolysis products such as ions, excited molecules and free radicals (atom, molecule or ions with at least one unpaired electron). Mostly $H^\bullet$, $HO^\bullet$ and $H_2O^\bullet$ radicals, H_3O^+, OH^- ions, H_2, O_2

and H_2O_2 molecules are produced by radiolysis. Therefore oxidising species can be produced under irradiation and their formation will engender an increase of the Electrochemical Corrosion Potential (ECP) causing a stronger general corrosion. However, in PWRs, as described previously, the medium is not solely pure water but deaerated pure water which contains dissolved hydrogen, boric acid and lithium hydroxide. The addition of dissolved hydrogen will inhibit the radiolytic dissociation and as a result oxidising species concentrations are greatly reduced and no increase of the corrosion potential is expected.

PWR media or simulated ones, referred further on, contain approximately 1000 ppm of boron (H_3BO_3) and 2 ppm of lithium (LiOH) with a pH close to 7.2 at 325 °C. The dissolved hydrogen concentration in PWR medium is of 25 - 30 cm^3 (STP)/kg H_2O (Standard Temperature and Pressure (STP) (0 °C, 1 atm)) while oxygen concentration stays under 10 ppb.

Primary water environment:

- T $\simeq$ 325 °C, P = 155 bar, [B] = 1000 ppm, [Li] = 2 ppm, [H_2]$\simeq$ 30 cc/kg, [O_2]$\leq$ 5 ppb and pH_{325C} = 7.2
- Radiolysis occurs in pure water environment and leads to the formation of oxidising species such as H_2, O_2 and H_2O_2. The addition of dissolved hydrogen in the medium inhibits radiolysis.

1.1.1.2 Oxide scales formed on austenitic stainless steels

Potter and Mann [19], followed by Tapping and Lister [20, 21] were among the first to investigate the oxidation of stainless steels observing a duplex oxide structure. Since then, such duplex structure was widely corroborated by several authors using a wide range of techniques in several corrosive environment including primary water [4, 5, 7, 12, 14, 20–32].

Numerous studies have shown that the two oxide layers formed on austenitic stainless steels in primary water have a M_3O_4 spinel structure (with M = Fe, Cr and Ni in variable proportions) [4, 5, 7, 12, 14, 24, 26–32]. The inner oxide grows into the metal at the metal/oxide interface whereas the outer oxide growth happens at the oxide/medium interface. Figure 1.1 summarises the duplex oxide formed in primary water on austenitic stainless steels. This duplex oxide layer is composed of:

- An iron-rich outer layer of crystallites with geometric shapes and sizes ranging from several nanometres to a few microns mostly found to be magnetite (Fe_3O_4) [4, 5, 7, 12, 14, 24, 26–32],
- A chromium rich compact and protective inner layer mostly described as mixed iron/chromium spinel [4, 5, 7, 12, 14, 24, 26–32],
- A nickel enrichment at the metal/oxide interface but its origin remains controversial [4, 5, 12, 26–31].

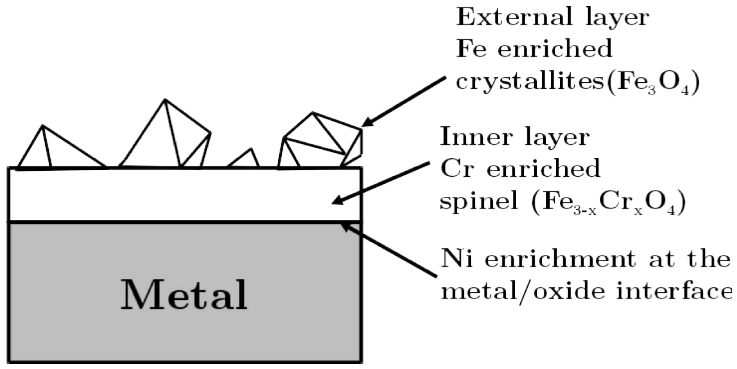

Figure 1.1: *Schematic of the duplex oxide formed on austenitic stainless steels in primary water*

Outer oxides, with crystallites shapes, appear at the surface of the inner oxides regardless of the oxidation time. Indeed, even after 1 minute oxidation Soulas observed a small outer oxide that tended to become faceted as the oxidation time increased [12]. The oxide coverage, size, number and density are different from one study to another since their formation and growth is contingent on the medium, the oxidation time and on other parameters that will be developed further on in section 1.1.2. However most authors observe bigger oxides as the oxidation time increases. The outer oxide formed at the surface of the inner layer tends to have well-shaped crystallites.

Few authors have observed a corundum structure of Cr_2O_3 type within the inner layer [20, 24, 33]. Tapping et al. [20], deduced the presence of a Cr_2O_3 oxide from its composition while Da Cunha Belo et al. [24] used Raman spectroscopy. Cheng et al. used X-ray Photoelectron Spectroscopy (XPS) measurements to find the Cr_2O_3 structure [33]. Such structure was only observed in very few studies while most authors attributed the inner layer as a spinel AB_2O_4 structure [4, 5, 7, 12, 14, 26–32].

A spinel structure of AB_2O_4 type contains 56 oxygen atoms, 8 tetrahedral site cations and 16 octahedral site cations [34]. The spinel type (normal or inverse) is defined according to the distribution of the A and B cations in the cell. In a normal spinel, the B cations are on octahedral sites and the A cations on tetrahedral sites, whereas in an inverse spinel the A cations are in octahedral sites and the B cations half in tetrahedral sites and half in octahedral sites. These two types of spinels can be written in the following manner: $[A^{2+}](B^{3+})_2O_4$ for normal spinels and $[B^{3+}](B^{3+}A^{2+})O_4$ for inverse spinels where square brackets represent tetrahedral sites and parentheses octahedral sites. From the crystal fields theory, the stabilisation energy of the different spinels can be calculated [35]. For an isolated atom, the energy level of the five 3d atomic orbitals are degenerated and possess the same energy. However, cations in octahedric or tetrahedric environment will be subjected to an electrostatic field due to the presence of respectively 6 or 4 ligands. These will induce a splitting Δ of the d-orbitals in two sets with different energies and thus there will be a degeneracy loss. For the octahedral configuration orbitals d_{xy}, d_{yz} and d_{xz} are stabilised and at a lower energy than d_{z^2} and $d_{x^2-y^2}$. The three lower orbitals are referred to as t_{2g} while the two higher ones are referred to as e_g. The tetrahedral configuration also possesses two sets of district orbitals, e (lower energy: d_{z^2} and $d_{x^2-y^2}$) and t_2 (higher energy: d_{xy}, d_{yz} and d_{xz}). The crystal field splitting energy for octahedral symmetry is referred as to Δ_o while it is referred as to Δ_t for tetrahedral symmetry. Fe^{2+}, Fe^{3+} and Cr^{3+} are all transition metals with respectively $[Ar]4s^03d^6$, $[Ar]4s^03d^5$ and $[Ar]4s^03d^3$ electron configuration. Fe^{3+} is a high-spin system with no Crystal Field Stabilization Energy (CFSE) while Fe^{2+} has a higher CFSE (CFSE = -0.4 Δ_o) thus explaining the inverse spinel configuration of Fe_3O_4 since the divalent ion has more gain in octahedral geometry than the trivalent ion. For the $FeCr_2O_4$ spinel, Cr^{3+} is a high-spin ion with a higher CFSE (CSFE = -1.2 Δ_0) that the divalent high-spin Fe^{2+} ion. Hence,

Cr^{3+} will occupy the octahedral sites resulting in a normal spinel configuration. For, the mixed iron/chromium spinel, Cr^{3+} cations, having a higher CFSE than Fe^{2+} and Fe^{3+} ions, will occupy octahedral sites while the iron cations can occupy both tetrahedral and octahedral sites. Thus, mixed iron/chromium spinel can be represented accordingly: $[Fe^{2+}_{1-x}Fe^{3+}_{x}](Fe^{2+}_{x}Fe^{3+}_{2-2y-x}Cr^{3+}_{2y})O_4$ with x and y between 0 and 1 [36, 37].

The spinel structure of the inner layer formed on 316L alloy oxidised in PWR medium for short times was investigated by Soulas [12]. He looked upon the type of spinel at different oxidation times by studying the Cr/Fe ratio obtained by Electron Energy Loss Spectroscopy (EELS) and found that the spinels' stoichiometry changes with time. He suggested that the inner layer has a structure of normal spinel type while the outer layer has a structure of inverse spinel type (cf. Table 1.1).

Table 1.1: *Spinel types according to the analysed layer and the oxidation time (data from [12])*

Oxidation time	$\frac{Cr}{Fe}interne$	Formula	Spinel type
1 min	0.44	$[Fe^{2+}](Fe^{3+}_{1.1}Cr^{3+}_{0.9})O_4$	Normal
2 min	0.54	$[Fe^{2+}](Fe^{3+}_{0.95}Cr^{3+}_{1.05})O_4$	Normal
10 min	1.05	$[Fe^{2+}](Fe^{3+}_{0.45}Cr^{3+}_{1.55})O_4$	Normal
1 h	1.09	$[Fe^{2+}](Fe^{3+}_{0.45}Cr^{3+}_{1.55})O_4$	Normal
5 h	0.91	$[Fe^{2+}](Fe^{3+}_{0.55}Cr^{3+}_{1.45})O_4$	Normal
24 h	1.06	$[Fe^{2+}](Fe^{3+}_{0.45}Cr^{3+}_{1.55})O_4$	Normal
Oxidation time	$\frac{Cr}{Fe}externe$	Formula	Spinel type
1 min	0.15	$[Fe^{3+}](Fe^{2+}Fe^{3+}_{0.6}Cr^{3+}_{0.4})O_4$	Inverse
2 min	0.14	$[Fe^{3+}](Fe^{2+}Fe^{3+}_{0.6}Cr^{3+}_{0.4})O_4$	Inverse
10 min	0.07	$[Fe^{3+}](Fe^{2+}Fe^{3+}_{0.8}Cr^{3+}_{0.2})O_4$	Inverse
1 h	0.04	$[Fe^{3+}](Fe^{2+}Fe^{3+}_{0.9}Cr^{3+}_{0.1})O_4$	Inverse
5 h	0.05	$[Fe^{3+}](Fe^{2+}Fe^{3+}_{0.85}Cr^{3+}_{0.15})O_4$	Inverse
24 h	0.1	$[Fe^{3+}](Fe^{2+}Fe^{3+}_{0.7}Cr^{3+}_{0.3})O_4$	Inverse

As mentioned above, several authors have studied the nickel enriched area underneath the oxide scale. The area thickness range from few nm to several tens of nm and its observation strongly depends on the sample preparations, their surface state and the oxide thickness. The nickel content can then locally reach twice that of the nickel content in the alloy. Observations made by Transmission Electron Microscopy (TEM) by Terachi et al. revealed its existence [26, 27]. Lozano-Perez et al. confirmed the presence of such area in 2009 and 2010 using two other techniques: Nano-Secondary Ion Mass Spectrometry (SIMS) and Atom Probe Tomography (APT) [28, 29]. They explain the presence of this zone enriched in nickel by a mechanism of diffusion of Ni from the oxide to the metal substrate. This enrichment was also highlighted at a grain boundary ahead of a crack tip by Herbelin et al. using Energy Filtered Transmission Electron Microscopy (EFTEM) nickel maps [38] . Soulas also observed this nickel enriched area by EFTEM imaging and EELS [12]. He proposes a two successive stages phenomenon: the nickel diffusion in the inner layer at the very first oxidation stages and then an inverse diffusion which would push back the nickel in the alloy. Kruska et al. agreed with the reverse diffusion mechanism hypothesis after analysing oxidised hardened samples and observing nickel enrichment at the crack tip [31]. They assume that nickel enrichment could serve as a diffusion barrier to

oxygen and thus prevent or slow the oxide growth. Moreover, from APT results, they made the hypothesis that hydrogen could be trapped in the nickel-enriched zone. Perrin et al. also noted this nickel enrichment and added that this enrichment seems to be linked to the presence of defects in this area [4]. The hydrogen diffusion through the oxide layer and its trapping in the alloy was studied by Dumerval [5]. She made the assumption that hydrogen accumulation at the metal/oxide interface results from an hydrogen trapping. Since the outer layer is formed by cationic diffusion (see section 1.1.1.3), vacancies are created at the metal/oxide interface and might act as hydrogen traps [39]. She also showed that the hydrogen and nickel accumulation are correlated, confirming the hypothesis made by Kruska et al. [31] that hydrogen is trapped in the nickel-rich area. Indeed, the hydrogen accumulation beneath the oxide layer results from a trapping in the alloy in the same area in which the nickel enrichment is observed as she demonstrated from Glow Discharge Optical Emission Spectroscopy (GDOES) analysis (Figure 1.2). The oxidation mechanism seems to induce at the metal/oxide interface an area enriched in both Ni and H.

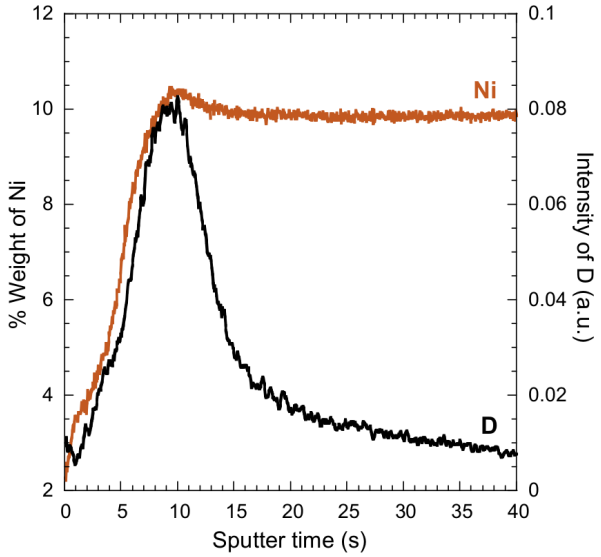

Figure 1.2: *Quantitative profiles of nickel (left axis) and qualitative one of deuterium (right axis), obtained by GDOES on 316L sample oxidised 600 hours in deuterated primary medium, and plotted against the sputtering time [40]*

Tables 1.2 and 1.3 attest of several studies made on oxides formed on stainless steels exposed in aqueous medium at high temperature or simulated PWR water. The oxide composition can vary from one study to another since the conditions (chemistry of the medium, composition of the alloy, oxidation time, etc.) are not exactly the same and the characterisation techniques used differ and have different sensitivities.

Table 1.2: *Literature overview of the oxide scale formed on austenitic stainless steels in aqueous media at high temperature (1980 - 2010)*

Reference	Material	Oxidation condition	Characterisation techniques	Oxide scale	Composition
Tapping (1986) [20]	304	Lithiated water, T = 300 °C, P = 103 bar, pH = 10.3, $H_2 = 18\,cm^3/kg$, t = 5 to 576 h	SEM, XPS, AES, NRA RBS	Outer oxide	$NiFe_2O_4$
				Inner oxide	$(Fe, Cr)_2O_3$
Lister (1987) [21]	304	Lithiated water, T = 279 °C, P = 120 bar, pH = 10.3., $H_2 = 18\,ml/kg$, t = 166 h	SEM, AES,	Outer oxide	$Ni_xFe_{3-x}O_4$
				Inner oxide	$FeCr_2O_4$ or $NiCr_2O_4$
Szklarska (1991) [22]	304	Lithiated water, T = 100 to 350 °C, P = n.c., pH = 8, $H_2 = 1.58\,ppm$, t = n.c.	AES, Impedance, OCP,	Outer oxide	Fe_2O_3 and FeOOH
				Inner oxide	Cr_2O_3
Da Cunha Belo (1998) [24]	316L	PWR medium*, T = 350 °C, P = n.c., pH = n.c., $H_2 = 27\,ppm$, t = 2000 h	SDL, TEM, GIXRD, Raman GDOES	Outer oxide	$Ni_{0.75}Fe_{2.25}O_4$
				In-between oxide	$Ni_{0.75}Fe_{2.25}O_4$ Fe_3O_4
				Inner oxide	Cr_2O_3, $FeCr_2O_4$ or Fe_3O_4
Ziemniak (2002) [25]	304	Ammoniated water T = 260 °C, P = n.c., pH = 6.7, $H_2 = 45\,cm^3/kg$, t = 1000 to 10000 h	SEM, XPS, GIXRD,	Outer oxide	$(Ni_{0.2}Fe_{0.8})$ $(Fe_{0.95}Cr_{0.05})_2O_4$
				Inner oxide	$(Ni_{0.2}Fe_{0.8})$ $(Fe_{0.3}Cr_{0.7})_2O_4$
Terachi (2005) (2008) [26, 27]	316	PWR medium*, T = 320 °C, P = 155 bar, pH = n.c., $H_2 = 1$ to $45\,cm^3/kg$, t = 245 to 500 h	SEM, GIXRD, AES, TEM	Outer oxide	Fe_3O_4
				Inner oxide	$FeCr_2O_4$

** for simulated environment*

Table 1.3: *Literature overview of the oxide scale formed on austenitic stainless steels in aqueous media at high temperature (2010 - 2018)*

Reference	Material	Oxidation condition	Characterisation techniques	Oxide scale	Composition
Soulas (2012) [12]	316L	PWR medium*, T = 325 °C, P = 155 bar, pH = 7.2, H_2 = 30 cm^3/kg, t = 1 min to 24 h	SEM, GIXRD, XPS, Raman TEM	Outer oxide	Fe_3O_4
				Inner oxide	$Fe_{1.5}Cr_{1.5}O_4$
Cisse (2012) [30]	304L	PWR medium*, T = 340 °C, P = 150 bar, pH = n.c., H_2 = 30 cm^3/kg, t = 500 h	SEM,	Outer oxide	Fe_3O_4 and $(Fe, Ni)Cr_2O_4$
			TEM,	Inner oxide	$(Fe, Ni)Cr_2O_4$
Perrin (2013) [4]	316L	PWR medium*, T = 325 °C, P = 155 bar, pH = n.c., $H_2 = 1.3 \times 10^{-3}$ mol/L, t = 620 h	SEM, TEM, SIMS	Outer oxide	Fe_3O_4
				Inner oxide	$Fe_xCr_{3-x}O_4$
Dumerval (2014) [5]	316L	PWR medium*, T = 325 °C, P = 155 bar, pH = 7.2, H_2 = 41 cm^3/kg, t = 600 h	SEM,	Outer oxide (at. %)	$(Fe, Cr, Ni)_3O_4$ Fe - Cr - Ni - O 28 - 6 - 3 - 63
			TEM,	Inner oxide (at. %)	$(Fe, Cr, Ni)_3O_4$ Fe - Cr - Ni - O 17 - 14 - 6 - 63
Gupta (2016) [7]	304L	PWR medium*, T = 340 °C, P = 155 bar, pH = n.c., H_2 = 25 - 35 cm^3/kg, t = ∼ 360 h	SEM,	Outer oxide	Fe_3O_4 and $(Fe, Ni)Cr_2O_4$
			TEM,	Inner oxide (at. %)	$(Fe, Ni)Cr_2O_4$ Fe - Cr - Ni 56 - 34 - 10
Chen (2017) [32]	316L	PWR medium*, T = 310 °C, P = 122 bar, pH = 7, H_2 = 30 ml/kg, t = 500 h	SEM,	Outer oxide	$(Ni, Fe)Fe_2O_4$
			TEM,	Inner oxide	$(Fe, Ni, Cr)_3O_4$

** for simulated environment*

Oxide scales formed on austenitic stainless steels:

- Formation of a duplex oxide even after 1 minute oxidation.
- The inner oxide grows into the metal at the metal/oxide interface whereas the outer oxide growth happens at the oxide/medium interface.
- The outer oxide is composed of crystallites of magnetite (Fe_3O_4) inverse spinel with geometric shapes and sizes ranging from several nanometres to a few microns that tend to become bigger and faceted as the oxidation time increases.
- The inner oxide is mostly found to be a chromium rich normal spinel with iron AB_2O_4 but few studies attest of a Cr_2O_3 oxide.
- Presence of a nickel enrichment underneath the inner oxide whose observation depends on the sample preparation, surface state, oxide thickness, etc. This enrichment is believed to result from an inverse diffusion which would push back the nickel from the inner oxide into the alloy.
- Hydrogen trapping occurs at the metal/oxide interface in the nickel enriched zone due to the presence of cationic vacancies injected.

1.1.1.3 Oxidation mechanisms

The formation of an oxide layer is the result of complex reactions at the metal/oxide and oxide/medium interfaces (metal oxidation, transport of reactive species (cations, anions, electrons)) through the oxide and possibly the metal. Diffusion of species through the oxide layer is generally considered as the kinetically limiting step of corrosion. Several types of mechanisms have been proposed, based either on diffusion process or on empirically constructed from oxidation kinetics. In the following paragraphs, focus is made on the long-time oxidation kinetics of the oxide scales, since those were much more studied than short-time oxidations.

Over the years, many authors concluded that the inner oxide grows with an anionic diffusion mechanism. Terachi et al. made the hypothesis that the inner oxide growth by an anionic diffusion phenomenon by observing the metal/oxide interface [27]. Perrin et al. using isotopic analysis studied the oxygen diffusion coefficient and the inner oxide growth mechanism [4]. They concluded that the inner oxide is growing by anionic diffusion through grain boundaries of the oxide. Dumerval also confirmed such mechanism using a gold deposit [5]. On the other hand, the outer oxide grows with a cationic diffusion mechanism and the medium-cation saturation plays a role in the crystallites dissolution and precipitation [27, 28]. Indeed, cations (especially iron and nickel) can be released into the medium and can then re-precipitate undergoing sursaturation in the boundary layer [4, 20, 21, 41].

Wagner: Solid state diffusion

Wagner's solid state diffusion model was proposed in 1933. Resulting from work on the oxidation of metals in dioxygen environment at high temperatures (> 400 °C), it allows to correlate the oxidation kinetics and the transport properties of the oxide. This model is based on the simultaneous transport of ions and electrons in the oxide layers. The growth of the oxide film is ensured by the ion diffusion in the metal thanks to crystalline defects. Wagner's theory allows to describe the formation of a compact, adhesive and protective oxide. However, this model requires a number of somewhat restrictive assumptions, which leads to a limitation of the number of applications of the model. For example, the model was established for a mono crystal without any grain boundaries. This model is also only valid for the formation of thermal oxide films in

air. But Wagner's theory served as a basis for several other models: Mott [42–44], Mott-Cabrera [45], Fehlner-Mott [46], McDonald's PDM [47–51], Bojinov's MCM [52–55] and the generalised Marcus-Seyeux model [56].

Macdonald: Point Defect Model

Macdonald's Point Defect Model (PDM) is taking the punctual defects into account [47–51]. This model is based on the idea that the main species involved in the growth of the oxide are these point defects and more particularly the vacancies (cationic and anionic). In this model, the passive film, developed on the surface of a metal, has a duplex structure. The inner layer acts as a protective barrier regarding the diffusion of metal species. It contains different types of defects: cationic vacancies ($V_M^{\chi'}$), interstitial cations ($M_i^{\chi+}$) and oxygen vacancies ($V_O^{\cdot\cdot}$). The outer layer is formed by hydrolyzing the cations leaving the barrier layer. The protective inner layer growth is then carried out by a vacancy mechanism: the transport of the species is effected by passing an atom from an occupied position of the lattice to another vacant site. The inner oxide growth is essentially due to the anionic vacancies migration whereas the dissolution of the metal is essentially due to the migration of the cationic vacancies and interstitials.

Regarding the 316L exposed to PWR medium, the PDM can be described as presented in Figure 1.3. Metallic species (M = Fe, Cr, Ni for example) will react at the metal/oxide interface and inject in the oxide interstitial cations ($Fe_i^{\chi_1+}$, $Cr_i^{\chi_2+}$), oxygen vacancies ($V_O^{\cdot\cdot}$) and cations in cation sites (Fe_{Fe}, Cr_{Cr}) while consuming cationic vacancies ($V_{Fe}^{\chi_1-}$, $V_{Cr}^{\chi_2-}$) and leaving vacancies in the alloy (V_m). These anionic vacancies will generate oxygen ions in anion sites (O_O) by reacting with water at the outer interface and oxygen will then migrate inward. Chromium, iron and oxygen in cation or anion sites will lead to the inner oxide growth. Interstitial cations (such as iron) will migrate through the inner oxide and annihilate at the oxide/solution interface. Doing so, aqueous iron cations will be released into the solution ($Fe_{(aq)}^{\delta_1+}$) forming the outer oxide by precipitation phenomena. Cations in cation sites will also generate aqueous cations as well as cation vacancies in the oxide at the same interface. These cation vacancies will tend to migrate toward the metal/oxide interface and react with metallic species as described previously, leading to vacancies in the alloy, therefore contributing to the metal dissolution.

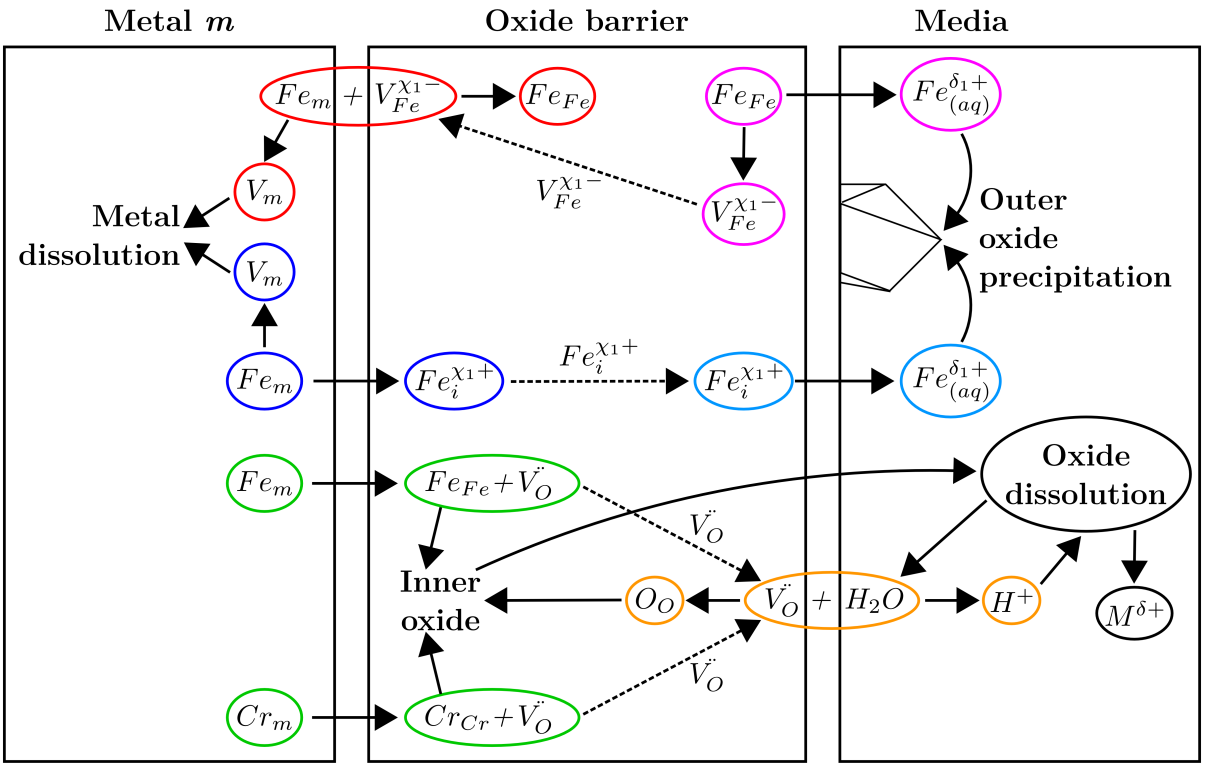

Reactions at the metal/oxide interface

(1) $m + V_M^{\chi'} \xrightarrow{k_1} M_M + V_m + \chi e'$

(2) $m \xrightarrow{k_2} M_i^{\chi+} + V_m + \chi e'$

(3) $m \xrightarrow{k_3} M_M + \frac{\chi}{2} V_O^{\cdot\cdot} + \chi e'$

Reactions at the oxide/media interface

$M_M \xrightarrow{k_4} M_{(aq)}^{\delta+} + V_M^{\chi'} + (\delta - \chi)e'$ **(4)**

$M_i^{\chi+} \xrightarrow{k_5} M_{(aq)}^{\delta+} + (\delta - \chi)e'$ **(5)**

$V_O^{\cdot\cdot} + H_2O \xrightarrow{k_6} O_O + 2H^+$ **(6)**

$MO_{\frac{\chi}{2}} + \chi H^+ \xrightarrow{k_7} M^{\delta+} + \frac{\chi}{2} H_2O + (\delta - \chi)e'$ **(7)**

Figure 1.3: *Simplified schematic of Macdonald's model applied to the studied system with M = Cr and Fe (according to Macdonald [50]) with $V_M^{\chi'}$ cation vacancy, $M_i^{\chi+}$ cation interstitial, $V_O^{\cdot\cdot}$ oxygen (anion) vacancy, $M_{(aq)}^{\delta+}$ cation in solution, M_M cation in cation site on the cation sublattice, O_O oxide ion in anion site on the anion sublattice, $MO_{\frac{\chi}{2}}$ stoichiometric barrier layer oxide, arrow: reactions, dotted arrow: species migration*

➔ Focused Ion Beam (FIB) walls observations will permit to confirm the duplex character of the oxide. However, the presence of vacancies and interstitials in the oxide and the alloy cannot be highlighted using TEM.

Nevertheless, if the model takes into account punctual defects, it does not take into consideration diffusion short-cuts, such as nanopores or grain boundaries across the oxide grains. Therefore, Castle and Masterson's model as well as Robertson's model are presented in the following paragraphs.

Castle and Masterson: Nanopores model

This model was developed from the study of mild steel samples oxidised in alkaline or acidic medium at 300 °C by Castle and Masterson [57]. The oxide observed at the surface of the samples is duplex, with an outer layer of magnetite. Yet for the inner layer of the oxide to grow, oxygen must be able to diffuse through the oxide layer to react with the metal/oxide interface. Potter and Man were one of the first to offer the hypothesis that the inner oxide is formed

by oxygen anionic solid state diffusion [19]. However, it appears that the diffusion coefficient of the O^{2-} ions in the outer oxide (magnetite Fe_3O_4) is much too low to explain the speed of corrosion kinetics and thus solid state diffusion cannot solely explain the oxidation kinetic. Castle and Masterson model predicts an interconnection between the metal surface and the medium through pores [57]. Such pores in the inner oxides are able to play the role of diffusion short-cuts. The medium can therefore take these diffusion paths and would access the metal/oxide interface via the pores in the oxide. Thus, the species can circulate in both directions: the oxidising species (OH^-) can reach the metal/oxide interface and come into contact with the metal, and conversely, the ferrous ions can reach the surface (cf Figure 1.4). Indeed, the iron dissolved in the pores, diffusing outward would precipitate on the outer layer. Such diffusion in liquid phase through the pores would be the limiting step of the oxidation kinetic growth. This model has flaws since one of its hypothesis is that no cation release happens. Moreover, thickness ratio between the inner and outer layer is supposed to be one in the model but cannot be considered a constant since it changes with the experimental conditions. Thus, the assumption that half of the cation participates to the inner oxide growth and the other half to the outer oxide one cannot be considered true. Finally, porosity is depending on the iron solubility in the corrosive environment and when this solubility is weak no oxide porosities were observed. Since the whole model is based on the presence of porosities and none were ever observed in PWR medium to the author knowledge it constitutes a real drawback.

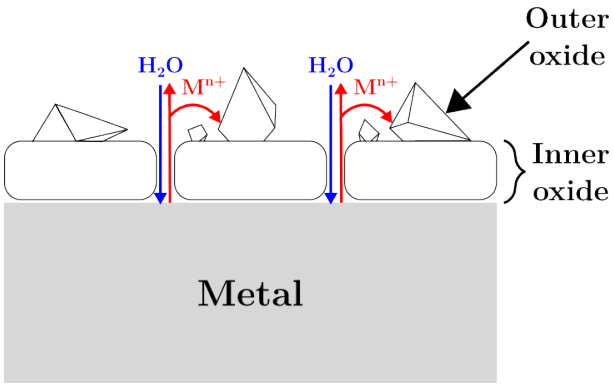

Figure 1.4: *Schematic of Castle and Masterson's model with diffusion of H_2O and cation metal through nanopores of the oxide (according to Castle and Masterson [57])*

Evans proposed a pore obstruction by precipitation phenomenon model [58]. This model is based on results of carbon steels in an alkaline medium, for temperatures above 250 °C showing a slowdown over time in the corrosion kinetics. These observations were later confirmed by Harrison [59]. The proposed mechanism involves the coupling of a liquid phase transport mechanism in the pores of the oxide with the possibility for these pores to become progressively clogged during oxidation time. The pores obstruction is supposed to be due to the precipitation reactions that can take place within the pores. Concerning the phenomenon of pores blockage, two mechanisms are envisaged. The first, self-locking pores, corresponds to the progressive closure of the pores during the growth of the oxide, leading to a slowing down of the oxidation rate. In the long term, this metal loss tends to reach a constant value, corresponding to the thickness reached by the oxide during its growth. The second mechanism envisaged by Evans corresponds to a "mutual blocking" of the pores. The pores adjacent to precipitation zone will end up closing under the effect of the compression stress generated by the precipitation. The main fault of this mechanism is that no experimental fact accredits this assumption since no pores were ever observed, to the author knowledge, in stainless steels oxidised in PWR medium.

➔ TEM observations of the oxide should allow to confirm or deny the nanopores presence in the oxide if these are big enough to be imaged.

Robertson: Grain boundary diffusion

Robertson offers to reconsider Castle and Masterson model and proposes a new one based on a solid phase limiting process to describe the growth of the oxide [60, 61]. In this model, the inner oxide consists of small and equiaxed grains and is growing toward the metal at the metal/oxide interface. Its growth requires that oxygen must attain the interface. Roberson supposes that the inner oxide still grows by the access of water to the metal through pores in the oxide. The growth of the inner oxide would thus be happening at the metal/oxide interface via oxygen diffusion through nanopores/grain boundaries (Figure 1.5). For Robertson, the diffusion of cations needed to form the outer oxide occurs through grain boundaries acting like diffusion short-cuts. It is this outward diffusion of cations at grain boundaries that would be the limiting process of the inner layer growth. However, the parabolic law offered in this model does not seem to correspond to the growth kinetics of the inner oxide observed by Machet [62] or Carrette [63].

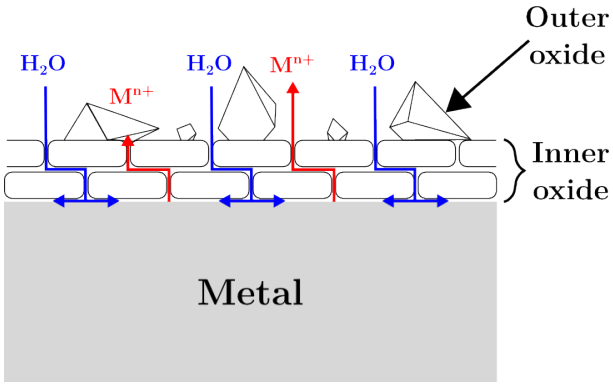

Figure 1.5: *Schematic of Robertson's model with diffusion of H_2O and cation metal through nanopores or grain boundaries of the oxide (according to Robertson [61])*

➔ Soulas recently demonstrated that the inner oxide is monocrystalline on each metal grain [13]. This result is at variance with Robertson model. TEM observations of the oxide should allow to confirm or deny the grain boundaries presence in the oxide and their density should affect the oxidation kinetic.

Lister: Dissolution and precipitation phenomenon

Lister et al. were the first to introduce the notion of species release in an aqueous medium in a model (Figure 1.6) [21]. This is based on experiments using radio tracers on type 304L stainless steels in aqueous medium lithiated at high temperature. Tests in a recirculation loop made it possible to highlight the effects of the metallic species saturation on the outer oxide growth and on cations release. Samples were exposed to cations saturated water and then to corrosion-free water and vice versa. Such corrosion sequences allowed to highlight that corrosion product released into the medium play a role on the outer oxide morphology. Crystallites were observed after oxidation in saturated medium whereas none were seen after oxidation in the unsaturated medium. Oxidation in unsaturated medium did not lead to the formation of a duplex layer, but only to the formation of a single and continuous chromium rich layer. When exposing samples firstly in saturated and then unsaturated medium, no outer layer was present, indicating that it was dissolved into the medium. By exposing the samples the other way around, once again no crystallites were observed. Thus, the precipitation of the outer oxide, although connected to the medium saturation should not occur if an inner layer is present. It would indicate that once the inner oxide is formed and established, it prevents the outer layer from growing. Therefore, the growth of the outer layer is not only due to the species present in solution but also there is a contribution from the diffusion of species through the inner layer. Lister assumes that all metal cation that cross the inner oxide layer does not fully participate in the formation of the outer

layer and that some are released into the water. The presence of external crystallites is therefore the product of two different mechanisms: the precipitation of ions released previously and of the cations diffusion through the inner layer. Lister model is then based on the existence of the diffusion of solid-phase metal ions in the inner layer, as in the case of Robertson's model. The model considers that all metal species passing through the inner oxide layer are not all released once they reached the oxide/solution interface, and that a part could participate in the formation of the outer layer. In addition, it requires the presence of nucleis of a different nature from those of the inner layer.

In conclusion, for Lister two conditions have to be meeting for an outer oxide to grow:
- The metal must not have chromium inner oxide prior oxidation acting as a barrier
- The medium must contain species present in solution

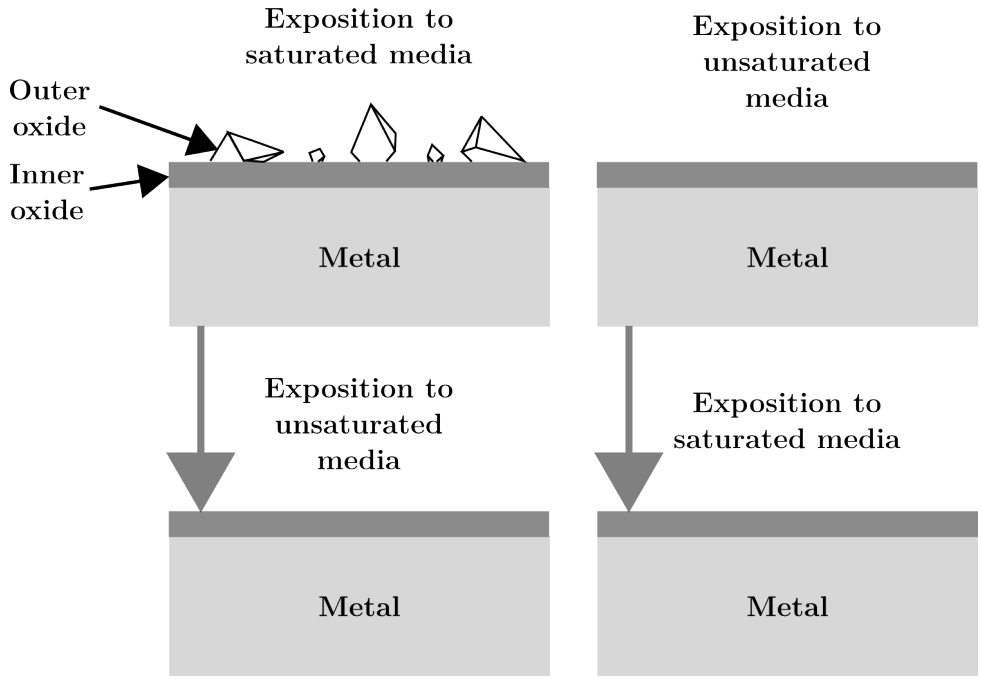

Figure 1.6: *Schematic of Lister's outer oxide growth model for alloys exposed to saturated and unsaturated water (according to Lister [21])*

Perrin et al. confirmed Lister's allegations by testing samples in a stainless steel loop and then in a titanium autoclave (without cation saturation) [4]. The outer layer formed in the stainless steel loop is dissolved after a short corrosion test in the titanium autoclave. If a longer oxidation is performed in the titanium corrosion device, a new outer layer will form on top of the inner layer after the dissolution of the one formed in the stainless steel loop. They concluded that the nucleation and growth of the outer layer is dependent on the substrate (metal or oxide) on which it grows.

However, few authors observed duplex oxide layers using titanium loop with unsaturated medium [13, 23, 64, 65]. Nevertheless, one should remember that local saturation of the boundary layer may act as saturated medium but the oxidation kinetic should be faster in fully saturated medium.

➔ Oxidation in a titanium recirculation loop and Scanning Electron Microscopy (SEM) observations of the sample surface should allow to confirm or deny Lister's allegations. According to this mechanism no outer oxide is supposed to form if the sample is exposed to unsaturated water. Nonetheless, local surstaturation might occur, still resulting in oxide precipitation.

Oxidation mechanisms:

- Inner oxide grows at the metal/oxide interface thanks the diffusion of anionic vacancies.
- Outer oxide grows by cationic diffusion through the inner oxide and precipitation of the cations present in solution. In unsaturated media, no outer oxide is formed according to Lister's model but this allegation is disputed. Nevertheless, the oxidation kinetic is supposed to be slower in unsaturated media.
- Nanopores or grain boundaries of the oxide might act as diffusion short-cuts for the vacancies but nanopores are yet to be seen on stainless steels oxidised in primary water.

1.1.1.4 Effect of short oxidation times

Machet is one of the few authors that have studied short oxidation times in PWR medium [62]. His work was based on 600 and 690 nickel based alloys for oxidation of less than 10 minutes. He developed a model based on three steps, with a first one regarding the oxide scale formation and the next two for the oxide growth (blocking and then resuming of the growth). On the 690 alloy, the chromium rich oxide layer is almost instantaneously created, afterward a blocking of the oxide growth occurs before a resumption of the oxide scale growth.

During his work, Soulas described the morphological, chemical and structural evolution of the oxide layers depending on the oxidation time for short oxidation times [12]. Samples were oxidised in PWR medium in a titanium loop to avoid redeposition phenomenon for oxidation times ranging from 1 minute to 24 hours. Figure 1.7 presents the evolution of the oxide scale as presented by Soulas. The film instantaneously formed in contact with the ambient air is passive (step 1). After 1 minute oxidation, the oxide is duplex as suggested in the literature (step 2). Globular crystallites are formed during the first step before becoming faceted as the oxidation time increases. These crystallites exhibit a clear preferential crystallographic orientation only after 24 hours oxidation. The inner layer, initially amorphous, passes in a nanocrystalline state (steps 3 to 6) before becoming monocrystalline (step 7). This inner layer gradually enriched in chromium between 2 and 10 minutes of oxidation. From a ratio Cr/Fe at 0.38, it will evolve into a ratio close to 1. In parallel the inner oxide crystallises and nanograins appear (step 3). The crystallisation carries on until the monocrystalline state is reached. Several nanograins will then start to create an epitaxial relation with the substrate. The oxide nanograin growth starts parallel to the interface oxide/metal by reduction of the interface energy until a single crystal is formed at this interface (step 5). Then the growth will continue perpendicularly to the interface (step 6). At this state, the inner oxide is in an epitaxial relation with the underlying metal grain. Depending on the crystallographic orientation of the underlying metal grain the oxidation kinetic is modified. Indeed the energy needed to form the oxide layer depends on the amount of misfit dislocations between the alloy and the oxide and this is depending on the metal orientation. According to Soulas, the equilibrium inner oxide is a $Fe_{1,5}Cr_{1,5}O_4$ spinel and the outer one is composed of magnetite (Fe_3O_4) which is also a spinel structure.

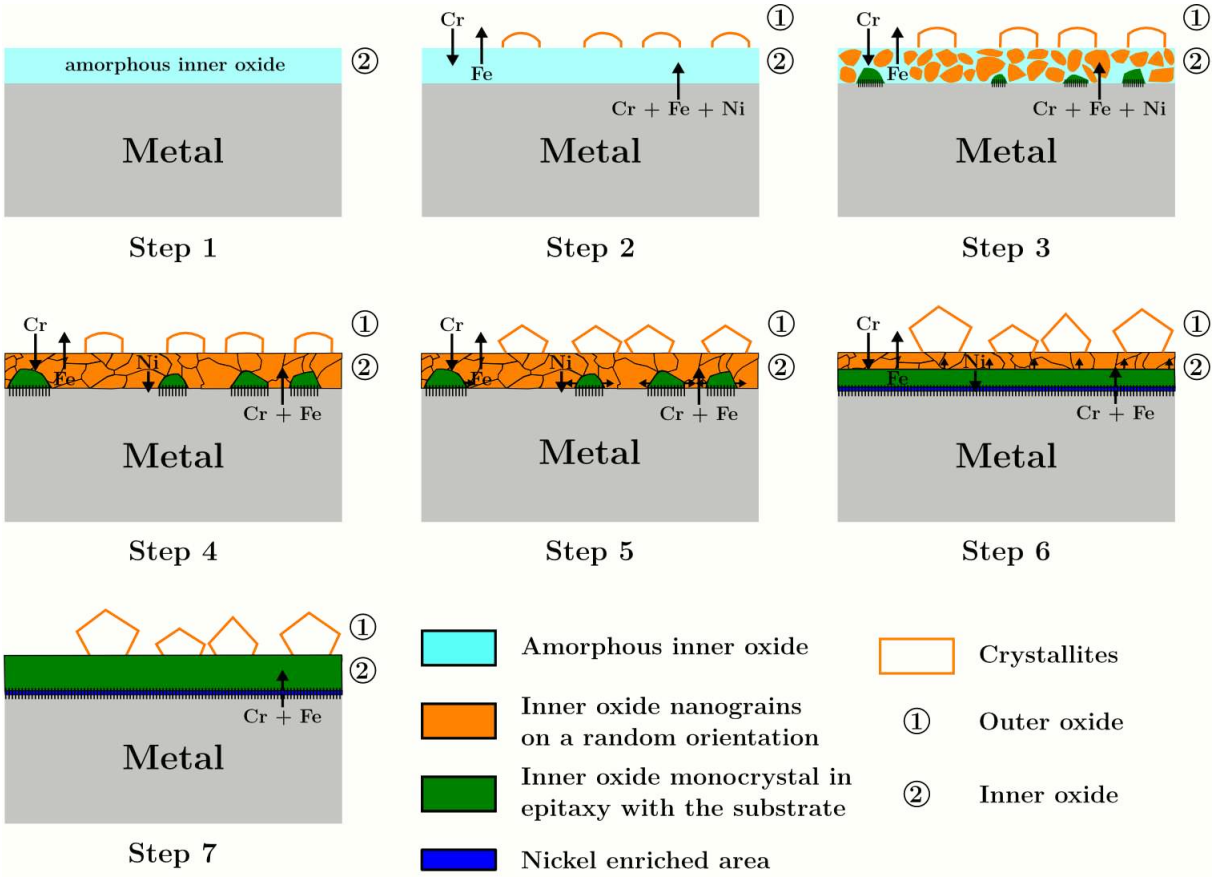

Figure 1.7: *Schematic of the inner layer crystallisation process on 316L stainless steel exposed in PWR medium during short time oxidation (according to Soulas [12])*

Effect of short oxidation times:

- The outer oxide tends to become bigger and faceted as the oxidation time increases.
- The inner oxide, initially amorphous, will become nanocrystalline and then monocrystalline with an epitaxial relationship with the metal grain underlying while enriching in chromium.

1.1.2 Parameters affecting stainless steels oxidation

If the understanding of the corrosion mechanism is essential, the parameters that can influence the oxidation kinetic and the oxide layers formed are numerous and have to be taken into consideration. Below are developed the parameters involved in this study but several others are not depicted below. For example, the alloy composition and especially the chromium content was studied among other by Terachi [27]. The effect of alloy grain size on the oxidation process was studied by several other but still remain unclear [66, 67].

1.1.2.1 Surface state and cold-work

Warzee et al. were of the first to introduce the surface state effect on the oxidation kinetic of stainless steels [68]. Their study was made on stainless steels oxidised in high-temperature water and steam for different surface states (polished with 600 grit paper, milled, ground and electropolished samples). The cold-work depths were measured using the half-width of the (111) austenitic line from X-Ray Diffraction (XRD). Hence, the polished sample had a cold-work depth

of 2 µm against 6 µm for the ground specimen whereas the milled one was still thoroughly cold-worked at a depth of 30 µm. The oxidation times ranged from 300 to 2000 hours and the metal losses are presented in Figure 1.8. They observed different behaviour between aqueous medium and steam oxidation. Thereby, the electropolished samples were the less oxidised as opposed to the three other samples for the oxidation in water while they were the most oxidised in steam due to the temperature difference. For both medium it is difficult to make assumptions on the oxidation kinetics of the polished, milled and grinded samples since they appear very close and no measurement uncertainties are presented. The oxidation kinetic is then depending on the surface state but have to be compared with care for different oxidation environment.

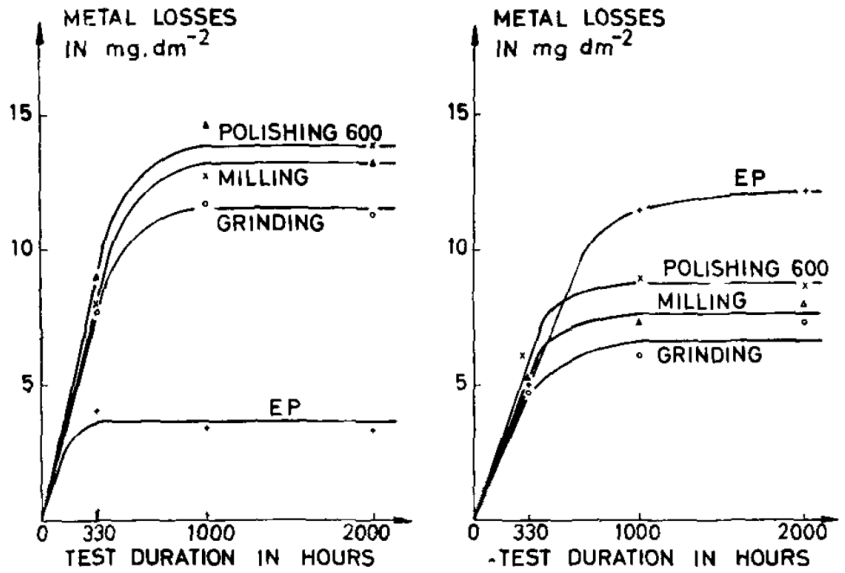

Figure 1.8: *Oxidation kinetic of a 304 alloy depending on its surface finish for a) water at 300 °C and b) steam at 400 °C, 200 kg/cm^2 [68]*

For Ziemniak et al. the corrosion rate is lowered by a factor greater than three on the electropolished surface compared to machined surface [69]. They concluded that since the surface microstrain is removed with the electropolishing, the inner oxide will have a more uniform growth and that it will decrease the porosity of the oxide and thus the oxidation kinetic. Indeed, the presence of strains, creates preferential nucleation sites for nucleation and growth of the inner oxide. As for the outer layer, the oxide is bigger but less crystallites are observed on cold-worked samples compared to electropolished surfaces.

Most authors, comparing mechanical polishing and electrochemical polishing agree that the corrosion rate increase with the degree of cold-work [41, 66, 69–71]. For the electrochemical polishing the oxidation kinetic is slowed down since a protective chromium rich layer is formed during the polishing. This kind of preparation does not induce any defect or cold-work in the material and create a barrier leading to a thin oxide scale formed in PWR or aqueous conditions. Several other authors [7, 10, 11], were able to compare different cold-work surfaces and their consequences on the corrosion layer formed for samples oxidised in PWR medium. Since the sample preparation can induce a certain amount of cold-work in the material close to the surface, it is a necessity to understand the impact of the sample preparation onto the observed oxides. A mechanical polishing might induce a residual hardening of the material at the surface. Doing so, a recrystallised area of nanograins may be formed at the surface [7, 11, 30, 63, 72].

Cisse compared polished down to Oxide Polishing-Silica (OP-S) samples and ground ones oxidised in PWR medium 500 hours at 340 °C [10]. She observed a thinner inner oxide on the

ground sample who had a deep nanograin structure below the inner oxide ($\sim 1.5\,\mu m$). The polished sample also possessed such a recrystallised area while being three times thinner ($\sim 500\,nm$). According to Cisse, the bigger the recrystallised area is, the thinner the inner oxide is. In Ghosh et al. study, solutions annealed machined, ground and reference (polished down to $0.1\,\mu m$) samples after a 360 h oxidation at 300 °C are compared [11]. The oxides formed on cold-work samples (machined and ground) are richer in chromium while thinner agreeing to Cisse's results. Indeed, the ground sample possessed an inner layer of $0.32\,\mu m$ and was the most cold-worked, the machined sample had an inner layer of $0.6\,\mu m$ while it was $1.2\,\mu m$ thick on the reference sample. Gupta compared vibratory polished with OP-S samples (without cold-work induced) and mechanically polished (down to $0.25\,\mu m$) ones oxidised 360 hours in PWR medium at 320 °C [7]. As observed by several authors, a nanograin area of about $1\,\mu m$ was found on the mechanically polished sample whereas none was detected on the vibratory polished sample. As opposed to Cisse and Ghosh results, she observed a thicker oxide on the cold-work samples. However, as Cisse and Gosh, Gupta showed that the oxide layer formed on the cold-work sample is richer in chromium. The higher density of grain boundaries in the material would enhance the outward diffusion of cations leading to this thicker oxide.

All authors agree that the cold-work leads to the formation of an inner oxide layer richer in chromium while the nanograin area influence on the oxide thickness is not clear [7, 10, 11]. Since the inner layer is formed by anionic diffusion, the presence of a high density of defects would facilitate the diffusion. And the higher density of grain boundaries in the nanograin layer would also increase the diffusion as grain boundaries are known to be diffusion short-cuts. Moreover, the defects can provide more preferential nucleation sites for the inner oxide formation. The more the sample possesses a deep nanograin area, the more the oxidation kinetic will be slow down since the diffusion processes are faster and the nucleation sites are plentiful; thus the inner oxide will be richer in chromium and established quickly. When the recrystallised area is deep the diffusion short-cuts are numerous and in depth, inducing the formation of a protective thin oxide (Figure 1.9).

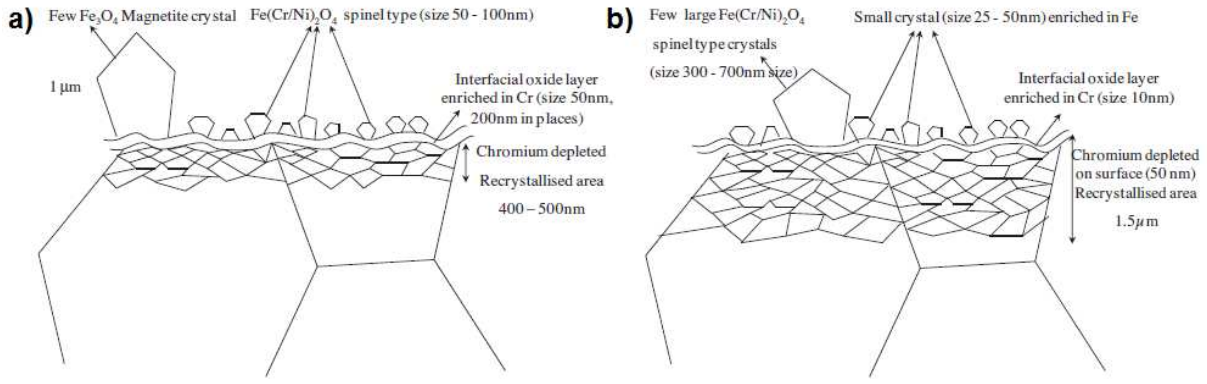

Figure 1.9: *Schematic of the oxide formed on 304L alloy exposed in PWR medium at 340 °C for 500h a) polished sample b) machined sample [10]*

The cold-work and surface finish effects on the crystallites were also investigated by other authors [7, 20, 30, 69]. They observed smaller crystallites and overall a denser oxide on electropolished samples [20, 69]. However, when the material possesses a recrystallised area the crystallites are bigger. The higher the degree of cold-work is, the smaller the crystallites are. Indeed, the more cold-work there is, the more defects are present inducing a higher number of preferential nucleation sites and overall the formation of smaller crystallites [7, 30].

In a nutshell, the material surface state before its oxidation will modify the oxide layers

formed but the aftermath of induced cold-work remains complex. To better understand this, further study have to characterise in-depth the cold-worked area before the oxidation (depth of the deformed layer, recrystallisation, presence of dislocations, etc.).

Surface state and cold-work:

- Electropolished surfaces are less sensitive to oxidation since they are defect-free and a protective passive chromium rich oxide is formed during the polishing. Overall, thinner oxides with homogenous growths are formed on top of electropolished samples.
- Cold-worked materials possess superficial layers with high strain and high density of dislocations as well as subgrain boundaries. These can act as short-cuts for the outward diffusion of cation and the inward diffusion of oxygen.
- Defects create preferential sites for the nucleation and growth of the inner oxide.
- Mechanical polishing could induce a nanograin layer leading to inner oxides richer in chromium due to the presence grain boundaries diffusion short-cuts. However its influence on the oxide thickness remains unclear.
- Cold-work provokes the formation a numerous small crystallites since defects may act as preferential nucleation sites.

1.1.2.2 Chemistry of the medium and installation effect

As previously stated, primary water environment contains boric acid in order to absorb neutrons and control, as well as reduce, the reactor core reactivity since boron is a neutronic poison. Lithium is also added to adjust the pH of the medium to a slight alkaline value. The influences of pH, as well as lithium/boron contents in the medium are still subjected to questioning.

Mazenc studied the influence of the chemistry of the medium on the corrosion and dissolution of corrosion products for a 690 nickel based alloy [64]. He showed that pH modify the oxidation kinetic. Sun et al. studied the effect of pH on the electrochemical behaviour of the oxide layers formed in a simulated PWR medium [73]. They concluded that thinner and more protective oxides are obtained for higher pH (alkaline solution). Dupin also came to the same conclusions, thicker oxides are formed on samples exposed to media with lower pH and chromium content in the oxide decreases with the pH increases [74]. Thus, pH influences the oxide thickness and might influence its composition. The boron content also modifies the oxidation kinetic and the oxide thickness. An increase in the boron content seems to lead to thinner oxides and to slow the oxidation kinetic. Moreover, the boron content in the oxide increases when this content is increased in the medium. No effect on the composition of the oxide was found by Mazenc apart from the boron enrichment.

Hydrogen is introduced in the desaerated water to provide a less oxidising medium in PWRs environment and reduce water radiolysis. This hydrogen added into the medium also comes, in lesser quantities, from the oxidation reaction (metal oxidation and reduced water). Few authors investigated the influence of dissolved hydrogen/oxygen as well as hydrogen peroxide contents on the oxide scale formed. Among them, the effect of water chemistry on the oxidising behaviour of 316L alloy was investigated by Chen et al. [32]. Their study included hydrogenated, deaerated and oxygenated primary waters at 310 °C. The oxide layers formed in deaerated and hydrogenated environments are similar in composition but possess different morphologies. In hydrogenated and deaerated water spinel oxides are formed while in oxygenated water both spinel and hematite (α-Fe_2O_3) are identified from Raman spectra. In addition, the morphology of the

outer layer is extremely dependent of the medium in which it is oxidised as visible in Figure 1.10. In hydrogenated water the distribution of the outer oxide is inhomogeneous with numerous crystallites of various sizes. For the outer oxide formed in deaerated medium, the crystallites are well-shaped and faceted but are less numerous and dispersed. Finally, in oxygenated water the crystallites are globular and numerous. The inner oxide formed on the sample exposed to oxygenated water was nickel-rich and porous as opposed to the inner layers formed on samples exposed to hydrogenated or deaerated environment which were chromium rich without porosities. The author found a higher inner oxide thickness on the samples exposed in deaerated and oxygenated water than on the sample exposed in hydrogenated water. However, all samples were exposed to their medium for different durations so the inner oxides thickness are to consider with care.

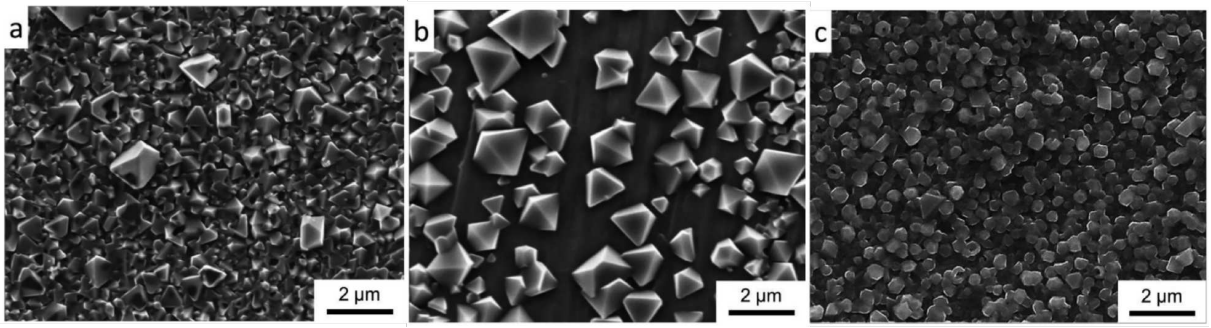

Figure 1.10: *SEM images of the outer oxide morphology formed on 316L alloy exposed to various primary water a) hydrogenated 500 hours, b) deaerated 1170 hours and c) oxygenated 1012 hours [32]*

In a nutshell, H_2O_2 [75, 76] and dissolved O_2 [32, 73, 76, 77], have been shown to affect the corrosion of stainless steels. Adding O_2 and H_2O_2 to the water engenders a significant decrease of the Cr content in the oxides (compared to the ones formed in hydrogenated water) while inducing hematite (Fe_2O_3) formation (Fe_3O_4 in hydrogenated water). Moreover, oxides formed in oxygenated water and water containing H_2O_2 are thicker than the ones formed in hydrogenated water [32, 76].

Regarding the installation, as previously seen in section 1.1.1.3, the oxide layer depends upon the loop material. Indeed, in stainless steel corrosion devices, the medium will be saturated thanks to the release of cations from the loop. In titanium loop the medium is believed to be unsaturated since the only release that can take place is the one from the exposed samples and such loops are often designed with big enough mixing tanks or ions-exchange resins to keep an unsaturated medium. Nevertheless, one should remember that local saturation of the boundary layer may act as saturated medium and thus crystallites could form thanks to cation precipitation. Therefore, the usage of a stainless steel loop should lead to the formation of a thicker outer oxide.

Overall, the chemistry of the oxidising medium can alter the oxide layer so one should keep in mind that modifying the medium can influence the oxide. Nonetheless, each contribution is still not well understood. The loop material can affect the oxide formed and comparisons between corrosion devices should be handled with care.

Chemistry of the medium and installation effect:

- Thinner oxides are formed at higher pH.
- O_2 and H_2O_2 contents in the medium engender thicker oxides and a decrease of the inner oxide chromium content as well as hematite formation.
- The loop material influences the medium saturation and thus the oxide layer (formation and/or thickness) since the outer oxide is believed to form thanks to cation precipitation.

1.1.2.3 Crystallographic orientation of the metal

Several authors such as Warzee, Moore and Gardey [68, 70, 78], observed that the crystallographic orientation of the underlying metal grain modify the oxidation kinetic of nickel-based alloy. An epitaxial relation is mentioned but no mechanisms are offered. Moreover, such observations were made for quite long oxidation times. For the sake of clarity, in the following, the terms "grain oriented [100]" or "[100] grain orientation" mean "grain having the vector <100> as the normal vector on the surface" and so on for the [110] and [111] orientations.

Miget observed different outer oxide morphologies and sizes, depending on the crystallographic orientation of the underlying metal grain (Figure 1.11) [66]. He supposed and demonstrated the presence of an epitaxial relationship between the metal and the oxide layers. Using TEM diffraction, he showed that the metal grain and crystallite orientation were identical and that an orientation relationship cube/cube is present. To this end it is necessary for the crystallographic orientation information to be transmitted through the inner layer, from the metal to the external oxide. The inner oxide layer must therefore have an epitaxial growth on the metal grain. Such epitaxy would favour the nucleation and/or growth of the outer oxide by accommodating the crystal lattices and the cations diffusion in preferential directions in the oxide. Continuing the work of Gardey [70], Miguet demonstrated that [100] and [111] grain orientations possess a lower outer crystallites density than [110] grains.

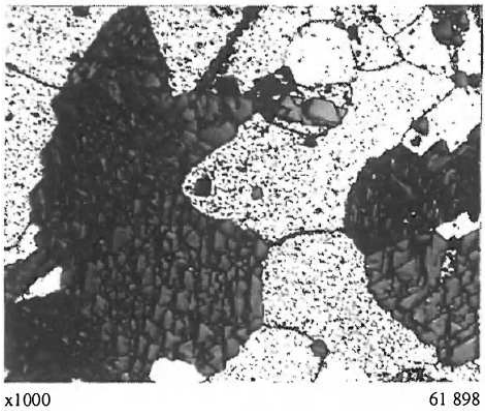

Figure 1.11: *SEM image of the outer oxide morphology formed on 600 alloy exposed to primary water during 1169 hours with outer oxide densities and morphologies depending on the underlying metal grain [66]*

Soulas was the first to study the setup of this epitaxial relation for short oxidation times on austenitic stainless steel [12]. Regardless of the grain orientation ([100], [110] and [111]), the epitaxial relation was found to be cube/cube type. This epitaxy is made possible thanks to a residual elastic deformation of the metal which accommodates the parametric misfit. Thanks to misfit dislocations, the theoric parametric misfit between the two lattices decreases and a residual elastic stress in the metal makes up for this parametric misfit. The number of dislocation needed

to accommodate the metal/inner oxide differ, depending on the grain orientation, modifying the energy to be brought to form the epitaxial relation. Soulas found that the [111] grains need fewer dislocations to accommodate the interface than the [110] (network of dislocations every 7 planes vs 5 planes). Thus the inner oxide growth is faster on [111] grains since they need less energy to be accommodated and this oxide will be thicker on this grain orientation. According to him, [111] grain orientation possesses the lower residual elastic stress of the three investigated orientations. However, crystallites possess the opposed kinetic. They will grow faster being bigger on [110] grains since the cation diffusion is faster when the oxide is nanocrystalline. Figure 1.12 present the growth of the oxide layers depending on the metal grain orientation according to Soulas. Soulas' conclusion regarding the outer layer is in agreement with Miguet [66] results on austenitic nickel based alloys.

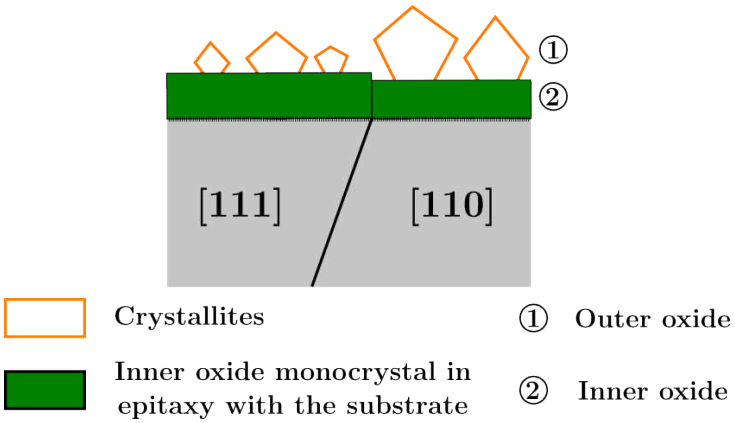

Figure 1.12: *Schematic of the oxide scales growth on [111] and [110] grain orientation [12]*

Recent work by Matthews and al. once again confirms that the inner oxide thickness is strongly dependent on the underlying grain orientation (Figure 1.13) [14]. They oxidised a 316L alloy in a simulated PWR environment at 320 °C during 1000 hours and observed that grains close to the [100] orientation seemed to be the more oxidised. Apart from this orientation they did not detect a great variability in the oxides thickness but several other clear grain orientations should be studied to confirm that the [100] grains are the most oxidised ones. Soulas [12], did not conclude on the same grain orientation for the preferential oxidation but its work was conducted for short oxidation times and thus the growth kinetic might change overtime.

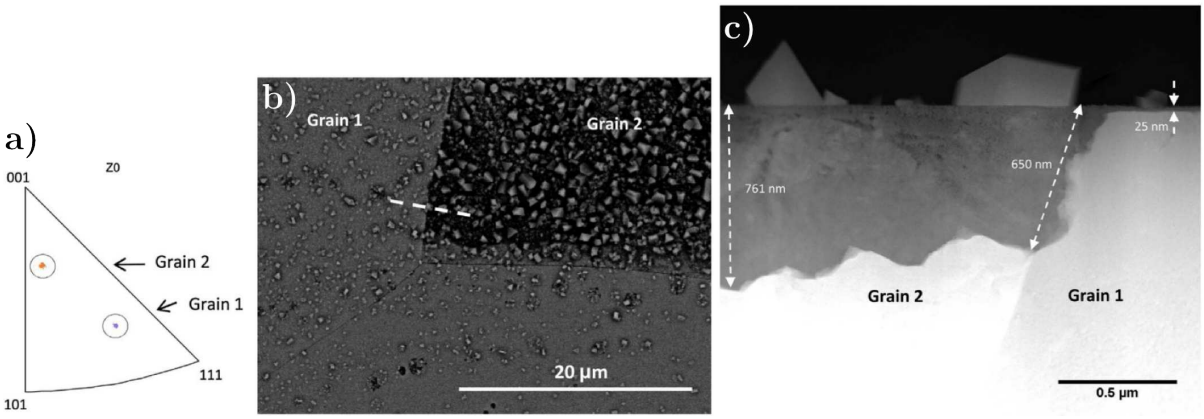

Figure 1.13: *Solution annealed 316L sample exposed in PWR media at 320 °C for 1000 hours a) Inverse pole figure for grains 1 and 2 b) Back-scatter electron SEM image at 15 kV with grain 2 appearing darker indicative of a thicker inner oxide (dashed line: location of the TEM lift-out) and c) STEM HAADF image confirming the thicker inner oxide formed on grain 2 [14]*

Overall, the inner and outer oxide thickness and their oxidation kinetic is dependent on the

crystallographic orientation of the underlying metal grains. Moreover, an epitaxial relationship is established between the metal and inner layer. Such epitaxial growth aims to minimise the oxide formation energy by accommodating both lattices with misfit dislocations to relieve the stress induced misfit. Regarding the outer oxide, its formation and growth results from cation precipitation (cf. section 1.1.1.3) on nucleation sites but the authors cited above showed that this phenomenon goes along with an epitaxial growth of the crystallites.

Crystallographic orientation of the metal:

- The outer oxide morphology, size and density depends upon the metal crystallographic orientation. Crystallites exhibit specific morphologies depending on the underlying metal grain after 24 hours oxidation. Bigger and higher density of crystallites are observed on [110] grains.
- Presence of an epitaxial relationship between the metal and oxide layers. Misfit dislocations accommodate the lattice parametric misfits.
- The crystallographic orientation of the underlying metal grain modifies the oxidation kinetic. The inner oxide thickness depends on the number of dislocation needed to accommodate the misfit.

1.1.2.4 Irradiation

Irradiation (without water radiolysis) was not found to change the oxide structure for stainless steels oxidised in PWR medium. The oxides are still found to be a spinel inner layer chromium-enriched and a spinel outer oxide close to magnetite [7, 79].

Regarding the outer layer, irradiation defects leads to smaller but more numerous crystallites according to several authors [5, 7]. Since irradiation induces defects in the material, those can act as preferential nucleation sites for the crystallites. Deng et al. observed that with increasing irradiation dose, the outer oxide growth is enhanced (Figure 1.14) [8].

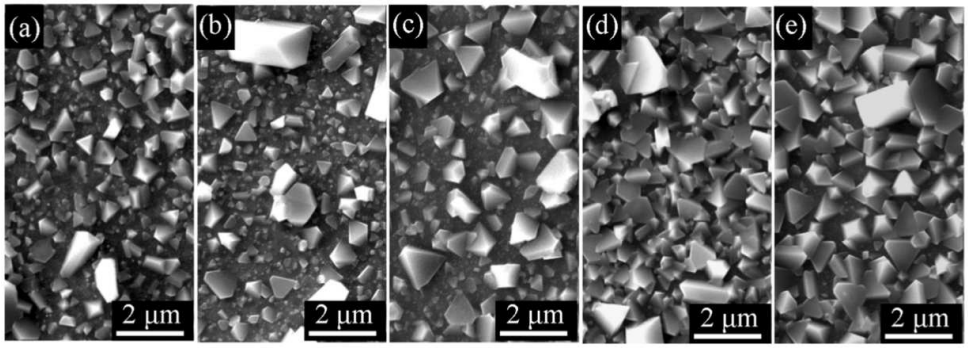

Figure 1.14: *SEM images of the outer oxide depending on the irradiation dose for 500 hours exposed samples in PWR medium at 320 °C a) Solution annealed b) 0.5 dpa c) 1.5 dpa d) 3 dpa and e) 5 dpa [8]*

Some authors observed that the presence of irradiation defects seems to induce thicker inner oxides as it was the case with cold-work samples (see section 1.1.2.1) [7, 8, 80]. Moreover, Gupta observed that the inner oxide is indeed thicker but that it is richer in chromium [7]. Deng et al. saw no inner oxide thickness differences between the solution annealed sample and the 0.5 dpa one both polished down to OP-S before the irradiation [8]. However, for higher irradiation doses the inner oxide is thicker on irradiated samples than on the solution annealed one agreeing with other works. They showed that the inner oxide thickness increases with increasing the irradiation dose (Figure 1.15). Irradiation defects may accelerate the cations diffusion inducing thicker inner

oxides. In contrast, Dumerval and Perrin observed thinner inner oxide for irradiated samples but these were also richer in chromium than the unirradiated ones [4, 5].

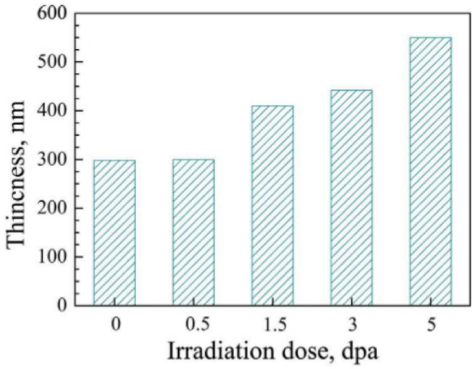

Figure 1.15: *Inner oxide thickness measured by XPS depending on the irradiation dose for 500 hours exposed samples in PWR medium at 320 °C [8]*

Using a specific installation, Raiman et al. oxidised 316L samples while irradiating them with a proton beam [81–85]. The medium was pure desaerated water containing 3 wppm of H_2 at 320 °C. The addition of 3 wppm H_2 was sufficient enough to suppress the Dissolved Oxygen (DO) content below detectable levels. Nonetheless, variations in the DO and water conductivity with the proton beam current suggested that irradiation was inducing radiolysis products in the water. The inner oxides formed on irradiated samples were found to be depleted in chromium, thinner and more porous when compared to the inner oxides on unirradiated samples. Raman spectroscopy revealed the presence of hematite (α-Fe_2O_3) solely on the surfaces of irradiated samples as no hematite was found on samples which were not irradiated. Areas which were exposed to the flow of irradiated water also exhibited inner oxide poorer in chromium and hematite on their surfaces. They concluded that water radiolysis was responsible for both effects and provoked an increase in the corrosion potential under irradiation. They also suggested that accelerated oxide dissolution is occurring under irradiation at the oxide/solution interface. According to them, the H_2O_2 production, due to radiolysis, raises the corrosion potential high enough to cause the dissolution of the inner oxide resulting in a thinner and less protective inner oxide layer on the irradiated areas.

Hanbury et al. [86], oxidised under proton flux a 316L alloy for 24 hours to 0.06 dpa in the same device as Raiman. They observed a higher outer oxide coverage on the oxidised under proton flux area compared to the unirradiated area (Figure 1.16). Moreover, the outer oxide morphologies in the oxidised under proton flux area and outside this area are different on their sample (Figure 1.16). According to them it is due to the difference in nature of the outer oxide. Indeed, they found the outer oxide in the oxidised under proton flux area to be hematite (α-Fe_2O_3) while magnetite (Fe_3O_4) is formed in the unirradiated area (Figure 1.17). Hematite was found in all area that have been exposed, according to them, to radiolysis (oxidised under proton flux area and downstream).

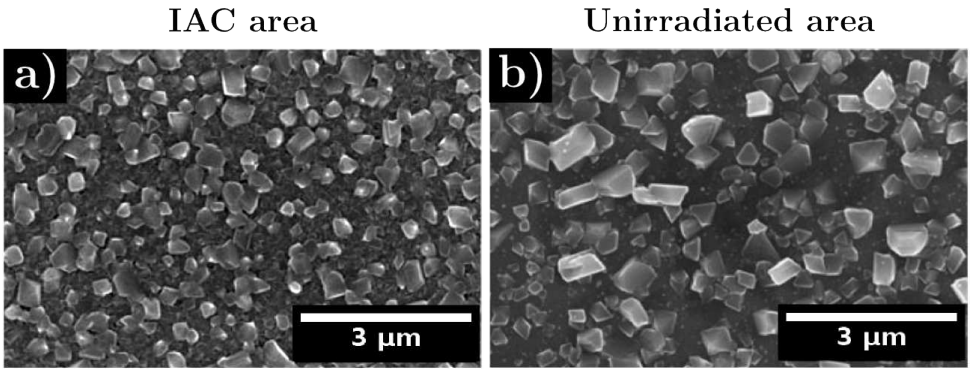

Figure 1.16: *SEM images of the outer oxide formed on a 316L alloy exposed to 320 °C water with 3 wppm H_2 for 24 hours on a) the oxidised under proton flux area and b) unirradiated area [86]*

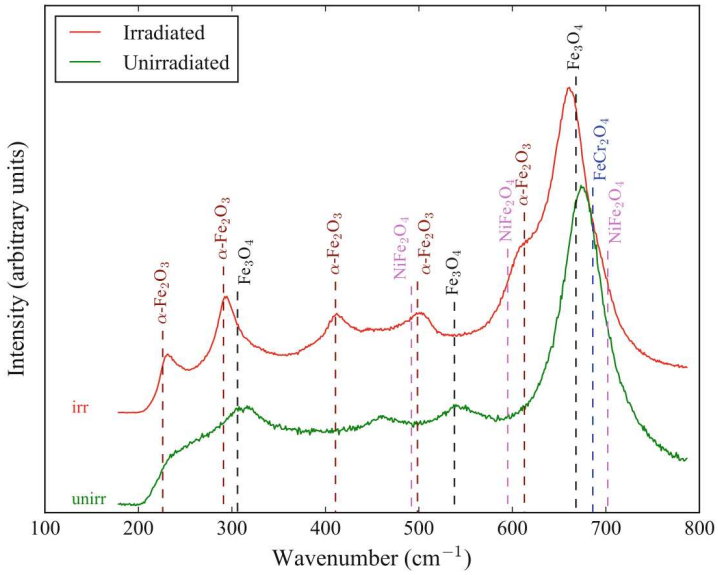

Figure 1.17: *Raman spectra of the oxides formed on a 316L alloy exposed to 320 °C water with 3 wppm H_2 for 24 hours on both the oxidised under proton flux area and unirradiated area [86]*

They also calculated inner oxide thickness ratios between two adjacent grains both in the oxidised under proton flux and unirradiated regions (Figures 1.18 and 1.19). They observed a strong dependence of the crystallographic orientation of the underlying metal grain on the inner oxide thicknesses outside the oxidised under proton flux area. The inner oxide is sometimes more than four times thicker on one grain than on the adjacent one (Figure 1.19). Nevertheless, they did not rule on a preferentially oxidised orientation but since the grain orientations were mostly random it cannot allow to conclude on a [100], [110] or [111] preferential oxidation (Figure 1.18). However, they did not draw the same conclusion on the oxidised under proton flux area. While the ratios calculated in the unirradiated area ranged mostly from 1 to 4, the ones calculated in the oxidised under proton flux area are all close to 1 (Figure 1.19). Yet the respective grain orientations of the adjacent grains on which the ratios were calculated were not given (and can potentially be close). It is then difficult to conclude from these data that crystallographic orientation does not modify the oxidation kinetic. Moreover, once again, the inner oxides thickness were measured on grains whose orientation were sometime far from the crystallographic orientation of interest of this study (ie [100], [110] and [111]).

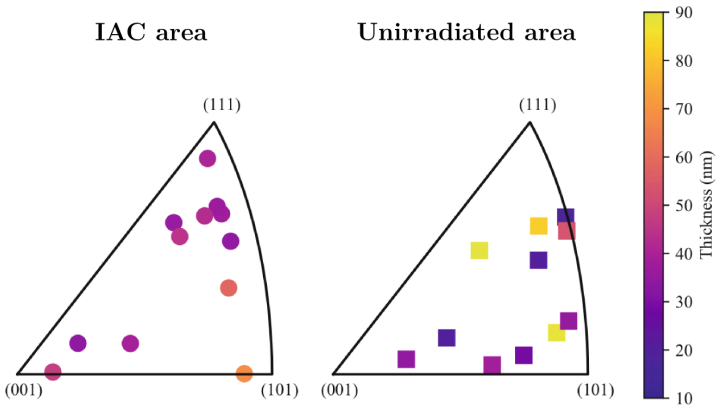

Figure 1.18: *Inner oxide thicknesses formed on a 316L alloy exposed to 320 °C water with 3 wppm H_2 for 24 hours as a function of grain orientation for both the oxidised under proton flux area and the unirradiated area [86]*

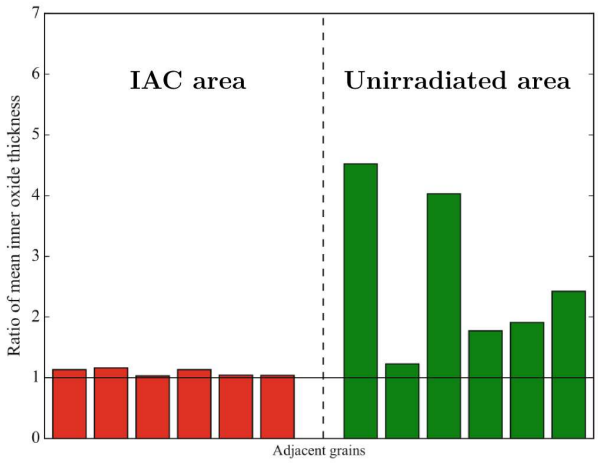

Figure 1.19: *Inner oxide thickness ratios between two adjacent grains for both the oxidised under proton flux area and the unirradiated area [86]*

Hanbury et al. observed a wavy metal/inner oxide and inner/outer oxide interfaces on the irradiated under proton flux area (Figure 1.20) [86]. Since on this area crystallites were found to be hematite they concluded that an Electrochemical Corrosion Potential (ECP) change is most likely induced by the oxidising radiolysis products. They suppose that it results in chromium dissolution since loss of original metal surface was observed. There is then a competition between oxide growth and dissolution in this region. Such dissolution would explain why no inner oxide thickness grain-to-grain differences were observed.

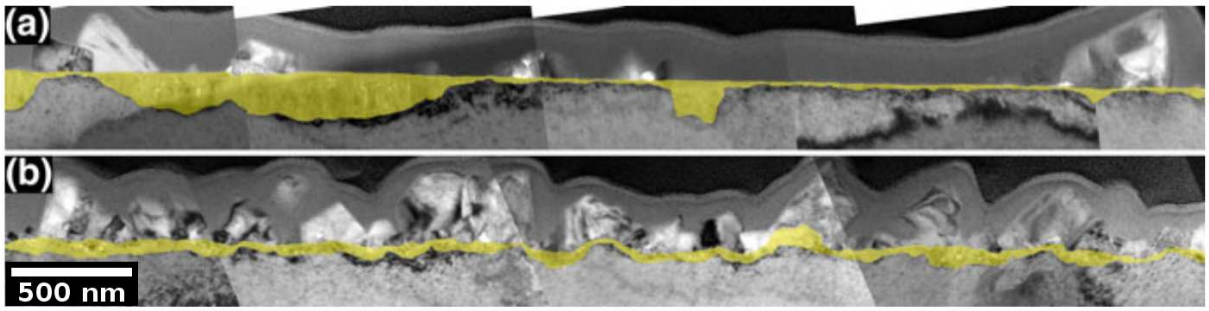

Figure 1.20: *Images of the oxide layers formed on a 316L alloy exposed to 320 °C water with 3 wppm H_2 for 24 hours on the a) unirradiated region b) oxidised under proton flux area [86]*

The effect of irradiation on the oxide layers formed is still controverted. Moreover, the effect

of the presence of irradiation defects for short time oxidation is still unknown mainly because only few works focused on it. Thereby, this study will allow a better comprehension of the influence of irradiation on the oxidation kinetics.

Irradiation:

- Irradiation accelerates the outer oxide growth and irradiation defects might act as preferential nucleation sites.
- Irradiation provokes the formation of an inner oxide richer in chromium, its effect on the oxide thickness is still unclear but defects are believed to accelerate the cations diffusion.
- Oxidation under proton flux generates oxidising radiolysis products which lead to hematite formation as well as inner oxide dissolution and thus a thinner inner oxide layer.

1.1.3 Austenitic stainless steels oxidation in PWRs: Synthesis

The studies presented above allow to establish a general pattern regarding the oxide layer formed on austenitic stainless steels in primary medium of PWRs. This description is proposed in Figure 1.1 and can be divided into three main parts:

- An outer layer composed of iron-rich crystallites,
- A continuous inner layer chromium enriched,
- A nickel enrichment in the underlying alloy.

This review of the different mechanisms stainless alloys oxidation in a primary water environment has made it possible to highlight two processes governing the growth of the duplex layer. The outer layer is believed to be growing from a cationic diffusion mechanism coupled with a precipitation mechanism of dissolved cations in the medium, originating from a diffusion process within the inner layer. The inner layer is formed by anionic diffusion. Finally, both the presence of an inner and outer layer were demonstrated on stainless steel exposed to simulated primary water even after 1 minute oxidation. Nonetheless very few studies focused on short time oxidation. In addition, only few authors studied the effect of the crystallographic orientation of the underlying metal grain on the oxide formed for austenitic stainless steels [12–14]. Crystallites tend to become faceted as the oxidation time increase and their morphology depend on the underlying grain orientation. Many authors reported a polycrystalline inner oxide [5, 6, 26, 27, 87–89] whereas Soulas observed a monocrystalline oxide [12, 13] sharing an epitaxial relationship with the substrate after 24 hours oxidation. There thus still uncertainty regarding the structure of the inner layer. Moreover, this epitaxial kinetic is depending on the crystallographic orientation of the metal. This bibliographic overview allowed to highlight the influence of the various parameters which can affect the oxidation kinetic, the morphology and the thickness of the oxide layer formed. Indeed, it has been shown that the alloy's surface state as well as cold-work, oxidising medium chemistry, crystallographic orientation and irradiation may play a role in the oxides formed. However, the duplex structure of the oxide or its composition will seemingly not be greatly impacted by these parameters. From the observations presented above, the effect of the surface state on the oxide layer formed is still to be studied taking into account the crystallographic orientation of the metal. Furthermore, the role of irradiation on the stainless steels oxidation in PWR medium is still poorly understood and was never studied taking the underlying metal grain orientation into consideration.

Oxide description:

- Duplex oxide right from 1 minute oxidation.
- Outer oxide (magnetite Fe_3O_4) grow by cationic diffusion through the inner oxide and precipitation of the cations present in solution. The crystallites tend to become bigger and faceted as the oxidation time increase and exhibit a clear crystallographic orientation.
- Inner oxide (chromium rich spinel) grow by anionic diffusion at the metal/oxide interface. Initially amorphous, the inner oxide will become nanocrystalline and then monocrystalline epitaxially grown on the metal grain underlying. Nanopores or grain boundaries in the inner oxide might act as diffusion short-cuts.
- Nickel enrichment in the metal underneath the inner oxide and hydrogen trapping at the metal/inner oxide interface in the nickel-rich area.

Parameters influencing the oxidation:

- Electropolished surfaces possess a thin chromium rich oxide at their surface and are defect-free thus being less sensitive to corrosion than mechanically polished ones. Mechanical polishing might induce strain and/or a nanograin layer which lead to inner oxides richer in chromium due to the presence grain boundaries diffusion short-cuts in the metal. Cold-work provokes the formation a numerous small crystallites as defects may act as preferential nucleation sites.
- The medium chemistry affects the oxide formed. H_2, H_2O_2 and O_2 present in the water modify the oxides thickness, morphology and composition.
- Existence of an epitaxial relationship between the metal and oxide layers with a residual elastic deformation which accommodates the parametric misfit between the lattices relieving the stress induced misfit. Crystallographic orientation of the underlying metal grain modifies the oxidation kinetic.
- Irradiation accelerates the outer oxide growth and irradiation defects might act as preferential nucleation sites. Irradiation provokes the formation of an inner oxide richer in chromium, its effect on the oxide thickness is still unclear. Oxidation under proton flux generates radiolysis products and modifies the oxides (thinner inner oxide, hematite formation, etc.).

1.2 Irradiation effect on austenitic stainless steels

As seen previously in section 1.1.2.4, the irradiation might be able to modify the oxide formed. However, to better understand this phenomenon, one first needs to fathom the irradiation effect on the metal since it could affect the oxidation process. In PWRs, neutron energy covers a wide range (from a few eV to several MeV) and includes the domain of thermal, epithermal and fast neutrons. Almost 95% of the damage due to irradiation are induced by fast neutrons (energy ($> 0.1\,\text{MeV}$) or epithermal ones. Therefore the most energetic neutrons are the ones damaging the materials. When a material is irradiated, collisions occur between neutrons and the atoms of the alloy, generating microstructural changes. It is then by interacting with matter that the neutrons will be brought to create defects in the crystal lattice. If, during an elastic shock between a neutron and an atom, the energy yielded by the neutron is sufficient, then the atom will be ejected from its crystalline site, leaving a vacancy in its place. This atom will then be found in interstitial position and will be called a Self Interstitial Atom (SIA). The energy needed to eject an atom from its site is greater than the displacement energy of the atom (threshold set

at 40 eV for α iron and unknown for γ iron but considered equivalent to the α iron threshold). This phenomenon is known as the creation of a Frankel Pair (FP) composed of a vacancy and a SIA. If the energy is insufficient, the atom will vibrate around its equilibrium position but will not be displaced. If the atom dislodged from its crystalline site also has sufficient energy, it can in turn eject another atom outside its site. Displacements cascades can thus be created from a Primary Knock-on Atoms (PKA) causing the formation of numerous FP [15]. 90 to 99% of the displaced atoms end up recombining with vacant crystalline positions. Nevertheless, some defects do not annihilate and remain in supersaturation. It is the presence of such vacancies or interstitial defects (free or in the form of clusters) that is responsible for the microstructural and chemical changes. Dislocation loops, "black dots" or cavities are the main microstructural changes observed in irradiated stainless steels. On top of causing irradiation damages, the neutrons can also initiate nuclear reactions leading to chemical changes by transmutation. Helium can then be generated by the nickel and boron transmutation leading to the presence of gaseous helium filling some cavities which cause additional swelling and embrittlement of the materials. In addition, chemical changes such as segregation and precipitation can be caused by irradiation, modifying locally the expected chemistry. The chemical segregation will result from a cross-flow between point defects and atoms of the alloy toward sinks such as grain boundaries, dislocations, precipitates, etc. inducing local chemical changes. The saturation of these phenomena occurs at a given dose, which results in a state of equilibrium in which induced defects no longer evolve. This saturation is dependent on many parameters, including the temperature, but also the composition of the alloy, the damage induced, etc. [90–94].

Quantification of irradiation damage is necessary in order to better understand the modifications induced by irradiation. In order to quantify the irradiation (neutron, ion or proton), a unit has been defined: Displacement Per Atom (dpa). This dpa represents the number of times an atom is dislodged from its initial site on average by ballistic shock. So, it evaluates the number of FP (SIAs and vacancies) created during neutron/atom collisions by atom. A convention resulting from ASTM E521-89 makes it possible to approximate the fluence to dpa with the following equivalence: $(\text{dpa}) = 7 \times 10^{24}\,\text{n/m}^2$. However, this relationship is only valid when the neutron energy is greater than 1 MeV (based on a displacement energy of iron at 40 eV).

Internals are especially subjected to high neutron flux due to their positioning. At the end of such materials lifetime the dose can locally reach 80 dpa. Moreover, irradiation is known to alter the material microstructure and chemistry and its mechanical properties (loss of ductility and toughness, localization of deformation and hardening) [90, 95]. In this bibliographic review, interest is drawn on PWR irradiation conditions. Thus, temperatures ranging from 270 °C and 370 °C will be discussed regardless of warmer zones due to gamma irradiation. Microstructural and chemical modifications induced by irradiation and several parameters influencing these modifications are described below. A focus is also made on synthetic irradiation that aims to emulate neutron irradiation happening in PWRs.

Shedding light on:

- Microstructural and chemical modifications induced by irradiation.
- Effect of various parameters on these modifications (alloy microstructure and composition, irradiation conditions, etc.).
- Synthetic irradiation aiming to emulate PWRs neutron irradiation.

1.2.1 Microstructural modifications

As presented above, point defects (SIAs and vacancies) induced by the irradiation modify the microstructure of irradiated material. In the following paragraphs are described the main microstructural changes induced by irradiation. These modifications can affect the overall mechanical properties of the material and lead to an increase in yield strength as well as a consequent decrease of the ductility and fracture toughness. Furthermore they can also affect the corrosion resistance.

1.2.1.1 Frank loops

Frank loops are the main defect observed in stainless steels neutron irradiated for PWR dose and service temperatures (Figure 1.21). They were observed by numerous authors for neutron irradiation [2, 90–92, 95–100], as well as ion or proton irradiations [5, 93, 94, 101–110]. The main imaging method of Frank loops is known as Rel-Rod Dark Field (RRDF) imaging which is developed in Appendix A. These are faulted loops because they contain one stacking fault and they are sessile. The formation of these Frank loops comes from the agglomeration of vacancies or interstitial defects in {111} planes. These loops act as obstacles to dislocation movement, leading to a hardening of the material well-known as irradiation induced hardening. These two-dimensional clusters may be vacancies or interstitials, but for irradiation temperatures above 300 °C in stainless steels, Frank loops are considered to be interstitials. Their Burgers vector is $\frac{a}{3}\langle 111\rangle$ (with a the lattice parameter). Their size usually ranges from 10 to 20 nm and their density is between 1×10^{22} to $3 \times 10^{23}\,\mathrm{m}^{-3}$. The density and the diameter of the loops increase with the dose before stabilising by saturation at low doses between 1 and 5 dpa for temperatures close to 300 °C [90, 92, 97]. Above 300 °C the loop sizes increase while their densities decrease [90, 92, 95, 103].

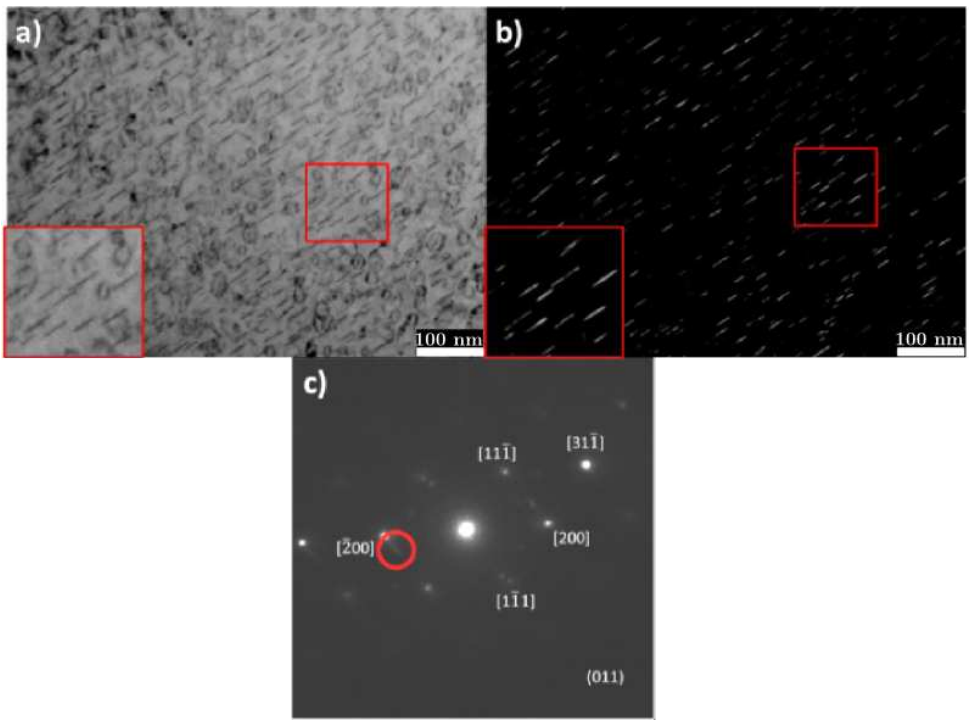

Figure 1.21: *TEM images of dislocation loops observed in a FeNiCr alloy irradiated at 5 MeV with Ni^{2+} ions at 450 °C a) BF image of the dislocation loops with g=[31$\bar{1}$], b) RRDF image of the same area with g=$\frac{1}{2}$ [$\bar{3}\bar{1}$1], c) Diffraction pattern associated with previous images (encircled diffraction streak was used to visualise Frank loop) [106]*

Frank loops: Main observed defects for irradiated austenitic stainless steels, the loops are believed to be interstitial defects.

1.2.1.2 "Black dots"

"Black dots" are clusters of small point defects, usually 2 - 3 nm in diameter, visible in Transmission Electron Microscopy in the form of black dots when imaged in Bright Field, hence their name. They were observed by a large variety of studies [2, 90–92, 95–98, 102, 103, 105–107]. Below 300 °C, these defects are the main microstructural change due to irradiation [92]. They have been assimilated to very small Frank loops [91, 95, 96, 107]. Pokor et al. assumed that these defects would be small Frank loops "edge-on" or inclined [95]. Other authors consider a contribution of vacancies in these "Black dots" [90, 102]. But, because of their size it is difficult to be certain of their nature. The cumulative density of "black dots" and dislocation loops usually saturates to a value between 2×10^{23} at $4 \times 10^{23}\,\mathrm{m}^{-3}$ [91]. At low temperatures, the density of these "black dots" seems independent of the temperature. This is no longer true for temperatures above 300 °C since above this temperature their density tends to decrease.

"Black dots": Small defects believed to be small Frank loops.

1.2.1.3 Cavities and helium filled bubbles

Cavities (or voids) are due to an agglomeration of vacancies and are formed, usually for temperatures between 300 and 700 °C [97, 99, 111]. When these cavities are observed by TEM they have a typical octahedron shape with the main faces in the type planes {111} (Figure 1.22). Often numerous, between 1×10^{22} and $1 \times 10^{23}\,\mathrm{m}^{-3}$, these cavities have an average diameter from 2 to 10 nm. Above 300 °C the cavity sizes increase while their densities decrease [90, 92, 103].

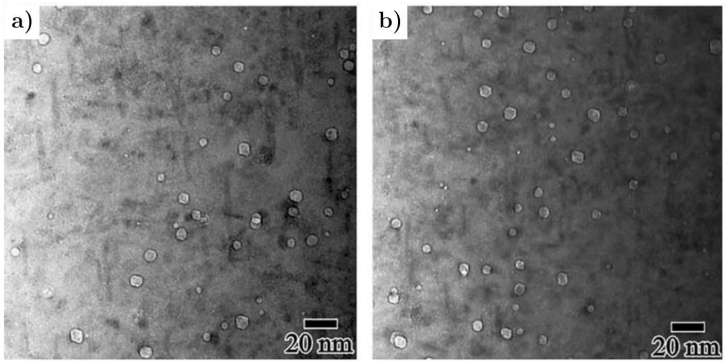

Figure 1.22: *TEM images of cavities formed in a CW 316 extracted bolt from Tihange, in the neutron irradiated area at 275 °C and 5.5 dpa in a) and b) two different areas [97]*

Sometimes these cavities contain helium and are called bubbles as previously stated in section 1.2. The creation of helium bubbles is due to the transmutation of boron and nickel during nuclear reactions [112] as presented in equations 1.1 and 1.2. Because of its low solubility in steel, helium will cause a stabilisation of cavities formed and is likely to cause swelling of the material as well as grain boundaries embrittlement at temperatures above 400 °C [112, 113].

$$^{59}Ni + n \longrightarrow ^{59}\,Ni + \gamma\; then\; ^{59}Ni + n \longrightarrow ^{56}\,Fe + ^{4}\,He \tag{1.1}$$

$$^{10}B + n \longrightarrow ^{7}\,Li + ^{4}\,He \tag{1.2}$$

Both cavities and helium bubbles were observed by numerous authors [2, 65, 90, 92, 93, 95–101, 106, 110, 114–116]. Bubbles coexist with cavities but at a given irradiation temperature, the bubble density is often one order of magnitude greater than that of the cavities. In general, these helium bubbles have a smaller diameter than cavities. In addition, bubbles and cavities have distinct geometric shapes, the first are spherical whereas the cavities are often faceted. However, the helium detection, to attest of the presence of helium filled cavities, can be very challenging. Electron Energy Loss Spectroscopy can be employed but the helium detection still remains complicated due to the helium edge position and its low intensity. Since the bubbles are cavities filled with helium, synthetic irradiation performed to simulate neutron irradiation does not induce bubbles within the material unless the irradiation is coupled with He ion irradiation.

Cavities and helium filled bubbles:

- Void/cavity results from an agglomeration of vacancies.
- Bubbles are cavities filled with helium created by the boron and nickel transmutation. They cannot be obtained by performing synthetic irradiation without helium implantation.

1.2.1.4 Stacking Fault Tetrahedra

Stacking Fault Tetrahedron (SFT) are tetrahedron with four intrinsic stacking faults in the {111} planes with dislocations along the corners of the tetrahedron. These are vacancy clusters that are visible by TEM in the form of triangles (Figure 1.23). These Stacking Fault Tetrahedra (SFTs) are the most stable form of vacancy clusters for materials with low stacking fault energy. Stainless steels having a relatively low stacking fault energy (between 20 and 40 $\mathrm{mJ\,m^{-2}}$) SFTs are theoretically likely to form under irradiation. Nevertheless, the formation of the latter within the austenitic stainless steels is controversial. Horiki and Kiritani observed SFTs in high purity Fe16Ni15Cr alloy neutron irradiated at temperatures ranging from 100 to 400 °C [117]. Edward et al. reported the presence of SFTs in high purity 304 alloy while observing none in commercial purity 304 and 316 alloys [91]. The presence of SFTs has been demonstrated in high purity austenitic stainless steels irradiated with neutrons but to date, SFTs have not been observed in PWR oxidised samples.

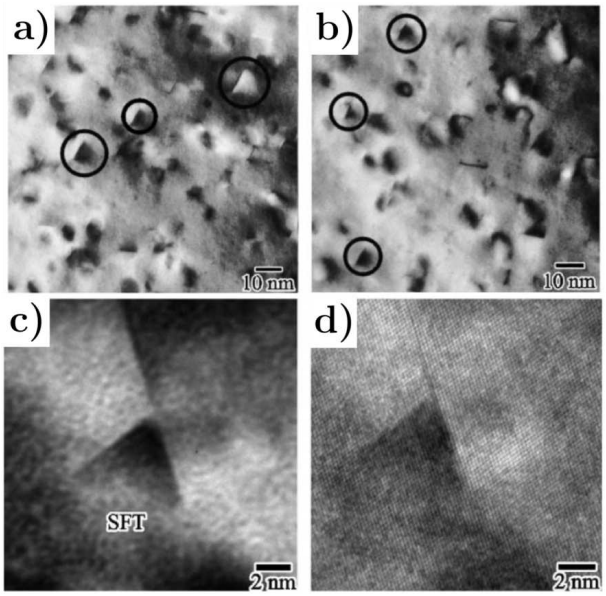

Figure 1.23: *a), b), c) and d) TEM images at different magnifications of SFT observed in high purity alloy neutrons irradiated at 1.2 dpa at 275 °C in the Barsebäck reactor [91]*

Stacking Fault Tetrahedra: Vacancy clusters with a tetrahedron shape due to the presence of four intrinsic stacking faults which were observed in high purity austenitic stainless steels but never to date in reactor materials.

1.2.1.5 Modification of the dislocation network

In PWRs internals some austenitic steels used are hardened by cold-work such as 316L steel used for stressed screws. However, on decommissioned components, the initial dislocation network has never been observed. By studying experimental irradiation in a fast neutron reactor Pokor observed the dislocation network at 1 dpa but it was no longer visible to 5 dpa [95]. He concluded that the initial network of dislocations tends to disappear under irradiation. The dislocations are annihilated between themselves or on defects such as grain boundaries [95].

Modification of the dislocation network: Initial dislocation network disappears under irradiation.

1.2.2 Chemical modifications

One of the main consequences of irradiation at elevated temperature is the spatial redistribution of solute and impurity elements in the metal. This phenomenon leads to the enrichment or depletion of alloying elements or even clustering and precipitation in specific regions such as dislocations, voids, grain boundaries, etc. called sinks. Such changes can cause modification of the solid local properties and may induce susceptibility that can result in a degradation of the component integrity. For this reason, understanding Radiation Induced Segregation (RIS) (developed in the first paragraph) and the phase precipitation phenomenon (second paragraph) is of great importance. However it is very difficult, because of their small size and density, to detect and quantify such chemical modifications using TEM. Small segregations can be detected using Atom Probe Tomography (APT) but the nature of the objects on which segregation and depletion occur (such as dislocation lines and loops) cannot be found out using APT (except grain boundaries which can be observed during the needle milling using a Focused Ion Beam). Coupling TEM observations and APT analyses allows to make links between the size, density and morphology of segregations and objects. Thus, a comparison between TEM images and APT analyses seems indicated. One of today challenge would be to characterise, on a same area, chemical segregation and defects on APT thin needles by both TEM and APT. If such segregation were to be investigated using TEM, High Angle Annular Dark Field (HAADF) Scanning Transmission Electron Microscopy (STEM) images coupled with EELS or Energy Dispersive X-ray Spectroscopy (EDXS) analyses using a high collection angle would be necessary.

1.2.2.1 Radiation Induced Segregation

This phenomenon of segregation under irradiation is called Radiation Induced Segregation (RIS). It is due to point defects that will be eliminated at sinks leading to a concentration gradient near them (enrichment or depletion). A great number of authors observed this segregation in their studies for neutron irradiation [90, 92, 96–98, 118–127], as well as ion or proton irradiations [101, 104, 108, 128–135]. There is then depletion or enrichment at the local scale of several elements. Mainly observed on grain boundaries such segregation can also happen on dislocation loops or cavities/bubbles [91, 97, 110, 119, 127, 131, 133]. Ni and Si enrichment as well as Cr depletion on the defects are thereby observed. Clusters of solutes such as Ni/Si can also be formed [110, 127, 131, 133, 136–139]. This Radiation Induced Segregation (RIS) is dependent on the irradiation flux and the irradiation temperature while being at its maximum between 250 and 400 °C [18, 90]. Fukuda et al., among other authors, showed that as the irradiation

temperature increases, the nickel enrichment and chromium depletion induced by the RIS are exacerbated [122]. Thus, in operation, segregation can be observed within the materials used in PWRs. Chromium will be depleted at grain boundaries while an enrichment of nickel is observed. Moreover, segregation of minor alloying elements such as an enrichment of Si and P and the depletion of Mn and Mo has been reported as well. This segregation saturates between 3 and 5 dpa for an irradiation temperature close to 300 °C. A typical Radiation Induced Segregation is presented in Figure 1.24. The segregation is usually narrow around the grain boundary ($\sim$ 5 to 10 nm). A significant chromium depletion might promote intergranular corrosion or cracking since chromium impairs the corrosion resistance.

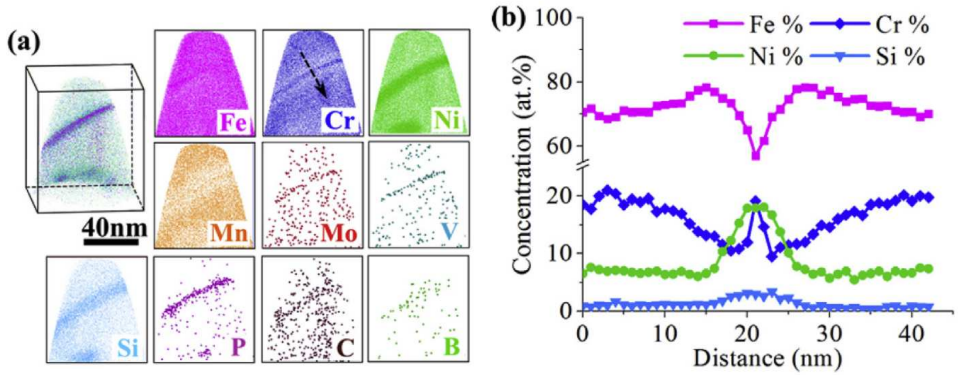

Figure 1.24: *RIS in 304 alloy neutron irradiated in the EBR-II reactor at 0.4 dpa and 416 °C a a) atomic maps of APT results b) line profiles [127]*

Two mechanisms explain this phenomenon: the inverse Kirkendall effect, which remains the preferred mechanism in the case of irradiation in PWR [101, 118, 121], and the association of interstitials. These two phenomena are in competition but it is probable that one of the two mechanisms prevails for a given composition and irradiation conditions. The Radiation Induced Segregation will cause a concentration gradient close to the sinks depending in particular on the diffusion coefficients (vacancy or interstitial) of the species but their size is also an important parameter. Indeed, only small solutes are able to diffuse by an interstitial mechanism by forming "Dumbbell". The solute–interstitial complexes resulting from the interstitial association mechanism are in general very mobile, and this mechanism predominates for low temperatures and doses of irradiation. When the temperature or the dose is high, the vacancy mechanism (inverse Kirkendall effect) then becomes predominant [92]. Etienne et al. having observed segregation on dislocation loops by APT assumed that the interstitial association mechanism might also induce segregation on other sinks that grain boundaries [137]. Some authors such as Allen et al. [121] believe that RIS at grain boundaries is only imputable to the inverse Kirkendall effect for irradiation conditions close to that happening in PWRs.

– Inverse Kirkendall effect:

The inverse Kirkendall effect mechanism is a vacancy diffusion mechanism in which vacancy flux and solute atom flux are opposite. In the case of a binary alloy A-B under irradiation, a flux of vacancies $\vec{J_v}$ will be established in the direction of the sink and there will be a gradient of concentration of vacancies (C_v) close to the sink. This vacancy flux causes a flux of atoms A and B ($\vec{J_A} + \vec{J_B}$) of norm equal to that of J_v but of opposite direction. If the atoms A and B have an equal vacancy diffusion coefficient (ie D_A^v=D_B^v) then the composition of the alloy near the sink will not be modified. If, on the contrary, their diffusion coefficient by vacancy mechanisms are different, then the norms of atomic flux A and B will no longer be identical. Therefore, if specie A has the greatest diffusion coefficient, it will diffuse more rapidly than B with the vacancies, and atoms A will go against the vacancies concentration gradient. This specie A will then be

depleted at the sink. More generally, the inverse Kirkendall effect induced by a vacancy flux will always cause depletion close to the sink of the fastest diffusing element (element having the greatest vacancy diffusion coefficient). This inverse Kirkendall effect for a vacancy diffusion mechanism is presented in Figure 1.25 a) for a binary alloy A-B as previously described. Thus, chromium is depleted at grain boundaries because it diffuses rapidly with present vacancies in supersaturation (Figure 1.25 b)). In contrast, nickel is the specie that diffuses the most slowly with the vacancies leading to its enrichment at grain boundaries.

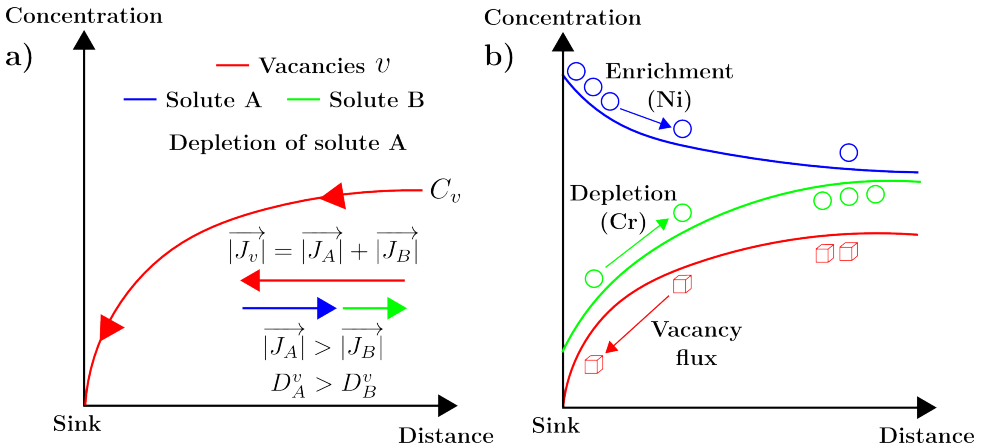

Figure 1.25: *Schematic of the Kirkendall vacancy diffusion mechanism close to a sink for a) a binary A-B alloy and b) a stainless seels alloy*

– Association of interstitials:

This mechanism is based on the formation of complexes between the solute and the defects. It entails the association of SIA with small atoms such as silicon, nickel or phosphorus in the form of mixed dumbbells. If the migration energy of this complex is lower than its dissociation energy, it then becomes mobile. The solute atoms are dragged to the sinks where interstitials are eliminated. There will thus be a concentration gradient of interstitials allowing an enrichment of the area around the sink in solute elements. Small atoms (such as Ni or Si) will be enriched near the sinks at the expense of bigger elements (Figure 1.26).

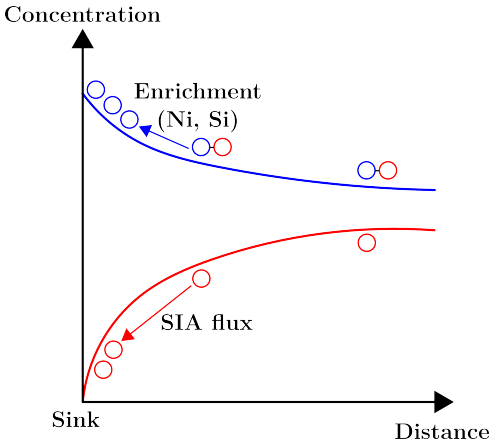

Figure 1.26: *Schematic of the interstitial association mechanism close to a sink*

Radiation Induced Segregation:

- Depletion (mainly Cr) or enrichment (mainly Ni and Si) at the local scale of elements near sinks such as grain boundaries, dislocation loops, voids and bubbles.
- The involved mechanisms are predominantly the inverse Kirkendall effect (vacancy mechanism) and the association of interstitials.

1.2.2.2 Phase precipitation

If irradiation causes local segregation of alloying elements at sinks, it is also responsible for changing phase or an acceleration/delay of the formation kinetics of several phases and the formation of precipitates under irradiation. Such precipitation was noted by several authors [90–92, 92, 96, 97, 100, 112, 114, 127, 129, 138, 140, 141]. This precipitation is, however, reported in the temperature for high irradiation temperatures (> 400 °C) and doses often greater than 10 dpa. TEM analysis such as diffraction and APT measurement are the main used techniques to characterise the precipitation in irradiated stainless steels. Figure 1.27 presents an example of precipitation in a neutron 304 irradiated alloy exhibiting G phase and carbides precipitates.

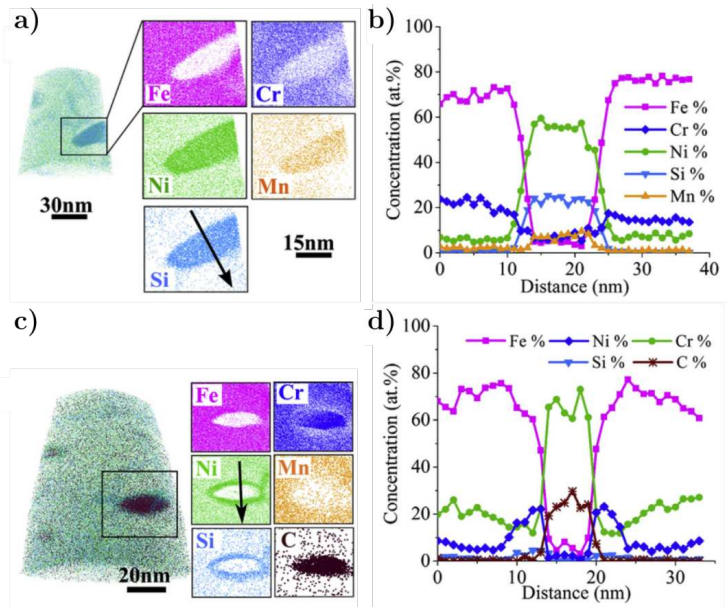

Figure 1.27: *Precipitation in 304 alloy neutron irradiated in the EBR-II reactor at 28 dpa and 450 °C a) atomic maps of APT results of G phase precipitate b) line profiles of the G phase precipitate c) atomic maps of APT results of the carbide precipitate b) line profiles of the carbide precipitate [127]*

In the presence of irradiation the precipitation can be classified according to the three following categories and the induced precipitated are presented in the Table 1.4:

- Precipitation accelerated or delayed by irradiation,
- Phases modification under irradiation,
- Irradiation-induced precipitation.

Table 1.4: *Observed precipitates in austenitic stainless steels under irradiation ([92, 96])*

	Precipitation accelerated or delayed by irradiation	Precipitation modified by irradiation	Precipitation induced by irradiation
Carbides	M_6C, $M_{23}C_6$, MC	M_6C	-
Intermetallic phases	Lava phases, sigma phase (σ), Chi phase (χ)	Lava phases	-
Phosphide	-	M_2P	MP, M_2P, M_3P
Silicides	-	-	G phase ($M_6Ni_{16}Si_7$) γ' phase (Ni_3Si)

Phase precipitation: At high doses, irradiation can induce phase modification/creation or an acceleration/delay of the formation kinetics of some phases.

1.2.3 Parameters affecting the changes induced by irradiation

Even if microstructural and chemical changes induced by irradiation were widely studied, one should still consider that those modifications are depending on several conditions or parameters (material ones or irradiation ones). Indeed, numerous parameters can influence the irradiation defects and changes and are to be taken into consideration such as the alloy surface state, composition, grain boundary character, etc. and irradiation conditions (temperature, dose, damage rate, etc.). Below are developed the main parameters involved in this study that can influence the modifications induced by irradiation.

1.2.3.1 Surface state and cold-work

A few authors studied the effect of cold-work and surface state on the Frank loops induced by dislocations [7, 97, 108]. Stephenson and Was, using data from several studies compared the dislocation average size and density from proton irradiated CP SA and CW 316 alloy [108]. The average loop size was of 7.6 ± 2.5 nm on the SA sample against 9.1 ± 4.4 nm on the CW one. The loop density was smaller on the CW sample than on the SA sample (0.16×10^{23} loops/m^3 versus 0.86×10^{23} loops/m^3). The effect of polishing induced defects on the irradiation defects was studied by Gupta [7]. Fe^{5+} ion irradiation of 316L alloy was performed to 10 dpa at 450 °C. Comparing a mechanically polished sample with nanograins under the surface and vibratory polished sample (without the nanograins area) she observed different Frank loop populations. The average loop size was found to be of 20.3 ± 2.7 nm in the mechanically polished sample while 14.9 ± 3.6 nm in the vibratory polished sample. The loop density, however, was higher in the vibratory polished sample ($2.55 \pm 1.05 \times 10^{22}$ loops/m^3 against $0.06 \pm 0.2 \times 10^{22}$ loops/m^3 in the mechanically polished sample). This is in agreement with Stephenson and Was [108] results for the effect of cold-work on both the average loop size and density. The nanograins seem to highly suppress the density of Frank loops and more generally irradiation induced defects. Maziaz et al. assume that the dislocation network competes with dislocation loops for interstitials [96]. Indeed, a cold-worked material must see its dislocation network recovers before Frank loops can nucleate. At higher doses when the initial dislocation network is recovered, this difference should fade. Therefore defects induced by the polishing (and notably the presence of nanograins) and the initial cold-work state of a material can alter the irradiation induced defects created.

Surface state and cold-work: In the presence of cold-work or a nanograin area, the density of the observed dislocation loops is smaller but their size is bigger. However, for higher doses, the initial dislocation network being recovered the loop population difference fades.

1.2.3.2 Irradiation dose

Other studies have focused on the effect of irradiation doses on the irradiation defects generated. Most authors [90, 91, 94, 101, 103], agree that increasing the dose increases cavity and dislocation loops sizes and densities. Nevertheless, after a given irradiation dose a steady state is reached and the density and size of these defects are then constant (Figure 1.28).

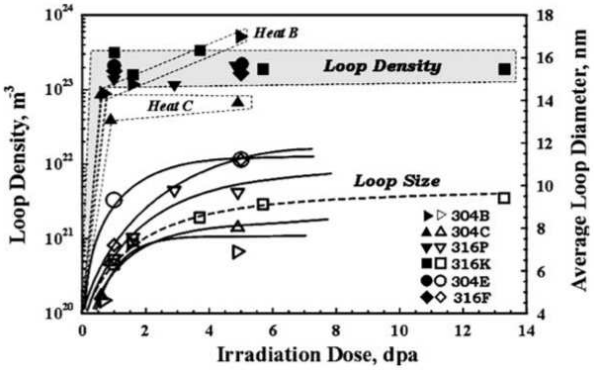

Figure 1.28: *Evolution of the dislocation loop size and density versus the irradiation dose for a neutron irradiation at 275 °C on 304 and 316 austenitic stainless steels [91]*

The Radiation Induced Segregation is also dependent on the irradiation dose. Several authors reported that the RIS is enhanced when the irradiation dose increase [90, 94, 98, 103, 142] (Figure 1.29).

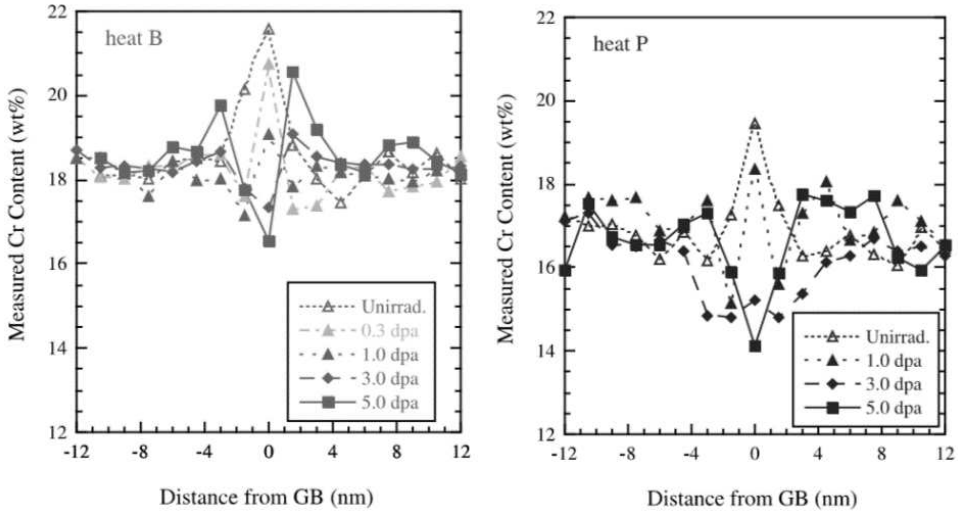

Figure 1.29: *Evolution of the chromium content at grain boundaries for a 304 alloy (heat B) and 316 alloy (heat P) proton pre-irradiated between 0 and 5 dpa at 360 °C [94]*

As for the irradiation defects, the segregation reaches a steady state from a given irradiation dose. Fukuya et al. studied the RIS of an extracted bolt from PWR [98]. The enrichment and depletion are enhanced by the dose but reach a steady state around 10 dpa as visible on Figure 1.30.

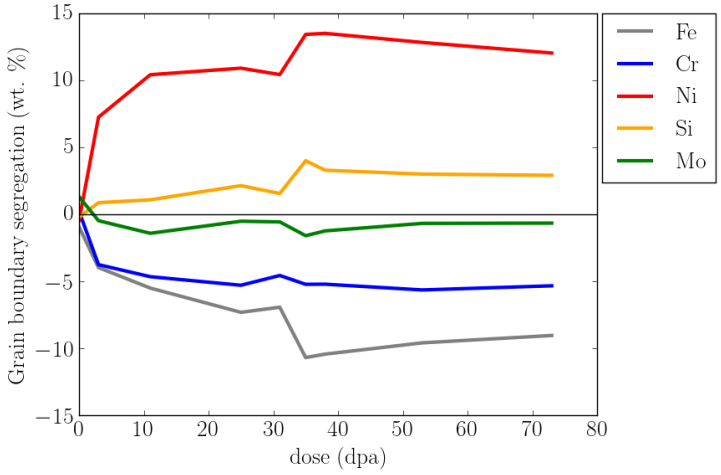

Figure 1.30: *Grain boundary segregation for a neutron irradiated in PWR CW 316 between 292 and 323 °C [98]*

Irradiation dose: When increasing the irradiation dose the cavity and dislocation loops sizes and densities increase as the amount of Radiation Induced Segregation before reaching a steady state.

1.2.3.3 Grain boundaries character

Grain boundaries separate two adjacent crystals of the same nature but with two different orientations. Among other, Priester and Lejcek book's give details on the theoretical and experimental comprehension of grain boundaries with information on the structure and a geometric and thermodynamic description of the grain boundaries [143, 144]. Several main grain boundary descriptions are detailed below.

One of the simplest ways to characterise a grain boundary is based on its θ misorientation. For small angles (generally $\theta \leq 15°$) the grain boundaries are referred as Low Angle Grain Boundaries (LAGBs) while grain boundaries with a misorientation $\theta \geq 15°$ are referred as High Angle Grain Boundaries (HAGBs). For grain boundaries with low misorientation, the latter is accommodated by network distortions caused by an array of dislocations.

Furthermore, the boundary plane orientation is used to characterise grain boundaries. The rotation axis $\vec{o}$ might be included in the grain boundary plane ($\vec{o} \parallel \vec{n}$) and is thus called a "twist" boundary or might be perpendicular to this plane ($\vec{o} \perp \vec{n}$) and then called a "tilt" boundary. It can even be a mix of these two situations ("mixed"/"general" boundary). A grain boundary is referred as "symmetrical" if the grain boundary plane $\vec{n}$ is the symmetry plane of the interface. In this case the same Miller indices are used for both crystals to describe the grain boundary plane ($\{hkl\}$). One should note that this kind of symmetry can only be reached for pure tilt grain boundaries. However it is referred as "asymmetrical" if the interface is asymmetric and thus the grain boundary plane is defined in the two crystals system coordinates $\{h_1k_1l_1\}|\{h_2k_2l_2\}$. Such representations of the grain boundary need to assume that the grain boundary is straight but in reality it can also be curved or faceted.

High Angle Grain Boundaries can be classified according to the Coincident Site Lattice (CSL) model presented below. The CSL network includes all the grain boundaries such as the positions of the crystallographic sites (thus the atoms) on both sides of the grain boundary coincide. Such coincidence is described with a coincidence index denoted Σ (odd integers in the case of cubic

materials) as presented in equation 1.3. The lower Σ, the higher the coincidence of two grains and thus the lower grain boundary energy.

$$\Sigma = \frac{Coincidence\ unit\ cell\ volume}{Primitive\ unit\ cell\ volume} = \frac{-1}{\rho} \tag{1.3}$$

With ρ the inverse of the density of crystallographic sites common to both crystal lattices in the CSL network.

CSL notation provides no information on the orientation of the grain boundary or its atomic structure. Thus, although this notation is widely used, it is not sufficient to describe and characterise a grain boundary. Indeed, two grain boundaries with the same Σ can be extremely different depending on their grain boundary plane. Table 1.5 groups together a few angles/direction of misorientation of the CSL boundaries in the face-centered cubic structures.

Table 1.5: *Couples angles/direction of misorientation of CSL boundaries in face-centered cubic structure (non-exhaustive) [145]*

Coincidence index Σ	Angle θ (°)	Axis $\langle uvw \rangle$
3	60	⟨ 111 ⟩
5	36.9	⟨ 100 ⟩
7	38.2	⟨ 111 ⟩
9	38.9	⟨ 110 ⟩

Moreover, in real materials CSL can deviate from the theoretical configurations presented in Table 1.5. Strain or additional defects such as dislocations or interface steps might induce a deviation from the optimum CSL misorientation. Brandon proposed a criterion [146] (equation 1.4) to estimate the deviation from the optimum CSL misorientation without losing the special CSL character of the grain boundary. According to this criterion, the tolerable deviation for Σ3, Σ5, Σ7 and Σ9 are respectively 8.7°, 6.7°, 5.7° and 5°. HAGB which is not considered as CSL is called Random High Angle Grain Boundary (RHAGB). These RHAGBs are the most present grains in a material if no specific heat treatment has been carried out in order to favour special grain boundaries.

$$\theta = \theta_0 \Sigma^{-\frac{1}{2}} \tag{1.4}$$

With θ the angle tolerance, θ_0 a constant approximated to 15° (misorientation angles $\theta_0 \geq 15°$ are considered LAGBs), and Σ the CSL coincidence index.

Several authors studied the effect on the grain boundary character on the RIS phenomenon [126, 130, 134, 135, 147–151]. Regardless of the irradiation performed (electron, heavy ion, proton or neutron) most authors agree that the coherent twin boundaries Σ3, being special low energy boundaries are not as sensitive to Radiation Induced Segregation as other Random High Angle Grain Boundary [126, 130, 134, 135, 148–150] (Figures 1.31 and 1.32). However a distinction is made between coherent and incoherent Σ3 twin boundaries. If almost no segregation is detected at coherent Σ3 twin, the incoherent ones behave as the RHAGBs (Figures 1.31 and 1.33).

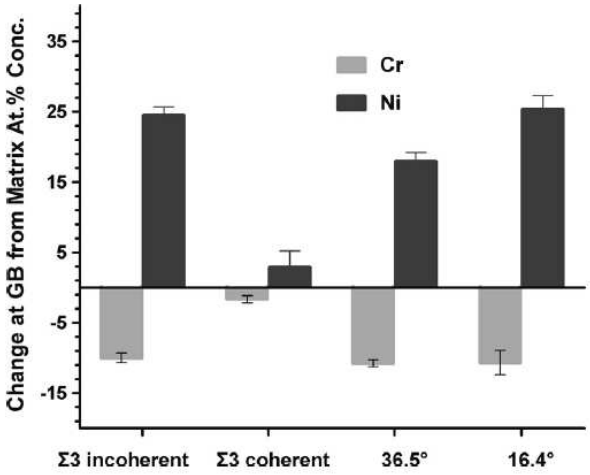

Figure 1.31: *Grain boundaries Cr and Ni concentration difference from the matrix of a 316L Cu^{2+} ion irradiated at 11 dpa and 500 °C depending on the nature and misorientation of the grain boundary [135]*

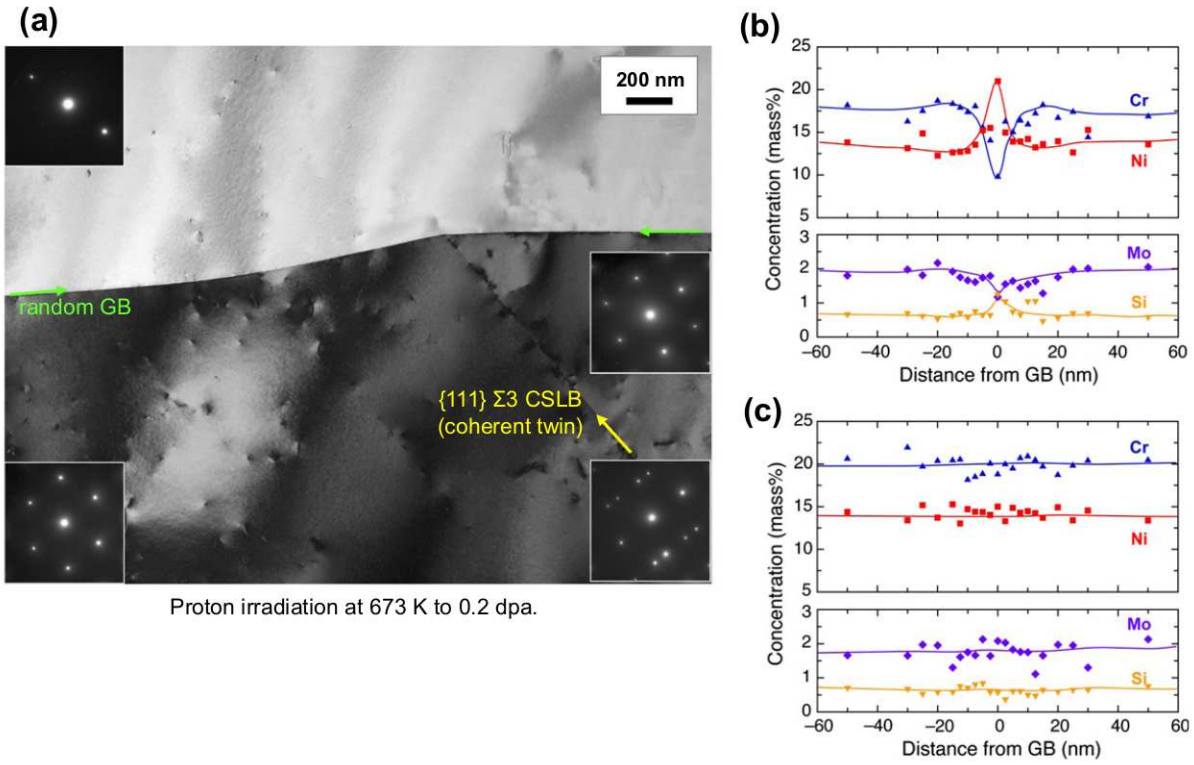

Figure 1.32: *a) TEM images of grain boundaries in a proton irradiated (400 °C, 0.2 dpa) 316L and Cr, Ni, Mo and Si concentration profiles across b) a RHAGB c) a Σ3 twin boundary [134]*

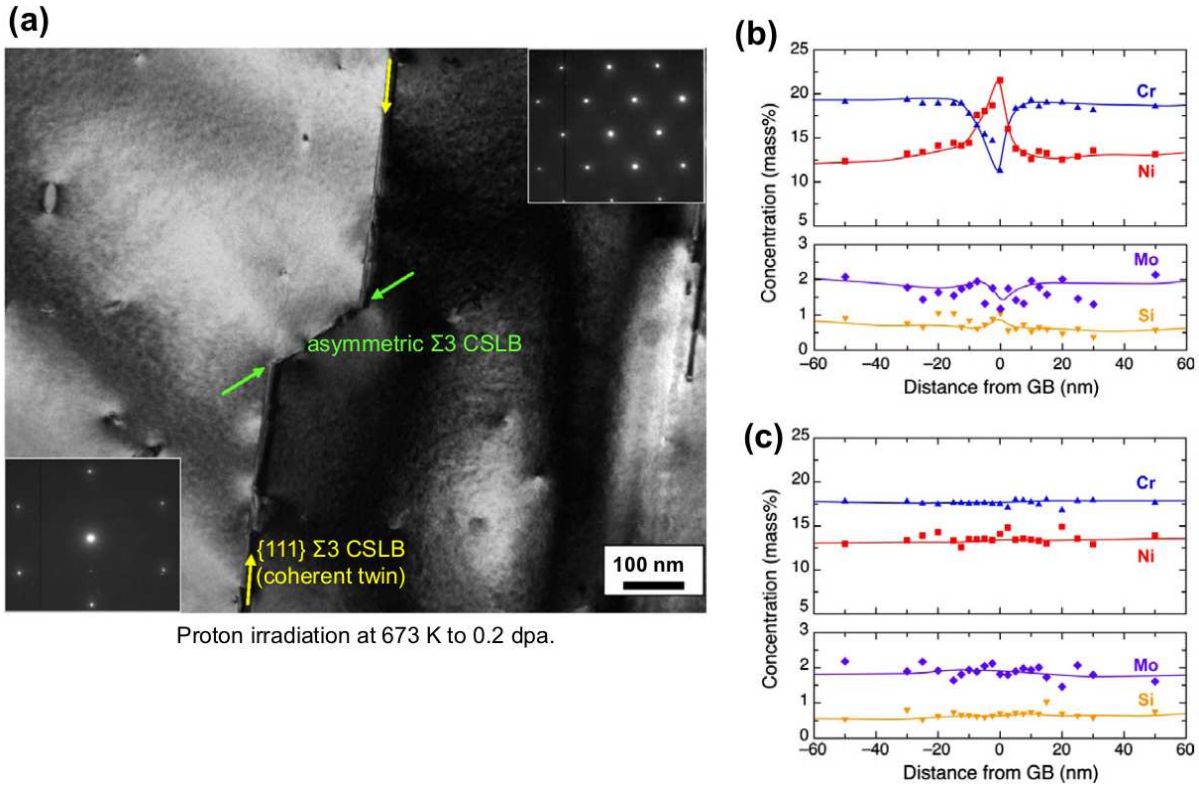

Figure 1.33: *a) TEM images of grain boundaries in a proton irradiated (400 °C, 0.2 dpa) 316L and Cr, Ni, Mo and Si concentration profiles across b) a Σ3 asymmetric boundary c) a Σ3 coherent twin boundary [134]*

Watanabe et al. showed in their study that RHAGBs are sensitive to Radiation Induced Segregation from the first dpa as opposed to Σ3 grain boundaries [149]. The Σ3 grain boundary became sensitive to RIS only after reaching 3 dpa meaning that before that the grain boundary was not acting as a point defect sink.

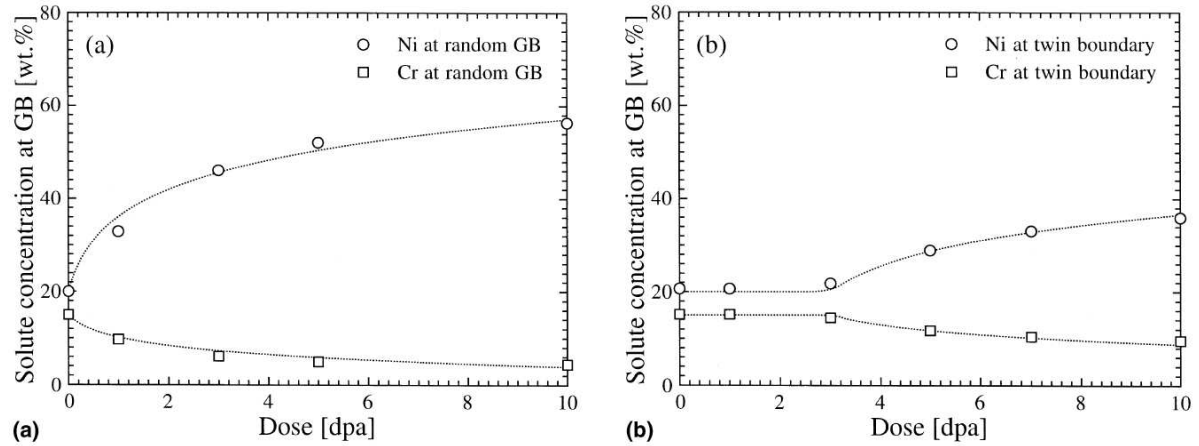

Figure 1.34: *Grain boundaries Cr and Ni concentration depending on the irradiation dose (electron irradiation up to 10 dpa at 350 °C for a) a RHAGB and b) a Σ3 twin boundary [149]*

Thus incoherent Σ3 twin boundaries and RHAGBs act as more powerful sinks than the Σ3 coherent twin boundaries. The latter might prevent Irradiation Assisted Stress Corrosion Cracking since less chromium depletion happens on these grain boundaries.

But the CSL description is not enough to fully describe a grain boundary and thus explain the segregation occurring. In order to give a microscopic description of a grain boundary, five independent Degrees of Freedom (DOFs) are needed to portray the misorientation between the two grains and the grain boundary plane. Two of them describe the rotation axis ($\vec{o}$, [uvw]), one the rotation angle (θ) and the last two the grain boundary plane ($\vec{n}$, $(h_1k_1l_1)/(h_2k_2l_2)$) as visible in Figure 1.35. Associated with these macroscopic parameters are four other microscopic parameters. Three more DOFs are needed to account for the translation of one crystal with respect to the other (mutual rigid-body translation vector: $\vec{t}$) and a last one indicates the plane position (vector normal to the grain boundary plane). All the intrinsic properties (including mobility and energy) of the grain boundaries are set by these nine parameters but the five macroscopic DOFs are enough to geometrically describe the grain boundary using the notation $\theta°[uvw](h_1k_1l_1)/(h_2k_2l_2)$.

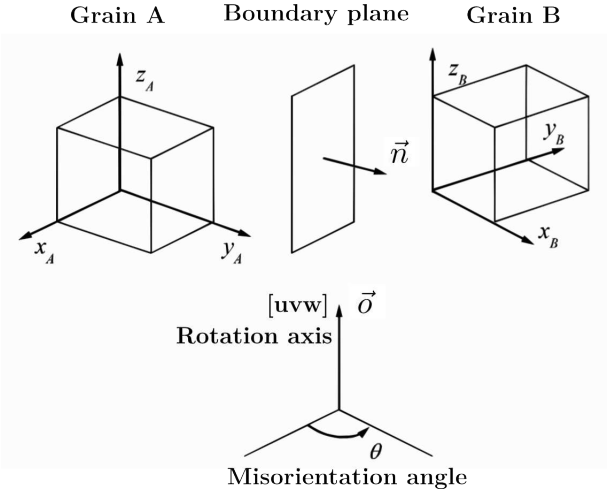

Figure 1.35: *Grain boundary description with x_A, y_A, z_A and x_B, y_B, z_B the axis of the coordinate parallel to crystallographic directions respectively in grain A and B. o: the rotation axis, θ: the rotation/misorientation angle needed to transfer both grains to an identical position and n: the orientation of the grain boundary plane (according to [152])*

Grain boundary character:

- Grain boundary character influence the amount of Radiation Induced Segregation occurring at a given grain boundary. Indeed, incoherent Σ3 twin boundaries and Random High Angle Grain Boundaries are more sensitive to Radiation Induced Segregation than the Σ3 coherent twin boundaries.
- Five independent Degrees of Freedom are needed to describe a grain boundary using the notation $\theta[uvw](h_1k_1l_1)/(h_2k_2l_2)$.

1.2.4 Synthetic irradiations

In neutron irradiated stainless steels, a high residual radioactivity due to the relatively high nickel content in austenitic stainless steels is present. Moreover, since the damage rate of neutron irradiation are very slow (approximately 10^{-8} dpa/s), doses of about several dpa are achieved in a few years and the samples can only be analysed in specialised facilities for radioactive samples and after decay times. All that happens in a very important financial cost and very complex experiments. Furthermore, a precise knowledge of the dose, dose rate and irradiation temperature within the PWRs is extremely delicate. For all these reasons, attempts are made to validate the use of other particles such as protons or ions to emulate neutron irradiation.

1.2.4.1 Generalities

Ion irradiation allows to reach doses of 1 to 10 dpa in several hours/days reducing the total cost of such an assay. However the particles penetration in the material is much less important for ion irradiation as shown in Figure 1.36. In addition, ion irradiation do not produce or produce very low radioactivity allowing a simpler handling of the samples without the need for specific precautions.

Since ions irradiations are conducted at much higher damage rates than neutron ones, the irradiation temperature needs to be adjusted to induce the same total flow of defects to sink (driving processes like Radiation Induced Segregation) or the net flux of one kind of defect over another (driving processes like loops or cavities growth). Mansur's equations (1.5 and 1.6) allow to link the neutron irradiation temperature and the ion irradiation one [15–17]. Thus, by changing the appropriated temperatures, irradiation studies can be made using heavy ions or protons. Was and Allen offer to simulate neutron irradiation happening in BWR (288 °C, 4.5×10^{-8} dpa/s) by proton irradiation at

For a damage rate modification, the temperature shift for an identical dose is obtained by keeping N_S constant (RIS):

$$T_2 - T_1 = \frac{\frac{kT_1^2}{E_m^v} \ln\left(\frac{K_{0_2}}{K_{0_1}}\right)}{1 - \frac{kT_1}{E_m^v} \ln\left(\frac{K_{0_2}}{K_{0_1}}\right)} \tag{1.5}$$

For a damage rate modification, the temperature shift for an identical dose is obtained by keeping N_R constant (loop):

$$T_2 - T_1 = \frac{\frac{kT_1^2}{E_m^v + 2E_f^v} \ln\left(\frac{K_{0_2}}{K_{0_1}}\right)}{1 - \frac{kT_1}{E_m^v + 2E_f^v} \ln\left(\frac{K_{0_2}}{K_{0_1}}\right)} \tag{1.6}$$

With:
- N_R the defect number by volume units recombined at a given time
- N_S the defect number lost at sink by volume units at a given time
- K_0 the defect production rate
- Φ the dose
- k the Boltzmann's constant (8.617×10^{-5} eV/K)
- E_m^v the vacancy migration energy ($\sim$ 1.3 eV)
- E_f^v the vacancy formation energy ($\sim$ 1.9 eV)

Thus, to simulate a typical neutron irradiation in BWR (288 °C, 4.5×10^{-8} dpa/s) he proposed a proton irradiation with a damage rate of 7×10^{-6} dpa/s at 400 °C for the RIS simulation (N_S invariant) and 300 °C for the dislocation loops study (N_R invariant). Most of the studies choose an irradiation temperature in between the two in order to obtain a compromise between the RIS and dislocation loops emulation.

The Table 1.6 gathers the advantages and inconvenience of heavy ion and proton irradiation.

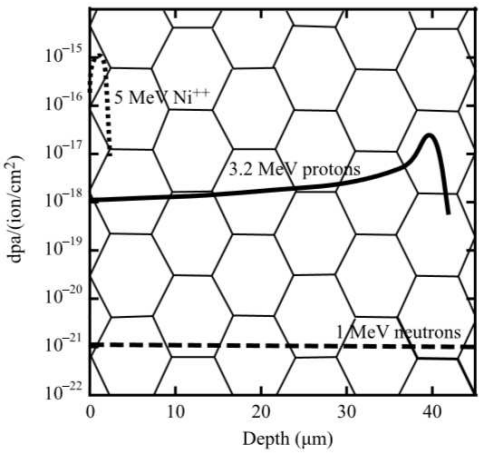

Figure 1.36: *Differences between defects created by various particles [153]*

Table 1.6: *Advantages and inconveniences of using heavy ions and protons to simulate neutron irradiation [153]*

	Heavy ions	**Protons**
Advantages	High dose rate Short irradiation times Dense cascade production	Moderate dose rate Moderate irradiation times Moderate temperature shift Good depth of penetration Flat damage profile over tens of µm
Disadvantages	Very limited depth of penetration Strongly peaked damage profile Very high damage rate Require high irradiation temperature No transmutation Potential ion implantation at high doses	Minor sample activation Smaller, widely separated cascades No transmutation

Since ion irradiation cannot cause transmutation reactions, some authors study the effects of helium on the microstructure with the means of irradiation coupled with a gas implantation [93, 107].

Generalities:

- Heavy ion or proton irradiations allow to reach doses of a few dpa in hours or days, thus decreasing the irradiation cost while creating low or even no radioactivity and allowing an easier sample handling.
- The irradiation temperature should be adjusted when performing a synthetic irradiation to simulate at best the Frank loops population and Radiation Induced Segregation phenomenon.

1.2.4.2 Proton irradiation

Proton irradiation (H^+) has the advantage of being able to reproduce, in a few days, the irradiation doses sustained by the materials within the reactors for several years. Since protons and neutrons have a close mass, they are capable of causing equivalent damage in terms of microstructural damage to a depth of several tens of microns (for protons with an energy of a few MeV). To simulate irradiation defects for neutron irradiation at about 300 °C for PWR operating temperature, it is necessary to perform ion irradiation at slightly higher temperatures. Indeed, in doing so the diffusion of the defects will be accelerated and the difference of the charge and

mass between the ions and the neutrons will be almost compensated. By using proton irradiation, it is easier to control the dose and temperature seen by the sample. In addition, after proton irradiation, the residual radioactivity being very low, the microstructural analysis can be performed more quickly and in a less expensive manner [103].

Stephenson and Was studied various 304 and 316 alloys, proton, and neutron (in BOR-60 fast reactor) irradiated at 5.5 dpa for respective temperatures of 360 °C and 320 °C [108]. The size of the dislocation loops are similar for both types of irradiation but slightly larger for the neutron irradiation (between 6 and 11.4 nm for neutron irradiated samples and between 5.2 and 9.1 nm for proton irradiated samples). The densities of dislocation loops range from 0.47 to $4.4 \times 10^{23}\,\mathrm{m}^{-3}$ for neutron irradiation versus 0.16 to $0.93 \times 10^{23}\,\mathrm{m}^{-3}$ for proton irradiation. Concerning the Radiation Induced Segregation, proton irradiation at 360 °C faithfully reproduces the segregation induced by neutrons at 320 °C (at 5.5 dpa) as visible in Figure 1.37.

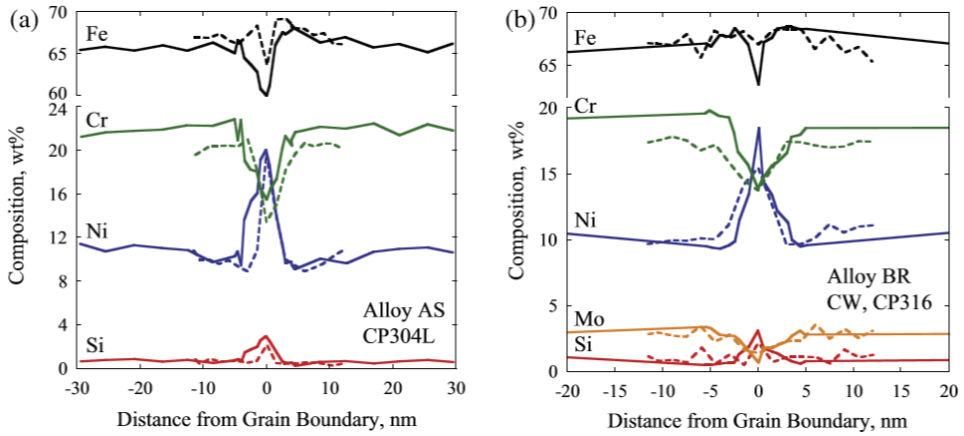

Figure 1.37: *Evolution of the iron, chromium, nickel, molybdenum and silicon content at grain boundaries for 304 and 316 alloys irradiated at 5.5 dpa with a) protons at 360 °C and b) neutrons at 320 °C [108]*

Gan et al. and Was et al. compared proton and neutron irradiations of 1, 3 and 5 dpa [94, 103]. The proton irradiation was performed at 360 °C and was compared with neutron irradiation performed on the same materials at 275 °C for similar doses. Their observations agreed with these of Stephenson and Was [108] even if the studied doses are different. An identical trend between proton and neutron irradiations is observed for the RIS, as well as the size and density of Frank's loops, despite some differences in the size or distribution of the irradiation defects. The loop density and size is slightly smaller after proton irradiation than after neutron irradiation.

Proton irradiation: Proton irradiation thus seems to be able to simulate the defects created by neutron irradiation.

1.2.5 Irradiation effect on austenitic stainless steels: Synthesis

The first two parts of this section are summarised in Figure 1.38 which presents all the microstructural and microchemical changes induced by irradiation in austenitic stainless steels. All defects are presented in the same sketch although they cannot be imaged at the same time. This sketch highlights the presence of dislocation loops, cavities or helium bubbles, black dots and dislocations for low irradiation doses and the presence of dislocation loops, cavities or helium bubbles, black dots and precipitates/clusters for higher irradiation doses. Moreover, regard-

less of the irradiation dose, Radiation Induced Segregation at grain boundaries can take place (enrichment Ni and Si, and depletion in Fe, Cr and Mo).

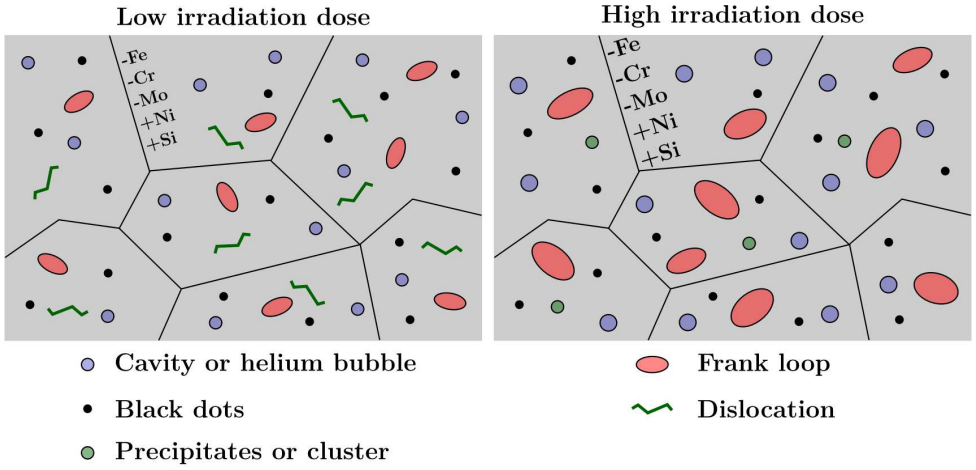

Figure 1.38: *Sketch of the irradiation changes induced in austenitic stainless steels according to the literature for high and low irradiation doses*

In the third part of this section various parameters were discussed (surface state, irradiation dose and grain boundary character). The surface state and cold-work were found to diminish the density of Frank loops. However, higher irradiation doses exacerbate the RIS and increase the size and density of dislocation loops and cavities. Regarding grain boundary character, it has a significant effect on the RIS phenomenon and is found highly reduced on coherent $\Sigma 3$ grain boundaries.

Finally, synthetic irradiation is able to emulate the microstructure of neutron irradiated stainless steels while being more convenient for handling.

Irradiation description:

- Vacancy and interstitial defects are responsible for the microstructural modifications induced by irradiation.
- Frank loops, "Black dots", cavities and helium-filled ones are the main microstructural defects created under irradiation.
- Radiation Induced Segregation modifies locally the solutes and impurities spatial distribution around grain boundaries, dislocations and voids (with primarily a depletion of chromium, manganese and molybdenum and an enrichment of nickel and silicon). The Inverse Kirkendall effect (vacancy mechanism) is the main mechanism attributed to Radiation Induced Segregation. At high doses irradiation also affects the precipitation occurring.

Parameters influencing the irradiation:

- The presence of a nanograin area induced by polishing and the initial cold-work state of a material provokes the formation of bigger and more numerous Frank loops.
- Irradiation doses and temperatures will all affect the density and size of Frank loops and the amount of Radiation Induced Segregation.
- Grain boundary character plays an important role on the Radiation Induced Segregation happening at grain boundaries and the $\Sigma 3$ coherent grain boundaries are the less sensitive to segregation.

Emulation of neutron irradiation:

- Synthetic irradiation such as ion and proton ones can emulate neutron irradiation by choosing accordingly the irradiation temperature for a given dose rate.

1.3 Bibliographic summary and experimental approach

In PWRs, core internals are exposed to high neutrons flux resulting in the formation of point defects in the microstructure and microchemistry changes. Since the 80's, baffle-to-former bolts cracks have been observed and are believed to be resulting of Irradiation Assisted Stress Corrosion Cracking (IASCC). In order to better understand the IASCC phenomenon, the study of the irradiation effect on the oxide scale and their formation and growth mechanisms is of great importance. It therefore passes through the understanding of the oxidation mechanisms and especially during the oxidation first stages as new surfaces will be exposed to the primary medium as the crack propagates. Moreover, the irradiation defects and microchemistry changes might modify the oxidation kinetics and oxide layers formed.

Based on all the experimental studies presented above, several authors offered different descriptions of the oxide layers formed on austenitic stainless steels in primary medium of PWRs. All authors agree that the oxide is duplex. The inner layer is chromium rich and formed by solid state diffusion according to Wagner model. Concerning the outer iron rich crystallites, the authors evaluate its formation as a balance between a solid state diffusion, the dissolution of this layer into the solution and the precipitation of corrosion products. The growth mode of the oxide layers remains today a point of disagreement as well as the crystallographic structure of the oxide layers. Although the majority of them describe it as having a cubic structure, some identify it with a hexagonal structure or even a mixture of the two structures. Contentions also

arise on the poly or monocrystalline nature of the inner oxide layer. Several authors evidenced the presence of a nickel-rich area underneath the inner oxide. The literature survey also highlighted the influence of the various parameters which can affect the oxidation kinetic, morphology, chemistry and thickness of the oxide layer formed. Indeed, it has been shown that the surface state and cold-work, oxidising medium chemistry, crystallographic orientation, grain boundary character and irradiation may play a role in the oxide formed. The effect of the surface state on oxidation needs to be further studied since it remains unclear and might influence the oxide layers. Only few authors studied the effect of the crystallographic orientation of the underlying metal grain on the oxide formed and most oxidations described in the above paragraphs were carried out at long oxidation times. However, both inner and outer oxides are formed during the first minutes of oxidation and the crystallographic orientation of the underlying metal grain was found to alter the crystallite morphologies and the epitaxial relationship between the inner oxide and the substrate. Thus, the crystallographic orientation of the metal should be taken into account since epitaxial relationships between the different oxide layers are established and influence the oxidation kinetic. The knowledge of such relationships is therefore essential to refine at best a corrosion model. Furthermore, the role of irradiation on the stainless steels oxidation in PWR medium is still poorly understood and was never studied taking the underlying metal grain orientation into consideration. This bibliographic overview highlighted the irradiation defects created under irradiation as well as the chemical modifications. These can affect the oxidation. Inner oxides formed on irradiated alloys were found to be richer in chromium than the ones formed on unirradiated specimens. Some authors observed that thicker inner layers are formed on irradiated materials while others observed thinner oxides. Changes in the inner layer thickness and chromium enrichment observed in irradiated samples are likely to be linked to the post irradiation microstructure since the diffusion of chromium is supposed enhanced by the irradiation defects. Moreover, since segregation of elements at grain boundary is one of the processes occurring in service of PWRs internals that could affect the oxidation phenomenon, its effect should be studied. The effect of Radiation Induced Segregation on the oxide layer growth has to be clarified. As the effect of irradiation on the oxidation is not yet clear, it should be investigated at short oxidation times to bring light on the involved mechanism in the oxidation first stages.

To extend the literature and have better understanding of the underlying mechanism of IASCC, it is necessary to study oxidised irradiated material in PWR medium. As neutron irradiation requires costly specialised facilities to investigate the materials, it is essential to emulate at best the PWR irradiation on laboratory samples. Proton irradiation can serve as an efficient tool to simulate neutron damage using correct temperature shifts. Indeed, proton irradiation has been successfully used in several studies to simulate neutron irradiation damages (loops, RIS, etc.) and will be used in this study. To study at best the IASCC mechanisms, one should focus on the investigation of the oxidation occurring at the crack tips. To do so, short time oxidations will be performed to study the oxidation first steps on irradiated materials. As described above, the sample preparation and its cold-work degree can greatly influence the oxide scales formed. Therefore we need to understand better the effect of cold-work induced by the polishing steps. Hence, to emulate the PWR oxidation, one must control the sample preparation at best.

The analysis of the above studies also made possible to perform a comparison of the characterisation techniques used to analyse the oxide layers. Analysing surfaces of thin layers (less than 20 nm) with macroscopic techniques such as Raman spectroscopy, X-Ray Diffraction (grazing or not) is very complex because of the lack of spatial resolution of both techniques. Moreover, when the surface to be analysed is rough due to the presence of an oxide scale the data analysis tends to become more complicated since the signals come from both the inner and the outer oxide layer. Currently, the techniques allowing to obtain accurate and precise results turn out to

be Scanning Electron Microscopy (SEM) and Transmission Electron Microscopy (TEM). These techniques make it possible to observe the thin oxide layers and the irradiation induced changes in transverse sections. However, TEM sample preparation should be optimised at best to lessen the artefacts generated and to obtain good quality thin lamellae. Although sample preparation may be challanging, the use of TEM allows to perform a morphological, chemical, crystallographic and atomic analysis of the oxide and the irradiation induced changes with a very high spatial resolution. The only weakness of electron microscopy is related to the very low material volume analysed which may not be perfectly representative of the whole material and thus requires multiple sampling. That is why the study presented below implements electron microscopy but also macroscopic analysis techniques (optical microscopy, Grazing Incidence X-Ray Diffraction (GIXRD), and Raman spectroscopy) in order to validate the results obtained by SEM and TEM.

Synthesis of the literature:

- Cold-work effect on oxidised materials should be further investigated since they remain unclear. Therefore, sample preparation must be meticulous enough not to induce cold-work in the sample prior to oxidation.
- Short time oxidations focusing on the crystallographic orientation of the metal grain underneath on both the inner and outer oxides are still to investigate to better understand the growth mechanisms of the oxide layers.
- The influence of irradiation defects on the oxidation kinetics was studied but their effects remain unclear especially for the first steps of oxidation taking the crystallographic orientation of the metal into account.
- The Radiation Induced Segregation at grain boundaries, depending on the grain boundary character was studied by several authors but the corrosion behaviour of such boundaries is to be examined since they might impair the Irradiation Assisted Stress Corrosion Cracking resistance.
- The analysis of such thin oxide layers on specific grain orientations entails the use of specific techniques with Transmission Electron Microscopy being one of the most advantageous one.

In this work, oxidised in simulated PWR environment reference samples as well as samples with various polishing were investigated. This will help to fathom the effect of sample preparation and more generally of cold-work on the oxidation kinetic and give information on the oxide scales formed on unirradiated materials. Short times oxidation to study the oxidation first steps to relate to the oxide formation and growth at the crack tips were performed while taking the crystallographic orientation of the metal into account. Proton pre-irradiated samples were prepared and oxidised to understand the influence of irradiation defects on the oxidation kinetic. Moreover, an oxidation under proton flux was performed at the University of Michigan to look upon the contribution of the proton flux on the oxidation process as occurring in PWRs. Finally, an oxidised crack tip of a decommissioned bolt was studied and compared to all the other samples before concluding on the representativeness of this study. The outer and inner layers were characterised using macroscopic and nanoscopic techniques from their morphology, thickness, structure to composition while investigating the intergranular oxidation. Ultimately, all the obtained results allowed to discuss the oxidation mechanisms and studied parameters.

Chapter 2

Experimental techniques and studied materials

Contents

2.1 Experimental techniques . . . 61
2.1.1 Optical microscopy . . . 61
2.1.2 Grazing Incidence X-Ray Diffraction . . . 61
2.1.3 Raman spectroscopy . . . 62
2.1.4 Scanning Electron Microscopy . . . 63
2.1.4.1 EBSD mapping before oxidation . . . 63
2.1.4.2 Surface observations after oxidation . . . 64
2.1.4.3 Oxide thickness measurements . . . 66
2.1.4.4 TEM lamellae preparation and optimisation . . . 66
2.1.5 Transmission Electron Microscopy . . . 69
2.1.5.1 Electron diffraction . . . 71
2.1.5.2 Bright Field images . . . 71
2.1.5.3 Dark Field images . . . 72
2.1.5.4 Scanning Transmission Electron Microscopy . . . 72
2.1.5.5 Energy Dispersive X-ray Spectroscopy . . . 73
2.1.5.6 Electron Energy Loss Spectroscopy . . . 74
2.1.6 Experimental techniques: Synthesis . . . 77
2.2 Materials and samples preparations . . . 78
2.2.1 Samples oxidised in simulated primary water . . . 78
2.2.1.1 Reference 316L alloy . . . 78
2.2.1.2 Cold-worked 316L alloy . . . 81
2.2.1.3 Proton pre-irradiated 316L alloy . . . 82
2.2.1.4 Oxidations in simulated PWR media . . . 84
2.2.2 Irradiation Assisted Corrosion . . . 86
2.2.3 Decommissioned bolt . . . 89
2.2.4 Materials and samples preparations: Synthesis . . . 91
2.3 Characterisation of the irradiated samples and proton irradiation representativeness . . . 91
2.3.1 Microstructural modifications characterisation . . . 92
2.3.1.1 Frank loops . . . 92
2.3.1.2 Cavities . . . 95
2.3.2 Chemical modifications characterisation . . . 99
2.3.2.1 Intragranular segregation and precipitation . . . 99
2.3.2.2 RIS at grain boundaries . . . 104
2.3.3 Proton irradiation representativeness . . . 107

The objective of this chapter is to present the studied materials as well as the experimental techniques used to investigate the oxidised samples. Focus will be brought upon the characterisation of the irradiated samples. The first section depicts the microscopic and macroscopic characterisation techniques used to study the samples and details will be given on the obtained information using these techniques. All the studied materials, the sample preparations and their oxidation are described in the second section. In this section, the first part will focus on samples oxidised in the Titane corrosion loop in simulated primary water. The second part will present a sample oxidised under proton flux in a dedicated device to study the Irradiation Assisted Corrosion. Then, the third part will introduce the decommissioned bolt neutron irradiated investigated in this study. Finally, the last section will focus on the investigation of the irradiated materials microstructure and chemistry. Proton irradiated samples will be compared to the extracted bolt. A discussion will be held on the proton irradiation representativeness compared to the neutron radiation.

2.1 Experimental techniques

The experimental techniques chosen for this study are detailed in the following paragraphs. These techniques range from macroscopic analysis techniques to microscopic analyses to characterise the studied oxide scales. They were chosen to give the required information on the oxide morphology, thickness, chemistry, structure, at the appropriate scale. The results from these techniques will help to conclude on the oxidation kinetics and the involved mechanisms.

2.1.1 Optical microscopy

Optical microscopy was used to observe the samples before and after oxidation. It permitted to assess the oxidation homogeneity and gave an overview of the oxidation effects. These images were primarily acquired to be compared with the Electron Back Scattered Diffraction (EBSD) maps. Optical images allowed to conclude if a relation could be established between the crystallographic orientation of the metal and the outer oxide growth kinetic. Indeed, such images can highlight a contrast due to the differences of reflexivity of the outer oxide depending on its thickness, morphology, coverage, etc.

Optical microscopy: This technique permitted to look upon the oxidation homegeneity. The images were compared to EBSD maps to conclude on the effect of crystallographic orientation on the oxidation behaviour.

2.1.2 Grazing Incidence X-Ray Diffraction

X-Ray Diffraction is a well-known technique used to characterise a sample crystallographic structure. Nonetheless, the signal emitted by "thin" (1 to 1000 nm) films is usually weak. One way to avoid that and to increase the contribution of the signal from the film is to perform a diffraction with small grazing angle using Grazing Incidence X-Ray Diffraction (GIXRD).

In order to characterise the crystallographic structure of thin oxide scale formed on the 316L alloy, the choice of GIXRD device was of great importance. As fluorescence can create an important background noise on iron based alloys and thus lose the oxide peaks searched, a device capable of handling fluorescence is recommended.

Grazing Incidence X-Ray Diffraction were performed at the CIRIMAT of Toulouse using a Bruker D8 Advance and processing was done using EVA software. This device possesses a copper anode (λ=1.5406 nm) and is equipped with a göbel mirror and a goniometer circle diameter (focusing circle) of 560 mm. Axial soller slit of 4° opening were used coupled with equatorial soller slit of 0.3° opening allowing to obtain resolved peaks. A beam mask of 2 mm x 10 mm was inserted and an anti-diffusion knife was placed above the sample. The device is coupled with a LynxEye XE-T detector. The acquisitions were performed with an incidence angle of 0.5 °, angular steps of 0.05° and a 15° to 80° angular range.

Calculations were made using the AbsorbDX software to determine the penetration depth in the expected compounds (Table 2.1). It is therefore expected to have on the diffraction pattern both the oxide scale and the matrix.

Table 2.1: *Penetration depth in the expected compounds*

Specie	Penetration depth (nm)
316L	~ 100
Fe_3O_4	~ 170
$FeCr_2O_4$	~ 210

Grazing Incidence X-Ray Diffraction: This technique allowed to characterise the oxide structure thanks to a very small incidence angle of 0.5 °.

2.1.3 Raman spectroscopy

Raman spectroscopy can provide information on the molecular structure and the characteristic fundamental vibration of a compound. Raman only allows to study materials which have a polarizability change (not suited for metals and alloys). Raman spectra plot the scattered intensity against the "wavenumber" shift (energy). The wavenumber ($\widetilde{\nu}$) is the most common unit in Raman spectroscopy and is linked to the frequency ν, the speed of light c and the wavelength λ by the equation 2.1.

$$\widetilde{\nu} = \frac{\nu}{c} = \frac{1}{\lambda}(\mathrm{cm}^{-1}) \tag{2.1}$$

The Raman vibrational bands are characterised by their wavenumber/frequency (energy), intensity (polar character of the bond) and the band shape (bond environment). As vibrational energies are unique for each molecule, Raman spectroscopy provides a specific "fingerprint" allowing to identify the molecule responsible for the band. The wavenumber or position of the band in the spectrum depends of the mass of the atoms, their geometric arrangement and the strength of the molecule chemical bond. It therefore provides information on the chemical nature and structure of the oxides by observing the active modes of vibration. In addition, it is also sensitive to the residual stresses present. Indeed, these stresses cause a deformation of the chemical bonds resulting in a displacement of the wavenumbers characteristics of the vibration mode. Details on Raman spectroscopy applied to spinel oxides can be found in Appendix B.

Raman spectroscopy was performed at the CIRIMAT of Toulouse using a confocal micro Raman Horiba Jobin Yvon Labram HR 800 with a 532 nm argon laser source. LabSpec 6 softaware was used for the fitting and processing of the Raman spectra and bands. A numerical aperture (N.A.) of 100 µm was used inducing a spot diameter (1.22λ/N.A.) of 0.72 µm and a spot depth (4λ/N.A.^{2}) of 2.6 µm. A grating of 600 lines per millimeter was used. The exposition times and accumulations were depending on the studied sample and thus emitted signal (contingent on the oxide crystallinity, its thickness etc.). The full laser power is of 13 mW without filter but a 90 % opacity filter was used reducing the laser power to 1.03 mW. Using a too opaque filter will engender a high signal/noise ratio and loss of power laser and therefore longer acquisition times. Therefore, a compromise was chosen to use a filter that did not modify the oxide scales but with a good enough signal/noise ratio. Figure 2.1 highlights the Raman spectra acquired on a sample oxidised 24 hours without a filter and using one. As one can see, without filtering a modification of the oxide occurs due to the high temperature induced by the laser power. Since magnetite is known to evolve under heating ($Fe_3O_4 \rightarrow \gamma Fe_2O_3 \rightarrow \alpha Fe_2O_3$ [154]), it suggests that a too high laser power is causing the oxide modification.

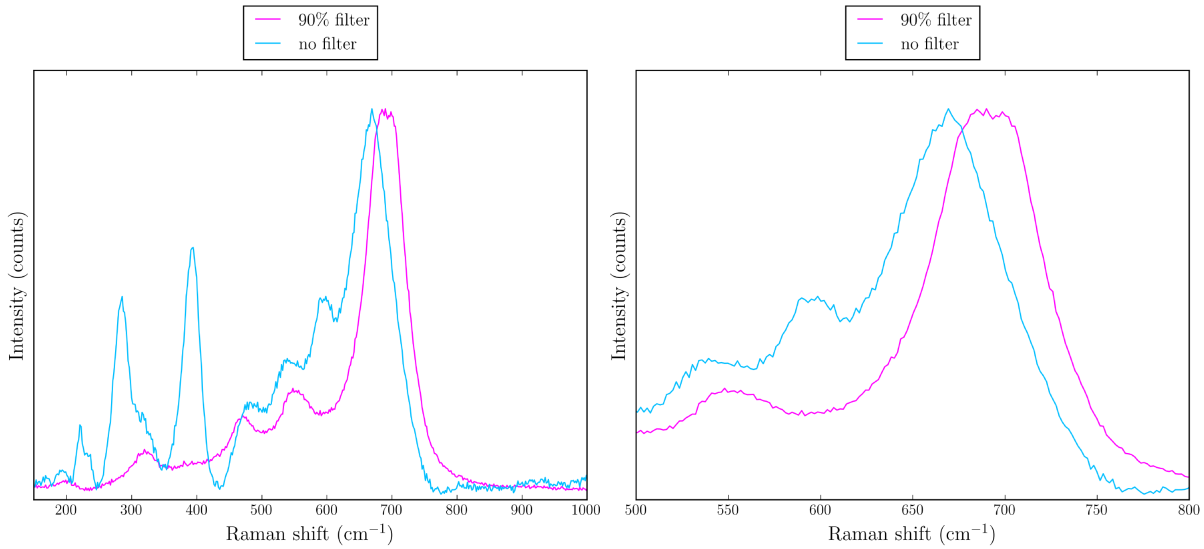

Figure 2.1: *Raman spectroscopy effect of the opacity filter on the oxide for a 90% opacity filter and no opacity filter*

As iron oxides are strongly absorbing materials, the penetration depth (z) is determined by the absorption depth of the incident laser beam: $z \simeq \frac{1}{\alpha}$ with α the absorption coefficient given for the material at a specific wavelength. Using a 532 nm laser beam, $\alpha \simeq 21\,873\,\mathrm{cm}^{-1}$ [155] and the estimated penetration depth in magnetite (Fe_3O_4) is $z \simeq 460\,\mathrm{nm}$. The whole oxide scale should therefore be investigated. Using such a device allowed to characterise oxides as a function of specific grain orientations since the micro Raman spectrometer was paired up with an optical microscope and the spot diameter was very small (0.72 µm). The obtained Raman spectra will be compared to a database of spectra or simulated ones.

Raman spectroscopy: This technique permitted to study the oxide structure and chemistry. Its paring with an optical microscope and it small probe size allowed to characterise the oxide formed on specific grain orientations.

2.1.4 Scanning Electron Microscopy

Scanning Electron Microscopy (SEM), was used to perform EBSD maps, surface observations and TEM lamellae which are all presented below. These microscopes are all equipped with an Field Emission Gun which generates electrons between 100 eV and 30 keV as well as magnetic lenses which focus the electron beam onto the sample and scan it across its surface.

2.1.4.1 EBSD mapping before oxidation

Electron Back Scattered Diffraction (EBSD) is a Scanning Electron Microscopy based technique that provides crystallographic information on a sample microstructure. It is primarily used to obtain crystallographic orientation maps, identify phases and obtain information on grain boundaries or even stresses and strains. To perfom EBSD mapping, samples must be polished down to as close as a defect-free surface and should be plane. The sample is then tilted at 70° toward the camera (Figure 2.2). During EBSD acquisitions, some backscattered electrons undergo a Bragg reflexion on specific crystallographic planes. These electrons are diffracted according to planes in a solid angle whose apex lies at the point of impact of the beam with the sample. They will create a number of paired large-angle cones matching the diffracting planes. The intersection of the cones with the screen forms an image called “Kikuchi” bands or “pseudo-Kikuchi” bands, which are recorded on a Charge-Coupled Device (CCD) camera. The number,

the position, the symmetry, the intensity and the spacing of the Kikuchi bands are characteristic of the crystallographic network and its orientation.

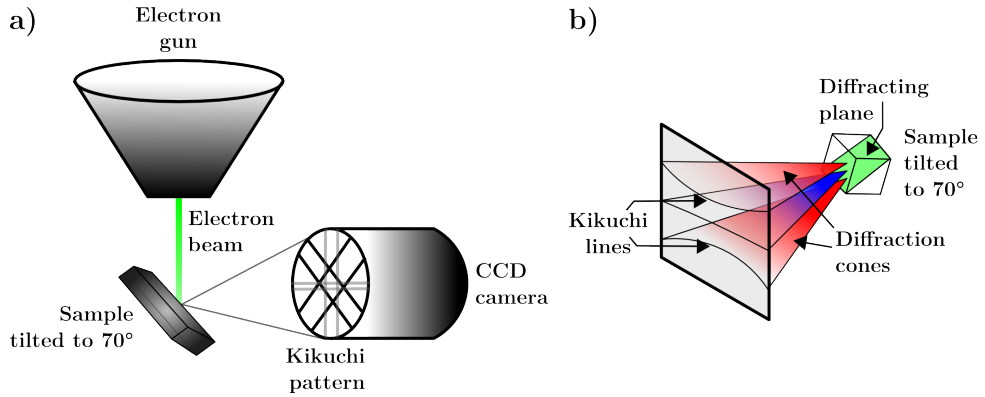

Figure 2.2: *Sketch of the EBSD a) detection geometry and b) diffraction cone and pattern formation*

EBSD mapping was carried out before oxidation using a SEM TESCAN Mira3. Since the main interest of these maps in this work was to obtain the metal orientation, the acquisition was grossly done in order to perform fast acquisitions. Mainly three orientations were of interest in this work: [100], [110] and [111]. It also allowed to determine if texture was present, the grain size and characterise grain boundaries. For the neutron irradiated material (cf. section 2.2.3) EBSD mapping was performed using a Zeiss EVO50 SEM installed in a hot cell of the LIDEC laboratories.

EBSD mapping before oxidation: This technique granted the obtention of maps revealing crystallographic orientations of the grains at the surface of the metal.

2.1.4.2 Surface observations after oxidation

All samples were observed with a FEI Dual Beam Helios nanolab 600 after oxidation. Using the EBSD maps acquired before oxidation, the oxide formed on specific grain orientation was observed with this SEM. To do so, the grains were imaged using > 15 kV Back Scattered Electrons (BSEs) and the microstructure was compared to the EBSD maps.

The average size, number, coverage and morphology of the external crystallites were observed with this microscope. Secondary electrons mostly at 5 kV were used. Image analyses were performed thanks to the ImageJ software taking into account the oxidation duration and the underlying metal grain orientation [156]. The error was reckoned to be $\pm$ 10 % of the measured value by performing unfitted thresholds. One needs to know that the coverage might by bias for high values since it was chosen to separate the crystallites in order to obtain their average size and number. When crystallites are touching each other such threshold induces an underestimation of the coverage.

BSEs were also used to investigate the oxide thickness. Indeed, atoms with high atomic number have a higher probability of producing an elastic collision because of their greater cross-sectional area. Consequently, the BSE number reaching the detector is proportional to the area mean atomic number. Therefore, a "brighter" BSE intensity correlates with greater mean Z, and "darker" areas have lower mean Z. Thus, since oxygen possesses a much lower Z than the atoms of the alloy, area with a thicker oxide will appear darker than thinner oxide areas. Calculations at several accelerating voltages were performed using the CASINO Monte Carlo software [157, 158] (Figure 2.3). A 316L substrate was simulated with a duplex oxide scale (50 nm of $FeCr_2O_4$ as the inner layer and 20 nm of Fe_3O_4 as the outer layer). The BSE penetration depth ranged from

$\sim$ 10 nm at 1 kV to $\sim$ 600 nm at 20 kV. Thus by changing the accelerating voltages one can obtain information on the oxide. Furthermore, this was used to help in finding the metal grains after oxidation by comparing to EBSD maps.

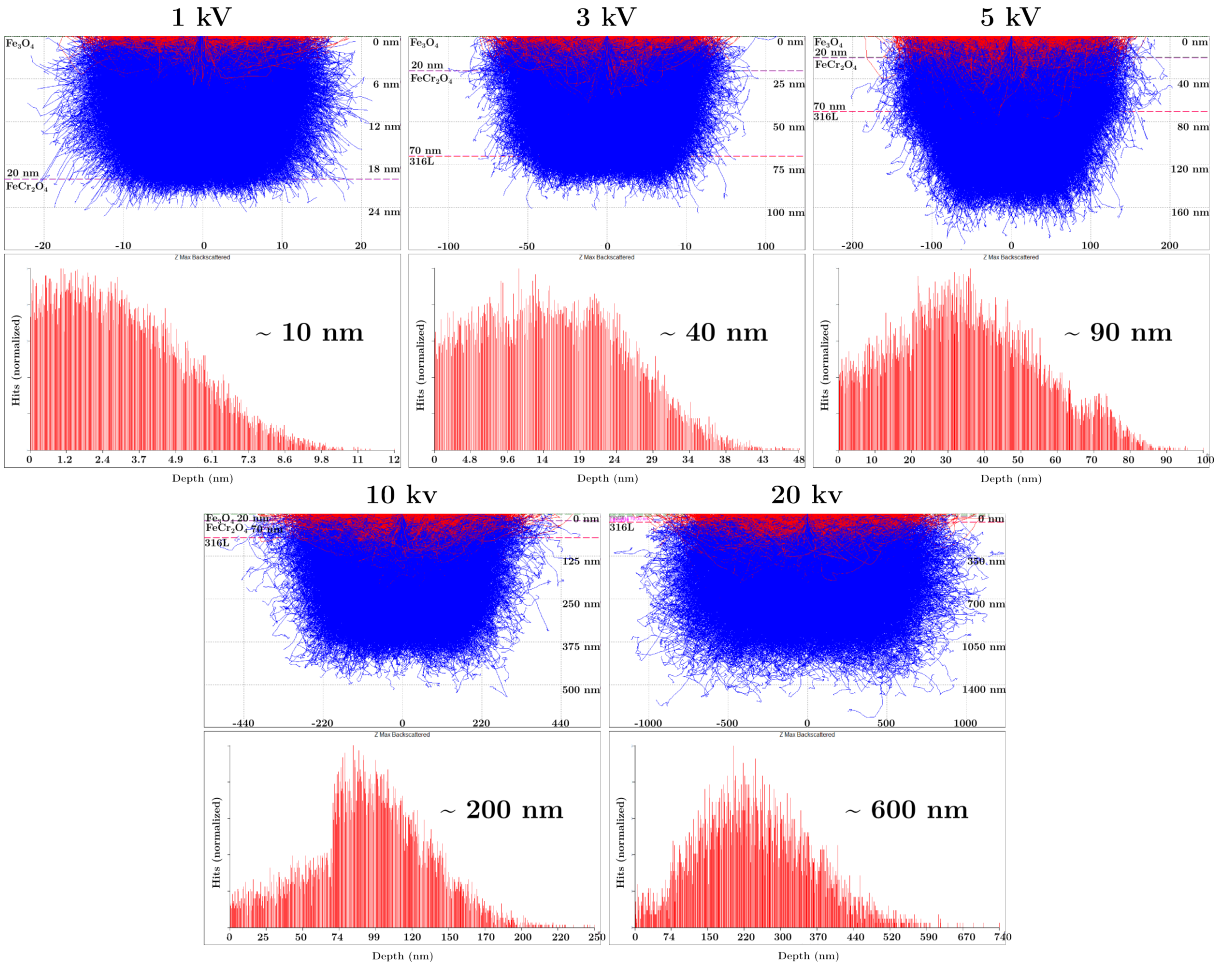

Figure 2.3: *Casino simulations on a 316L alloy substrate and a duplex oxide layer (20 nm Fe_3O_4 / 50 nm $FeCr_2O_4$) at various kV and associated BSE penetration depth*

From BSE imaging at several accelerating voltages, contrast variations are highlighted depending upon the underlying metal grain (Figure 2.4). These differences could arise from disparate oxide thicknesses since BSE contrast is based on differences in the mean atomic number or average density. As the oxides have a lower atomic mass than the metal, they will emit less BSE signal, hence regions of thicker oxide are darker. However, not all accelerating voltages make appear the same contrasts therefore hinting that not all accelerating voltages are suitable for such assessment. Indeed, using a too high voltage, the thin oxide scales and a high volume of the underlying metal grain will contribute to the observed contrasts. Thereby, channelling contrasts from the alloy will be present and will modify the contrasts which render interpretations difficult. On the contrary, using too low accelerating voltages will not help the image interpretation since the electrons will penetrate only in the oxide scale and observed contrasts result from channelling in the oxide layer. For the study of oxide layers of $\sim$ 10 to 100 nm, 3 kV and 5 kV appear the optimum accelerating voltage.

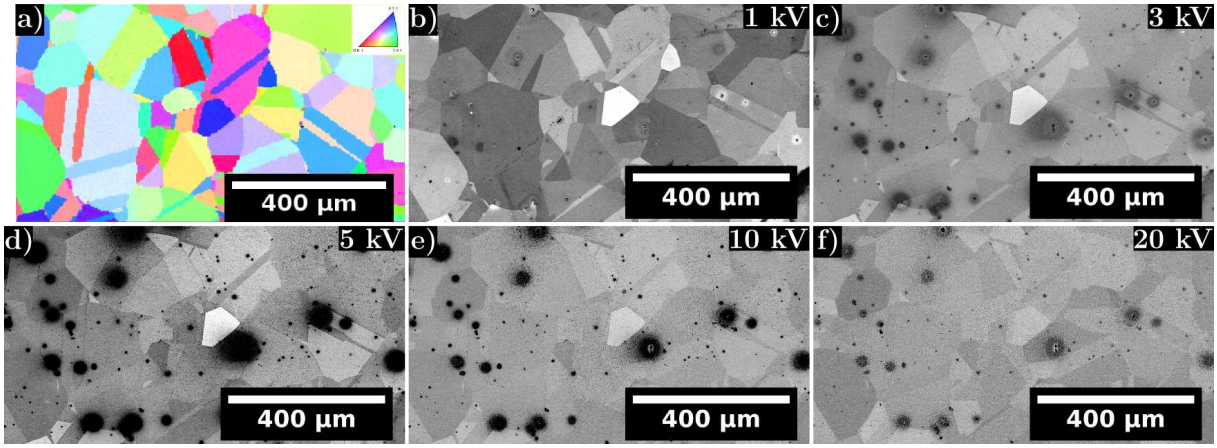

Figure 2.4: *EBSD map and SEM BSE images on the same area on a REF sample oxidised 24 hours a) EBSD maps, b) 1 kV, c) 3 kV, d) 5 kV, e) 10 kV and f) 20 kV*

Surface observation after oxidation: This imaging technique allowed to look upon the outer oxide after oxidation taking the underlying metal grain orientation into account. The outer oxide morphology, size, coverage, etc. and the overall oxide thickness were investigated. Using the appropriate accelerating voltage (5 kV) BSE imaging can be used to identify regions of thicker/thinner oxides.

2.1.4.3 Oxide thickness measurements

The oxide thicknesses were investigated using the Oxford Instrument AZtec LayerProbe software. This technique is developed for planar thin film analyses in SEM. It was coupled to an environmental FEI QUANTA SEM equipped with Field Emission Gun (FEG) source and an EDXS Silicon Drift Detector (SDD) X-Max detector of 80 mm^2 from Oxford Instruments. By coupling the SEM imaging and the previously acquired EBSD maps, acquisitions on specific grain orientations were made. The LayerProbe software allow the measurement of the composition and thickness of a planar multi-layer sample. The 316L substrate composition as well as a bi-layer were simulated to run the LayerProbe software. The layer on top of the substrate was chosen to be Chromite while the outer oxide was chosen to be Magnetite. However, a 5% variation in both oxide composition was allowed since the stoechiometry of the oxide might not be perfect. As the oxide scales formed on the samples are far from being planar it causes inaccuracy in the obtained thicknesses. The results will thus be looked upon only in a qualitative way. The LayerProbe software uses the data from an obtain spectrum and refines a model of the layered structure in order to obtain their thickness and composition.

Oxide thickness measurements: This technique granted the investigation of the oxide layer thicknesses and permitted to select areas on specific grain orientations when coupled to the EBSD maps.

2.1.4.4 TEM lamellae preparation and optimisation

Thin samples were required for TEM observations and characterisations. TEM sample preparation used to be mainly performed on electro-thinned foils which, however, present residual oxide layers on both lamella sides that can evolve under the electron beam during observation. Moreover, such sampling cannot be used on heterogeneous samples such as oxides formed on metal. FIB allows an easy sampling of a small amount of material with controlled thickness and location, thus minimising the volume of extracted material compared to electropolished foils. However,

FIB preparation induces artefacts such as gallium implantation, irradiation defects (black dots) and an amorphous layer of about 30 nm on both sides of the foil [159–161]. In neutron irradiated materials, the spontaneous disintegration of certain elements generates background noise and makes quantitative studies of segregation in EDXS very difficult. Thus, samples with a very low activity, or even better with no measurable activity, are required to quantify segregation on neutron irradiated materials using EDXS. To do so, FIB sampling appears to be the best choice for preparing TEM lamellae for IASCC studies.

The preparation of TEM lamellae was carried out with a Dual Beam Helios nanolab 600 (Figure 2.5) FIB as presented in Figure 2.5. The cross-sections as well as FIB cleaning and thinning were performed following the protocol presented by Legras [162]. Such technique permits to cut thin slices of material thus allowing observation of both the oxide layer at the surface and the material underneath and allows to prepare samples on selected areas. TEM lamellae on neutron irradiated material (presented in section 2.2.3) were prepared using a Tescan Lyra 3 FIB/SEM installed in a hot cell at LIDEC laboratories. Since a Ga^+ ion source is coupled to a SEM, the device is then called a "Dual-Beam" and allows the observation of the sample at the same time as the use of ions to cut the sample. The ionic column is inclinated from the electron column (typically by 52 °).

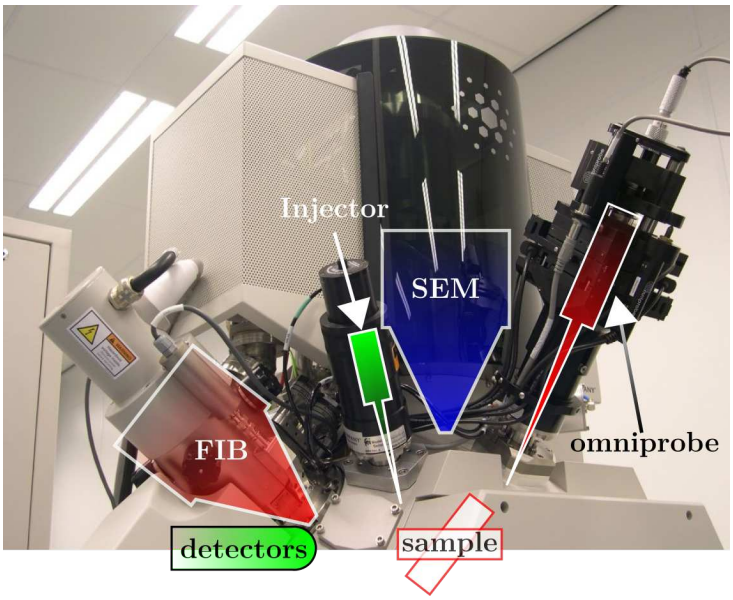

Figure 2.5: *Dual beam Helios nanolab 600 used*

Figure 2.6 presents the main operating mode of a FIB. Firstly, the emission of secondary ions and electrons can be used to form images using low ion current (Figure 2.6 a). Secondarily the chemical interaction with other gases such as carbon or platinum can induce depositions or enhance preferential etching (Figure 2.6 b). Deposits of platinum and carbon have been made via gas injectors (Figure 2.5). Carbon deposit permits to adjust the astigmatism for TEM/STEM observations and create a sharp contrast between the outer oxide and the platinum deposit during TEM imaging. Platinum deposit protects the surface to be machined and is done after the carbon deposit. Thirdly, the sputtering of substrate atoms induce milling when using high ion current (Figure 2.6 c). In this case, the focused Ga^+ used erodes the material by ion abrasion.

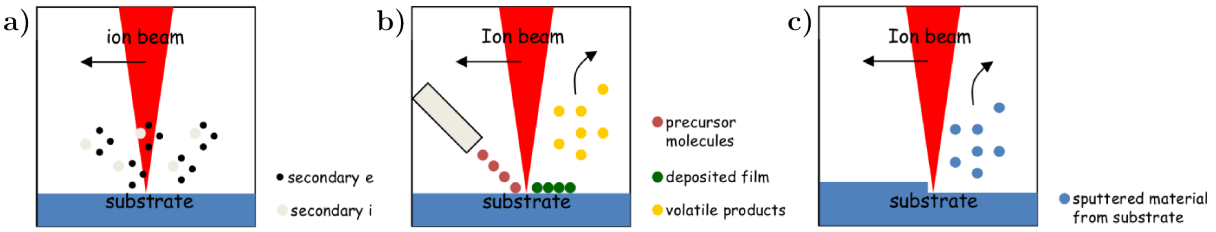

Figure 2.6: *Main usages of a FIB from [163] a) ion imaging, b) ion deposition and c) ion sputtering*

Lamellae were extracted on selected grain boundaries as presented in Figure 2.7. Doing so, two different grain orientations of interest can be obtained on one TEM sample. Lamellae with [100], [110] and [111] grain orientations were chosen. Once a cross section is made, its extraction is carried out via a micromanipulator (omniprobe visible in Figure 2.5 and 2.7) and the deposition of ionic platinum. The sample is then "welded" on a TEM grid using Pt deposit and thinned with low ion beam current.

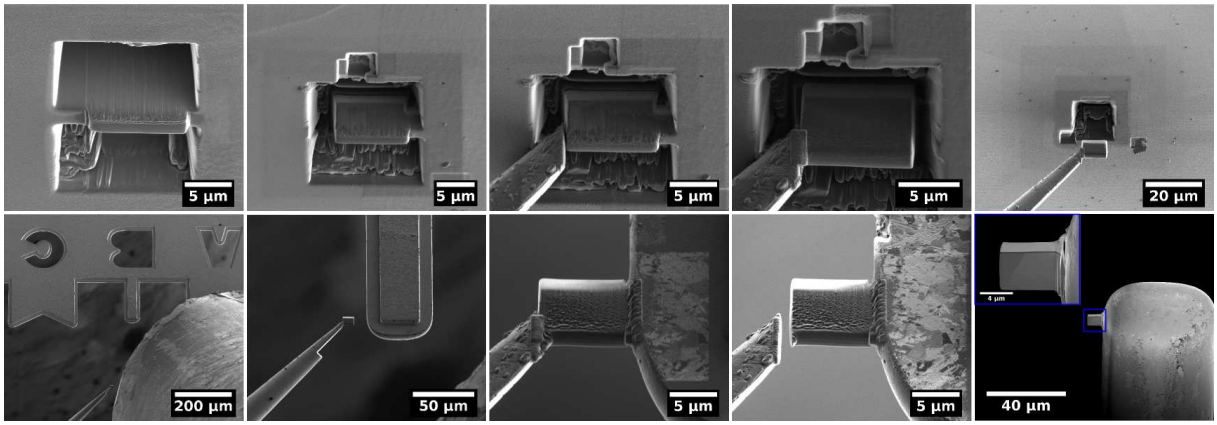

Figure 2.7: *FIB lift-out*

To counterbalance the unwanted artefacts (gallium implantation, irradiation defects, amorphous layer) an optimisation of the FIB preparation is needed. Post FIB cleaning with low-voltage argon ions allows to further thin the sample while removing the artefacts. This state-of-the-art preparation protocol provides lamellae located on a region of interest (such as grain boundaries, cracks) with a controlled thickness, without any spurious irradiation defects and amorphous layer or residual oxide layer as shown by Legras et al. [161]. The lamellae were prepared following this protocol. 500V Ar^+ ions were used to perform this final thinning of the lamellae in a Precision Ion Polishing System (PIPS) II ion polishing system. Each one was cleaned repeatedly until the desired thickness was reached depending on the characterisation to be done. Indeed, thin samples ($<$ 60 nm) can be needed for High Resolution Transmission Electron Microscopy (HRTEM) imaging or EDXS/EELS quantifications but are more rapidely subjected to degradation under the beam and are even more delicate to handle. The lamella thickness (t/λ) is measured using the ratio between an unfiltered image acquired in EFTEM mode and a zero-loss (elastic) image from the same area under identical conditions. Figure 2.8 presents TEM Bright Field (BF) images of one of the obtained lamellae after the FIB preparation and after the ionic polishing cleaning.

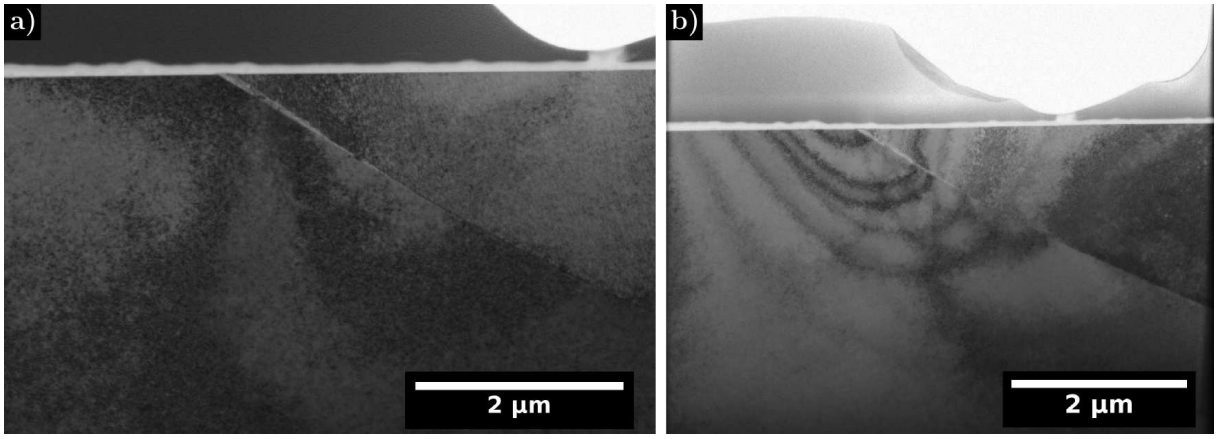

Figure 2.8: *TEM BF images of a lamella a) after the FIB preparation ($e \approx$ 150–200 nm) b) after the PIPS cleaning ($e \approx$ 30 nm)*

TEM lamellae preparation and optimisation: FIB sampling allowed to prepare thin TEM foils on area of interest. The induced artefacts were erased and the foils thinned by a post FIB cleaning using low voltage argon ions until the desired lamellae thicknesses were obtained. Such thicknesses depended upon the analyses to be made on the foil (EDXS and/or EELS analyses, HRTEM, imaging of small defects).

2.1.5 Transmission Electron Microscopy

All the techniques presented above provide information on the morphology, chemistry and structure of oxide layers formed on 316L steels at macroscopic scale. But their resolution and the observation of the sample from the surface will limit the obtained information. Indeed, with GIXRD and Raman spectroscopy it is particularly difficult to attribute the collected information to a single layer. Especially since the oxides formed have close structure and chemistry. The only alternative to overcome these constraints is to examine the cross-sectional oxide layers with a high spatial and analytical investigation technique such as Transmission Electron Microscopy (TEM). Doing so, the oxide layers can be examined independently. In addition, TEM makes it possible to collect, on the same experiment, information on the microstructure as well as on the chemistry and/or structure of the sample.

A sketch of a typical microscope is presented in Figure 2.9 with the gun, the illumination system, the objective lens, apertures, the imaging system and the screen. In a microscope three types of electromagnetic lenses are found: condensers, the objective lens and the projector lenses (diffraction, intermediate and projection lenses). They are coils traversed by a stabilised electric current which generate a magnetic field allowing the control of the electron trajectories in the column. A current variation thus modifies the convergence of the beam. Three different apertures can be distinguished. The condenser one which is under the second condenser lens and centered on the optical axis. This aperture allows to keep only the center part of the incident beam. The objective aperture is located in the back focal plane of the objective lens and is called the contrast aperture. It allows to select part of the diffracted beam to form an image. And the area selection aperture is found in the image plane and it can select part of the object in order to form its diffraction pattern.

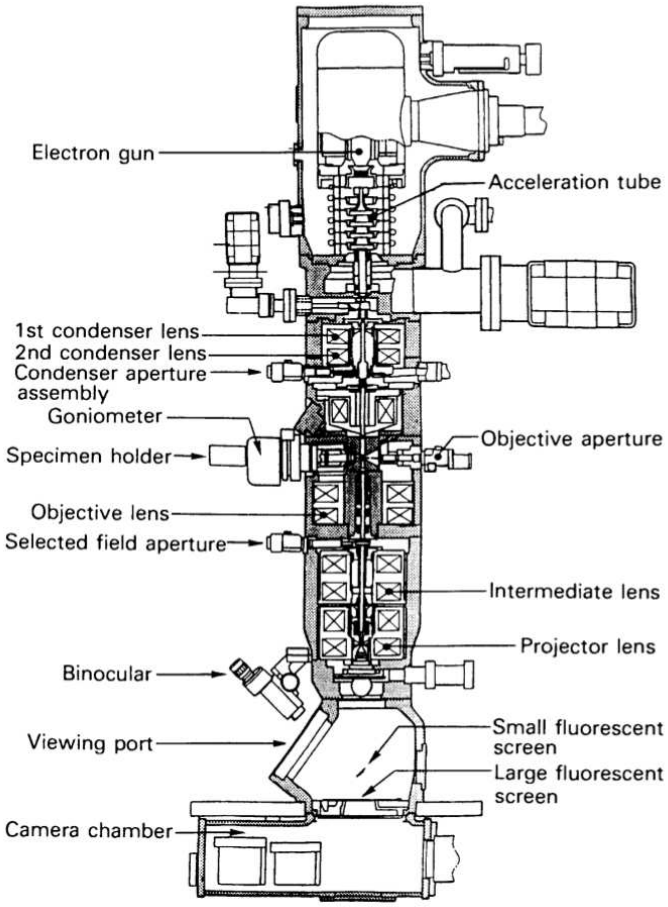

Figure 2.9: *TEM sketch [164]*

The Transmission Electron Microscope used is a FEI Tecnai Osiris 200 kV S/TEM optimised for high-speed and high-sensitivity chemical analysis measurements in STEM mode with a Super-X SDD EDXS detector. This detection system possesses four windowless SDD dectors located above the sample which offer a total collection angle about 0.9 steradian (almost seven times higher than a conventional collection angle). This microscope is equiped with an X-FEG high brightness Schottky gun that provides 2-3 times more electron current than a conventional FEG source. It is suitable for both conventional BF/DF and high resolution TEM imaging and is coupled with a Charge-Coupled Device (CCD) camera. A QUANTUM Gatan Imaging Filter (GIF) is installed on the microscope allowing to perform EELS spectroscopy and EFTEM mapping. EELS quantification required to record both low and high energy losses which is not easy using standard spectrometer due to the high brightness variation across the entire spectrum (cf. Appendix C). Included in the QUANTUM GIF, the DualEELS technology enable to record simultaneously two spectra from different energy range. It uses the electrostatic drift tube in the spectrometer to quickly switch the energy range and the electrostatic shutter to control the exposure time therefore allowing to acquire in the same region the low loss spectrum and the core loss one. Moreover, it is possible, using DigitalMicrograph software, to aquired joint EDXS/EELS spectra on a same area. The BF, two Annular Dark Field (ADF) and HAADF STEM detectors in the microscope provide a wide range of diffraction and Z-contrast conditions for STEM imaging and analysis. The microscope possesses a 0.24 nm resolution in TEM mode and 0.18 nm in STEM resolution.

2.1.5.1 Electron diffraction

In diffraction mode one should consider the wave behaviour of electrons. As the beam passes through the sample, crystalline plane in Bragg condition will diffract. It scatters the electrons in a predictable manner depending on the crystal structure. The incident beam diffracted into several beams recombine at the exit of the objective lens and form the diffraction pattern in the focal plane of the objective lens. The insertion of a selected area aperture allow to get a diffraction pattern from a specific area. The diffraction pattern is interpreted by means of the Bragg law (eq. 2.2).

$$2d_{\mathrm{hkl}}sin(\theta) = n\lambda \tag{2.2}$$

In electron diffraction $\lambda \approx 0.001$ nm therefore $\lambda \ll \mathrm{d_{hkl}}$. We can thus work using a small angle approximation and the following equation: $2\ \mathrm{d_{hkl}}\theta \approx \mathrm{n}\lambda$. Selected Area Electron Diffraction (SAED) patterns were acquired mostly to study the crystallographic relationship between the matrix and the oxides.

Electron diffraction: This technique allows to study the metal and oxide structures and orientations.

2.1.5.2 Bright Field images

The TEM imaging mode, called Bright Field (BF) mode, consists in observing the image formed by the transmitted beam in the image plane of the objective lens. In this mode, the TEM condenser lenses purpose is to control the spot size and beam convergence. An objective aperture can be added and will control the collection angle of the electron as well as the aberrations and the resolution. In BF mode, the objective aperture is centered on the optical axis onto the transmitted beam (Figure 2.10). Several constrasts arise from this imaging mode. Thick regions, areas with heavy atoms, and crystalline areas oriented along low indices zone axis will appear with a dark contrast (mass-thickness and diffraction contrasts). BF imaging allows to observe the sample as a whole, to appreciate the quality of the lift-out and to identify the thinnest areas that can be observed. By imaging the sample under and over-focus it allowed to look upon oxide porosities or the presence of oxide grains. This under/over focus technique was also used to image the cavities created under irradiation by observing the surrounding contrast associated to Fresnel fringes.

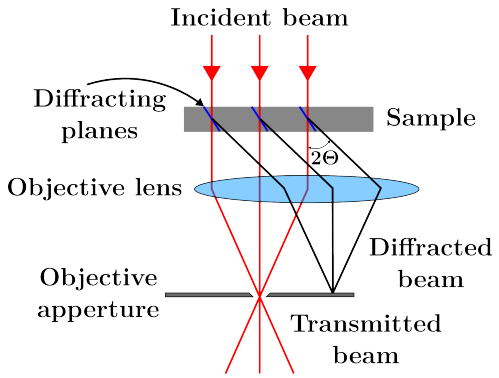

Figure 2.10: *Sketch of the Bright Field imaging mode*

Bright Field images: These images were used to look upon the lamellae, the oxide and the irradiation induced cavities (in over/under focus).

2.1.5.3 Dark Field images

As opposed to Bright Field imaging mode, in the Dark Field (DF) imaging mode the objective aperture select only diffracted electrons (scattered electrons) in order to form an image (2.11 a). When moving the objective aperture to select the wanted scattered beam, the Dark Field (DF) is called a Displaced-Aperture Dark Field (DADF). As in BF imaging the objective aperture is critical and control aberrations, the collection angle and the resolution. However, the aberration and astigmatism will be greatly increased when going further off-axis. To counterbalance that phenomenon and thus not move the objective aperture too far off-axis to select the scattered electrons, the beam can be tilted to deflect the selected diffraction spot on the optical axis. Such DF is then called a Centered Dark Field (CDF). Doing so, the objective aperture will stay on axis and one have to center the wanted scattered beam on axis by tilting the beam (Figure 2.11 b). In the current work, CDF was used to image the loop population, the potential intragranular precipitation, and the crystallographic relationship of the oxide with respect to the matrix.

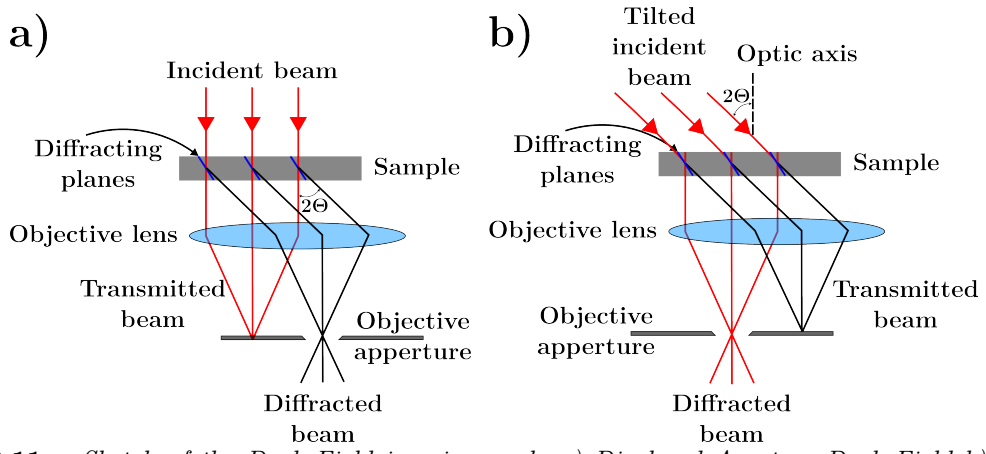

Figure 2.11: *Sketch of the Dark Field imaging mode a) Displaced Aperture Dark Field b) Centered Dark Field*

Dark Field images: Such images were used to image the Frank loops induced by irradiation, the precipitation induced by irradiation and the oxide orientation with respect to the matrix.

2.1.5.4 Scanning Transmission Electron Microscopy

In Scanning Transmission Electron Microscopy (STEM) mode, the electron probe is focused on the sample. The spatial resolution is then directly correlated to the electron probe size. A defined area of the sample can be scanned to reform a point-by-point image owing to a specific lens system. The excitation conditions of the lenses in STEM mode make that the intrinsic defects to the latter are different from the TEM mode. Three differents detectors are used to obtain STEM images (BF, DF and HAADF detectors). The BF detector, centered on the optical axis of the column, allows to obtain images having the same characteristics as a BF TEM image. The Dark Field (DF) detector has a ring shape centered on the optical axis (of internal diameter between 2 and 4 mm). Using such detector, it is then possible to form an image from electrons scattered at higher or smaller angles. By playing on the distance to the optical axis or the camera length, the angle in which the electrons will be collected can be chosen. Finally, the electrons collected by the High Angle Annular Dark Field (HAADF) detector corresponds to electrons scattered at a very wide angle, typically more than 50 mrad. The contrast of the image then essentially results from the elastic diffusion due to the interaction of the electrons with the atoms nucleus and carries a chemical signature of the sample. By assimilating the elastic scattering

to a Rutherford-type diffusion, it can be shown that the intensity of the signal collected by the HAADF detector is proportional to the atomic number of the atoms that have interacted with the beam according to the relationship $I_{HAADF} \sim Z^2$ [165]. The Figure 2.12 represents the various STEM detectors presented above.

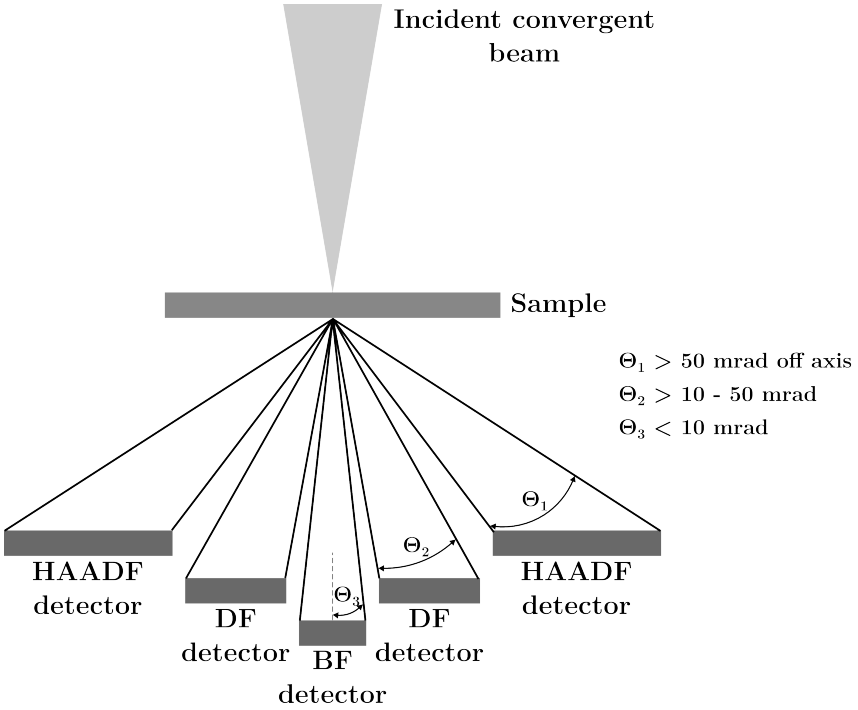

Figure 2.12: *Sketch of the STEM detectors positions*

The STEM images were primarily used to measure the inner oxide thickness using ImageJ software [156] and to look upon the cavity distribution. The contrast variation induced by the cavities in STEM HAADF images is more uniform than that of the Fresnel fringes observed in TEM BF images as the latter are contingent on the foil thickness. Therefore, some cavities not easily visible on over/under focused images are evidenced in STEM HAADF ones.

Scanning Transmission Electron Microscopy: Such images were used to assess the oxide formed and the cavities induced by irradiation.

2.1.5.5 Energy Dispersive X-ray Spectroscopy

When illuminated by the electron beam, electrons from the inner shell might become excited and finally ejected inducing the formation of a pair electron-hole. An electron from an outer shell with an higher energy then fill the vacancy created, and X-rays (X photons) are emitted with an energy corresponding to the energy difference between the higher energy shell and the lower one. X-rays emitted are then analysed in the spectrometer (number and energy) and used to identify the elemental composition of materials (Figure 2.13).

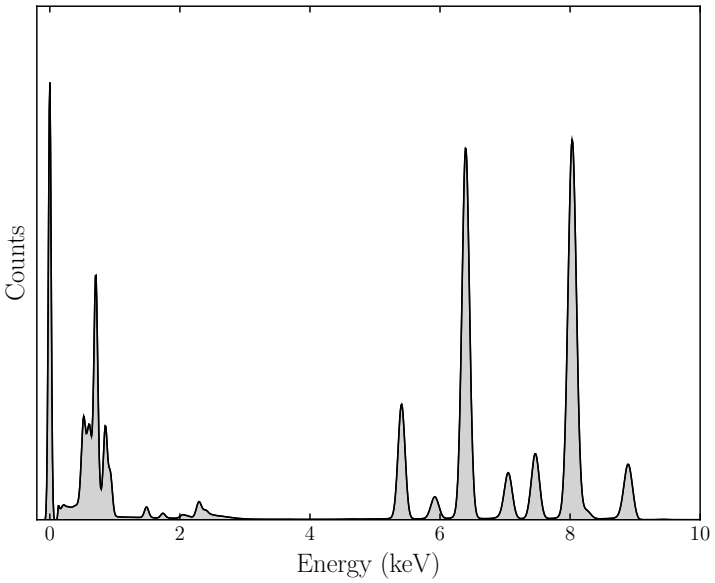

Figure 2.13: *EDXS sprectrum*

Energy Dispersive X-ray Spectroscopy combines a qualitative and semi-quantitative elemental analysis. The spatial resolution is of the order of magnitude of the probe size and the energy resolution is about 130 eV. The generated data consist of spectra showing peaks corresponding to the elements and their shell. The spectrum displays the intensity as a function of the energy of the photons detected (in keV). The peaks are characteristic of the energy of the radiation levels K, L and more rarely M of the elements present in the sample. The background noise is characteristic of Bremsstrahlung braking radiation. Bremsstrahlung X-rays are generated due to the slowing down of electrons from the electron beam by the electric field surrounding the atoms nuclei from the sample. In the results presented below regarding the oxide composition, the evolution of oxygen concentration will only be given using arbitrary units. Indeed, its quantification can be impaired due to the close vicinity of Cr-L lines (0.45-0.57 keV) and O-K lines (0.52 keV) as deconvolution of both signals can prove difficult. Furhter information on the EDXS quantifications are presented in Appendix C.

Energy Dispersive X-ray Spectroscopy: EDXS spectra were acquired to quantify the oxide composition. The oxygen content will only be displayed in arbitrary units.

2.1.5.6 Electron Energy Loss Spectroscopy

The Electron Energy Loss Spectroscopy (EELS) is based on the elastic and inelastic diffusion. Three regions can be distinguished on the obtained spectrum.

– Zero loss region (centered on 0 eV energy)

As the electrons pass through the sample, a large part of the incident electrons crosses the material without interaction. They are then transmitted without energy loss, angular deviation or undergo a very small deviation if their trajectory passes in the electronic field of the nucleus. After passing through the sample, these electrons are characteristic of the elastic or quasi-elastic diffusion. This signal corresponds, on the energy loss spectrum, to the "zero-loss" peak. This very intense peak is centered at a 0 eV energy and has a finite width indicating the instrumental energy resolution.

– Low losses region (from 0 eV to approximately 50 eV)

A large fraction of the remaining electrons (approximately 90%) interacts individually and collectively with the electron cloud surrounding the atoms (conduction electrons, valence electrons).

This inelastic interaction occurs with low energy losses and low angular deviations of electrons. This signal corresponds, on the spectrum, to the loss domain of transitions inter or intra-band and the "plasmons". It provides information on the chemistry, structure and dielectric properties of the sample.

– High losses region (extends from 50 eV up to several thousand electronvolts)

The fraction of electrons remaining interacts with the core electrons that gravitate on the electronic layers surrounding the nucleus. This interaction takes place with a more or less significant energy loss, characteristic of the chemical specie atomic number, and a more or less strong angular deviation. This signal corresponds on the spectrum to the core loss region. It is reflected on the spectrum by peaks associated with a jump in intensity superimposed on the continuous background. The threshold area, which extends over almost 20 eV beyond the threshold front, is the domain of fine structures called Energy Loss Near Edge Structure (ELNES). These structures reflect the density of unoccupied states and depend on the chemical environment and the valence of the atom considered.

The acquisition of the spectra is carried out thanks to, in our case, a Gatan Imaging Filter (GIF) which is a post-column energy filter. It is composed of a magnetic prism which is positioned below the spectrometer entrance aperture and bends, disperses as well as focuses the incident electron beam. Two techniques allow to collect the information obtained by the electron energy filtering system. These correspond to two distinct acquisition modes presented below and in Figure 2.15:

– Electron spectroscopy

This technique consists in forming a spectrum through the GIF. No slit is inserted in the electron output path and the intensity variations of the scattered electrons are directly recorded on a CCD camera and classified by increasing energy loss to form a spectrum. This type of acquisition is called Electron Energy Loss Spectroscopy (EELS). The choice of the diaphragm spectrometer makes it possible to optimise the signal-to-noise ratio and the resolution of the spectrum.

– Energy filtered imaging

By introducing an energy selection slit after the magnetic prism, a chemical image of the selected area is reformed. The slit will only let through a selected energy range and solely the electrons of the chosen energies will reach the camera. This type of acquisition is called Energy Filtered Transmission Electron Microscopy (EFTEM) imaging. In this work solely the three windows method presented in Figure 2.14 has been used allowing to estimate in a relative way the chemical concentration between several elements. Lamella thickness measurements were performed by acquiring an unfiltered image and a zero-loss (elastic) image from the same area under identical conditions. The thickness (t/λ) is then automatically calculated using the Poisson statistics of inelastic scattering.

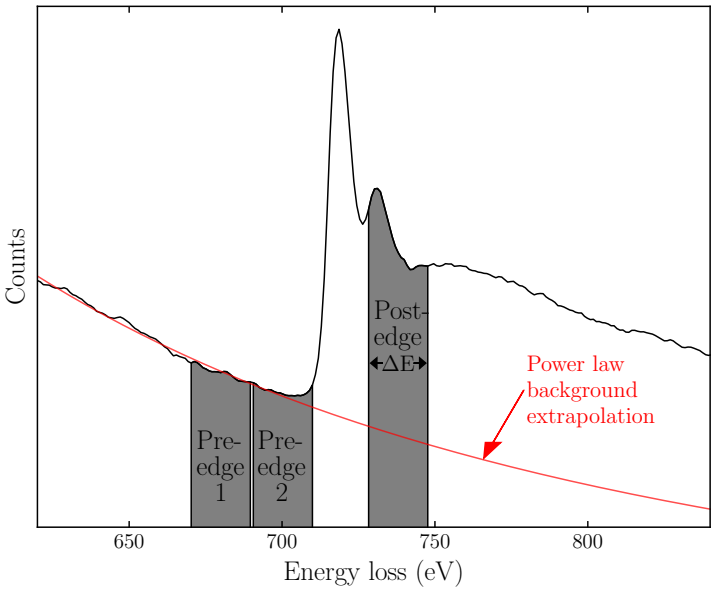

Figure 2.14: *EFTEM acquisition with the three windows method*

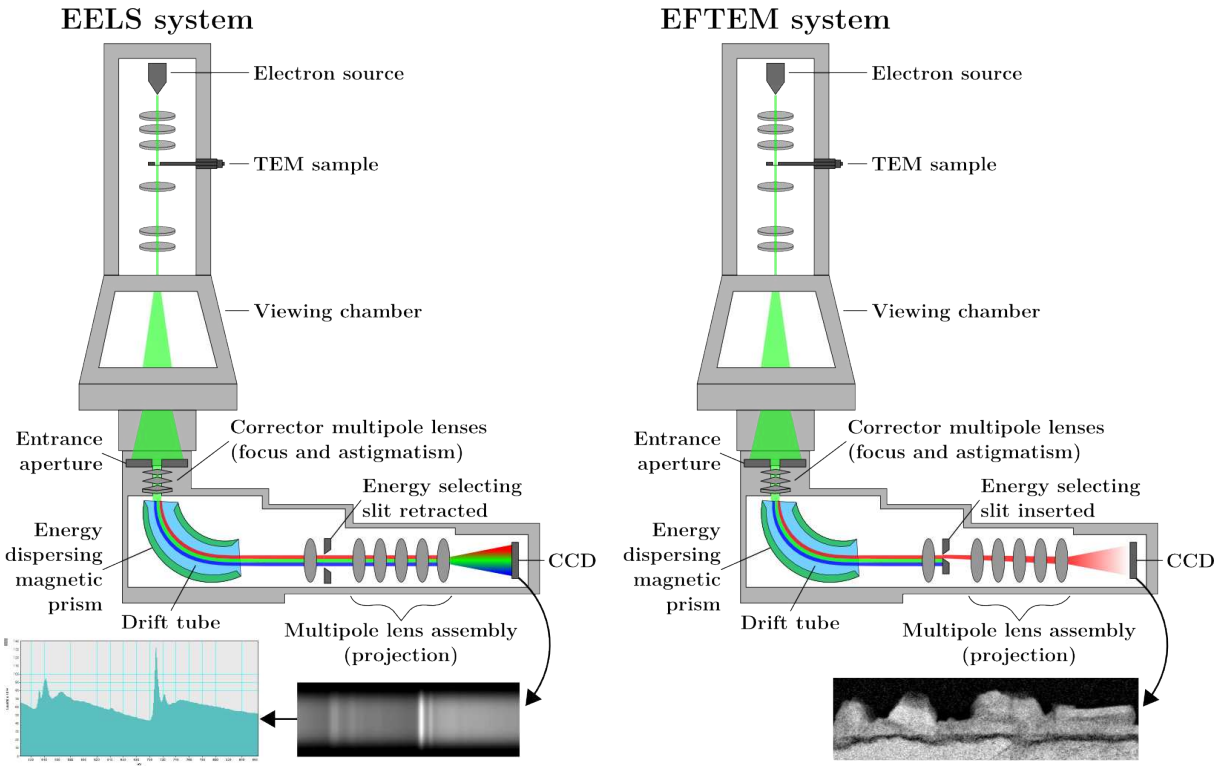

Figure 2.15: *Schematic of the EELS and EFTEM mode in TEM*

Details on the EELS quantifications performed (convergence and collection angles, background extraction, edge-identification etc.) can be found in Appendix C.

Electron Energy Loss Spectroscopy:

- Thickness maps were obtained by acquiring an unfiltered and a zero-loss image on the same area.
- EFTEM imaging allowed to look upon the oxide composition in a qualitative way.
- EELS spectra were acquired to quantify the oxide composition.

2.1.6 Experimental techniques: Synthesis

Below are summarised the main points of interest of this study that need to be investigated to better understand the oxidation mechanisms and the associated techniques that were used. Each technique and its physical principle was briefly described in the above paragraphs.

Sample preparation:

- Electron Back Scattered Diffraction mapping to obtain the metal grain crystallographic orientations.
- Focused Ion Beam sampling using Scanning Electron Microscopy Back Scattered Electrons imaging coupled with the EBSD maps.
- Energy Filtered Transmission Electron Microscopy imaging for TEM lamella thickness measurements.
- Precision Ion Polishing System II cleaning and thinning of the lamellae.

Microstructural and chemical modifications induced by irradiation:

- Under and over-focus Transmission Electron Microscopy Bright Field imaging of the cavities.
- Transmission Electron Microscopy Dark Field imaging on the rel-rod strikes of the dislocation loops in 2-beam condition near [101] zone axis.
- Electron Energy Loss and Energy Dispersive X-ray Spectroscopies mapping of the inter/intragranular Radiation Induced Segregation and precipitation.

Morphological evolution of the oxide layers:

- Optical microscopy coupled with the EBSD maps.
- Scanning Electron Microscopy Secondary Electron and Back Scattered Electron imaging coupled with the EBSD maps.
- Transmission Electron Microscopy Bright Field and Scanning Transmission Electron Microscopy imaging on selected grain orientations.

Structural evolution of the oxide layers:

- Grazing Incidence X-Ray Diffraction.
- Raman spectroscopy on specific grain orientations coupled with the EBSD maps.
- Diffraction and Dark Field Transmission Electron Microscopy on selected grain orientations.

Chemical evolution of the oxide layers:

- Raman spectroscopy on specific grain orientations coupled with the EBSD maps.
- Energy Filtered Transmission Electron Microscopy mapping, Electron Energy Loss and Energy Dispersive X-ray Spectroscopies on selected grain orientations.

2.2 Materials and samples preparations

2.2.1 Samples oxidised in simulated primary water

Below are presented the samples oxidised in simulated primary water. The 316L alloy with both reference samples and cold-worked ones are depicted as well as the proton pre-irradiated samples. The sample preparation will be detailed in-depth. With regard to the study of the irradiation effect on the oxidation, different types of defects have been created in the material by proton implantation before oxidation. The irradiation conditions will be detailed as well the choices made to simulate neutron irradiation following indications given in the literature. The oxidation tests in the TITANE corrosion cell using simulated primary water environment and campaigns performed will be described.

2.2.1.1 Reference 316L alloy

The austenitic stainless steel studied was provided by EDF R&D. It is a commercial heat of solution annealed Z2CND17.12 (X2CrNiMo17-12-2), more commonly called 316L, from Creusot Loire Industrie. The metal sheet was hot rolled and then solution annealed between 1050 and 1150 °C. The chemical composition of the alloy is presented in the following Table 2.2. This analysis was carried out by X-ray Fluorescence Spectrometry (XFS) for the heavy elements. The carbon content was determined by combustion then Infrared Absorption Spectrometry (IAS). Nitrogen and oxygen contents were ascertained by thermal conductivity measurement and by IAS respectively. The alloy composition is compared in Table 2.2 to the French RCC-M specifications of nuclear units. As can be seen, the composition of the studied 316L alloy is in agreement with the specifications except for the phosphorus content (0.028 wt. % vs 0.02 required).

Table 2.2: *Studied 316L alloy composition compared to RCC-M specifications [3]*

Element	C	Cr	Ni	Mo	Mn	Si	N	S	P	Cu	O	Fe
RCC-M specifications (wt. %)	≤ 0.03	16-19	10-14	2.25-2.75	≤ 2	≤ 1	-	≤ 0.015	≤ 0.02	≤ 1	-	Bal.
Studied 316L (wt. %)	0.027	17.1	11.5	2.58	1.9	0.4	0.051	0.005	0.028	0.2	0.009	Bal.
Studied 316L (at. %)	0.13	18.3	10.9	1.5	1.9	0.8	0.2	0.01	0.05	0.18	0.03	Bal.

Samples were machined using Electrical Discharge Machining (EDM) with the following dimensions: 10.85 mm x 11.85 mm x 1.7 mm from the metal sheet. A reference polishing procedure was applied down to OP-S (colloidal silica) for "reference" samples called further on **REF** samples. This polishing methodology was validated by Sun [166] and is presented in Appendix D (Tables D.1 and D.2). The point was to obtain samples without any induced hardening or dislocations brought by the polishing steps.

Figure 2.16 presents an optical image acquired on the polished 316L alloy before oxidation. Several inclusions in the material are highlighted and those were found to be MnS precipitates and Cr, Mn, Ti, Al oxides from SEM EDXS characterisations (Figure 2.17).

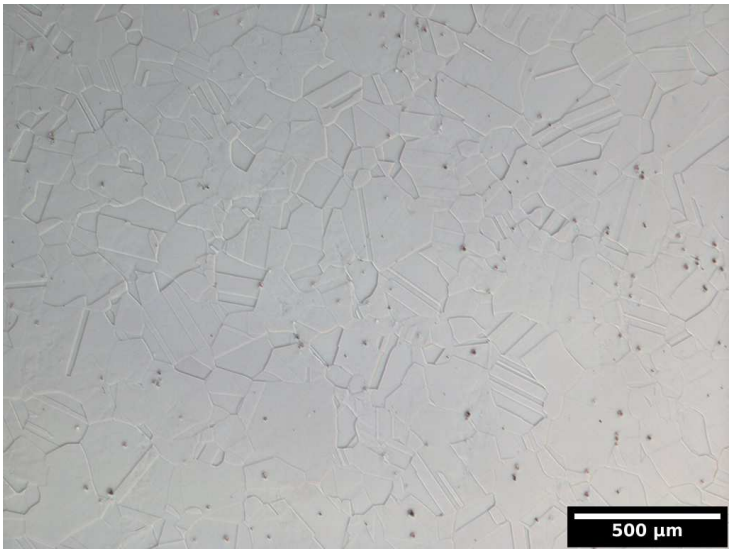

Figure 2.16: *Optical image of the microstructure of the polished 316L alloy before oxidation*

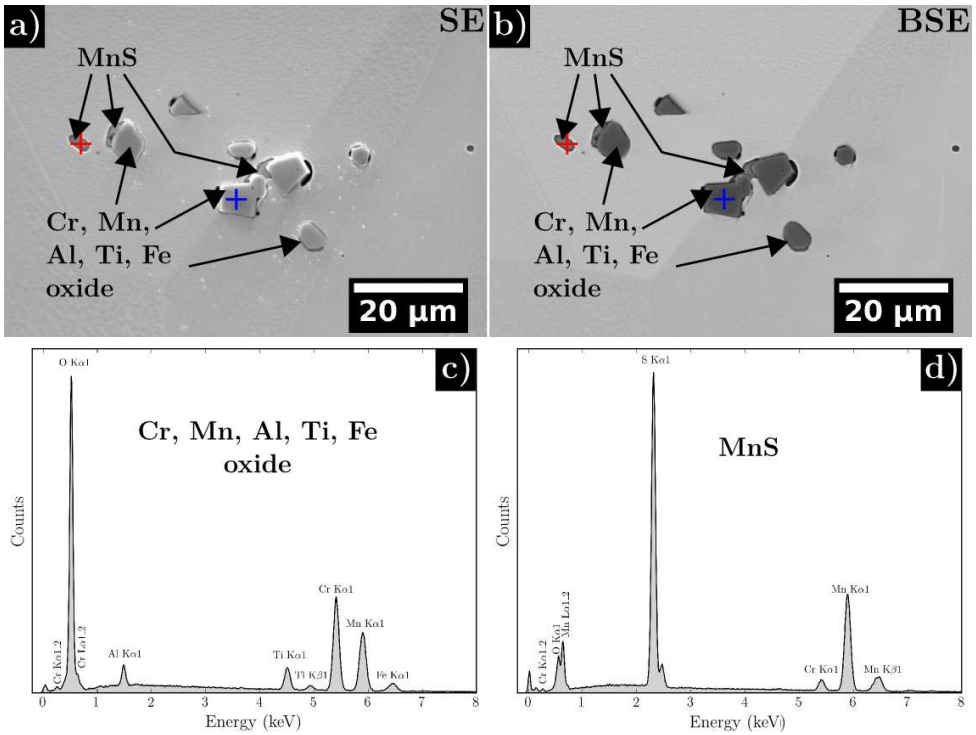

Figure 2.17: *a) SEM SE image of the inclusions present in the 316L alloy b) SEM BSE image on the same area c) EDXS spectrum on the blue cross d) EDXS spectrum on the red cross*

Average grain size was obtained thanks to EBSD mapping and data treatments using the OIM analysis software. The imposed misorientation for the grain calculation was of five degrees allowing to represent at best the grain population. The grain size calculated results from three averaged data collection of each 16 mm^2. The grain size was calculated with and without taking into account the $\Sigma 3$ recrystallised twin boundaries (Figure 2.18). The average grain size of the 316L alloy is about 90 µm (Table 2.3).

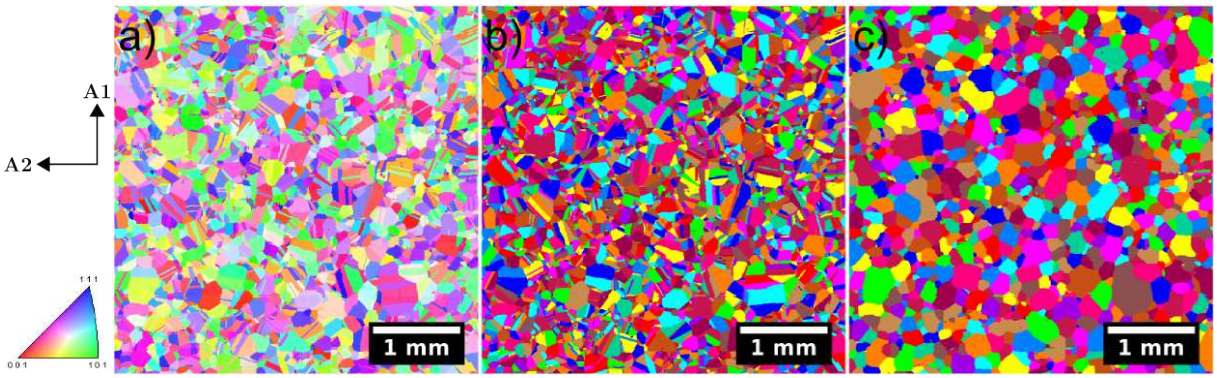

Figure 2.18: *EBSD data treatment of the 316L alloy a) inverse pole figure map b) grains map with the Σ3 twins c) grains map without the Σ3 twins*

Table 2.3: *Average grain size of the 316L alloy over three EBSD data collection of 16 mm² each*

	With Σ3 twin boundaries	Without Σ3 twin boundaries
Average size (µm)	50	92
Standard deviation (µm)	41	72
Number of analysed grains	4782	1476

Since the alloy was hot-rolled, its texture was investigated using EBSD data collection. The local crystallographic orientation of the grain being registered on each point of the acquisition, the data representation using stereographic projection provides information on the sample texture. Figure 2.19 presents the pole figures calculated along <100>, <110> and <111> directions. The analysis of these projections shows that the crystallographic orientations are isotropically distributed

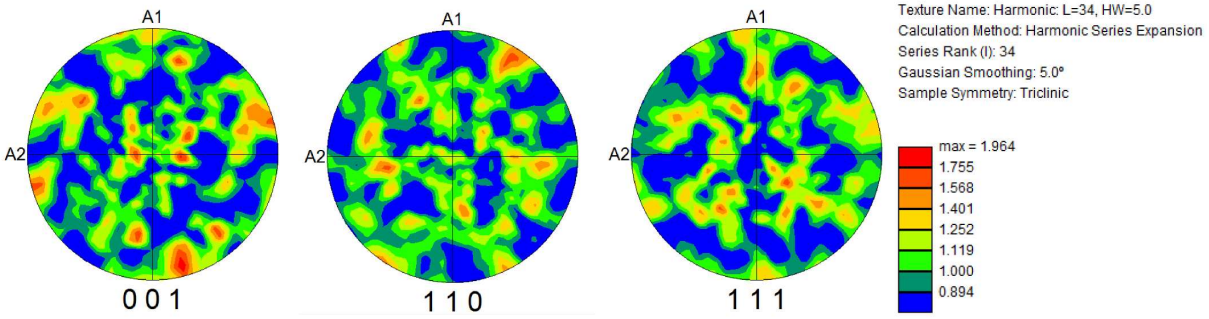

Figure 2.19: *Texture of the 316L from EBSD data treatment, pole figures of the studied 316L alloy along <100>, <110> and <111> directions*

To better understand the obtained spectra from X-Ray Diffraction (XRD) on oxidised 316L, an unoxidised sample was firstly analysed. The Figure 2.20 highlights the peaks of the 316L alloy.

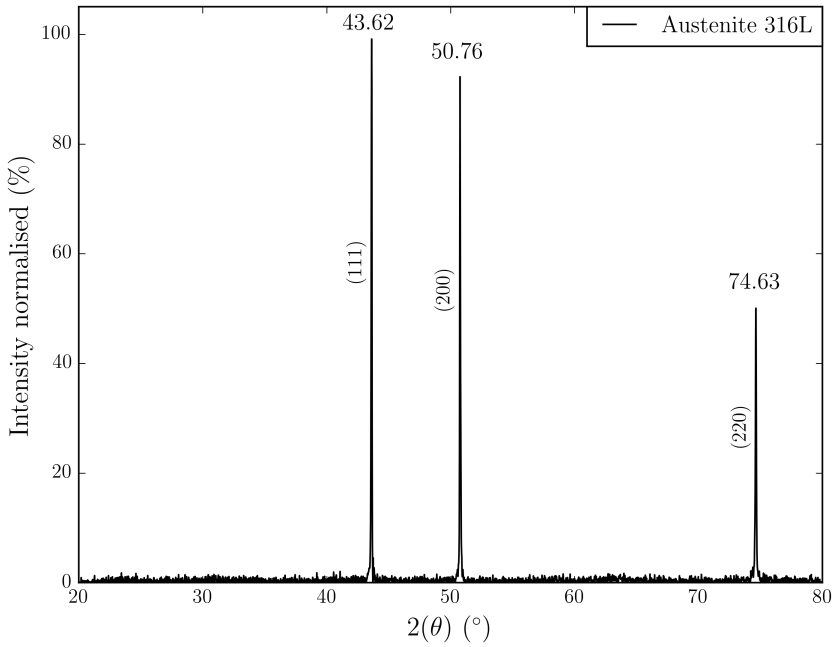

Figure 2.20: *XRD of an unoxidised 316L sample ($K_{\alpha 2}$ removed)*

Using the 2Θ obtained on the diffractogram of the bare metal (Figure 2.20) the lattice parameter of the 316L was calculated (Table 2.4). The lattice parameter is close to 3.59 ± 0.01 Å as expected for a 316L alloy.

Table 2.4: *Lattice parameters calculated from 2Θ obtained using a copper anode on the studied 316L unoxidised (λ_{Cu}=1.5406 Å)*

2Θ (deg)	Θ (deg)	Θ (rad)	hkl	$D_{spacing}$	a (Å)
43.62	21.81	0.31	111	2.07	3.59 ± 0.01
50.76	25.38	0.43	200	1.80	3.59 ± 0.01
74.63	37.32	0.61	220	1.27	3.59 ± 0.01

Reference 316L alloy (REF):

- The studied alloy is a commercial heat of SA 316L alloy in agreement with nuclear standards.
- Samples were polished using a reference polishing procedure to obtain samples without cold-work induced by polishing.
- The presence of various precipitates (MnS and oxides) which could affect the oxidation in the near regions was highlighted.
- EBSD analysis revealed that the crystallographic orientations are isotropically distributed.

2.2.1.2 Cold-worked 316L alloy

Cold-worked samples were obtained by using **REF** samples and doing-over an already done polishing step of the reference polishing procedure presented in Appendix D. Thus, a deformation layer was induced at the surface due to a rougher polishing. This allowed to study the effect of the polishing induced cold-work on the oxide layers. Two polishing steps were chosen: SiC foil P4000 and 6 µm diamond paste corresponding to 5.3 ± 0.5 µm and 6 µm abrasive size respectively. According to Sun [166], the SiC foil P4000 induced a strained layer of 1.2 ± 0.2 µm and the

diamond paste 0.44 ± 0.01 µm. In the following the cold-worked samples are referred as **SIC** and **6UM** samples respectively. The 6UM samples were polished 1 minute while the SiC samples were polished 30 seconds to induce the desired cold-work. Figure 2.21 presents optical images before oxidation of the studied cold-worked samples.

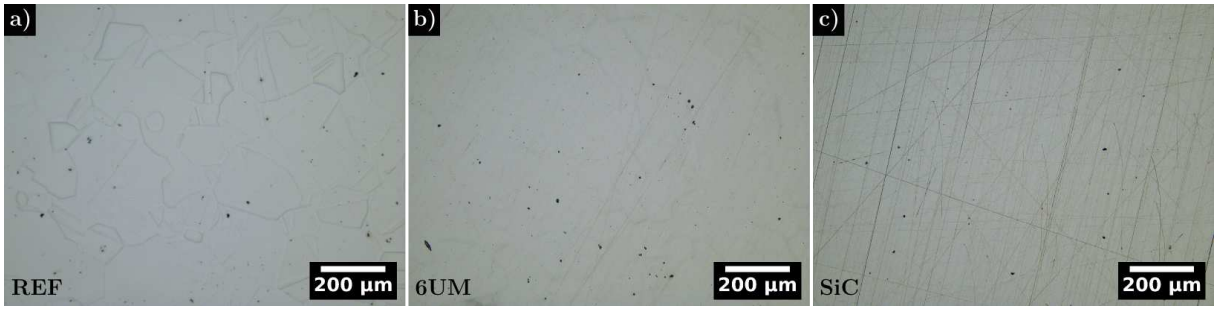

Figure 2.21: *Optical images before oxidation of a a) REF sample, b) 6UM sample and c) SIC sample*

Cold-worked 316L alloy (SIC and 6UM):

- The studied cold-work samples come from the same 316L alloy polished using the reference polishing procedure and then polished with a rougher polishing step to induce a controlled deformed layer.
- Two polishing steps were studied: the SiC foil P4000 and the 6 µm diamond paste inducing a strained layer of 1.2 ± 0.2 µm and 0.44 ± 0.01 µm respectively.
- These samples will help fathom the effect of laboratory polishing on the oxidation phenomenon.

2.2.1.3 Proton pre-irradiated 316L alloy

Proton pre-irradiated samples were prepared from the same 316L alloy. Thin samples with polishing on both sides were required to insure a good thermal transfer during irradiation. To do so, samples were machined using EDM with a thickness of 0.7 µm. They were then polished on one side following the reference polishing procedure (Appendix D) ended at 1 µm diamond paste. The samples were stripped from the resin, turned over and coated again using the same resin before being polished using the entire reference polishing procedure. Proton pre-irradiations were performed at the CEMHTI of Orléans. An irradiation dose of 1 dpa was chosen to be close to the saturation of the dislocation loops and the RIS phenomenon. Indeed, the loop size and density saturation occurs at approximately 1 dpa and the RIS tends to saturate between 0 and 5 dpa [90–94]. One irradiation at 0.5 dpa and then another one at 1.5 dpa were also performed in order to study the effect of the dose on oxidation. The diameter of the irradiated zone in each sample was of 4 mm, so that all samples had both irradiated and unirradiated regions. This directly enables comparative studies of the oxides formed on irradiated and unirradiated areas on a sample with the exact same oxidation conditions. In the following **IRR** sample will refer the irradiated area while **UNIRR** sample to the unirradiated area of these proton irradiated samples. These proton irradiations were performed at 380 ± 7 °C and with a dose rate close to 1.06×10^{-5} dpa/s with 1.5 MeV protons. Stopping and Range of Ions in Matter (SRIM) [167] calculations were performed with Kinchin-Pease cascades to obtain the damage profile and using a displacement energy of 40 eV [168] (Figure 2.22). The total penetration depth of the 1.5 MeV protons was about 15 µm. Irradiation temperature was followed during the irradiation using pyrometers. The irradiation temperature was chosen according to the equations proposed by Was [15, 153], in order to simulate neutron irradiation occurring in PWRs (developed previously

in Chapter 1 section 1.2.4). The damage rate K_{01} was fixed at 4.5×10^{-8} dpa/s and T_1 was fixed at 288 °C to simulate neutron irradiation. The two equations allow optimisation of the irradiation conditions to better simulate the Frank loops size and density, and the radiation-induced segregation. Due to technical issues, the targeted dose rate of 1.4×10^{-5} dpa/s was not achievable. The irradiations were therefore performed close to 1.06×10^{-5} dpa/s and the ideal irradiation temperature would have been 375 °C. At a constant dose rate, an increase of the irradiation temperature is known to exacerbate the RIS and the size of Frank loops and cavities increase. This tend to benefit this study since it aims to look upon the effect of irradiation defects and segregation on the oxidation. Irradiated samples were then polished with OP-S to remove the possible oxide formed during the irradiation and to reach the irradiation plateau at the desired dose at a depth of about 2 µm (Figure 2.22). This final OP-S polishing and its calibration is described in Appendix D.

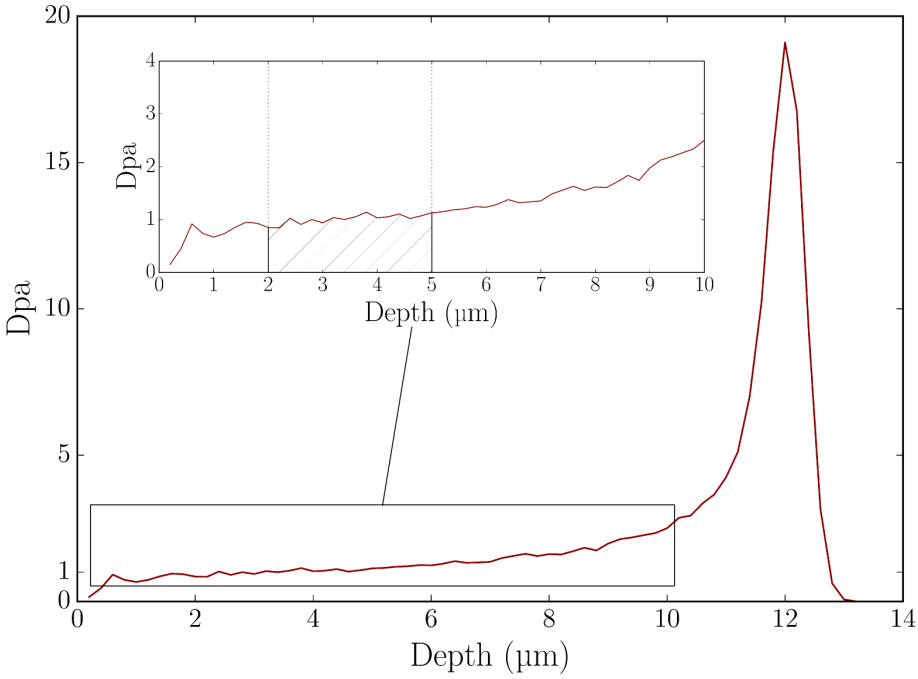

Figure 2.22: *SRIM calculation and zoom on the area of interest*

Proton pre-irradiated 316L alloy (UNIRR and IRR):

- The samples were prepared from the same heat of 316L using the reference polishing procedure. They were then proton pre-irradiated on a 4 mm disk at the sample center allowing to study directly both the unirradiated and irradiated area on the sample with the exact same oxidation conditions.
- Irradiation conditions were chosen to emulate the neutron irradiation occurring in PWR and a compromise was made between the Frank loop emulation and the Radiation Induced Segregation emulation. The slightly higher irradiation temperature at which were performed the irradiation might benefit this study by increasing the irradiation defects sizes and exacerbate the RIS.
- Irradiations were performed at 380 °C to 0.5, 1 and 1.5 dpa with a dose rate close to 1.06×10^{-5} dpa/s with 1.5 MeV protons.
- These samples will help fathom the irradiation effect on the oxidation phenomenon.

2.2.1.4 Oxidations in simulated PWR media

Once the samples polished, Vickers indentations were performed in order to help to navigate on the samples after their oxidation (Figure 2.23).

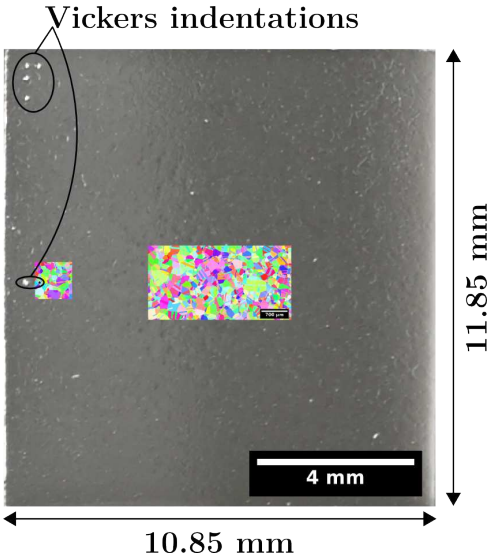

Figure 2.23: *Sample with the position of the EBSD maps acquired and the Vickers indentations performed*

In order to take the crystallographic orientation of the metal into account, several EBSD maps were acquired on the samples center (cf. section 2.1.4.1). TEM lamellae were extracted using FIB (detailed in section 2.1.4.4) in order to control the surface state before oxidation (presence of cold-work, native oxide, etc.). Finally, right before oxidation, samples were polished using an argon ion polishing (Precision Etching and Coating System (PECS) II from Gatan) to remove the native chromium rich oxide and to remove the carbon contamination induced by the EBSD maps. The following condition for the argon polishing were used: 4 keV, 180 seconds, 50° rocking angle, 25 rocks/s 30 rpm.

Oxidations were made using a specific corrosion loop developed at EDF R&D and called "TITANE loop" (Figure 2.24). The high pressure and high temperature part of the loop is made of Titanium to avoid metallic contamination coming from the circuit. Ion concentration in the water is brought to a minimum by using a 400 liters mixing tank. The chemistry of the medium was controlled before and after each oxidation test.



Figure 2.24: *TITANE loop*

A small cell is coupled to the main loop to carry out short time oxidation (down to 1 min). The sample holder is presented in Figure 2.25. It is made in Zircaloy 4 and was oxidised for 500 hours at 550 °C to form a protective oxide avoiding galvanic corrosion. In this cell the samples are in contact with the PWR simulated medium only during the oxidation time. Firstly, an argon flux is used for 5 minutes to flush out any unwanted oxygen inside the cell. Samples are then heated to the test temperature under argon flux and 5% hydrogen to avoid high temperature oxidation before introducing the medium. At the end of the exposure, the medium is flushed out by an argon flux for 5 minutes. The cell is then sealed with the argon inside for the cooling down of the cell before its opening.

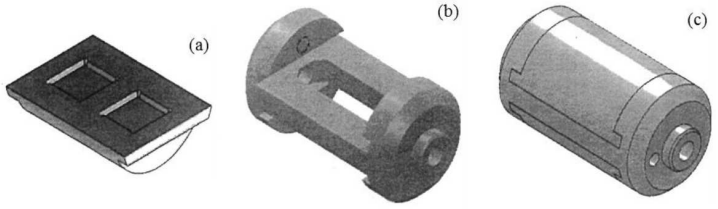

Figure 2.25: *Sketch of the TITANE sample holder*

Oxidations were performed in simulated PWR environment (T = 325 °C, P = 155 bar, [B] = 1000 ppm, [Li] = 2 ppm, $[H_2]$ = 30 cc/kg, $[O_2]_{dissolved} \leq 5$ ppb and $pH_{325\ °C} = 7.3$). Oxidation times ranging from 5 minutes to 96 hours were performed.

Oxidations in simulated PWR media:

- EBSD maps were acquired before oxidation on the samples to take, later on, the crystallographic orientation of the metal into account.
- Polishing using argon ions was performed right before the oxidation to remove the native chromium rich oxide and the carbon contamination induced during EBSD mapping.
- The TITANE corrosion loop is made of titanium and the medium contain 1000 ppm of boron, 2 ppm of Li, 30 cc/kg of dissolved hydrogen and is deoxygenated. The media is maintained at 325 °C and 155 bar for a pH of 7.3 at 325 °C.
- Samples were oxidised using a specific corrosion cell allowing short oxidation durations. The samples were thus in contact with the medium only during the oxidation time and not during the conditioning and deconditioning phases.
- Oxidation times investigated in this work ranged from 5 minutes to 96 hours.

2.2.2 Irradiation Assisted Corrosion

The following paragraphs relate to a sample oxidised under proton flux to study the Irradiation Assisted Corrosion. This experiment was performed using an oxidation under proton flux device available at the University of Michigan in the Michigan Ion Beam Laboratory (MIBL). This sample will be referred further on as the Michigan **IAC** sample. This experiment aimed to better understand the influence of a simultaneous oxidation and irradiation as occurring in PWRs. Indeed, after performing pre-irradiation and then oxidation in simulated PWR medium, it is necessary to look upon the contribution of the proton flux on the oxidation process and thus to study the effect of Irradiation Assisted Corrosion (IAC). This experiment aims to compare data on oxidised pre-irradiated samples to the oxidation under proton flux. Details will be given on the sample preparation and irradiation conditions used in the following paragraphs. Similarely to the experiments conducted on pre-irradiated samples, only part of the sample exposed to the medium was proton pre-irradiated beforehand. Thus both the unirradiated area and the proton pre-irradiated one were oxidised at the same time with identical oxidation conditions. Moreover, during the oxidation a small area in the pre-irradiated zone was oxidised under proton flux. It thus enabled a direct comparison of the three areas. The proton pre-irradiation performed on half of the sample will be introduced as well as the IAC experiment condition. The differences between this corrosion medium and the one used previously will be described. The oxides formed on this sample will be compared to the ones formed on the proton pre-irradiated and unirradiated samples oxidised in TITANE loop.

The **IAC** sample was prepared partly at EDF and at the University of Michigan. The same 316L alloy as presented in section 2.2.1.1 was used. A plate of 20 x 20 x 1 mm in size was machined by EDM and polished using the reference polishing procedure (Appendix D). Half of this plate has been proton pre-irradiated using 1.23 MeV protons. The plate was mounted on a copper stage electrically isolated from the beam line. The stage was heated using a resistive cartridge heater and the air at room temperature served as coolant from the back of the stage. A thin layer of molten Indium between the stage and the plate provided an effective thermal contact. The sample was irradiated at a dose of 0.94 dpa using a damage rate of 5.9×10^{-6} dpa/s at 360 $\pm$ 13 ° C. Irradiation temperature was controlled during the irradiation using thermocouples. The damage profile is presented in Figure 2.26 and was obtained using the Stopping and Range of Ions in Matter (SRIM) software [167] and Kinchin-Pease cascades.

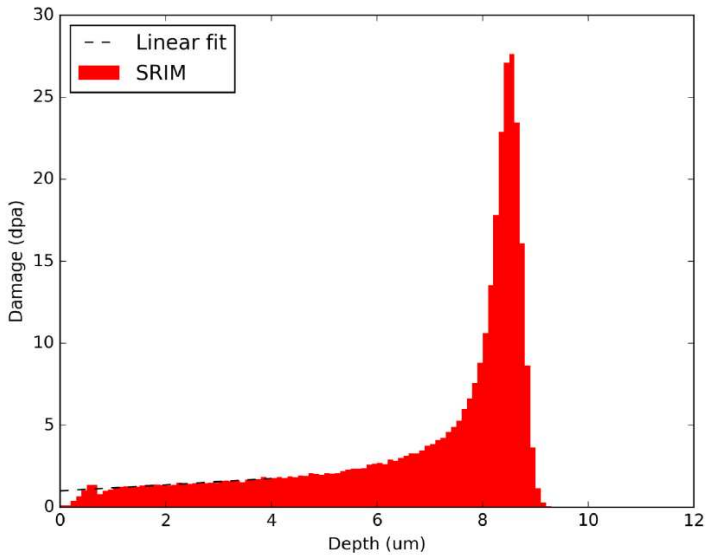

Figure 2.26: *Damage profile of the proton pre-irradiation of the Michigan IAC sample*

A 8 mm diameter disk was cut by Electrical Discharge Machining straddling the pre-irradiated area and the unirradiated area. OP-S polishing was performed on the disk to remove the first outer two microns and to be on the irradiation plateau (cf. Appendix D). Then EBSD mapping was acquired on the whole area. Lastly, a final polishing was carried out from the back side of the sample reducing its thickness down to 46 µm. This thinned sample was welded to a 17-4 PH disk of the same diameter with a thickness of 36 µm. The sample, having been welded and subjected to high mechanical stresses due to the differences in pressure between the vaccum required for the proton beam and the pressure of the media, is strained. A sketch of the whole irradiation under proton flux system is presented in Figure 2.27 with the 2-disks configuration. Such 2-disk assembly reduces the activity of the 316L sample after the experiment and allow a better mechanical resistance.

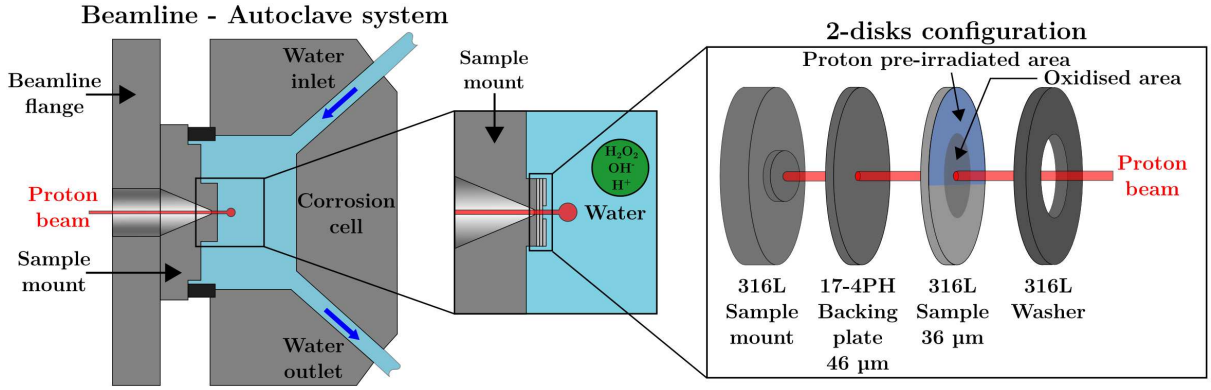

Figure 2.27: *Sketch of the Beamline–Autoclave system and mount assembly with a two-disks configuration for the IAC experiment*

The corrosion cell of the device is made of stainless steel, thus, a phenomenon of dissolution/precipitation is likely to occur. The medium consist of water at 131 bar with the addition of 3 wppm of hydrogen at a temperature of 320 °C and a $pH_{320\,°C}$ of 6.2 (calculated using Caolin software (EDF property)). The dissolved O_2 content was kept under 0.2 wppb and no boron or lithium were added into the medium. The medium flow inside the cell is of 15 mL/min. Since the medium is slightly different than the one used in the TITANE corrosion loop (presented in section 2.2.1.4), the oxidation might differ. Indeed, the literature survey highlighted that the pH of the medium is likely affect the oxidation kinetic.

Oxidation under proton flow was carried out during 24 hours using 5.4 MeV protons. The received dose was 0.064 dpa and the damage rate of 7.43×10^{-7} dpa/s. The irradiated area was a disk of 1 mm diameter located in the sample center and thus in the pre-irradiated area. Therefore, the cummulated dose in this area is 1 dpa. The damage profile of the oxidation under proton flux is presented in Figure 2.28 and was obtained using the SRIM software [167].

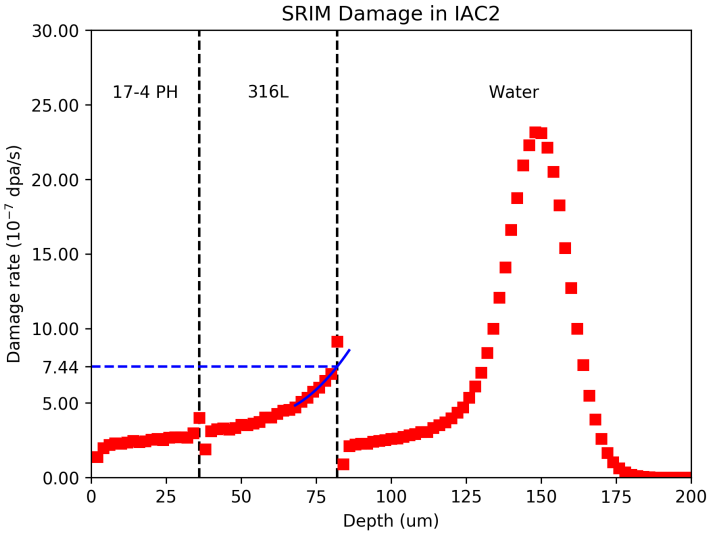

Figure 2.28: *Damage profile of the oxidation under proton flux of the IAC sample*

Four different areas are observable after oxidation on the Michigan **IAC** sample as shown in Figure 2.29.

1. Oxidised area on the unirradiated part of the sample (**IACUNIRR**)
2. Pre-irradiated and oxidised area (0.94 dpa) (**IACIRR**)
3. Pre-irradiated and oxidised under proton flux area to emulate Irradiation Assisted Corrosion (0.94 + 0.06 dpa) (referred as oxidised under proton flux area or **IACIAC**)
4. Radiolysis area and/or dissolution/precipitation phenomenon (caused by the stainless steel corrosion cell)

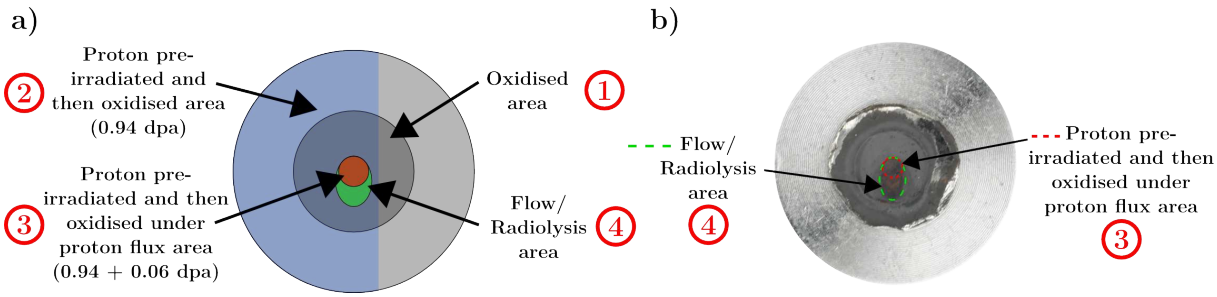

Figure 2.29: *a) Sketch of the different area of the IAC sample and b) IAC sample after the 24 hours oxidation under proton flux*

Irradiation Assisted Corrosion:

- A proton pre-irradiation was conducted on half of a 316L sample polished using the reference polishing procedure using 1.23 MeV protons to a dose of 0.94 dpa at 360 °C.
- The sample was thinned to 46 µm and welded to a 17-4PH backing plate to reduce the activity of the studied sample and increase mechanical resistance.
- The corrosion cell is made of stainless steel and is thus subjected to dissolution/precipitation phenomenon of metallic species in the medium.
- The medium consists of water at 320 °C in which 3 wppm of dissolved hydrogen is introduced. No boron or lithium were added in the medium, thus the medium pH was of 6.2, this can affects the oxides formed since the pH is different from the one in the TITANE loop.
- Oxidation under proton flux was carried out during 24 hours using 5.4 MeV protons at 320 °C and the received dose was of 0.064 dpa. The irradiated area consists of a disk of 1 mm diameter located in the pre-irradiated area.
- Four areas of interest are present on the sample: 1) an oxidised area (**IACUNIRR**), 2) a proton pre-irradiated area (**IACIRR**, $\sim$ 1 dpa, 360 °C), 3) a proton pre-irradiated and then oxidised under proton flux area with a total dose of 1 dpa (**IACIAC**) and 4) a flow/radiolysis area visible after oxidation.

2.2.3 Decommissioned bolt

The following paragraphs present the composition, irradiation conditions and sample preparation of a decommissioned bolt of a French PWR. This bolt, that cracked during service, is a great asset to study the IASCC phenomenon. The oxide formed at the crack tip will be compared to the ones formed on the surface of irradiated materials presented above. It was extracted from an upper former (7th) level of the internal structures (CP0 power plant) after 29 years of operation. The bolt length is 71.5 mm and its diameter at the shank is 12.8 mm.

The studied bolt is made of CW Z3CND17.12 (X2CrNiMo18-14-3) austenitic stainless steel. Since the initial dislocation network is believed to recover under irradiation the cold-work of the bolt should not impair the crack tip. The 316L bolt chemical composition in presented in Table 2.5. Inductively Coupled Plasma (ICP) was used to measure the material composition for all elements except for the carbon and sulphur contents which were determined by Infrared Absorption Spectrometry (IAS) after combustion technique. These values are in good agreement with the RCC-M specifications except for the sulphur and carbon contents which both appears higher than the requirement (respectively 0.038 wt. % vs 0.015 wt. % required and 0.042 wt. % vs 0.03 wt. %).

Table 2.5: *Chemical composition of the extracted bolt made of 316L compared to RCC-M specifications (wt. %) [2, 3]*

Element (% wt.)	C	Cr	Ni	Mo	Mn	Si	S	P	Cu	Co	Fe
Decommissioned bolt	0.042 ± 0.003	16.20 ± 0.8	12.90 ± 0.6	2.721 ± 0.092	1.82 ± 0.09	0.76 ± 0.06	0.038 ± 0.013	0.012 ± 0.003	0.061 ± 0.003	0.078 ± 0.004	Bal.
RCC-M specifications	≤ 0.03	16-19	10-14	2.25-2.75	≤ 2	≤ 1	≤ 0.015	≤ 0.02	≤ 1	≤ 0.20	Bal.

Numerical simulations were run by EDF in a previous work to determine the bolt temperature and fluence [2]. The final dose in dpa includes contributions from Fe, Ni, Cr and Si. Neutron dose and temperature along the baffle-to-former bolt from the numerical simulations are shown

in Figure 2.30. The dose received by the bolt ranges from approximately 10 dpa at the head to 6 dpa at the bottom locations. The average dose received at the head-to-shank junction is estimated to 7 dpa and the temperature to 325 °C. From these data, the dose rate was calculated and found to be close to 7.65×10^{-9} dpa/s.

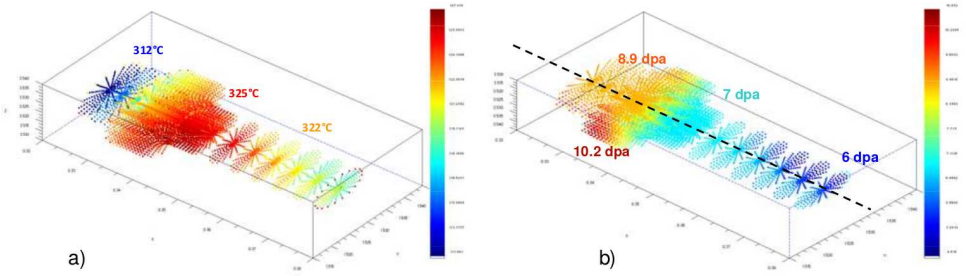

Figure 2.30: *a) Temperature and b) fluence estimated by numerical simulation [2]*

The extracted bolt was cut with a diamond saw following a longitudinal axis. The obtained cross section was then mechanically polished to reveal the IASCC cracking at the head-to-shank junction. TEM lamellae were extracted at crack tips in the head-to-shank junction. To do so, the cracks were localised thanks to SEM imaging in a specialised facility due to the sample activity induced by neutron irradiation (Figure 2.31 a). Focused Ion Beam lamellae were prepared using a Tescan Lyra 3 FIB/SEM installed in a hot cell at LIDEC laboratories. After the lamellae extraction, EBSD mapping was performed using a Zeiss EVO50 SEM also installed in a hot cell of the LIDEC laboratories to obtain information on the cracked grain boundaries (Figures 2.31 b and c). The lamellae were cleaned using argon ions accelerated at low voltage in a PIPS II polishing system as described in section 2.1.4.4 down to the desired thickness.

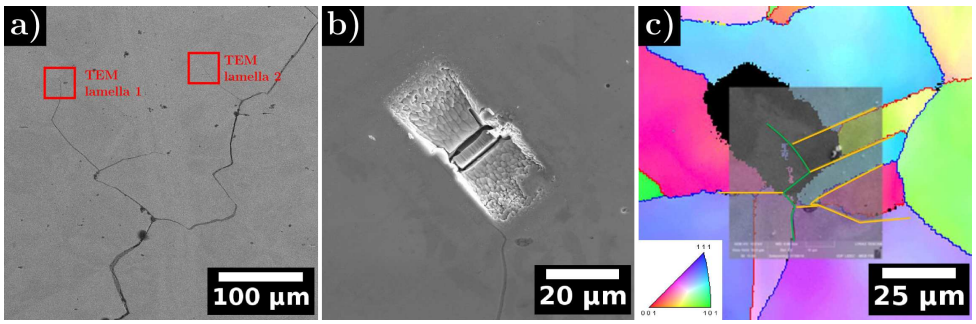

Figure 2.31: *a) SEM 15kV BSE imaging of the cracks in the junction between the head and the shank of the bolt b) SEM 20 kV SE imaging of the location of the first extracted lamella and c) zoom on the EBSD map of the location of the extracted lamella (green: IASCC cracking, yellow: adjacent grain boundaries)*

Decommissioned bolt:

- The studied bolt is made of CW 316L. It was extracted from an upper former level of a French internal structure after 29 years of operation.
- The average dose received at the head-to-shank junction is estimated to 7 dpa and the temperature to 325 °C.
- FIB lamellae were extracted at crack tips in a specialised facility able to handle radioactive samples.

2.2.4 Materials and samples preparations: Synthesis

From an experimental point of view, the medium and the materials were chosen so as to best represent the operating conditions of a Pressurized Water Reactor. Below are summarised the studied materials, their preparation, irradiation conditions and oxidations.

Oxidation in PWR media: Titane samples

- **REF** samples were polished using the reference polishing method to study the oxidation phenomenon without the addition of dislocations.
- Cold-worked 316L samples (**SiC** and **6UM**) were subjected to a polishing inducing a controlled deformed layer below the surface to study the influence of cold-work induced by polishing on the oxidation.
- Proton pre-irradiated 316L samples were irradiated at 380 °C to 0.5, 1 and 1.5 dpa to study the influence of irradiation on the oxidation. On each irradiated samples **IRR** and **UNIRR** areas enable to study solely the effect of irradiation.
- Oxidations (5 minutes to 96 hours) were performed in a titanium recirculating loop (TITANE loop) in simulated PWR environment.

Irradiation Assisted Corrosion: Michigan sample

- Four areas of interest are present on this sample: 1) an oxidised area (**IACUNIRR**), 2) a proton pre-irradiated area (**IACIRR** $\sim$ 1 dpa, 360 °C), 3) a proton pre-irradiated and then oxidised under proton flux area (**IACIAC** total dose of 1 dpa) and 4) a flow/radiolysis area. This sample enables the study of the effect of irradiation and of an oxidation under proton flux on a unique sample. Oxides on this sample will compared to the ones oxidised in the Titane loop.
- The oxidising medium did not contain boron or lithium, which can modify the oxides formed since the pH is different from the one in the TITANE loop. A phenomenon of dissolution/precipitation is likely to occur since the corrosion cell used is made of stainless steel.

Decommissioned bolt:

- The extracted bolt is made of CW 316L. The average dose received at the head-to-shank junction after 29 years of operation is of 7 dpa and the irradiation temperature was estimated at 325 °C. Lamellae were carefully extracted at the bolt crack tips. The oxidation at crack tips will be compared to the other studied samples.

2.3 Characterisation of the irradiated samples and proton irradiation representativeness

The sample microstructures were characterised using TEM to visualise the irradiation defects and induced chemical modifications. As previously explained, sample preparation is of great importance since the image qualities and chemical quantification accuracies greatly depends upon the sample quality. Protons were used in this study to perform the irradiations that aimed to emulate the microstructure of neutron irradiated materials. The studied irradiations are presented in Table 2.6. As the employed damage rate was higher than that of neutrons, a calculated temperature shift was applied as presented beforehand in section 2.2.1.3.

Table 2.6: *Summary of the irradiations performed*

Particules	Dose (dpa)	Temperature (° C)	Fluence (dpa/s)
Proton	1	380	1.06×10^{-5}
Proton	1.5	380	1.06×10^{-5}
Proton	~ 1	360	5.90×10^{-6}
Proton	1	360/320	5.90×10^{-6}
Neutron	7	325	7.65×10^{-9}

Among the induced defects, focus will be made on the Frank loops and cavities. Their size and density will be investigated and compared. Then the chemical modifications such as the Radiation Induced Segregation at grain boundaries and the intragranular precipitations and segregations will be presented. Supplementary characterisations and details are reported in Appendix E. The microstructural and chemical modifications on proton pre-irradiated samples will be compared to the ones observed on the neutron irradiated bolt. Ultimately, the proton irradiation representativeness will be discussed for the different pre-irradiations.

2.3.1 Microstructural modifications characterisation

Franks loops and cavities are the main microstructural defects induced by irradiation. The present section thus aims to investigate and quantify such defects. Both cavities and Frank loop are found close to the polished surface as visible in Figure 2.32. Therefore, the mechanical polishing aiming to remove the first two microns to reach the irradiated area of interest did not disturb the irradiation defects close to the surface.

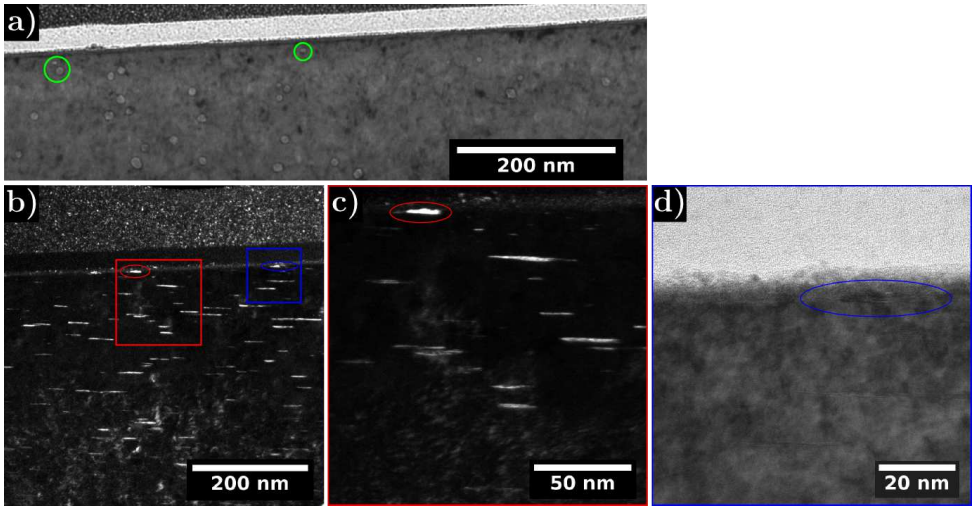

Figure 2.32: *TEM images near the surface of a sample proton pre-irradiated after the OP-S polishing removing the first microns a) BF image of the cavities under-focus b) and c) DF image of the loops edge-on d) BF image of the loops edge-on*

2.3.1.1 Frank loops

Among the defects induced by irradiation, Frank loops are one of the main observed defects (cf. section 2.3.1.1). On each irradiated sample Frank loops were present. Figure 2.33 presents a TEM BF image of the loops edge-on on the Titane **IRR** sample irradiated at 1 dpa.

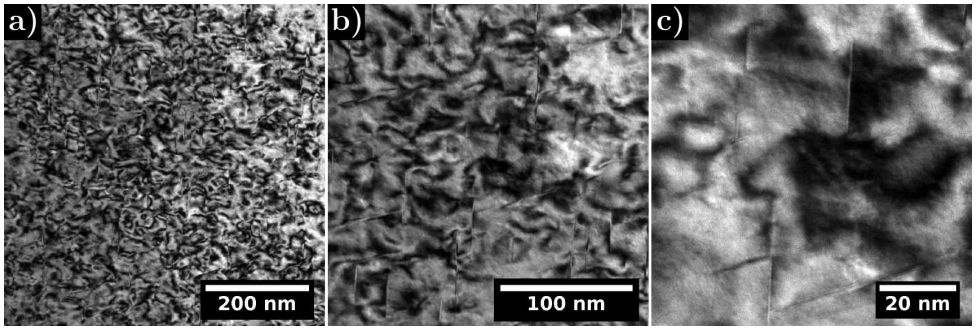

Figure 2.33: *Frank loops egde-on imaged in TEM BF on a [101] zone axis on the Titane 1 dpa IRR sample*

For each sample, at least one of the four families of Frank loops was imaged thanks to the Rel-Rod Dark Field technique as introduced in Figure 2.34 on the Titane 1 dpa **IRR** sample. Details on this technique are given in Appendix A. Samples were oriented close to [101] zone axis with g= $\frac{1}{2}$ <131>. Efforts were made to characterise the loop population both qualitatively and quantitatively. The total loop densities were obtained by multiplying by four the measured density on one family. Indeed, the loop distribution was considered isotropic along {111} crystallographic planes. To represent at best the loop population, the quantitative analysis of the loop size and density was made on a area big enough to be representative but with a magnification allowing to image small loops. All the quantifications were performed on the same magnification. Efforts were made to estimate the uncertainties at best. Thus, for the loop densities, they were considered for the lamella thickness and the measured loop number. As for the loop sizes, the uncertainties given take into account the standard deviation and an uncertainty on the measurement itself. Figure 2.34 d highlights one loop threshold performed using the ImageJ software [156].

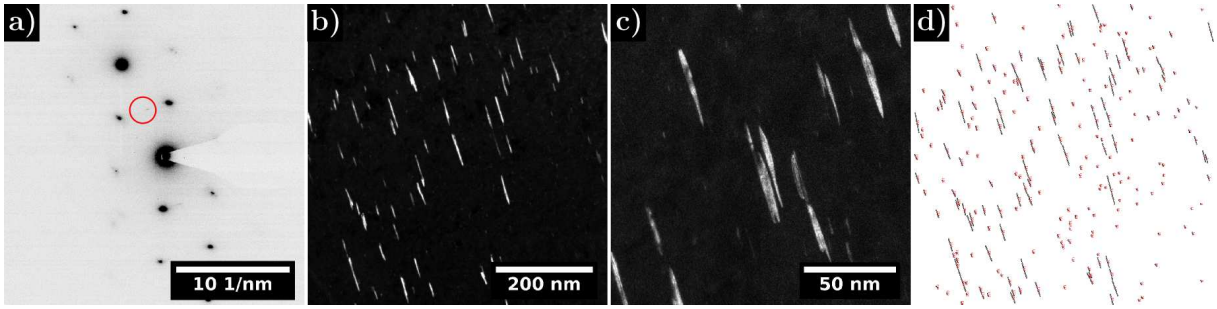

Figure 2.34: *Frank loops on the Titane 1 dpa IRR sample imaged in TEM a) diffraction pattern on [101] zone axis in 2-beam conditions along $\frac{1}{2}$ [$\bar{1}\bar{3}$1] (red circle: objective aperture centered on the rel-rod streak) b) and c) DF images on the rel-rod streak imaging one loop family edge-on d) loop quantification performed on the area presented in b)*

Figure 2.35 images the loop distribution on all the studied irradiated samples. Each loop distribution and imaging with details on the studied areas can be found in Appendix E. The loop sizes and densities are summarised in Table 2.7 depending on the observed sample and its irradiation condition.

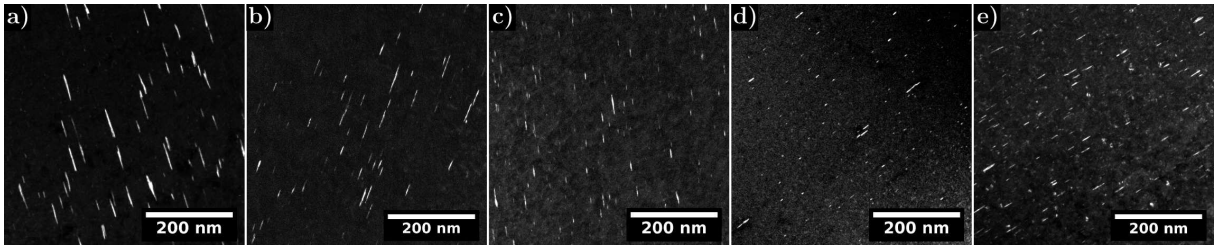

Figure 2.35: *Frank loops edge on imaged in TEM DF in 2-beam condition close to [101] zone axis on the a) Titane 1 dpa IRR sample b) Titane 1.5 dpa IRR sample c) IACIRR area of the Michigan sample d) IACIAC area of the Michigan sample and e) decommissioned bolt*

Table 2.7: *Summary of the Frank loop distribution and size depending on the irradiation*

Sample	Dose (dpa)	Temperature (° C)	Density ($\times 10^{22}$ m^{-3})	Average size (nm)	Min size (nm)	Max size (nm)
Titane IRR	1	380	2.5 ± 0.7	18.4 ± 15.9	2.2	85.6
Titane IRR	1.5	380	2.3 ± 0.9	21.4 ± 14.1	3.6	91.8
IACIRR	∼ 1	360	3.1 ± 0.9	11.0 ± 5.8	2.1	35.9
IACIAC	1	360/320	2.6 ± 0.5	8.5 ± 4.8	3.3	35.2
Bolt	7	325	15.7 ± 6.8	5.0 ± 2.9	1.0	18.8

Comparing the loop population on both Titane **IRR** samples irradiated at 380 °C, it appears that the loop density and size are close. As no clear differences are seen it suggests that the irradiation plateau is reached or closed to be reached for such irradiations. However, loops are slightly bigger on the **IRR** 1.5 dpa sample. Thus, the higher dose could be responsible for this slightly bigger loop size. As for the Michigan sample, in the **IACIRR** area the loops are twice as small as the ones on the Titane **IRR** samples. On this area the loop density was found to be slightly higher than on the **IRR** samples. This is consistent with the results obtained by several authors who observed bigger loops but a smaller loop density when the irradiation temperature increases [92, 101, 103]. Moreover, the **IACIAC** area of the Michigan sample possesses the smaller and the fewer loops of the proton irradiated samples. Therefore, defects might have undergone a recombination process during the oxidation under proton flux. For the decommissioned bolt neutron irradiated at 7 dpa and 325 °C, the loop density is more than 5 times higher than on all the previous presented samples. This is certainly partially due to the higher irradiation dose and the lower irradiation temperature. Moreover, the high quality and low thickness of the lamellae (∼ 30 nm) might allow an easier recognition of the loops and facilitate their observation contributing to the much higher loop density on this sample. This would also explain the higher loop density measured on our sample compared to Panait et al. results on the same bolt as their sample was electropolished and hence the presence of an amorphous layer would prevent the visualisation of defects [2]. The loop mean size is also the lowest on this sample, and might result from the easier visualisation of such small loops.

Our results bode well with other works as visible on Figure 2.36. Comparing our data to the literature available, it seems that the loop mean size of the samples proton irradiated at 380 °C is in the middle high of the measured loop sizes. This probably results from the high irradiation temperature used.

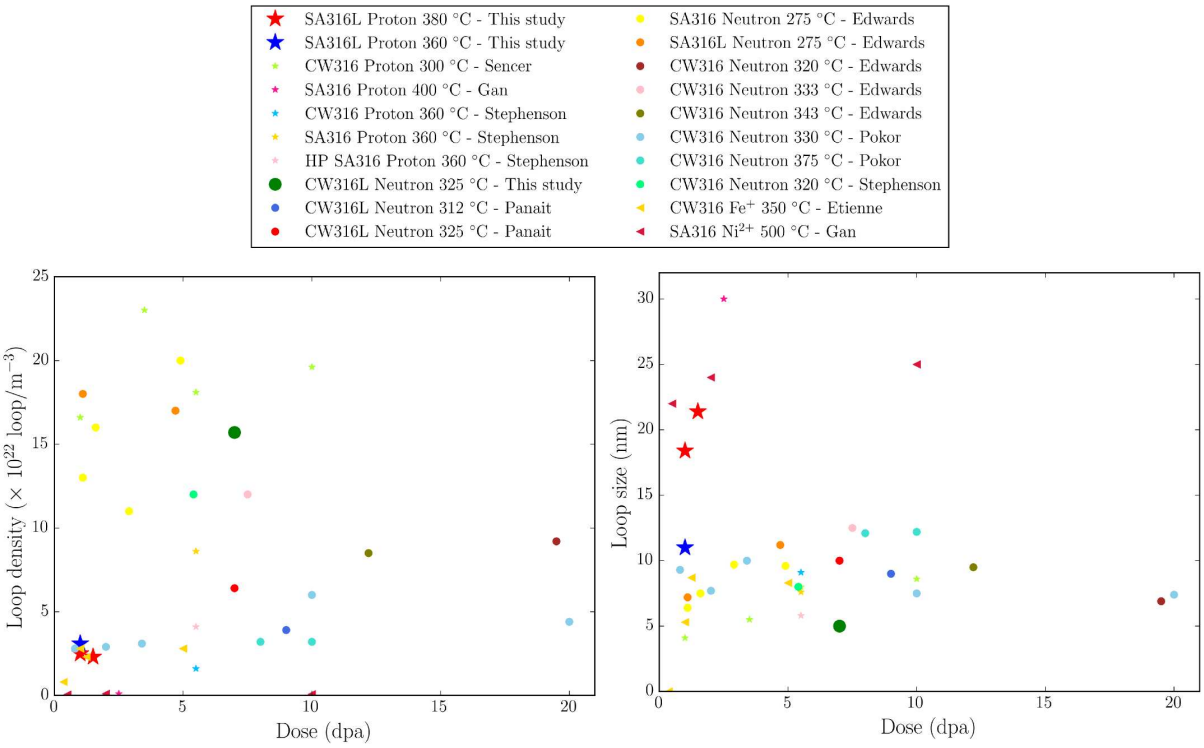

Figure 2.36: *Loop densities and sizes for various 316 alloy with different irradiation conditions (data from [2, 91, 93, 95, 97, 108, 142, 169])*

Frank loops: Frank loops were observed on all the irradiated samples. All the obtained results are in good agreement with the literature data.

- The loop densities are close on both the Titane 1 and 1.5 dpa **IRR** samples. Loops are slightly bigger on the 1.5 dpa sample due to the higher irradiation dose.
- The **IACIRR** area of the Michigan sample possesses a higher loop density but smaller loops compared to the Titane 1 dpa **IRR** sample. This is believed to results from the lower irradiation temperature.
- In the **IACIAC** area of the Michigan sample the loop size and density is slightly lower possibly due to defects recombination during the oxidation under proton flux.
- Finally, the loops formed on the decommissioned bolt are the smallest but have the higher density. The small foil thickness could explain the higher visibility of small defects.

2.3.1.2 Cavities

Bubbles and/or cavities were imaged in TEM by the under/over focus technique. Cavities appear surrounded by a dark fringe in under-focus condition while surrounded by a bright fringe in over-focus condition as shown in Figure 2.37 on the 1.5 dpa Titane **IRR** sample. Only voids are formed on the proton irradiated samples since no helium is introduced during the irradiation nor is formed due to transmutation as occurring for neutron irradiation (cf. Chapter 1 section 1.2.1.3). However, for neutron irradiated materials, TEM images cannot allow to differentiate helium filled cavities (bubbles) with voids. TEM observations highlighted the presence of more or less faceted cavities in several irradiated samples. As for the loops, efforts were made to characterise the void population both qualitatively and quantitatively. All the quantifications were performed on close magnifications except for the sample which had the smallest cavities

and thus needed a higher magnification to measure the void sizes. Uncertainties were also evaluated. Thus, for the void densities, uncertainties were considered for the lamella thickness and the measured cavity number. As for the void sizes, the uncertainties given take into account the standard deviation and an uncertainty on the measurement itself.

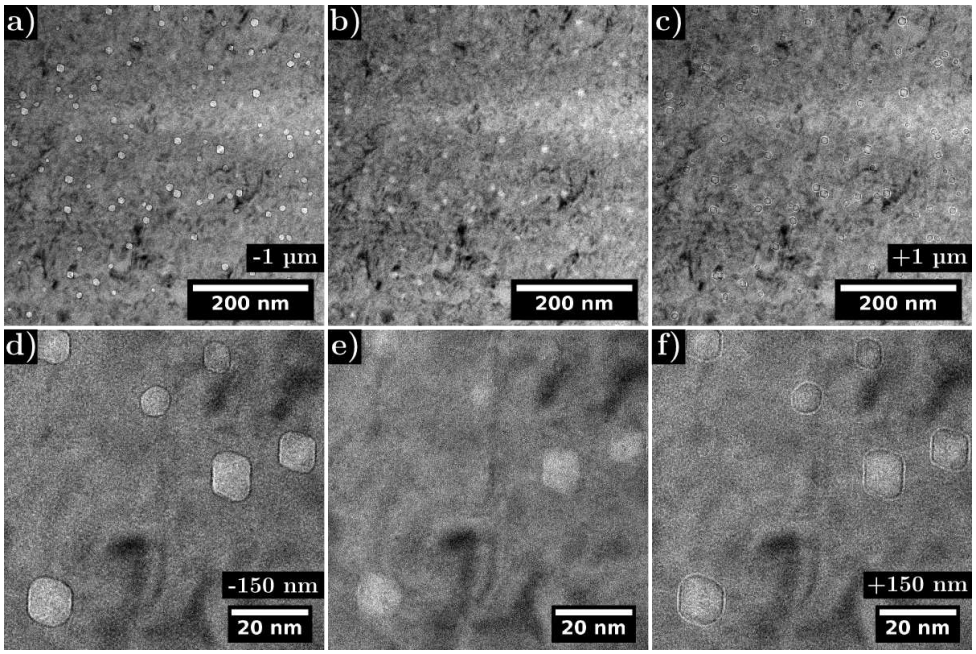

Figure 2.37: *TEM BF imaging of the cavities distribution on focus, under-focus and over-focus on the Titane 1.5 dpa IRR sample a) and d) under-focus, b) and e) focus c) and f) over-focus*

The cavity distribution for all samples is reported in Figure 2.39 and Table 2.8. All the cavity imagings along with details on the studied areas can be found in Appendix E. Due to the sufficient size of the cavities, on both the Titane samples and the decommissioned loop, faceted cavities with facets all parallel from one faceted void to the other were observed. These faceted cavities can be described as regular hexagons stretched along one direction. Further analyses revealed that four facets lie in {111} planes (shown by the red arrows) while the others two lie in {020} planes (shown by the blue arrows) as evidenced in Figure 2.38. Longest facets are the {111} facets.

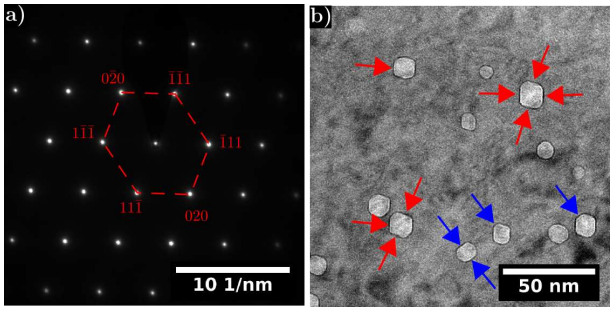

Figure 2.38: *a) Diffraction pattern in [101] zone axis and b) associated TEM BF under-focus imaging of the cavities distribution on the Titane 1.5 dpa IRR sample (facets lying in {111} planes are shown by the red arrows, facets lying in {020} planes showed by the blue arrows)*

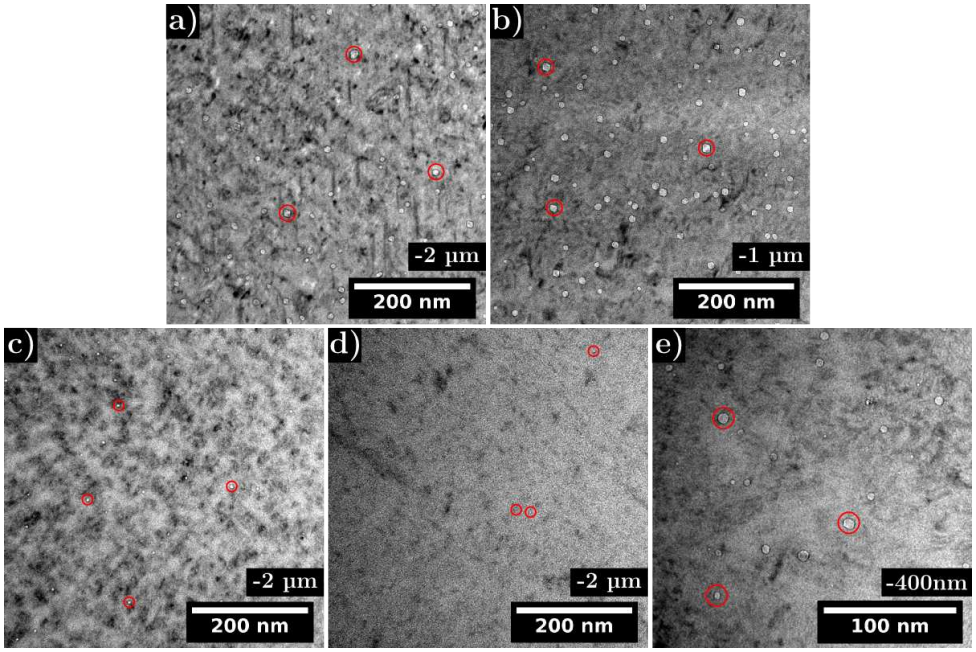

Figure 2.39: *TEM BF under-focus imaging of the cavities distribution on the a) Titane 1 dpa IRR sample b) Titane 1.5 dpa IRR sample c) IACIRR area of the Michigan sample d) IACIAC area of the Michigan sample and e) decommissioned bolt*

Table 2.8: *Summary of the cavity distribution and size depending on the irradiation*

Particules	Dose (dpa)	Temperature (° C)	Density ($\times 10^{21}$ m^{-3})	Average size (nm)	Min size (nm)	Max size (nm)
Titane IRR	1	380	3.8 ± 1.6	8.2 ± 2.0	1.1	15.0
Titane IRR	1.5	380	4.7 ± 1.8	11.4 ± 2.4	0.9	19.5
IACIRR	∼ 1	360	1.6 ± 0.7	5.0 ± 1.2	1.0	7.1
IACIAC	1	360/320	0.3 ± 0.2	2.2 ± 0.9	1.1	3.7
Bolt	7	325	30.9	3.8 ± 2.0	0.9	11.2

Cavity Denuded Zone (CDZ) near the grain boundary were noticed on the Titane 1.5 dpa **IRR** sample and the decommissioned bolt (Figure 2.40). The grain boundary acting as sink for the vacancies could induce this voids depleted area. No CDZ were highlighted on the Michigan sample due to the low cavity density.

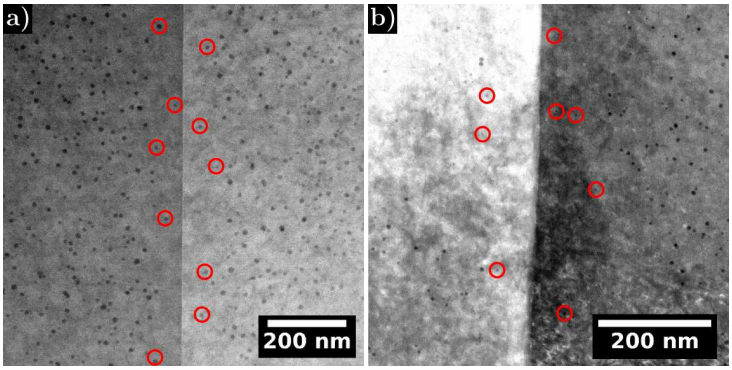

Figure 2.40: *STEM HAADF imaging of the Cavity Denuded Zone near the grain boundary (cavities are darker than the matrix) on the a) Titane 1.5 dpa IRR sample and b) decommissioned bolt (the cavities nearest to the grain boundary are circled in red)*

Among the obtained results it appears that the void density is higher and the cavities are bigger on the Titane 1.5 dpa **IRR** sample compared to the 1 dpa sample. This is consistent with the results from previous studies which stated that increasing the irradiation dose increases both

the void sizes and densities [90–92]. In addition, the voids on both the **IACIRR** and **IACIAC** areas of the Michigan sample are much smaller than the ones formed on the Titane **IRR** samples and fewer cavities were present. The irradiation temperature might not be high enough to induce bigger and more numerous voids. Indeed, as the irradiation temperature decreases, the void size tends to decrease too [92, 101, 103]. According to the literature their density should increase as the temperature decrease which is the opposite of the obtained results. It might be caused by a void size too small thus inducing a error in the number of cavities counted. Moreover, the oxidation under proton flux might have caused a recombination of defects explaining such low void size and density on this specific **IACIAC** area. As for the decommissioned bolt, the cavity density is the highest, probably resulting from the combination of the higher irradiation dose, irradiation temperature and the lower foil thickness ($\sim$ 30 nm). Cavities were smaller on this sample than on the samples proton irradiated at 380 °C and might be caused by the lower irradiation temperature. As explained previously, the foil higher quality and lower thickness might promote the visualisation of small defects explaining the higher void density and their smaller size measured on our sample compared to Panait et al. results on the same bolt [2]. Finally, the grain boundaries acting as sink for the vacancies could induce the CDZ observed.

Comparing our data to the literature available, it appears that our results bode well with other works as visible on Figure 2.41.

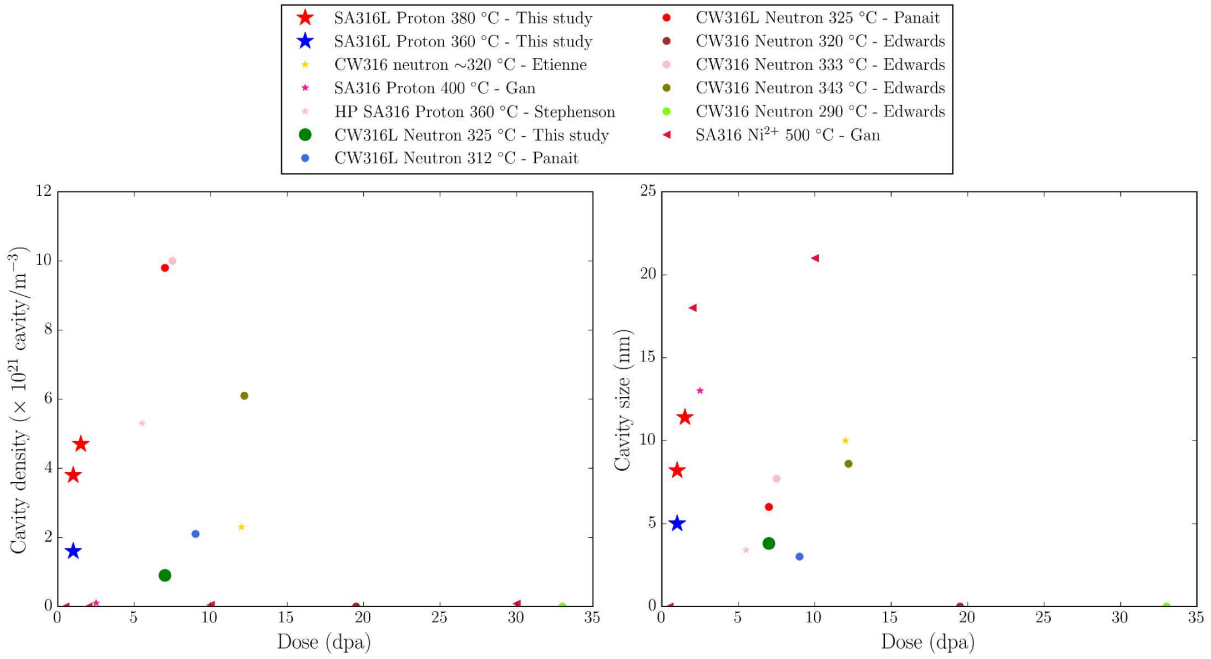

Figure 2.41: *Cavity densities and sizes for various 316 alloy with different irradiation conditions (data from [2, 95, 97, 108, 142, 169])*

Cavities: Cavities were observed on all irradiated samples and appear faceted when big enough to be imaged with facets lying in {111} and {020} planes.

- Cavities are more numerous and bigger on the Titane 1.5 dpa **IRR** sample than on the 1 dpa sample. This is believed to result from the higher irradiation dose.
- Few small voids were observed on the Michigan sample both in the **IACIRR** and **IACIAC** areas. The proton irradiation temperature might not be high enough (compared to the one used for the irradiation of the **IRR** samples) to induce bigger and more numerous voids. Moreover, the oxidation under proton flux might have caused a recombination of defects.
- Numerous cavities were observed on the decommissioned bolt. The morphological analysis of the cavities could not allow to differentiate voids and helium filled bubbles. Their high density and small size result from a combination of the irradiation dose, temperature and the foil thickness.

2.3.2 Chemical modifications characterisation

As irradiation can induce segregation and precipitation these phenomena were investigated on all the irradiated samples. Such RIS was characterised at grain boundaries but also on dislocations and voids since these can act as sinks. Results from quantifications will be given in the form of Δ = (RIS − matrix) in at. % with regards to the matrix composition where + and − indicate enrichment and depletion respectively.

2.3.2.1 Intragranular segregation and precipitation

Intragranular segregation and precipitation was studied on all the irradiated samples using EDXS and/or EELS. Segregation on such defects was already observed by several authors [91, 97, 98, 110, 131, 133]. Most of them evidenced segregation by APT [110, 131, 133], while Edward et al. reported segregation on voids surfaces but did not present any imaging of it [97]. The segregation around cavity was studied either far off a zone axis or on a [110] zone axis to study at the same time the segregation around Frank loops. However, one should remember that measured concentration can be diluted to some extent since the defects are buried within the foil. Moreover, silicon and manganese quantification using EELS are sometimes not presented due to their low concentration and/or their difficulties to be detected. Results from quantifications are detailed in Appendix E.

The EDXS and EELS maps acquired on the Titane 1 and 1.5 dpa **IRR** specimens highlight an obvious segregation on cavities and Frank loops (Figures 2.42 and 2.44). Quantifications were performed on areas 70 ± 10 and 60 ± 10 nm thick respectively. However, diffraction patterns did not evidence an precipitation on these samples (cf. Appendix E). Further mappings were carried out on a loop and a cavity and are reported in Appendix E. The cavities appear nickel and silicon enriched while chromium, iron and manganese depleted. By superimposing the STEM image and the segregation mapping, it appeared that segregation occurs on the void surfaces. The loops edge-on are also segregated. A Ni/Si enrichment is seen on some loops and is coupled to a Cr, Fe and Mn depletion. This segregation is especially marked at the loop tips due to a geometric effect. Since the loops are analysed edge-on, the contribution of segregation at the loops extremities in the foil depth is higher. In addition, the iron segregation possesses a M-shaped profile at the loop tip indicating that iron is pushed back. Figures 2.43 and 2.45 highlight the amount of segregation occurring around both a cavity and a loop. From the profile acquired through the cavity, the segregation appear marked around the cavity and seem not to

be homogeneous. From quantification performed the maximum amount of segregation around both defects appear close reaching around $\Delta_{Cr} \approx -$ 3–6 at. %, $\Delta_{Ni} \approx +$ 8–13 at. % and $\Delta_{Si} \approx +$ 3–5 at. % for chromium, nickel and silicon respectively. However, segregation is slightly more marked on the 1.5 dpa **IRR** sample.

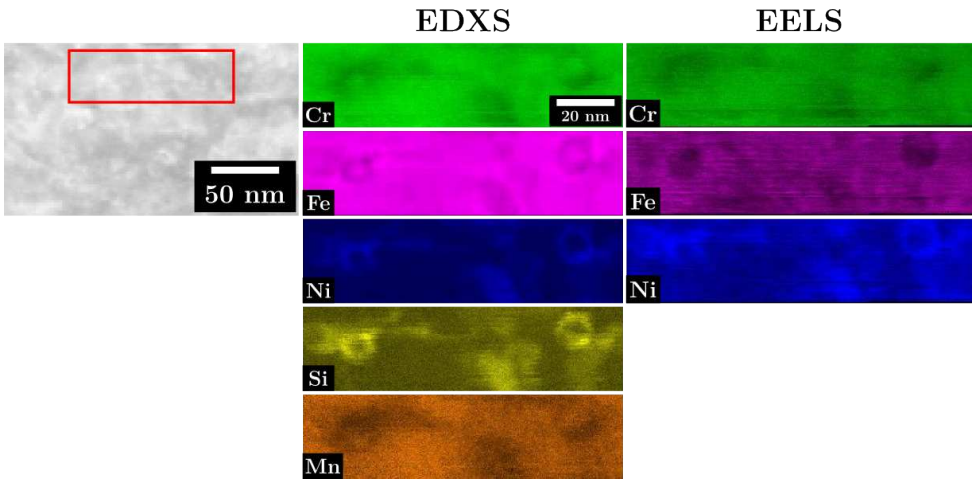

Figure 2.42: *HAADF image and associated EDXS/EELS quantitative mapping of Cr, Fe, Ni, Mn and Si of the intragranular segregation on the Titane 1 dpa IRR sample (close to [101] zone axis)*

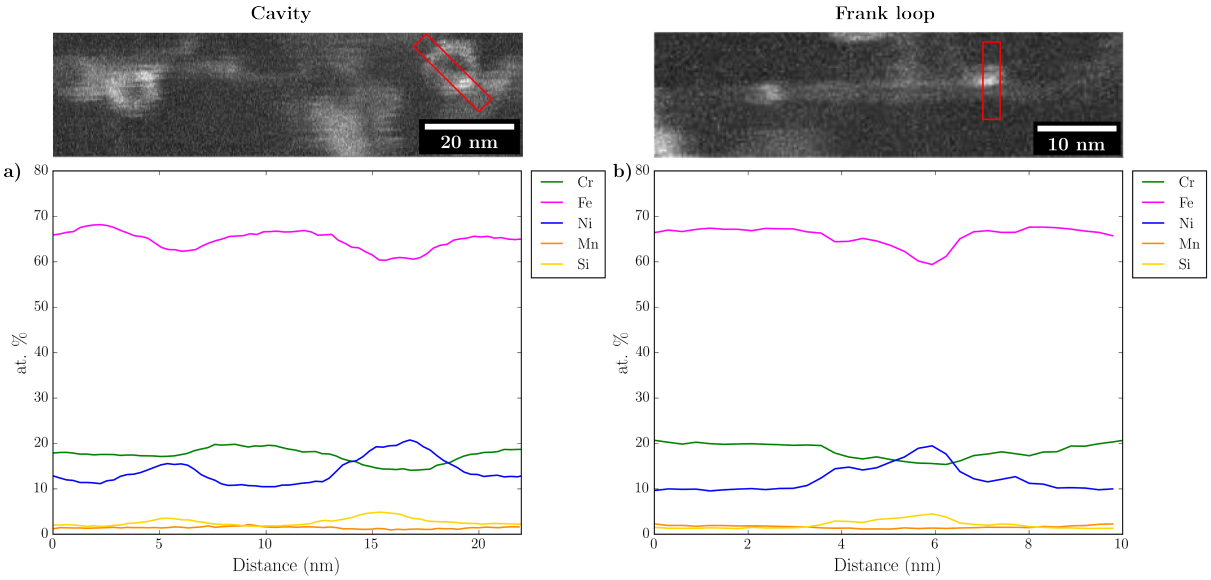

Figure 2.43: *EDXS Quantitative linescan on the Titane 1 dpa IRR sample a) on a cavity b) on a loop edge-on (near [101] zone axis)*

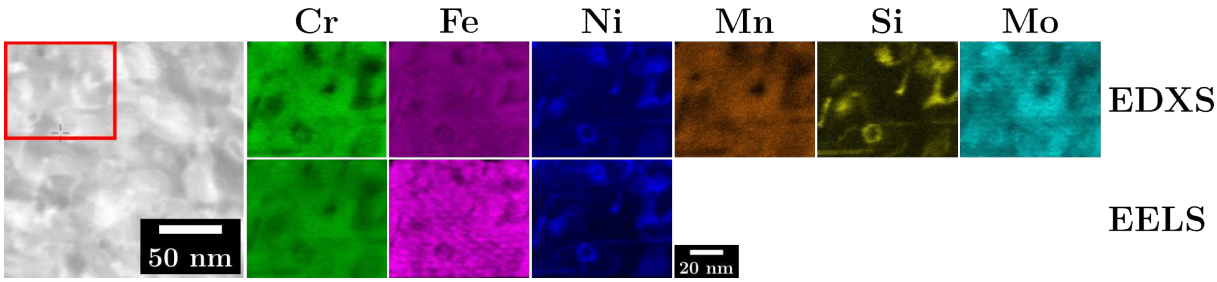

Figure 2.44: *HAADF image and EDXS/EELS mapping of Cr, Fe, Ni, Mn, Si and Mo of the intragranular segregation on the Titane 1.5 dpa IRR sample*

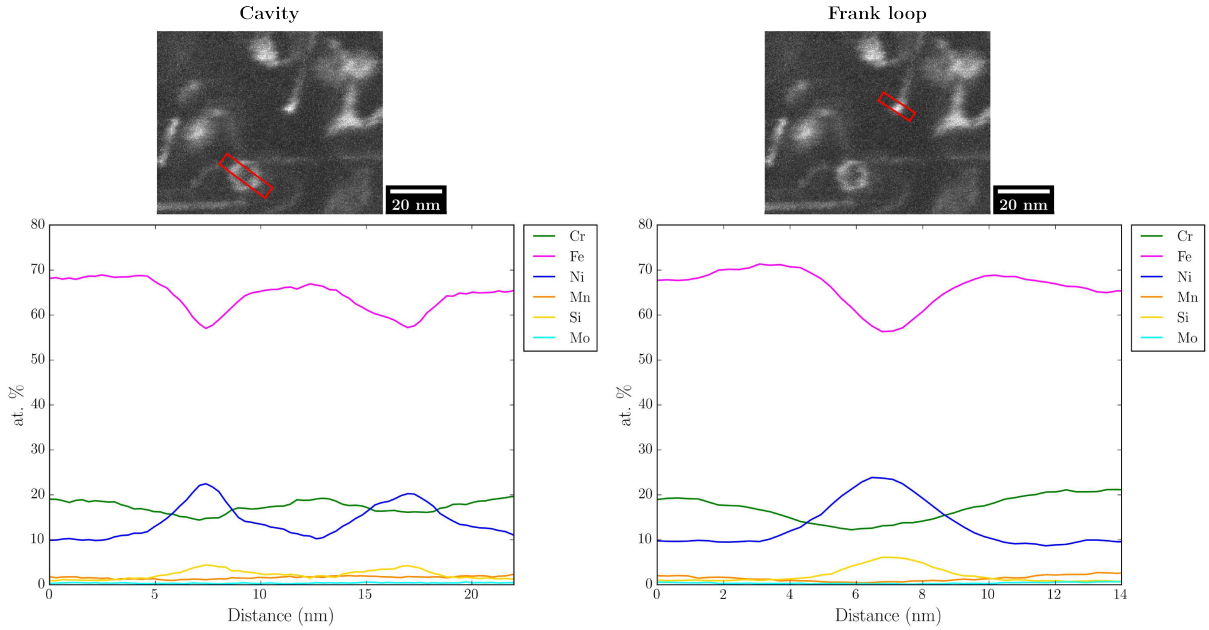

Figure 2.45: *HAADF image and EDXS/EELS mapping of Cr, Fe, Ni, Mn, Si and Mo of the intragranular segregation on the Titane 1.5 dpa IRR sample*

Figures 2.46 and 2.47 present the segregation occurring at the Frank loops on the **IACIRR** area of the Michigan sample. The quantification was performed on a 70 ± 10 nm thick area. Once again the loops are Ni/Si enriched while, Cr, Fe and Mn depleted. Nonetheless, the amont of segregation is lower than the one observed previously ($\Delta_{Cr} \approx -1$, $\Delta_{Ni} \approx +4$–8 at. %, $\Delta_{Si} \approx +2$ for chromium, nickel and silicon respectively) probably due to the lower irradiation temperature of this specimen (360 °C against 380 °C for the Titane **IRR** samples). The segregation around cavities was not studied for this sample due to the too small size of the voids. Since segregation was seen around cavities for the other sample proton pre-irradiated, such segregation might occur on this sample too. The intragranular segregation on the **IACIAC** area of the Michigan sample was not investigated. However, since Frank loops and cavities were observed on this sample, segregation is likely to arise around such objects.

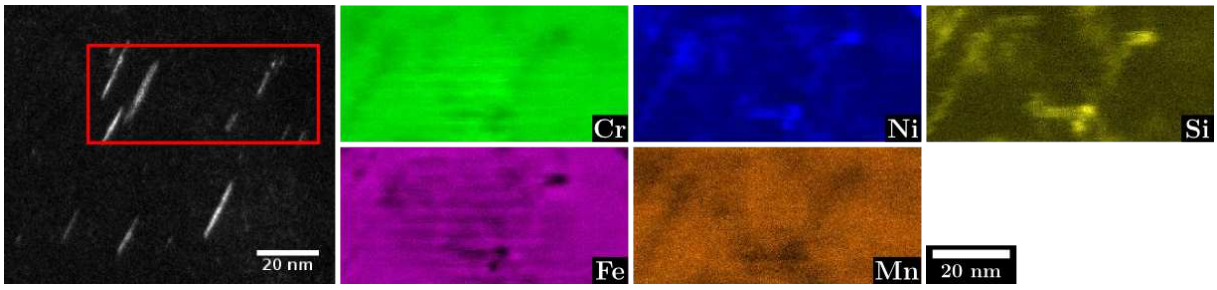

Figure 2.46: *TEM DF image of the loops edge-on near [101] zone axis and EDXS mapping of Cr, Fe, Ni, Mn and Si of the intragranular segregation on the IACIRR area of the Michigan sample*

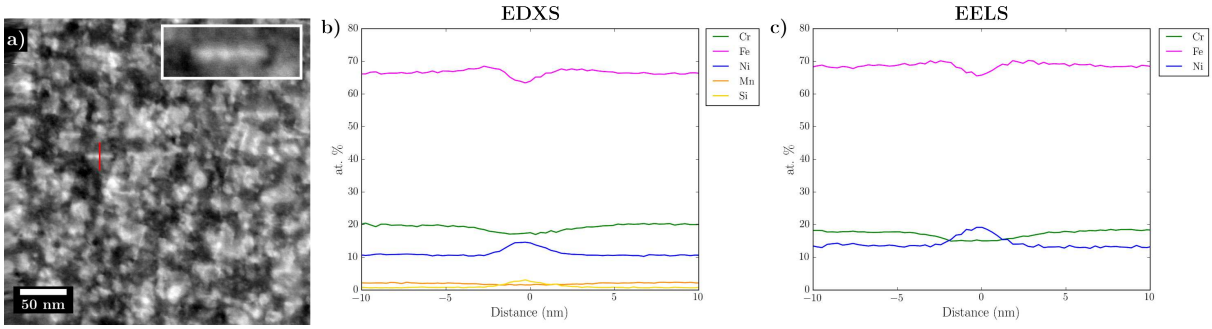

Figure 2.47: *Segregation on a Frank loop edge-on (close to [101] zone axis) on the IACIRR area of the Michigan sample a) HAADF image and b) EDXS quantitative linescans and c) EELS quantitative linescans*

Finally, intragranular segregation on the decommissioned bolt irradiated to 7 dpa was investigated. While additional diffraction spots coming from precipitates were difficult to be observed especially on [100] zone axis (Figure 2.48 a), some were evidenced on [111] zone axis thanks to the higher spacing between the diffracting spots of the matrix (Figure 2.48 b). A BF image of the studied area on [111] zone axis is shown on Figure 2.48 c while Figures 2.48 d to f and g to i are the DF images of the reflections positioned at $\frac{1}{2}$ <220> and $\frac{1}{3}$ <422> respectively. All the DF images showed evidence for precipitation. Even if the smallest objective aperture available on the TEM was used ($\varnothing \approx 10\,\mu m$) it remains too big to finely and accurately image this precipitation.

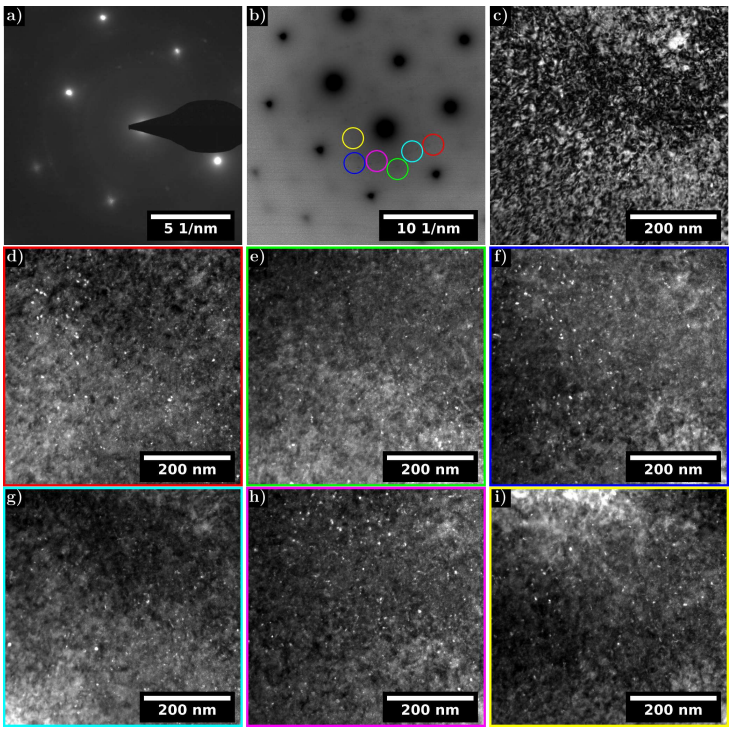

Figure 2.48: *DF investigation of the presence of precipitates on the decommissioned bolt a) SAED pattern on [100] zone axis b) SAD pattern on [111] zone axis with the objective aperture placement for the following DF c) BF of the transmitted beam d) to i) DF images of the corresponding coloured circles from b)*

EELS and EDXS chemical analyses also showed a clear clustering/precipitation. Indeed, Figure 2.49 highlights the intragranular segregation and mainly Ni/Si clusters with iron enrichment around them. These clusters/precipitates appear unevenly distributed and sometimes aligned (Figure 2.50). This suggests that some might have nucleated on former dislocations. Clusters

Cr-rich, Cr+Ni-rich and Ni-rich are also evidenced on the EELS maps from Figure 2.50. These Ni-rich cluster are believed to be silicon enriched as at lower magnification Ni/Si cluster were observed on EDXS maps.

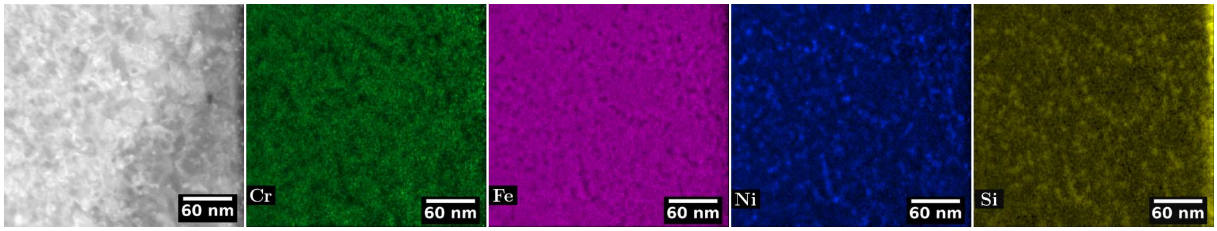

Figure 2.49: *HAADF image and EDXS quantitative mapping of intragranular segregation of Si, Ni, Fe and Cr on the decommissioned bolt*

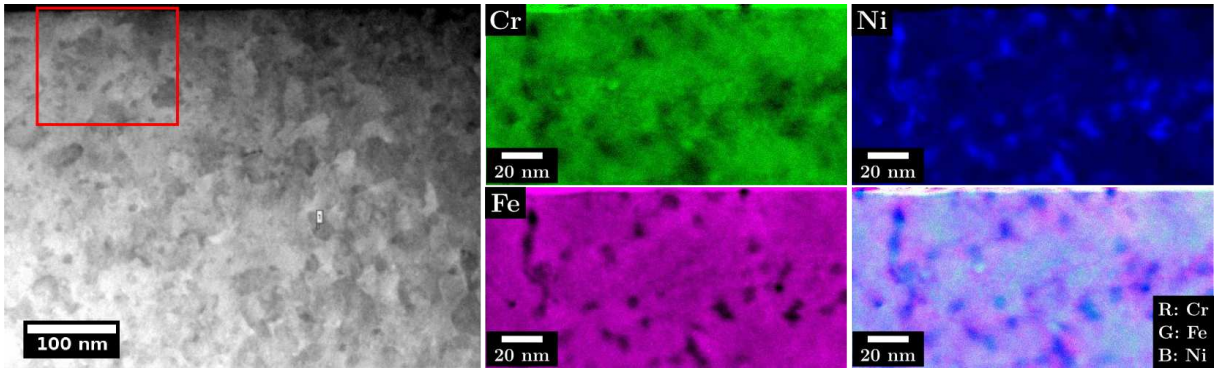

Figure 2.50: *HAADF image on a [110] zone axis and EELS mapping of intragranular segregation of Cr, Fe and Ni on the decommissioned bolt*

Chemical mapping was performed on cavities, loops edge-on or in plane view (Figure 2.51, Figure 2.50, Figure 2.52). Segregation of nickel and depletion of iron and chromium was detected around cavities (Figure 2.51). Figure 2.52 shows EDXS maps acquired on a [110] zone axis with the Frank loops edge-on. One of the loops (red arrow) is Ni/Si segregated and Fe/Cr depleted while iron enriched on both sides (see profile on Figure 2.52) whereas a second one (blue arrow) appears not to be segregated. The amount of segregation on the segregated loop reaches $\Delta_{Si} \approx +22$ at. %, $\Delta_{Ni} \approx +5$ at. %, $\Delta_{Cr} \approx -7$ at. %. A loop in plane view was analysed by EELS mapping (Appendix E) clearly pointing out that the segregation on loops is not homogeneous as on the voids surface. The maximal amount of segregation occurring on both defects reaches $\Delta_{Ni} \approx +19$ at. % and $\Delta_{Cr} \approx -7$ at. %.

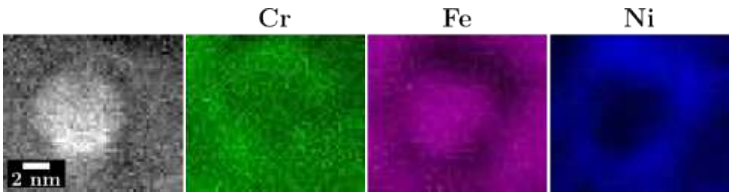

Figure 2.51: *HAADF image and EELS mapping of Cr, Fe and Ni on a cavity on the decommissioned bolt*

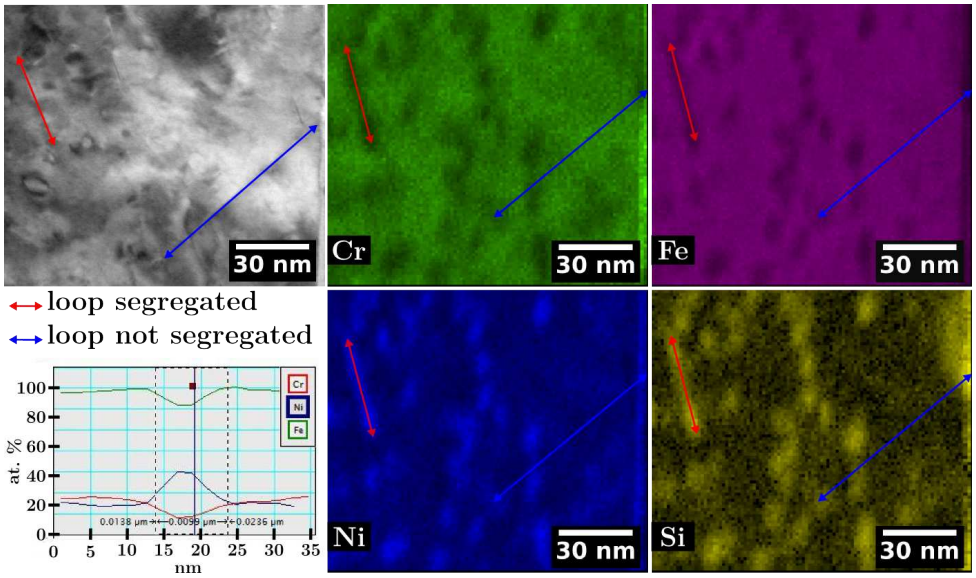

Figure 2.52: *HAADF image on a [110] zone axis and associated EDXS quantitative mapping of Ni, Si, Fe and Cr around edge-on Frank loops with the chemical composition profile across the segregated loop (normalised to the maximum value) on the decommissioned bolt*

In conclusion, intragranular segregation was evidenced on all irradiated samples. However, diffraction patterns did not allow to evidence an obvious precipitation on the proton pre-irradiated samples. Nonetheless, the several EDXS and EELS mappings carried out around cavities and Frank loops highlighted a clear segregation around these defects. Both loops and cavities act as sinks for the RIS but this segregation is not homogeneous on these defects. Segregation at dislocation loops and cavities is consistent with that at grain boundaries. Fe, Cr and Mn are depleted while Ni and Si are enriched at both the grain boundary and the irradiation defects. The amount of segregation is close on all sample but slightly lower on the Michigan sample due to the lower irradiation temperature. This Ni/Si segregation at irradiation defects might be precursor to γ' (Ni_3Si) or G ($M_6Ni_{16}Si_7$) phases [90, 92, 96]. Indeed, if solute concentrations in some local/specific regions exceed their solubility, a new phase can grow [170]. This TEM analysis allowed to correlate the defects nature and the segregation. Yet, it has limitations as it is needed, to provide accurate chemical composition of this segregation, to deconvolute the signal coming from the matrix and the signal hailing from the segregation. Such deconvolution should prove difficult and therefore these results should be combined to APT measurements.

Intragranular segregation and precipitation: Radiation Induced Segregation was observed around both cavities and Frank loops and was found to be heterogeneous. TEM EDXS and EELS analyses allowed to correlate the nature of the defects and the segregation occurring around them. Nickel and silicon enrichment was highlighted coupled with iron, chromium and manganese depletion. These site may act as nucleation sites for γ' or G phases. However, not all Frank loops were found segregated.

2.3.2.2 RIS at grain boundaries

To look upon intergranular RIS the grain boundaries were set edge-on. Both Energy Dispersive X-ray Spectroscopy (EDXS) and Electron Energy Loss Spectroscopy (EELS) quantifications were performed if possible. Molybdenum segregation was only quantified when foils were sticked on copper grids. Moreover, its quantification was only performed by EDXS since the molybdenum edge was too far off and was not included in the acquired EELS spectrum. One should note that phosphorus and silicium quantification using EELS could be underestimated. This is due to

their low concentration and thus low counts received and to low sensitivity of EELS spectroscopy for elements with higher energy losses.

All the grain boundaries were found chromium, iron and manganese depleted while enriched in nickel and silicon. Iron depletion often possessed a M-shaped profile while nickel enrichment sometimes presented a W-shaped profile. Enrichment in phosphorus and molybdenum depletion were also evidenced on some grain boundaries. Figures 2.53 and 2.54 image the Radiation Induced Segregation at the grain boundary of the Titane 1.5 dpa **IRR** sample[1]. All the other maps and linescans acquired on the samples can be found in Appendix E. Segregations were found between 4 and 9 nm wide and relatively homogeneous along the grain boundary. The RIS quantifications at grain boundaries for all studied samples are summarised in Table 2.9.

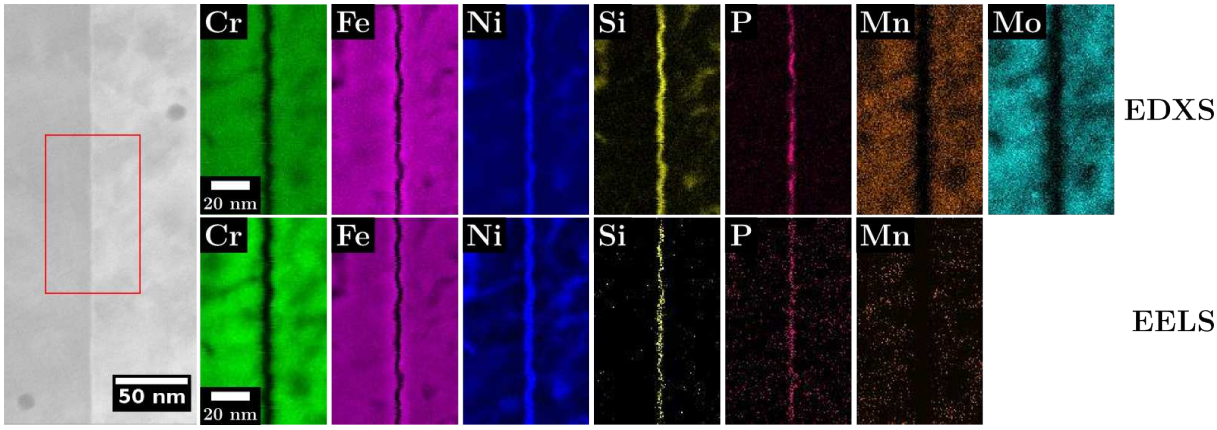

Figure 2.53: *HAADF image and associated EDXS and EELS quantitative maps of the grain boundary composition on the Titane 1.5 dpa IRR sample*

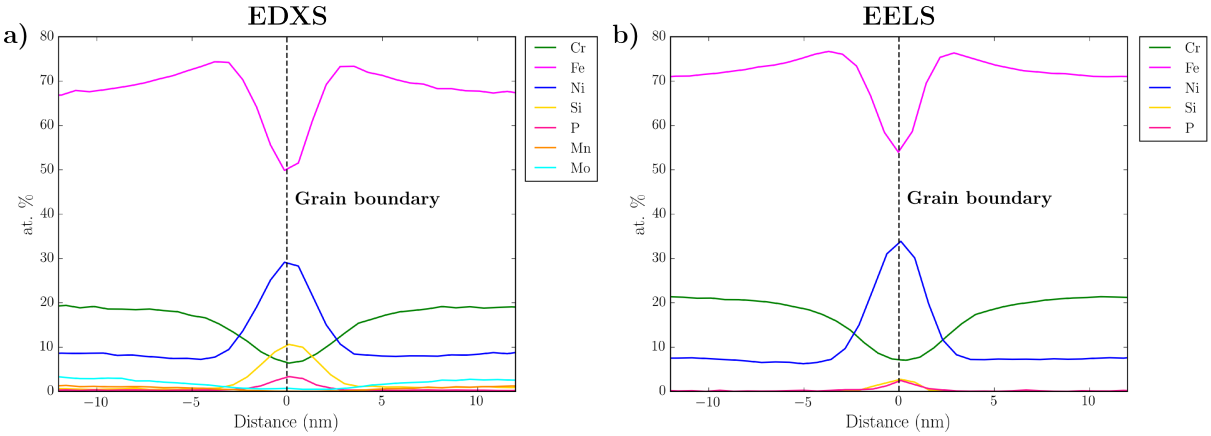

Figure 2.54: *Quantitative linescans along the grain boundary on the Titane 1.5 dpa IRR sample a) EDXS profiles b) EELS profiles*

[1]The tortuous appearance of the grain boundary is caused by the drift that occurred during the acquisition.

Table 2.9: *EDXS and EELS quantitative analyses of the grain boundaries RIS – Results given in the form of Δ = (RIS − matrix) in at. % with regards to the matrix composition (+ and − indicate enrichment and depletion respectively)*

Element	Titane 1 dpa IRR		Titane 1.5 dpa IRR		IACIRR		IACIAC		Bolt
	EDXS	EELS	EDXS	EELS	EDXS	EELS	EDXS	EELS	EDXS
Fe	−6	−3	−16	−13	−3	≤ −1	−7	−3	−21
Cr	−9	−9	−12	−11	−4	−7	−4	−4	−8
Ni	+11	+10	+18	+23	+6	+10	+5	+5	+5
Mn	−1	−1	≤ −2	≤ −2	≤ −2	≤ −2	≤ −2	≤ −2	−1
Si	+7	+4	+10	+2	+4	+1	+4	+2	+24
Mo	-	-	≤ −2	-	-	-	-	-	≤ −2
P	-	-	+3	+2	+1	+1	+4	+3	-

The RIS at grain boundaries observed for all samples is consistent with the literature data for neutron [90, 96–98, 122] and proton irradiations [101, 108, 128]. The segregation is found enhanced at 1.5 dpa compared to the one that occurred on the Titane 1 dpa **IRR** sample. In addition, the amount of RIS at grain boundary is not as high on the **IACIRR** area of the Michigan sample as the one occurring on the Titane **IRR** samples. However, the segregation is close on both the **IACIRR** and the **IACIAC** area of the Michigan sample. Finally, the RIS occurring on the grain boundary of the extracted bolt is close to the one measured on the sample proton irradiated except for the silicon enrichment which was found much higher. Since silicon content in the decommissioned bolt alloy is almost twice that in the 316L proton irradiated, this higher silicon content might be responsible for the higher silicon segregation at grain boundary on the decommissioned bolt. Figure 2.55 compares the amount of chromium and nickel RIS at grain boundaries on the studied irradiated samples. The smallest segregation is seen on the Michigan sample in both the **IACIRR** and **IACIAC** areas. The smaller irradiation temperature can probably be held accountable for the smaller RIS. The higher segregation is observed on the Titane 1.5 dpa **IRR** sample followed closely by the on the Titane 1 dpa **IRR** sample and the decommissioned bolt. This is in agreement with the literature since it is believed that both dose and the irradiation temperature exacerbate the RIS [90, 98, 122]. Moreover, all these resuts are in agreement with the ones on intragranular segregation presented in the above section, both in terms of segregation contents and trends.

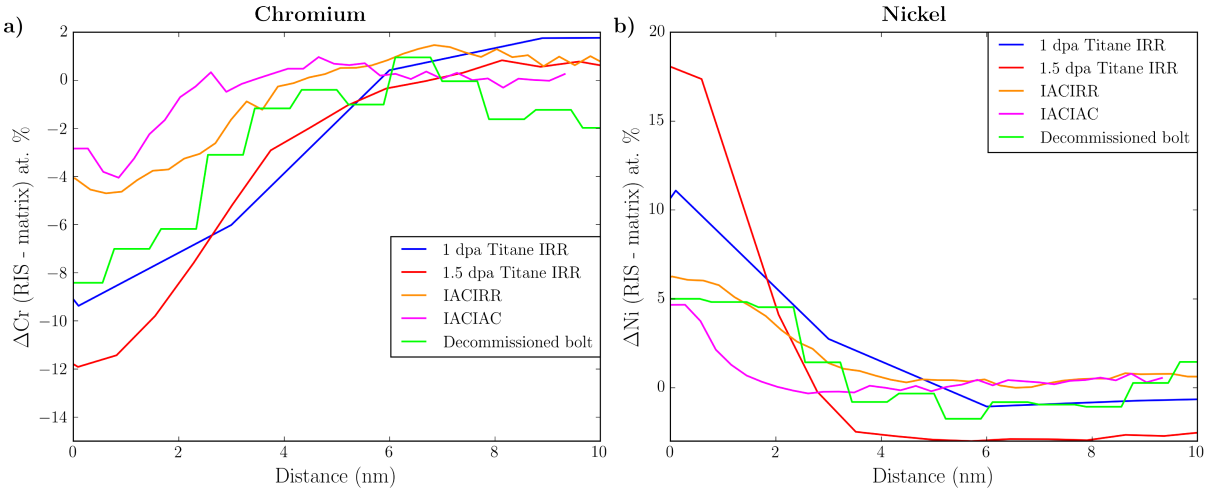

Figure 2.55: *EDXS quantitative linescans near grain boundaries depending on the irradiation condition of a) chromium and b) nickel*

RIS at grain boundaries: Radiation Induced Segregation at grain boundaries was observed on all irradiated samples and is consistent with the literature data.

- Grain boundaries are enriched in Ni and Si, while deleted in Cr, Fe, and Mn. Enrichment in phosphorus and molybdenum depletion were observed on some samples. This segregation is homogeneous along the grain boundaries.
- RIS is enhanced on the Titane 1.5 dpa **IRR** sample compared to the 1 dpa sample thus indicating that the RIS plateau is not reached yet.
- RIS is lower on the **IACIRR** area than on the Titane 1 dpa **IRR** sample area due to the lower irradiation temperature.
- Segregation at grain boundary on the decommissioned bolt is close to the one observed Titane **IRR** samples except for the silicon enrichment which is much higher due to the higher silicon content in the bolt.

2.3.3 Proton irradiation representativeness

Proton irradiation were carried out to emulate the microstructure of neutron irradiated materials after an adjustment of the irradiation temperature to emulate neutron irradiation with protons as suggested by the literature [15–17]. As previously stated, Frank loops, cavities and segregation were observed on all irradiated samples. The number of features per unit volume and their sizes were determined for each sample and the segregation was quantified. Thus the microstructure and segregation on samples proton irradiated were compared to the neutron irradiated extracted bolt as well as to the literature data. For the first time, TEM analyses of the intragranular segregation permitted to link the segregated area to the defect nature. Nonetheless, these analyses should be combined to APT measurements to provide chemical compositions of the segregated areas with a better accuracy.

The higher irradiation dose of the 1.5 dpa Titane **IRR** sample compared to the 1 dpa sample, induced slightly bigger loops and cavities and more numerous cavities. This is consistent with the literature since their size and density have been reported to increase with the irradiation dose before reaching a saturation plateau [90–92]. The saturation is believed to take place between 1 and 5 dpa for temperatures close to 300 °C. Moreover, RIS is supposed to be exacerbated as the irradiation dose increases and such phenomenon was seen between the 1 and 1.5 dpa doses [90, 98]. However, the irradiation temperature is known to influence the Frank loops and cavities sizes and densities [92, 101, 103]. Above 300 °C, as the irradiation temperature increases both the loop and cavity sizes increase while their densities decrease. This was seen on the Michigan sample in the **IACIRR** area compared to Titane 1 dpa **IRR** sample. Cavities and loops were both less numerous and smaller on the sample irradiated at the lower irradiation temperature. Smaller sizes of both defects are consistent with the literature. Their smaller density is probably due to a higher difficulty to image and count such small defects. In addition, RIS at grain boundary was found lower on the **IACIRR** and **IACIAC** areas of the Michigan sample which is consistent with the literature data stating that RIS increases with the irradiation temperature [122]. The **IACIAC** area of the Michigan sample possessed smaller and fewer defects than the other samples. It might stem from a defect recombination that occurred during the oxidation. Finally, the decommissioned bolt possessed small but numerous Frank loops and cavities. It results from the combinaison of the lower irradiation temperature, higher irradiation dose and the TEM foil low thickness and high quality. TEM imaging of the cavities could not allow to differentiate voids and helium filled bubbles. RIS at grain boundary was in agreement with the ones measured on the samples proton irradiated. Compared to Panait results on the same bolt

[2], our results bode well but the defect sizes are lower and their densities higher probably due to the higher quality sample preparation and lower lamella thickness. Indeed, an amorphous layer is usually present on top of electropolished lamellae prepared on neutron irradiated materials. Its presence would add unwanted contrasts that could be mistaken for defects or could prevent their observation. The higher quality of the PIPS cleaned FIB lamellae made in this work, partially due to the reduction of the amourphous layers present, allow an easier quantification of irradiation defects. Nonetheless, one should be careful when considering and comparing such data as we highlighted that the measurements and quantifications are extremely contingent on the foil quality. Thus, both microstructural defects and segregation induced by neutron irradiation are closely replicated using proton irradiation.

Proton irradiation representativeness: As expected from the literature survey, Frank loops, cavities and Radiation Induced Segregation at grain boundaries were observed on all irradiated samples. For the first time, segregation on irradiation defects was analysed using TEM and compared to the defects nature.

Frank loops: Frank loops sizes ranged from $\sim$ 1 to 90 nm while their density ranged between $\sim$ 2 and 16×10^{22} loop/m^3.

Cavities: Cavities sizes ranged from $\sim$ 1 to 20 nm while their density ranged between $\sim$ 0.3 and 31×10^{21} cavity/m^3 and they appear faceted when big enough to be imaged (facets lying in {111} and {020} planes).

RIS at grain boundaries: Grain boundaries were found Ni and Si enriched, while Cr, Fe, and Mn depleted as expected. Enrichment in phosphorus and molybdenum depletion were observed on some samples. Nickel enrichment reached $\sim$ 30 at. % and the maximum chromium depletion was measured at $\sim$ 6 at. %.

Intragranular segregation and precipitation: EDXS and EELS mapping revealed a Ni/Si enrichment as well as Fe, Cr and Mn depletion around both cavities and Frank loops. These sites may act as precursor to γ' or G phases formation. However, not all Frank loops were found segregated.

➔ Proton irradiation was shown to be an efficient tool to emulate both the microstructure and segregation induced by neutron irradiation.

Chapter 3

Characterisation of the oxides formed in simulated primary water

Contents

3.1 Description of the oxides formed on 316L exposed to simulated PWR medium 112
3.1.1 Morphological description of the oxide layers . . . 112
3.1.1.1 Optical microscopy study of the oxidised samples . . . 112
3.1.1.2 SEM characterisation of the outer oxide surface morphology . . . 112
3.1.1.3 Oxides morphology and thickness at nanoscopic scale . . . 113
3.1.1.4 Morphological description: Summary . . . 114
3.1.2 Analysis of the crystallographic structure of the oxide layers . . . 115
3.1.2.1 SEM description of the outer oxide morphology . . . 115
3.1.2.2 GIXRD analysis . . . 115
3.1.2.3 Raman spectroscopy . . . 117
3.1.2.4 TEM Dark Field and diffraction study . . . 118
3.1.2.5 Crystallographic structure: Summary . . . 121
3.1.3 Chemical analysis of the oxide layers . . . 122
3.1.3.1 Raman spectroscopy analysis . . . 122
3.1.3.2 EFTEM mapping . . . 123
3.1.3.3 EELS and EDXS quantitative analyses . . . 124
3.1.3.4 Chemical analysis: Summary . . . 126
3.1.4 Grain boundaries oxidation . . . 126
3.1.4.1 Morphological description . . . 126
3.1.4.2 Chemical analysis . . . 128
3.1.4.3 Grain boundaries oxidation: Summary . . . 130
3.1.5 Oxides formed on 316L exposed to simulated PWR medium: Synthesis, discussion and oxidation mechanism . . . 130
3.2 Crystallographic orientation effect on the oxide scales . . . 134
3.2.1 Morphological description of the oxide depending on the underlying grain orientation 134
3.2.1.1 Optical microscopy study . . . 135
3.2.1.2 Description of the oxides using SEM . . . 135
3.2.1.3 TEM study of the inner oxides thickness . . . 137
3.2.1.4 Morphological description: Summary . . . 138
3.2.2 Chemical analysis of the oxide layers depending on the underlying grain orientation 139
3.2.2.1 Raman spectroscopy analysis . . . 139
3.2.2.2 EDXS and EELS quantitative analyses . . . 140
3.2.2.3 Chemical analysis: Summary . . . 142

3.2.3 Crystallographic orientation: Synthesis, discussion and oxidation mechanism . . . 142
3.3 Cold-work effect on the oxide scales . . . 145
3.3.1 Characterisation of the oxides morphology and thickness on cold-worked samples . 145
3.3.2 Chemistry of the oxides formed on cold-worked samples . . . 148
3.3.3 Cold-work effect: Synthesis, discussion and oxidation mechanism . . . 149
3.4 Effect of the presence of inclusions on the oxide scales . . . 151
3.4.1 Characterisation of the oxides morphology and thickness near inclusions . . . 151
3.4.2 Chemistry of the oxides near inclusions . . . 154
3.4.3 Effect of the presence of inclusions: Synthesis, discussion and oxidation mechanism 154
3.5 Oxide scales formed in simulated primary water: Synthesis . . . 156

The literature overview given in Chapter 1 highlighted that oxides formed on austenitic stainless steels exposed to primary water are duplex [12, 13, 26–29, 32]. This duplex oxide layer is known to be composed of an iron-rich outer layer mostly found to be magnetite with sometimes nickel in it and a chromium rich compact inner layer mostly described as a mixed iron/chromium spinel [24, 26]. In addition, a nickel-rich layer was reported by several authors at the metal/oxide interface [12, 13, 26, 28]. However, the literature review evidenced some disagreement among several authors regarding the structures of the oxides formed on stainless steel alloys exposed to PWR environments. This point of contention arises from the observation of Face Centered Cubic (FCC) structures [26, 27], hexagonal ones [22, 33] or even a mix of both [24]. Moreover, the inner oxide layer was reported sometimes monocrystallite [12, 13] and other times polycristalline [5, 6, 26, 27, 87–89].

Therefore, the following chapter aims to bring lights on the oxides formed on a 316L alloy exposed to simulated primary water. It will provide reference for further comparision with irradiated specimens in the next chapter. The properties of oxide films formed, including morphology, thickness, structure and chemical composition, etc. are thought to play important roles in the oxidation process, especially at the initial stages and at crack tips. Indeed, as Stress Corrosion Cracking (SCC) and IASCC cracks will further propagate, they will present oxidised areas corresponding to the oxidation first stages at the crack tips. Thus, samples were oxidised during short times, between 5 minutes and 96 hours, to investigate the oxidation first stages. Only few authors studied short time oxidation, among them, Soulas depicted the oxides scales formed and the oxidation mechanism proposed will be discussed [12, 13]. Hence, given the few amount of data, short time oxidations on unirradiated 316L alloy were perform to act as reference and be compared to short time oxidations performed on irradiated 316L alloy in Chapter 4. An overview of the oxide scale formed on a 316L alloy exposed to primary water will be given in the first section focusing on the outer oxide morphology, the oxide scale structure and composition as well as the oxide formed at grain boundaries. As the crystallographic orientation of the underlying metal grain was shown to influence the oxidation [12–14, 66], the oxide layer investigation was made on a sole grain orientation. Then, further investigation of the oxide layers considering the crystallographic orientation of the underlying metal grain will be developed. The outer oxide morphologies, inner oxide thicknesses and overall oxide compositions will be detailed depending upon the underlying metal grain orientation. The last two sections aim to reveal how surface heterogeneities such as cold-work induced by a poorly controlled polishing and inclusions can affect the oxidation. Therefore, their effect onto the oxides morphology, thickness and chemistry will be depicted. Finally, a synthesis on the oxide scales formed in simulated water environment will be given.

The investigation of the oxide scales presented in the following sections was carried out using adapted techniques for the analysis of such thin oxide layers as described in Chapter 2 section 2.1. The outer oxide morphologies were studied using optical images as well as SEM images. The

inner oxide thicknesses were measured from TEM and STEM images and these images allowed to give an overview of the inner layer. The investigation of the oxide crystallographic structures were made from a macroscopic scale using GIXRD and Raman spectroscopy down to the nanometric scale using SAED analysis and TEM DF imaging. From a macroscopic point of view, the chemistry of the oxide layers was studied using Raman spectroscopy. Several TEM techniques were employed to investigate the oxide compositions at a nanometric scale. EFTEM imaging made it possible to visualise enrichment in a given element and EDXS, EELS analyses allowed to quantify these enrichments seen in EFTEM mapping.

Oxide scales formed in simulated primary water:

- Description of the oxide scales formed on a 316L alloy exposed to simulated PWR medium for short time oxidation on a sole grain orientation.
- Investigation of the influence of the crystallographic orientation of the underlying metal grain.
- Effect of surface heterogeneities: cold-work induced by the polishing carried out and the presence of inclusions.

3.1 Description of the oxides formed on 316L exposed to simulated PWR medium

This section focuses on the investigation of Titane **REF** and **UNIRR** samples oxidised between 5 minutes and 96 hours. Solely results on [100] grain orientation will be presented. First and foremost, the morphology of the oxide layers was studied as a function of the oxidation time. Then, the crystallographic structure of the oxide was investigated from the macroscopic scale down to the nanometric scale. Thirdly, the chemistry of the oxide layers was looked upon after 24 hours oxidation.

3.1.1 Morphological description of the oxide layers

In the following paragraphs, the outer oxide will be depicted in plane view in the optical and SEM images whereas TEM cross-section imaging will provide information on the oxides thicknesses and morphologies.

3.1.1.1 Optical microscopy study of the oxidised samples

Optical images were used to look upon the **REF** specimens oxidised between 5 minutes and 72 hours (Figure 3.1). The sample oxidised 5 minutes is the less oxidised of all as its surface looks whiter/brighter. As the oxidation time increases contrasts between grains appear. This variation of contrast is due to a different light reflectivity on the grain surfaces after oxidation. So there is certainly a difference in morphology, size or density of crystallites as the oxidation duration increases. The longer the samples are exposed in the medium, the more oxidised the samples look. The influence of the crystallographic orientation of the underlying metal grain and of the inclusions will be described in sections 3.2 and 3.4.

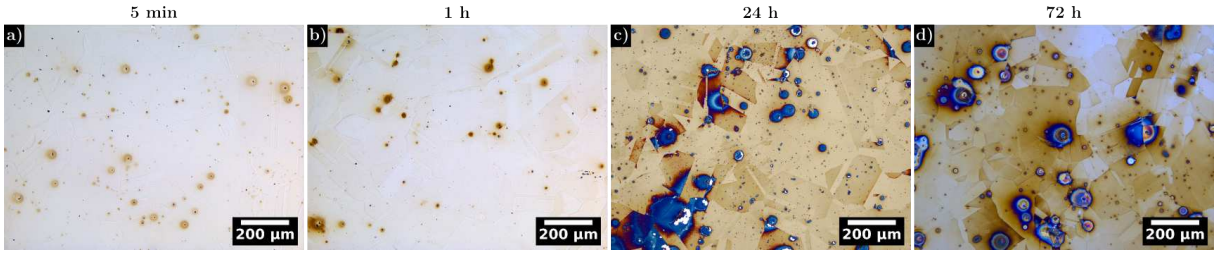

Figure 3.1: *Optical images of the REF samples oxidised in simulated PWR water a) 5 minutes b) 1 hour c) 24 hours and d) 72 hours*

3.1.1.2 SEM characterisation of the outer oxide surface morphology

SEM images acquired on the **REF** specimens oxidised between 5 minutes and 72 hours are presented in Figure 3.2 and the measurements performed in Table 3.1. These images allowed to look upon the outer crystallite distributions, their sizes and densities but were acquired on solely one grain orientation ([100]) since, as already mentioned in Chapter 1, the underlying metal grain is known to affect the outer oxide formed. Before 24 hours oxidation, the outer oxide formed is globular and without any specific crystallite shapes. The coverage is higher after 1 hour oxidation than after 5 min ($\sim$ 58 % vs 51 %) and the crystallites are slightly bigger ($\sim$ 37 vs 23 nm) but less numerous ($\sim$ 580 vs 376 crystallite/µm^2). Since fewer crystallites are observed after 1 hour oxidation, it suggests that some crystallites were dissolved into the medium and have re-precipitated while growing the still existing ones. This explains the smaller number of bigger crystallites and the higher coverage observed on the 1 hour oxidised sample compared to the 5 minutes oxidised one. After 24 hours oxidation, bigger faceted crystallites are visible. Small germs (from a few nm to $\sim$ 20 nm) with undefined shapes are still present on top of

the inner oxide meshed with the bigger faceted crystallites. The oxide structure and chemistry of these crystallites could differ. Moreover, the outer oxide coverage is higher after 24 hours oxidation since the small germs cover most of the inner oxide surface. The number of faceted crystallites that appeared after 24 hours oxidation is even higher after 72 hours oxidation ($\sim$ 72 vs 25 crystallite/µm^2). However, between the two samples, the crystallite mean sizes were found to be close and not bigger as could be expected from a longer oxidation duration. This arises from the higher number of faceted crystallites that are formed and still remain small and thus lower the mean crystallite sizes. Nonetheless, the biggest crystallite observed on each sample was getting bigger as the oxidation duration increased. Thus, as the oxidation time increases after 24 hours, the number of faceted crystallites increases and they grow. It is believed that, as the oxidation progresses, faceted crystallites will cover the whole inner oxide and will continue to grow if they remain adhered to the inner layer.

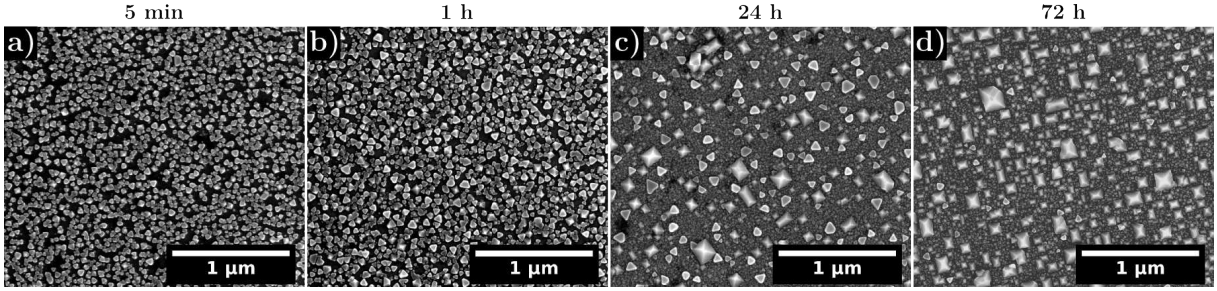

Figure 3.2: *SEM SE images (5 kV) on [100] grain orientation of REF samples oxidised a) 5 minutes b) 1 hour c) 24 hours and d) 72 hours*

Table 3.1: *Quantitative analysis of the crystallite distribution on REF samples oxidised 5 minutes, 1 hour, 24 hours, and 72 hours (for 24 h and 72 h the number of crystallites and their mean sizes per µm^2 are given for the big-faceted crystallites)*

Oxidation time	5 minutes	1 hour	24 hours	72 hours
mean size ± standard deviation (nm)	23 ± 9	37 ± 15	71 ± 50	66 ± 35
min – max size (nm)	6 – 50	7 – 105	9 – 175	10 – 200
crystallite/µm^2	580 ± 40	376 ± 40	25 ± 3	72 ± 7
coverage (%)	51 ± 5	58 ± 5	68 ± 5	68 ± 5

3.1.1.3 Oxides morphology and thickness at nanoscopic scale

After 1 hour and 24 hours oxidation, the oxide formed on top of a 316L alloy oxidised in simulated PWR media is duplex (Figures 3.3 and 3.4). This duplex layer consists of a continuous inner oxide layer and a non-continuous outer oxide layer, as expected from the literature [12, 13, 26–29, 32]. The presence of the carbon deposit granted a clear visualisation of the discontinuous outer layer. Crystallites are formed on top of the thin inner oxide layer and not directly on top of the metal. The oxide thicknesses were measured on [100] grain orientations from the STEM HAADF images (Figures 3.3 and 3.4). The oxide is less than 5 nm thick after 1 hour oxidation while it is $\sim$ 10 ± 2 thick after 24 hours oxidation. Crystallite sizes range from a few nm to $\sim$ 50 nm. This is in accordance with Soulas' results who observed inner layers about $\sim$ 3 to 15 nm between 5 minutes and 24 hours oxidation [12].

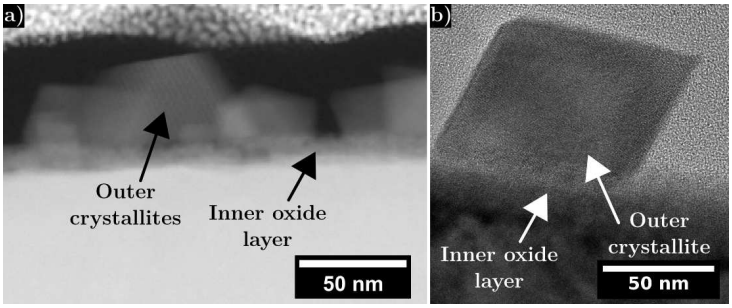

Figure 3.3: *a) STEM HAADF image and b) HRTEM image on an UNIRR sample oxidised 1 hour*

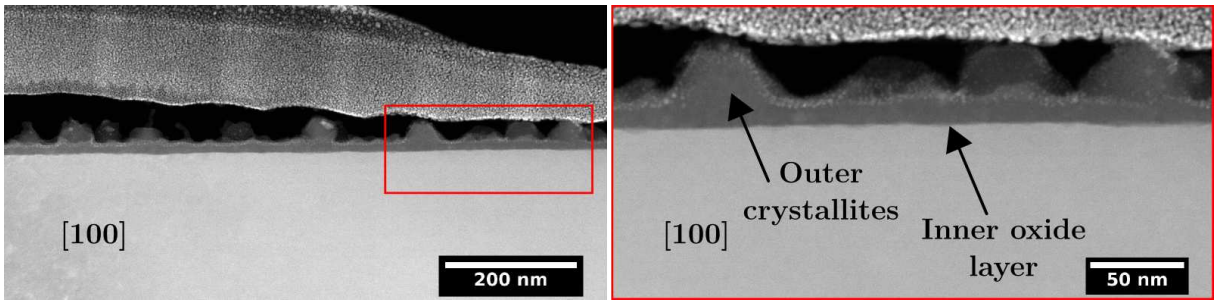

Figure 3.4: *STEM HAADF image on an UNIRR sample oxidised 24 hours on a [100] grain orientation and associated zoom of the red framed area*

Under and over-focus BF images allowed to appreciate the inner oxide density (Figure 3.5). The inner oxide is dense without the appearance of porosities big enough to be imaged.

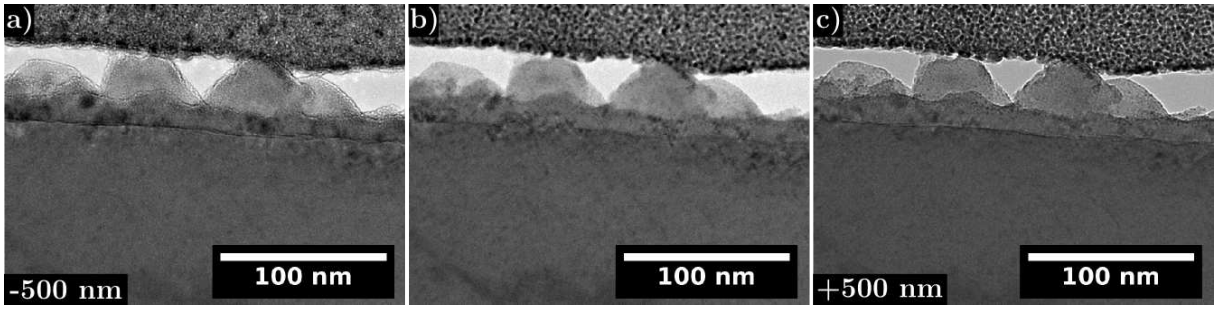

Figure 3.5: *TEM BF images on an UNIRR sample oxidised 24 hours on a [100] grain orientation a) under-focus b) focus and c) over-focus*

3.1.1.4 Morphological description: Summary

The oxide formed on top of 316L alloy oxidised in simulated PWR medium is confirmed to be duplex with a dense inner oxide and a discontinuous outer oxide as suggested by the literature [5, 7, 12, 24, 26, 27, 30, 32]. As the oxidation duration increases the inner oxide layer grows (from less than 5 nm to $\sim$ 10 nm). This inner layer is dense and crystallites are formed directly on top of the inner oxide layer. SEM imaging revealed that an outer oxide is formed even after 5 minutes oxidation and the crystallites are globular. As the oxidation time increases, bigger crystallites are formed but germs are believed to be dissolved into the medium before re-precipitating and contributing to the growth of surrounding crystallites. After 24 hours oxidation, faceted crystallites cohabit with smaller germs. The number of faceted crystallites was found to increase for longer oxidation durations and they continuously grow. Therefore, their growth seem privileged compared to the globular crystallites one.

Morphological description: A duplex oxide layer is formed on 316L alloy exposed to simulated PWR medium consisting of a continuous inner oxide layer and a non-continuous outer oxide layer. The inner oxide grows as the oxidation duration increases and after 24 hours oxidation the inner layer is dense and $\sim$ 10 nm thick. Crystallites are present even after 5 minutes oxidation without any distinct morphology and are believed to dissolve and re-precipitate. After 24 hours oxidation faceted crystallites mesh with smaller germs.

3.1.2 Analysis of the crystallographic structure of the oxide layers

In the following paragraphs focus was made on the investigation of the oxide crystallographic structures from a macroscopic scale using SEM imaging, GIXRD and Raman spectroscopy down to the nanometric scale thanks to SAED analysis and TEM DF imaging. Calculations for both GIXRD and Raman spectroscopy indicated a penetration depth in the oxide of $\sim$ 170 – 210 nm and 460 nm respectively (cf. Chapter 2 sections 2.1.2 and 2.1.3). Since the oxides were found thinner ($<$ 100 nm) both oxide layers will be probed.

3.1.2.1 SEM description of the outer oxide morphology

As seen on Figure 3.6, after 24 hours oxidation, a favoured outer oxide morphology is present among the faceted crystallites. Indeed, squared bases pyramids are the main crystallite morphology as the oxidation time increases on the [100] grain orientation. This outer oxide favoured morphology suggests that an epitaxial relationship exists between the outer oxide, inner oxide and the 316L substrate. Such relationship would be an heteroepitaxy since both the oxide and the substrate are different materials with different lattice parameters. The existence of an epitaxial relationship between the inner oxide layer and the underlying metal grain was investigated and demonstrated by Soulas but no epitaxial relationship with the outer oxide layer was described in his work [12, 13]. On nickel based alloys, Miguet suggested the existence an epitaxial relationship with the outer crystallites but did not describe it further [66] whereas Sennour proposed an orientation relationship ($(111)_{\text{Outer}} \parallel (101)_{\text{Inner}/\gamma}$ and $[110]_{\text{Outer}} \parallel [010]_{\text{Inner}/\gamma}$) [171].

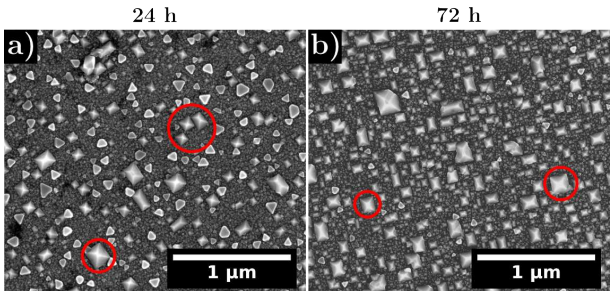

Figure 3.6: *SEM SE images (5 kV) on [100] grain orientation of REF samples oxidised a) 24 hours and b) 72 hours*

3.1.2.2 GIXRD analysis

Figure 3.7 introduces the GIXRD results for the **REF** samples oxidised 5 minutes, 1 hour, 24 hours and 96 hours in simulated primary water. After each oxidation test, independently of its duration, the metal is clearly visible on the three more intense peaks, as on the unoxidised metal (cf. Figure 2.20). Smaller and less intense peaks are present and seem to correspond to a spinel structure AB_2O_4 [172, 173] with a lattice parameter calculated close to 8.37 $\pm$ 0.05 Å. No further analysis on the peak were performed since GIXRD inherently induce a small shift and broadening of the Bragg peaks [174]. The observation of such structure is in agreement with the results of several authors who also observed a spinel oxide structure on stainless steel alloy

using x-ray diffraction [25, 26, 69, 175–180]. Contrary to the finding of a few authors [20, 24, 33], no corundum structure (Cr_2O_3 type oxide) was observed on top of the studied samples. If such structure was present in sufficient quantity (> 1 %), associated peaks would be detected at $\sim$ 24.5, 33.5 and 54.9 ° [181]. Therefore, spinel structure is the only detected structure. However, no distinction can be made between the outer and inner layer as these are both supposed to be spinel structures with close lattice parameters. As one can see, as the oxidation time increases, the peaks corresponding to the oxide are more intense (when normalising the maximum intensity corresponding to the 316L alloy to 100 %). Since fixed grazing angles were used it suggests that thicker oxides are formed and/or that the oxide scale crystallised as the oxidation duration increased.

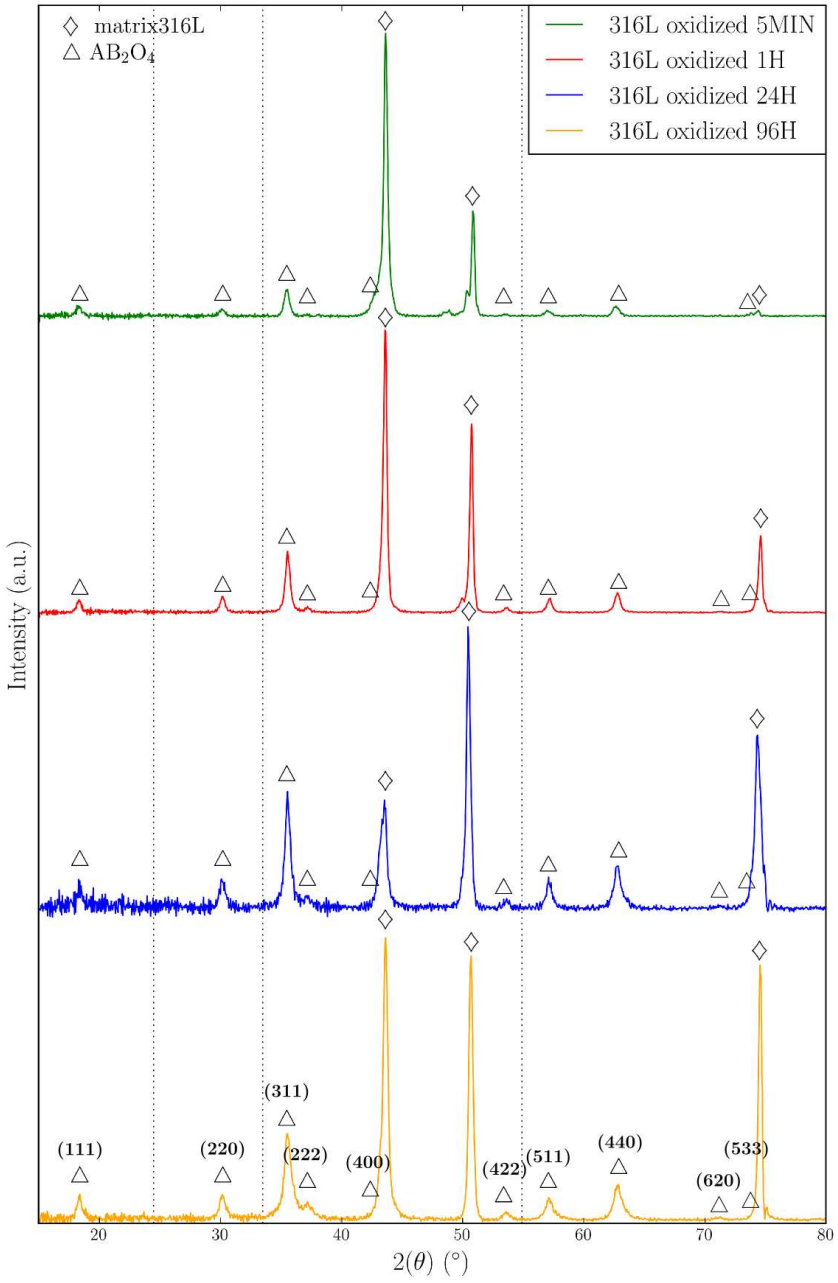

Figure 3.7: *GIXRD results of the REF samples oxidised between 5 minutes and 96 hours*

3.1.2.3 Raman spectroscopy

Figure 3.8 presents the Raman spectra obtained on **UNIRR** specimens oxidised 5 minutes and 24 hours. Raman spectrum of a crystalline material consists of sharp and mostly narrow bands whereas that of the amorphous phases manifests very broad peaks with widths of up to several hundred cm^{-1}. Therefore, the acquired spectra indicate the presence of at least partially crystalline oxides or highly strained oxides. At least 6 bands can be identified (cf. red stars on Figure 3.8) demonstrating that a surface oxide is detected even after 5 minutes oxidation. Looking upon the sample oxidised 24 hours, a similar Raman spectrum was observed as after 5 minutes oxidation but it is much less noisy. The noise on the spectrum obtained on the 5 minutes oxidised sample suggests that the oxide scale formed is thinner on this specimen.

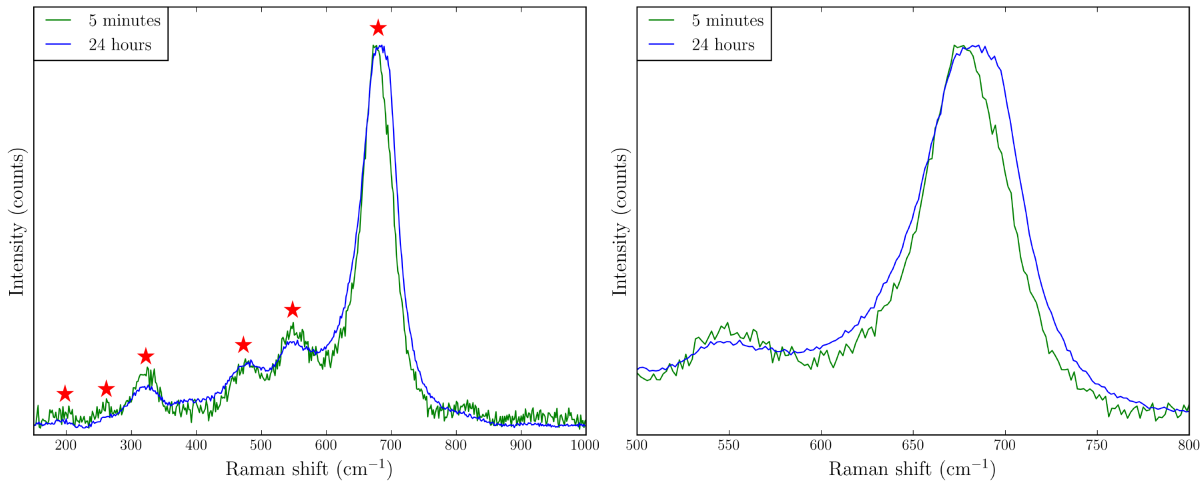

Figure 3.8: *Raman spectra on UNIRR samples oxidised 5 minutes and 24 hours (red stars indicate the detected bands)*

The TEM morphological description of the oxides formed highlighted the presence of a duplex oxide layer (cf. section 3.1.1). As only spinel structure was detected from the GIXRD analysis, both oxide scales should be spinel oxides. Moreover, since the penetration depth is higher than the whole oxide thickness, both oxide scales are supposed to be probed during the acquisition. Spinel oxides possess five active vibrational bands often found close to one another (cf. Appendix B). Thus 10 bands are supposed to be present. However, on each spectrum only 6 bands are easily detected but the spectra cannot be fitted using only six bands with theoritical Gaussian/Lorentzian band shapes as seen in Figure 3.9. The observation of asymmetric bands and the improper quality of fitting obtained with theoritical band shapes indicate the convolution of several bands within one. This confirms that at least two species are present, even after 5 minutes oxidation and that the oxides are likely to have close/similar compositions.

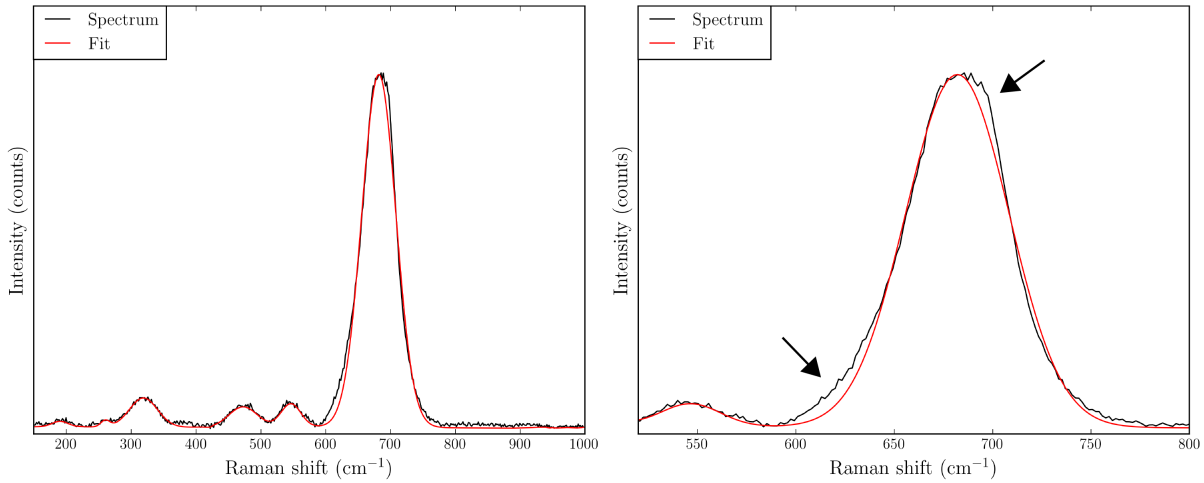

Figure 3.9: *Raman spectrum on an UNIRR sample oxidised 24 hours and the fit realised with six bands (black arrows indicate areas where the fit do not match the spectrum)*

The strongest band was found in both cases (5 minutes and 24 hours oxidations) at $\sim$ 680 cm^{-1} and is wider toward higher wavenumbers after 24 hours oxidation (Figure 3.8). The observation of the broadening of the most intense band on the 24 hours oxidised sample indicates that one of the oxide layers with a different composition grew and induced a shouldering of the band. In all likelihood no additional specie is formed after 24 hours oxidation since no additional band is detected and the only change concerns the most intense band.

Comparing our results with spectra acquired on powder and from the literature data (cf. Appendix B), the oxides formed match with a AB_2O_4 spinel structure. Moreover, it appears that neither hematite (α-Fe_2O_3) nor chromium oxide (Cr_2O_3) are detected on the samples. As these corundum-type compounds were not observed using GIXRD or Raman spectroscopy it can be assumed that neither are present (if there were any, it would be in really small quantity ($\leq$ 1 %)). Only a few authors used Raman spectroscopy to investigate the oxide scales formed on stainless steel alloys exposed to PWR environment [12, 24, 89, 178]. Their spectra (Figure 3.10) are very close to ours presented above. They also concluded, using other techniques, to the presence of duplex oxide layer of spinel oxides.

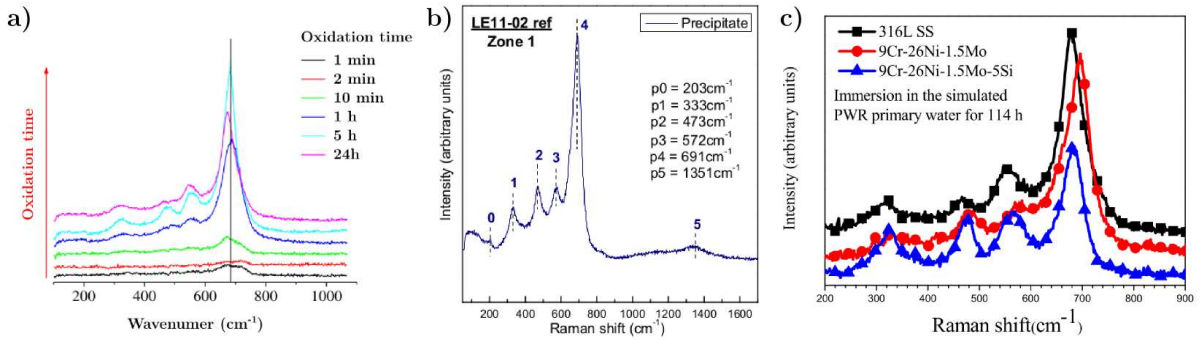

Figure 3.10: *Raman spectra obtained on 316L alloy exposed to PWR media a) between 5 minutes and 24 hours [12], b) 72 hours [178] and c) 144 hours [89]*

3.1.2.4 TEM Dark Field and diffraction study

Figure 3.11 introduces several SAED patterns on the **UNIRR** sample oxidised 24 hours and acquired with the matrix in [001], [101] and [111] zone axis respectively. Due to the small oxide thicknesses compared to the size of the smallest selected area aperture ($\varnothing \approx$ 200 nm) the

diffraction patterns contain information on the metal and both oxide scales. It is thus difficult to perform a complete analysis of the oxide structures independently. Nonetheless, small spots corresponding to diffracted spots from the oxide can be distinguished close to the diffracting spots of the matrix for [001], [101] and [111] zone axis. Whatever, the substrate orientation, the oxide is indexed as spinel phase AB_2O_4 (space group $Fd\bar{3}m$) with a lattice parameter a $\approx$ 8.33 $\pm$ 0.10 Å. No rings suggesting the presence of nanocrystals with an "isotropic" crystallographic orientation distribution were observed on the diffraction patterns (Figure 3.11). In our case we observed isolated spots at specific diffraction angles compared to the matrix indicating the presence of an overall oriented oxide. Since the spinel oxide was each time indexed in the same zone axis as the substrate, it reveals that a cube/cube epitaxial relationship exists between the inner oxide and the underlying metal grain. The presence of an epitaxial relationship between the inner layer and the substrate was already mentioned by several authors [12–14, 66, 171]. Among them, Sennour and Soulas also proposed a cube/cube relationship between the inner layer and the metal substrate [13, 171]. In addition, the blue arrows and associated zooms evidence some elongated diffracting spots corresponding to the oxide. Such diffracting behaviour might come from the presence of strain in the oxide and/or a slight disorientation.

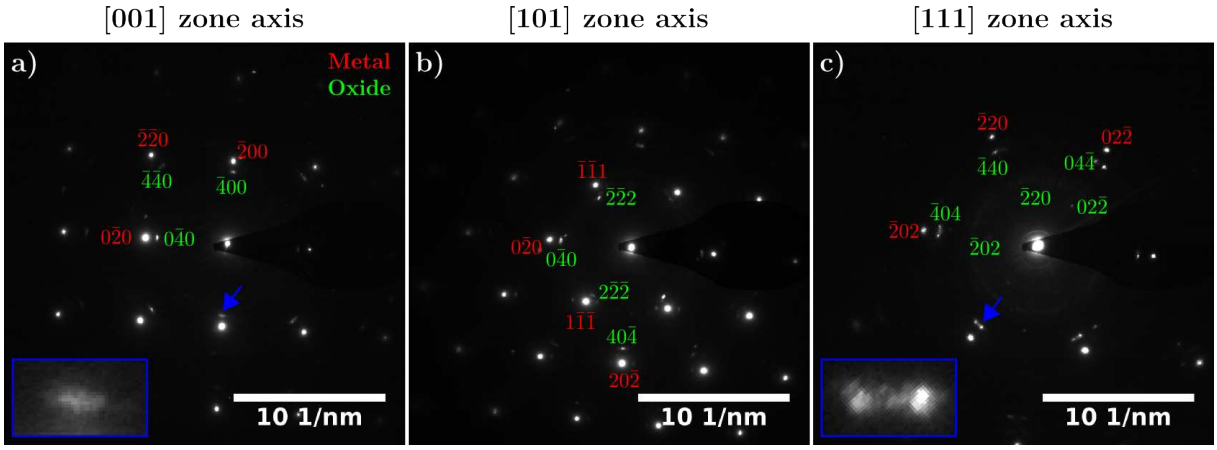

Figure 3.11: *SAED patterns on an UNIRR sample oxidised 24 hours close to a) [100] zone axis b) [110] zone axis and c) [111] zone axis (red: austenite matrix, green: oxide, blue arrow: elongated spots and associated zoom on these spots in the inserts framed in blue)*

To acquire DF images on the oxide, the smallest objective aperture available on the TEM ($\varnothing \approx$ 10 µm) was used and positioned as to take mainly the intensity coming from the diffracting spot corresponding to the oxide and as to avoid the nearby diffracting spot of the matrix. Hence, as imaged in Figure 3.12, the objective aperture was not placed centered on the oxide diffracting spot but slightly shifted. However, such aperture positioning modifies the diffraction conditions and therefore the areas appearing in DF imaging as diffracting. An even smaller objective aperture would allow an easier visualisation of the oxide by selecting smaller areas on the diffraction pattern and thereby less contribution and noise from other diffracting spots (as the ones from the matrix for example). As it can prove difficult/sometimes impossible to reach all three main zone axis using only a double-tilt sample-holder not all the three main zone axis could be investigated in DF imaging. Moreover, when reachable, such images cannot always be interpreted, especially when the tilt angles are too high, as the matrix and oxide layer overlap.

DF imaging performed on [100] zone axis highlights that the main diffracting specie in cube/cube relationship with the substrate is the inner oxide layer (Figure 3.12). However, some areas appear to diffract better (as circled and shown by the arrow in Figure 3.12) indicating that some regions are better oriented with respect to the matrix than others.

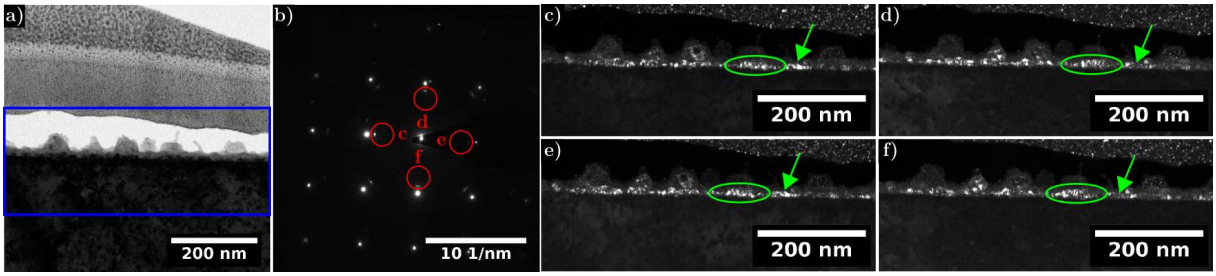

Figure 3.12: *UNIRR sample oxidised 24 hours on a [100] grain orientation in [100] zone axis a) BF image b) SAED pattern (red circle: objective aperture) c) to f) DF on the spots circled in b)*

HRTEM images and associated Fast Fourier Transforms (FFTs) on the inner layer revealed that the inner oxide layer is in the same zone axis as is the matrix ([101] zone axis – Figure 3.13). Therefore, the oxide layer is entirely epitaxially grown. Nevertheless, we observed in the FFTs small rotations (< 10 °) of the structure around [101] zone axis. This indicates that the inner oxide layer is heavily strained. Numerous defects (points defects, dislocations, etc) are believed present and distort the lattice. Hence, the high level of strain in regions of the inner layer will locally slightly disorient it and modify its diffracting conditions explaining why some areas do not appear properly oriented in DF imaging. As for the outer oxide, faceted crystallites are in the same zone axis as the inner layer. Some of these crystallites grew on the inner oxide layer with an epitaxial twin-like relationship (with a $(\bar{1}\bar{1}1)$ twin plane) as evidenced in Figure 3.13 for the crystallites framed in magenta and blue while others grew (as the one framed in cyan) with a cube/cube epitaxial relationship with the inner layer.

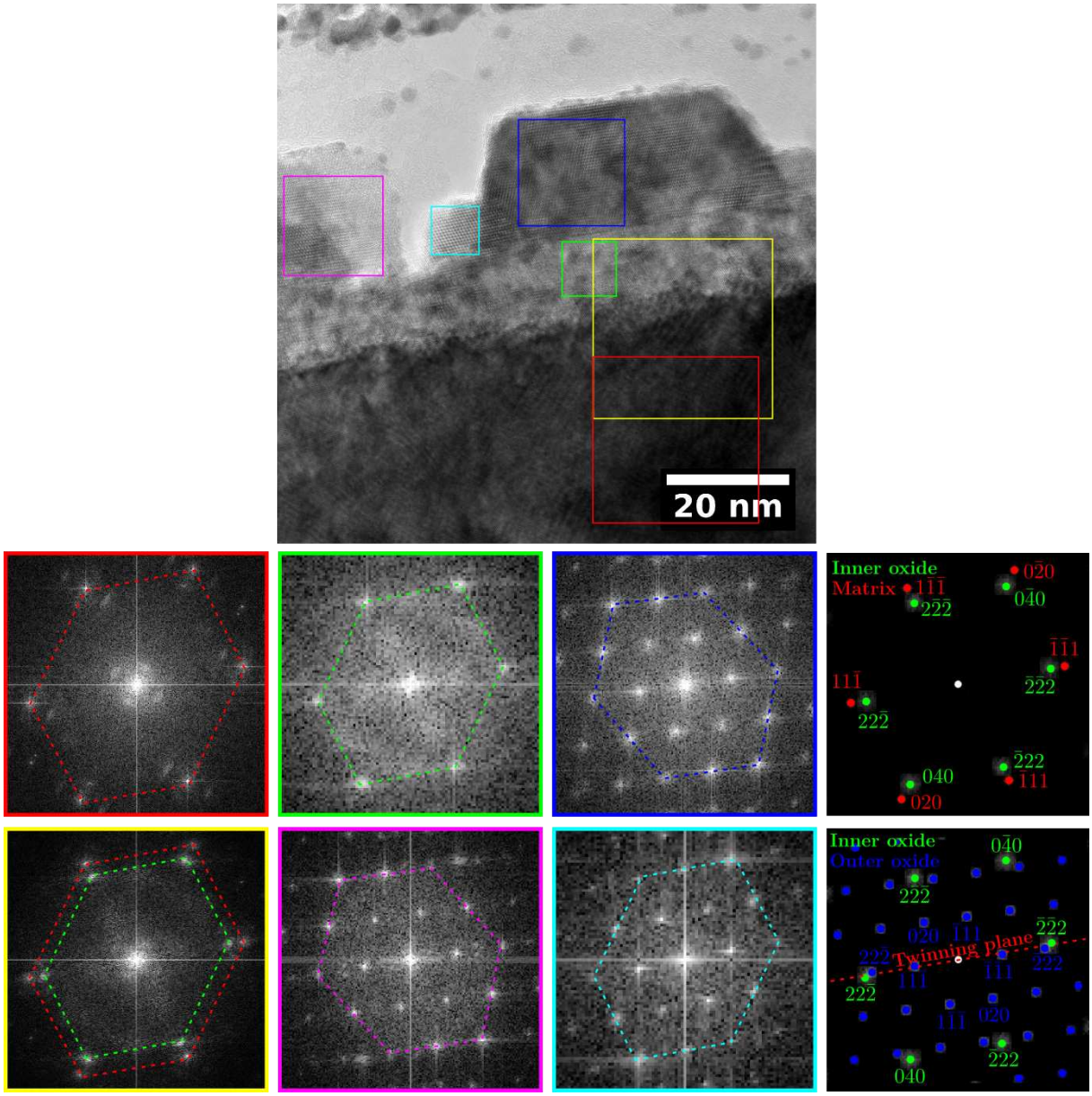

Figure 3.13: *HRTEM image of the metal/inner oxide interface of a [111] grain in [101] zone axis and associated reduced FFTs corresponding to the framed areas*

3.1.2.5 Crystallographic structure: Summary

The structure of the oxide scales was investigated in the previous paragraphs, however, it is difficult, due to the small thickness of the oxide layers to differentiate both oxide scales. Nonetheless two species are present onto the Raman spectra confirming the duplex character of the oxide. Both GIXRD and Raman spectroscopy highlighted the presence of AB_2O_4 spinel oxides. The observation of a favoured crystallite morphology suggested that an epitaxial relationship exist between the some outer crystallites, the inner oxide layer and the substrate. This was confirmed by TEM observation of the oxide structures. The latter analysis revealed that the inner layer is a spinel oxide that share a cube/cube epitaxial orientation relationship with the underlying metal grain. Nevertheless, stresses in the oxide are present resulting in a strained oxide in which small areas are not properly oriented with the matrix. As for the outer crystallites, some of them share an epitaxial twin-like orientation with the inner layer while a few are in cube/cube epitaxy.

Crystallographic structure: Both oxide layers are of spinel structure (AB_2O_4). The inner oxide is a spinel sharing a cube/cube epitaxial orientation relationship with the matrix but is severely strained and hence slightly disoriented. The outer faceted crystallites share a twin-like or a cube/cube epitaxial orientation relationship with the underlying inner oxide.

3.1.3 Chemical analysis of the oxide layers

The following paragraphs introduce results on the chemistry of the oxide layers from a macroscopic scale (Raman spectroscopy) down to nanometric scale (EFTEM, EDXS and EELS analysis).

3.1.3.1 Raman spectroscopy analysis

Comparing the spectra obtained on a specimen oxidised in PWR water and spectra of powder reference spinel oxides it appears that no nickel chromite ($NiCr_2O_4$) is detected on the studied samples (Figure 3.14). However, magnetite (Fe_3O_4), chromite ($FeCr_2O_4$) and nickel ferrite ($NiFe_2O_4$) are potential candidates based on their band positions and relative intensities.

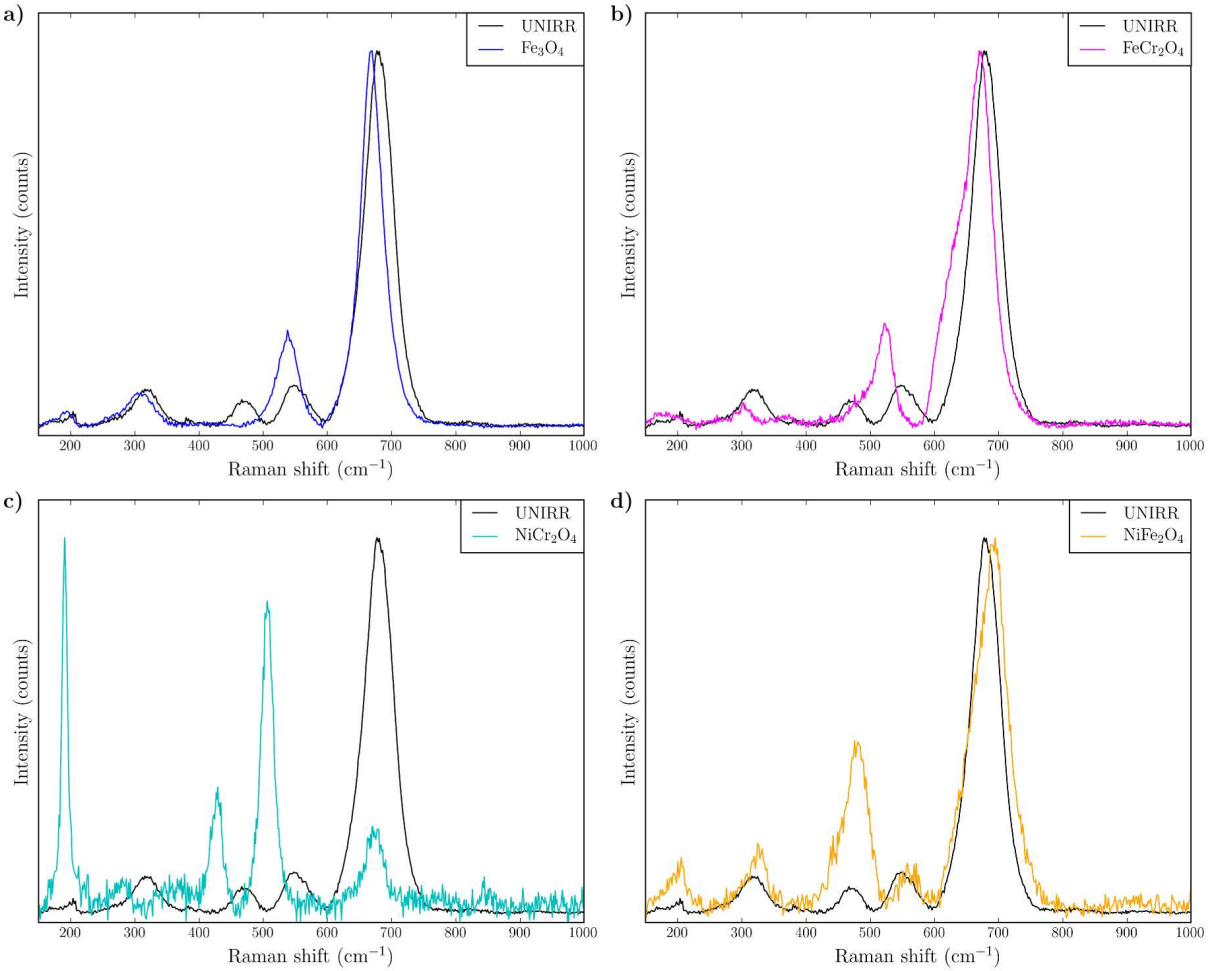

Figure 3.14: *Raman spectrum of an UNIRR sample oxidised in simulated PWR media compared to spectra of a) Fe_3O_4, b) $FeCr_2O_4$, c) $NiCr_2O_4$ and d) $NiFe_2O_4$*

As previously stated two spinel oxides are present and detected onto the samples and more than six asymmetric bands can be detected (Figure 3.15). Due to the close vicinity of the bands resulting from spinel oxide it can prove difficult to assign a position to each one of them.

However, at first sight, neither specie cited above nor a mix of them seem to match perfectly the experimental spectra (Figure 3.15). Therefore, several assumptions can be made. The oxides formed might not be pure oxides spinels but rather mixed solid solution spinel oxides and stresses and defects (observed in section 3.1.2.4) are present within the oxides. Such deviation from "perfect" oxides influenced the band positions in the spectra and induced shifts thus explaining that no compound perfectly matches the oxide formed. Hence, the oxide layers are likely to be $(Fe^{2+}_{1-x}Fe^{3+}_{2-y}M^{2+}_{x}M^{3+}_{y})O^{-2}_{4}$ with M^{2+}: Fe^{2+} or Ni^{2+} and M^{3+}: Fe^{3+} or Cr^{3+}.

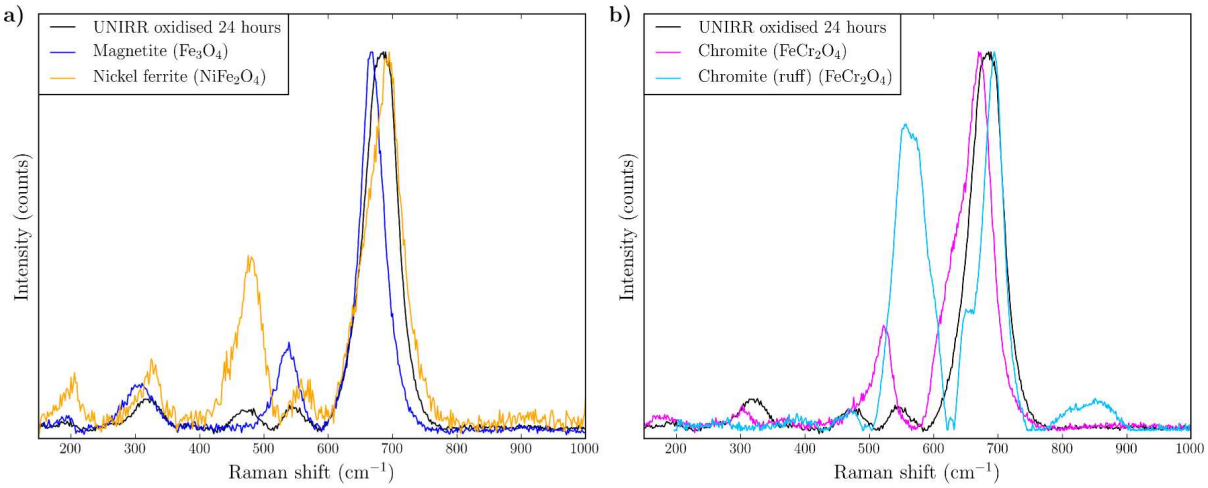

Figure 3.15: *Raman spectrum on an UNIRR sample oxidised 24 hours compared to Raman spectra of a) magnetite (Fe_3O_4) and nickel ferrite ($NiFe_2O_4$) and b) chromite ($FeCr_2O_4$) (analysed power and chromite from [182])*

The most intense band located near 680 cm^{-1} can be assigned to the A_{1g} mode of spinel oxides. At least two bands compose this band as previously demonstrated in section 3.1.2.3 (Figure 3.9). One of them is believed to be coming from the outer oxide (spinel oxide close to magnetite) and the other from the inner layer mixed spinel oxide. Numerous authors observed that the A_{1g} mode of magnetite is located at lower wavenumber than that of chromite and nickel ferrite [175, 183–185] (see Appendix B for details). They also reported a shouldering of the A_{1g} band of chromite and nickel ferrite that can further complicate the analysis of the A_{1g} band. It can be assumed that one band is located between 665 and 675 cm^{-1} and correspond to the outer oxide while a second one and its potential shouldering are located between 675 and 710 cm^{-1} and before 660 cm^{-1} and correspond to the inner layer.

3.1.3.2 EFTEM mapping

EFTEM qualitative mapping was performed on a the **UNIRR** specimens oxidised 1 hour and 24 hours. Both imagings revealed the same oxide scales, thus only the 24 hours oxidised sample is presented in Figure 3.16 as the oxide are thicker and hence more easily discernable. Both the outer and inner layers are highlighted on the oxygen map. The inner layer is chromium-rich while the crystallites are enriched in iron. Therefore, the inner layer is more likely to have a composition close to chromite than nickel ferrite (as proposed from the Raman spectra analysis). Moreover, an enrichment in nickel is visible from the nickel map at the metal/oxide interface as indicated by the red arrow and is 5 – 7 ± 2 nm thick. All of this is in agreement with previous analyses of oxides scales formed on stainless steels exposed to PWR media [5, 7, 12, 24, 26, 27, 30, 32].

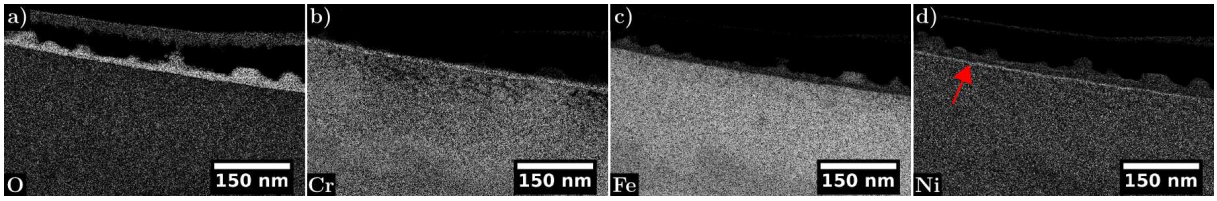

Figure 3.16: *EFTEM maps on an UNIRR sample oxidised 24 hours a) oxygen map b) chromium map c) iron map and d) nickel map (red arrow indicates the Ni-enriched area at the metal/oxide interface)*

3.1.3.3 EELS and EDXS quantitative analyses

Following EFTEM qualitative analysis on the **UNIRR** samples, quantitative measurements of the chemical composition of the oxides was carried out using EDXS and EELS. Linescans acquired on the 24 hours oxidised sample are presented in Figure 3.17. EELS and EDXS analyses gave slightly different oxide compositions[1] and are reported in Table 3.2. As presented in Appendix C, two different EELS quantifications were performed. The first one took into account the oxygen content while the second one did not and allowed to obtain metallic species ratios. The latter was also used to compare to EDXS quantifications performed without oxygen as its Kα x-ray line overlaps the Cr-Lα one. Titanium was observed in the oxide scales in low concentration ($<$ 4 at. %) but each time a higher content is detected in the outer layer. Moreover, less and less titanium was detected when going into the inner layer toward the metal. Titanium is believed to come from the oxidation loop which is made of titanium. Small amount of titanium would be dissolved into the medium and be incorporated into the oxide by a re-precipitation phenomenon. As seen previously, the outer layer is iron-rich but titanium, chromium and nickel are detected. As for the inner layer, it is, independently of the oxidation time, a nickel, iron and chromium mixed spinel oxide. However, chromium content in the inner oxide is lower than that of iron after 1 hour oxidation ($\frac{Cr}{Fe}_{1h} \leq 1$) while it is higher after 24 hours oxidation ($\frac{Cr}{Fe}_{24h} > 1$). As proposed by Soulas the inner layer is gradually enriched in chromium as the oxidation duration increases before reaching its equilibrium composition [12]. He reported a $\frac{Cr}{Fe}$ ratio of 1 constant between 10 minutes and 24 hours oxidation while our results indicate that chemical equilibrium is not reached yet after 1 hour oxidation as the chromium:iron ratio in higher after 24 hours than after 1 hour oxidation. After 1 hour oxidation the ratios obtained in this work are in good agreement with Soulas results for oxidation in between 2 minutes and 1 hour. Moreover, $\frac{Cr}{Fe}$ ratios were above 1 after 24 hours oxidation revealing that the inner oxide layer is not an $Fe_{1.5}Cr_{1.5}O_4$ oxide as suggested by Soulas [12] but keep being enriched in chromium.

After 24 hours oxidation, both profiles indicated a nickel enrichment on $\sim 4-5$ nm coupled with a chromium depletion at the metal/oxide interface, as already highlighted in numerous studies [12, 26–29]. This nickel-rich area reached $\sim$ 17 at. % nickel content from EELS analysis against $\sim$ 30 at. % from EDXS analysis[2]. As it appears from the profiles and associated STEM image, the metal/oxide interface was not perfectly planar. Hence, oxide is still detected in this area explaining for instance oxygen detection in this region in EELS analysis and lowering the amount nickel of nickel detected. Moreover, a thin amorphous layer present on the foil would also increase the amount of oxygen detected.

[1] Measured contents were rounded to provide whole numbers

[2] One should note that nickel was always better detected in the EDXS analyses than in the EELS ones since its edge is not very sharp and the signal is lost in the background when the nickel content is not high enough. It relates to EELS sensitivity being lower at higher energy losses while its Kα line is well detected and quantified in EDXS analysis.

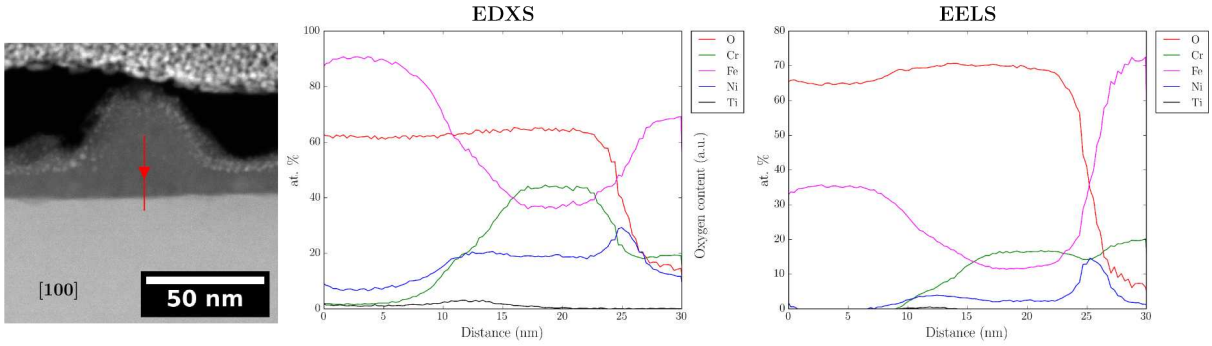

Figure 3.17: *STEM image and associated quantitative EDXS and EELS linescans on a UNRIRR sample oxidised 24 hours on a [100] grain orientation*

Table 3.2: *EDXS and EELS quantitative analyses of the oxides formed on [100] grain orientation on the UNIRR samples oxidised 1 hour and 24 hours*

Analysed region	Oxidation time	Method	O (at. %)	Cr (at. %)	Fe (at. %)	Ni (at. %)	Ti % (at. %)
Outer oxide	1h	EELS	66	0	29	5	-
		EELS	-	3	82	12	-
		EDXS	-	4	81	14	1
	24h	EELS	65	0	33	1	< 1
		EELS	-	4	88	5	3
		EDXS	-	1	91	7	1
Inner oxide	1h	EELS	63	15	16	6	-
		EELS	-	38	48	14	-
		EDXS	-	30	55	15	-
	24h	EELS	71	14	12	3	0
		EELS	-	50	36	14	-
		EDXS	-	44	37	19	0
Ni-rich area	24h	EELS	30	14	39	17	0
		EELS	-	20	55	25	-
		EDXS	-	25	45	30	0

As both oxides are spinel oxides, their compositions can be written according to AB_2O_4. A stoichiometric spinel oxide consists of 57.1 at. % oxygen and 42.9 at. % metal. However, EELS results always overestimated the oxygen content of the oxides compared to stoichiometric spinels (cf. Table 3.2). It could be due to a thin amorphous layer present onto the FIB lamella but, in addition, the oxide formed are, in all likelihood, not stoichiometric. Therefore, to write the oxides according to AB_2O_4, the EELS and EDXS analyses without oxygen content were used and the Cr+Fe+Ni+Ti sum was set equal to 3 (Table 3.3). The spinel iron-rich outer oxide can be written: $(Ni,Cr,Ti)_{3-x}Fe_xO_4$ with $3 \geq x \geq 2.5$ according to the quantification results. Many authors concluded that the inner layer is a close to be a chromite oxide ($FeCr_2O_4$) [5, 7, 12, 26, 27, 30]. For a stoichiometric chromite, the Cr:Fe ratio should be 2, however, our results suggest a ratio closer to $\sim 1.2 - 1.4$ after 24 hours oxidation. Thus it seems that nickel ions occupy some of the Fe^{3+} sites and some iron ions occupy some of the Cr^{3+} sites. The spinel can hence be written as $(Ni_xFe_{1-x})(Cr_yFe_{1-y})_2O_4$ with $1 \geq x \geq 0$ and $1 \geq y \geq 0$. From the quantitative analyses carried out, the inner oxide layer composition can be narrowed down to: $(Ni_xFe_{1-x})(Cr_yFe_{1-y})_2O_4$ with $0.6 \geq x \geq 0.4$ and $0.8 \geq y \geq 0.65$. These results are in agreement with the previously made assumption from Raman spectroscopy (cf. section 3.1.3.1) that the oxides are rather solid solution oxides.

Table 3.3: *EDXS and EELS analyses of the oxides formed on [100] grain orientation on the UNIRR samples oxidised 1 hour and 24 hours*

Oxide	Oxidation time	Method	AB_2O_4
Outer	1h	EELS	$Ni_{0.4}Fe_{2.5}(Cr,Ti)_{0.1}O_4$
	24h	EELS	$Ni_{0.2}Fe_{2.5}(Cr,Ti)_{0.3}O_4$
		EDXS	$Ni_{0.2}Fe_{2.7}(Cr,Ti)_{0.1}O_4$
Inner	1h	EELS	$Cr_{1.3}Fe_{1.3}Ni_{0.6}O_4$
	24h	EELS	$Cr_{1.5}Fe_{1.1}Ni_{0.4}O_4$
		EDXS	$Cr_{1.3}Fe_{1.1}Ni_{0.6}O_4$

3.1.3.4 Chemical analysis: Summary

The oxides scales formed on 316L alloy oxidised in primary water investigated in this study are in good agreement with the literature data. EFTEM mapping revealed that the outer oxide layer is iron-rich while the inner oxide is chromium rich and therefore combined to Raman spectroscopy analysis that the outer crystallites are close to magnetite and the inner oxide is close to chromite. The outer and inner oxide layers composition were defined by the chemical quantitative analyses. The outer layer can be written $((Ni,Cr,Ti)_{3-x}Fe_xO_4$ with $3 \geq x \geq 2.5$ while the inner oxide can be written as $(Ni_xFe_{1-x})(Cr_yFe_{1-y})_2O_4$ with $0.6 \geq x \geq 0.4$ and $0.8 \geq y \geq 0.65$. In addition, EELS analyses evidenced that the inner layer is progressively enriched in chromium as the oxidation goes by. Titanium was found incorporated primarily in the outer oxide in low concentration. Titanium from the oxidation loop could be dissolved into the medium and re-precipitate into the outer oxide. The EFTEM mapping highlighted the presence of nickel at the metal/oxide interface and the presence this nickel-rich region was corroborated by EELS and EDXS analyses. These analyses confirmed that mixed solid solution spinel oxides are formed on the 316L alloy exposed to simulated primary water. Moreover, it appears that the oxides stoichiometry is not respected and that defects and stresses are present in the oxides.

Chemical analysis: The oxides formed are non-stoichiometric. Crystallites are found to be close to magnetite with a small amount of nickel, chromium and titanium ($(Ni,Cr,Ti)_{3-x}Fe_xO_4$ with $3 \geq x \geq 2.5$). The inner layer is a solid solution oxide containing iron, chromium and nickel $(Ni_xFe_{1-x})(Cr_yFe_{1-y})_2O_4$ with $0.6 \geq x \geq 0.4$ and $0.8 \geq y \geq 0.65$. This oxide layer is gradually enriched in chromium. A nickel enrichment is present at the metal/oxide interface.

3.1.4 Grain boundaries oxidation

The extraction of lamellae across two grains allowed the investigation of grain boundaries oxidation. These oxidation sites are especially of interest since SCC is likely to occur at grain boundaries if the material is not too cold-worked. Therefore, the grain boundary oxidation was looked upon and the intergranular oxides formed were compared to the ones formed on the samples surface. Such characterisation was made on **UNIRR** specimens oxidised 1 hour and 24 hours. The following paragraph focus on the morphological description and chemical analysis of the grain boundaries oxidation using SEM images and TEM analysis.

3.1.4.1 Morphological description

SEM imaging evidences that some grain boundaries are preferentially oxidised as it can be seen in Figure 3.18 with the appearance of bigger crystallites close to the grain boundary. It suggests that some grain boundaries acted as diffusion short-cuts, enhancing diffusion to form these bigger crystallites of magnetite.

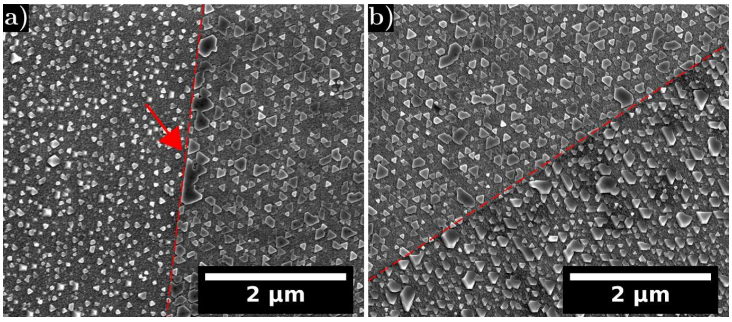

Figure 3.18: *SEM SE images (5 kV) of oxidised grain boundaries (REF sample oxidised 24 hours) with a) enhanced crystallites growth on the grain boundary and b) no enhanced grain boundary oxidation*

The oxide penetration is found 42 ± 2 nm deep and relatively narrow after 24 hours oxidation while it is solely of 21 ± 2 nm after 1 hour oxidation (Figure 3.19). As on the oxide formed on the surface, no porosities were seen. However, TEM imaging each time revealed that the oxide penetration is asymmetric as shown by the magenta dashed lines in Figure 3.19. The oxide penetration is more pronounced on one side of the grain boundary. This preferential oxidation and the formation of facets should relate to the grain boundary plane orientation and its affinity to be oxidised.

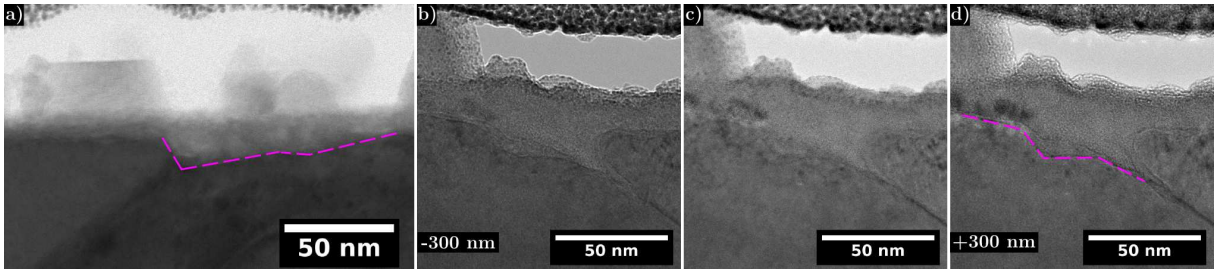

Figure 3.19: *TEM images on the oxidised grain boundary on UNIRR samples a) STEM BF image on the sample oxidised 1 hour and TEM BF images on the sample oxidised 24 hours b) under-focus c) focus d) over-focus*

After having set edge-on the grain boundary, three distinct regions can be distinguished in the oxide penetration of the **UNIRR** sample oxidised 24 hours. Interestingly, STEM HAADF contrasts evidence a brighter region below the intergranular oxide penetration (circled in blue in Figure 3.20) which is ∼ 30 nm long. This area (1) appears to have a different composition from the matrix and should be richer in an heavier element. Above this area a slightly darker region (2) can be seen as shown by the green arrow. This area contain lighter elements and is likely to be oxidised. The third one (3) (shown by the red arrow) is a straight area aligned on the former grain boundary that look even darker than region (2). As no porosities were evidenced and thus no density difference, this ∼ 27 ± 3 nm deep region should contain more lighter elements than the previous one and is thought to be even more oxidised. No evidence of grain boundary migration was observed but a further analysis at a finer scale would be needed to confirm that point.

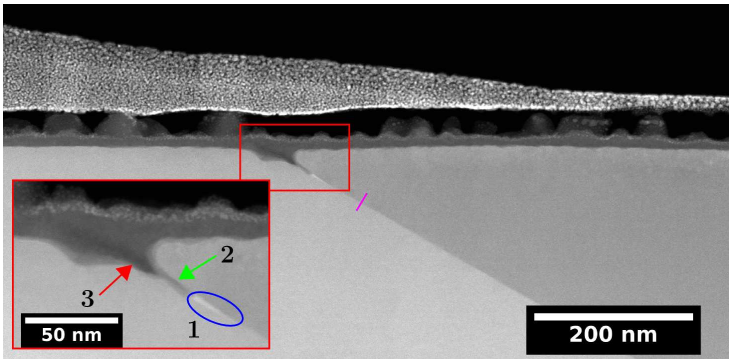

Figure 3.20: *STEM HAADF image on the oxidised grain boundary on a UNIRR sample oxidised 24 hours*

3.1.4.2 Chemical analysis

First of, EDXS and EELS linescans were acquired across this grain boundary (profile line shown in magenta in Figure 3.20) below the oxide penetration (Figure 3.21). These profiles highlight a slight iron depletion and chromium enrichment.

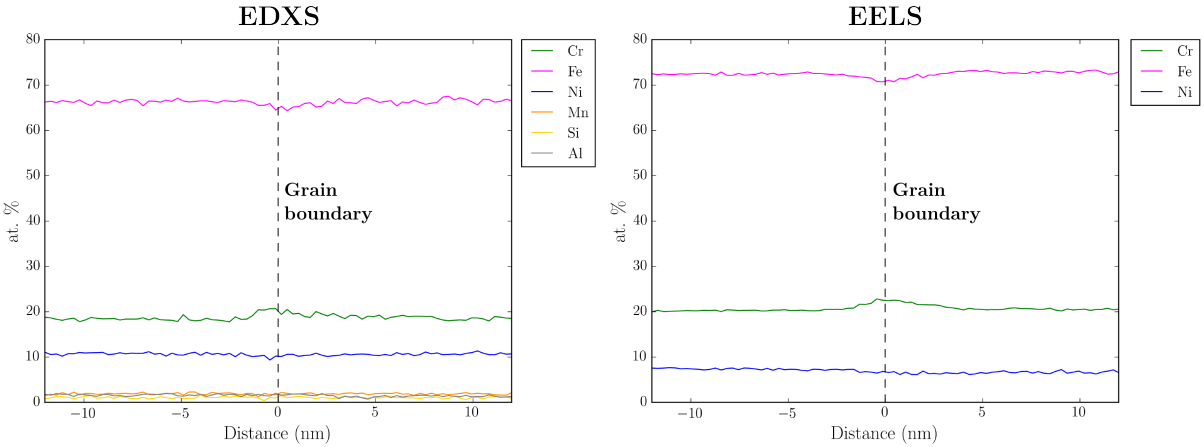

Figure 3.21: *EDXS and EELS quantitative linescans across the grain boundary on an UNIRR sample oxidised 24 hours*

EFTEM mapping was made on the same grain boundary. The oxygen map evidences the oxide penetration. The intergranular oxide seems to be even richer in chromium and is likely to correspond to the previously imaged dark area (3) aligned with the former grain boundary. An iron and chromium depletion is visible below this oxide penetration coupled with nickel enrichment that corresponds to the whitest area (1) observed previously.

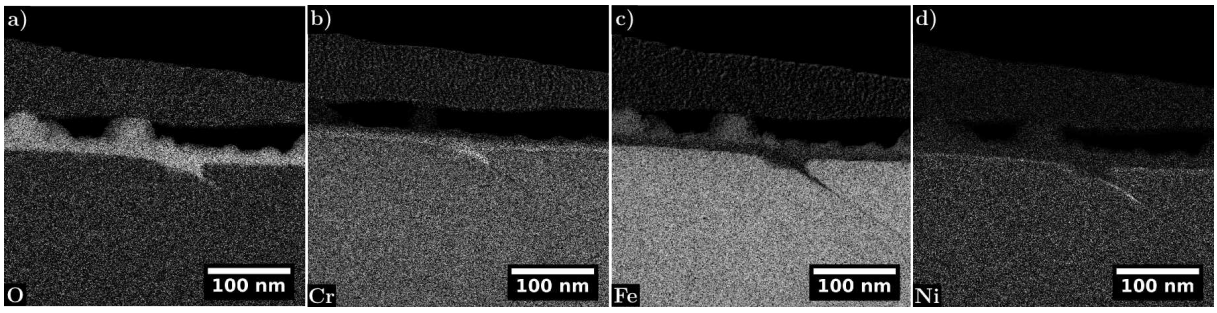

Figure 3.22: *EFTEM maps on the oxidised grain boundary on a UNIRR sample oxidised 24 hours*

EDXS and EELS analyses were carried out on this oxide penetration (Figure 3.23) to gain

information on its composition[3]. The chemical composition of the nickel-rich area (1) that appear the whitest in STEM images was investigated. As highlighted by EFTEM mapping, this region is a clustering of unoxidised Ni coupled with a Fe/Cr depletion. This area is $\sim$ 30 nm deep while $\sim$ 3 nm thick. The nickel enrichment is close to 40 at. % in this area (Figure 3.24). Ni enrichment below oxidised grain boundaries and crack tips was already observed by a few authors [9, 26, 31, 186]. Above this area, a slightly oxidised area (2) nickel-rich is present (Figure 3.23). This region must result from the oxidation of this nickel-rich area. Moreover, since this oxidised region is located in the foil depth it suggests that the oxidation front is not perpendicular to the foil surface. Hence, as signal comes from the alloy under and over this penetration, chemical quantifications were not performed as they would be improper. A chromium rich oxide is formed in the oxide penetration (3) (Figure 3.23) and the chromium content reaches up to $\sim$ 30 at. % (Table 3.4). The $\frac{Cr}{Cr+Fe+Ni}$ ratio is $\geq$ 0.7 in this region. EELS quantitative analysis was also performed on an oxidised grain boundary of the **UNIRR** 1 hour oxidised sample. It also highlighted that the intergranular oxide formed is richer in chromium than that formed at the sample surface ($\frac{Cr}{Cr+Fe+Ni} \sim 0.65$). Hence, the oxide at grain boundary is, in all likelihood, of corundum structure and can be written as $Cr_x(Fe,Ni)_{2-x}O_3$ with $2 \geq x \geq 1.3$. No such structure was previously detected in the GIXRD and Raman spectroscopy analyses of the oxide layer structures. Nevertheless, the presence of such small areas containing Cr_2O_3 like oxides would not provide, in all likelihood, sufficient signal to be detected. A nickel enrichment border the oxide penetration similarly to the one observed previously at the metal/oxide interface.

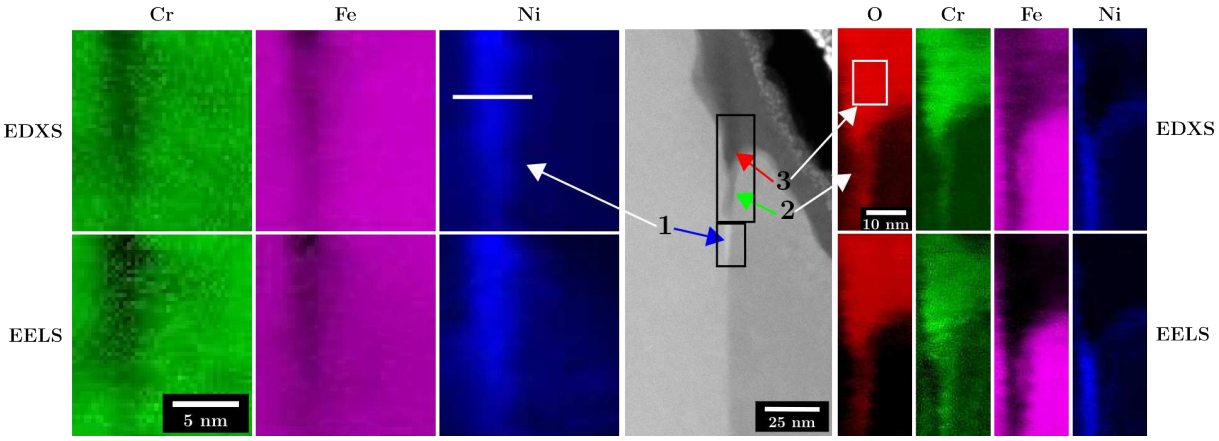

Figure 3.23: *EDXS and EELS quantitative maps of the unoxidised area (1) and grain boundary oxidation (2 and 3) on an UNIRR sample oxidised 24 hours*

[3]The tortuous appearance of the grain boundary oxidation is caused by the drift that occurred during the acquisition that lasted several hours.

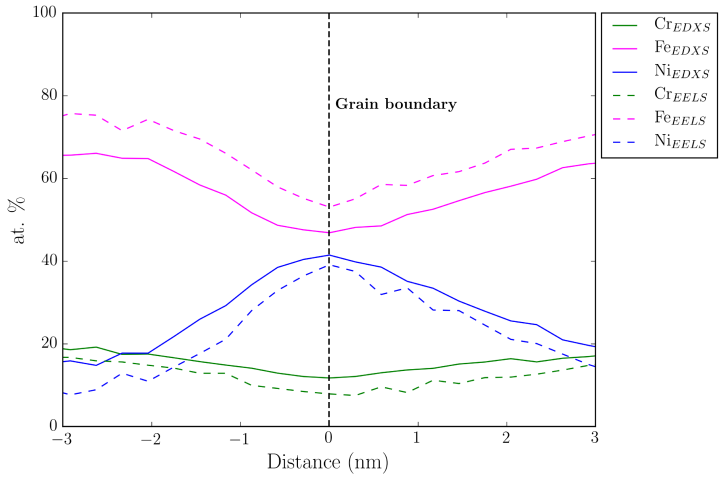

Figure 3.24: *EDXS and EELS quantitative linescans of the unoxidised area (1) below the grain boundary oxidation (profile along the white line shown in the previous maps) on an UNIRR sample oxidised 24 hours*

Table 3.4: *EDXS and EELS quantitative analyses of the grain boundary oxidation on an UNIRR sample oxidised 24 hours in the area framed in white (3) in the previous maps*

Method	O (at. %)	Cr (at. %)	Fe (at. %)	Ni (at. %)
EELS	69	29	2	0
EELS	-	77	22	1
EDXS	-	71	23	6

3.1.4.3 Grain boundaries oxidation: Summary

Some grain boundary appeared preferentially oxidised since big outer crystallites were observed on top of grain boundaries hence revealing that some preferentially act as diffusion shortcuts. Moreover, TEM images highlighted that the oxide penetration is asymmetric and faceted without porosities. The EDXS and EELS linescans showed that below this intergranular oxide chromium is slightly enriched and iron depleted. A nickel-rich area was detected below the oxidised grain boundary and the measured Ni concentration was as high as $\sim$ 40 at.%. Above this region, the slightly oxidised area at the tip of the oxide penetration was found enriched in nickel and is believed to result from the oxidation of this nickel-rich area. Nickel enrichment was also found pushed sideways at the oxide flanks (metal/oxide interface) as it was observed previously for surface oxidation. The oxide formed in the oxide penetration is chromium rich and the $\frac{Cr}{Cr+Fe+Ni}$ ratio is higher than 0.65. This oxide can be written $Cr_x(Fe,Ni)_{2-x}O_3$ with $2 \geq x \geq 1.3$. Comparing this oxide to the one formed on the surface, the presence of an oxide richer in chromium but depleted in iron was highlighted.

Study of the grain boundaries oxidation: The grain boundary oxide penetration is asymmetric and faceted and the oxide formed is richer in chromium than the one formed on the sample surface. This oxide is believed to be of corundum structure ($Cr_x(Fe,Ni)_{2-x}O_3$ with $2 \geq x \geq 1.3$). The tip of the oxide penetration was found nickel-rich and a clustering of unoxidised nickel was highlighted below this oxide penetration.

3.1.5 Oxides formed on 316L exposed to simulated PWR medium: Synthesis, discussion and oxidation mechanism

This section aims to summarise the results on the oxide scales formed on a 316L austenitic stainless steel alloy exposed to primary water environment for short oxidation durations. Below are reported the main results from the above sections. These results will be compared to the

literature data and a proposed oxidation mechanism of a 316L alloy in PWR media is discussed. The overall oxidation mechanism proposed is presented in Figure 3.25.

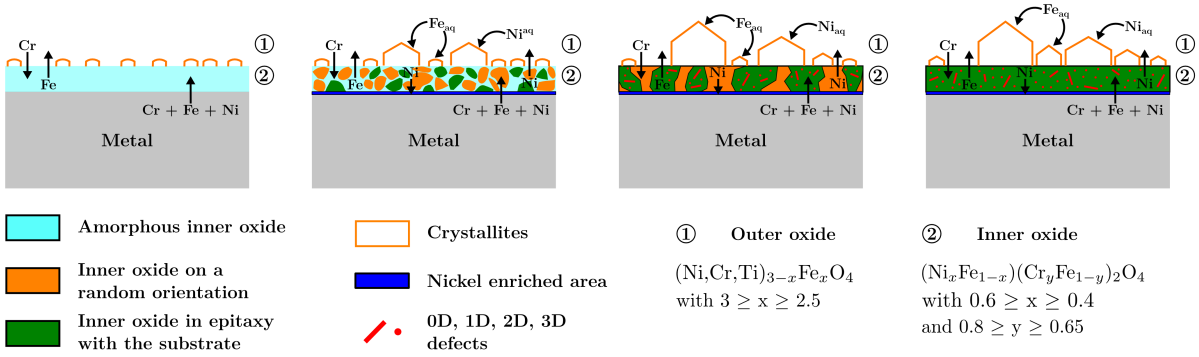

Figure 3.25: *Schematic of the oxidation mechanism of a 316L austenitic stainless steel exposed to PWR medium during short time oxidation and as the oxidation duration increases*

A duplex oxide layer is formed even after 5 minutes oxidation and, at the earlier oxidation stages, crystallites are globular without any specific shape. The observation of a duplex oxide layer is in accordance with numerous author's observations on stainless steels alloy exposed to primary water [12, 13, 26–29, 32]. Numerous small and globular germs are formed on top of the samples at the early stages of oxidation ($<$ 24 hours) and fewer crystallites are present after 1 hour oxidation than after 5 minutes but these are bigger. They are believed to dissolve into the medium before re-precipitating. This is consistent with Lister's oxidation model [21], however oxidations were not performed in saturated media. Nonetheless, metallic species released into the media will saturate a close boundary layer before re-precipitating. The outer oxide grows as the oxidation time increases and after 24 hours oxidation a favoured crystallite morphology appears and these crystallites mesh with small germs ($<$ 20 nm). The inner oxide thicknesses measured varied between $\sim$ 5 and 10 nm which is in accordance with Soulas' results who reported inner layers $\sim$ 3 to 15 nm thick between 5 minutes and 24 hours oxidation [12].

Both the oxide layers are found to be spinel oxides (AB_2O_4). The observation of such structure is in agreement with the results of several authors who also observed a spinel oxide structure on stainless steel alloys using diffraction [25, 26, 69, 175–180]. Contrary to the finding of a few authors [20, 24, 33], no corundum structure of Cr_2O_3 type oxide was present, at least in a sufficient amount, to be evidenced on top of the studied samples. At short oxidation times ($<$ 24 hours) the oxide is likely to present both amorphous and crystalline regions as shown by Soulas [12, 13]. An epitaxial orientation relationship is established after 24 hours oxidation between the outer oxide, the inner oxide and the 316L substrate and is responsible for the observation of a favoured outer oxide morphology. The inner oxide share a cube/cube epitaxial orientation relationship with the matrix and crystallites are epitaxially grown onto the inner layer with a twin-like or a cube/cube epitaxial orientation relationship. However, not the whole inner oxide layer is properly epitaxially grown and some areas were slightly disoriented due to stress and strain in the oxide. This oxide layer can be assimilated to an oxide exhibiting an epitaxial relationship with the underlying metal grain but strongly stressed and strained in which numerous defects are present. Therefore this oxide layer is not polycrystalline as reported by many authors [5, 6, 26, 27, 87–89] but closer to monocrystalline as suggested by Soulas [12, 13]. The presence of such a relationship was already mentioned by several authors [12–14, 66]. Among them, Soulas also proposed a cube/cube relationship between the inner layer and the metal substrate [13]. When a thin layer is epitaxially grown onto a substrate, a lattice parameter mismatch between the film and the substrate usually exists. Thus the interface can be strained or relaxed depending upon the magnitude of the difference between the two lattice parameters.

Dislocations are likely to compensate, at least partially, this misfit as proposed by Soulas [12, 13].

Regarding the oxide layer composition, chemical analyses revealed the presence of titanium primarily in the outer oxide in really low concentration. It is believed to come from the oxidation loop made of titanium. Small amount of titanium will dissolve into the medium and be incorporated into the oxide by a re-precipitation phenomenon. The oxide layer investigation revealed a discontinuous outer layer composed of iron-rich crystallites of spinel structure close to magnetite ($(Ni,Cr,Ti)_{3-x}Fe_xO_4$ with $3 \geq x \geq 2.5$) and a dense inner oxide layer. The inner oxide is found to be a mixed solid solution spinel of iron, nickel and chromium ($(Ni_xFe_{1-x})(Cr_yFe_{1-y})_2O_4$ with $0.6 \geq x \geq 0.4$ and $0.8 \geq y \geq 0.65$). However, the chromium content into the inner layer is gradually increasing as the oxidation goes by as already observed for such short oxidation times by Soulas [12]. Both these oxide compositions are in accordance with the literature data [5, 7, 12, 24, 26, 27, 30, 32]. Since the diffusion rates of metal ions in the oxides are found to be sorted by the following order: $Fe^{2+} > Ni^{2+} > Cr^{3+}$ [61], faster diffusing species such as Fe will primarily diffuse to form the outer layer, while slower diffusing ones as Cr will remain in the inner layer. A clear nickel enrichment of $\sim$ 4–5 nm associated with a chromium depletion was highlighted at the metal/oxide interface. Therefore, the Ni enrichment highlighted by numerous studies at the metal/oxide interface was confirmed in this study [12, 26–29]. No nickel depletion was detected in the substrate underneath this region, which suggests that the Ni was rejected from the oxide toward the metal during its formation and growth. This area will, in all likelihood, have a slightly different lattice parameter than the substrate and could generate stress at the metal/oxide interface. However, due to its small thickness it would prove difficult to estimate the change in lattice parameter. As Fe and Cr possess a higher affinity to oxygen than Ni, the rate of incorporation of the latter element in the oxide scale will be smaller than that of Fe and Cr. Ni would be expected and is concentrated at the metal/oxide interface since it is rejected from the inner layer. It is plausible that nickel close to the surface would go into the medium and then re-precipitates as part of the outer oxide while the one close to the metal/oxide interface would accumulate at this interface and a small amount would still remain incorporated into the oxide.

The investigation of the oxide layers formed on the 316L alloy exposed to PWR media revealed that these are not "pure" spinel oxides but rather mixed oxides of spinel structure that are stressed and strained. The inner layer is believed to contain a significant number of ionic defects [47–51]. Their presence offers routes for ionic species to be transported through the oxide allowing the dissolution of the metal and the overall oxidation process. It can be generally stated that the more defects the oxide contains and the higher their mobility, the more susceptible the underlying alloy is to corrosion. Thereby, the presence of stresses, strains and defects in the inner oxide layer will, in all likelihood, induce a decrease of its protectiveness as the oxide growth is dependent on the amount of defects within the oxide scale. In this oxide layer, generation, transport, and consumption of ionic point defects, (interstitial cations, and both cation and anion vacancies) occur. The growth of the inner layer proceeds into the alloy by ingress oxygen transport via oxygen vacancies [5, 27, 47–51]. In addition, diffusion through this inner oxide layer limits the rates of both outer oxide growth and corrosion release. Indeed, the outer layer is supposed to grow by a dissolution/re-precipitation mechanism involving the transport of interstitial cations through the inner oxide as the rate-limiting step [21, 47–51]. After the outward cationic diffusion of metal ions through the inner layer they then dissolve into the medium. The medium will then locally saturate and a precipitation phenomenon occurs leading to the crystallites growth onto the alloy surface and the formation of the outer crystallites. Therefore, the growth of the outer oxide crystallites is dependent on the outward cationic diffusion through inner layer. This diffusion will be affected by the amount of stress and defect present within the layer and thereby by the more or less protective/barrier character of the inner oxide layer. The extent of oxide

precipitation is governed by the solubilities of Fe and Ni in high-temperature water. Hence, it can be assumed that the precipitation reaction is close to local equilibrium, enabling the growth of the large crystallites observed.

As for the grain boundary oxidation, the overall oxidation process proposed is depicted in Figure 3.26. Some grain boundaries are preferentially oxidised and big outer crystallites are formed on top of them. It is likely that grain boundaries, acting as diffusion short-cuts, accelerated diffusion to the surface, promoting the formation of outer crystallites on top of the grain boundaries. Intergranular oxides were asymmetric and faceted but did not contain porosities. The grain boundary oxidation is thought to unfold in two stages. First, a protective surface oxide will be formed on the surface of the grain boundary. In a second step, the grain boundary acting as a diffusion short-cut will be oxidised preferentially but also on both sides. Moreover, this intergranular oxide is richer in chromium than the one formed at the sample surface and likely to be of corundum structure. Its composition is close to $Cr_x(Fe,Ni)_{2-x}O_3$ with $2 \geq x \geq 1.3$. Cr_2O_3 is supposed to be the most stable oxide formed on Ni-Cr-Fe alloys [171]. As a slender iron depletion coupled with chromium enrichment below the oxide penetration was highlighted, it suggests that iron is diffusing along the grain boundary and then through the inner oxide layer to the surface inducing an iron depleted area near the grain boundary. The grain boundary acting as a diffusion short-cut would pump iron from the metal faster and provide a depleted iron area. As oxygen affinity for Cr is larger than that for Fe, chromium would be oxidised more readily by reacting with inward diffused oxygen inducing the formation of the observed chromium-rich oxide. Thus, the formation of a corundum-type $(Cr,Fe,Ni)_2O_3$ inner oxide at grain boundaries on the 316L alloy (with the total Cr concentration about 30 at.%) can be related to the low iron content near the grain boundary.

Additionally, a highly Ni-enriched region (up to $\sim$ 40 at. %) was found ahead of the grain boundary oxide as reported by a few authors primarily below crack tips [9, 26, 31, 186]. Since grain boundaries are a fast diffusion path, nickel seems to be preferentially pushed away along them. This nickel enrichment could slow down and delay further oxygen diffusion along the grain boundaries. Nickel was also found pushed sideways at the oxide flanks as observed previously for surface oxidation. Ni enrichment near the oxide/metal interface or ahead of the intergranular oxide may be related to its lower oxidation rate compared with Fe and Cr during the formation of the oxide film. The selective oxidation of chromium and potentially iron yielded the formation of a nickel enriched area at the inner oxide/metal interface and below the grain boundary oxide penetration.

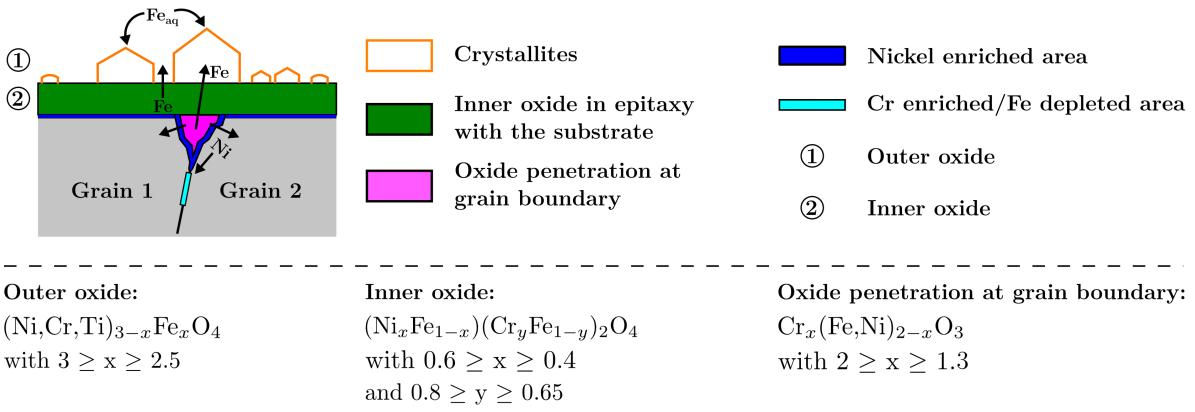

Figure 3.26: *Schematic of the grain boundary oxidation mechanism of a 316L austenitic stainless steel exposed to PWR medium*

To conclude, the results obtained for the **REF** and **UNIRR** samples are in agreement with most of the studies conducted on stainless steel alloys exposed to high temperature aqueous media [20–22, 25] or PWR media [5, 7, 12, 24, 26–30, 32]. All of the results mentioned above lead to several conclusions introduced below.

Synthesis on the oxides formed on 316L exposed to simulated PWR medium:

- The oxide scale formed is duplex even after 5 minutes oxidation with outer crystallites and a dense inner oxide layer. As the oxidation time increases both oxide layer grow. The inner oxide layer is strongly strained and contains numerous defects. The presence of these stresses, strains and defects will lower its protectiveness.
- Both oxides possess a AB_2O_4 spinel structure and the inner oxide layer share a cube/cube epitaxial orientation relationship with the underlying metal grain. A crystallographic orientation relationship between the metal, the inner layer and outer crystallites exist and is responsible for the favoured outer oxide morphology observed after 24 hours oxidation.
- The crystallites are found to be close to magnetite and contain nickel ($(Ni,Cr,Ti,Fe)_3O_4$) while the inner layer is a mixed spinel oxide containing iron, chromium and nickel ($(Fe,Ni)(Fe,Cr)_2O_4$) and this layer is progressively enriched in chromium. Moreover, the oxides were not found stoichiometric and hence point defects will compensate the stoichiometric deviance and will promote oxidation.
- A nickel enrichment is present at the metal/oxide interface due to its rejection from the inner oxide. The region is thought to have a slightly different lattice parameter and thereby will induces stresses at the metal/oxide interface.
- The intergranular oxide is asymmetric, faceted and richer in chromium than the one formed at the surface. It is of corundum structure and can be written $(Fe,Ni,Cr)_2O_3$. The fast pumping of iron at the grain boundaries results in an iron depleted area and lead to the formation of a chromium-rich oxide. As grain boundaries are a fast diffusion path, nickel is preferentially pushed along them inducing a clustering of unoxidised nickel below the intergranular oxide.

3.2 Crystallographic orientation effect on the oxide scales

This section focus on the influence on the crystallographic orientation of the underlying metal grain on the oxidation (kinetic, chemistry, etc.). To do so, EBSD maps acquired before oxidation were used to choose the appropriate grain orientation of interest. This study aims to investigate on the oxides formed on top of [100], [110] and [111] grain orientations. This section focuses once again on the investigation of Titane **REF** and **UNIRR** samples oxidised between 5 minutes and 72 hours.

3.2.1 Morphological description of the oxide depending on the underlying grain orientation

The following paragraphs focus on the morphological description of the oxide layers depending on the underlying grain orientation. These oxides will be looked upon using optical microscopy, SEM and TEM as in section 3.1.1.

3.2.1.1 Optical microscopy study

Optical images were used to analyse at a macroscopic scale the effect of the crystallographic orientation of the metal on the oxidation process. No clear contrast can be seen between adjacent grain after 5 minutes oxidation (Figure 3.27 a). However, from 1 hour oxidation some slight changes in the contrasts can be seen and these are for the 24 hours and 72 hours oxidised samples. The observed contrasts vary depending on the underlying metal grain orientation indicating that the crystallographic orientation of the underlying metal grain affect the oxidation. Hence, there is certainly a difference in morphology, size or density of crystallites between these orientations.

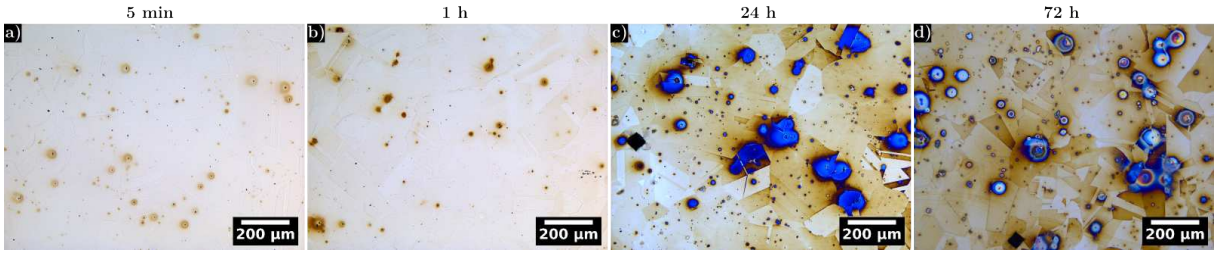

Figure 3.27: *Optical images on REF samples oxidised a) 5 minutes b) 1 hour c) 24 hours and d) 72 hours*

After oxidation, [111] grain orientation look the whiter while [100] orientation is the darkest of the three studied orientations (Figure 3.28). As [100] and [111] orientations presented the most obvious contrasts, TEM lamellae were extracted on these orientations and their analysis is presented in paragraphs 3.2.1.3 and 3.2.2.2. Therefore, the oxidation kinetic seem contingent upon the underlying metal grain orientation.

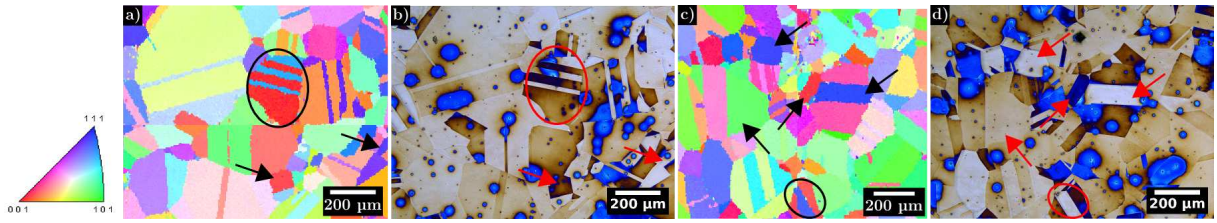

Figure 3.28: *b) and d) Optical images on an UNIRR sample oxidised 24 hours and a) and c) associated EBSD maps*

3.2.1.2 Description of the oxides using SEM

SEM images were acquired on **REF** specimens oxidised between 5 minutes and 72 hours (Figure 3.29) and each image contained at least one grain boundary in the frame. Before 24 hours oxidation, no crystallographic orientation effect can be seen between two adjacent grains on the outer oxide morphology, size and/or density. However, after 24 hours oxidation clear differences can be seen between the outer oxide morphologies depending on the underlying metal grain orientation.

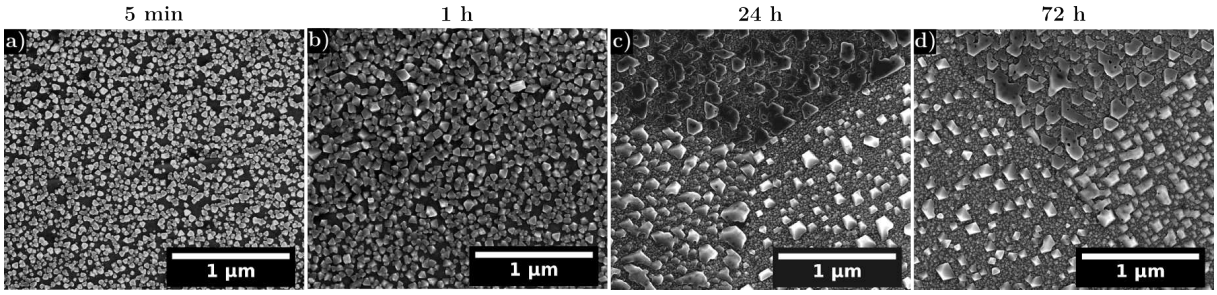

Figure 3.29: *SEM SE images (5 kV) on grain boundaries on REF samples oxidised a) 5 minutes b) 1 hour c) 24 hours and d) 72 hours*

Images acquired on a **REF** sample oxidised 24 hours on specific grain orientations ([100], [110] and [111]) are presented in Figure 3.30. On each grain orientation, big-faceted crystallites cohabit with small germs. Depending on the underlying crystallographic metal grain orientation the outer oxide morphology vary. On [100] grain orientation most of the biggest crystallites are squared base pyramid while reflecting prisms are observed on [110] orientation and flat triangles are formed on [111] grain orientation. Therefore, a distinct favoured outer oxide morphology is observed depending upon the underlying grain orientation. It hints toward the existence of a crystallographic orientation relationship between the outer crystallites, the inner oxide layer and the underlying metal grain as assumed previously in section 3.1.5. This relationship is likely to be hinging on the underlying grain orientation. Soulas and Matthews et al., for example, studied 316L alloys exposed to PWR media for up to 24 hours and 1000 hours respectively [12–14]. Both authors observed differences in the size and density of crystallites depending on the crystallographic orientation but did not evidence the existence of an epitaxial relationship between the outer layer and the inner layer/substrate. Moreover, to the author's knowledge, the description of these favoured crystallite morphologies (as presented above) depending upon the underlying grain orientation was never reported. The crystallite sizes, however, do not differ on the three studied orientations (Table 3.5). Regarding the bigger faceted crystallites, the measurements indicate that a smaller number of them are formed on the [100] orientation ($\sim$ 25 $\pm$ 3 crystallite/µm^2) compared to [110] ($\sim$ 32 $\pm$ 3 crystallite/µm^2) and [111] ($\sim$ 46 $\pm$ 5 crystallite/µm^2) orientations. Most of the crystallites formed on top of [111] grain orientation possess the favoured crystallite morphology, even the small germs, while it is not the case for [100] orientation. This suggests that a higher number of nucleation sites for the faceted crystallites are available on [111] grain orientation.

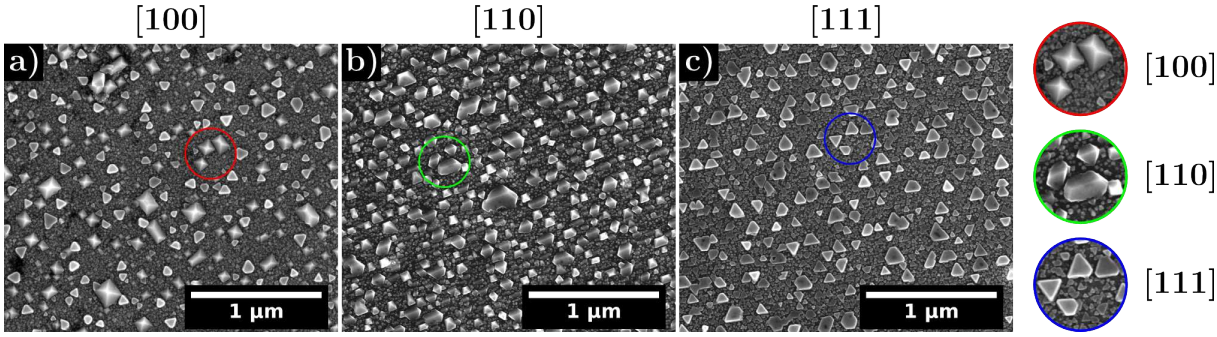

Figure 3.30: *SEM SE images (5 kV) on a REF sample oxidised 24 hours on a a) [100] grain orientation b) [110] grain orientation and c) [111] grain orientation*

Table 3.5: *Quantitative analysis of the crystallite distribution on a REF sample oxidised 24 hours on [100], [110] and [111] grain orientations (the number of crystallites per µm² and the mean crystallite sizes are given for the big-faceted crystallites)*

Grain orientation	[100]	[110]	[111]
mean size ± standard deviation (nm)	71 ± 35	72 ± 40	69 ± 35
min – max size (nm)	9 – 167	12 – 288	14 – 176
crystallite/µm²	25 ± 9	32 ± 7	46 ± 3
coverage (%)	68 ± 5	67 ± 5	73 ± 5

LayerProbe analysis (cf. Chapter 2 section 2.1.4.3) was carried out on the **UNIRR** sample oxidised 24 hours (Figure 3.31). These results can only be looked at in a qualitative way since the outer oxide layer is not planar. Nonetheless, the measured oxide thickness varies from one grain orientation to another. It confirms, once again, that the underlying metal grain orientation modifies the oxidation kinetic. Moreover, a trend can be distinguished as the oxide formed on top of orientations close to [111] are often found thinner than on orientations close to [100].

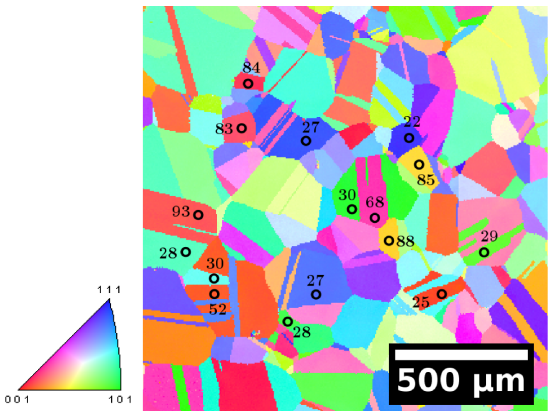

[100]	[110]	[111]
84	30	30
83	28	27
93	29	22
52	28	27
68		
25		

Figure 3.31: *EBSD map and LayerProbe measurements of the oxide thickness (in nm) on the UNIRR sample oxidised 24 hours*

3.2.1.3 TEM study of the inner oxides thickness

After 1 hour oxidation, no clear variation was seen between the inner oxide thicknesses depending on the underlying grain orientations as both oxides were thin (≤ 5 nm). However, after 24 hours oxidation, STEM HAADF images acquired on both [100] and [111] grain orientations (Figure 3.32) revealed an inner oxide thickness difference between the two studied grain orientations. The inner oxide thicknesses on both orientation vary from 10 ± 2 nm on [100] to 7 ± 2 nm on [111]. The inner oxide is thicker on [100] orientation than on [111] grain orientation. This corroborates the previous LayerProbe results. The inner oxide layer thickness is then contingent on the crystallographic orientation of the underlying metal grain. Such behaviour was already observed by Soulas and Matthiew [12–14]. However, these results are not in accordance with Soulas who observed thicker oxides on [111] grain orientation after short oxidation times [12]. Matthews et al, observed thick oxides on orientation close to [100] after 1000 hours oxidation at 320 °C but concluded that the oxidation kinetic as a function of the underlying metal grain was greatly influenced by the oxidation temperature [14]. Therefore, depending on the crystallographic orientation of the underlying metal grain the oxidation kinetic is modified.

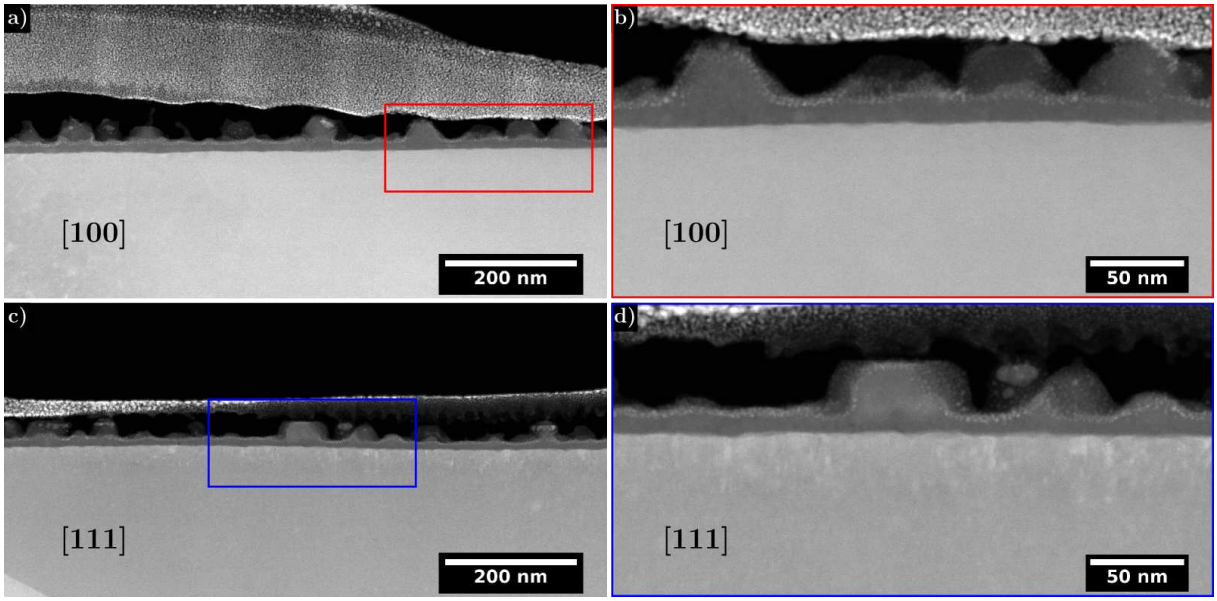

Figure 3.32: *STEM HAADF images on an UNIRR sample oxidised 24 hours on a) and b) a [100] grain orientation, c) and d) a [111] grain orientation*

TEM BF images did not evidence porosities big enough to be imaged within the inner layer (Figure 3.33).

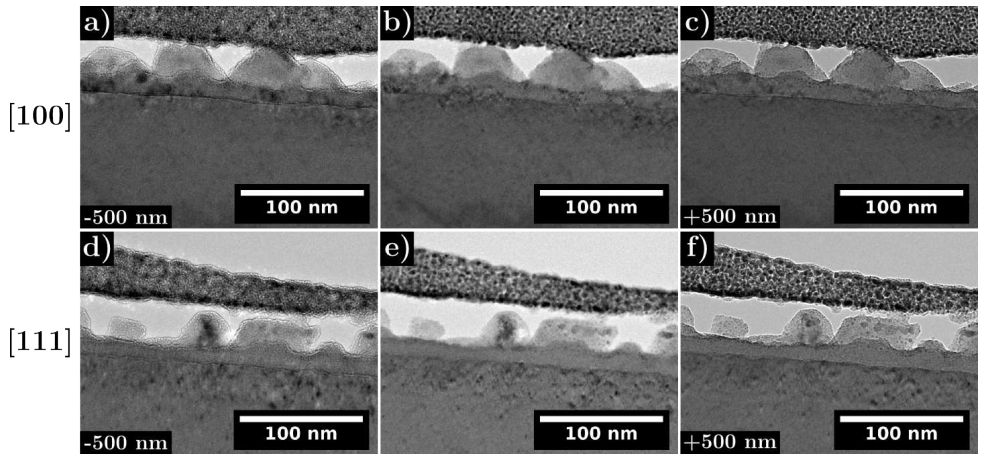

Figure 3.33: *TEM BF images on an UNIRR sample oxidised 24 hours on a), b) and c) a [100] grain orientation respectively under-focus, focus and over-focus and c), d) and e) a [111] grain orientation respectively under-focus, focus and over-focus*

3.2.1.4 Morphological description: Summary

No effect of the crystallographic orientation can be seen before 24 hours oxidation. However, after 24 hours oxidation, some grains are more oxidised than others from the optical images. Moreover, favoured crystallites morphologies are observed and their shapes depend upon the underlying metal grain orientation. This hints toward the existence of an epitaxial relationship between the oxide layer and the substrate. The number of established crystallites is contingent upon the underlying metal grain and more nucleation sites are available on [111] grain orientation for the favoured crystallites. LayerProbe analysis revealed that the overall oxide thickness is hinging on the underlying metal grain crystallographic orientation and further TEM analysis highlighted and confirmed that the inner oxides are thicker on top of [100] grains than on [111] ones.

Morphological description: After 24 hours a clear effect of the crystallographic orientation of the underlying metal grain can be observed. Faceted crystallites with a favoured morphology are formed and the crystallite shape depends upon the crystallographic orientation. Moreover, more nucleation sites are present for the formation of these favoured crystallites on [111] grain orientation. The crystallographic orientation affect the inner oxide thickness. Oxides are thicker on [100] grain orientation than on [111] grain orientation.

3.2.2 Chemical analysis of the oxide layers depending on the underlying grain orientation

The chemistry of the oxide layers contingent on the underlying grain orientation was investigated using Raman spectroscopy and quantified by EELS and EDXS analyses.

3.2.2.1 Raman spectroscopy analysis

The Raman spectra obtained on [100], [110] and [111] grain orientations on the **UNIRR** sample oxidised 24 hours are presented in Figure 3.34. As previously explained, the band located at ~ 680 cm^{-1} can be decomposed in two distinct A_{1g} bands. Comparing the three orientations it appears that there is a slight shift and/or a broadening in the A_{1g} band corresponding to the inner oxide toward the higher wavenumber according to [111]>[110]>[100][4]. This band is wider on the [100] orientation and more symmetrical. This could arise from different inner oxide composition, the presence of strains or various oxide thicknesses. The inner layer might be richer in chromium or nickel or thicker on the [100] grain orientation. An inner oxide richer in chromium/nickel would induce a shift in the band toward the higher wavenumber, while an inner oxide thicker would increase the ratio A_{1g} (Inner oxide):A_{1g} (Outer oxide). If different oxide thicknesses are responsible for the observed band shift/broadening it would solely come from the inner oxide. Indeed, the morphological description did not highlight differences in the outer layer sizes while the inner layer thickness was found to differ depending upon the underlying metal grain. Since both oxides are probed, more signal will come from the inner oxide with respect to the outer one on grains on which thicker inner oxides are formed. This appears to be the case, indeed, slightly thicker inner oxides are formed on [100] grain orientation. Moreover, on the [100] orientation the ratio of the contribution inner oxide:outer oxide for the A_{1g} band is close to 1 while it is below 1 on the [111] orientation. On the [111] orientation the band is clearly asymmetric and the contribution of the outer oxide prevails on the one from the inner oxide. Raman spectroscopy analysis therefore confirm that the inner oxide is thicker on [100] grain orientation and thinner on [111] grain orientation. In a nutshell, the main shift/broadening observed of the A_{1g} band in the Raman spectra is believed to be induced by differences of inner oxide thicknesses. However, strains and chemical differences in the oxides might also induce slight shifts of the bands but their close vicinity do not allow to better interpret these differences.

[4]The term "shift" will further on refers to movement of the center-of-mass of the combined bands.

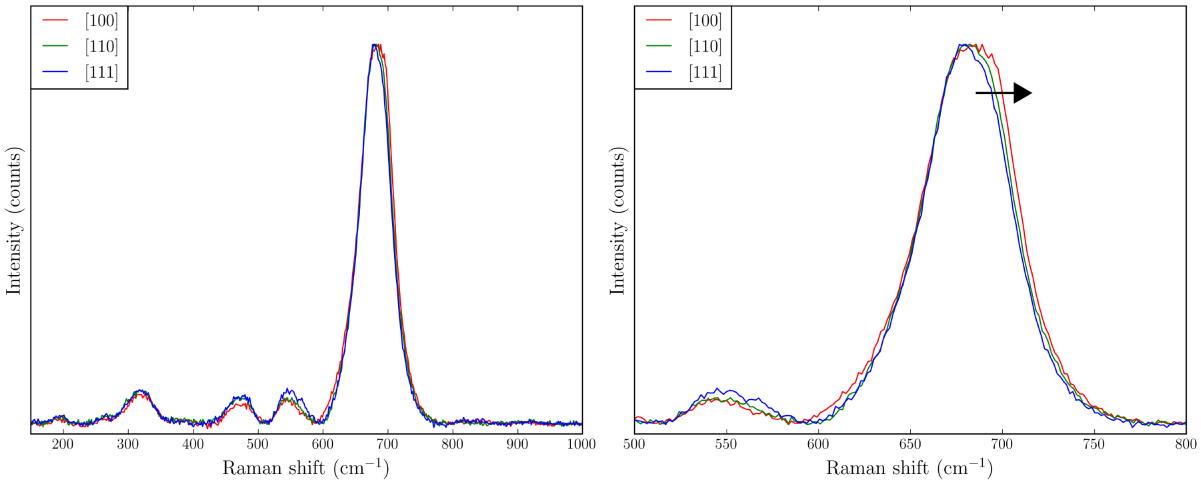

Figure 3.34: *Raman spectra on the UNIRR sample oxidised 24 hours depending on the crystallographic orientation of the underlying metal grain*

3.2.2.2 EDXS and EELS quantitative analyses

As EFTEM mapping did not indicate any noticeable change in the oxides, further quantitative analyses were carried out. Due to the small thickness of the inner oxide layers after 1 hour oxidation and the potential overlapping of the oxide with the substrate, EELS analysis performed did not evidence clear chemical differences between the oxide scales. However, after 24 hours oxidation, EDXS and EELS quantitative linescans acquired on the oxide formed on [100] and [111] grain orientations (Figure 3.35) on the **UNIRR** specimen oxidised 24 hours highlight chemical variation depending upon the underlying metal grain. The quantitative analysis of the outer and inner oxide layer are presented in Table 3.6 while Table 3.7 reports the AB_2O_4 notations for each oxide with respects to the technique employed. Both outer oxides were found to be iron oxides having a close composition and containing nickel as well as traces of chromium and titanium. Similarly, inner oxides are, on both crystallographic orientation, solid solution spinel iron, chromium, nickel oxides. However, the inner layer is found slightly richer in chromium on the [111] orientation as evidenced from the cf. $\frac{Cr}{Cr+Fe+Ni+Ti}$ ratios in Table 3.7. This suggests that chromium diffusion is faster on [111] grain orientation leading to the formation of inner oxide richer in chromium. Both profiles indicate a nickel enrichment at the metal/oxide interface but this enrichment was always higher on the [111] orientation (EELS analysis: $\sim$ 17 at. % on [100] against $\sim$ 21 at. % on [111] and EDXS analysis: $\sim$ 30 at. % on [100] against $\sim$ 33 at. % on [111]).

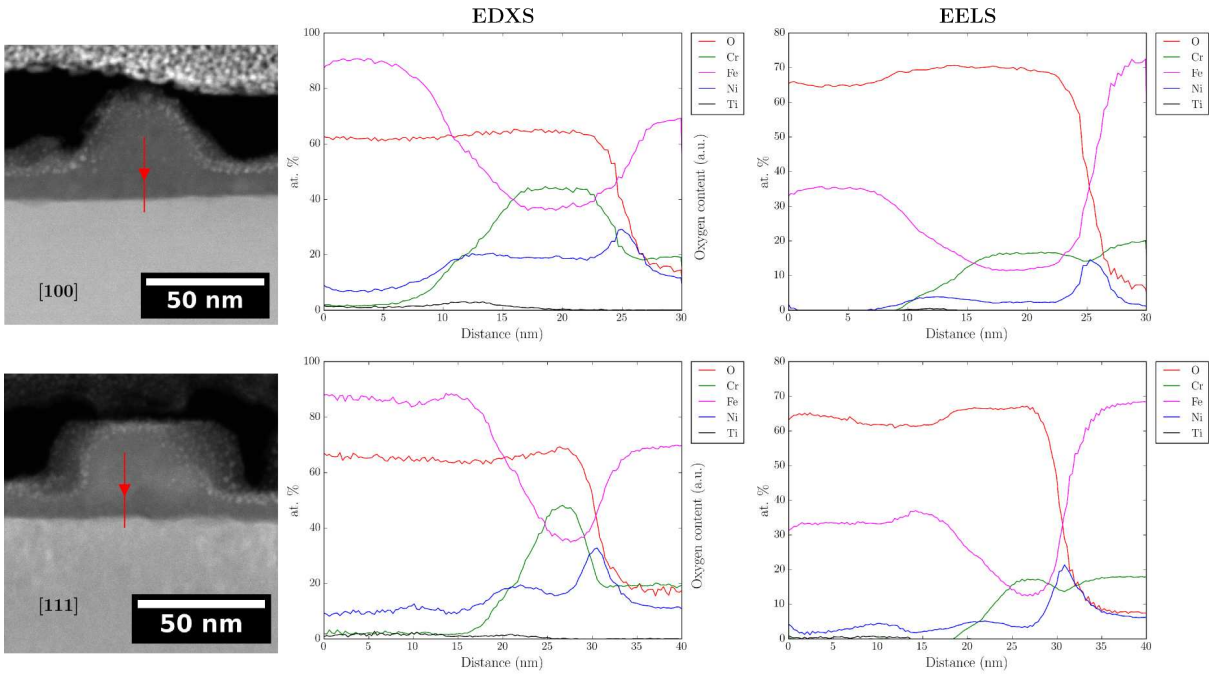

Figure 3.35: *STEM image and associated quantitative EDXS and EELS linescans on a sample oxidised 24 hours on both a [100] and [111] grain orientations*

Table 3.6: *EDXS and EELS quantitative analyses of the inner oxides formed on [100] and [111] grain orientations on the UNIRR sample oxidised 24 hours*

Analysed region	Grain orientation	Method	O (at. %)	Cr (at. %)	Fe (at. %)	Ni (at. %)	Ti % (at. %)
Outer oxide	[100]	EELS	65	0	33	1	< 1
		EELS	-	7	84	6	3
		EDXS	-	1	91	7	1
	[111]	EELS	62	0	33	4	< 1
		EELS	-	4	88	5	3
		EDXS	-	2	87	10	1
Inner oxide	[100]	EELS	71	14	12	3	0
		EELS	-	50	36	14	-
		EDXS	-	44	37	19	0
	[111]	EELS	67	17	12	4	0
		EELS	-	53	34	13	-
		EDXS	-	47	37	16	0
Ni-rich area	[100]	EELS	30	14	39	17	0
		EELS	-	20	55	25	-
		EDXS	-	25	45	30	0
	[111]	EELS	29	14	36	21	0
		EELS	-	25	46	29	-
		EDXS	-	21	46	33	0

Table 3.7: *EDXS and EELS analyses of the oxides formed on [100] and [111] grain orientations on the UNIRR sample oxidised 24 hours*

Analysed region	Grain orientation	Method	$\frac{Cr}{Cr+Fe+Ni+Ti}$	AB_2O_4
Outer oxide	[100]	EELS	< 0.1	$Ni_{0.2}Fe_{2.5}(Cr,Ti)_{0.3}O_4$
		EDXS	< 0.1	$Ni_{0.2}Fe_{2.7}(Cr,Ti)_{0.1}O_4$
	[111]	EELS	< 0.1	$Ni_{0.2}Fe_{2.6}(Cr,Ti)_{0.2}O_4$
		EDXS	< 0.1	$Ni_{0.3}Fe_{2.6}(Cr,Ti)_{0.1}O_4$
Inner oxide	[100]	EELS	0.50	$Cr_{1.5}Fe_{1.1}Ni_{0.4}O_4$
		EDXS	0.44	$Cr_{1.3}Fe_{1.1}Ni_{0.6}O_4$
	[111]	EELS	0.53	$Cr_{1.6}Fe_{1.0}Ni_{0.4}O_4$
		EDXS	0.47	$Cr_{1.4}Fe_{1.1}Ni_{0.5}O_4$

3.2.2.3 Chemical analysis: Summary

The Raman spectra acquired on different grain orientations highlighted slight modifications between the three studied orientations. These are believed to be related to the inner oxide thicknesses. Both outer oxides have close composition and did not seem dependent upon the underlying metal grain orientation. However, on [111] grain orientation, the inner layer is richer in chromium and a higher nickel enrichment is present at the metal/oxide interface.

Chemical analysis: Variations in the oxides chemistry can be seen between the three studied orientations and confirm that the oxide formed on [100] grain orientation is thicker. On [111] grain orientation the inner oxide is richer in chromium. In addition, on this same orientation, the underlying Ni-enrichment is higher.

3.2.3 Crystallographic orientation: Synthesis, discussion and oxidation mechanism

This section aims to summarise the effect of the crystallographic orientation of the underlying metal grain onto the oxide scales formed on a 316L austenitic stainless steel alloy exposed to primary water environment. Below are reported the main results from the above sections. These results will be discussed and compared to similar work carried out by Soulas [12]. Moreover, the proposed oxidation mechanism of a 316L alloy in PWR media depending on the crystallographic orientation presented in Figure 3.36 is discussed.

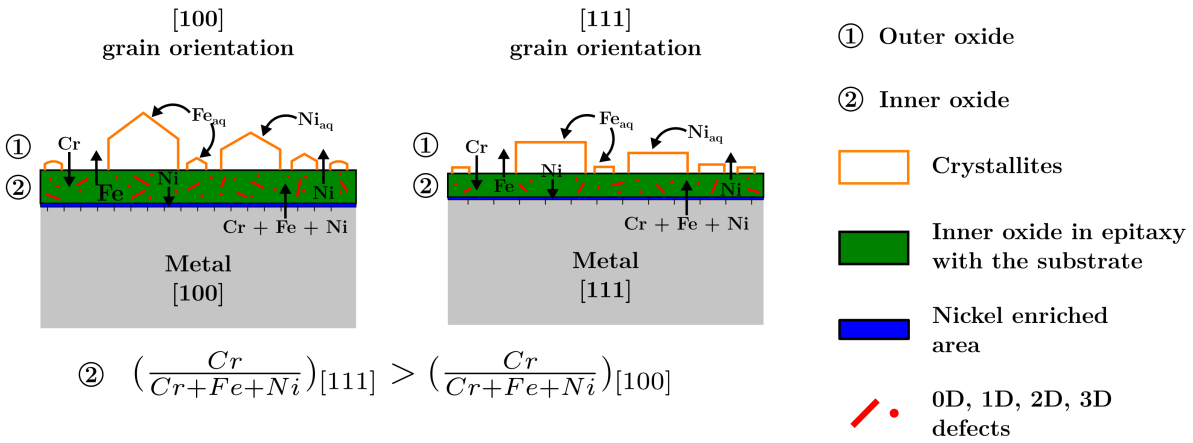

Figure 3.36: *Schematic of the oxidation mechanism depending on the underlying grain orientation of a 316L austenitic stainless steel exposed to PWR medium*

SEM imaging revealed that a preferential crystallite morphology is developed on top of each

studied orientation ([100], [110] and [111]) and that these crystallite shapes are related and specific to the underlying grain orientation. It therefore hints toward the existence of a crystallographic orientation relationship between the outer crystallites, the inner oxide layer and the underlying metal grain and this relationship is likely to be hinging on the underlying grain orientation. The same cube/cube epitaxial relationship between the inner oxide and the matrix is believed to be established on all metal grain orientations after 24 hours oxidation as described in section 3.1. However, as previously mentioned, not all the inner layer is properly epitaxially grown and some areas are strongly strained and hence slightly disoriented. Some inner layers might be more strained than others depending on the underlying metal grain and the epitaxial relationship. Moreover, it is thought that epitaxially grown crystallites will only nucleate and grow on areas properly oriented to develop the epitaxial orientation relationship between the two layers. Numerous authors never observed an effect of the underlying crystallographic orientation of the metal grain onto the outer oxide scale. This could arise from the longer oxidation times usually performed that could, past one point, erase this effect once the crystallites big enough. In addition, the establishment of the epitaxial relationship is likely to be contingent on the substrate surface state and therefore sample preparation. Sample preparation usually varies between different laboratories and we showed that this could greatly influence the outer oxide formation and growth. Indeed, if a sufficient strained layer was induced by the polishing, the outer oxide might loose the crystallographic information coming from the substrate and inner oxide as no epitaxial orientation relationship would be established and therefore, no specific crystallite shapes would be observed (cf. section 3.3).

According to Soulas, the establishment of an epitaxial relationship is made possible thanks to a residual elastic deformation of the metal which accommodates the parametric misfit [12, 13]. These misfit dislocations will decrease the theoric parametric misfit between the two lattices and a residual elastic stress in the metal makes up for this parametric misfit. The number of dislocation needed to accommodate the metal/inner oxide differ, depending on the grain orientation, modifying the energy to be brought to form the epitaxial relationship. Thus, the energy required to form an epitaxial oxide layer hinges on the amount of misfit dislocations between the alloy and the oxide and is contingent on the metal orientation. Soulas found that the [111] grains need fewer dislocations to accommodate the interface than [100] and [110] grain orientations (network of dislocations every 7 planes on [111] vs 5 planes on [110]). Therefore [111] grains need less energy to be accommodated and possess the lower residual elastic stress of the three investigated orientations. Since the oxide growth is contingent on the interfacial reactions at the metal/oxide interface [47–51], it is believed that the rate of the metal oxidation is influenced by the coherency, the residual stresses as well as the rate of the establishment of the epitaxial relationship across metal/oxide interface. In all likelihood, the inner oxides epitaxially grown will have different levels of growth strain depending on their orientation relationship with the substrate and therefore the underlying metal grain orientation. The accommodation of internal strains will likely, in addition, be made by the formation of non-stoichiometric oxides of slightly different lattice parameters. This stoichiometry deviation will be compensated by a higher number of point defects within the oxide layer to preserve the oxide electrical neutrality. As ionic defects are responsible for the oxidation process, a higher number of them will enhance oxidation. Hence, the higher the strain in the oxide and stoichiometry deviance, the faster the inner oxide growth. In addition, it is likely that, once the epitaxy established, diffusion through the inner layer will be slowed down as a more coherent interface is formed. In a nutshell, the network of misfit dislocations will relieve the interface coherency stress but the number of dislocations required to accommodate the interface and therefore the energy needed and resulting strain will affect the overall oxidation kinetic.

The observation of a much higher number of faceted crystallites with the favoured morphol-

ogy on the [111] grain orientation indicates that the inner layer is probably less strained and disoriented and that hence more regions can act as preferential germination sites for the faceted crystallites. Indeed, in all likelihood, at a given short oxidation time, a higher volume of oxide will be properly epitaxially grown on the [111] orientation since the establishment of the epitaxial relationship is believed the less energy-consuming of the three studied orientation. Thereby, the epitaxial relationship will be established faster and will induce less strain and defects on this grain orientation. In addition, as the inner oxide growth progress by ingress oxygen transport via oxygen vacancy diffusion, the observation of thicker oxides on [100] grain orientation indicates that oxygen diffusion is faster on this given orientation compared to the [111] one. Since the establishment of the epitaxial relationship is harder on [100] grain orientations and more energy consuming, the inner layer epitaxially grown will be more strained. Thus, on [100] grain orientation, more defects will be present in the inner layer. Hence, the higher oxide strain and stoichiometry deviance are responsible for the faster growth rate on [100] grain orientation. Since the metal/oxide interface on the [111] is the more coherent of the three and the less strained one, it is possible that diffusion across this interface will be slower. Regarding the oxide layer composition, only slight chemical changes between the two studied grain orientations were observed. The inner oxide layer is richer in chromium on top of [111] grain orientation. Moreover, the nickel enrichment underneath the alloy at the metal/oxide interface was higher on this given orientation. As diffusion through the inner layer is slower for oxides richer in chromium [5, 27], it would thus contribute to the thinner oxides formed on [111] grain orientation. The presence of an oxide layer richer in chromium would tend to decrease the growth rate of the oxide scale, acting as a barrier against the diffusion of metal and oxygen ions.

As previously stated, in his work Soulas proposed an oxidation mechanism in which the epitaxial relationship between the inner oxide layer and the substrate is established faster and is less energy-consuming on [111] grain orientation [12]. He also indicated that thicker oxides are formed on [111] grain orientations due to their faster crystallisation. However, he did not take into consideration that the interface coherency and oxide strain and defects could affect the oxidation kinetic. Therefore, even if the underlying metal grain orientation indeed control the oxidation kinetic, our results indicate that thinner inner oxides are formed on [111] grain orientation and that the oxidation kinetic is linked to the epitaxial orientation relationship established and to the amount of strain and defect within the inner oxide layer.

A parallel can be drawn between the preferential oxidation contingent on the underlying metal grain orientation and the grain boundaries oxidation (cf. section 3.1.4). Indeed, as presented above, on the samples surface, some grain orientations are preferentially oxidised compared to others. As for the grain boundaries oxidation, the asymmetric and faceted character of the intergranular penetration is thought to hail from a preferential oxidation of grain boundary planes along specific directions. Thereby, particular attention should be paid to the grain boundary planes and their oxidation as their preferential oxidation could be detrimental for the IASCC and the crack propagation. Grain boundary plane oxidations could be studied by looking upon surface oxidation of different grain orientations to account for the diversity of grain boundary plane.

Synthesis: Crystallographic orientation effect The underlying metal grain orientation affects the oxidation kinetic, outer oxide morphology, inner oxide thickness, oxide chemistry, etc.

- The outer and inner oxides share an epitaxial orientation relationship with the underlying metal grain.
- Thinner oxides are formed on top of [111] grain orientation compared to [100]. The faster oxygen diffusion through the inner layer on the layer arises from the higher level of stress in the inner layer on this given orientation since the establishment of the epitaxial relationship is more energy-consuming.
- The inner oxide is richer in chromium on [111] grain orientation and the underlying Ni-enrichment is higher.
- The rate of the metal oxidation is influenced by the coherency, the residual strain as well as the rate of the establishment of the epitaxial relationship across metal/oxide interface.

3.3 Cold-work effect on the oxide scales

As most studied samples to investigate PWR oxidation are prepared and polished in laboratory it is necessary to study the discrepancies induced by different polishing steps onto the oxidation. This section therefore aims to look upon oxides scales formed on samples prepared with different polishing. This study will focus on the **SiC** and **6UM** samples polished using SiC P4000 paper and 6 µm diamond paste respectively (presented in Chapter 2 section 2.2.1.2). The specimens investigated were oxidised between 24 hours and 72 hours. After polishing, controlled strained layers are induced and are 1.2 ± 0.2 µm and 0.44 ± 0.01 µm deep on the **SIC** and **6UM** specimens respectively [166]. The oxide formed on these samples will be compared to the ones formed on **REF** ones to fathom the influence of this induced deformation. The oxide layers were characterised using optical microscopy, SEM images and FIB cross-sections.

3.3.1 Characterisation of the oxides morphology and thickness on cold-worked samples

After 72 hours oxidation, a close oxidation behaviour can be observed on the **REF** and **6UM** samples (Figure 3.37). The crystallographic orientation of the underlying metal grain still controls the oxidation process for both samples but scratches resulting from the polishing are visible on the **6UM** sample. However, the **SiC** sample appear much more oxidised than the **6UM** one and the underlying metal grains become much more difficult to identify. The blue colour of the surface of the **SiC** sample probably results from a thicker oxide layer. Since this sample is the rougher polished of the three studied ones and has the deeper/more strained layer (1.2 ± 0.2 µm) [166], it suggests that the higher degree of cold-work induced accelerates the oxidation kinetic.

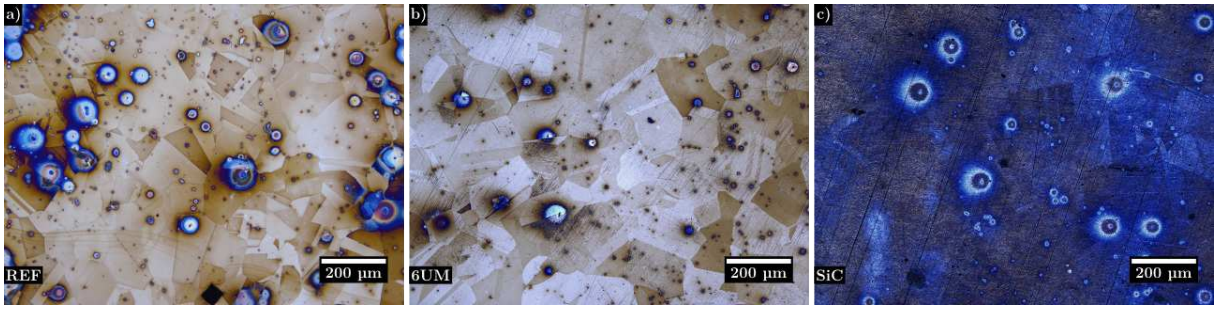

Figure 3.37: *Optical images on a) REF, b) 6UM and c) SiC samples oxidised 72 hours*

On the **6UM** samples, scratches coming from the polishing are present and preferentially oxidised as visible in Figure 3.38. Bigger crystallites are formed on these specific sites. Since a larger surface area is locally exposed to the medium and oxidised in the scratches it would locally promote the redeposition process inducing the formation of the bigger crystallites. Moreover, the darker area visible in the Back Scattered Electron image (Figure 3.38 a) around the crystallites formed on the scratches imply that the inner layer is thicker. These observations indicate that underlying defects such as dislocations and the presence of strain in these regions accelerates the growth kinetic of both oxide layers.

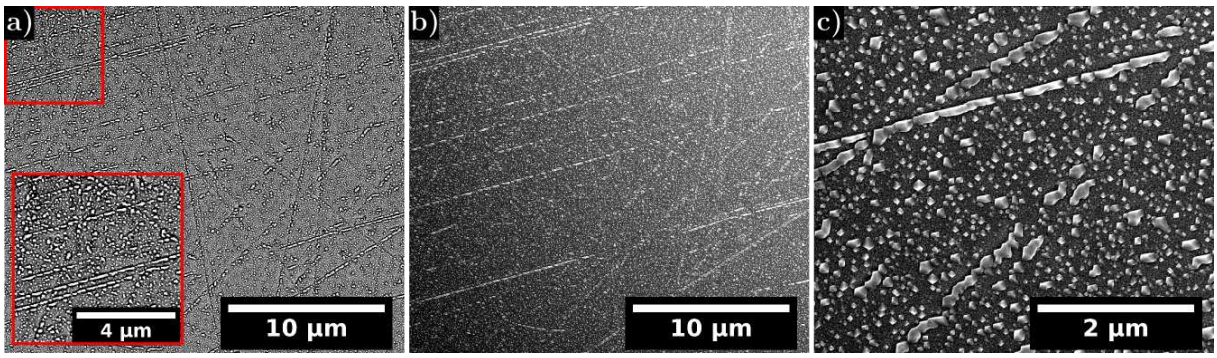

Figure 3.38: *SEM images (5 kV) on the 6UM sample oxidised 24 hours a) BSE imaging (zoom in insert of the framed area) b) and c) SE imaging on the same area*

Figure 3.39 presents SEM images on **REF**, **6UM** and **SiC** samples oxidised 24 and 72 hours. After 24 hours oxidation, faceted crystallites and smaller germs are formed on both the **REF** and **6UM** samples as opposed to the **SiC** sample who presents disorganised crystallites of homogeneous sizes. The observation of specific crystallites shapes as seen on the **REF** and **6UM** sample is revealing of the epitaxial relationship existing between the oxide layers and the substrate. Therefore, the amount of cold-work induced on the **6UM** sample in its strained layer ($0.44 \pm 0.01\,\mu m$) by the polishing did not modify the epitaxial relationship establishment. Moreover, a higher number of big-faceted crystallites are present on the **6UM** sample for both 24 and 72 hours oxidised samples compared to the **REF** samples. Since a rougher polishing is susceptible to induce defects such as dislocations, they may act as preferential germination sites. In addition, the faceted crystallites mean sizes are bigger on the **6UM** samples. As the outer oxide is believed to form from the diffusion of cations through the inner layer before being dissolved into the medium and re-precipitating, this suggests that diffusion is faster into the oxide layer formed on **6UM** samples. Hence, cold-work accelerates the outer oxide growth kinetic and the diffusion through the inner layer.

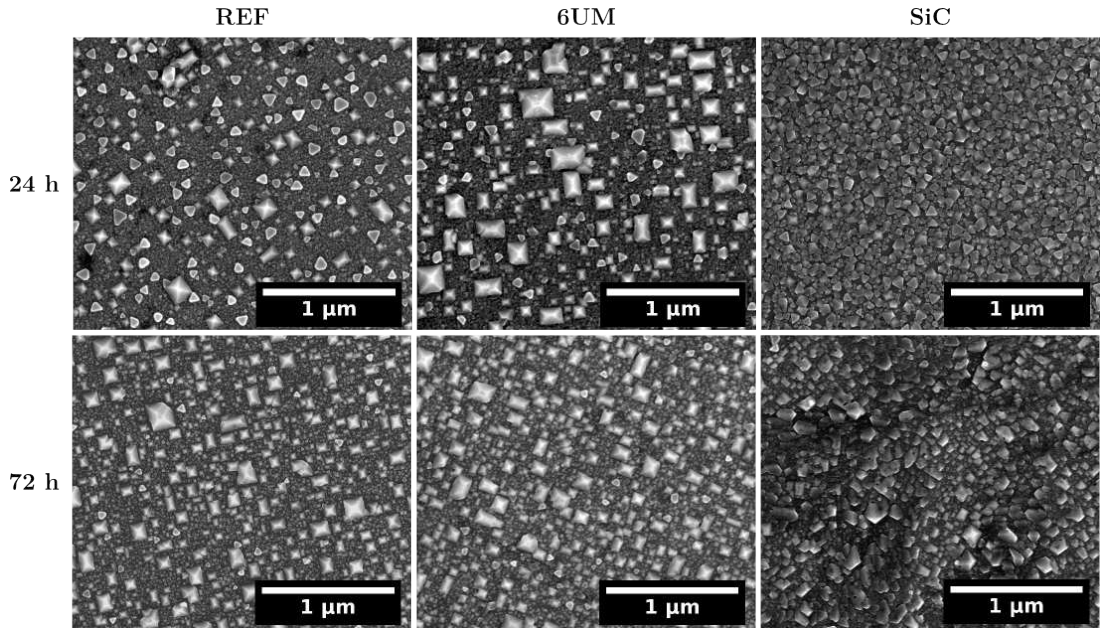

Figure 3.39: *SEM SE images (5 kV) on REF, 6UM and SiC samples oxidised 24 and 72 hours on a [100] grain orientation*

However, the expected crystallites morphologies are not observed on the **SiC** sample oxidised 24 hours (Figure 3.39). This suggests that the deeper and more strained layer induced on this specimen ($1.2 \pm 0.2\,\mu m$) is enough to affect the establishment of the epitaxial relationship. Nonetheless, after 72 hours oxidation, on a sole grain orientation ([100] here), several outer oxide favoured morphologies can be found on the **SiC** sample (Figures 3.39 and 3.40). Squared bases pyramids crystallites are observed (circled in red) and mesh with reflecting prism crystallites (circled in blue). These squared based pyramid are the favoured crystallite morphology formed on [100] grain orientation while reflecting prisms are usually observed on [110] grain orientation (cf. section 3.2.1.2). This entails that a crystallographic orientation relationship is established between the oxide layers but stress and strain present near the alloy surface are likely to disturb this orientation relationship therefore inducing the formation of several preferential crystallites shapes. Since an epitaxial relationship can be detected on this specimen only after 72 hours oxidation, it entails that the amount of cold-work induced by the polishing delays the establishment of an epitaxial relationship. As a different oxidation behaviour was seen on this sample, a cross-section was made on this area across the bigger reflecting prism crystallites and the square based pyramid ones seen in Figure 3.40 d.

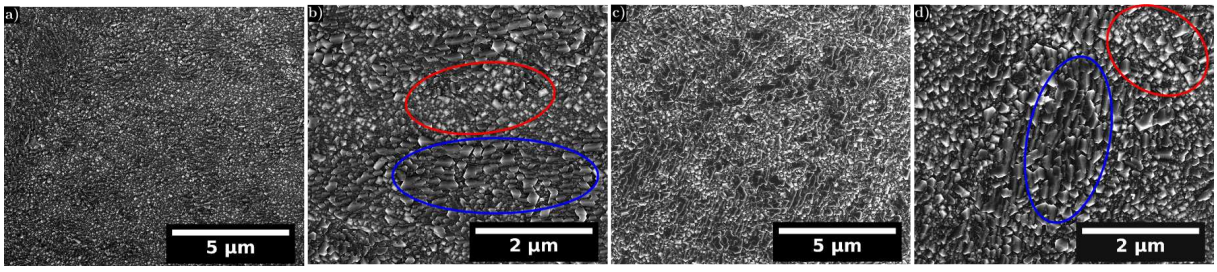

Figure 3.40: *SEM SE images (5 kV) on the SiC sample oxidised 72 hours on a [100] grain orientation*

Two FIB cross-sections were made on the **SiC** sample oxidised 72 hours (Figure 3.41). An heavily strained layer induced by the polishing is clearly visible on these images as shown by the red arrows. In this region, a high number of defects are believed to be present and dislocation cells are likely to be formed. A thick inner oxide penetration ($\sim$ 120 $\pm$ 20 nm) is visible on Figure 3.41 d (shown with the green arrow) while outside of this area the inner oxide is thinner

than 20 nm and therefore not observable on the cross-sections. The region with the intragranular oxide penetration corresponds to the area on which bigger crystallites with a reflecting prism morphology were formed. The presence of dislocation cells in the heavily strained layer could locally disturb the interface and the epitaxial relationship explaining the disturbed outer layer formed on these samples and thicker inner oxide.

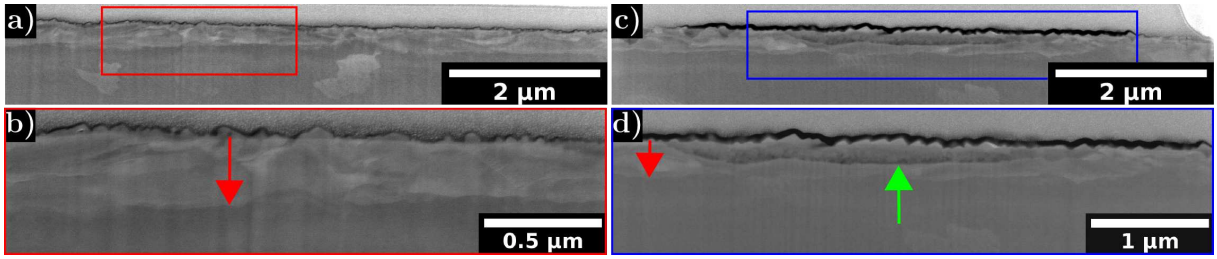

Figure 3.41: *SEM SE images (5 kV) on the SiC sample oxidised 72 hours on a [100] grain orientation a) lamella made on an area with homogeneous crystallites, b) zoom on area framed in red in a), c) lamella made one an area with several crystallites morphologies and d) zoom on the area framed in blue in c) (red arrow: strained layer, green arrow: oxide penetration)*

Characterisation of the oxide morphology and thickness on cold-worked samples
The different samples polishing affected the oxides morphology and thickness.

- The amount of cold-work induced by a 6 µm diamond paste polishing is not enough to prevent the establishment of the epitaxial relationship between the oxide layers and the underlying metal grain. However cold-work engendered by SiC P4000 paper polishing prevented or delayed this epitaxy.
- Defects induced by the polishing act as preferential nucleation sites for the outer crystallites and diffusion in the inner layer is faster. Thereby, the cold-worked layer induced by polishing enhances the oxidation kinetic.
- The dissolution/re-precipitation phenomena are enhanced in the scratches due to the larger area exposed locally to the medium. Thus, crystallites growth is enhanced on polishing scratches and defects induced by the polishing are believed to accelerate the oxide growth kinetic.

3.3.2 Chemistry of the oxides formed on cold-worked samples

Raman spectra of the **REF**, **6UM** and **SiC** samples oxidised 24 hours are presented in Figure 3.42. All the spectra are similar indicating that spinel oxides of close compositions are formed on all the studied samples. Nonetheless, the spectra obtained on both the **REF** and **6UM** on [111] grain orientations are perfectly superimposed. Therefore, the same oxides are believed to be formed on these samples and no differences in the oxide layer chemistry can be highlighted. The spectra on the **SiC** sample was acquired on an unknown grain orientation and is slightly different from the other two. On this specimen, the A_{1g} band is not symmetric and the contribution of the inner layer is higher than that of the outer one (ratio A_{1g} (Inner oxide):A_{1g} (Outer oxide) $>$ 1) inducing a shouldering. This suggests that the inner oxide formed on this sample is probably thicker.

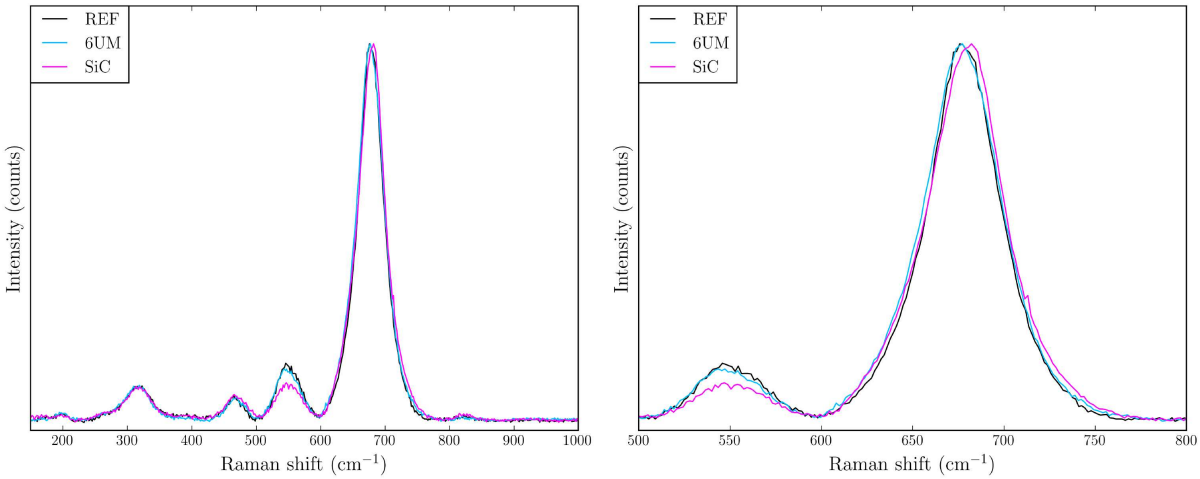

Figure 3.42: *Raman spectra on the REF, 6UM and SiC samples oxidised 24 hours (on [111] grain orientation for the REF and 6UM sample, orientation unknown for the SiC sample)*

Chemistry of the oxides formed on cold-worked samples: No differences could be observed between the oxides formed on the sample well polished and the one polished using 6 µm diamond paste whereas thicker oxides are likely to be present on the SiC P4000 polished specimen.

3.3.3 Cold-work effect: Synthesis, discussion and oxidation mechanism

In this section the effect of the polishing onto the oxide scales formed on 316L alloy exposed to PWR medium was investigated. This work focused on samples polished using SiC 4000 abrasive paper and 6 µm micron paste. Both of these polishing possess a close abrasive size but the polishing of **SiC** samples, performed on a paper, is rougher than the polishing of **6UM** samples done on polishing cloth since they induce strained layers 1.2 ± 0.2 and 0.44 ± 0.01 µm deep respectively [166]. Comparing the **REF**, **6UM** and **SiC** samples after oxidation, it appears that the **SiC** one is the most oxidised of the three. Such different oxidation behaviour contingent on the polishing method used was already mentioned by several authors [7, 10, 30]. Indeed, surface preparation can induce a high degree of cold-work at the material surface such as dislocations and dislocation cells and can lead to the appearance of a recrystallised layer composed of nanograins whose depth depends on the roughness of the polishing. Different surface preparations are therefore likely to have different oxidation behaviours. The overall oxidation process is depicted in Figure 3.43.

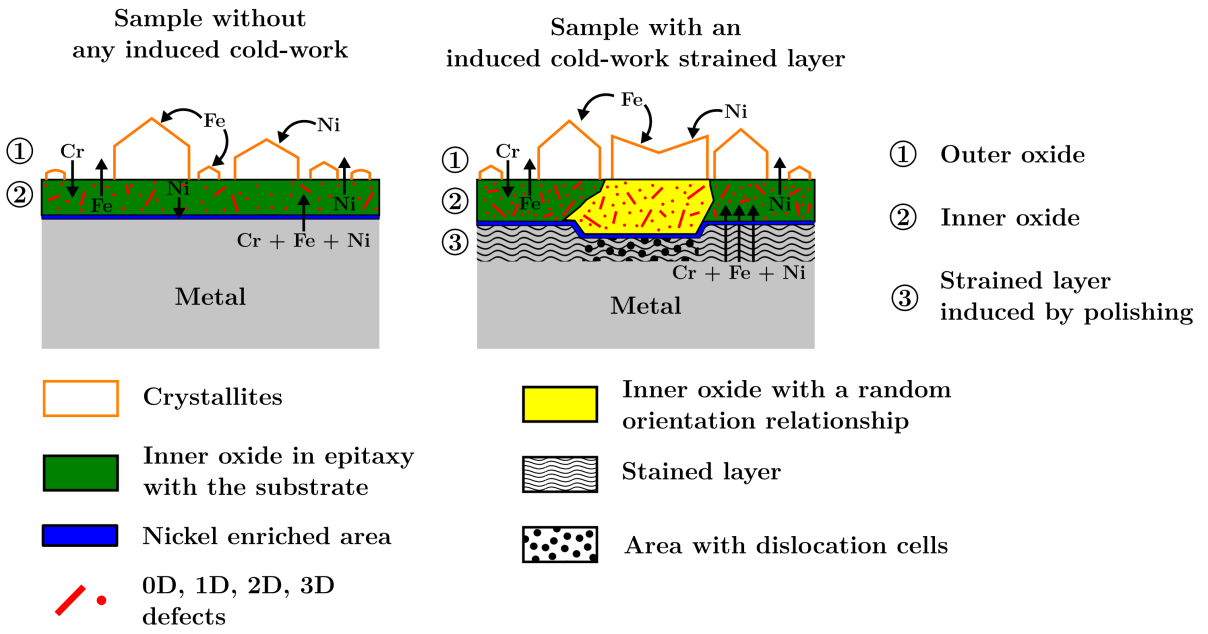

Figure 3.43: *Schematic of the oxidation mechanism depending on the sample preparation of a 316L austenitic stainless steel exposed to PWR medium*

As mentioned previously in section 3.1.2, the appearance of specific crystallites shapes as observed on the **REF** and **6UM** specimens indicates that a crystallographic relationship exists between the metal and the oxide scales. Hence, it is believed than on the **6UM** sample, the underlying metal grain orientation still controls the oxidation kinetic. However, on the **SiC** samples, crystallites of homogeneous sizes were observed after 24 hours oxidation while several specific crystallites shapes were seen on top of a sole grain orientation after 72 hours. Since the **SiC** specimens are polished with a coarse SiC grit, the extent of strain in its $1.2 \pm 0.2\,\mu m$ deep stained layer is expected high [166]. Dislocations cells could be formed and would prevent/delay the establishment of the epitaxial relationship. Thereby, areas of the inner oxide layer would be misoriented and the outer layer will appear without favoured morphologies. If/when an epitaxial relationship is established, the presence of dislocations and strain would prevent or delay the proper epitaxial growth of the inner and outer oxides on the whole grain. Some areas will still epitaxially grow and sometime another epitaxial relationship more favourable will be probably established in the areas in which dislocation cells are present explaining the presence of, at times, more than one preferential outer crystallite morphology. On the area where a different orientation relationship is established, thicker oxides will be formed since the oxides will likely be highly strained to accommodate the more favourable epitaxial relationship. However, if the cold-work induced by the polishing is too important it is assumed that no epitaxial relationship will be established, even at longer oxidation times, therefore modifying the overall oxidation kinetic. This will in all likelihood be the case for oxides formed on the as received components as they are cold-worked. Nevertheless, an epitaxial relationship could be formed at crack tips as the initial network of dislocations tends to disappear under irradiation (cf. Chapter 1 section 1.2.1.5).

As a higher number of crystallites was observed on the **6UM** samples compared to the **REF** ones it suggests that defects induced by the rougher polishing of the **6UM** specimen in the strained layer would act, in the first stages of oxidation, as preferential sites of nucleation for the outer crystallites. In addition, bigger crystallites were formed on cold-worked samples indicating that diffusion through the inner layer is faster. The presence of defects brought by the polishing in the alloy might engender the formation of even more stressed and strained oxides in which diffusion will be accelerated due to the presence of numerous defects. Hence, species such as iron

and nickel will be faster transported toward the surface and will locally saturate the solution and precipitate resulting in the formation of bigger crystallites. It is worth noticing that defects in the strained layer would provide a faster diffusion path for metallic species as the quantity of diffusion short-cuts available near the metal/oxide interface will be higher. Moreover, optical images revealed that the oxide layer formed on the **SiC** sample is bluer and thereby probably thicker. Since the **SiC** specimen is the rougher polished of the three studied ones and possesses the deeper and more strained layer, it suggests that the higher degree of cold-work induced accelerates the oxidation kinetic. The presence of defects within the oxide layers will also quicken the ingress diffusion of oxygen thus inducing the formation of thicker oxides on cold-worked specimens. Furthermore, scratches coming from the polishing were found preferentially oxidised. Bigger crystallites and thicker oxides were formed on these specific sites. The larger surface area available in the scratches will enhance the overall dissolution/redeposition process and therefore induce the formation of bigger crystallites on top of the scratches. These observations indicate that underlying defects such as dislocations and the presence of strain in these regions accelerate the growth kinetic of both oxide layers.

In a nutshell, if the sample polishing is not well controlled, it will greatly affect the oxidation kinetic, especially at short oxidation times. As numerous laboratory tests focus on better understanding oxidation, the sample surface preparation should be of very great care. The above conclusions can be extrapolated to cold-work generally speaking and suggest that cold-work will promote oxidation.

Synthesis: Cold-work effect Cold-work is found to accelerates the overall oxidation kinetic.

- Underlying defects such as dislocations and the presence of strain accelerate the growth kinetic of both oxide layers. Defects induced by the polishing act as preferential germination sites and diffusion through the inner layer is faster.
- Too high a degree of cold-work near the interface is believed to lead to dislocation cells formation that will disturb the establishment of the epitaxial relationship between the metal and inner oxide layer and therefore lead to the formation of a disorganised outer oxide layer.

3.4 Effect of the presence of inclusions on the oxide scales

Inclusions are present in the industrial 316L alloy investigated. These inclusions were described in Chapter 2 section 2.2.1.1 and mainly consist of manganese sulphur (MnS) precipitates and Cr, Mn, Ti, Al oxides. This section focuses on their effects onto the oxidation and how the oxide layers are affected by the presence of inclusions. The oxidation near inclusions was investigated using optical microscopy as well as SEM imaging. A FIB cross-section was made to look upon the inner oxide thickness near an inclusion and the chemistry of the oxide layer close to an inclusion was studied with Raman spectroscopy.

3.4.1 Characterisation of the oxides morphology and thickness near inclusions

The blue colour observed around the inclusions indicates that an inhomogeneous and preferential oxidation occurs around the inclusions (Figure 3.44). Thicker oxides are likely to be formed around the precipitates but changes in the oxides morphologies or compositions could also engender these contrasts. Therefore, precipitates are found to affect the overall oxidation

process and the oxidation kinetic is enhanced close to these. As the oxidation time increases the oxidised area around the precipitates is more and more oxidised.

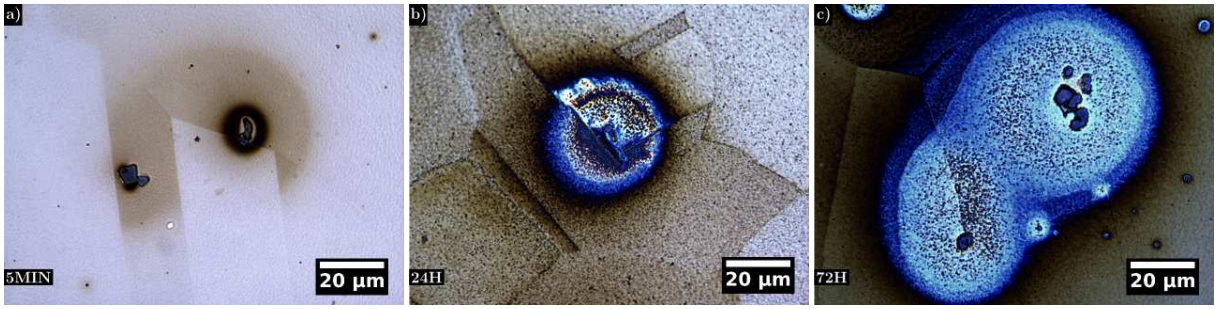

Figure 3.44: *Optical images near inclusions on REF samples oxidised a) 5 minutes, b) 24 hours and c) 72 hours*

SEM images were acquired near inclusions. On Figure 3.45, pitting is even observed after 5 minutes oxidation as shown by the red arrows. This pitting is linked to the partial dissolution of MnS inclusions that are often found underneath oxide precipitates as seen in Chapter 2 section 2.2.1.1. The bigger inclusions however remain unoxidised after 5 minutes oxidation. At longer oxidation times, a preferential oxidation occurred around the former inclusions and MnS are completely dissolved (Figures 3.46 and 3.47). The crystallites are bigger and denser indicating that the outer oxide growth is enhanced near inclusions. The outer oxide formed on [100] grain orientation is much bigger and denser while the oxide formed on [111] grain orientation is almost unaffected (Figure 3.46 c). The establishment of the epitaxial relationship is not affected by the precipitate's presence since the same outer oxide favoured morphologies are observed. Therefore, the oxidation kinetic around the precipitates is still controlled by the crystallographic orientation of the underlying metal grain.

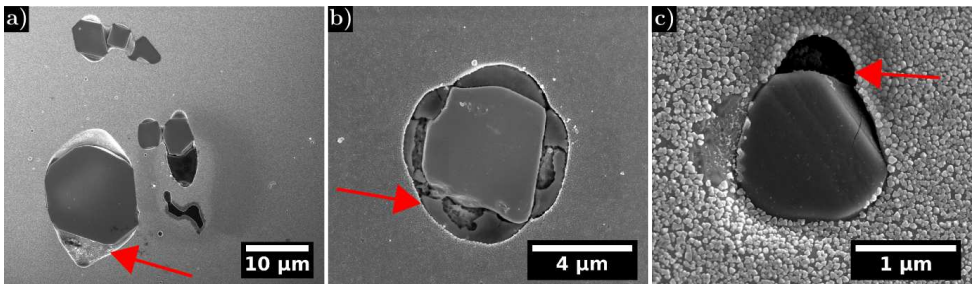

Figure 3.45: *SEM SE images (5 kV) near inclusions on samples oxidised 5 minutes a), b) and c) different inclusions*

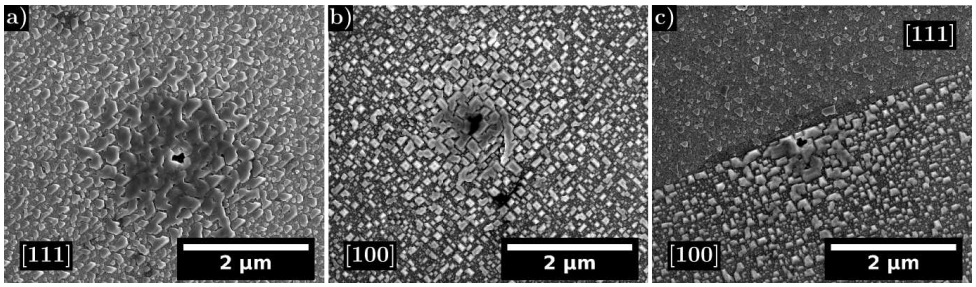

Figure 3.46: *SEM SE images (5 kV) near former inclusion on samples oxidised a) and b) 24 hours and c) 72 hours*

The BSE image reported in Figure 3.47 d confirm that the inner oxide is thicker close to the inclusion as areas surrounding the inclusion are darker and thus thicker. A smaller darker region is observed on the [111] grain orientation compared to the [110] one. Therefore, the inner oxide thickness influenced by the precipitate presence is also dependent on the underlying grain

orientation and the oxidation kinetic is slower on the [111] grain orientation. Since close to the oxide precipitates, the same oxidation kinetic with respect to the underlying metal grain occurs as far away from them, it suggests that precipitates accelerate the overall oxidation kinetic without modifying the underlying mechanism.

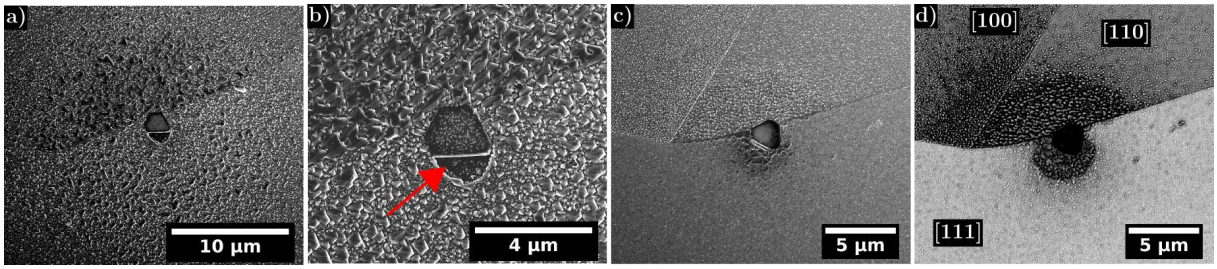

Figure 3.47: *SEM images (5 kV) near inclusions on REF samples oxidised a) and b) 24 hours (SE) c) and d) 72 hours with c) SE and d) BSE*

LayerProbe software analyses were performed near inclusions. The oxide layer was found ∼ 45 nm thick away from an inclusion while almost 5 times thicker (∼ 220 nm) near the inclusion. It therefore confirms that precipitates enhance the oxide growth kinetic.

A FIB cross-section was made near a former inclusion (area framed in red in Figure 3.48 a) to confirm that the inner oxide layer is thicker close to the former precipitate as supposed from the BSE image (Figure 3.48 a, b and c) and LayerProbe analysis. While further away from the inclusion the inner layer is measured 10 nm thick (shown by the green arrow at the edge of the cross-section), a ∼ 80 nm thick inner oxide is formed close to the former precipitate (cyan arrows). Regarding the outer oxide, SEM images were acquired near the former inclusion and far away from it to provide information on its influence on the crystallites (Figure 3.48 c to f). On either side of the grain boundary, each outer oxide morphology remains the same attesting once again that the precipitates do not modify the epitaxial relationship established. However, crystallites are much bigger close to the former inclusion. Moreover, the crystallite growth at grain boundary is much more pronounced near the former inclusion. Thereby, their presence also enhanced the grain boundary oxidation.

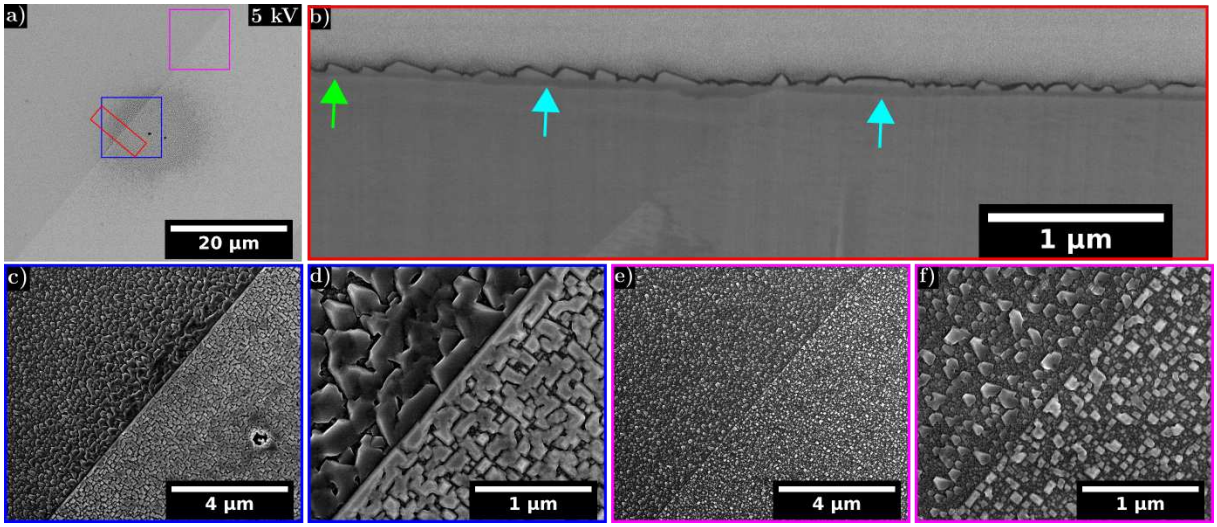

Figure 3.48: *SEM images (5 kV) on a REF sample oxidised 24 hours near a former inclusion and further away from it a) area on which was made the cross-section and SEM images b) oxide scale in cross-section (green arrow thin inner oxide further away from the inclusion, cyan arrow thicker oxide close to the inclusion) c) and d) outer oxide close to the inclusion, e) and f) outer oxide away from the inclusion*

Characterisation of the oxide morphology and thickness near inclusions: Precipitates were found to affect the oxide morphologies and thicknesses near inclusions.

- The dissolution of MnS inclusions engendered pitting and S as well as Mn release into the medium. A preferential oxidation around precipitates is observed. Both the inner and outer oxide layers are thicker. Precipitates are found to enhance both oxides growth kinetic and the grain boundary oxidation.
- The oxidation still is contingent on the underlying metal grain orientation and the oxidation kinetic is slower on [111] grains. Hence, precipitates do not modify the underlying metal grain orientation oxidation kinetic.

3.4.2 Chemistry of the oxides near inclusions

Raman spectra were made on an inclusion, close to this inclusion and far away from it (Figure 3.49). On the oxidised inclusion, the Raman spectra completely differ from the one acquired on the surface oxide (far away from the inclusion). This is mainly due to the precipitate composition which contains Cr, Mn, Ti, Al oxides and therefore induce shifts and new band apparitions. A spectrum was acquired on the oxide formed close to the inclusion and highlights a composition difference in the oxide layer formed. Indeed, new bands are detected. Thus, the presence of the precipitates induces a change in the oxide chemistry. The dissolution of MnS precipitates might introduce manganese ions into the medium that could re-precipitate and be included in the oxide layers.

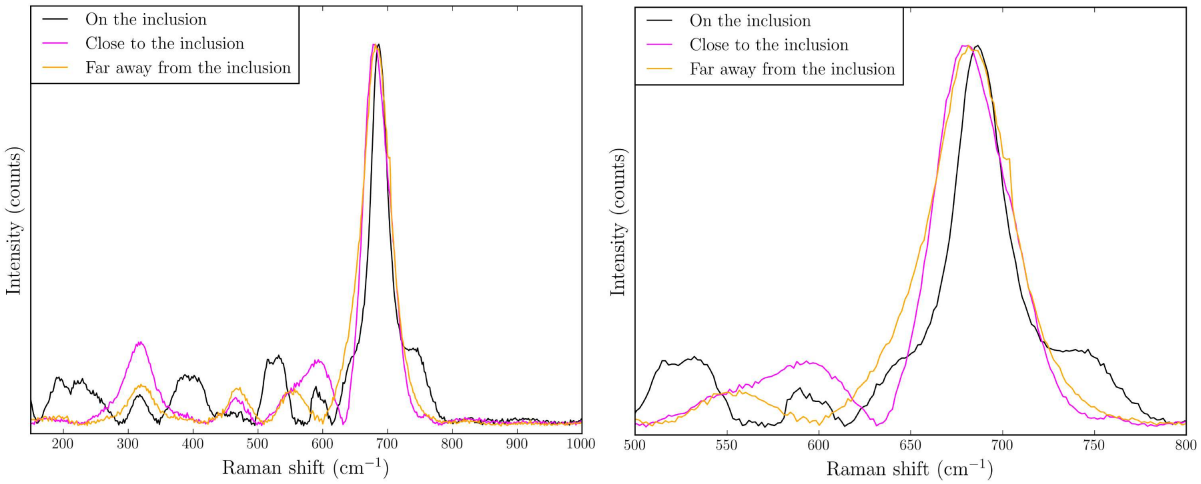

Figure 3.49: *Raman spectra on and close to an inclusion on a sample oxidised 24 hours*

Chemistry of the oxide near inclusions: The presence of inclusions induces a change in the oxide chemistry. MnS dissolution could release manganese into the medium that would re-precipitate and be included into the oxide layers.

3.4.3 Effect of the presence of inclusions: Synthesis, discussion and oxidation mechanism

The presence of inclusion was found to affect the overall oxidation. The investigation of the oxide scales near inclusions and associated oxidation mechanism are summarised below and in Figure 3.50.

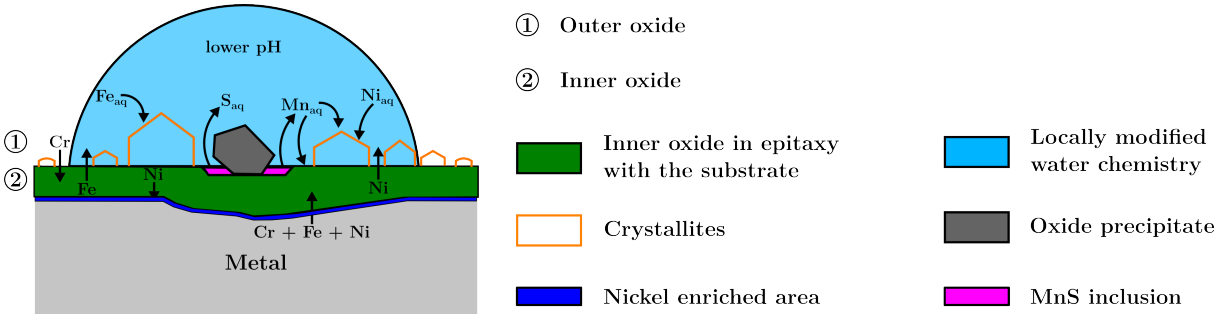

Figure 3.50: *Schematic of the oxidation mechanism near precipitates of a 316L austenitic stainless steel exposed to PWR medium*

Optical and SEM imaging evidenced a preferential oxidation around the precipitates. After 5 minutes oxidation, MnS precipitates start to dissolve inducing pitting while the oxide inclusion remains unoxidised. At longer oxidation times, the MnS are completely dissolved. The crystallites were found bigger and denser and the inner oxide is thicker close to the precipitates. Hence, near oxide precipitates and former MnS inclusions the oxidation kinetic was found enhanced. Regarding the oxide chemistry near precipitates, it was highlighted that the oxide layer composition is affected by the presence of the inclusions. The MnS precipitates, undergoing an oxidative dissolution, will induce local changes in the water chemistry and therefore the oxidation behaviour since sulphur-rich anions and manganese cations are released into the medium. The sulphur-rich anions might decrease locally the pH of the boundary layer while manganese ions could saturate the boundary layer and re-precipitates into the oxides. Sulphur could also be incorporated in the oxide or at the metal/oxide interface [187, 188]. Several studies shown that decreasing pH induced the formation of thicker oxides [73, 74]. Therefore, the boundary layer close to the precipitate having a lower pH is responsible for the formation of thicker oxides. Moreover, near inclusions the grain boundary is especially oxidised and bigger outer crystallites are formed on top of it. As precipitates were found to enhance the overall oxidation kinetic they therefore also enhanced the grain boundary oxidation. In a nutshell, the precipitate presence enhanced both the outer and inner oxide growth. As outer oxides were formed near precipitates with the favoured crystallites morphologies expected depending on the underlying metal grain orientation, it reveals that the establishment of the epitaxial orientation relationship between the oxide layers and the substrate is not affected by the presence of inclusions. The underlying metal grain orientation still controls the oxidation kinetic while precipitates enhance the latter without modifying the oxidation mechanism.

This behaviour near inclusions can be assimilated to the oxidation occurring in a stainless steel loop or in media with lower pH for example. Indeed, in such loop, metal ions such as iron will be dissolved into the solution and saturate it as manganese was dissolved near the precipitates and locally saturated the medium. As near the inclusion, in a stainless steel loop, the metallic species will then re-precipitate onto the specimen surface. It is expected that the water chemistry (with respect to saturation concentration of the soluble metal ions) will affect the quantity of outer layer. Moreover, lower pH media will affect the overall oxidation by affecting the oxides thickness and potentially chemistry as it was noticed near MnS precipitates.

Synthesis: Effect of the presence of inclusions The precipitate presence enhances both the outer and inner oxide growth and overall oxidation kinetic.

- Pits were initiated at the former manganese sulphur (MnS) inclusions which dissolved during oxidation. This MnS dissolution induces the release of manganese and sulphur ions into the medium and could saturate the boundary layer and decrease locally the pH of the medium.
- Manganese coming from the dissolution of MnS inclusion is believed to be incorporated into the oxide scale. Sulphur could also be present in the oxide scales or at the metal/oxide interface.
- This oxidation behaviour near inclusions can be assimilated to the oxidation occurring in saturated medium (a stainless steel loop for example).

Since the presence of manganese sulphur inclusion is found detrimental and induced pit initiation, their formation should be avoided if possible. The sulphur-rich anions released might decrease locally the pH and could increase the steel anodic dissolution in the crevices that could provide starting point of Stress Corrosion Cracking. One of the ways to avoid the MnS formation and therefore their dissolution is to manufacture steels with extremely low sulphur content.

3.5 Oxide scales formed in simulated primary water: Synthesis

All of the results mentioned in paragraphs 3.1, 3.2, 3.3 and 3.4 regarding the oxide formed on a 316L type stainless steel exposed to simulated PWR primary environment for short oxidation times led to several conclusions.

First and foremost, the oxide layer is confirmed to be a duplex structure with an outer oxide layer composed of Fe-rich crystallites and a continuous Cr-enriched inner layer. In addition, both parts of the oxide have a spinel structure and nickel enrichment has been observed at the metal/oxide interface. A crystallographic orientation relationship between the metal, the inner layer and outer crystallites is established and responsible for the favoured outer oxide morphology observed after 24 hours oxidation. Moreover, the inner oxide layer appears overall epitaxially grown onto the underlying metal grain with a cube/cube orientation relationship but is highly stressed and strained. Outer crystallites are epitaxially grown onto the inner layer with a twin-like or a cube/cube orientation relationship. The grain boundary oxide penetration is chromium-rich and, in all likelihood, of corundum structure. A clustering of unoxidised nickel was highlighted at the oxide penetration tip and is pushed back from the oxide along the grain boundary.

The underlying metal grain crystallographic orientation was found to control the oxidation kinetic at short time oxidations. Discrepancies in the outer oxide morphology, inner oxide thickness and chemistry were highlighted hinging on the grain crystallographic orientation. Among the observed results, thinner inner oxides are formed on [111] grain orientation and are richer in chromium. Favoured crystallite morphologies are formed on top of each grain orientation and these crystallites shapes are specific to each grain. The oxidation kinetic contingent on the underlying metal grain is influenced by the metal/oxide interface coherency, the defects introduced in the inner oxide and its strain as well as the rate of the establishment of the epitaxial relationship. In a nutshell, the strain engendered by the epitaxial growth of the inner oxide layer induce an evolution of the diffusion through the oxide and thus growth kinetic. A similar behaviour was highlighted for the grain boundaries oxidation as it is dependent on the grain boundary plane. The preferential oxidation occurring along specific directions induces an asymmetric oxide pen-

etration with facets that could prove detrimental for IASCC and crack propagation.

The several polishing investigated revealed that sample preparation has a strong effect on the oxidation kinetic. Overall, cold-work near the surface was found to enhance both the crystallites and inner oxides growth. A higher number of crystallites was present on top cold-worked specimens hinting that defects induced by the polishing act as preferential germination sites. However, too high a degree of cold-work near the interface was found to disturb the oxide layers and the establishment of the epitaxial relationship.

Inclusions within the alloy also affected the oxidation kinetic. Precipitates presence was found to enhance both the outer and inner oxide growth and overall oxidation kinetic. Moreover, the dissolution of MnS inclusions induced pitting. MnS dissolved during oxidation are likely to release manganese and sulphur ions into the boundary layer of the medium. Sulphur ions are believed to locally decrease the pH and manganese and sulphur are likely to be included into the oxides or at the metal/oxide interface.

All of these observations lead to think that careful investigations should be made to study the oxidation in PWR media. Studies should take into account the underlying metal grain orientation and prepare at best the studied samples to overcome cold-work effect and control the sample preparation to study representative and reproducible samples. If precipitates are present within the alloy, investigations of the oxide scales should be made further away from them. Therefore, in the following chapter investigating the effect of irradiation, the study of the oxide scales will be made on samples properly polished and away from the precipitates. In addition, the study will take into consideration the underlying metal grain orientation.

Oxide scales formed in simulated primary water:

- Oxides formed in PWR medium possess a duplex oxide structure of spinel oxides. The outer layer of crystallites is close to magnetite while the inner layer is a mixed chromium, iron and nickel spinel oxide. A nickel enrichment is present underneath the inner oxide. Both oxide layers seem to share an epitaxial relationship with the 316L substrate. The oxide formed at the grain boundary penetration is chromium-rich and in all likelihood of corundum structure. Moreover, a segregation of unoxidised nickel is present at the oxide penetration tip.
- The underlying metal grain crystallographic orientation was found to control the oxidation kinetic at short time oxidations and should be considered in further investigations of the oxide scales. Moreover, the grain boundary oxidation is also dependent of the grain boundary plane.
- Sample preparation has a strong effect on the oxidation kinetic and therefore should be controlled to prepare representative and reproductive samples.
- Inclusions were found detrimental and enhanced the overall oxidation kinetic, thereby representative studies on industrial alloys should take place away from the precipitates.

Chapter 4

Irradiation effect on the oxide scales formed in primary water

Contents

4.1 Description of the oxides formed on proton pre-irradiated samples 161
4.1.1 Morphological description of the oxides 161
4.1.1.1 Optical microscopy study of the oxidised samples 161
4.1.1.2 SEM characterisation of the outer oxide 161
4.1.1.3 TEM study of the oxides at nanoscopic scale 163
4.1.1.4 Effect of irradiation on the oxides morphology: Summary 166
4.1.2 Crystallographic structure and epitaxy of the oxide layers 167
4.1.2.1 Structure of the oxide scales 167
4.1.2.2 Study of the epitaxial relationship 168
4.1.2.3 Effect of irradiation on the oxides crystallographic structure and epitaxy: Summary 170
4.1.3 Chemical analysis of the oxide layers 171
4.1.3.1 Raman spectroscopy analyses 171
4.1.3.2 EFTEM mapping 172
4.1.3.3 EELS and EDXS quantitative analyses 172
4.1.3.4 Effect of irradiation on the oxides chemical composition: Summary . . . 175
4.1.4 Study of the intergranular oxidation on grain boundaries affected by RIS 175
4.1.4.1 Morphological description 176
4.1.4.2 Chemical analysis 177
4.1.4.3 Irradiation effect on the grain boundaries oxidation: Summary 179
4.1.5 Oxides formed on proton pre-irradiated samples: Synthesis, discussion and oxidation mechanism 179
4.2 Study of the Irradiation Assisted Corrosion 183
4.2.1 Characterisation of the oxides formed on the IACUNIRR area 184
4.2.1.1 Description of the oxides morphology and thickness 184
4.2.1.2 Analysis of the oxides structure 186
4.2.1.3 Chemical analysis of the oxide layers 187
4.2.1.4 Grain boundary oxidation 190
4.2.1.5 Unirradiated area characterisation: Summary 190
4.2.2 Characterisation of the oxides formed on the IACIRR area 191
4.2.2.1 Description of the oxide scales 191
4.2.2.2 Proton pre-irradiated area characterisation: Summary 193
4.2.3 Characterisation of the oxides formed on the IACIAC area 193

4.2.3.1 Description of the oxide scales . . . 194
4.2.3.2 Oxide formed under proton flux characterisation: Discussion and summary 199
4.2.4 Irradiation Assisted Corrosion experiment: Synthesis, discussion and oxidation mechanism . . . 202
4.3 Oxides formed at the crack tips of a decommissioned bolt . . . 203
4.3.1 Oxides description . . . 204
4.3.2 Synthesis and discussion on the representativeness of short-time oxidations of proton pre-irradiated specimens . . . 208
4.4 Oxide scales formed on irradiated materials: Synthesis . . . 209

This last chapter addresses the effect of irradiation on the oxide scales formed in primary water. It aims to study how irradiation can modify the oxides morphology, thickness, structure and chemistry. Irradiation defects (Frank loops and cavities) and the intragranular segregation and RIS at grain boundaries (as evidenced in Chapter 2 section 2.3) could potentially affect the oxide scales formed, the oxidation kinetic and overall oxidation mechanisms. Moreover, the literature review conducted in Chapter 1 highlighted that irradiation affects the oxide scales [4–9]. Some authors observed that irradiation influences the outer oxide as well as the inner oxide layer thickness [5–9], and the inner layer composition [4, 5, 7]. However, up to date, irradiation was not found to modify the duplex character of the oxide nor the oxide layer structures [4–9]. The investigation of short time oxidations conducted on irradiated materials will help to conclude if and how irradiation defects affect the oxidation behaviour and kinetic. To the author's knowledge, no study has yet investigated short time oxidation on irradiated 316L alloy. The study of short time oxidations could then be related to the oxidation first stages at the IASCC crack tips.

Firstly, the oxide scales formed on proton pre-irradiated samples oxidised in the Titane loop (**IRR** samples) will be presented. The oxides morphology, structure, composition and grain boundary oxidation will be depicted and compared to the oxide formed on unirradiated materials (**REF** and **UNIRR** samples). Focus will then be made on a sample oxidised under proton flux to study the Irradiation Assisted Corrosion. The oxide layers formed on the unirradiated area (**IACUNIRR**), proton pre-irradiated area (**IACIRR**) and oxidised under proton flux area (**IACIAC**) will be described in-depth and compared among themselves as well as with the Titane **UNIRR** and **IRR** samples. And finally, the investigation of the oxide formed at the crack tip of a decommissioned bolt will be introduced. The results on this extracted bolt will be compared to the ones obtained on samples oxidised in simulated primary water and described previously. Ultimately, a global synthesis on the effect of irradiation on the oxide scales formed in primary water environment will be given.

Influence of irradiation on the oxide layer formed in simulated primary water:

- Study of the influence of the concentration of irradiation defects at the surface on the oxidation first stages.
- Investigation of the influence of the oxidation under proton flux.
- Representativeness of synthetic proton irradiation and of the study of surface oxides to emulate oxidation at crack tips.

4.1 Description of the oxides formed on proton pre-irradiated samples

One of the simplest ways to study the effect of irradiation defects onto the oxide layers formed is to perform pre-irradiations and then oxidise the samples in PWR media. Therefore, the following paragraphs describe the oxide layers investigated on the Titane **IRR** samples. As, during this work, no effect of irradiation was highlighted on the oxide scales formed on the 0.5 dpa **IRR** sample, solely the 1 and 1.5 dpa **IRR** specimens are presented in the following. The outer oxide morphology, inner oxide thickness, oxide scale composition and oxide formed at grain boundaries were investigated using the same methodology and experimental techniques as used for the unirradiated oxidised samples in Chapter 3. Since no differences were evidenced in the oxides formed on **UNIRR** and **REF** samples, the oxides formed on the **IRR** specimens will be compared either one. However, as the **UNIRR** specimens correspond to unirradiated areas of the **IRR** samples, their comparison directly enables comparative studies of the oxides formed on irradiated and unirradiated areas on a sample with exactly the same oxidation conditions.

4.1.1 Morphological description of the oxides

This section focuses on the morphological description of the oxide layers formed on top of **IRR** samples oxidised between 5 minutes and 24 hours.

4.1.1.1 Optical microscopy study of the oxidised samples

The **IRR** areas look darker than the **UNIRR** areas in optical microscopy images (cf. Figure 4.1). This indicates a variation between the oxide formed in the **IRR** and **UNIRR** areas. The latter probably due to a difference in coverage, size or morphology of the outer oxide or even composition. Moreover, the preferential oxidation occurring around precipitates is enhanced in the **IRR** area. Therefore, irradiation affects the oxidation and its effect is visible even at the macroscopic scale. Irradiation thus appears the accelerate the oxidation kinetic.

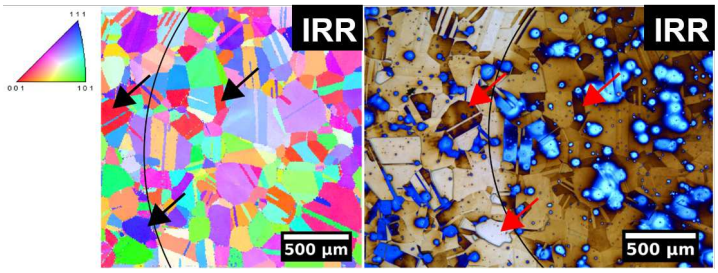

Figure 4.1: *EBSD map and optical image on a same area on the IRR sample oxidised 24 hours including both the unirradiated and the irradiated area*

4.1.1.2 SEM characterisation of the outer oxide

SEM images of the outer oxide on a [100] grain orientation on the **UNIRR** and 1 dpa **IRR** samples oxidised between 5 minutes and 24 hours are reported in Figure 4.2. The associated measurements made are introduced in Table 4.1. The outer oxide formed on both the **UNIRR** and 1.5 dpa **IRR** samples are depicted in Figure 4.3.

After 5 minutes oxidation, crystallites formed in both the **UNIRR** and **IRR** samples are very small ($\sim$ 30 nm). However the outer oxide has a higher coverage on the **IRR** one and crystallites are more numerous. This greater outer oxide coverage on **IRR** specimens is seen regardless of the oxidation duration. After 1 hour and 24 hours oxidation, faceted crystallites are observed and a

higher number of them are present onto the **IRR** samples. Hence, the nucleation rate is higher on **IRR** samples and irradiation defects are likely to induce more propitious nucleation sites for the outer oxide. As already observed in Chapter 3 section 3.1.1.2, less crystallites are present after 1 hour oxidation than after 5 minutes. Therefore, crystallites are still believed to dissolve gradually into the medium and then re-precipitate to participate to the growth of surrounding faceted crystallites. In addition, these faceted crystallites are bigger on **IRR** specimens as seen in Figure 4.3 for the 1.5 dpa **IRR** sample. This is not seen clearly from the sizes given in Table 4.1 for the 1 dpa **IRR** sample since numerous small crystallites are quantified but the overall bigger size of the outer oxide can be noticed in the maximum crystallite size given. Since, on the **IRR** specimens, the crystallites are bigger, it suggests that diffusion of cation through the inner layer is faster [21, 50]. Some authors observed that irradiation influenced the outer oxide [4–8]. The observed tendancies are contrary to observations made thus far by other authors [4, 5, 7] who observed smaller crystallites on irradiated material. However, Deng et al. and Fukumura et al. observed a higher number and a bigger size of crystallites as the irradiation dose increase [6, 8], which is in accordance with our results.

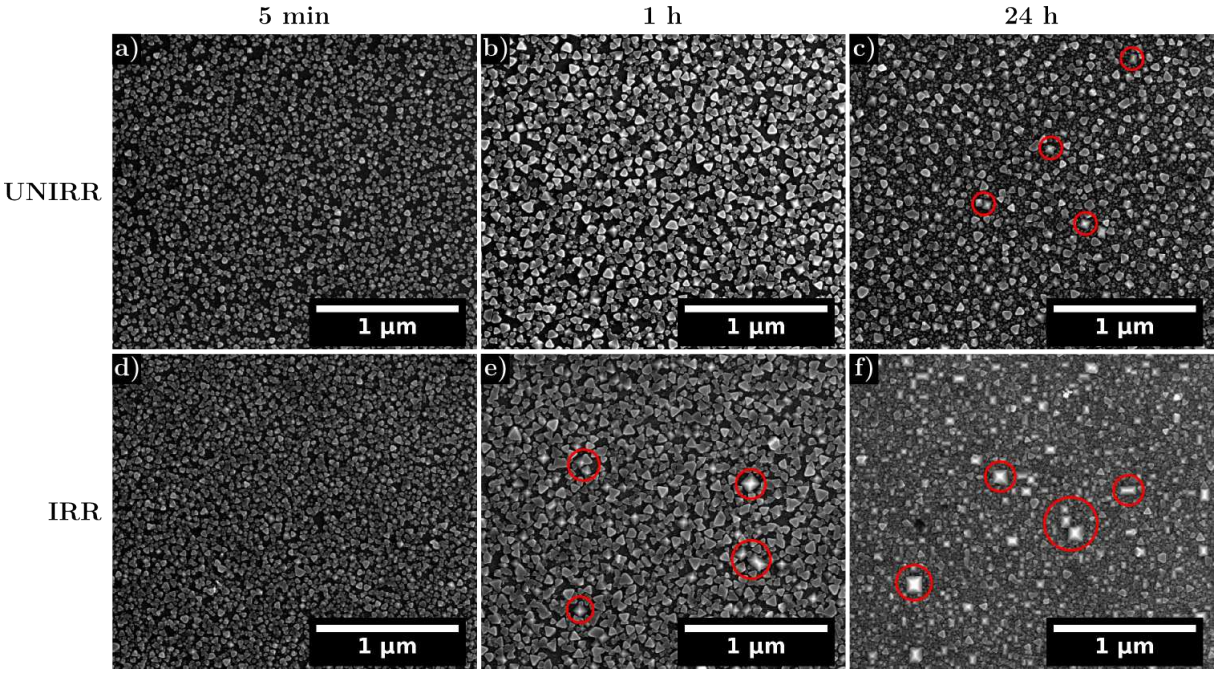

Figure 4.2: *SEM SE images (5 kV) on [100] grain orientation of both UNIRR and 1 dpa IRR samples oxidised 5 minutes, 1 hour and 24 hours*

Table 4.1: *Quantitative analysis of the crystallite distribution on UNIRR and IRR samples oxidised 5 minutes, 1 hour and 24 hours (for 1 h the number of crystallite per µm² is given for both the whole distribution and the big faceted crystallites, for 24 h the number of crystallites per µm² and their mean sizes are given for the big-faceted crystallites)*

Oxidation time	5 minutes		1 hour		24 hours	
Sample	UNIRR	IRR	UNIRR	IRR	UNIRR	IRR
mean size ± standard deviation (nm)	23 ± 9	28 ± 11	37 ± 16	43 ± 17	43 ± 14	42 ± 23
min – max size (nm)	6 – 50	5 – 70	7 – 105	10 – 113	10 – 85	11 – 121
crystallite/µm²	580 ± 40	627 ± 50	376 ± 40 26 ± 7	382 ± 40 42 ±9	30 ± 11	101 ± 16
coverage (%)	51 ± 5	64 ± 5	58 ± 5	64 ± 5	58 ± 5	75 ± 5

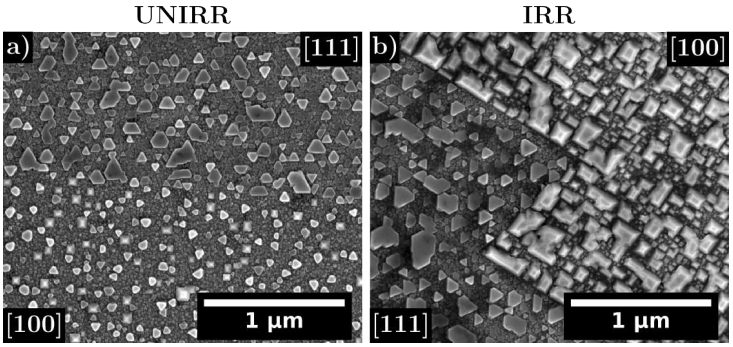

Figure 4.3: *SEM SE images (5 kV) on a [100]/[111] grain boundary on a) an UNIRR sample and b) a 1.5 dpa IRR sample*

LayerProbe analysis was performed on the **UNIRR**, 1 and 1.5 dpa **IRR** samples oxidised 24 hours. The mean oxide thicknesses were estimated independently of the underlying metal grain orientation and measurements were realised on several random grain orientations. On each sample, between 10 and 35 grains were analysed to obtain a good qualitative representativity of the oxide thicknesses. The oxides were found 1.1 and 1.5 times thickers on the 1 dpa and 1.5 dpa **IRR** samples respectively compared to the **UNIRR** ones. Thus, LayerProbe analysis indicates that thicker oxides are formed on **IRR** samples and that their thickness increases with the irradiation dose as already mentionned by Deng [8].

4.1.1.3 TEM study of the oxides at nanoscopic scale

As observed on cross-section views of the **UNIRR** samples, the oxide formed on irradiated material is duplex (Figures 4.4 and 4.5). This is consistent with the findings of several authors [4–9]. Regarding the inner oxide thickness, measurements are reported in Table 4.2. Comparing the inner oxide thickness measurements to the ones performed on **UNIRR** samples, the oxide is thicker on the 1 dpa **IRR** specimens after both 1 hour and 24 hours oxidation. Therefore, irradiation enhances the inner oxide growth and the ingress diffusion of oxygen appears faster on **IRR** specimens resulting in these thicker oxides. This is coherent with results of a few authors [6–9], but in disagreement with Perrin and Dumerval ones [4, 5]. Thicker inner layers on irradiated specimen suggests that they are less corrosion resistant compared to their unirradiated counterpart. The dose effect was also studied by comparing the oxides formed on the 1 dpa and the 1.5 dpa **IRR** samples oxidised 24 hours. On both orientations, the oxide is thicker on the 1.5 dpa **IRR** sample indicating that an increase of the irradiation dose affects the oxidation kinetic and accelerates the inner layer growth. This is in agreement with Deng et al. results [8]. Moreover, it is worth noticing that the metal/oxide interface is always wavy on [111] grain orientation and that intragranular inner oxide penetrations are observed (cf. magenta lines highlighting the metal/oxide interface in Figures 4.4 and 4.5). On this given orientation, the inward oxide growth appears to process preferentially along <112> directions ({112} planes are preferentially oxidised). As this behaviour is only observed on the **IRR** samples, irradiation is thought responsible for these intragranular oxide penetrations and will be discussed further on.

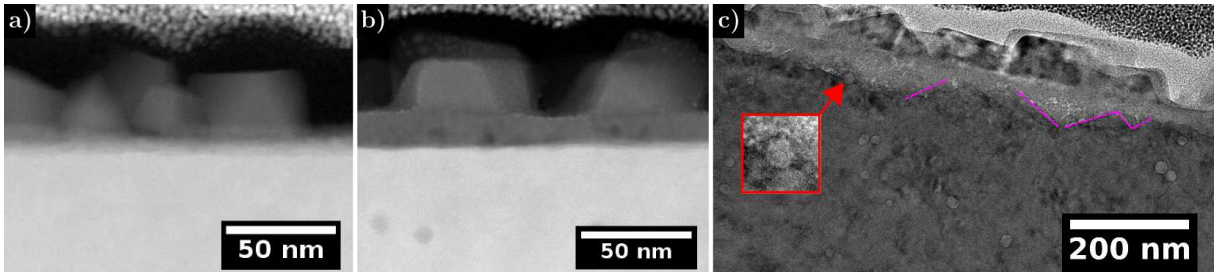

Figure 4.4: *TEM images on samples oxidised 1 hour a) STEM HAADF image on the UNIRR sample on a [100] grain b) STEM HAADF on the 1 dpa IRR sample on a [100] grain and c) under-focus BF image on the 1 dpa IRR sample on a [111] grain evidencing porosities in the inner oxide layer (red arrow highlights a cavity at the metal/oxide interface)*

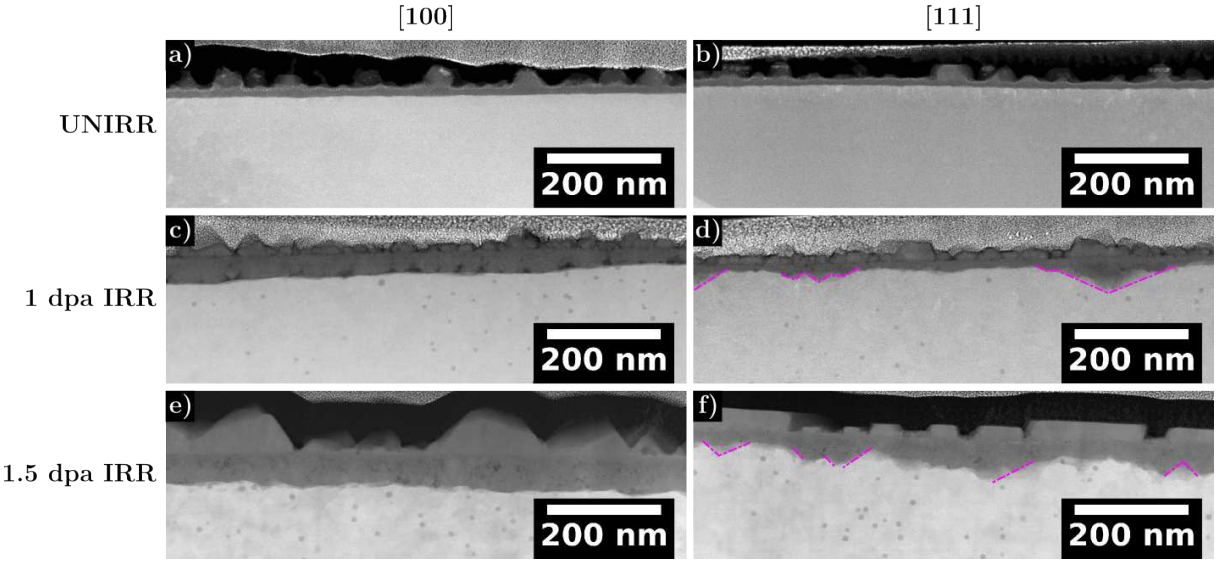

Figure 4.5: *STEM images on specimens oxidised 24 hours a) and b) UNIRR sample, c) and d) 1 dpa IRR sample, e) and f) 1.5 dpa IRR sample on [100] and [111] grain orientation respectively*

Table 4.2: *Inner oxide thicknesses on UNIRR, 1 and 1.5 dpa IRR samples oxidised 1 hour and 24 hours*

Oxidation time	Grain orientation	Inner oxide thickness (nm)		
		UNIRR	1 dpa IRR	1.5 dpa IRR
1 h	[100]	≤ 5	14 ± 2	-
	[111]	≤ 5	10 ± 6	-
24 h	[100]	10 ± 2	36 ± 6	53 ± 6
	[111]	7 ± 2	18 ± 10	33 ± 16

BF under and over focused images on the oxides after 1 hour and 24 hours oxidation evidence the presence of porosities in the inner oxide layer formed on the **IRR** specimens (Figure 4.4 c and 4.6). Fewer and smaller porosities were present in the oxide formed on top of [111] grain compared to [100] grain orientation. These porosities are thought to provide interconnections between the media and the inner oxide layer/substrate and therefore act as preferential diffusion paths. They are believed responsible for the observed enhanced oxide growth on **IRR** specimens.

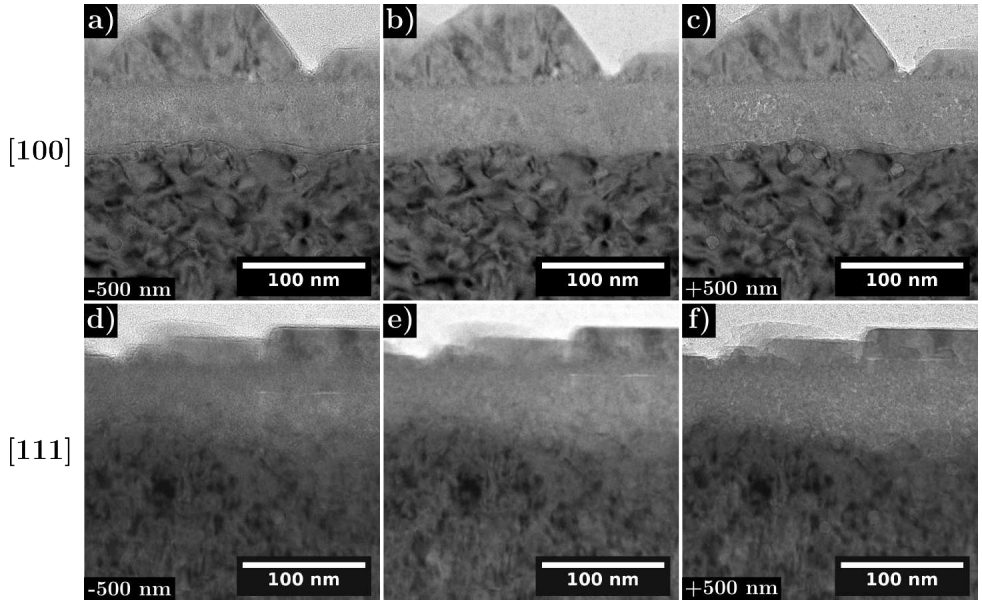

Figure 4.6: *TEM BF images on the 1.5 dpa IRR sample oxidised 24 hours of the oxide formed under-focus, focus and over focus on a) b) and c) a [100] grain and d) e) and f) a [111] grain*

As seen previously in Chapter 2 section 2.3.1.1, Frank loops and cavities were formed on the **IRR** samples due to the proton pre-irradiation. Some of these defects were found at the metal/oxide interface (Figures 4.4 c and 4.7). However, no preferential oxidation around these defects is observed. On [111] grain orientations, one family of Frank loops is parallel to the initial alloy surface. As the oxide thickness is uneven on this grain orientation, it might originate from the presence of these loops parallel to the surface. The propinquity of these loops at the metal/oxide interface could accelerate or delay the oxidation kinetic, resulting in oxide penetrations on the loops or in between them respectively. This means that, on [111] grain orientation, when reaching a loop parallel to the alloy initial surface, the inner oxide will further propagates along <112> direction to keep growing while avoiding the loop if the latter delay the oxidation kinetic, whereas if the loop is preferentially oxidised, {112} oxide facets will be formed. More generally, as the oxidation front progress, it will encounter Frank loops, and the previous observation (Figure 4.7) suggests that, depending upon the inclination of the latter with regards to the metal/oxide interface, it will affect more or less the oxidation kinetic. It is believed that the more the loops are perpendicular to the initial substrate surface, the less they will affect the oxidation kinetic. The oxide preferential growth along specific crystallographic directions can be related to the oxidation kinetic controlling the inner oxide thickness according to the underlying metal grain orientation. Thus, this intragranular oxidation behaviour is comparable to the surface oxide growth.

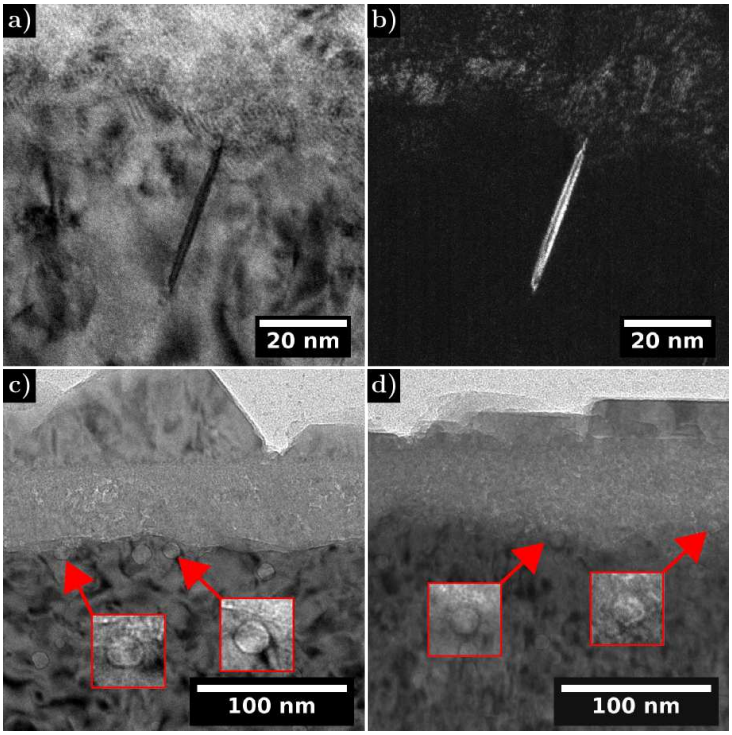

Figure 4.7: *Irradiation defects found close to the metal/oxide interface on the 1.5 dpa IRR sample oxidised 24 hours a) TEM BF image of a Frank loop and b) associated DF image of the Frank loop (2-beam conditions close to [101] zone axis) c) TEM BF image of cavities on [100] grain orientation d) TEM BF image of cavities on [111] grain orientation (cavities shown by the red arrows and associated zooms)*

4.1.1.4 Effect of irradiation on the oxides morphology: Summary

Numerous similarities were seen between the oxide morphologies on **UNIRR** and **IRR** specimens. The duplex character of the oxide was not to be found affected by irradiation. However, irradiation affects the oxidation as differences were evidenced in the outer oxide size, coverage, number of crystallites and inner oxide thicknesses. The outer and inner oxides nucleation and growth are likely to be disrupted by the concentration of irradiation defects at the surface during the oxidation first steps.

A higher outer oxide coverage and number of crystallites are seen independently of the oxidation duration on **IRR** samples indicating that nucleation is enhanced on these specimens. Irradiation defects would act as preferential nucleation sites inducing this higher number of crystallites during the oxidation first stages. In addition, thicker oxides are observed on **IRR** samples and their thickness increased with increasing the irradiation dose. Irradiation therefore accelerates the oxide growth. Diffusion is believed faster in the inner oxides formed on **IRR** specimens and the latter are porous. These porosities are likely to act as diffusion short-cuts, promoting the oxides growth. Irradiation defects were also observed near the metal/oxide interfaces but were not clearly preferentially oxidised. They were found to affect the oxidation kinetic especially on [111] grain orientation with the presence of Frank loops parallel to the interface. The inclination of these Franks loops with regards to the oxidised surface is thought to affect the inner oxide growth. The more the latter are parallel to the oxidised surface, the more they will affect the oxidation kinetic. However, at this time, it is not possible to rule on their role on the oxidation kinetic (promoting or delaying). Nonetheless, when reaching such defect, the oxide growth will progress along preferential directions and thus can be related to the surface oxidation whose oxidation kinetic is controlled by the crystallographic orientation of the underlying metal grain.

Main effects of irradiation on the oxides mophology:

- Outer oxide nucleation is enhanced on irradiated samples and irradiation defects, in all likelihood, act as preferential nucleation sites. Moreover, cation diffusion through the inner oxide layer is faster.
- Thicker and porous inner oxides are formed on irradiated specimens and are even thicker with increasing the irradiation dose. Oxygen diffusion through the inner layer is therefore faster on irradiated specimens and this enhanced growth results from the porosities acting as diffusion short-cuts.
- Irradiation defects at the metal/oxide interface are not preferentially oxidised but still affect the oxidation kinetic. The Frank loop inclination with regards to the oxidised surface will more of less affect the oxidation kinetic. Intragranular oxide penetrations induced by these loops progress along preferential crystallographic directions.

4.1.2 Crystallographic structure and epitaxy of the oxide layers

To see if irradiation modify the oxide crystallographic structure or the epitaxial relationship between the oxide layers and the substrate, the oxide structure was investigated on **IRR** specimens and compared to **UNIRR** ones.

4.1.2.1 Structure of the oxide scales

GIXRD was performed on a 1 dpa **IRR** sample (Figure 4.8). Since the analysis is made on the whole sample and only a 4 mm disk was pre-irradiated, the acquired diffractogram was only compared to the diffractogram obtained on the **REF** sample presented in section 3.1.2.2. The only oxide detected is an AB_2O_4 oxide as seen on the **REF** specimens (cf. Chapter 3 section 3.1.2.2). Neither hematite (Fe_2O_3) nor chromium oxide (Cr_2O_3) were detected. Thereby it can be assumed that irradiation does not modify the oxide structure. This is consistent with the similar morphologies of the outer oxides formed on the **IRR** and **UNIRR** specimens (cf. section 4.1.1).

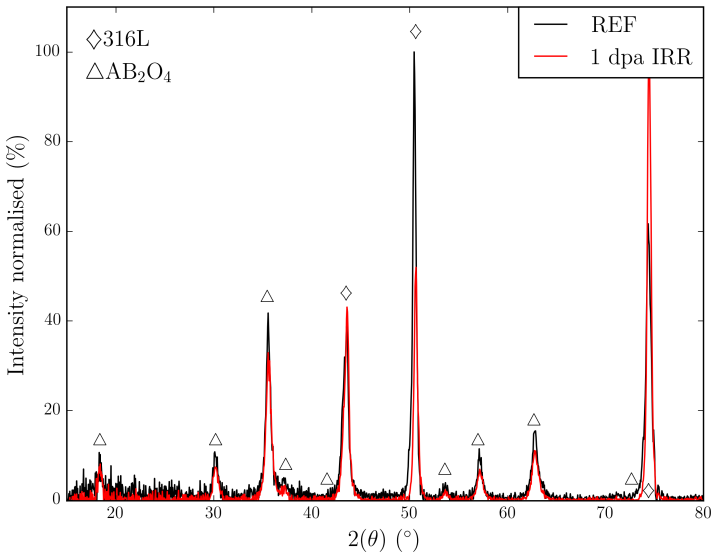

Figure 4.8: *GIXRD spectra on the REF and 1 dpa IRR samples oxidised 24 hours (normalised on the most intense peak)*

The Raman spectra obtained on the **IRR** sample did not attest of the presence of any

additional specie (Figure 4.9) compared to spectra obtained on **UNIRR** or **REF** samples (cf. Chapter 3 section 3.1.2.3). Therefore, spinel oxides are also supposed to be formed on **IRR** samples. The shifts of the bands will be discussed in section 4.1.3.1.

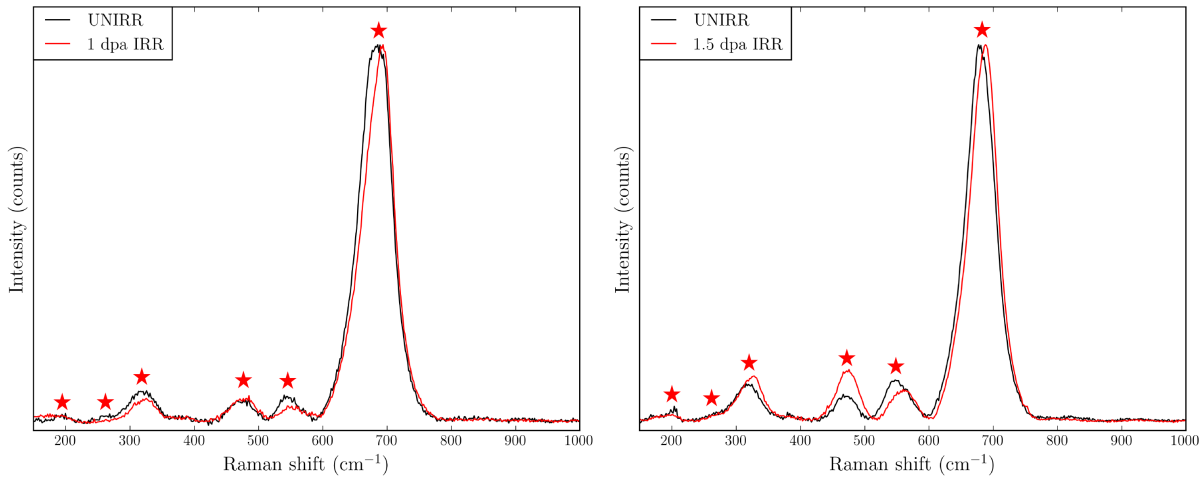

Figure 4.9: *Raman spectra on UNIRR samples compared to 1 and 1.5 dpa IRR samples oxidised 24 hours on a [100] grain orientation (red stars show the observed bands)*

To extract more information about the oxide crystalline structures, SAED patterns were collected in TEM (Figure 4.10). Since the oxides formed on **IRR** samples were thicker, it was proven easier to look upon the oxide structure using electron diffraction. As on **UNIRR** samples, diffraction pattern indexed the inner layer as spinel phase (space group Fd$\bar{3}$m) with a lattice parameter a $\approx 8.33 \pm 0.1$ Å.

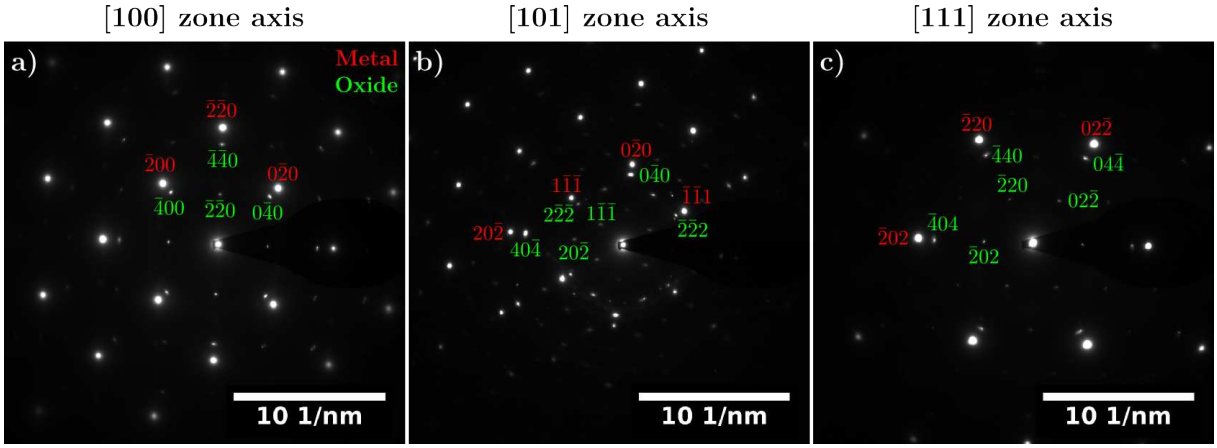

Figure 4.10: *SAED patterns on IRR samples oxidised 24 hours close to a) [100] zone axis b) [110] zone axis and c) [111] zone axis (red: austenite matrix, green: oxide)*

4.1.2.2 Study of the epitaxial relationship

An optical image of the 1 dpa **IRR** sample highlighted that [100] grains are the darkest of the three studied orientations, as on the **UNIRR** specimens (cf. arrows in Figure 4.1, section 4.1.1.1). Therefore, the underlying metal grain orientation is still believed to influence the oxidation kinetic. In fact, after 1 hour and 24 hours oxidation, some crystallites have the expected faceted crystallites with the favoured squared based pyramid morphology on both the **UNIRR** and **IRR** samples but a higher number of them are present onto the **IRR** samples (cf. Figure 4.2 in section 4.1.1.2). Moreover, these faceted crystallites are bigger on **IRR** specimens (cf. Table 4.1 in section 4.1.1.2). As evidenced in Figure 4.11, the faceted crystallites on the three orientations of

interest possess the same morphologies as previously observed on **UNIRR** samples (cf. Chapter 3 section 3.2.1.2). The triangular morphology seen on the surface [111] grain orientation is, in cross-section, observed as flat crystallites while the squared based pyramids formed on [100] grain orientation can be noticed in cross-section (cf. Figure 4.5 in section 4.1.1.3). Since the favoured crystallite morphologies are observed after 1 hour and 24 hours oxidation on the three grain orientations on the **IRR** specimens, it shows that irradiation do not modify the crystallographic orientation relationship established. Thereby, irradiation and irradiation defects did not disturbe the establishment of the epitaxial relationship. Nevertheless, a higher number of crystallites with the favoured morphology are seen on the **IRR** samples suggesting that a higher number of preferential nucleation sites exists on the **IRR** samples for the favoured crystallites. Hence, the inner oxide layer is probably better established allowing the growth of more crystallites with the favoured morphology on the **IRR** samples than on the **UNIRR** ones. The establishment of the crystallographic orientation relationship is likely to be accelerated by irradiation. In addition, the inner oxide layer is each time found thinner on the [111] grain orientation than on the [100] one (cf. Figure 4.5 and Table 4.2). This indicate that the underlying metal grain orientation still controls the oxidation kinetic on **IRR** specimens.

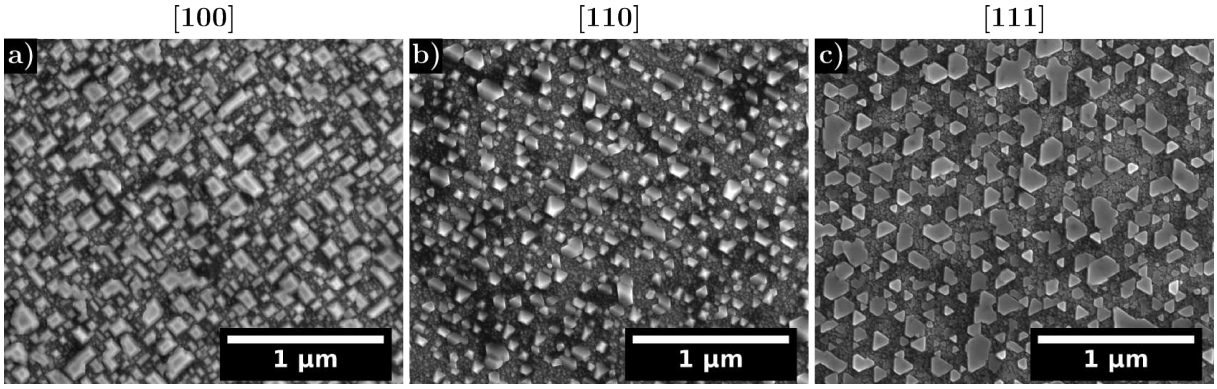

Figure 4.11: *SEM SE images (5 kV) on the 1.5 dpa IRR sample oxidised 24 hours on a) [100] b) [110] and c) [111] grain orientation*

Diffracting spots from the oxides formed on **IRR** specimens were each time, independently of the substrate orientation, indexed in the same zone axis as the matrix (Figure 4.10). It confirms that the inner layer share a cube/cube epitaxial orientation relationship with the underlying metal grain and that irradiation do not affect the nature of the epitaxial relationship established. TEM Dark Field imaging on both the oxides formed on the 1 and 1.5 dpa **IRR** samples was carried out but solely these made on the 1 dpa **IRR** specimen are reported below in Figure 4.12. The higher spacing between the diffracting spots on [111] zone axis allow a weaker contribution from surrounding diffracting spots and thereby improve the resulting images quality. The DF images evidence that only small areas are properly epitaxially grown as previously observed on **UNIRR** specimens. HRTEM images and associated FFT and Inverse Fast Fourier Transform (IFFT) on the inner oxide layer of the 1 dpa **IRR** are reported in Figure 4.13. This IFFT was obtained after applying a bandpass mask whose diameter is plotted in blue on the FFT presented on the green insert in Figure 4.13 a. It evidences that some regions are in proper epitaxy and well oriented (as shown in the magenta circle) while other are highly strained (as seen in the cyan circle). These strained area are thereby slightly disoriented and thus not in the befitting diffracting condition to be visualised in DF imaging.

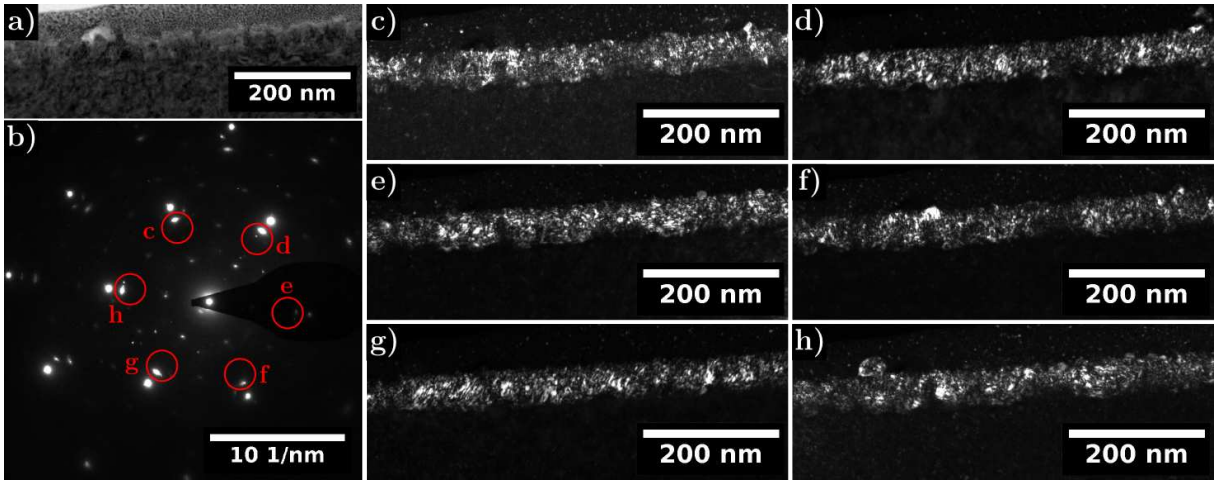

Figure 4.12: *1 dpa IRR sample oxidised 24 hours on a [100] grain orientation in [111] zone axis a) BF image b) SAED pattern (red circle: objective aperture) c) to h) DF on the spots circled in b)*

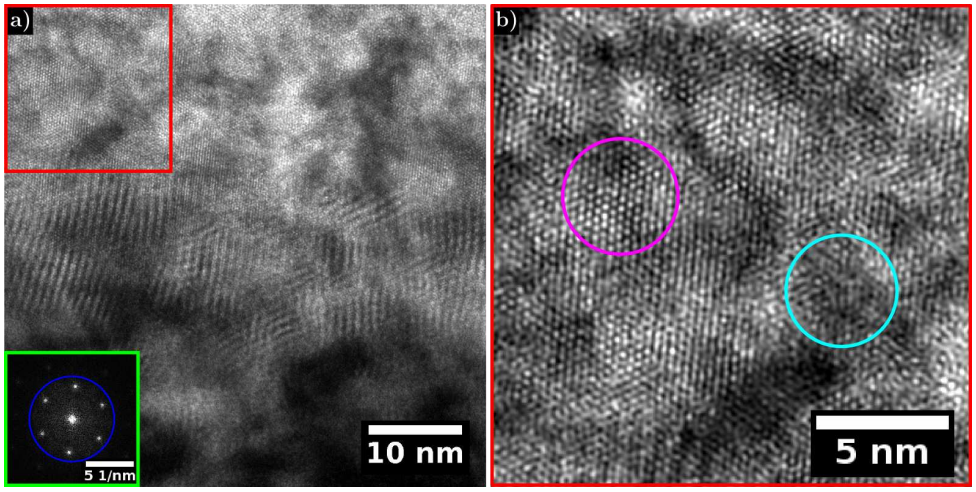

Figure 4.13: *a) HRTEM image of the metal/inner oxide interface of a [100] grain in [111] zone axis and associated FFT in the green framed area with the bandpass mask diameter drawn in blue b) IFFT of the area framed in red in a) with a well oriented region circled in magenta and a strained one circled in cyan*

4.1.2.3 Effect of irradiation on the oxides crystallographic structure and epitaxy: Summary

As expected from the literature [4–9], irradiation was not found to have an effect on the crystallographic structure of the oxide layers. Both oxides are AB_2O_4 spinels alike that on the **UNIRR** specimens. As contrasts between grains were observed after oxidation in optical images, the underlying metal grain still influences the oxidation kinetic. SEM imaging highlighted the same favoured crystallite morphologies as on **UNIRR** specimens contingent on the metal grain orientation. This hints that same crystallographic orientation relationship is established on **IRR** and **UNIRR** samples. Further TEM analysis confirmed that the inner oxide layer formed on the **IRR** specimens is epitaxially grown with a cube/cube orientation relationship with the underlying metal grain. This inner layer is, once again, heavily strained with a high density of defects. Hence, irradiation did not modify the epitaxial orientation relationships established between the oxide layers and the substrate. Nevertheless, more crystallites with the favoured morphology are present on **IRR** samples and these are bigger than on **UNIRR** samples. This suggests that more inner oxide regions share a proper epitaxial relationship with the substrate on the **IRR** specimen at a given oxidation time. These regions in epitaxy at the surface would

provide propitious nucleation sites for the faceted crystallites. Hence, the establishment of the crystallographic orientation relationship is likely to be accelerated by irradiation. In addition, since thicker oxides are still observed on [100] grain orientation, the underlying metal grain orientation still controls the oxidation kinetic.

Main effects of irradiation on the oxides crystallographic structure and epitaxy: Irradiation do not modify the crystallographic structure of the oxide layers:

- The duplex oxide layer consists of spinel oxides (AB_2O_4).
- The same cube/cube crystallographic orientation relationship is established between the substrate and the inner oxide layer. Nonetheless the latter is highly strained and contains numerous defects. The establishment of the epitaxial relationship between the inner layer and the substrate is accelerated by irradiation.
- The underlying metal grain still controls the oxidation kinetic on irradiated specimens.

4.1.3 Chemical analysis of the oxide layers

The chemical composition of the oxide layer formed on **IRR** samples was investigated and compared to the **UNIRR** specimens. Raman spectroscopy was used to look upon the overall oxide chemistry while nanoscopic investigations were performed with EFTEM mapping and EDXS and EELS analyses.

4.1.3.1 Raman spectroscopy analyses

Raman spectra were acquired on **UNIRR**, 1 and 1.5 dpa **IRR** samples on the three crystallographic orientations of interest (Figure 4.14). Differences in the A_{1g} band can be seen for all the orientations studied. A shouldering of the A_{1g} band is noticed for all the **IRR** specimens and the centre of mass of the A_{1g} band of both the inner and outer oxide is shifted toward higher wavenumbers. Since the inner oxide formed on **IRR** samples are thicker, the contribution from the A_{1g} band of the inner oxide prevails on the one from the outer oxide (A_{1g} (Inner oxide) > A_g (Outer oxide)) while there was a close competition between them on the **UNIRR** samples. Hence, this increase in inner oxide thickness is thought primarly responsible for the observed shifts. However, differences in chemical composition between the oxide layers formed on **UNIRR** and **IRR** sample could, also, in all likelihood, engender band shifts. Oxides richer in chromium on irradiated samples, as suggested by the literature [4, 5, 7], would induce a shift of the A_{1g} band toward the higher wavenumbers (cf. Appendix B). Nevertheless, it is difficult to conclude on band shifts for each oxide layer due to potential chemical variations since the thickness of the oxide layer already induced a shift and, in addition, the A_{1g} bands of the duplex oxide scale are in close proximity.

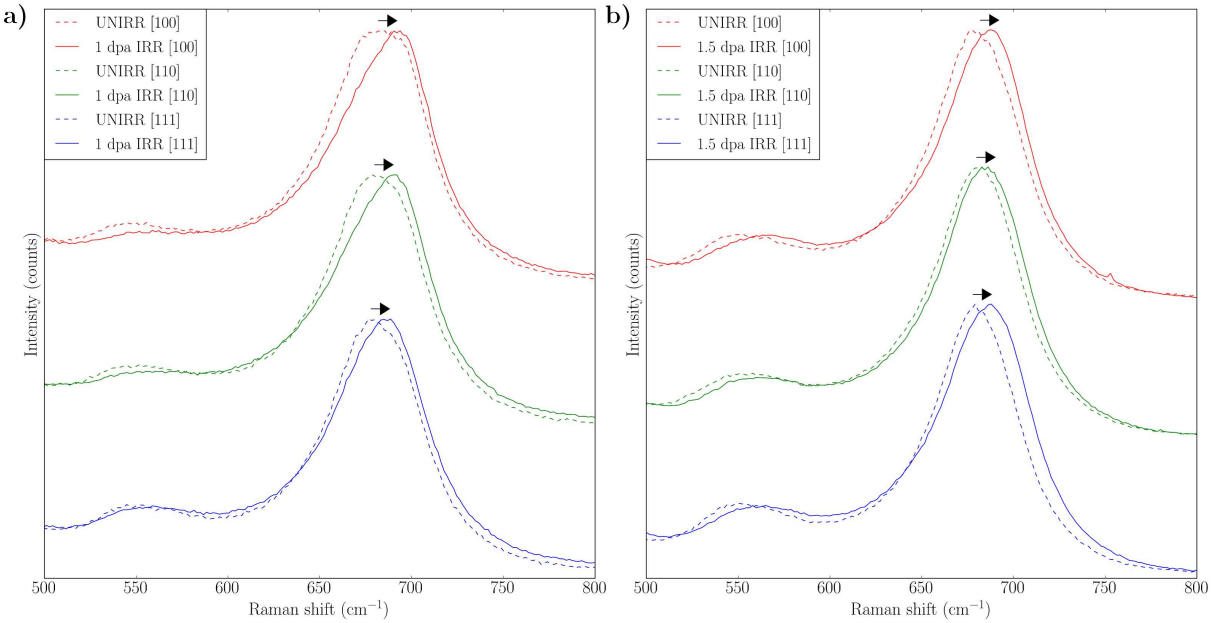

Figure 4.14: *Zoom on the A_{1g} band of the Raman spectra acquired on a) the UNIRR and 1 dpa IRR samples oxidised 24 hours and b) the UNIRR and 1.5 dpa IRR samples oxidised 24 hours*

4.1.3.2 EFTEM mapping

EFTEM mapping revealed, as for the **UNIRR** and **REF** samples, an iron-rich outer oxide and a chromium-rich inner oxide for the 1 and 1.5 dpa **IRR** samples (Figure 4.15). A slight Ni-enrichment is seen at the metal/oxide interface but the low magnification and the low thickness of this area renders its observation difficult. Moreover, these images highlight a nickel enrichment and chromium depletion at the grain boundary resulting from the grain boundary RIS as presented in Chapter 2 section 2.3. These results suggest that irradiation did not qualitatively modified the oxide scales chemical composition.

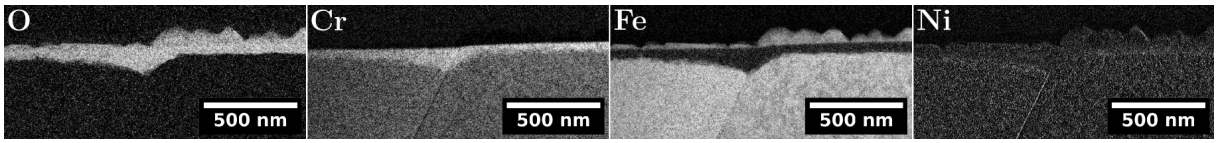

Figure 4.15: *EFTEM mapping of oxygen, chromium, iron and nickel on the 1.5 dpa IRR sample oxidised 24 hours*

4.1.3.3 EELS and EDXS quantitative analyses

As suggested from EFTEM qualitative mapping, EELS and EDXS analyses performed highlighted that the same kind of oxide layers are formed on **IRR** samples as on **UNIRR** ones for both 1 hour and 24 hours oxidation. The outer oxide layer is an iron-rich oxide with chromium, iron and nickel while the inner oxide is a iron, chromium, nickel oxide. However, EELS analysis after 1 hour oxidation revealed that the inner oxide layer is richer in chromium on the 1 dpa **IRR** sample than on the **UNIRR** one (for a [100] grain orientation) ($(\frac{Cr}{Cr+Fe+Ni})_{UNIRR} \sim$ 0.30–0.38 against $(\frac{Cr}{Cr+Fe+Ni})_{IRR} \sim$ 0.37–0.50 for EDXS and EELS analysis respectively). EDXS and EELS quantitative linescans were acquired on both [100] and [111] orientation on the 1 and 1.5 dpa **IRR** samples oxidised 24 hours but only EELS profiles are introduced in Figure 4.16. Results from quantification of the inner oxide layers and comparison to the **UNIRR** sample are presented in Table 4.3 for specimens oxidised 24 hours. From the quantitative analyses performed the inner oxide layer, its composition can be narrowed down to $(Ni_xFe_{1-x})(Cr_yFe_{1-y})_2O_4$ with $0.6 \geq x \geq 0.3$ and $0.9 \geq y \geq 0.65$. A higher amount of chromium is present onto the inner oxide

scales formed on **IRR** specimen as seen from the $\frac{Cr}{Cr+Fe+Ni}$ ratios introduced in Table 4.3. Several authors also reported oxides richer in chromium on irradiated samples [4, 5, 7]. Irradiation defects are believed to enhance metallic cation diffusion inducing the formation of oxides richer in chromium [4, 5, 7]. The formation of inner oxide layer richer in chromium is likely to be, at least partially, responsible for the shifts observed previously in the Raman spectra. Oxides richer in chromium are supposed to be more protective and slow down the oxidation kinetic [5, 27]. Nevertheless, thicker oxides are established on **IRR** specimens, thereby indicating that the primarily process responsible for the oxygen diffusion is the contribution of porosities as faster diffusion pathways and not the chromium content. Moreover, as on **UNIRR** samples, the chromium content is higher on [111] grain orientation. It indicates that the oxidation mechanism depending upon the underlying metal grain is not modified by irradiation. In addition, nickel enrichment at the metal oxide interface was also highlighted in the profiles. This enrichment varied between 18 and 27 at. %.

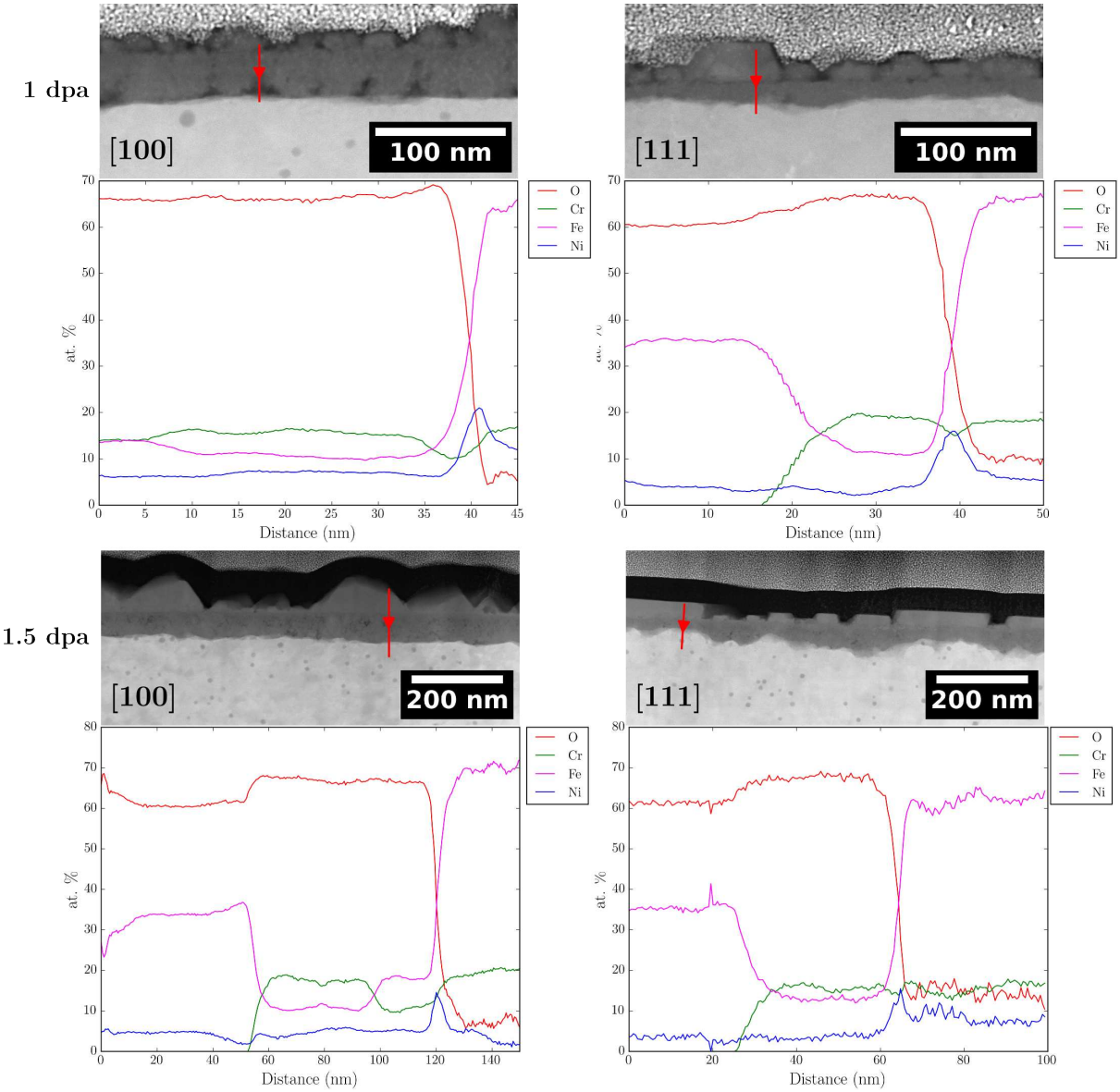

Figure 4.16: *STEM images and associated EELS quantitative linescans on the 1 and 1.5 dpa IRR samples oxidised 24 hours on both [100] and [111] grain orientations*

Table 4.3: *EDXS and EELS quantitative analyses of the inner oxides formed on [100] and [111] grain orientations on the UNIRR, 1 dpa and 1.5 dpa IRR samples oxidised 24 hours*

Grain orientation	Method	Analysed sample	O (at. %)	Cr (at. %)	Fe (at. %)	Ni (at. %)	$\frac{Cr}{Cr+Fe+Ni}$	AB_2O_4
[100]	EELS	UNIRR	71	14	12	3	-	-
		1 dpa IRR	66	16	11	7	-	-
		1.5 dpa IRR	64	17	12	7	-	-
	EELS	UNIRR	-	50	36	14	0.50	$Fe_{1.1}Cr_{1.5}Ni_{0.4}O_4$
		1 dpa IRR	-	49	32	19	0.49	$Fe_{0.9}Cr_{1.5}Ni_{0.6}O_4$
		1.5 dpa IRR	-	56	27	17	0.56	$Fe_{0.9}Cr_{1.7}Ni_{0.4}O_4$
	EDXS	UNIRR	-	44	37	19	0.44	$Fe_{1.1}Cr_{1.3}Ni_{0.6}O_4$
		1 dpa IRR	-	-	-	-	-	-
		1.5 dpa IRR	-	49	33	18	0.49	$Fe_{1.0}Cr_{1.5}Ni_{0.5}O_4$
[111]	EELS	UNIRR	67	17	12	4	-	-
		1 dpa IRR	65	20	11	4	-	-
		1.5 dpa IRR	66	16	14	4	-	-
	EELS	UNIRR	-	53	34	13	0.53	$Fe_{1.0}Cr_{1.6}Ni_{0.4}O_4$
		1 dpa IRR	-	56	31	13	0.56	$Fe_{0.9}Cr_{1.7}Ni_{0.4}O_4$
		1.5 dpa IRR	-	61	28	11	0.61	$Fe_{0.9}Cr_{1.8}Ni_{0.3}O_4$
	EDXS	UNIRR	-	47	37	16	0.47	$Fe_{1.1}Cr_{1.4}Ni_{0.5}O_4$
		1 dpa IRR	-	50	35	15	0.50	$Fe_{1.0}Cr_{1.5}Ni_{0.5}O_4$
		1.5 dpa IRR	-	51	37	12	0.51	$Fe_{1.1}Cr_{1.5}Ni_{0.4}O_4$

The EELS and EDXS linescans highlight two different areas in the inner oxide layer of the 1.5 dpa **IRR** sample on [100] grain orientation (Figure 4.16). The first one is richer in chromium while, underneath and close to the metal/oxide interface, the inner layer is richer in iron. The chromium and iron contents are reversed in the latter. One should note that such duplex character of the inner oxide layer was only observed on the sample irradiated with the highest studied irradiation dose and therefore irradiation is, in all likelihood, responsible for this phenomenon. As the lower part of the inner oxide is poorer in chromium, it indicates that this layer is less protective that the outer part. These oxides are likely to have different properties with respect to the anionic transport within the oxide. Such duplex character of the inner layer was already observed by Dumerval on irradiated specimens [5] but she reported an iron-rich part of the inner oxide located on top of the chromium-rich region. Only small regions exhibited this duplex behaviour while on the major part of the inner oxide layer a chromium-rich oxide is established. The observation of two sublayers in the inner oxide cannot be yet fully explained. Nevertheless, a higher density of segregated defects (depleted in chromium) initially present in the observed iron-rich areas could be responsible for this oxidation behaviour and play a role on the properties of the oxide formed.

Figure 4.17 introduces the EDXS maps acquired near the metal/oxide interface. This mapping was carried out on an area where a Frank loop lied at the interface. As previously shown in Chapter 2 section 2.3.2.1 the Frank loop is Ni/Si segregated. However, the extremity of the loop at the metal oxide interface is not as silicon enriched as the other loop tip[1]. It seems to indicate that silicon left the loop tip and is diluted into the surrounding substrate or into the medium. No narrow oxygen penetration is observed toward the loop and iron still has a M-shaped profile at the metal/oxide interface. Hence, no obvious preferential oxidation is evidenced around the loop. It therefore suggests that, apart from the Si dissolution, segregation around irradiation defects is not destabilised by the oxidation front and the oxidation process.

[1]This more pronounced segregation results from the higher volume of segregated loop in the foil depth since the loop is analysed edge-on.

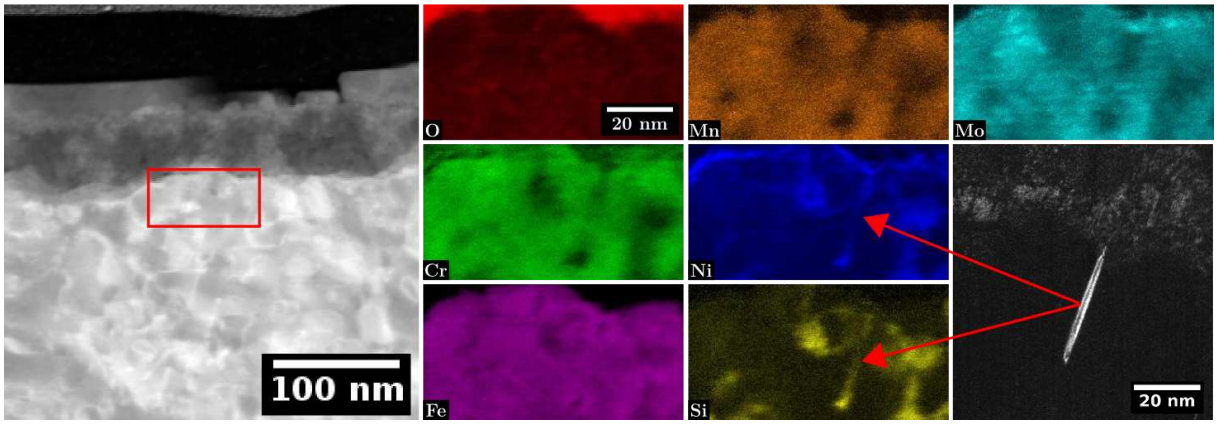

Figure 4.17: *STEM HAADF image and associated EDXS quantitative maps on the 1.5 dpa IRR sample oxidised 24 hours near the metal/oxide interface and the DF image associated with the Frank loop detected*

4.1.3.4 Effect of irradiation on the oxides chemical composition: Summary

As on **UNIRR** samples, the outer oxide formed on **IRR** specimens is iron-rich and the inner oxide is chromium-rich. Moreover, Ni enrichment is present at the metal/oxide interface. From the quantitative analyses performed the inner oxide layer, its composition can be narrowed down to $(Ni_xFe_{1-x})(Cr_yFe_{1-y})_2O_4$ with $0.6 \geq x \geq 0.3$ and $0.9 \geq y \geq 0.65$ and was always found richer in chromium on the **IRR** samples. The high concentration of defects engendered by irradiation at the metal/oxide interface, such as vacancies, is thought to promote cation diffusion toward the metal/oxide interface inducing the formation of oxides richer in chromium. Even if oxygen diffusion through the inner layer is slower for Cr-rich oxides [5, 27], thicker oxides are observed on **IRR** specimens. Therefore, porosities in the inner layers are responsible for the enhanced diffusion in **IRR** specimens and promote the growth of the inner oxide layer. In addition, a few scarce inner oxide areas presented a duplex character with an outer part chromium-rich and an inner part iron-rich. This could arise from the initial presence of an higher density of segregated defects (depleted in chromium) in the observed iron-rich areas that could affect the oxides formed. Irradiation defects close to the metal/oxide were not found preferentially oxidised but silicon was depleted at the oxidation front. Moreover, as on **UNIRR** samples, the chromium content is higher on [111] grain orientation hence confirming that irradiation did not affect the oxidation mechanism depending on the crystallographic orientation of the underlying metal grain.

Main effects of irradiation on the oxides chemical composition:

- Inner oxides are richer in chromium on the irradiated specimens and this chromium content increases with increasing irradiation dose. Irradiation defects are believed to accelerate diffusion.
- A few scarce inner oxide areas present a duplex character and are believed to be resulting from a higher density of irradiation defects in these regions.
- Segregated irradiated defects do not show evidence any obvious preferential oxidation but silicon was dissoved at the oxidation front.

4.1.4 Study of the intergranular oxidation on grain boundaries affected by RIS

Since the grain boundary of irradiated 316L is known to be subjected to Radiation Induced Segregation, this local chemical modification could modify the grain boundary oxidation. Chromium depleted grain boundaries might be especially more sensitive to intergranular oxida-

tion. The morphology and chemistry of the oxide penetration at grain boundaries were therefore studied on **IRR** specimens and compared to **UNIRR** ones for samples oxidised 1 hour and 24 hours. To do so, in the following are presented TEM and STEM imaging of the grain boundary oxidation as well as EDXS and EELS analyses of the oxide penetration.

4.1.4.1 Morphological description

A different behaviour is observed with regards to the oxide penetration at grain boundaries in both **UNIRR** and **IRR** samples. Grain boundaries analysed were, each time, Random High Angle Grain Boundary (RHAGB) and therefore were susceptible to RIS as presented in Chapter 2 section 2.3.2.2. Grain boundary oxidation was found much wider and deeper on **IRR** samples (both 1 and 1.5 dpa) than on **UNIRR** samples (Figures 4.18, 4.19 and 4.20). Measurement of the oxide penetration depths are reported in Table 4.4. Promoted intergranular corrosion by irradiation was already observed by a few authors [6, 8, 9]. After 1 hour oxidation, the oxide penetration is twice as deep in the **IRR** specimens than in the **UNIRR** one (43 ± 2 nm vs ∼ 21 ±).

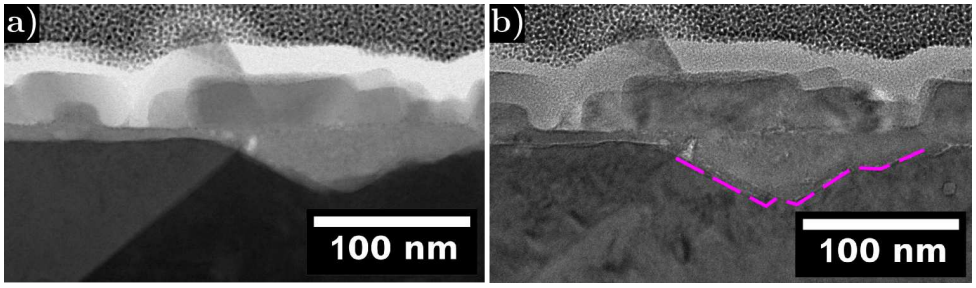

Figure 4.18: *TEM images on the grain boundary oxidation of the 1 dpa IRR sample oxidised 1 hour a) STEM BF image b) under-focus BF image*

Similarly, after 24 hours oxidation the oxide penetrations are ∼ 2-3 times deeper on **IRR** specimens than on the **UNIRR** sample (Table 4.4). The chromium depletion at grain boundaries induced by irradiation might sensitise the grain boundaries and promote deeper intergranular oxide penetration. Moreover, numerous porosities were observed in the oxide penetrations and could act as diffusion short-cuts by providing interconnections between the medium and oxide. (Figures 4.18, 4.19 and 4.20). Even if the grain boundary oxide penetration is wider and porous, it remains asymmetric as on the **UNIRR** specimen (Figures 4.18, 4.19 and 4.20). The oxide penetration is more pronounced on one side of the grain boundary and should relate to the grain boundary plane orientation affinity to be oxidised. Moreover, by drawing the metal/oxide interface (in magenta in Figures 4.18, 4.19 and 4.20), it appears that the oxide penetration is faceted and that the oxidation front progresses perpendicularly to specific crystallographic planes.

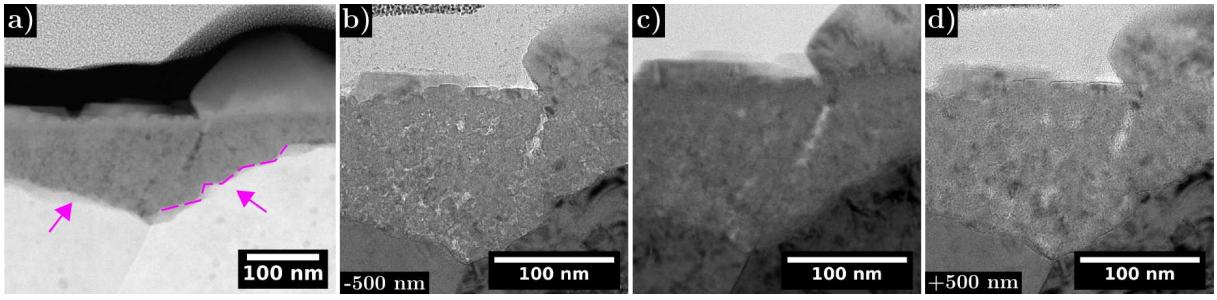

Figure 4.19: *TEM images of the grain boundary oxidation on the 1.5 dpa IRR sample oxidised 24 hours a) STEM image b) BF under-focus, c) BF focus and d) BF over-focus*

Table 4.4: *Grain boundary oxide penetration depth depending on the sample and oxidation duration*

	1 hour	24 hours
UNIRR	21 ± 2 nm	42 ± 2 nm
1 dpa IRR	43 ± 2 nm	111 ± 2 nm
1.5 dpa IRR	-	141 ± 2 nm

As imaged in Figure 4.20, the outer part of the oxide penetration formed at grain boundary on the 1 dpa **IRR** sample is on zone axis (shown by the blue arrows) while the inner and deeper part appears to be off-axis (shown by the green arrows). The on-axis regions correspond to the inner oxide layers that share the epitaxial orientation relationship with the substrate while the other ones are the oxide penetration areas in which are observed the porosities. An HRTEM image and associated FFT on both the on-axis (framed in blue) and off-axis (framed in green) areas are reported in Figure 4.20 c. The on-axis area is indeed epitaxially grown onto the underlying metal grain while a loss of epitaxy is observed in the off-axis area. Therefore, not the whole oxide penetration at grain boundary share a proper epitaxial orientation relationship with the substrate. The underlying off-axis region is likely to be severely strained and the presence of numerous defects, as these big porosities, might be responsible for this local epitaxy loss. These observations confirm that the grain boundary oxidation process unfold in two steps. First, an epitaxially grown surface oxide is formed on the surface of the grain boundary and then, the grain boundary acting as a diffusion short-cut is oxidised preferentially. The oxidation progresses along specific directions hinging on the grain boundary plane and the intragranular oxide is porous, highly strained and hence slightly off-axis.

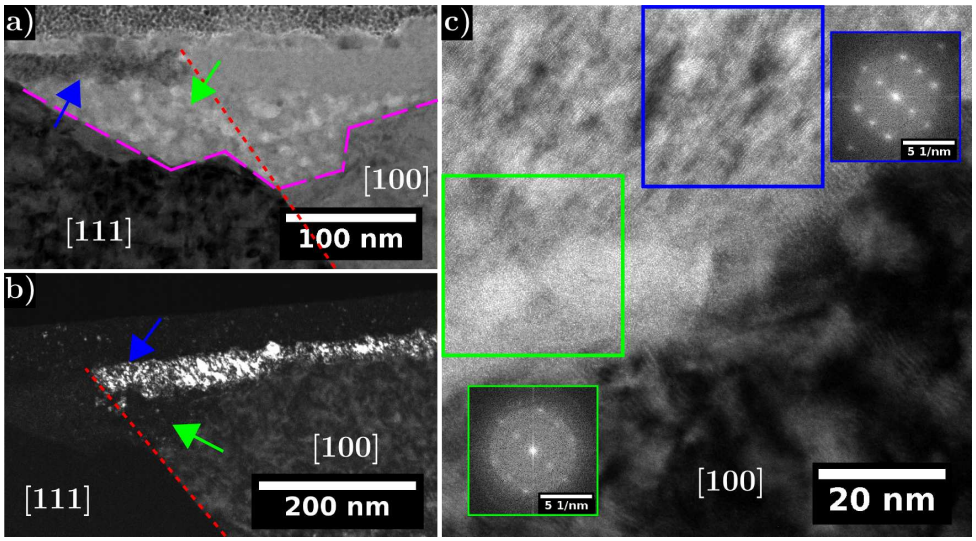

Figure 4.20: *TEM images of the grain boundary oxidation on the 1 dpa IRR sample oxidised 24 hours a) BF image with the [111] grain in [110] zone axis b) DF image with the [100] grain in [114] zone axis and c) HRTEM image on the [100] grain in [112] zone axis and associated FFT on the on zone axis and off-axis areas framed in red and blue respectively (red dashed line: grain boundary, green arrow: off-axis area, blue arrow: on-axis area)*

4.1.4.2 Chemical analysis

The composition of the oxide penetration on the 1.5 dpa **IRR** sample was investigated using EDXS and EELS quantitative mapping but solely the EDXS maps are reported in Figure 4.21. The mapped region is indicated by the red framed area in the STEM image. The grain boundary RIS is clearly visible below the oxide penetration. Quantifications performed on the grain boundary oxidation (in the area framed in white in Figure 4.21) are reported in Table 4.5. Comparing the composition of this intragranular oxide penetration to the one on the **UNIRR**

sample it appears that it is much less chromium-rich but contain more nickel. The oxide formed at grain boundary on the 1.5 dpa **IRR** sample is likely to be a spinel written $Fe_{0.8}Cr_{1.9}Ni_{0.3}O_4$ and not of corundum structure as it was the case on the **UNIRR** sample. Since RIS at grain boundaries engender a chromium depletion and a nickel enrichment, it would explain that the oxide formed is less chromium-rich while enriched in nickel. Nevertheless, as on the **UNIRR** specimen, the intragranular oxidation is richer in chromium than the surface oxide.

When comparing the intergranular nickel, silicon and phosphorus RIS at the oxidation front, it appears that the Si and P contents progressively decrease going from the intergranular RIS ($\sim$ 10 and 3 at. % respectively) toward the oxidation front over 10 nm whereas the Ni tends to accumulate reaching $\sim$ 50 at. % at the tip of the oxide penetration. The nickel content then decreases to attein its average RIS content. These observations suggest that Si and P are preferentially dissolved into the medium while Ni preferentially concentrates at the tip of the oxide penetration without being included into the oxide. This behaviour is analogous to the one observed for the loop lying at the metal/oxide interface as Si was also found to be sucked probably into the medium (cf. 4.1.3.3).

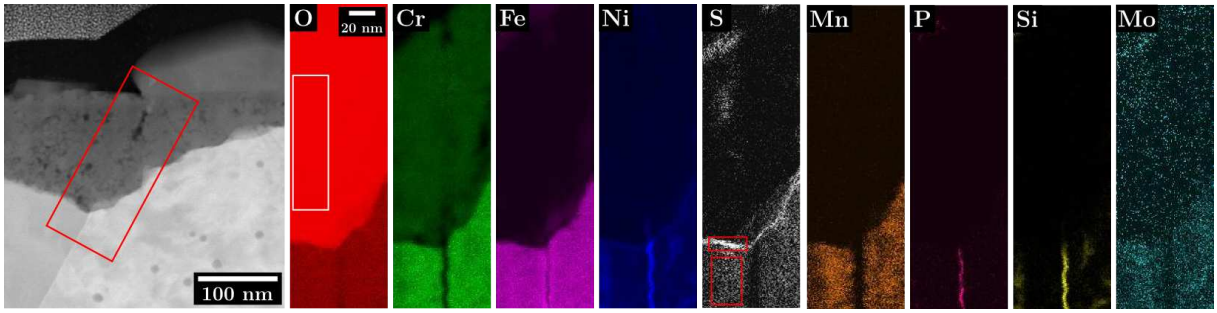

Figure 4.21: *STEM images and associated quantitative EDXS maps of the grain boundary oxidation on the 1.5 dpa IRR sample oxidised 24 hours*

Table 4.5: *EDXS and EELS quantitative analyses of the grain boundary oxidation framed in white in the previous mapping on the 1.5 dpa IRR sample oxidised 24 hours*

Method	O (at. %)	Cr (at. %)	Fe (at. %)	Ni (at. %)
EELS	64	20	11	5
EELS	-	59	27	14
EDXS	-	61	27	12

Moreover, the analysis evidenced a sulphur enrichment at the metal/oxide interface. To confirm its presence, two EDXS spectra were extracted, one from the matrix and the other on the believed S-enriched region (Figure 4.22). As the S-Kα line is really close to the Mo-Lα line, the spectra were normalised on the Mo-Kα line and attention was paid on the relative intensity of the overall S-Kα and Mo-Kα line. Thereby, the overall increase of the intensity of the line seen in Figure 4.22 indicates that sulphur is indeed present and hence genuinely detected at the metal/oxide interface. A few other authors evidenced sulphur at the metal/oxide interface [187, 188]. As in our case, even if the lamella was extracted away from any visible inclusion, as they were shown to affect the outer oxide (cf. Chapter 3 section 3.4), sulphur is believed to come from the dissolution of a nearby MnS inclusion.

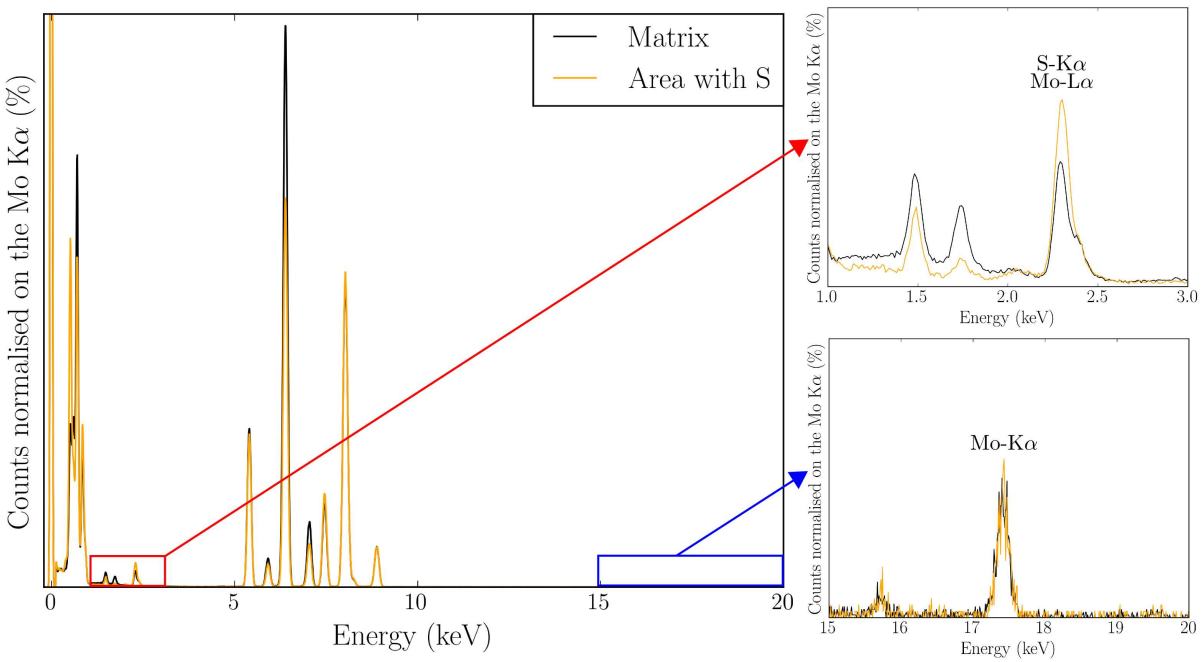

Figure 4.22: *EDXS spectra extracted from the areas framed in red in the previous quantitative mapping of the grain boundary oxidation on the 1.5 dpa IRR sample oxidised 24 hours*

4.1.4.3 Irradiation effect on the grain boundaries oxidation: Summary

The oxide penetration at the grain boundary in **IRR** specimens is much deeper and wider and contain numerous porosities. It is a spinel chromium-rich, iron, nickel oxide ($Fe_{0.8}Cr_{1.9}Ni_{0.3}O_4$) richer in chromium than the surface oxide. The segregation at grain boundaries induced by irradiation and hence local composition changes are thought to be responsible for the grain boundary preferential oxidation and the formation of an oxide less chromium-rich while richer in nickel compared to intragranular oxides at unirradiated grain boundaries. The presence of porosities and strains induce a local loss of epitaxy of the inner oxide. These could lead to oxide failure and cracking at grain boundaries. In addition, the intragranular oxide grow from the boundary toward the alloy along specific directions. The asymmetric oxidation of grain boundaries is enhanced on **IRR** samples as the overall oxidation kinetic is promoted. Silicon and phosphorus are assumed to be dissolved into the medium since their enrichment from RIS at grain boundary gradually increases over 10 nm after the oxidation front whereas nickel is enriched probably due to its rejection from the oxide therefore increasing its already high content due to RIS at the tip of the oxide penetration. The observation of sulphur at the oxide flanks is believed to result from the dissolution of a nearby MnS inclusion.

Main effects of irradiation on the grain boundaries oxidation: RIS promotes the intragranular oxidation and induces the formation of porous intragranular oxides less chromium-rich. Ni is further enriched at the oxide penetration tip while Si and P are thought to be dissolved into the medium.

4.1.5 Oxides formed on proton pre-irradiated samples: Synthesis, discussion and oxidation mechanism

This part summarises the results on the effects of a proton pre-irradiation on the oxides formed in PWR medium while taking into account the crystallographic orientation of the underlying metal grains. The set of results presented above revealed several effects of irradiation defects on the oxide layers formed on austenitic stainless steel exposed to primary water. The overall

oxidation mechanism on irradiated materials proposed is presented in Figure 4.23 and compared to the oxidation occurring on unirradiated materials.

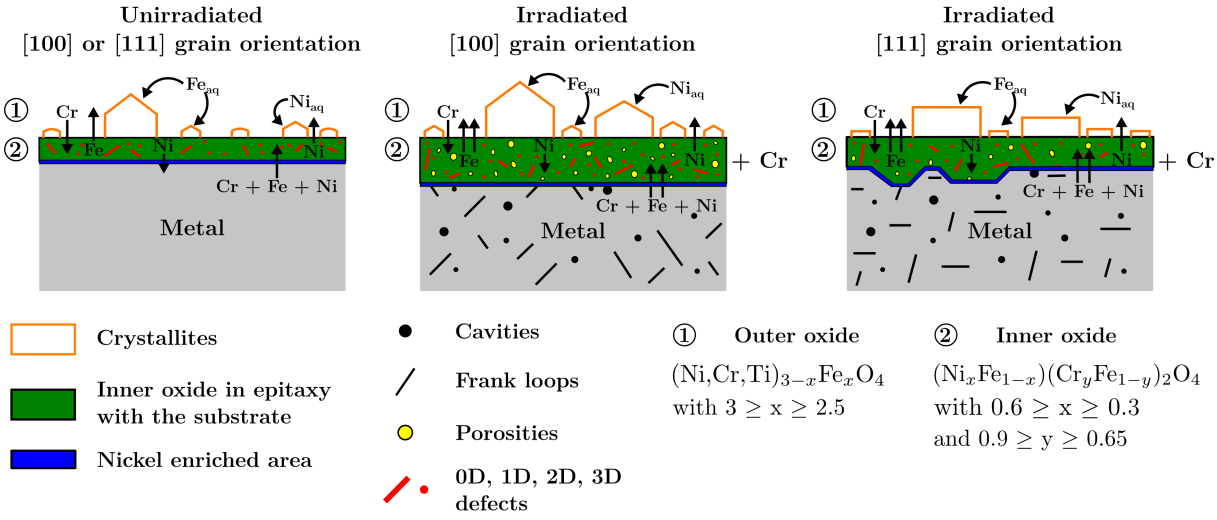

Figure 4.23: *Schematic of the oxidation mechanism of unirradiated and irradiated 316L austenitic stainless steel exposed to PWR medium during short time oxidations*

Below 1 dpa, the irradiation dose was not found high enough to induce any noticeable change into the oxide layers. However, an evolution of the morphology, the thickness and the composition of the oxides was noticed above 1 dpa. The duplex character of the oxide layer, as expected from the literature [4–9], was not observed to be modified. It was shown that irradiation does not modify the crystallographic structure of the oxide layers (both oxides are of spinel structure) as reported by other authors [4–9]. In addition, the outer crystallites possess the favoured crystallites morphologies contingent on the underlying metal grain orientation and the inner layer share a cube/cube epitaxial orientation relationship with the substrate. This oxide layer is however heavily strained and contains a high density of defects. This entails that the presence of irradiation defects near the metal/oxide interface did not disturb the establishment of the epitaxial relationship nor the oxide epitaxial growth. Since thinner oxides richer in chromium are formed on [111] grain orientation, as on the **UNIRR** specimens, it means that the crystallographic orientation of the underlying metal grain still controls the oxidation kinetic on irradiated materials. As more crystallites with the favoured crystallites morphology are present on **IRR** samples it means that a higher volume of inner oxide share a proper epitaxial relationship with the substrate allowing the growth of crystallites with the favoured morphology. Hence, the establishment of the crystallographic orientation relationship is likely to be accelerated by irradiation.

The initial microstructure was found to play a role in the germination and growth of crystallites since changes in size and density of crystallites were observed. On **IRR** samples, the crystallite density is higher while they are bigger even after 5 minutes oxidation. These findings reveal an effect of irradiation on both the crystallites density and size. Indeed, the evolution of the crystallite density is related to germination processes whereas their change of size is due to growth phenomena. This entails that irradiation enhances both the crystallite nucleation and growth. This is contrary to observations made thus far by other authors [4, 5, 7] who observed smaller crystallites on irradiated material. However, Fukuya et al. and Deng et al. observed a higher number and size of the oxide particles as the irradiation dose increase [6, 8] which is in accordance with the obtained results. Irradiation defects such as Frank loops are believed to act as preferential nucleation sites for the outer oxide nucleation during the oxidation first steps inducing a higher number of crystallites. As the outer layer is formed by cationic diffusion within the inner layer and a dissolution/repecipitation process [21, 50], it suggests that cation diffusion

is enhanced in the inner layers formed on **IRR** specimens.

Irradiation was found to promote the oxidation kinetic and thicker oxides are formed on **IRR** samples. In addition, an increase of the irradiation dose was found to enhance the oxidation kinetic and the oxide layers growth. This is coherent with several authors' results [6–9], but in disagreement with Perrin and Dumerval ones [4, 5]. As thicker oxides are formed, inward diffusion of oxygen responsible for the inner layer growth is promoted on irradiated materials. This enhanced diffusion should result from the high concentration of defects (point defects, dislocations, porosities, etc.) in the oxide scale [50]. Porous inner oxide layers were formed on **IRR** samples whereas none were evidenced in **UNIRR** samples. These porosities act as diffusion short-cuts promoting diffusion and the oxide growth by providing fast diffusion paths and interconnection between the medium and inner oxide/alloy surface. Therefore, as thicker and porous are formed on irradiated samples the inner oxide layers are less protectives than the ones formed on **UNIRR** samples. The inner oxide layers formed on the **IRR** samples are found richer in chromium than the ones formed on **UNIRR** specimens. The oxidation is, in all likelihood, disrupted by the high concentration of defects at the metal/oxide interface. Vacancies induced by irradiation or more generally displacement of atoms from their lattice should result in enhanced point defect concentration in the alloy that could be responsible for the faster diffusion of metal cations toward the metal/oxide interface. Such behaviour was already reported by several authors [4, 5, 7]. Oxides richer in chromium are supposed to be more protective and oxygen diffusion is slower through chromium-rich oxides [5, 27]. However, as previously stated, thicker oxides richer in chromium were observed on **IRR** specimens. Although it may seem appealing to correlate the protectiveness of inner layer to the chromium content, the observation of thick oxides Cr-rich on irradiated samples hints that caution must be exercised. The porosities observed in the inner oxide layers are believed responsible for this promoted oxygen diffusion and these fast diffusing paths would overstep the slower oxygen diffusion in Cr-rich oxides. Since we previously demonstrated that dislocations and stresses induced by mechanical polishing prior to the oxidation test could affect the oxides nucleation and growth (cf. Chapter 3 section 3.3) we can assume that differences of results in the open literature regarding the oxide scales formed on irradiated materials are partially explained by this phenomenon.

At the higher irradiation dose studied (1.5 dpa), a duplex character of the inner oxide layer was highlighted. Such behaviour was not observed on the whole oxide scale but only in some scarce areas. In these regions, the outer part of the inner oxide layer is chromium-rich while the inner part is iron-rich. Such inner region will be less protective as it is less chromium-rich. A higher density of segregated defects (depleted in chromium) initially present in the observed iron-rich areas could be responsible for this oxidation behaviour. Indeed, the substrate below the oxidation front will thereby be locally depleted in chromium and thus an iron-rich oxide will be formed.

Frank loops and cavities were not found preferentially oxidised and remained segregated at the oxidation front but Si appeared to be sucked from the loop tip and is assumed dissolved into the medium. Nevertheless, the presence of Frank loops near the metal/oxide interface is thought to affect the oxidation. Indeed, on [111] grain orientation, intragranular oxides penetrations are observed while none were evidenced on the other orientations. Since this was observed only on **IRR** specimens and since on this given orientation one family of Frank loops is parallel to the initial alloy surface, these loops are thought responsible for the observed intragranular oxide penetration. More generally, as the oxidation front progress, it will encounter Frank loops, and depending upon the inclination of the latter with regards to the metal/oxide interface, it will affect more or less the oxidation kinetic. It is believed that the more the loops are parallel to the initial substrate surface, the more they will affect the oxidation kinetic. If these loops

promote the oxidation kinetic a preferential oxidation of the loops will occur whereas if they delay the oxidation kinetic the oxide will preferentially progress around the loop. Previous work showed that a model alloy whose composition aimed to emulate the intergranular RIS content was much less oxidised than a 316L alloy (both exposed in simulated PWR medium during a short duration) [189]. As the segregation on the loops is analogous to that at grain boundaries (cf. Chapter 2 section 2.3.2.2) is it likely that these will delay the oxidation. When reaching such defect, the oxide growth will progress along preferential crystallographic directions (<112> for [111] grain orientation). This preferential growth of the intragranular oxide along specific directions can be related to the oxidation kinetic controlling the inner oxide thickness of the surface oxides according to the underlying metal grain orientation. Thus, this intragranular oxidation behaviour is comparable to the outer oxide growth. As, at crack tips, the oxidation and therefore crack propagation are contingent on the grain boundary plane orientation affinity to be oxidised, this preferential oxidation with regards to the loop inclination should be further studied.

While intergranular corrosion occurred at the grain boundary in both the **UNIRR** and **IRR** specimens, the oxide penetration is deeper and wider for the **IRR** samples. Deeper oxide penetration on irradiated materials were already reported by a few authors [6, 8, 9]. This suggests a promoted intergranular corrosion by irradiation. Moreover, a lower chromium content was evidenced on **IRR** intergranular oxide penetration compared to the **UNIRR** one indicating that this oxide is less protective on **IRR** samples. As grain boundary RIS occurs on most grain boundaries and especially on Random High Angle Grain Boundary (RHAGB) as the ones observed previously, RIS is likely to be responsible for this preferential oxidation. In particular, the low chromium content at grain boundaries induced by RIS is thought to increase the grain boundary sensitivity, resulting in higher corrosion susceptibility. Indeed, Terachi et al. [27] reported that the oxidation kinetic is linked to the chromium content in the alloy. The less chromium in the alloy, the more oxidation is promoted. Although, surface and grain boundary oxidations differ, it is likely that a preferential oxidation would occur at RIS Cr-depleted grain boundaries. In addition, the RIS was found affected by the oxidation front. Si and P contents were found gradually decreasing toward the oxide penetration hinting that both are sucked from the grain boundary and dissolved into the medium as already observed on the loop lying at the metal/oxide interface. Nickel, however was found preferentially segregated at the oxide tip. It is thought to accumulate ahead of the oxide front due to its rejection from the oxide thereby increasing the nickel content from $\sim$ 30 to 50 at. % in the oxide penetration tip near region. As RIS occurring at grain boundaries is dependent on the nature of the grain boundary (cf. Chapter 1 section 1.2.3.3), we can assume that grain boundaries less affected by RIS will present narrower and shorter oxide penetration closer to the ones evidenced on the **UNIRR** specimens. In addition, a surface oxide in epitaxy with the substrate is formed in the oxidation first steps while the intergranular oxide penetration is porous, highly strained and slightly off-axis. The grain boundary acting as a diffusion short-cut is preferentially oxidised and then the grain boundary planes are oxidised along specific crystallographic directions inducing the formation of facets. This behaviour can be related to the surface oxidation contingent on the underlying metal grain as well as the intragranular oxidation along specific crystallographic planes observed on the [111] grain orientation on **IRR** samples. Moreover, the presence of numerous porosities in the oxide penetration, as observed, could impair the grain boundary resistance and provide preferential cracking site. In a nutshell, the chemical composition changes at grain boundaries induced by RIS affect the oxidation and overall SCC resistance. Since grain boundary nature can play a role on the oxide penetration morphology, depth etc, several grain boundaries of different natures should further be investigated.

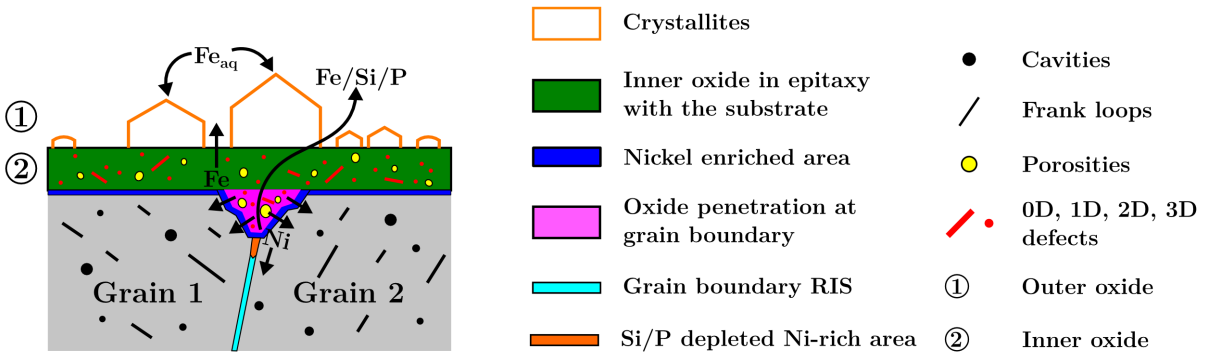

Figure 4.24: *Schematic of the oxidation mechanism of the grain boundary oxidation of an irradiated 316L austenitic stainless steel exposed to PWR medium during short time oxidations*

Main conclusions on the effect of irradiation on the oxidation: Irradiation promotes the overall oxidation kinetic and is dose dependent.

- Porosities act as diffusion short-cuts and are responsible for the enhanced growth of the oxide layers on irradiated specimens.
- The higher concentration of point defects near the metal/oxide interface are thought to promote chromium diffusion inducing the formation of oxides richer in chromium.
- A duplex character of the inner layer was evidenced and the observation of an oxide iron-rich is believed to result from the oxidation of a area with numerous chromium depleted defects.
- Frank loops and cavities did not appear preferentially oxidised but Si was observed sucked from the loop tip at the oxidation front. The loop relative inclination with regards to the oxidised surface is believed to play a delaying role in the oxidation process.
- RIS is accounted responsible for the promoted intergranular oxidation. The observed porosities in the oxide penetration could act as preferential cracking sites.
- RIS was found affected by the oxidation front. Si and P are dissolved into the medium while rejected Ni is enriched at the oxide penetration tip.

4.2 Study of the Irradiation Assisted Corrosion

In PWR reactors, the oxidation occurring at the crack tips, as the crack propagates, can be related to an oxidation under neutron flux on an already irradiated material. Therefore, to better understand the oxidation at crack tips, it is necessary to look upon the contribution of the simultaneous oxidation and irradiation processes. In order to investigate the influence of the irradiation flux on the oxidation process, a sample was proton pre-irradiated on half of its surface and then oxidised under proton flux on an even smaller area at the Michigan Ion Beam Laboratory (MIBL) of the University of Michigan (details on the sample can be found in Chapter 2 section 2.2.2). This sample was oxidised during 24 hours. It allowed to investigate the Irradiation Assisted Corrosion (IAC) phenomenon by comparing the oxides formed on the three areas (**IACUNIRR**, **IACIRR** and **IACIAC**). Such comparison among themselves will help to conclude on the irradiation effect and oxidation under proton flux on the oxide scales. The next paragraphs describe the oxide layers investigated regarding the oxide morphology, structure and composition as well as the oxides formed at grain boundaries. These results will also be compared to similar works done on the same device and to the oxides formed on the Titane samples. One

should remember that the medium in which was immersed the sample did not contain any boron or lithium and thus the $pH_{320°C}$ is of 6.2. Moreover, the stainless steel material of the loop is susceptible to lead to dissolution/redeposition phenomena.

4.2.1 Characterisation of the oxides formed on the IACUNIRR area

First and foremost, the oxides formed on the **IACUNIRR** area were investigated. Their morphologies, thicknesses and compositions were looked upon and compared to those of the oxide formed on Titane samples oxidised in a titanium loop with a slightly higher pH (pH_{IAC} = 6.2 vs. pH_{Titane} = 7.3).

4.2.1.1 Description of the oxides morphology and thickness

Optical images on the **IACUNIRR** area of the Michigan sample evidenced a heavy oxidation of the sample as the blue colour indicates (Figure 4.25). The oxide is supposed thick and uniform on almost all the sample surface since the underlying grain can rarely be distinguished. However, a different oxidation behaviour on top of grain oriented close to [111] can be seen. Indeed, big triangular crystallites are observed and the outer oxide coverage is much lower than on the rest of the orientations. Outside of [111] grain orientations big crystallites seem to cover the whole surface. The crystallographic orientation therefore played a role in the oxidation.

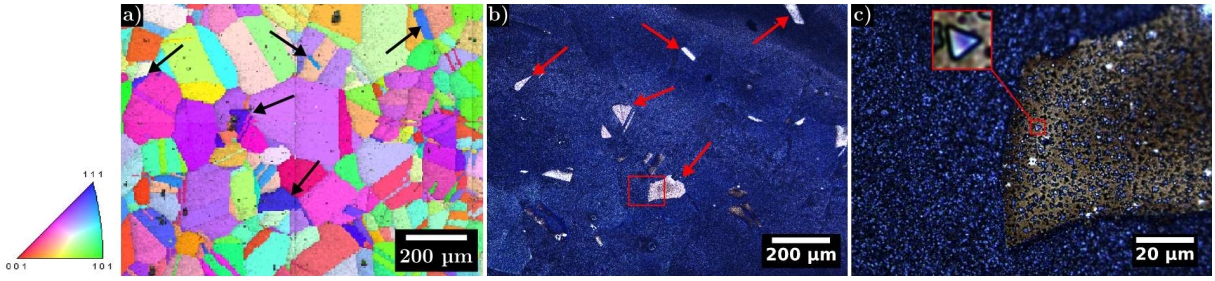

Figure 4.25: *Optical images of the oxide formed on the IACUNIRR area of the Michigan sample a) associated EBSD map b) overall oxide and c) zoom on a [111] grain orientation on the previously red framed area*

SEM images in the **IACUNIRR** area revealed the presence of large crystallites (sizes between 200 nm and 2 µm) as well as nucleis of several tens of nm (Figure 4.26). The outer oxide formed is clearly much bigger (sometimes up to 15 – 20 times bigger) than the one formed on Titane samples. The oxidation of the Michigan sample in a stainless steel loop is, in all likelihood, responsible for the observation of much bigger crystallites. Indeed, the medium is believed saturated in cations (especially iron) that will tend to precipitate and to participate to the outer oxide growth. As two crystallites families are present (small germs and big crystallites) it suggests that some crystallites are preferentially grown while germs remain small and are not suitable sites for the crystallite growth. These images highlighted a clear difference in the outer oxides morphology and coverage on the [111] grain orientation compared to [100] and [110] grain orientations. Apart of [111] grain orientation, no distinctions could be made between the outer oxide morphologies. Indeed, as seen in the optical images, the outer oxide formed on top of [111] grains is mostly composed of big and faceted triangular crystallites and small nucleis while coarse polygonal crystals with flat facets (and small nucleis) are formed on top of the other grains. Approximately 1 crystallite/µm^2 present the triangular morphologies on [111] grains and the outer oxide coverage is much lower on this given orientation. In addition, the outer oxide coverage is slightly higher on [110] grain orientation than on the [100] one. As much bigger crystallites are noticed on the other orientations, this suggests than it is less favourable to grow the outer crystallites formed on [111] grain orientation. This triangular shape of the outer crystallites observed on [111] grain orientation was already noticed on the Titane sample

(cf. Chapter 3 section 3.2.1.2) and is a proof that the inner oxide layer share a cube/cube epitaxial orientation relationship with the substrate and that the favoured crystallites also share an epitaxial relationship. As the expected favoured crystallite morphologies are not observed on the other two orientations, the inner layer might not be epitaxially grown or might be too highly strained or containing numerous defects/porosities inducing a loss of epitaxy at least for the outer oxide.

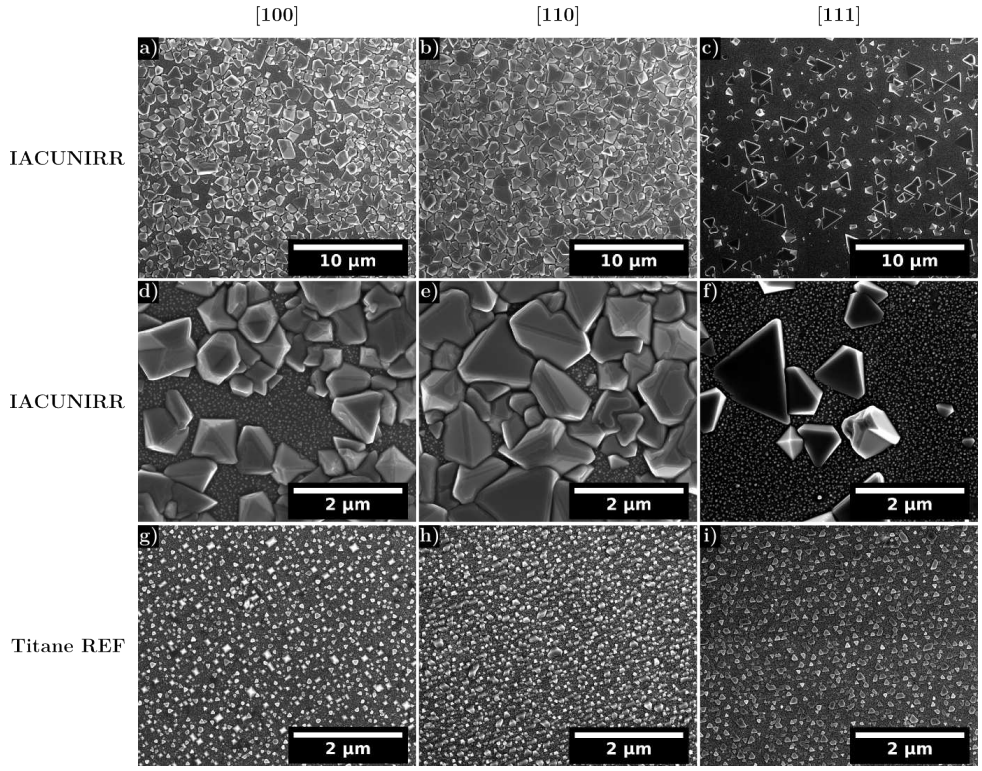

Figure 4.26: *SEM SE images (5 kV) of the outer crystallites formed on both the Titane REF sample and the IACUNIRR area of the Michigan sample*

A 5 kV BSE image acquired on a [111]/[100] grain boundary confirms that the coverage of the outer oxide is indeed much lower on the [111] grain orientation (Figure 4.27 a). It, moreover, appears that the inner oxide is thinner on this orientation since this area looks darker on the [100] grain orientation hinting that a thicker inner layer is formed. Cross section STEM imaging showing the duplex oxide layer formed on the **IACUNIRR** area is reported in Figure 4.27. This difference in inner oxide thicknesses depending on the crystallographic orientation was confirmed as the oxide is much thicker on [100] grain orientation than on the [111] one. However, the inner layer formed on [100] is extremely uneven, with thin oxide areas ($\sim$ 20 nm thick) and deep oxide penetration up to 425 nm. The mean oxide thickness is estimated at $\sim$ 152 $\pm$ 111 nm against 22 $\pm$ 15 nm on the [111] orientation. On this latest grain orientation, the inner oxide thickness ranged from 7 nm to 85 nm. Comparing these measurements to the ones made on samples oxidised at pH = 7.3 in the TITANE loop made of titanium ($\sim$ 10 nm thick), it clearly appears than the oxides are much thicker on the Michigan sample. This is agreement with a the literature data as thicker oxides are usually formed at lower pH [73, 74, 190]. Thereby, this preferential oxidation behaviour could arise from the lower pH of the media but also from the strain induced by the sample welding as both would accelerate the oxidation kinetic. Nonetheless, the observation of thicker oxides on [100] grain orientation is in agreement with the previous results on the Titane samples regarding the effect of the underlying grain on the oxidation kinetic (cf. Chapter 3 section 3.2). As thicker oxides are formed on the **IACUNIRR** area of the

Michigan samples, it reveals that oxygen diffusion is enhanced through these oxides. Porosities in the oxide layers were clearly evidenced on the oxide formed on [100] grain orientation (Figure 4.27 f) and fewer were also observed on [111] grain orientation (see Appendix F). On the thick oxide formed on [100] grain orientation the porosities form a channel from the outer surface to the metal/oxide interface. These could act as diffusion short-cuts for the oxygen diffusion and inner oxide layer growth. The lower pH of the medium is held accountable for the formation of a porous inner oxide layer. Furthermore, as noticed from SEM images, the outer oxide layer consists of faceted crystallites of size reaching as high as $\sim$ 500 nm on the [100] grain orientation and of small crystallites in between the bigger ones of sizes ranging from a few nm up to $\sim$ 30 nm. The big-faceted crystallites formed on the [111] grain orientation were found thinner ($\sim$ 80 – 120 nm) and very flat compared to the ones formed on the [100] grain (Figure 4.27 c and e).

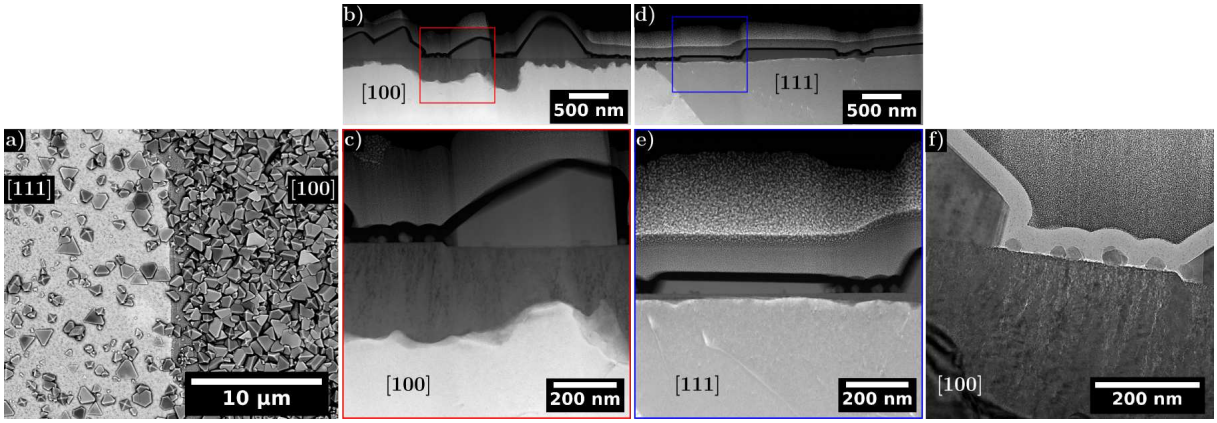

Figure 4.27: *Images on the IACUNIRR area of the Michigan sample a) SEM BSE image (5 kV) of a [111]/[100] grain boundary, b) c) d) and e) SEM STEM images on b) and c) a [100] grain orientation and d) and e) a [111] grain orientation and f) BF image under-focus revealing porosities in the inner oxide formed on [100] grain orientation*

4.2.1.2 Analysis of the oxides structure

Due to the sufficient thickness of the inner layer formed on [100] grain orientation, SAED patterns could be obtained solely on the inner layer. Even if the outer oxide morphology did not indicate that an epitaxial orientation relationship is formed between the oxide layer and the substrate, the SAED patterns revealed that the inner oxide scale is of spinel structure and is overall epitaxially grown with a cube/cube epitaxial relationship with the substrate (cf. Appendix F). Once again, only small regions are diffracting in DF indicating that the oxide is heavily strained. As most of the areas that were not in diffracting conditions were areas in which porosities were observed, it indicates that the presence of strain and porosities locally affect the orientation of the inner oxide explaining why some regions are better oriented than others. The presence of numerous porosities near the oxide surface close to the medium is thought to be responsible for the loss of epitaxy between the outer crystallites and the inner oxide layer. On [111] grain orientation, even if the inner layer is thinner and SAED pattern contain information on the substrate and both oxide scales, the inner oxide was also of spinel structure and is epitaxially grown with a cube/cube orientation relationship. However, a lot more oxide is in proper epitaxy with the underlying metal grain on this orientation. Thus, less defects are believed present into the oxide formed on this orientation as previously assumed in Chapter 3 section 3.2.3 and it would lessen the oxidation kinetic.

4.2.1.3 Chemical analysis of the oxide layers

Since the outer layer was sparse on [111] grain orientations and the crystallites were bigger than 1 µm, it was possible to acquire Raman spectra on a crystallite and on the inner layer independently (Figure 4.28). As depth probed by Raman spectroscopy is of ∼ 460 nm, both oxide layers will contribute to the observed band when acquiring a spectrum onto the crystallites. Moreover, small germs of the outer layer will be probed when acquiring a spectrum on the inner oxide layer. Nonetheless, each time, the contribution of the oxide of interest should prevail on the other. As supposed previously, the A_{1g} band of the inner layer is located at higher wavenumbers than the one of the outer layer. The fits indicate that the A_{1g} band of the inner layer is located at ∼ 701 cm^{-1} and a shouldering of the band around is seen at ∼ 644 cm^{-1}. The outer layer seem well crystallised and bands are observed around 192, 311, 412, 464, 545 and 674 cm^{-1} consistent with magnetite (cf. Appendix B).

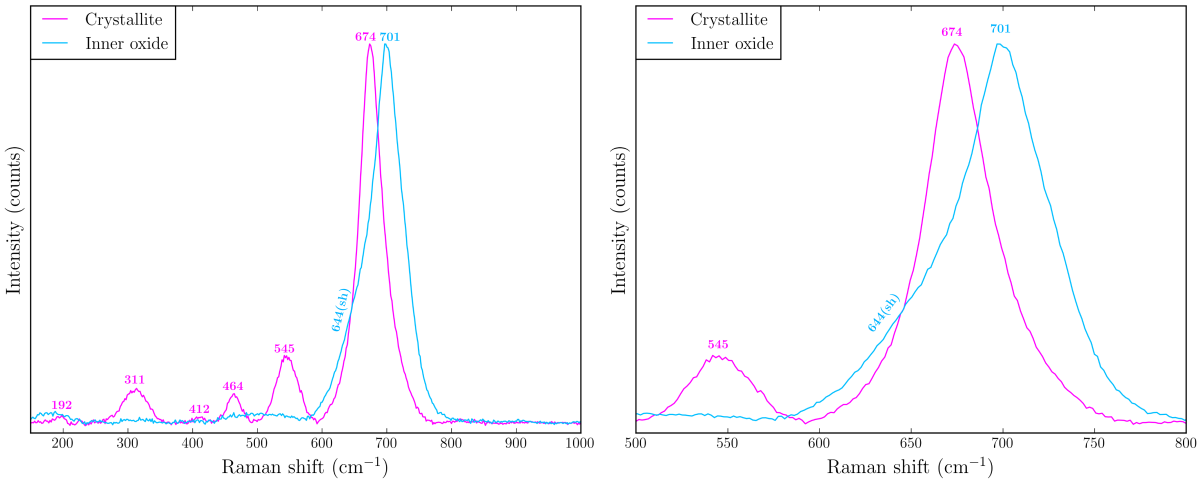

Figure 4.28: *Raman spectrum on the IACUNIRR area of the Michigan sample*

The chemistry of the oxide was investigated on the three orientations of interest using Raman spectroscopy but using bigger acquisitions windows to take into account both the big crystallites and the inner layer on each orientation (Figure 4.29). The obtained spectra are close for both [100] and [110] grain orientations but the A_{1g} band is wider on the [100] grain orientation. For both these orientation, the main response on the Raman spectra come from the outer layer but on the [100] grain orientation inner oxide is detected inducing a shouldering of the band near 703 cm^{-1}. As ∼ 460 nm are probed by the analysis, it means that the inner oxide layer is detected on the [100] orientation while its contribution is close to none on the [110] orientation. Indeed, the ratios A_{1g} (Outer oxide):A_{1g} (Inner oxide) are found to be > 2 and > 20 for [100] and [110] grain orientations respectively. Since a higher outer oxide coverage was observed on [110] orientation, it should lower the contribution from the inner oxide in the spectra. It means that in the ∼ 460 nm probed, much more outer oxide is detected on the [110] grain orientation and that therefore, more outer oxide or bigger crystallites are present or the inner oxide is thinner if both layers are entirely probed. On the [111] grain orientation, the inner oxide layer is the main detected oxide and therefore the A_{1g} band is wide and the detection of the A_{1g} band of magnetite induces a shouldering near 674 cm^{-1}. The ratio A_{1g} (Outer oxide):A_{1g} (Inner oxide) is < 1 on this orientation. This should result from the lower coverage of the outer oxide on this grain orientation inducing the main detection of the inner layer. In addition, small variations in the oxides chemistry would also induce small shifts of the bands but, once again, due to their close vicinity it is complex to conclude on each band shift.

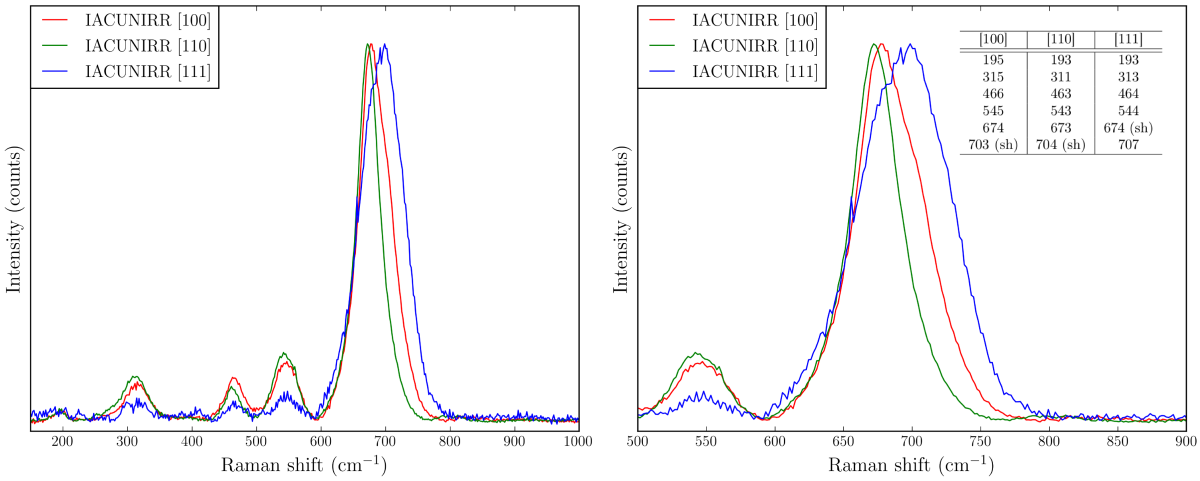

Figure 4.29: *Raman spectra on the IACUNIRR area of the Michigan sample depending on the grain orientation with band positions (cm^{-1}) depending on the grain orientation in insert (sh: shouldering)*

Comparing the Raman spectra on both the **IACUNIRR** area of the Michigan sample and the Titane **UNIRR** sample, band shifts can be observed (Figure 4.30). For the [100] grain orientation, on the **IACUNIRR** the response from the outer oxide is the main one inducing a better detection and intensity of the bands located near 470 and 545 cm^{-1}. Moreover, both these bands are shifted toward lower wavenumbers. The big crystallites covering the inner oxide are responsible for the better detection of the signal of the outer oxide. As for the A_{1g} band, the main response comes from the outer oxide while less inner oxide is detected but still present on the **IACUNIRR** area of the Michigan sample. On the Titane **UNIRR** sample the ratio A_{1g} (Outer oxide):A_{1g} (Inner oxide) is close to 1 while it is above 1 for the **IACUNIRR** area. The big crystallites that cover a huge part of the grain are responsible for the weakened detection of the inner oxide. The same things can be seen on the [110] grain orientation but the observations are even more pronounced since the outer oxide coverage is higher on this grain orientation for the **IACUNIRR** area. Therefore bands are even more shifted toward the lower wavenumbers and almost no inner oxide is detected (ratio A_{1g} (Outer oxide):A_{1g} (Inner oxide) >> 1 for the Michigan sample while close to 1 for the Titane sample). However, on [111] grain orientation the A_{1g} and is located toward higher wavenumbers compared to the one of the Titane **UNIRR** sample. This arises from the main detection of the inner oxide on this grain orientation since the outer oxide coverage is low.

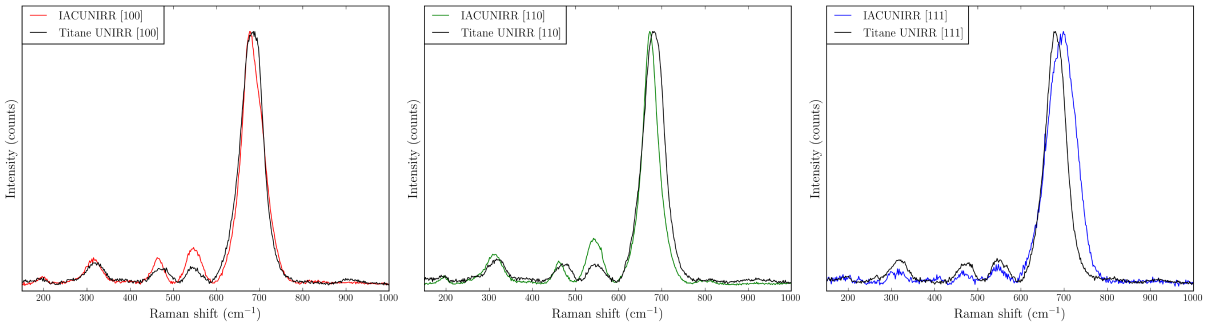

Figure 4.30: *Raman spectra on the IACUNIRR area of the Michigan sample compared to Raman spectra on the Titane UNIRR sample depending on the grain orientation*

EFTEM mapping on both grain orientation showed iron-rich crystallites and a chromium-rich inner oxide (cf. Appendix F). Both these oxide scales are similar to the ones formed on the Titane samples as seen in Chapter 3 section 3.1.3.2. No Ni enrichment was visible at the metal/oxide interface probably due to the low thickness of this enrichment and the low magnification at which

were performed the EFTEM maps. Therefore EELS and EDXS analyses were carried out on both [100] and [111] grain orientations are presented in Figure 4.31. Associated quantifications on the inner oxide layers are introduced in Table 4.6. The outer oxide formed are alike those formed on the Titane samples and can be written $Fe_3(Cr,Ni)_{3-x}O_4$ with $3 \geq x \geq 2.5$. The inner oxide layer is still an iron, chromium, nickel oxide and can be written $(Ni_xFe_{1-x})(Cr_yFe_{1-y})_2O_4$ with $0.5 \geq x \geq 0.2$ and $0.85 \geq y \geq 0.7$. Moreover, the nickel enrichment not visible in the EFTEM maps is highlighted from the EELS and EDXS linescans and is of the same order of magnitude as on the Titane samples. As on Titane samples, the thinner inner oxide formed on [111] grain orientation is richer in chromium. Thus, underlying metal grain orientation still controls the oxidation kinetic on the **IACUNIRR** area of the Michigan sample. Nonetheless, slight variations of the oxide composition can be seen between the quantitative linescans. Toward the medium, the inner oxide layer is richer in chromium (52 at. % Cr, 35 at. % Fe, 13 at. % Ni) while it is richer in nickel toward the metal (46 at. % Cr, 35 at. % Fe, 20 at. % Ni). This variation in composition might result from the presence of porosities. Chromium could segregate toward these porosities to restore a more protective character of the oxide in these regions.

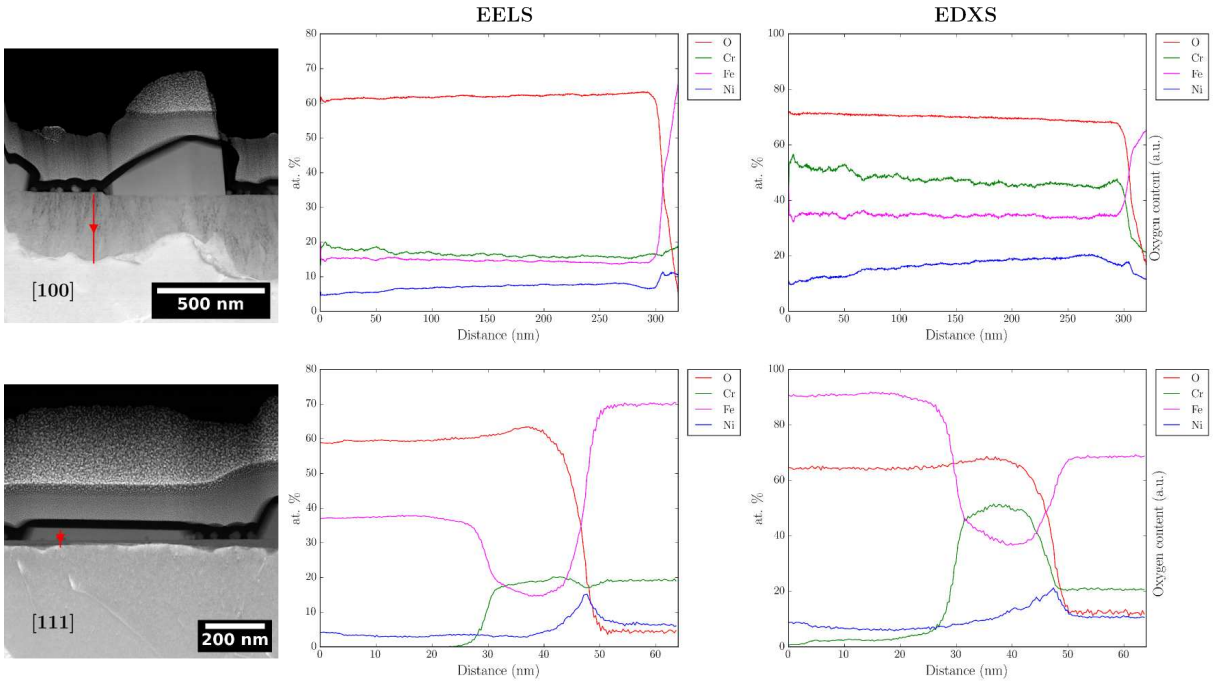

Figure 4.31: *STEM image and associated quantitative EELS and EDXS linescans on the IACUNIRR area of the Michigan sample on both a [100] and [111] grain orientations*

Table 4.6: *EDXS and EELS quantitative analyses of the inner oxides formed on [100] and [111] grain orientations on the Michigan sample in the IACUNIRR area*

Grain orientation	Method	O (at. %)	Cr (at. %)	Fe (at. %)	Ni (at. %)	$\frac{Cr}{Cr+Fe+Ni}$	AB_2O_4
[100]	EELS	62	17	14	7	-	-
	EELS	-	53	33	14	0.53	$Fe_{1.0}Cr_{1.6}Ni_{0.4}O_4$
	EDXS	-	47	35	18	0.47	$Fe_{1.1}Cr_{1.4}Ni_{0.5}O_4$
[111]	EELS	63	19	14	4	-	-
	EELS	-	56	36	8	0.56	$Fe_{1.1}Cr_{1.7}Ni_{0.2}O_4$
	EDXS	-	50	39	11	0.50	$Fe_{1.2}Cr_{1.5}Ni_{0.3}O_4$

4.2.1.4 Grain boundary oxidation

EELS and EDXS quantitative maps were acquired on the grain boundary oxidation[2] of the **IACUNIRR** area of the Michigan sample (Figure 4.32). On this region, the grain boundary oxide penetration was located in the foil depth as the oxidation front is not perpendicular and therefore quantification was wronged. Nonetheless, the oxide formed is chromium-rich and could be of corundum structure. Moreover, nickel is pushed along the oxide flanks and along the grain boundary as previously seen on Titane samples. In addition, as on Titane samples, the oxide penetration at grain boundary is asymmetric.

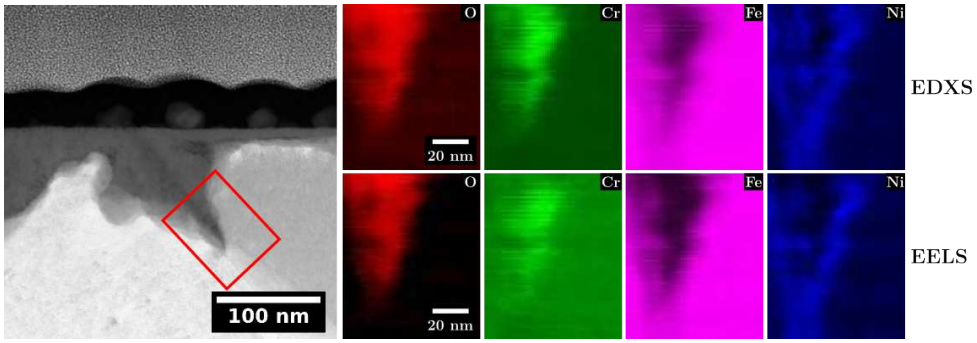

Figure 4.32: *STEM image and associated quantitative EDXS and EELS mapping on the grain boundary in the IACUNIRR area of the Michigan sample*

4.2.1.5 Unirradiated area characterisation: Summary

The oxides formed on the **IACUNIRR** area of the Michigan sample share a lot of similarities with the ones oxidised in TITANE loop. These similarities are listed below:

- The oxide scale is duplex and of spinel structure.
- The inner oxide layers are epitaxially grown with a cube/cube orientation relationship with the substrate.
- The outer oxide is close to magnetite while the inner oxide is a mixed chromium, iron and nickel spinel oxide and a nickel enrichment is present at the metal/oxide interface.
- The inner oxide is thinner on [111] grain orientation and richer in chromium than on the [100] one indicating that the underlying metal grain orientation still controls the oxidation kinetic.
- The oxide penetration at grain boundary is chromium-rich and nickel is pushed back at the oxide flanks and along the grain boundary.

However, compared to the oxides formed after exposure in the TITANE loop, the outer oxide is much bigger on the **IACUNIRR** area of the Michigan sample. This hail from the stainless steel loop used as a dissolution/re-precipitation process (mainly of iron) will contribute to the oxide growth and thus induce the formation of bigger crystallites. In addition, inner oxide are up to 15 – 20 times thicker on the **IACUNIRR** areas than the ones formed on the Titane samples. The formation of much thicker inner oxides (especially on [100] grain orientation) compared to the ones formed on the **UNIRR** Titane sample also oxidised 24 hours is thought to arise from the lower pH of the media in which the Michigan sample was exposed. Moreover, the sample having been welded is likely to be strained and these strains could enhance the oxidation as depicted in Chapter 3 section 3.3. The numerous porosities observed in the inner oxide layers could also act as diffusion short-cuts for the oxygen ingress diffusion inducing these thicker oxides. Apart from [111] grain orientation, coarse crystallites of polyhedral morphologies are formed while triangular crystallites are noticed on [111] grain orientation with a much lower outer oxide coverage. Thus,

[2]The tortuous appearance of the oxide penetration results from the drift that occurred during the acquisition.

the favoured crystallite morphology was solely observed on the [111] grain orientation. This confirms that the epitaxial relationship is quickly established on this orientation. As for the other orientations, no epitaxial relationship between the outer crystallites and the inner oxide layer could be evidenced. Since the inner oxide is believed even more strained on the two other orientations studied and containing numerous defects, among them numerous porosities, it is believed to induce the loss of epitaxy between the two oxide layers.

Unirradiated area characterisation:

- The oxidation in a stainless steel loop engenders a dissolution/re-precipitation process which enhances the outer oxide growth.
- The lower pH of the medium, the sample strain and the porosities in the inner oxide layer are thought to be responsible for the increased corrosion rate.

4.2.2 Characterisation of the oxides formed on the IACIRR area

On the same Michigan sample oxidised 24 hours, an **IACIRR** area was proton pre-irradiated to ~ 1 dpa and then oxidised (cf. Chapter 2 section 2.2.2). The oxides formed on this area will be compared to the ones observed on the **IACUNIRR** area to help fathom the effect of the proton pre-irradiation. These conclusions will be put in parallel with those obtained on the Titane **IRR** samples also irradiated at 1 dpa and oxidised 24 hours.

4.2.2.1 Description of the oxide scales

Several results on the **IACIRR** area are in agreement with that of those on the **IACUNIRR** area and will only be briefly summarised below (details can be found in Appendix F).

- STEM imaging confirmed the duplex character of the oxide.
- The outer oxide is composed of big-faceted crystallites meshing with small germs as seen from SEM imaging.
- Triangular crystallites are formed on [111] grain orientation while polyhedral ones are observed on the other orientations with a higher outer oxide coverage (SEM imaging).
- The inner oxide is thinner on [111] grain orientation than on the [100] one (Raman spectroscopy and STEM imaging).
- The inner oxide is porous (under-focus and over-focus TEM BF imaging).
- EFTEM maps highlighted an outer layer iron-rich and an inner layer chromium-rich.
- Raman spectra confirmed the presence of a duplex oxide layer of spinel structure.
- Electron diffraction revealed that the inner oxide layers are epitaxially grown with a cube/cube orientation relationship with the substrate.
- EELS and EDXS linescans evidenced that the outer oxide is close to magnetite while the inner oxide is a mixed chromium, iron and nickel spinel oxide.
- The grain boundary oxide penetration is asymmetric and chromium-rich.
- Nickel enrichment is present at the metal/oxide interface and also at the oxide penetration flanks and pushed along the grain boundary (EELS and EDXS linescans and mapping).

However, differences could be seen between the oxides formed on both the **IACUNIRR** and **IACIRR** areas. SEM imaging of the outer oxide revealed that approximately 2 crystallite/μm^2 present the triangular morphologies on [111] grain orientation which is twice that of on the **IACUNIRR** area (Figure 4.33). Moreover, it can be noticed on [100] grain orientation that the outer oxide coverage is higher on the **IACIRR** area. As on the **IRR** Titane samples, irradiation

defects are thought to act as preferential germination sites for the crystallites in the oxidation early stages.

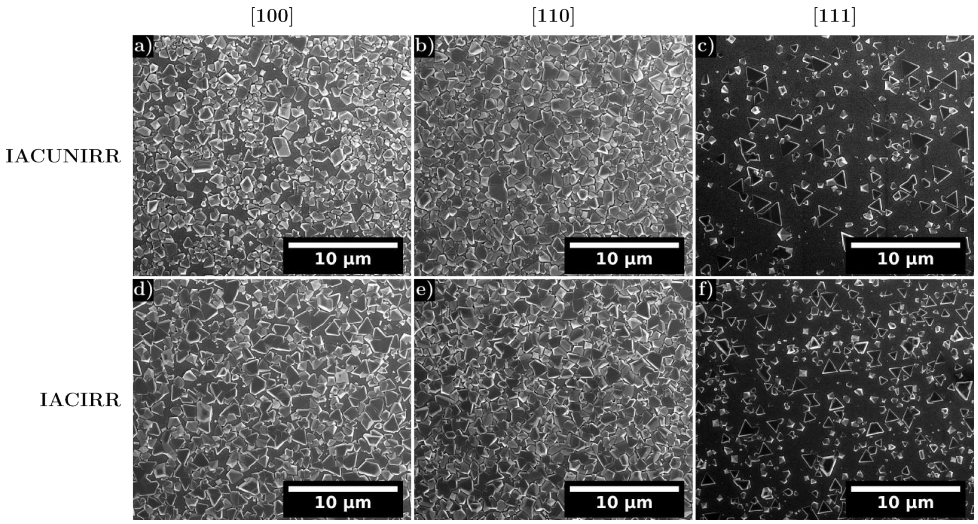

Figure 4.33: *SEM SE images (5 kV) on the IACUNIRR and IACIRR area of the Michigan sample depending on the crystallographic orientation*

The measured inner oxide thicknesses from STEM images are reported in Table 4.7 and highlight that, as previously, slightly thicker oxides are formed on the irradiated area. Large variations in inner oxide thicknesses are observed and therefore these measurements should be considered with care as only a lamella was extracted. Nevertheless, as assumed previously in section 4.1.5, oxygen diffusion is thought enhanced in the inner oxide layers formed on irradiated materials.

Table 4.7: *Inner oxide thicknesses on both [100] and [111] grain orientations for the IACUNIRR and IACIRR areas of the Michigan sample*

Sample	orientation orientation	mean thickness ± standard deviation (nm)	min – max thickness (nm)
IACUNIRR	[100]	152 ± 111	15 – 435
	[111]	22 ± 15	7 – 85
IACIRR	[100]	200 ± 100 (285 ± 12 in the even region)	20 – 320
	[111]	29 ± 9	15 – 70

By comparing the Raman spectra acquired on both the **IACUNIRR** and **IACIRR** areas it appears that the spectra are really close on [100] and [110] grain orientations. Nonetheless, on [100] grain orientation the slightly higher outer oxide coverage on the **IACIRR** area is thought responsible for the lessen detection of tha A_{1g} band of the inner oxide toward higher wavenumbers. As for the [110] grain orientation, since, on both areas, the outer oxide coverage is of almost 100 %, no differences were evidenced between the two spectra. As not the whole inner oxide scale could be probed on these grain orientations, it is not possible to conclude on variation of the inner oxide thicknesses. Moreover, since spectra on [100] and [110] grain orientations are almost superimposed, it means that the oxide compositions are close. On [111] grain orientation, more outer oxide contribution is seen toward the A_{1g} lower wavenumbers and is thought to result from the higher number of big crystallites observed on the **IACIRR** area on this orientation inducing a higher outer oxide coverage and thus detection. The broadening of the A_{1g} band toward the higher wavenumber on the **IACUNIRR** area probably result of the higher response of the inner oxide since less outer oxide is probed on this region therefore diminishing the intensity of the inner oxide response on the **IACIRR** area.

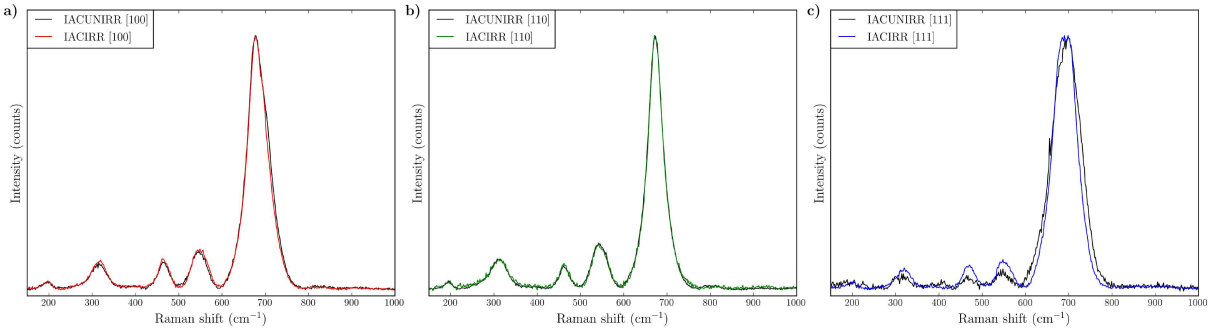

Figure 4.34: *Raman spectra on both the IACUNIRR and IACIRR areas of the Michigan sample a) on [100] grain orientation b) on [110] grain orientation and c) on [111] grain orientation*

EELS and EDXS linescans revealed that the inner oxide layers are richer in chromium on the **IACIRR** area than on the **IACUNIRR** area for both grain orientations (Table 4.8). This is coherent with the previous results on Titane samples since inner oxides were richer in chromium on the **IRR** specimens than on the **UNIRR** ones. Moreover, once again, inner oxides richer in chromium are formed on [111] grain orientation indicating than even in the **IACIRR** area, the underlying metal grain orientation control the oxidation kinetic.

Table 4.8: *EELS analyses of the inner oxides formed on [100] and [111] grain orientations on the Michigan sample in the IACUNIRR and IACIRR area*

Grain orientation	Sample	$\frac{Cr}{Cr+Fe+Ni}$	AB_2O_4
[100]	IACUNIRR	0.53	$Fe_{1.0}Cr_{1.6}Ni_{0.4}O_4$
	IACIRR	0.58	$Fe_{1.0}Cr_{1.7}Ni_{0.3}O_4$
[111]	IACUNIRR	0.56	$Fe_{1.1}Cr_{1.7}Ni_{0.2}O_4$
	IACIRR	0.64	$Fe_{0.8}Cr_{2.0}Ni_{0.2}O_4$

4.2.2.2 Proton pre-irradiated area characterisation: Summary

On the Michigan sample, irradiation was not found to greatly affect the oxide scale apart from the higher outer oxide coverage and slightly thicker inner oxide richer in chromium. As on the Titane samples, irradiation defects are thought to act as preferential germination sites and irradiation enhances the oxidation kinetic. In addition, irradiation does not modify the crystallographic orientation effect on the oxidation kinetic on the irradiated area.

Proton pre-irradiated area characterisation:

- Irradiation defects acts as preferential sites for the outer oxide nucleation and growth at the oxidation early stages.
- Thicker oxides richer in chromium are formed indicating that irradiation enhances the oxidation kinetic.
- The underlying metal grain still controls the oxidation kinetic on pre-irradiated materials.

4.2.3 Characterisation of the oxides formed on the IACIAC area

The following paragraphs focus on the **IACIAC** region that was proton pre-irradiated at $\sim$ 1 dpa and then oxidised under proton flux. The investigation of this area will provide information on the influence of a simultaneous oxidation and irradiation. Irradiation could induce the formation of radiolysis species into the medium (however in PWR water hydrogen is added to

suppress radiolysis) and will definitely induce point defects in the metal and the oxide as these grow. Both these processes could affect the oxide scales and will be discussed.

4.2.3.1 Description of the oxide scales

Figure 4.35 evidences that the oxidation of the **IACIAC** area differs from the one of the **IACUNIRR** and **IACIRR** regions. As on the **IACUNIRR** area, a specific oxidation behaviour can be seen on [111] grain orientations. Moreover, a flow region can be distinguished on the right side of this **IACIAC** area. A computational fluid dynamics simulation performed in Raiman's work [191], revealed that this flow region is engendered by the heating induced by the proton beam that caused an upward flow in the direction of the oblong-shaped region.

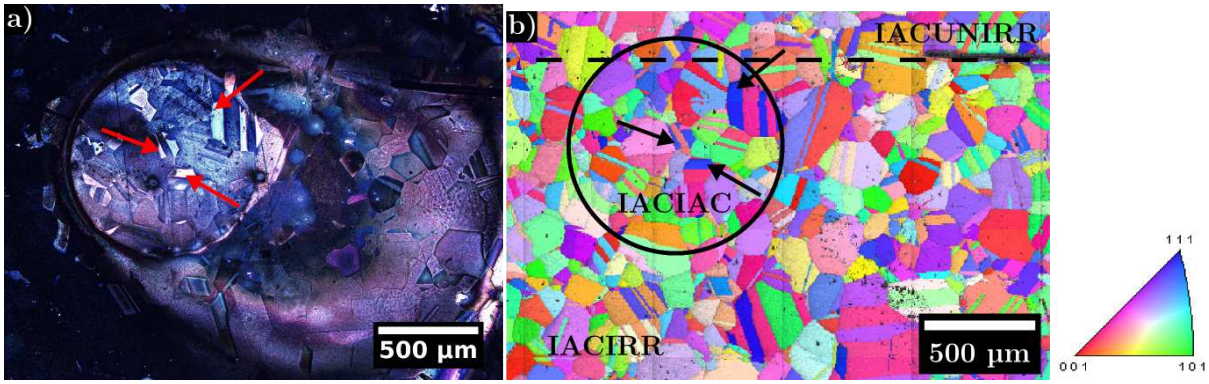

Figure 4.35: *a) Optical image on the IACIAC area of the Michigan sample and b) associated EBSD map*

The outer oxide formed in IACIAC area is much smaller than that formed in the other two zones of the sample with the presence of small crystallites (10 – 50 nm) and larger ones (50 – 500 nm). In addition, the overall outer oxide coverage is close to 100 % on all the grain orientations and the smaller crystallites are densely packed. The sizes, densities and morphologies of crystallites in this area are relatively similar regardless of the crystallographic orientation of the underlying metal grain. Nevertheless, on [111] grain orientation few small crystallites of the expected specific morphology are observed (flat triangles circled in red in Figure 4.36). This suggests that the inner layer, at least partially, epitaxially grown with the underlying metal grain. Moreover, some crystallites present different faceted six-sides morphologies suggesting that their crystallographic structure differs (circled in green in Figure 4.36). Their chemical composition might also differ from the other faceted crystallites. Raiman and Hanbury both mentioned the presence of hematite (Fe_2O_3) on areas oxidised under proton flux [84–86, 191].

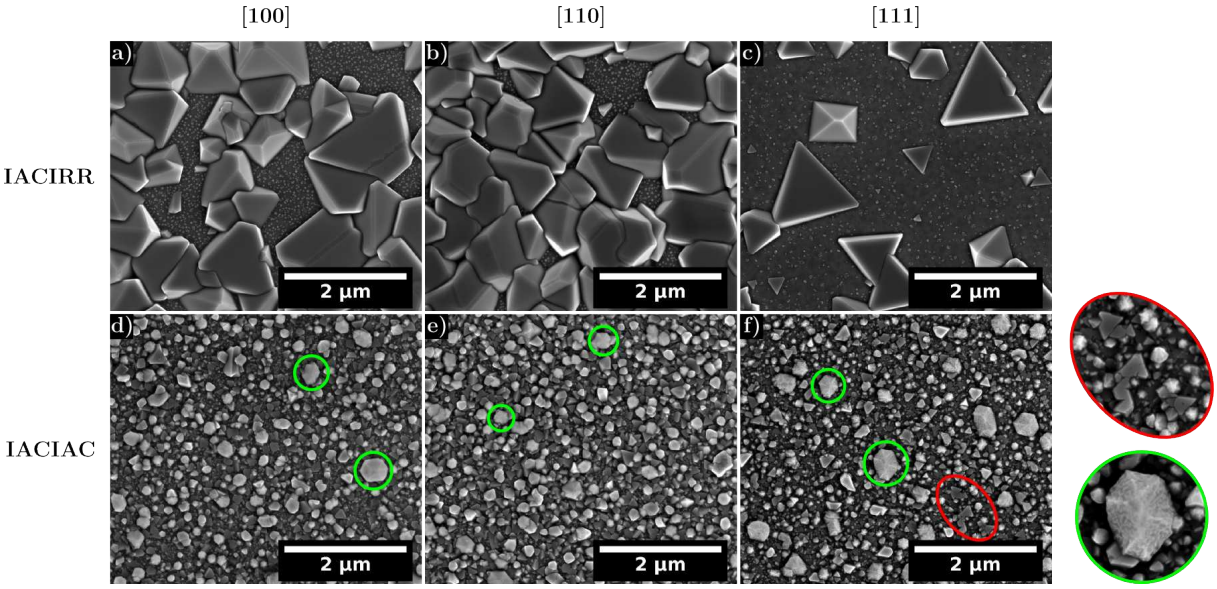

Figure 4.36: *SEM SE images (5 kV) on both the IACIRR and IACIAC area of the Michigan sample depending on the underlying metal grain orientation*

TEM imaging confirms the presence of bigger crystallites as well as numerous smaller ones densely packed (Figure 4.37). Among the faceted crystallites, some present the six-sides morphology as shown by the green arrows. As for the inner oxide layer, is it much thinner than on the **IACIRR** area ($\sim 15 \pm 8$ nm on both grain orientations). No clear effect of the underlying metal grain orientation could be evidenced on the inner oxide thicknesses. In addition, the darker area (as circled in red) in the STEM HAADF images are evidenced to be porosities in the TEM BF under-focus images (explicitly shown by the red arrow). Therefore, the inner oxide layers appear extremely porous and the oxide seems less compact on the [111] grain orientation than on the [100] one. This reveals that the crystallographic orientation of the underlying metal grain modifies the oxidation in **IACIAC** area.

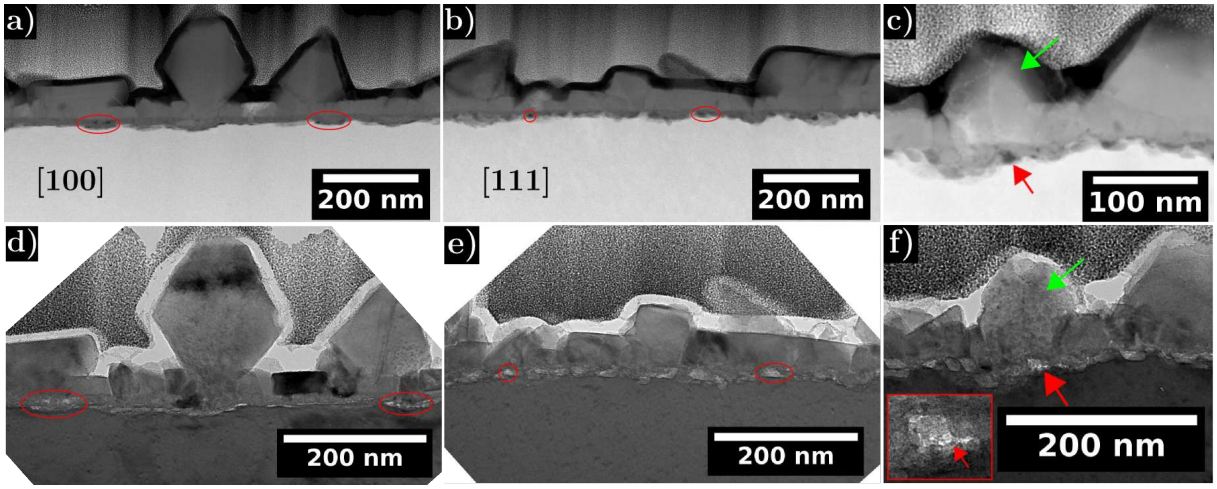

Figure 4.37: *TEM images on the IACIAC area of the Michigan sample a), b) and c) STEM images d), e) and f) TEM BF images under-focus (a) and c) on a [100] grain orientation and b), d) e) and f) on a [111] grain orientation*

Raman spectra acquired on the **IACIAC** area were compared to the one on the **IACIRR** area for each orientation (Figure 4.38). On the **IACIAC** area, the bands located at $\sim$ 226, 245, 294, 411, 493, 609 cm^{-1} are consistent with hematite (Fe_2O_3) (cf. Appendix B). Therefore, it can be concluded that hematite is indeed formed on the **IACIAC** area while none was detected on the **IACIRR** area. This hematite is assumed to be the six-sides crystallites observed previously

in the SEM and TEM images. Hematite was also detected on areas oxidised under proton flux using Raman spectroscopy by Raiman and Hanbury et al. who oxidised samples in the same device [84–86, 191]. Nevertheless, contributions from the outer and inner layers are seen in the spectra, indicating that at least three different chemical species are detected. The most intense contribution hails from the outer oxide (magnetite) then followed by the hematite and by the inner oxide layer.

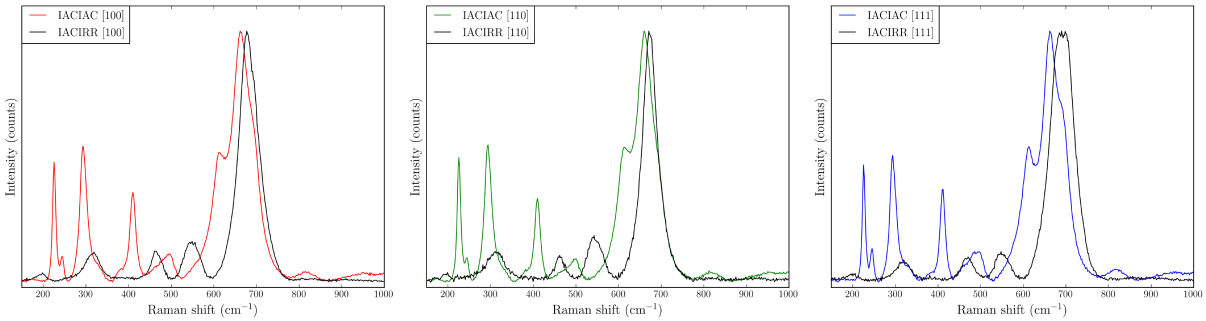

Figure 4.38: *Raman spectra on the IACIAC and IACIRR areas of the Michigan sample depending on the underlying metal grain orientation*

When observing the outer oxide further and further away from the **IACIAC** area going toward the flow region, the outer oxide morphology gradually differs (Figure 4.39). This area has a mix of small six-sides crystallites and larger faceted ones. The number of six-sides crystallites (assumed to be hematite) progressively decreases when going further away from the **IACIAC** area. On Figure 4.39 c, it clearly appears that magnetite is indeed dissolved and hematite crystals are formed attached to the magnetite crystallites. The observation of hematite downstream was already made but the authors never reported imaged proof of the magnetite crystallite dissolution [85, 86, 191].

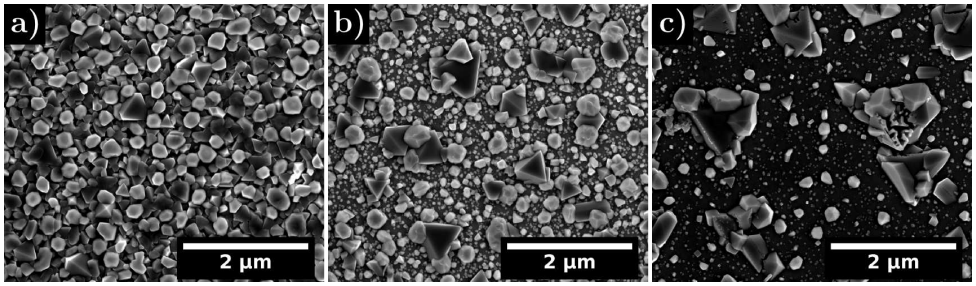

Figure 4.39: *SEM SE images (5 kV) on the flow area of the Michigan sample on [111] grain orientation*

The Raman spectrum on the flow region confirms the presence of hematite as the hematite signature bands are detected as evidenced in Figure 4.40.

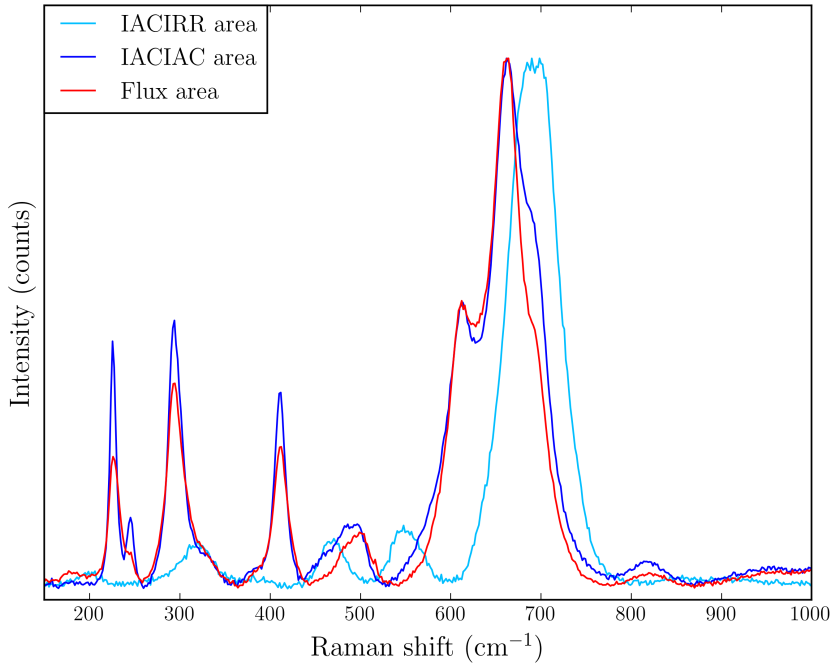

Figure 4.40: *Comparison of Raman spectra on the IACIRR, IACIAC and flow areas of the Michigan sample on a [111] grain orientation*

Electron diffraction study on this **IACIAC** area proved extremely difficult due to the low thickness of the oxide layers and the presence of several oxides with different orientations and structures (spinel and corundum structures) (Figure 4.41). Nonetheless it appears that the oxide scales are preferentially oriented as no rings were observed on the diffraction patterns. Some of the oxides appear to be in <101> zone axis as shown by the green dashed lines.

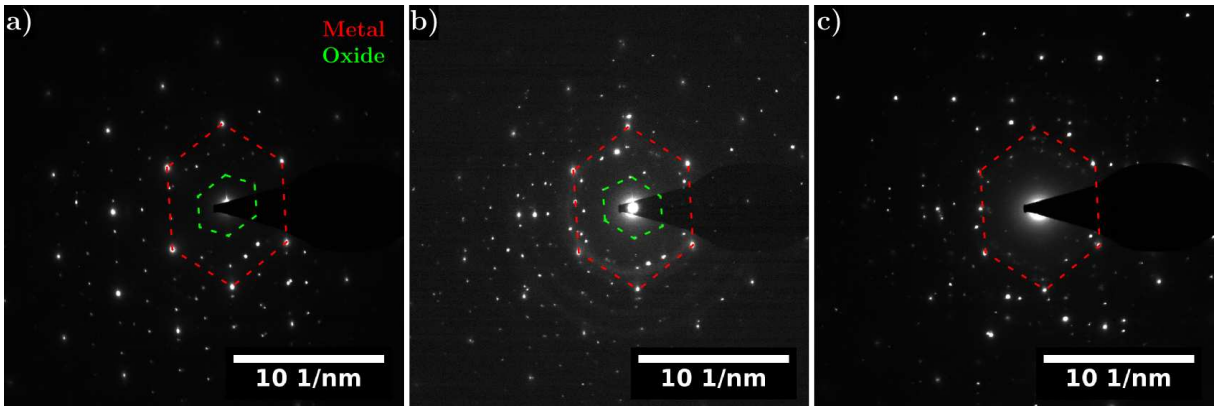

Figure 4.41: *Diffraction on a [110] zone axis on the [100] grain of the IACIAC area of the Michigan sample (red dashed lines: metal in [101] zone axis, green dashed lines: oxide in <101> zone axis)*

The EFTEM mapping clearly evidences that the outer oxide is iron-rich while the inner oxide is chromium-rich (Figure 4.43). It also highlights a nickel enrichment at the metal/oxide interface. However, some areas, located below red dashed lines in Figures 4.42 and 4.43 illustrating the outer/inner oxide interface, appear depleted in chromium while richer in iron compared to the rest of the inner oxide layer as indicated by the red arrows both on the STEM image and EFTEM maps. This loss of the original metal surface could reveal a potential dissolution of the inner layer as alleged by Raiman and Hanbury [84–86, 191]. Hanbury et al. used a marker layer (helium implantation) to measure the assumed oxide dissolution [192]. They followed the implantation peak location (ie the depth of the induced layer of bubbles) and observed that, $\sim 40 \pm 10$ nm of oxide is dissolved into the oxidised under proton flux area while no dissolution occurs in the

unirradiated area. The intragranular oxide penetration was not found deeper or possessing a different oxidation behaviour than intergranular oxide penetrations observed on Figures 4.42 and 4.43.

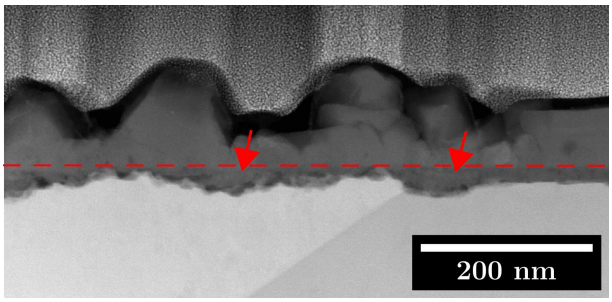

Figure 4.42: *STEM image on the grain boundary oxidation on the IACIAC area of the Michigan sample (dashed red line: outer/inner oxide interface)*

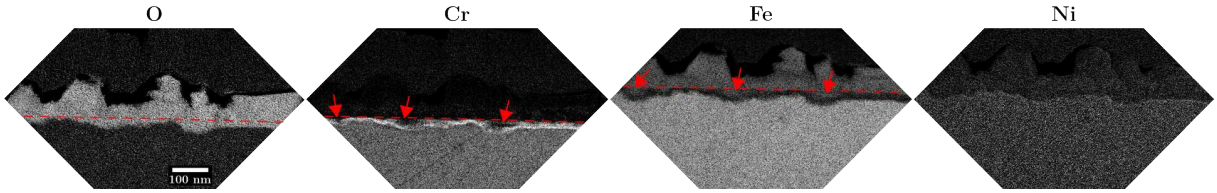

Figure 4.43: *EFTEM maps on the IACIAC area of the Michigan sample (dashed red line: outer/inner oxide interface, red arrows: areas iron-rich and chromium depleted)*

To better look upon the oxide scales compositions, EELS and EDXS punctual acquisitions and linescans were acquired on the oxide scales as introduced in Figures 4.44 and 4.45. These analyses reveal that the big outer crystallites have a different chemical composition than the smaller densely packed ones. The latter are richer in chromium and nickel compared to the bigger faceted crystallites. Their chemical composition can be written: $Fe^{2+}_{1-x}(Mn,Ni)_x(Cr^{3+}_yFe^{3+}_{1-y})_2O_4$ with $0.6 \geq x \geq 0.4$ and $0.2 \geq y \geq 0.05$. The outer faceted crystallites possess a composition close to magnetite (Fe_3O_4) and the six-sides crystallite on [111] grain orientation (n°2), have a chemical composition coherent with hematite (Fe_2O_3). EELS and EDXS linescans reported in Figure 4.45 clearly attest of the inhomogeneity of the inner oxide layer. Some areas are iron-rich while other are chromium-rich. Further analysis of the inner layer reveals that the $\frac{Cr}{Cr+Fe+Ni+Mn}$ ratios range from 0.3 to 0.7 while calculated $\frac{Cr}{Fe}$ ratios range from 0.3 to 2.8. Due to the presence of numerous porosities in the inner oxide layers as evidenced previously, chemical quantification would be impaired and therefore no inner oxide composition can be given for this oxide layer. Nevertheless, these results can be looked upon in a qualitative way. The linescans crossing porosities evidence a net increase of the chromium content in the porosity regions. The oxide is seemingly chromium-rich in the porosities hinting that iron is preferentially lacking in these areas. However, it also appears that the inner oxide layer is overall less chromium-rich than the one formed on the **IACUNIRR** and **IACIRR** areas. EDXS and EELS mapping carried out on the grain boundary oxide penetration did not evidence any specific oxidation behaviour at the grain boundary. Finally, nickel enrichment was highlighted from the profiles at the metal/oxide interface and reached up to $\sim$ 40 at. %.

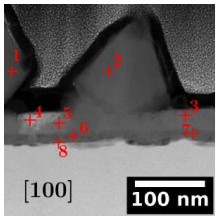

Analysed region	Cr (at. %)	Mn (at. %)	Fe (at. %)	Ni (at. %)
1	0	2	98	0
2	0	2	98	0
3	2	0	81	17
4	8	2	78	12
5	12	1	75	12
6	40	2	52	6
7	42	2	46	10
8	19	1	37	43

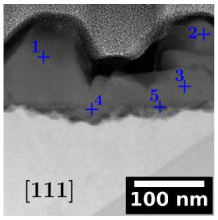

Analysed region	Cr (at. %)	Mn (at. %)	Fe (at. %)	Ni (at. %)
1	4	5	90	1
2	1	3	95	1
3	4	2	78	16
4	7	3	72	18
5	30	2	57	11

Figure 4.44: *STEM image and associated quantitative EDXS analyses on the IACIAC area of the Michigan sample on both [100] and [111] grain orientation*

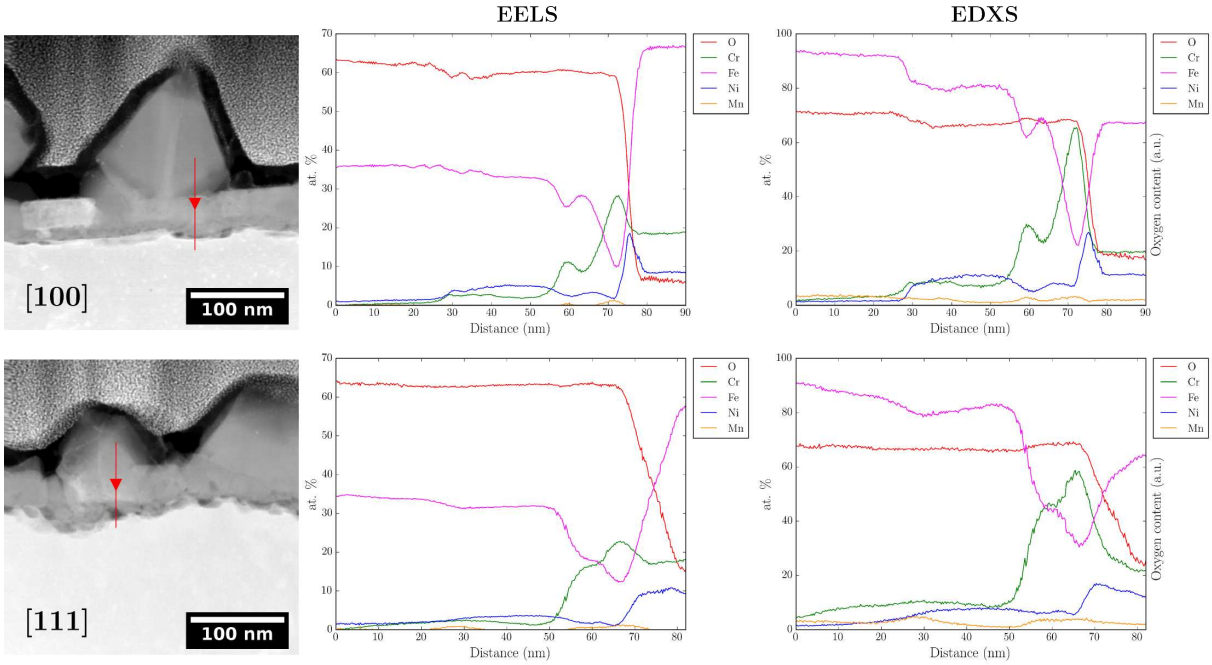

Figure 4.45: *STEM image and associated quantitative EELS and EDXS linescans on the IACIAC area of the Michigan sample on both [100] and [111] grain orientation*

4.2.3.2 Oxide formed under proton flux characterisation: Discussion and summary

Hematite was only observed in the **IACIAC** and flow areas and is not known to be formed and stable in PWR normal operating conditions, even at pH = 6.2. Calculated Pourbaix diagrams of iron extracted from other studies indicate that the presence of hematite is revealing of an increase of Electrochemical Corrosion Potential (ECP) (Figure 4.46). Indeed, to form stable hematite at this pH, an increase in ECP up to ∼ -0.5 V/SHE (Standard Hydrogen Electrode) is needed and believed to happen in the area oxidised under proton flux [27, 84]. This increases in ECP will affect the thermodynamic stability of the species formed. Thus, under this elevated potential magnetite will dissolve and form hematite as observed in Figures 4.36 and 4.39. The magnetite dissolution engenders formation hematite according to Equation 4.1.

$$2Fe_3O_4 + H_2O \rightarrow 3Fe_2O_3 + 2H^+ + 2e^- \tag{4.1}$$

Since, hematite presence was only evidenced in the **IACIAC** and flow area, both these regions are believed to be exposed to a medium with a higher ECP than the other areas. As the flow region is not affected by displacement damages, the latter are not believed responsible for the hematite formation and increased ECP. Hence, the proton beam irradiation is thought to induce a change in the water chemistry. Irradiation is likely do engender radiolysis and the production of species by radiolysis (long-lived species like O_2 and H_2O_2 along with short-lived radical oxidising species) should be held accountable for this increase in ECP. The amount of radiolytic species can result in modifications in oxides composition, thickness, ECP, etc. The main water chemistry

changes will happen in the **IACIAC** area but this medium will be carried away through the flow region and thus this contaminated water will also affect this area as previously observed. Thereby, water flow will carry radiolysis products and create a flow region exposed to these products without being affected by displacement damage. Nonetheless, radiolitic species will be created in the **IACIAC** area whereas less and less will be detected when drawing away from this area in the flow region. The difference in the amount of radiolysis products should be responsible for the differences in the outer oxide morphology between the **IACIAC** and flow regions. This explains why less and less hematite crystals are observed going further away from the **IACIAC** area as evidenced in Figure 4.39. Moreover, the addition of radiolysis products decreased the outer oxide size as already reported by [32, 76, 85, 193].

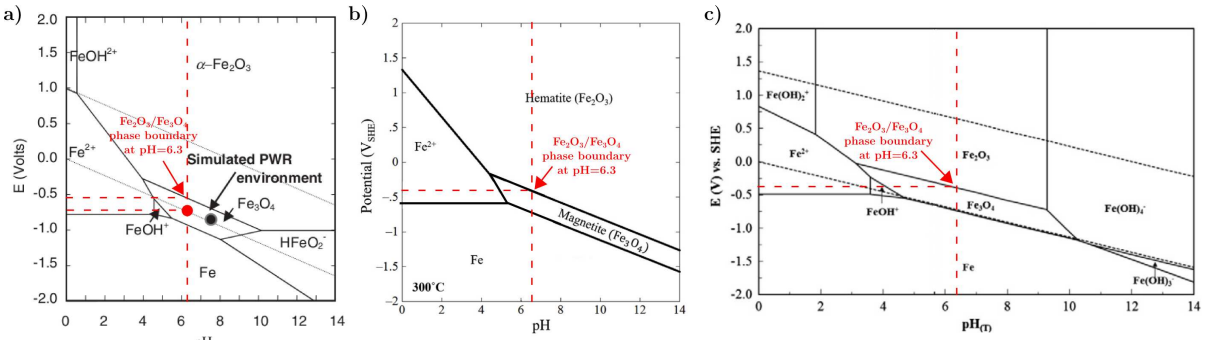

Figure 4.46: *Pourbaix diagram of iron a) in 320 °C water from [27] and b) in 300 °C water from [84] c) in 300 °C water from [194]*

Usually, the effect of radiolysis is suppressed by the addition of hydrogen. However, for this experiment, hydrogen content is not believed sufficient enough to suppress radiolysis and the ECP increase and therefore magnetite dissolution/hematite formation. Addition of O_2 and H_2O_2 in the medium is known to affect the oxide scales formed and overall oxidation kinetic [32, 73, 75, 76, 193] (hematite formation, thicker inner oxide porous and depleted in chromium). Raiman et al. showed that H_2O_2 formation under radiolysis exceeds O_2 production by more than an order of magnitude and [84, 191] (Figure 4.47). These simulations were realised for a dose rate of 7×10^{-7} dpa/s as used in our work but with 1.4 MeV protons. Moreover, the Dissolved Oxygen (DO) content was undetectable (< 8 ppb), indicating that the 3 wppm H_2 addition suppressed oxygen produced by radiolysis below detectable levels. H_2O_2 is hence believed primarily responsible for this increase in ECP and therefore the dissolved hydrogen addition is not enough to suppress radiolysis.

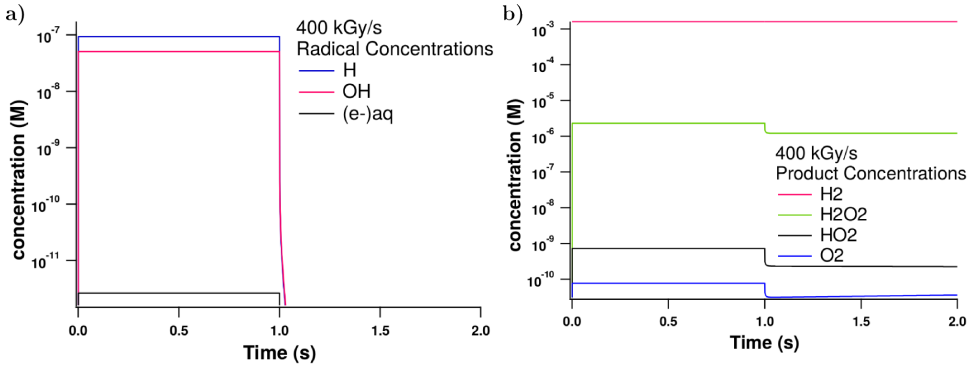

Figure 4.47: *Concentration of species produced by a 1 second pulse of 1.4 MeV protons in 300 °C water with 3 wppm H_2 at a dose rate of* 7×10^{-7} dpa/s *a) radical species b) long-lived species [191]*

Regarding the inner oxides, those formed in the **IACIAC** area are thinner, depleted in chromium and present an extensive amount of porosities compared to the ones formed in the

IACIRR area (Figures 4.37 and 4.45). The previously assumed ECP increases above -0.5 V/SHE cannot be accounted responsible for these observations. Nevertheless, it is known that, when producted in sufficient amount, O_2 and H_2O_2 (and therefore at higher ECP) the chromium rich inner oxide layer can be dissolved to form $HCrO_4^-$ soluble in water (Figure 4.48 and Equation 4.2). Therefore chromium deficient oxides are formed [76, 85, 86, 193]. The production of enough H_2O_2 by water radiolysis engendering a significant raise of ECP above $\sim 0 - 0.2$ V/SHE could lead to chromium dissolution explaining the thinner, porous inner oxides depleted in chromium observed. Thereby, it is likely that, in the **IACIAC** area (and potentially the flow region), the potential will be raised enough to cause dissolution of the inner oxide layer and be the reason for the observed loss of inner oxide and chromium depleted oxide. This entails that passivity is lost under irradiation in favour of transpassive corrosion with both active oxide growth and dissolution. When diffusion is as fast as the dissolution process, then the oxidation rate is equal to the dissolution rate and the inner oxide is likely to reach a steady state thickness. Porosities form as a result of chromium depletion in the oxide and chromium will segregate toward these porosities to reform a protective oxide layer explaining why the porosities were found chromium-enriched (Figure 4.45). The presence of porosities induced by the chromium dissolution will further grant access of the medium to the metal/oxide interface and therefore interfacial reactions should be the controlling mechanism for the oxide growth and dissolution. In addition, as the small crystallites were found nickel-enriched it is likely that nickel released into the water will be incorporated into the outer crystallites.

$$(Fe, Ni)Cr_2O_4 + 4H_2O \rightarrow (Fe^{2+}, Ni^{2+}) + 2HCrO_4^- + 6H^+ + 6e^- \quad (4.2)$$

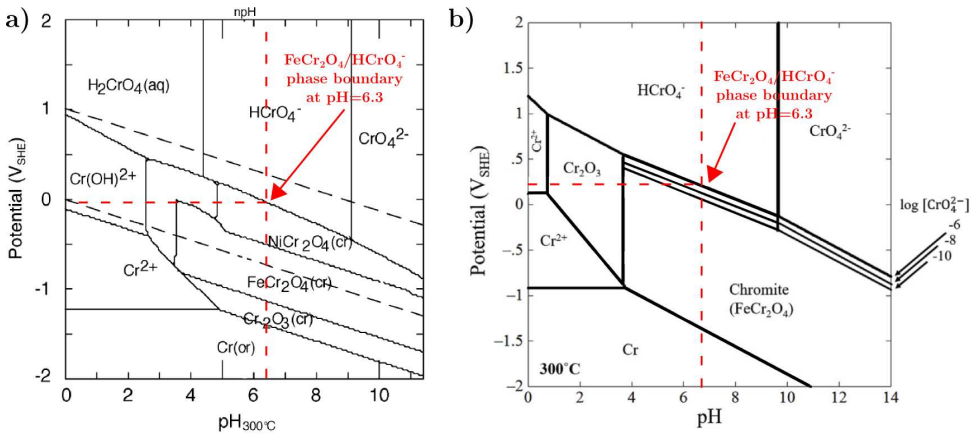

Figure 4.48: *Pourbaix diagrams of chromium a) in the ternary system of Fe-Cr-Ni in 300 °C water from [195] and b) in the binary Fe-Cr system in water in 300 °C water from [84]*

As the oxidation cell is heated with the sample being exposed to the medium, a first oxide scale will be formed before activating the proton beam. The observation of crystallites of a triangular shape on the [111] grain orientation in the **IACIAC** area reveals that the outer and inner oxide were initially and up to some point sharing an epitaxial relationship with the underlying metal grain. After a while, it is likely that all previously epitaxially grown crystallites will have dissolved to form magnetite due to the ECP increase engendered by irradiation. Moreover, during the oxidation under proton flux, as the inner oxide dissolve it will erase the differences of the inner oxide thicknesses depending on the underlying grain orientation. In all likelihood, the high dissolution rate will prevent the inner oxide to grow with an epitaxial relationship as the epitaxy establishment rate is thought slower than the dissolution rate. Thereby, grain orientation effects are thought diminished with chromium dissolution explaining why no differences in inner oxide thicknesses were observed in the **IACIAC** area.

In addition, in the **IACIAC** area, a high number of processes not taken into consideration above could still influence the oxidation and some of them are mentioned below:

- Under the proton beam, the medium and the sample are likely to be heated and it could affect the oxidation kinetic and the stability of the oxides formed.
- Proton irradiation will induce H^+ protons into the medium and could locally increase the pH of the medium hence affect the stability of the oxides formed and the oxidation rate.
- Short lived radicals are produced in small concentration and could alter the oxidation kinetic.
- Point defect enhanced diffusion in the metal and oxide during irradiation may promote oxidation rates of in situ radiation corrosion.

Oxide formed under proton flux characterisation: Water radiolysis under the proton beam affected the oxides stability and the ECP. It engendered dissolution of magnetite and hematite (α-Fe_2O_3) formation in the oxidised under proton flux and flow areas. It also induced chromium dissolution and the formation of porosities in the inner oxide layer. Therefore a thin and porous inner oxide grows and is at the same time dissolved.

4.2.4 Irradiation Assisted Corrosion experiment: Synthesis, discussion and oxidation mechanism

This section presents a synthesis on the IAC experiment performed using an oxidation under proton flux stainless steel device available at the MIBL of the University of Michigan. It aimed to replicate the simultaneous oxidation and irradiation occurring at crack tips by performing a 24 hours oxidation to study the oxidation first stages. This in situ irradiation-corrosion experiment allowed to investigate the contribution of irradiation on the oxidation behaviour. Compared with PWR medium, pure water without H_3BO_3 nor LiOH as used in this experiment had a lower pH (pH_{IAC} = 6.2 vs pH_{Titane} = 7.3). Both an **IACUNIRR** and **IACIRR** area were investigated and compared to the 24 hours oxidation performed in the TITANE loop. It also focus on the effect of an oxidation under proton flux (**IACIAC** area) to bring light on the IAC phenomenon. The overall oxidation mechanisms are presented in Figure 4.49.

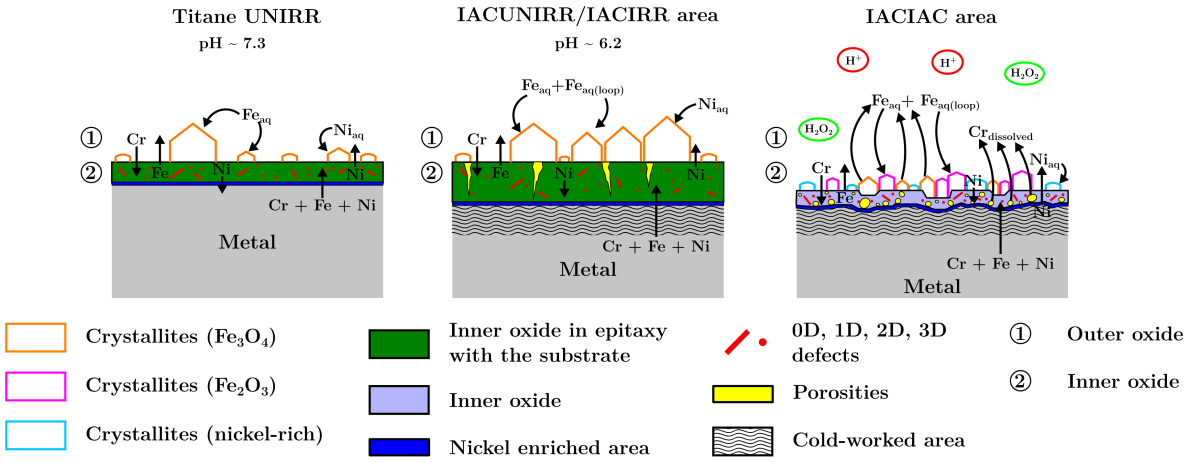

Figure 4.49: *Schematic of the oxidation mechanism of Titane UNIRR and IACUNIRR/IACIRR area compared to that of the IACIAC area of the Michigan sample*

By realising oxidation in a stainless steel loop, a dissolution/re-precipitation process (mainly of iron) contribute to the oxide growth and thus induce the formation of bigger crystallites (sometimes micrometric size). Moreover, the coupling of the lower pH and the resulting strains are

believed to promote the oxidation kinetic inducing the formation of thicker oxides. The lower pH is also assumed responsible for the formation of porous oxides. The porosities form a channel from the solution toward the metal and provide interconnections. They act as preferential diffusion paths and promote oxidation.

Regarding the effect of irradiation on the oxide formed on this sample, the reader is referred to section 4.1.5 as the analysis of the **IACIRR** area of the Michigan sample evidenced the same oxidation behaviour as the Titane **IRR** samples.

Finally, the oxidation mechanism is disrupted under irradiation. Water radiolysis induced by the proton irradiation elevates the ECP of the media by producing long-lived species (like O_2 and H_2O_2) along with short-lived radicals. Addition of 3 wppm H_2 was enough to suppress O_2 content below detectable level but not H_2O_2. This ECP increase is responsible for the formation of outer crystallites of hematite. These hail from the dissolution of magnetite. Since hematite (α-Fe_2O_3) was identified exclusively in the areas exposed to radiolyzed water, both under the beam and downstream and the flow and other two regions did not experience displacement damage, the flow of radiolysis products is thought responsible for the hematite formation. Thinner oxides depleted in chromium are formed on this **IACIAC** area. The wavy interface of the inner oxide tends to indicate that a dissolution process happened. Radiolysis-driven potential is believed to have been increased above the $FeCr_2O_4/HCrO_4$ phase boundary engendering the chromium-rich inner oxide dissolution. This dissolution induces the formation of porosities in the inner oxide layer. The observation of chromium deficient inner oxides on the **IACIAC** area compared to that on the **IACIRR** area can be related to the chromium dissolution. During the oxidation, nickel and chromium mainly coming from the oxide dissolution are thought to be incorporated in the small crystallites densely packed while hematite continues to form and magnetite to dissolve.

Irradiation could nonetheless affect the oxidation mechanism due to displacement damage and the generation of numerous point defects in both the oxides and the substrate. As the oxidation kinetic is dependent on the diffusion process, a small change in diffusivity should alter the oxidation rate. The generation of a high density of point defects under irradiation in the oxides could lead to enhanced diffusion and hence could promote oxidation. However, due to radiolysis being the dominant mechanism by which irradiation affected the nature and formation of the oxides in this experiment, its contribution should be suppressed by the addition of an higher H_2 content to look upon the contribution of irradiation on diffusion.

Irradiation Assisted Corrosion experiment:

- Oxidation in a stainless steel loop at a lower pH than that of PWR media enhances the oxidation kinetic.
- Irradiation under proton flux caused the ECP to rise substantially due to radiolytic production of oxidising species (such as H_2O_2). It affected the oxides stabilities and engendered inner oxide dissolution and the formation of hematite.
- Further works should be conducted to study the effect of irradiation on diffusion and the oxidation kinetic in a medium with a higher H_2 content to prevent radiolysis.

4.3 Oxides formed at the crack tips of a decommissioned bolt

This section focus on the investigation of a cracked baffle to former bolt extracted from a french PWR (see Chapter 2 section 2.2.3 for details). Two FIB lamellae were extracted at the

oxidised crack tips and cautiously cleaned and thinned using PIPIS. The results will be compared to the ones obtained on samples previously studied in this work and to the open literature to discuss on the representativeness of short-time oxidations and surface observations of proton pre-irradiated specimens.

4.3.1 Oxides description

First of all, Figure 4.50 evidence an asymmetric oxidation behavour as seen previously on proton pre-irradiated samples in section 4.1.4.1. Each time, one side of the intergranular crack is more oxidised than the other. The observation of an asymmetric growth of the oxides on both sides of grain boundaries confirms that the grain boundary plane has a noticeable influence on the oxidation kinetic. The plane with the lowest symmetry ($(\bar{2}\bar{1}\bar{3})$ plane) clearly exhibited a preferential oxidation behaviour with regular oxidised facets while the $(10\bar{1})$ plane was much less oxidised and possessed a planar metal/oxide interface (Figure 4.50). Such behaviour is consistent with the preferential intragranular and intergranular oxidation along specific crystallographic directions seen previously (cf. sections 4.1.1.3 and 4.1.4.1). It can also be related to the differences in oxidation kinetic observed as a function of the underlying metal grain orientation shown in this work or by a few authors [13, 14, 86]. The grain boundary plane affinity to be oxidised will hence play a role in the IASCC process and preferential oxidation of grain boundaries plane could be detrimental for IASCC and the crack propagation. Moreover, fine porosities (< 10 nm) in the oxide with a higher number density near the metal/oxide interface were noticed (Figure 4.50) in agreement with observation on an extracted bolt from Tihange [196, 197]. Porosities were also observed in proton pre-irradiated samples on surface oxides and grain boundaries oxides penetration as seen previously in sections 4.1.1.3 and 4.1.4.1. The porosities could be detrimental for the crack propagation. No evidence of grain boundary migration as mentionned by Bertali et al. [198] on a nickel base alloy exposed to simulated PWR environment was seen.

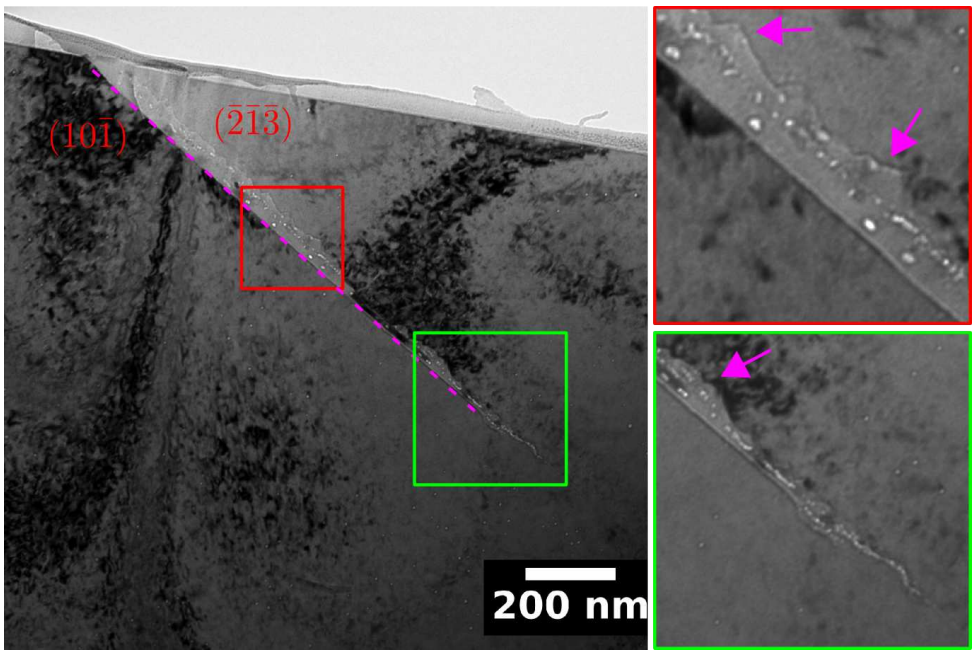

Figure 4.50: *TEM BF image on a crack tip of the neutron irradiated decommissioned bolt (grain boundary planes are written in red, magenta dashed lines indicate the homogenous oxidation behaviour, magenta arrows indicate the oxide penetration)*

Indexing FFTs obtained on the oxide (Figure 4.51) highlighted a spinel structure (AB_2O_4) as expected and coherent with previous findings (cf. sections 3.1.2 and 4.1.2.1) and the Tihange's bolt [196, 197]. Further investigation of the oxides formed reveals well oriented crystals indicating

that potential epitaxial relationships might be established between the oxide scales and the substrate as previously observed in sections 3.1.2.4 and 4.1.2.2. Nevertheless, the macroscopic strains and stresses seen by the bolt and those locally induced by the crack propagation at crack tip are likely to disturb and change locally the epitaxial relationship established.

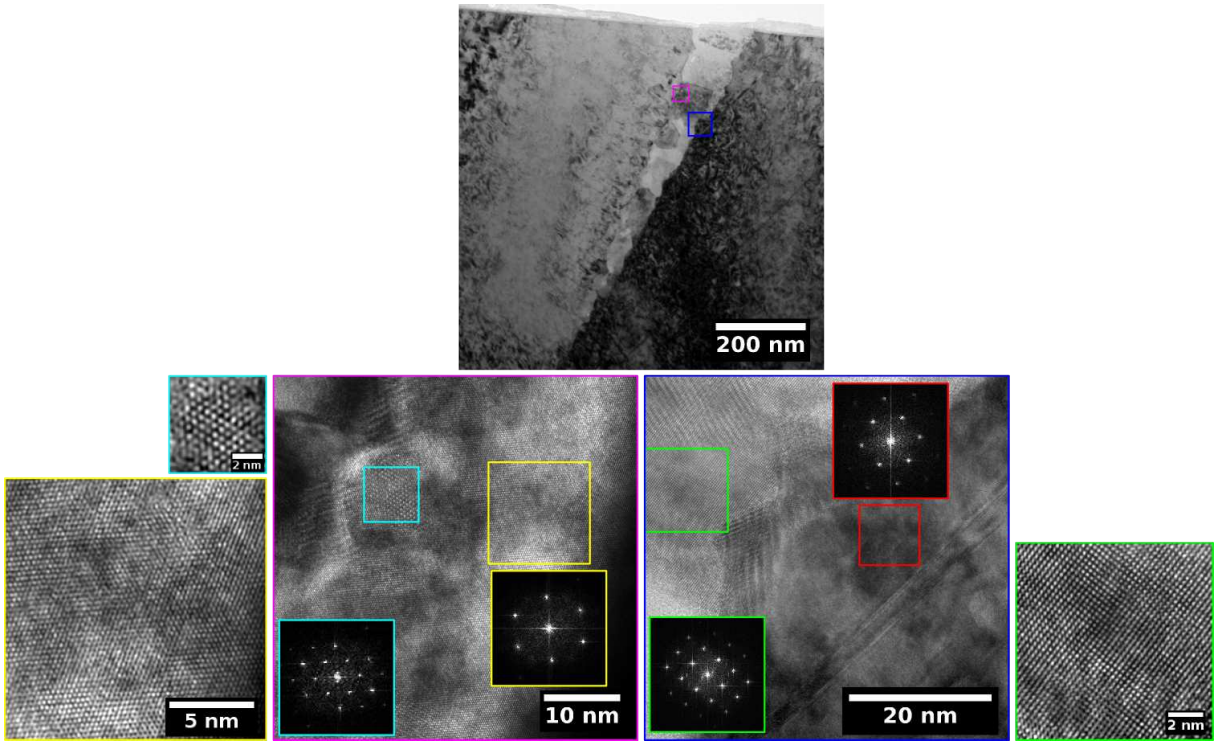

Figure 4.51: *HRTEM images on the crack tip of the neutron irradiated decommissioned bolt and associated FFTs and IFFTs (grain on the right is in [101] zone axis)*

To gain information on the oxide scales, EFTEM, EELS and EDXS mappings were carried out on the oxide formed at the crack tips. They revealed that the latter are filled with an iron-rich oxide while a chromium-rich oxide is formed at the crack flanks (Figure 4.52, 4.53 and 4.54). These observations are consistent with results on a PWR extracted bolt from Tihange at crack tip [196, 197]. Both these oxide scales (chromium-rich one and magnetite) are very similar to those observed on the surface of unirradiated and proton pre-irradiated 316L exposed to simulated PWR media as previously presented in this work (cf. sections 3.1.3 and 4.1.3) and by other authors [13, 21, 26–29, 32] but differs from outer Fe_2O_3 oxides observed locally after an oxidation under proton flux in simulated PWR media (cf. section 4.2.3). This shows that radiolysis is, as expected, indeed suppressed by the H_2 addition in PWRs unlike in the IAC experiment. At the crack tips, the inner oxide thicknesses varied from a few nm up to $\sim$ 35 nm while the oxide formed in the crack centre had a thickness that ranged from $\sim$ 10 to 30 nm. Moreover, Ni-enrichment was highlighted at the oxide flanks (Figures 4.52 and 4.54). Ni-enrichment at the metal/oxide as already observed previously in this work on samples oxidised in simulated primary water (cf. sections 3.1.3 and 4.1.3) and by authors on a decommissioned bolt [196, 197]. In addition unoxidised nickel clusters ($\sim$ 50 nm) were evidenced from the EFTEM maps (Figure 4.52) in the crack centre aligned with the former grain boundary. These nickel-rich areas are believed to result from the preferential oxidation of chromium and iron and the rejection of nickel during the Cr-rich oxide formation.

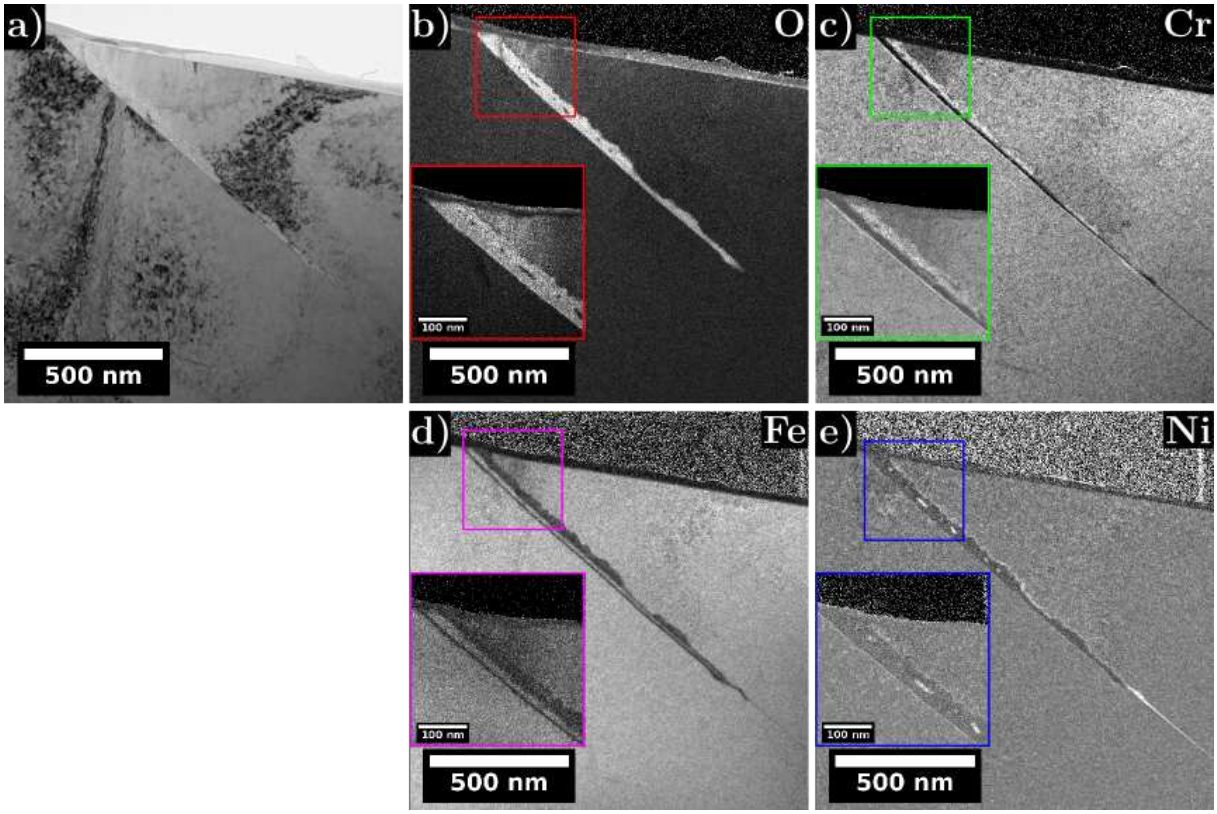

Figure 4.52: *EFTEM maps on the decommissioned bolt a) associated BF image b) oxygen map c) chromium map d) iron map and e) nickel map*

The segregation occurring in the hundreds of nanometre ahead of the crack tips was shown to be slightly different from the intergranular RIS presented in Chapter 2 section 2.3.2.2. Indeed, intergranular RIS is affected by the IASCC crack propagation (Figure 4.52 and Figure 4.53). A marked nickel enrichment extended over 1 µm at the crack tip as seen from EFTEM, EELS and EDXS mapping (Figures 4.52, 4.53 and 4.54). Such nickel enrichment below oxidised grain boundaries or crack tips was already reported by a few authors [9, 26, 31, 186, 196, 197, 199]. Nickel thus tends to accumulate ahead the oxide front. Moreover, the presence of oxidised silicon was highlighted at the crack tips over $\sim$ 200 nm while silicon depletion is observed over about 100 nm long ahead oxidised silicon at the crack tip (Figure 4.54). Silicon is assumed to be dissolved into the media since no Si was detected downstream in the crack. This looks close to the preferential dissolution of Si segregated at grain boundaries or on Frank loops at the oxidation front as previously observed on the proton irradiated sample either on intergranular oxide penetration or at the surface (see sections 4.1.3.3 and 4.1.4.2). Oxidised silicon (SiO_2) at the inner oxide/metal interface and at crack tip was already reported by Behnamian [186]. It is believed that to form this SiO_2 oxide, silicon segregated at grain boundaries due to RIS is sucked at the crack tips inducing the observed Si depletion over $\sim$ 100 nm in front of the oxidised silicon. Hence, Si segregation is modified at the crack tip and local release of Si into the medium at the crack tip could locally affect the oxidation. In addition, a clustering of sulphur was detected in the Si-depleted area ahead of the crack tip and sulphur-enrichment was seen at the metal/oxide interface (Figure 4.54).

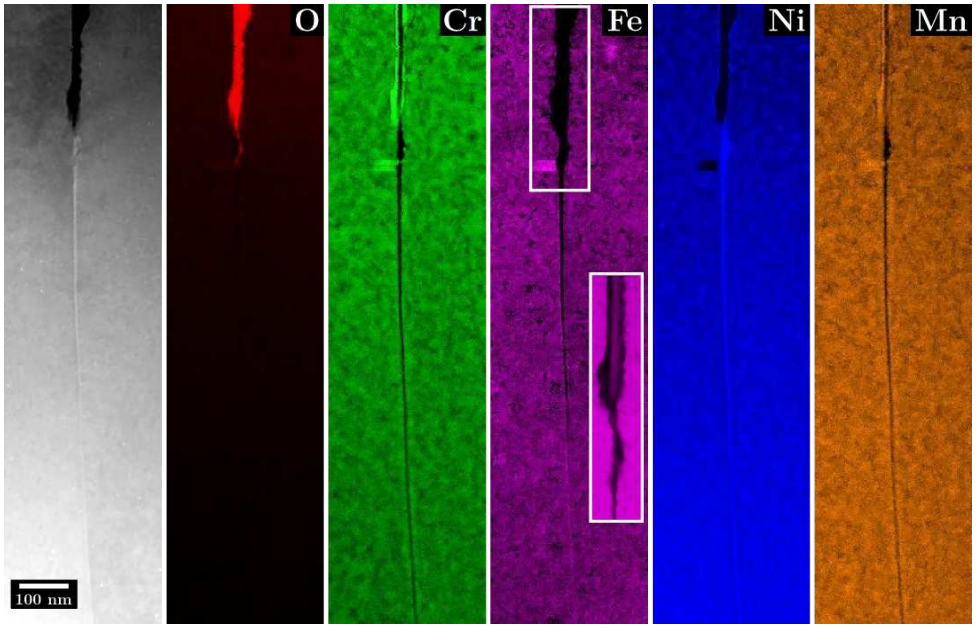

Figure 4.53: *STEM image and associated quantitative EELS mapping of the crack tip of the neutron irradiated decommissioned bolt*

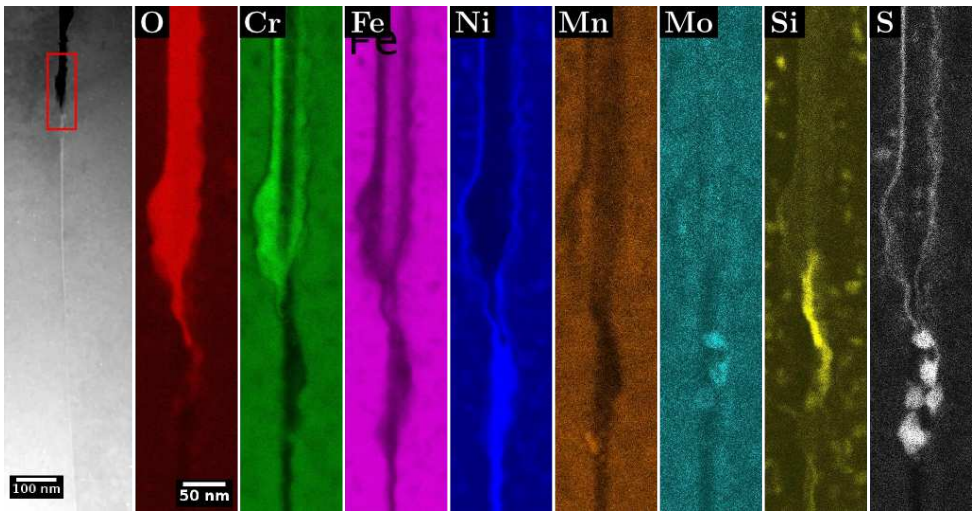

Figure 4.54: *STEM image and associated quantitative EDXS mapping of the crack tip of the neutron irradiated decommissioned bolt*

To confirm the presence of sulphur, two EDXS spectra were extracted, one from the matrix and the other on the believed S-enriched region (Figure 4.55). After normalising the spectra on the Mo-Kα line, it clearly appears that the relative intensity of the overall S-Kα and Mo-Kα line is higher. Thus, it demonstrates that sulphur is indeed responsible for the intensity increase and hence genuinely detected at the metal/oxide interface. Such S-rich enrichment at the oxide flanks was already seen on the grain boundary oxidation of the proton irradiated sample (cf. section 4.1.4.2). A few authors also evidenced sulphur segregation at the metal/oxide interface [187, 188, 197]. Detection of sulphur at the metal/oxide interface suggests that sulphur species were present in the crack-tip media. Release of sulphur from MnS inclusions, interacting with the medium in cracks appears likely. Therefore, this segregation might be a consequence of the release of sulphur from the MnS inclusions always present in industrial 316L alloys although in small amount. Their dissolution would induce a high concentration of sulphur species in the crack that could locally modify the medium chemistry and its pH in the crack. S-rich inclusions are believed to be former MnS inclusions and the lack of Mn into these might result from the transmutation of Mn to Fe [200]. Since sulphur is well known to weaken the SCC resistance

of metals, such sulphur segregation at the crack tip might play a detrimental role in IASCC cracking.

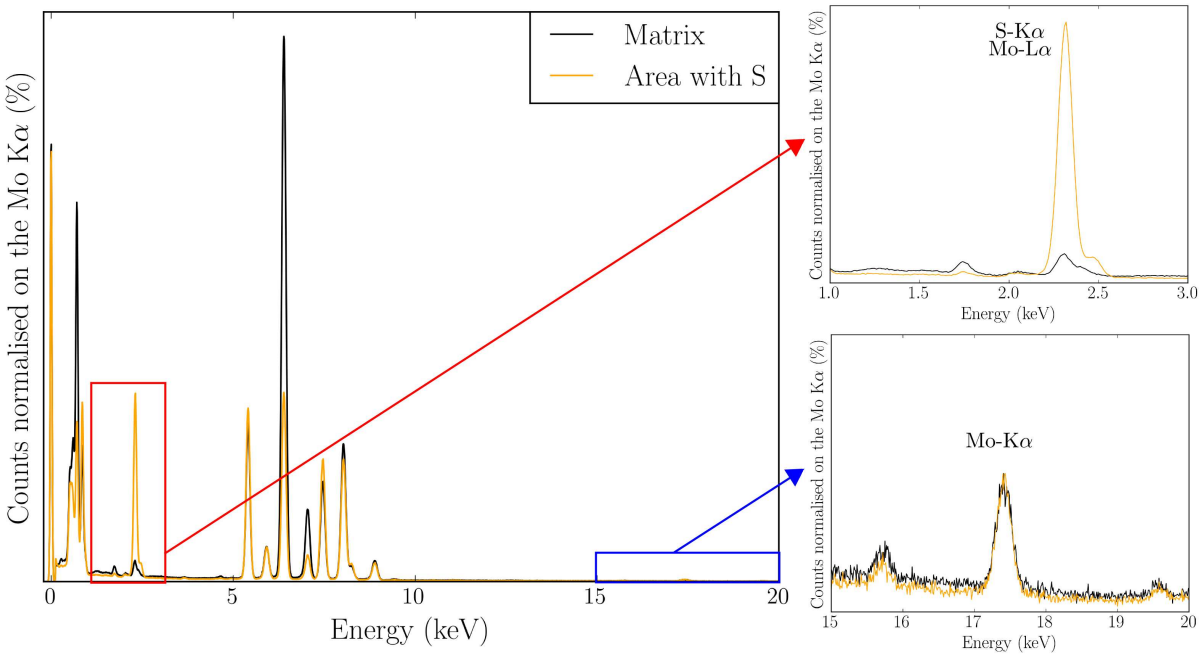

Figure 4.55: *EDXS spectra extracted from the matrix and the area thought to contain sulphur of the neutron irradiated decommissioned bolt*

4.3.2 Synthesis and discussion on the representativeness of short-time oxidations of proton pre-irradiated specimens

The main results on the oxides formed at crack tips are summarised below. Comparing the oxide scales formed at crack tips of the decommissioned PWR bolt with those formed on specimens proton pre-irradiated and oxidised during short durations, several similarities can be highlighted:

- The oxide is duplex and consituted of an inner chromium-rich oxide and an outer iron-rich oxide found for the bolt in the crack centre both of spinel structures.
- Ni-enrichment is present at the metal/oxide interface.
- The oxidation kinetic is contingent on the underlying metal grain for surface oxide and on the grain boundary plane for their intragranular oxidation and for the oxide formed at crack tips.
- Porosities are observed in the oxides.
- The grain boundary RIS is affected by the intergranular oxide penetration inducing a Ni-enrichment and a depletion/dissolution of silicon.
- Sulphur is segregated at the metal/oxide interface of the intergranular oxide.

All these analogous observations attest that performing short time oxidations of proton pre-irradiated specimens is an appropriate tool to mirror the oxides formed at crack tips.

Oxides formed at the crack tips of a decommissioned bolt:

- An iron-rich oxide (magnetite Fe_3O_4) is formed in the crack centre while a chromium-rich oxide is present on both sides of the cracks coherent with oxide scales formed on samples oxidised in simulated PWR media (synthetically irradiated or not). Clustering of unoxidised nickel is observed in the crack centre.
- Grain boundary plane greatly influences the oxidation and could prove detrimental. Facets are growing along specific preferential crystallographic directions as already observed on unirradiated and irradiated grain boundary oxide penetrations.
- Combination of RIS and IASCC induced a marked Ni segregation and the formation of oxidised silicon coupled with its depletion downstream.
- Segregation/clustering of sulphur at the crack tips is believed to result from release of S from MnS inclusions.

➔ Performing short time oxidations of proton pre-irradiated specimens is an efficient tool for emulating the oxides formed at crack tips.

4.4 Oxide scales formed on irradiated materials: Synthesis

Irradiation can affect oxidation kinetics by two different ways: modifying material properties through damage production and changing the media through water radiolysis. The main modifications in stainless steels induced by neutron irradiation are microstructural changes (formation of cavities, Frank loops, etc.) and Radiation Induced Segregation (on defects, at grain boundaries, etc.). These were emulated by synthetic irradiations such as proton ones as shown in Chapter 2 section 2.3.2.2 and therefore significant modifications alike those on neutron irradiated materials were induced in the irradiated specimens.

In PWRs water radiolysis only has a negligible influence on the primary water since radiolysis products quickly disappear through reactions with the added dissolved hydrogen. This was confirmed by the observation of oxides at crack tips analogous to those formed in simulated PWR environment but different from those formed under proton flux during the IAC experiment. Indeed, study of the latter in which radiolysis appeared to be the main process affecting the oxidation revealed that hematite formation and chromium dissolution wholely modified the oxidation process.

The results on proton pre-irradiated materials indicates that irradiation enhanced the oxidation kinetic but did not change the basic oxidation process. Thicker oxides are formed on irradiated samples and are richer in chromium due to enhanced diffusion of oxygen through the inner layer and promoted chromium diffusion due to the numerous defects induced by irradiation. The oxides formed on irradiated material were found porous. These porosities are thought the primary reason for the enhanced diffusion in the inner oxide layers. Since well-polished surfaces were exposed to simulated PWR media, the near surfaces contained numerous irradiation defects (Frank loops, cavities). On irradiated materials, bigger and a higher number of crystallites were formed. Such irradiation defects are believed to provide preferential nucleation sites and increase the nucleation rate enhancing oxidation. These defects were also found segregated as highlighted in Chapter 2 section 2.3.2.1 but not preferentially oxidised. Silicon was however depleted at the oxidation front on the loop tip and could be dissolved into the medium. The loops are believed to affect the oxidation kinetic and the inclination of Frank loops with regards to the oxidised surface will slow the growth of the inner oxide layer inducing intragranular oxide penetrations.

In addition, in irradiated materials, grain boundary oxidation was promoted. It is considered that modification of the grain boundary composition due to RIS was the driving process to this enhanced oxidation. RIS was found affected by the grain boundary oxidation. Silicon and phosphorus are sucked at the intergranular oxide tip and believed dissolved into the medium whereas nickel accumulated. Silicon and phosphorus released could locally modify the medium at crack tips and thereby the oxidation process. Intragranular and intergranular oxide penetration were found to grow along preferential crystallographic directions.

To bring light on the IASCC mechanisms and the representativeness of this work, the oxide formed at the crack tips of a damaged bolt was investigated. IASCC crack propagation will, among other, depend on the oxides formed, the crack tip chemistry as well as its surrounding matrix. At the crack tip of the extracted bolt, narrow bands of Cr-rich spinel formed along the crack walls and Fe-rich spinel filled the crack centre consistent with surface oxides formed in simulated PWR media observed previously. The oxides were porous as those formed on proton pre-irradiated samples exposed to simulated PWR medium. These porosities will likely weaken the grain boundary, promote IASCC and the crack propagation. Moreover, the asymmetric character of the oxidation contingent on the grain boundary plane was also evidenced on the crack of the oxidised neutron irradiated bolt. This preferential oxidation behaviour inducing facets growing along specific crystallographic directions were already observed on unirradiated and irradiated intergraular oxide penetrations. The preferential affinity of some grain boundary planes to be oxidised could prove detrimental and would promote cracking. Combination of RIS and IASCC resulted in a marked Ni enrichment ahead of the tip and the formation of oxidised silicon near the crack tip coupled with its depletion downstream. Therefore, the intragranular RIS of the cracked bolt was similarly affected by the oxidation process as on the pre-irradiated samples. Nevertheless, the presence of oxidised silicon and Ni-rich clusters in the crack centre, not observed on the synthetically irradiated samples, indicates a different oxidation stage at the crack tip compared to the short times studied.

Main conclusions on the oxide scales formed on irradiated materials:

- The basic oxidation process is not considered to be changed due to irradiation but oxidation kinetic is promoted by irradiation.
- Porous oxides are formed on irradiated material while they were not found porous on unirradiated materials (for media whose pH $\approx$ 7.3).
- Segregated irradiation defects (cavities and Frank loops) were not found preferentially oxidised. Silicon segregated on the loop was observed sucked near the oxidation front and is thought released into the medium. These loops are believed, with respect to their inclination, to slow down the oxidation kinetic.
- Intergranular RIS promote the oxidation rate at grain boundaries but is affected by the intergranular oxidation inducing depletion of silicon and phosphorus and nickel enrichment near the tip of the oxide penetration.
- Radiolysis is suppressed in PWR water by the addition of H_2 but if not suppressed completely modify the oxidation process (hematite formation, inner oxide dissolution).
- Performing short time oxidations on proton pre-irradiated specimens is an appropriate tool to emulate crack tips oxidation.

Conclusions and perspectives

In order to better understand the IASCC phenomenon, the study of the irradiation effect on the oxide scales and their formation and growth mechanisms is of great importance. Therefore, the purpose of this study was to investigate the effect of irradiation on the oxidation first stages of a 316L austenitic stainless steel exposed to simulated PWR environment. It aimed to emulate the oxidation at IASCC crack tips by performing short times oxidations. This thesis provides experimental data on surface oxidation of irradiated stainless steels in simulated primary water for the oxidation first stages. As the study of the effect of irradiation on the corrosion of austenitic stainless steels involves many parameters related to the material, the medium and the irradiation, this work is a first step in understanding the role of irradiation defects on corrosion.

Since only few studies have investigated the oxidation first stages of austenitic stainless steel in PWR environment and even fewer have reported the effect of irradiation on oxidation, both unirradiated and irradiated samples were oxidised in simulated PWR during short oxidation durations (from 5 minutes to 96 hours). Hence, in a first step, unirradiated samples were characterised while taking into consideration the underlying metal grain crystallographic orientation. Focus was also brought on surface inhomogeneities such as surface preparation and inclusions. Proton pre-irradiations were performed up to 1.5 dpa at $\sim$ 380 °C to emulate neutron induced defects and chemistry. The proton irradiation temperature was chosen to provide a compromise between microstructural and microchemical changes induced by irradiation similar to that of neutrons. The irradiation induced changes (cavities, Frank loops, RIS at grain boundaries and RIS on irradiation defects) were looked upon, characterised and quantified to conclude on the proton pre-irradiation representativeness and its ability to emulate neutron irradiation. Then, samples proton pre-irradiated and oxidised in simulated primary water were investigated and compared to unirradiated ones to rule on the role of irradiation defects on the oxide formed and oxidation kinetics. Such comparison allowed to provide a direct connection between radiation-induced changes and oxidation rate as well as mechanisms. In-depth characterisations of the oxide layers were carried out. The oxides morphology, thickness, structure, composition and epitaxial relationship were investigated. The crystallographic orientation of the underlying metal grain was taken into account in this work and its role on the oxidation kinetic was investigated. Since the main bolt cracks appear to be intergranular ones, attention was drawn on grain boundaries oxidation. The oxide penetration at grain boundaries was analysed from its composition to the penetration depth and linked to the RIS. Moreover, an oxidation under proton flux was made at the University of Michigan to study the IAC phenomenon and look upon the contribution of the proton flux on the oxidation process as occurring in PWR. Unfortunately the loop was made of stainless steel whereas the Titane loop is made of titanium and both media pH differed inducing a bias in this study. Nonetheless it permitted to look upon both these effects. Finally, a cracked decommissioned PWR bolt was studied. The oxide layers at crack tips were compared to the ones formed on proton irradiated samples to conclude on the representativeness of the investigation of surface oxides formed during short oxidation times.

➔ Proton irradiation representativeness

As neutron irradiation requires costly specialised facilities able to handle radioactive samples to investigate the materials, it is essential to emulate at best the PWR irradiation on laboratory

samples. Since synthetic irradiations can serve as an efficient tool to simulate neutron damage using correct temperature shifts proton pre-irradiation were performed. They allowed to reach, in a few hours, higher doses than that when using neutrons thus decreasing the irradiation cost while creating low or even no radioactivity and allowing an easier sample handling. Irradiation temperature was chosen to be a compromise for emulating both the microstructure and microchemistry similar to that of neutron at PWR relevant temperatures. The microstructures and segregation were characterised using TEM. It consisted of Frank loops and cavities of sizes and densities in accordance to neutron and proton literature. RIS at grain boundaries was also found both qualitatively and quantitatively consistent with neutron irradiated materials. For the first time, TEM in-depth analyses of the intragranular segregation permitted to link the segregated area to the defect nature. Nonetheless, these analyses should be combined to APT measurements to provide chemical compositions of the segregated areas with a better accuracy. One of today challenge would be to characterise, on a same area, chemical segregation and defects on APT thin needles by both TEM and APT. Thus, both microstructural defects and segregation induced by neutron irradiation are closely replicated using proton irradiation. TEM sample preparation and especially thickness and quality of the foil was shown to greatly affect the defects quantification. The optention of thin high quality samples to investigate irradiation defects and segregation is required. Therefore, efforts should be made to prepare at best the cleanest and as thin as needed TEM samples for the studies of irradiated materials.

➔ On the importance of sample preparation

Different samples preparations were implemented from a reference polishing that did not induce cold-work or dislocations to samples whose final polishing step was rougher (6 µm diamond paste and SiC P4000 paper). The latter induced controlled deformed layers at the sample subsurface. The investigations of the oxides scales on these samples revealed that the surface preparation greatly affected the oxide layers formed. Cold-worked brought by the polishing and cold-work generally speaking accelerates the overall oxidation kinetic. These findings also propose that the presence of surface hardened layer can induce of loss of epitaxy between the oxide layers and the substrate that can locally enhance the oxidation kinetic. If the sample polishing is not well controlled, it will greatly alter the oxidation kinetic, especially at short oxidation times. As numerous laboratory tests nowadays focus on better understanding oxidation process, sample surface preparations should be of very great care to produce representative and reproducible samples. Validation of these results using mechanically polished proton (or neutron) irradiated samples is needed to see if the induced cold-work overcome the influence of irradiation. In addition, this will make these results more appropriate to be used for actual PWR internals since the bolt are cold-worked and crack propagation will engender stresses and strains at the crack tips.

➔ Influence of the chemistry of the medium and installation effect

Oxidation in a stainless steel loop engenders a dissolution/re-precipitation process that enhances the outer oxide growth by up to ~ 100 times for 24 hours oxidation compared to the loop made of titanium. To carry out a representative study of the effect of short time oxidations, oxidations in a titanium loop are better suited as the outer oxide formation and growth will only be linked to the studied material and diffusion through its inner layer. Moreover, oxidation in a slightly lower pH than that of PWR medium was found to enhance the oxidation kinetic and induce the formation of porous inner oxide layers. Therefore at such pH the inner oxide loses some of its protectiveness and representative studies should be made at pH close to that of PWR media.

➔ Characteristics of the oxides formed in PWR medium

The oxide formed was always found to be duplex and of AB_2O_4 structure, regardless of the oxidised sample and the oxidation duration. The inner oxide layer is dense, continuous and chromium-rich (close to $FeCr_2O_4$) and is progressively enriched in chromium while the outer crystallites are dispersed on top of the inner oxide layer close to magnetite (Fe_3O_4). A nickel-rich area was also observed at the metal oxide interface and this region is likely to have a different lattice parameter than the matrix. It could induce strains at the metal/oxide interface and should be further investigated using HRTEM in an aberration corrected TEM. During this work it was evidenced that after 24 hours oxidation an epitaxial relationship is established between the metal and the oxide layers and engenders specific outer oxide morphologies. The inner layer is then epitaxially grown and is not a fine grains oxide as often reported. Such oxidation behaviour should be implemented in corrosion models as it will greatly influence diffusion and hence the oxidation kinetic. Micro-Raman spectroscopy was proven a useful tool for the study of the oxides. Further analyses combined to Ab initio calculations should be made to look upon the influence of strain in the oxide on the band shifts and of the amount of chromium in the oxide layers and therefore allow a better interpretation of the spectra. As Raman spectroscopy give information on the local chemistry it would benefit to be combined with High Resolution Electron Energy Loss Spectroscopy (HREELS) to yield a fuller description of the oxides. Moreover, in-depth studies of the ions distribution contingent on their valence in the oxide layers would provide information on the growth mechanism of these oxides. For example, Energy Loss Near Edge Structure (ELNES) study of both the oxygen and the iron/chromium edges would grant information on the oxide layers but local regions such as the Ni-rich area and intergranular oxides should also be looked upon.

➔ Influence of the crystallographic orientation of the underlying metal grain on the oxidation mechanisms for the oxidation first stages

The underlying metal grain crystallographic orientation was found to control the oxidation kinetic at short oxidation times. Oxides formed on [111] grain orientation are thickers and richer in chromium than those formed on [100] grain orientation. This oxidation kinetic lays on the inner oxide stresses coming from the more or less easy and energy-consuming establishment of the epitaxial orientation relationship between the substrate and the oxide layers. The higher the strain in the oxide scale and the stoichiometry deviance the faster the diffusion through this layer and hence the growth rate. As the crystallographic orientation clearly play a role on the oxidation kinetic, further work should be done to conclude on preferential oxidised orientations. Since in this work this effect was only studied for high symmetry orientations further investigations should be carried out on orientations with lower symmetries. The investigation of various grain orientations could help to better represent the diversities in grain boundary planes and their oxidation behaviour. Ab initio calculations should be made to confirm these observations and to investigate cations and anions diffusion through the inner layer depending upon the spinel orientation and therefore underlying metal grain orientation. HRTEM imaging would provide information on the epitaxial relationship established depending upon the oxidised surface orientation and on the dislocation network at the metal/oxide interface.

➔ Effect of irradiation on the oxidation kinetic and mechanisms

Results from this work clearly attested that irradiation accelerates the oxidation of austenitic stainless steel. Irradiation enhanced both the inner and outer oxide growth. It also promoted the nucleation rate of outer crystallites and defects are thought to act as preferential nucleation sites. Porous oxides were observed on irradiated material and these porosities are likely to promote diffusion and the oxidation kinetic. To confirm these assumptions, tracer experiments should be

carried out to study oxygen diffusion through these oxides. Moreover, inner oxide layer richer in chromium were formed on irradiated specimens hinting that defects induced by irradiation accelerated chromium diffusion from the allow toward the inner oxide layer. Nonetheless, to provide a strong enough database, studies on the effect of irradiation should also be carried out at longer oxidation times and on different grain orientations. Irradiation defects were not found preferentially oxidised but silicon was observed sucked at a loop tip located at the oxidation front. This silicon is believed dissolved and released into the medium. The inclination of Frank loops with regards to the oxidised interface revealed that these play a role on the oxidation kinetic that have to be further studied. In addition, a promoted oxidation was noticed at grain boundaries of irradiated samples and is thought to hail from the RIS at grain boundaries and especially their lower chromium content. Combination of RIS and oxidation induced a marked Ni-enrichment and a depletion of silicon and phosphorus at the tip of the intergranular oxide. Both silicon and phosphorous are thought released into the medium and could locally affect it and modify the oxidation process. Nevertheless, to be more conclusives, extensive investigations should be made on numerous oxidised grain boundaries, fully characterising them while taking into consideration the grain boundary plane. This could provide correlation between preferential oxidation at grain boundaries and cracking (crack initiation, propagation, etc). HREELS investigations should be carried out focusing on local phenomena such as on irradiation defects near the oxidation front, the intergranular Si/P depleted region etc. as the latter are likely to affect the oxidation. These, coupled to APT analyses would provide even more reliable chemical compositions. Doing so would confirm the delaying effect of the segregated defects on the oxidation kinetic and would bring light on the contribution of the intergranular Ni-rich or Si/P depleted areas.

➔ On the representativeness of the study of short oxidation duration and surface oxides to emulate the crack tips oxidation

Oxides formed at crack tips were found similar to those formed on sample surfaces both in terms of structure and chemistry with the observation of a duplex oxide layer and a underlying nickel enrichment. The same oxidation behaviour interacting with RIS was also observed at grain boundaries. Hence, the study of surfaces oxidised during short durations appears an appropriate and less expensive solution to emulate the crack tips oxidation. As on unirradiated and proton pre-irradiated specimens, the grain boundary oxidation at the crack evidenced an asymmetric oxidation with the formation of facets. Our results show that the intergranular oxide growth proceeds along specific crystallographic orientations that should be linked to the grain boundary plane and thus can be related to surface oxidation. In-depth studies of preferential oxidations contingent on the crystallographic orientation appear required as cracking often occurs at grain boundaries. Thereby, considering only the grain boundary coincidence is not sufficient and particular attention should be paid to the grain boundary planes and their oxidation since a preferential oxidation of the grain boundaries could lead to cracking and would further promote the crack propagation. Investigation of numerous oxidised grain boundaries should therefore be carried out with a full characterisation of the grain boundaries and the grain boundary planes. Doing so could bring some understanding on the preferential oxidation of some grain boundaries and the crack initiation and propagation. This could be coupled to studies of model alloys emulating the measured concentrations at irradiated grain boundaries. It would in addition provide numerous information on the effect of each (or at least several) elements segregated due to the RIS on the oxidation process occurring at crack tips. The formation of oxidised silicon and its dissolution as well as the observation of sulphur rich-areas hailing from the dissolution of MnS precipitates at crack tips should be further investigated. More lamellae should be extracted at crack tips to confirm the representativity of these observations. Alike sulphur segregation from that at crack tip was observed at the flank of an intergranular oxide on a sample exposed to simulated PWR medium. Since MnS inclusions are always present in industrial alloys, the

investigation of grain boundaries oxidised near such inclusions could give information of the effect of sulphur on the oxidation. In addition, the Irradiation Assisted Corrosion experiment was found to induce a noticeable change in the oxidation mechanism as hematite formation and dissolution of the inner oxide layer were evidenced. Water radiolysis under the proton beam was found the main driving mechanism for this oxidation. Due to radiolysis the simultaneity of the corrosion and irradiation processes (displacement damages/creation of point defects) has not been taken into account and is likely to further complicate the study of the phenomena involved. Indeed, vacancies induced by the irradiation are likely to affect the oxidation process as they participate to the oxide growth. Therefore further studies adding a higher hydrogen content would be required to investigate the effect of displacement damage on the oxides growth. Such experiments of simultaneous exposure to the primary medium and to the neutron/synthetic flux seem necessary to complete the results acquired in this work. It would allow to achieve a more accurate and complete description of the effects of irradiation on the oxidation process and kinetic occurring at crack tips.

Appendix A

Rel-Rod Dark Field

Widely used in literature [91, 93, 98, 106, 107, 142, 169, 201, 202], the Rel-Rod Dark Field (RRDF) technique allows to image and quantify nanometric dislocation loops. This technique makes it possible to image the loops stacking fault without the unneeded contrast generated by the matrix, which facilitates the loops counting and their size determination. In most works of the literature the minimum loop size pictured is of 1 nm. Measurements are almost always made for foil thicknesses of about 80 nm. By working on thinner samples results will be even more accurate since the assumption of kinematic diffraction can be reached. Thus electrons will only scatter once in the specimen and will not subsequently interact with each other or undiffracted electrons. The presence of Frank's loops cause the appearance of distinct streaks of the matrix spots in diffraction patterns (Figure A.1). These white streaks are called Rel-Rods and are associated with stacking faults responsible for Frank's loops in the {111} planes. In order to image these loops it is necessary to work in two-waves condition. Thus it is necessary to tilt far away from a zone axis (often <110>) along a selected reflection g (commonly [311]). The Dark Field images obtained by selecting a streak with the objective diaphragm image Frank's loops edge-on. However, it is not possible, using RRDF to differentiate extrinsic or intrinsic faults (ie faults associated with vacancy or interstitial type loops). One of the main drawbacks of this technique is the difficulty of visualising the four families of Frank's loops. Indeed, this technique allows observation only from one of the four loop families onto a Rel-Rod image. Even the use of a double tilt holder does not allow to affirm that all Frank loops families can be reached. In addition, at large tilt angles and after a short time spent on an area to be analysed, it is possible that some loops become hardly observable, due to surface contamination. Frank's total loop density is, in most works, obtained by multiplying by 4 the obtained density for a family of loops considering an isotropic loop distribution. Nevertheless, one should remember that the size and density of these dislocation loops are strongly dependent on the irradiation conditions, the dose received and the irradiated material.

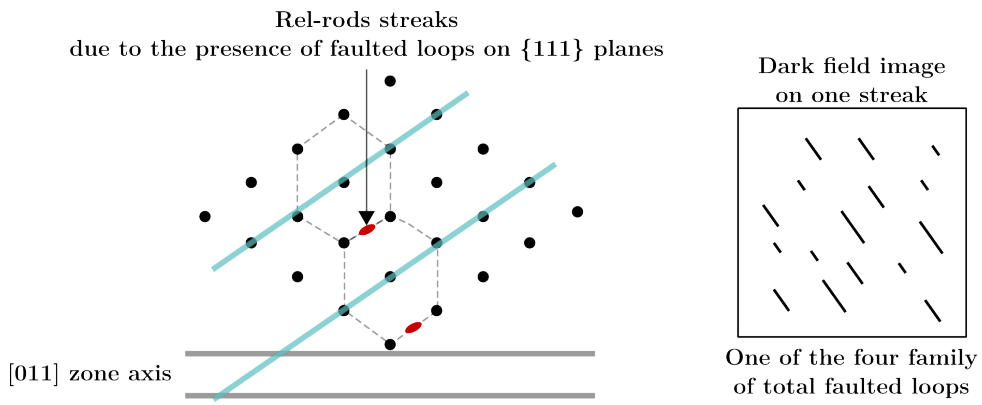

Figure A.1: *Schematic of the Rel-Rod Dark Field imaging*

Appendices

Appendix B

Raman spectroscopy applied to spinel oxides

Raman spectroscopy allow to look upon the structure and chemistry of a compound by identifying the bands that act as fingerprint. This technique can be used to study corrosion layers. Once a spectrum acquired it is common to identify the corrosion product by comparing the spectrum to Raman spectra of known oxide compound. A matching can be done to identify the special fingerprint of the observed bands and identify the oxide formed.

From the literature data, it is widely believed that the oxides formed on stainless steel alloy exposed to PWR medium are composed of an outer layer of magnetite and a mixte spinel inner layer. Five active vibrational modes are allowed regarding the spinel oxides, A_{1g}, E_g and three F_{2g} modes ($F_{2g}(1)$ being at the lower wavenumbers and $F_{2g}(3)$ at the highest) [203, 204]. Their intensity is usually ranked as such: $A_{1g} \geq F_{2g}(3) \geq F_{2g}(2) \geq E_g$.

Only a few authors studied, using Raman spectroscopy, the oxide scales formed on 316L alloy oxidised in PWR medium [12, 89, 178]. Soulas analysed the oxide formed on top of a 316L oxidised in PWR medium during 5 minutes to 24 hours on the same TITANE loop as used in this work (Figure B.1) [12]. As the oxidation duration increases, the signal coming from the oxide increases too due to the oxide progressive crystallisation. In addition, sprecta show four bands typical of a iron/chromium spinel AB_2O_4 with the most intense one close to ~ 690 cm^{-1}. Wang also studied a 316L exposed to PWR medium [178]. She observed five bands on each spectrum with the most intense one located at ~ 690 cm^{-1} (Figure B.2). Since the oxide formed on stainless steel alloy exposed to PWR media is know to be duplex and both oxide mostly found to be iron containing spinels, it can complicate the spectra interpretation due to the band proximity. Moreover, one should remember that a slight variation of the oxide chemistry of the presence of strain in the oxide should cause peak shifts. Therefore it complicates the spectra interpretation.

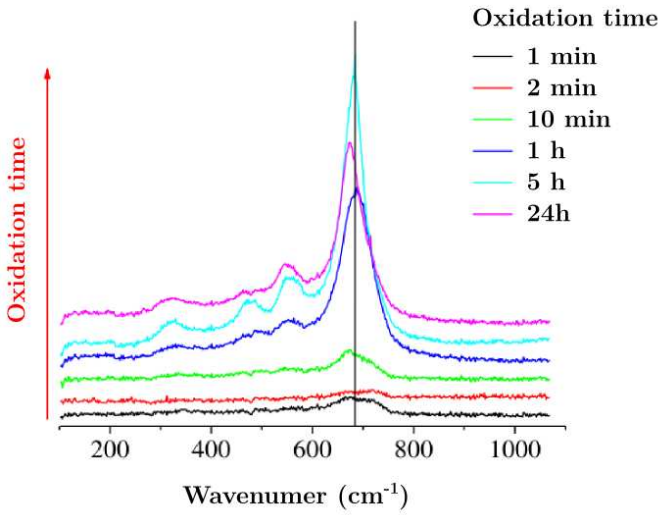

Figure B.1: *Raman spectra of 316L alloy oxidised from 1 min to 24 hours in simulated PWR medium [12]*

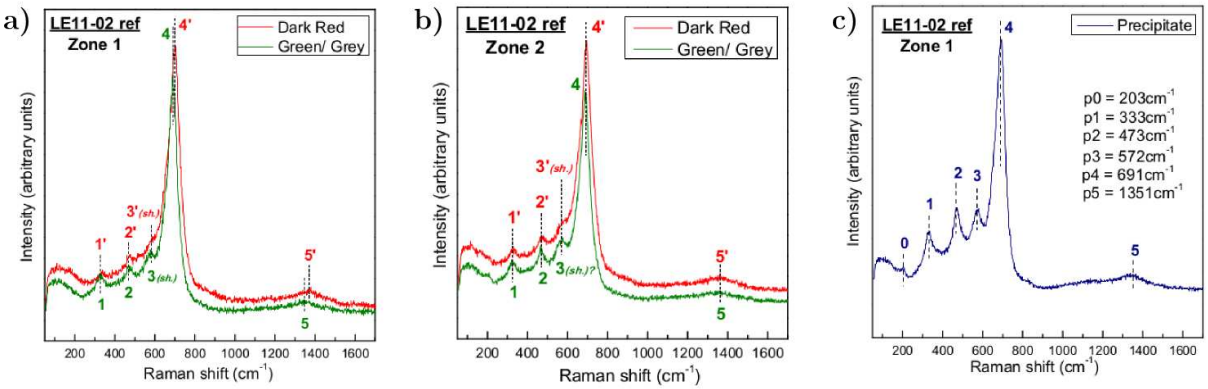

Figure B.2: *Raman spectra of 316L alloy oxidised 72 hours in simulated PWR medium a) in the central zone, b) in the confined zone and c) on a precipitate [178]*

To better inteprate the Raman spectra obtained on stainless steels oxidised in PWR environment, one should look upon pure oxide spectra. Therefore spectra were acquired onto references oxides in the form of powders (Figure B.3). Gaussian/Lorentzian curve fitting was used to find the band positions as presented in Table B.1.

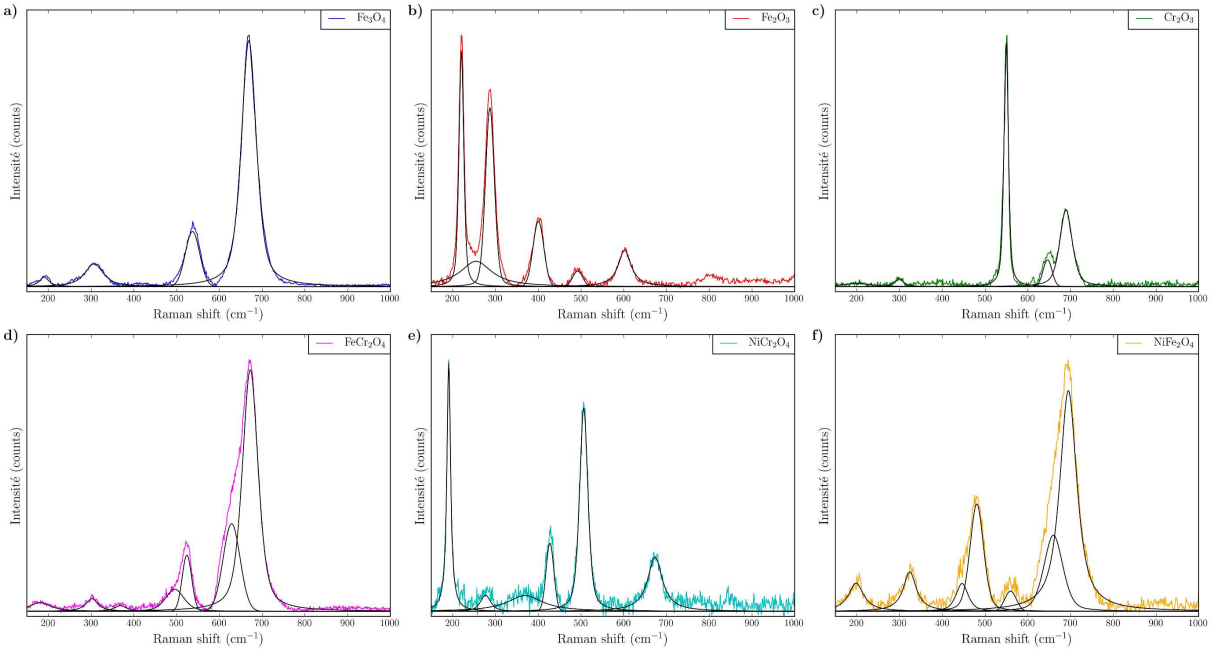

Figure B.3: *Raman spectra and associated Gaussian/Lorentzian fits of a) Fe_3O_4, b) Fe_2O_3, c) Cr_2O_3, d)$FeCr_2O_4$, e) $NiCr_2O_4$ and f) $NiFe_2O_4$ (Cr_2O_3 data from [205])*

Table B.1: *Band positions (cm^{-1}) of Fe_3O_4, Fe_2O_3, Cr_2O_3, $FeCr_2O_4$, $NiCr_2O_4$ and $NiFe_2O_4$ (sh: shouldering, ♢: most intense band)*

Fe_3O_4	Fe_2O_3	Cr_2O_3	$FeCr_2O_4$	$NiCr_2O_4$	$NiFe_2O_4$
190	202 ♢	199	180	191 ♢	198
307	255	299	302	277	324
537	287	550 ♢	369	370	446(sh) - 481
669 ♢	400	646	496(sh) - 525	427	560
	492	689	629(sh) - 672 ♢	507	660(sh) - 695 ♢
	602			673	

Hosterman conducted a study of several oxide and the obtained spectra that might form on stainless steels exposed to PWR medium are reported in Figure B.4. Table B.2 presents the band positions of the oxides presented in Figure B.4.

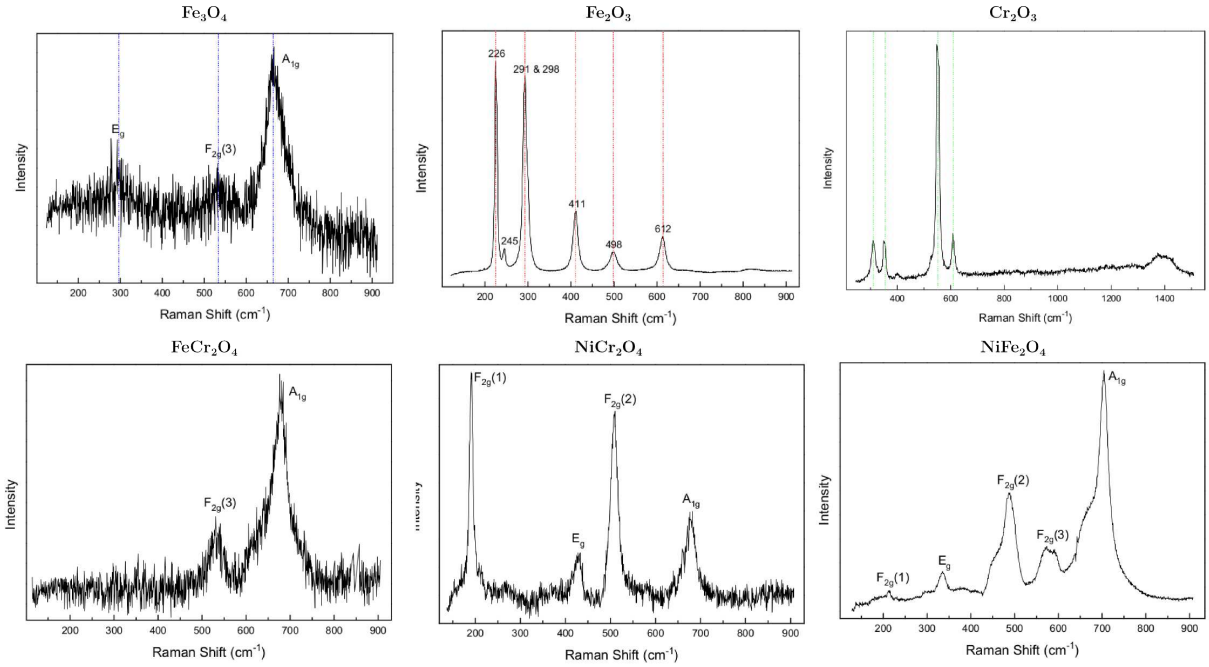

Figure B.4: *Raman spectra of Fe_3O_4, Fe_2O_3, Cr_2O_3, $FeCr_2O_4$, $NiCr_2O_4$ and $NiFe_2O_4$ [184]*

Table B.2: *Band positions (cm^{-1}) of Fe_3O_4, Fe_2O_3, Cr_2O_3, $FeCr_2O_4$, $NiCr_2O_4$ and $NiFe_2O_4$ (sh: shouldering) [184]*

Fe_3O_4	Fe_2O_3	Cr_2O_3	$FeCr_2O_4$	$NiCr_2O_4$	$NiFe_2O_4$
-	226	310	531	191	189(sh) - 211
295	245	351	635(sh) - 678	429	333
-	291	531		508	456(sh) - 487
531	298	552		-	568(sh) - 590
667	411	609		676	663(sh) - 704
	498				
	612				

For the oxides of interest (Fe_3O_4 and $FeCr_2O_4$) and the mixed spinel oxides in general, the strongest band appears between 660 and 680 cm^{-1} and is related to the A_{1g} mode [204]. Several authors reported a shift of the band toward the higher wavenumbers from the magnetite to the chromite (or spinel mixed oxide) regarding the A_{1g} mode [175, 183–185]. The wider gap between the A_{1g} mode from magnetite and chromite was observed by Wang et al. [183]. This gap was of about 17 cm^{-1} from 667 cm^{-1} for Fe_3O_4 to 684 cm^{-1} for $FeCr_2O_4$. There is then a shift in the observed bands depending on the iron/chromium content that can be related to the cation substitution as presented in Figure B.5. All the authors agree that when the chromium content increases the band associated to the A_{1g} mode is shifted toward higher wavenumbers. D'ipolito et al. [185] completed this saying that it is linked to the cation radius. According to them, the larger the radius of the cation the more shifted the A_{1g} band is toward higher wavenumbers. This explains the lower wavenumber for the magnetite against the chromite since the average cation radius size is smaller for the magnetite. Moreover, a shouldering of the band associated with the A_{1g} mode was observed by Wang et al. [183], McCarty [175] as well as Hosterman [184].

The intensity of the bands is known to be related to the degree of covalent character. Thus, the most intense band is produced by the bond having the strongest degree of covalent character. Regarding the magnetite, molecular vibration of the Fe^{3+}–O bonds in octahedral and tetragonal structure are responsible for the A_{1g} mode because they have a higher degree of covalent character than Fe^{2+}–O bonds. As for the chromite and more generally mixed spinel, the A_{1g} mode is due to the (Cr^{3+}, Fe^{3+})–O bonds in the chromite octahedral structure. The trivalent ions

inducing a compact structure formation with a higher degree of covalent character than in the tetrahedral structure Fe^{2+}–O is responsible for the A_{1g} mode.

Table B.3 presents a literature survey of observed Raman bands and their associated modes for magnetite, chromite and mixed spinels.

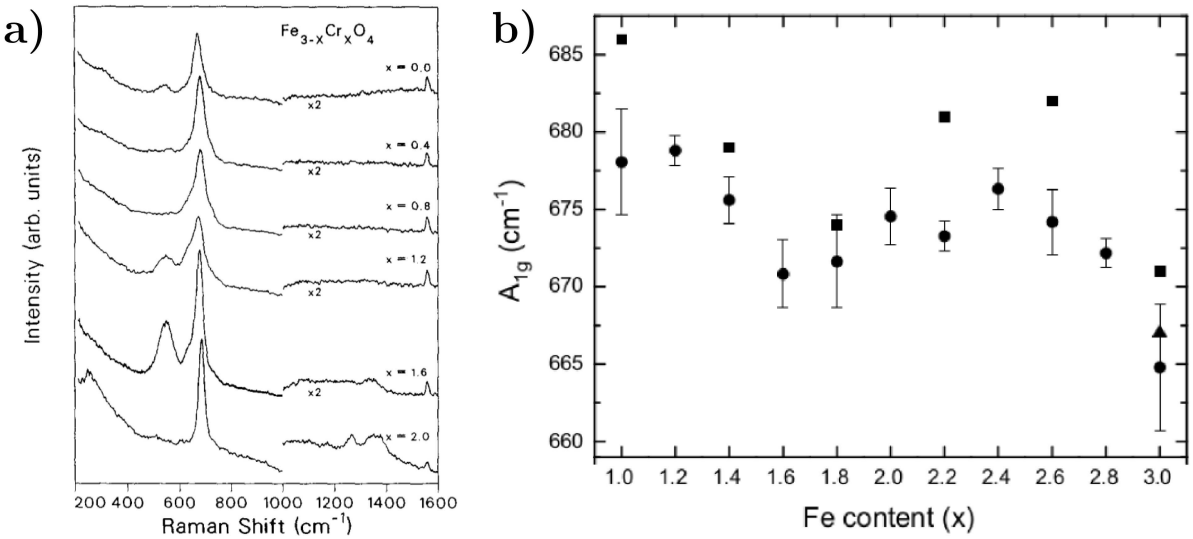

Figure B.5: *a) Raman spectra of solid solutions of $Fe_{3-x}Cr_xO_4$ (x = 0 - 0,4 - 0,8 - 1,2 - 1,6 - 2) [175] b) Bands shift for A_{1g} mode of $Fe_xCr_{3-x}O_4$ [184] (circles: [184], square: [175])*

Table B.3: *Literature survey of Raman bands for magnetite (Fe_3O_4) (cm^{-1}), chromite ($FeCr_2O_4$) and mixed spinels (cm^{-1})*

	McCarty [175] Fe_3O_4	Gasparov [204] Fe_3O_4	Shebanova [206] Fe_3O_4	Wang [183] Fe_3O_4	Hosterman [184] Fe_3O_4		D'Ippolito [185] Fe_3O_4
A_{1g}	671	670	668	667	667		667
F_{2g}	542	540	538	539	531		548
F_{2g}		308		305			474
E_g			306		295		312
F_{2g}		193	193				
	McCarty [175] $FeCr_2O_4$	McCarty [175] $Fe_{1,4}Cr_{1,6}O_4$	Chen [207] $FeCr_2O_4$	Wang [183] $FeCr_2O_4$	Hosterman [184] $FeCr_2O_4$	Hosterman [184] $Fe_{1,4}Cr_{1,6}O_4$	D'Ippolito [185] $FeCr_2O_4$
A_{1g}	686	679	677	684	678	676	674
F_{2g}		636	631 (F_{2g} ?)	639	635		591
F_{2g}		550	595 (F_{2g} ?)	$\sim$ 610	531	536	493
E_g			500 (E_g ?)	522			436
F_{2g}				$\sim$ 450			

Appendices

Appendix C

EELS and EDXS quantifications

EDXS data were acquired in DigitalMicrograph 3 software simultaneously with the EELS ones [208]. The probe size varied depending on the acquisition but was kept below 1 nm. The acquisitions lasted for several hours up to a few days depending on the acquisition. Hence, drift correction was not always enough to suppress the effective drift that still can be seen in some maps (tortuous appearance of the grain boundaries, interfaces etc.) No uncertainties were calculated in this work and the results can be assimilated to semi-quantitative ones but will be referred to quantitative since enough counts were each time obtained to perform the quantifications presented.

EELS analyses and quantifications

The fundamental aim of EELS quantification is to identify, extract and quantify species present on the specimen. By doing so, spectra can be converted into meaningful analytical quantities. The spectra processing was made using DigitalMicrograph 3 software. Once EELS spectra acquired the next step is to extract its information to determine the analysed region composition. To perform meaningul quantitative EELS analysis, the specimens should be sufficiently thin to prevent multiple inelastic scattering. The usage of the DualEELS system allowed to record both low loss and core loss regions of the spectrum. Therefore, the zero loss peak was each time recorded along the core-loss region and allowed the deconvolution of the plural scattering. Firstly, the edge-positions were indicated from their inflexion point. Then background windows were positionned to extract the background. It allowed to extract the intensity of each edge while removing the underlying background intensiy. The position and size of the background windows used for quantification and to remove the background intensity have a great impact onto the resulting quantification and therefore were choosen with care. Then the measured intensity were related to concentrations using Hartree-Slater model cross-sections. White lines were excluded from the quantification analysis. Indeed, they are strongly dependent upon the chemical state of the specie and are not well modelled in cross-section calcultation. In order to quantify the obtained spectra, the collection semi-angle (β) and the convergence semi-angle (α) have to be known (Figure C.1). The collection semi-angle corresponds to the EELS maximal scattering angle. This angle depends on the camera length and the spectrometer entrance aperture. Usually, large collection angles will give high intensity but poor energy resolution. To measure such angle, one have to calibrate a diffraction pattern from a known Bragg reflexion and convert the angles in mrad. The angle is then given by the radius of the entrance aperture shadow. The convergence semi-angle directly depends and is proportional to the last limiting aperture, thus the C2 condenser aperture. By choosing a smaller aperture, a smaller angle of scattered electrons enter the spectrometer. It can be calibrated for a specimen with a known Bragg angle by measuring the width of the diffraction disks. Both angles were measured and calibrated for a chosen camera length (CL= 87 mm), spectrometer entrance aperture (5 mm) and C2 aperture

(70 µm) used in this work. The convergence semi-angle was found to be α= 10.5 mrad while the collection semi-angle was found to be β = 15.82 mrad.

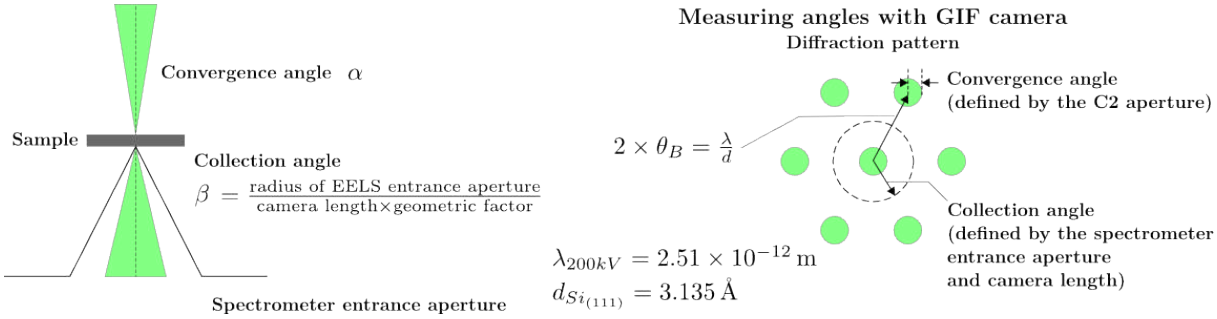

Figure C.1: *Schematic of the convergence and collection angles*

First, EELS quantifications were performed with every edge present and taking into account oxygen. In this case, attention must be drawn onto the oxygen and chromium overlapping edges. Indeed, the overlapping of two or more edges can render the quantification harder and they need to be considered with care. Their analysis if not properly done could be inaccurate therefore, a method should be used to separate the edges or they should be modelled as an ensemble. An example of the background fitting and edge quantification fits is reported in Figure C.2. A single background fit was realised and edges were modelled as overlapping each other.

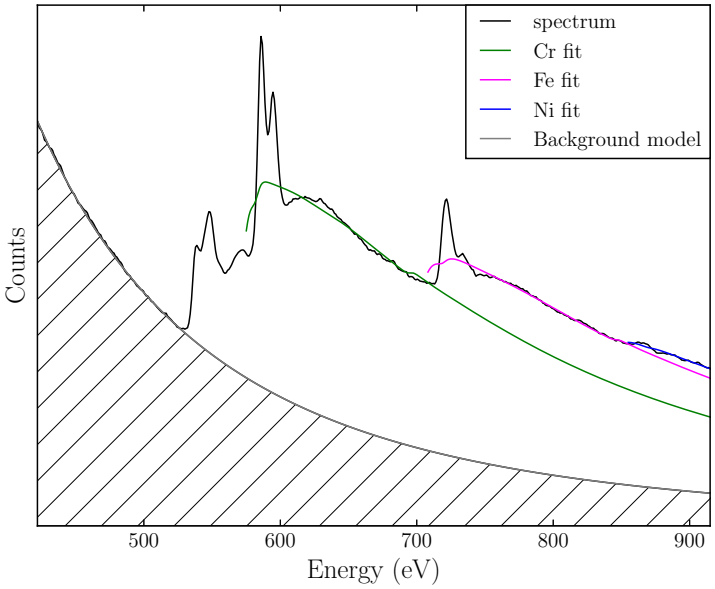

Figure C.2: *EELS spectrum and associated background and edges with O quantification*

A second round of EELS quantifications were realised without oxygen. These quantifications were used to provide ratios of metallic species and to write the spinel oxides accordingly to AB_2O_4. An example of the background fitting is reported in Figure C.3. Three background windows were used and each edge was quantified individually.

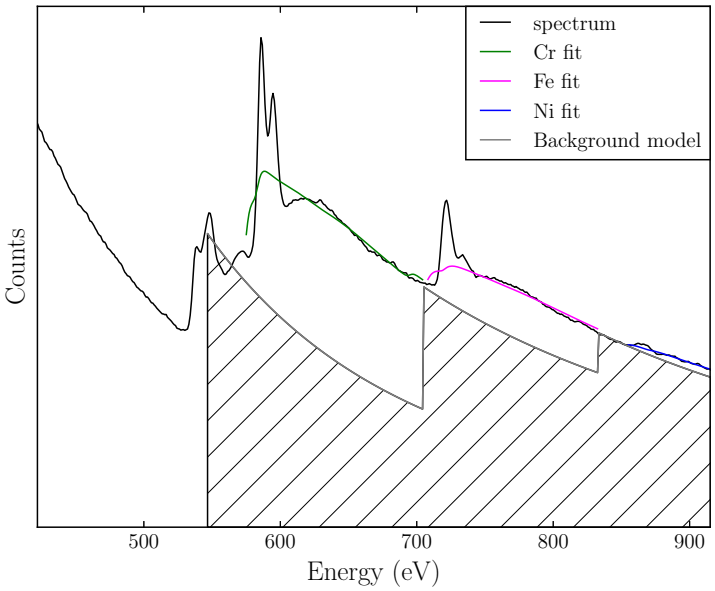

Figure C.3: *EELS spectrum and associated backgrounds and edges without O quantification*

EDXS analyses and quantifications

For the EDXS analyses, dead times were kept between 20 and 30 % to provide enough counts and semi-quantative analyses. The background was subtracted and Full Width Half Maximums (FWHM) integrated intensities were used for quantifications using k-factors and the Cliff Lorimer method. Dwell time per pixel ranged between 0.01 and 2 seconds depending on the acquisition. A Casnati cross-section model [209] was used for the quantification but no matrix correction was applied (such as thin-foil absorption corrosion or ZAF correction) [165].

Appendices

Appendix D

Sample polishing

A reference polishing procedure was implemented in this study. It allow to prepare sample without any induced hardening or dislocations brought by the polishing steps. Tables D.1 and D.2 present the polishing steps realised on the samples. To perform this polishing samples were coated in a conductive resin improving the reproducibility of the preparation. A thin aluminum foil was placed at the back of the samples allowing an easy stripping. Each sample was heavily rinced under water and then cleaned using ultrasonic water bath between each polishing steps and dried with argon.

Table D.1: *Reference polishing*

Abrasive Type	Duration (min)	Plate Rotation (rpm)	Holder Rotation (rpm)	Applied Force (N)	Grain size (µm)
SiC Foil P800	3	150 a	150 a	20	21.8 ± 1.0
SiC Foil P1000	3	150 a	150 a	20	18.3 ± 1.0
SiC Foil P1200	3	150 a	150 a	20	15.3 ± 1.0
SiC Foil P2000	4.5	150 a	150 a	20	10.3 ± 0.8
SiC Foil P4000	4.5	150 a	150 a	20	(5.3 ± 0.5)
Floc 6 µm	4	150 a	150 a	20	6
Floc 3 µm	8	100 a	100 a	15	3
Nap 1 µm	10	100 a	100 a	10	1
Nap 0.25 µm	12	100 a	100 a	10	0.25
Nap 0.1 µm	14	100 a	100 a	10	0.1
OP-S 0.04 µm	20	40 a	50 c	5	0.04

Note: 'a' anti-clockwise rotation; 'c' clockwise rotation

Table D.2: *Polishing suspensions*

Abrasive type	Suspension	Lubricant	Cooling
Floc 6 µm	8/1	2/1	2
Floc 3 µm	8/2	2/1	3
Nap 1 µm	8/3	2/1	4
Nap 0.25 µm	8/3	2/1	4
Nap 0.1 µm	8/4	2/1	4
OP-S 0.04 µm	10/4	-	4

The proton pre-irradiated samples needed to be polished to reach the irradiated area at the desired dose. To do so, an OP-S polishing to remove between 2 to 5 µm was calibrated. Such calibration was realised using Vickers indentation of 500 grams to measure the abraded depth. The latter is calculated using the following equation (eq. D.1). A sketch of the indentation is presented in Figure D.1 along with the measurement realised.

$$p = \frac{1}{tan(68) \times 2\sqrt{2}} \times (average(d_{1A}, d_{1B}) - average(d_{2A}, d_{2B})) \tag{D.1}$$

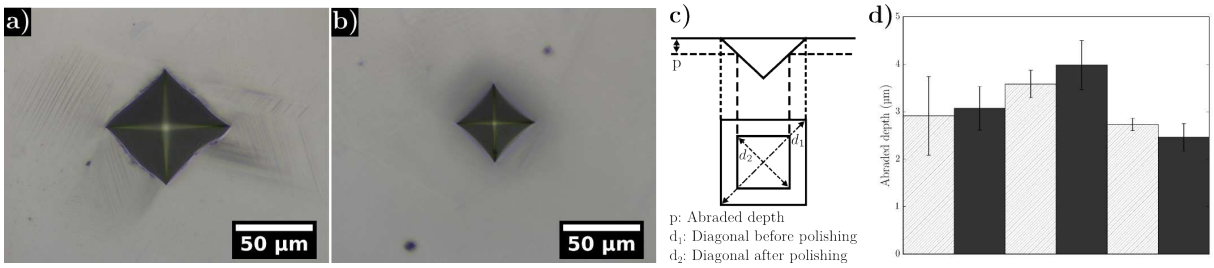

Figure D.1: *a) Optical image of the Vickers indentation before the polishing b) Optical image of the Vickers indentation after the polishing c) sketch of the abraded depth and d) measured abraded depth on several samples*

Appendix E

Additional characterisations on the irradiated samples

This appendix reports supplementary characterisations carried out on irradiated samples.

Frank loops

Figures E.1 and E.2 highlight the loop population on the Titane 1 dpa and 1.5 dpa **IRR** samples respectively. The quantification was performed on areas 100 and 70 ± 10 nm thick respectively. Loop densities and sizes were found to be close on the two samples. The loop density on the sample irradiated at 1 dpa was of $2.5 \pm 0.7 \times 10^{22}\,\mathrm{loop/m^3}$ while it was of $2.3 \pm 0.8 \times 10^{22}\,\mathrm{loop/m^3}$ on the 1.5 dpa sample. Loops were slightly bigger on the 1.5 dpa sample (mean size of 21.4 ± 14.1 nm versus 18.4 ± 15.9 nm). The loop sizes ranged from approximately 2 to 86 nm on the 1 dpa sample and from 4 to 92 nm on the 1.5 dpa sample.

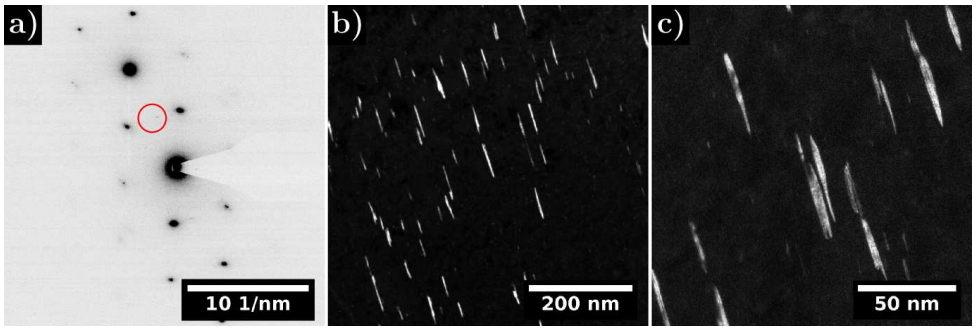

Figure E.1: *Frank loops on the Titane 1 dpa IRR sample imaged in TEM a) diffraction pattern on [101] zone axis in 2-beam conditions along $\frac{1}{2}$ [$\bar{1}\bar{3}1$] (red circle: objective aperture used to image the loops), b) and c) DF images on the rel-rod streak imaging one loop family edge-on*

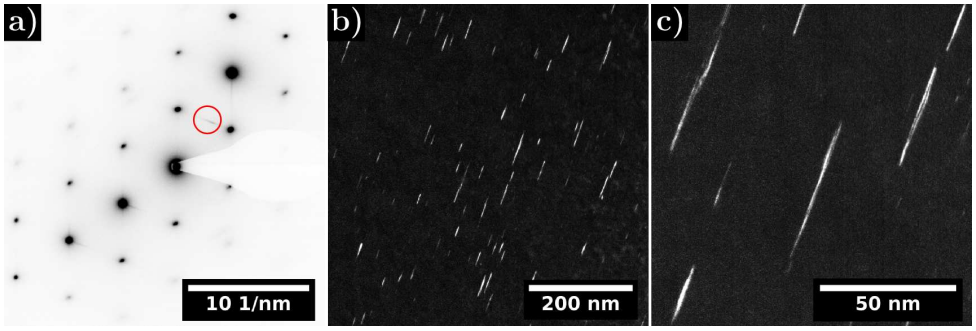

Figure E.2: *Frank loops on the Titane 1.5 dpa IRR sample imaged in TEM a) diffraction pattern on [101] zone axis in 2-beam conditions along* $\frac{1}{2}$ *[1$\bar{3}\bar{1}$] (red circle: objective aperture used to image the loops), b) and c) DF images on the rel-rod streak imaging one loop family edge-on*

Frank loops were also present on the **IACIRR** area of the Michigan sample (Figure E.3). The quantification was made on a area 110 ± 10 nm thick. The loop mean size is of 11.0 ± 5.8 nm with the biggest loop measured at 35.9 nm. Their density is of $3.1 \pm 0.9 \times 10^{22}$ loop/m^3.

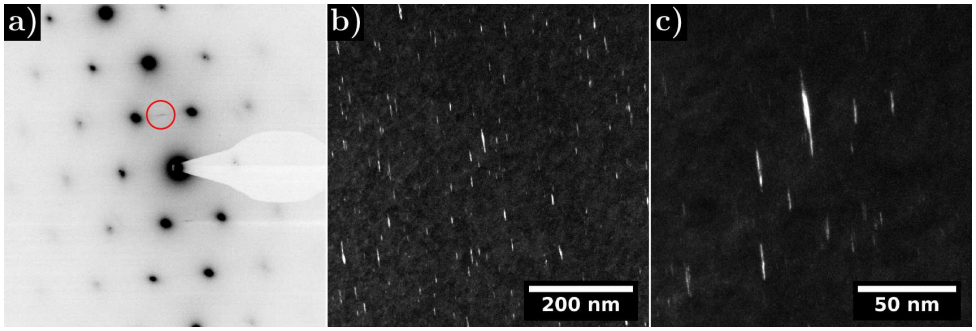

Figure E.3: *Frank loops on the IACIRR area of the Michigan sample imaged in TEM a) diffraction pattern on [101] zone axis in 2-beam conditions along* $\frac{1}{2}$ *[$\bar{1}\bar{3}$1] (red circle: objective aperture used to image the loops), b) and c) DF images on the rel-rod streak imaging one loop family edge-on*

The quantification of the Frank loops on the **IACIAC** area of the Michigan sample was performed on a 70 ± 10 nm thick area (Figure E.4). The loop mean size is 8.5 ± 4.8 nm and their density is of $2.6 \pm 0.5 \times 10^{22}$ loop/m^3.

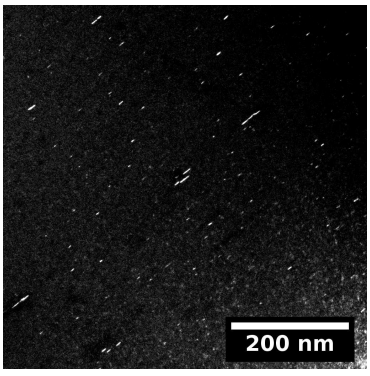

Figure E.4: *TEM DF image, imaging family of Frank loops edge-on on the IACIAC area of the Michigan sample (close to [101] zone axis in 2-beam conditions along* $\frac{1}{2}$ *[$\bar{1}$31])*

The Frank loop population of the decommissioned bolt is presented in Figure E.5. The analysis was performed on a 30 ± 5 nm thick area. The loop size ranges from about 1 nm to almost 19 nm with a mean size of 5.0 ± 2.9 nm. The loop density was found to be $15.7 \pm 6.8 \times 10^{22}$ loop/m^3.

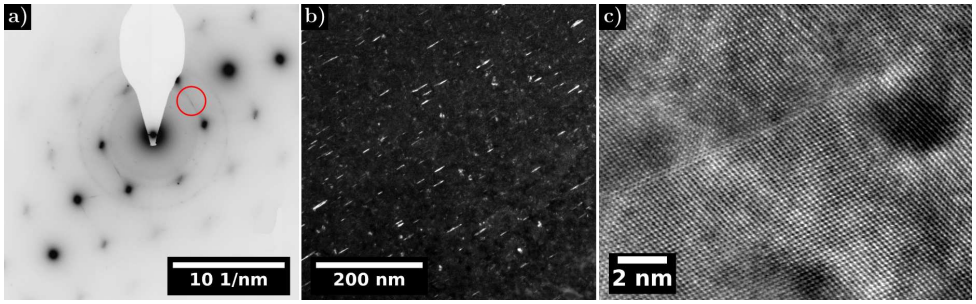

Figure E.5: *Frank loops imaged in TEM on the decommissioned bolt a) diffraction pattern on [101] zone axis in 2-beam conditions along $\frac{1}{2}$ [1̄31] (red circle: objective aperture used to image the loops) b) DF image on the rel-rod streak imaging one loop family edge-on c) HRSTEM image of a Frank loop edge-on*

Cavities

Figures E.6 and E.7 present the void population on the Titane 1 and 1.5 dpa **IRR** samples respectively. Quantifications were performed on area 60 ± 10 nm and 70 ± 10 nm thick respectively. The 1 dpa sample has an average void size of 8.2 ± 2.0 nm (ranging from approximately 1 to 15 nm). On this sample the void density was found to be $3.8 \pm 1.6 \times 10^{21}$ void/m^3. The void ranged from about 1 to 20 nm with a mean size of 11.4 ± 2.4 nm on the 1.5 dpa sample while void density is of $4.7 \pm 1.8 \times 10^{21}$ void/m^3. The cavities appear on both samples faceted with facets all parallel from one faceted void to the other one as visible on Figures E.6 and E.7.

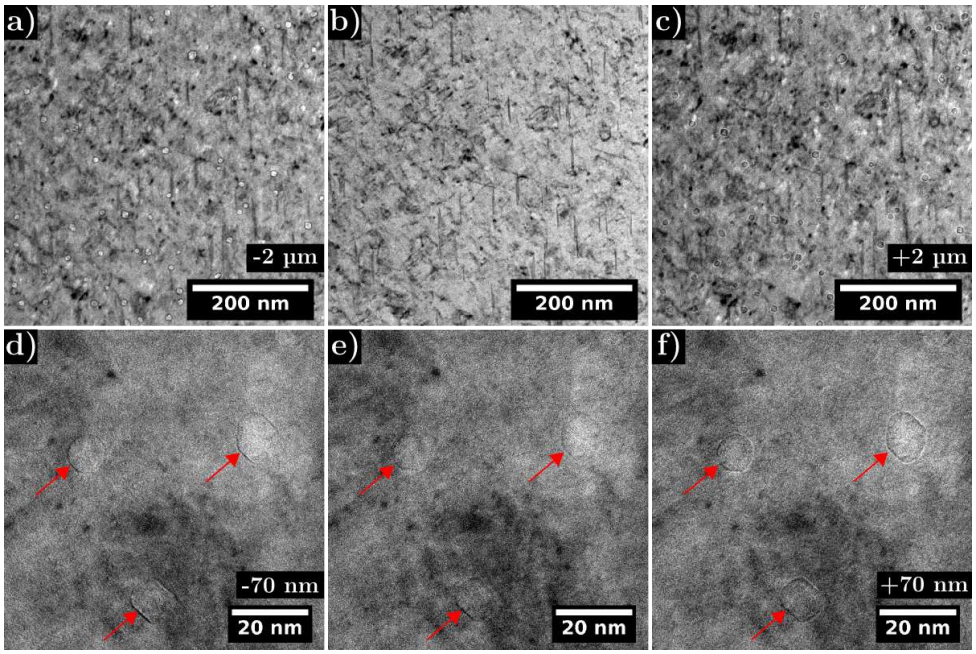

Figure E.6: *TEM BF imaging of the cavities distribution on focus, under-focus and over-focus on the Titane 1 dpa IRR sample a) and d) under-focus, b) and e) focus c) and f) over-focus*

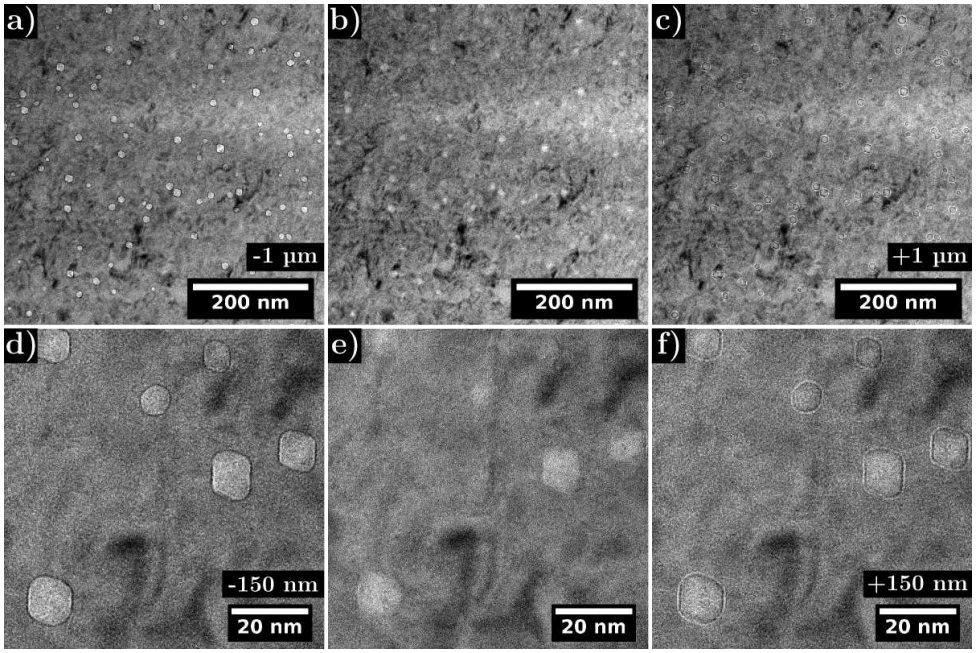

Figure E.7: *TEM BF imaging of the cavities distribution on focus, under-focus and over-focus on the Titane 1.5 dpa IRR sample a) and d) under-focus, b) and e) focus c) and f) over-focus*

Few small cavities were observed on the **IACIRR** area of the Michigan sample (Figure E.8). As one can see, less voids are present on this sample and their size is much smaller than on the Titane **IRR** samples. The cavity density is found to be $1.6 \pm 0.7 \times 10^{21}$ cavity/m^3 while the cavity mean size is of 5.0 ± 1.2 nm. The biggest void observed measured 7.1 nm.

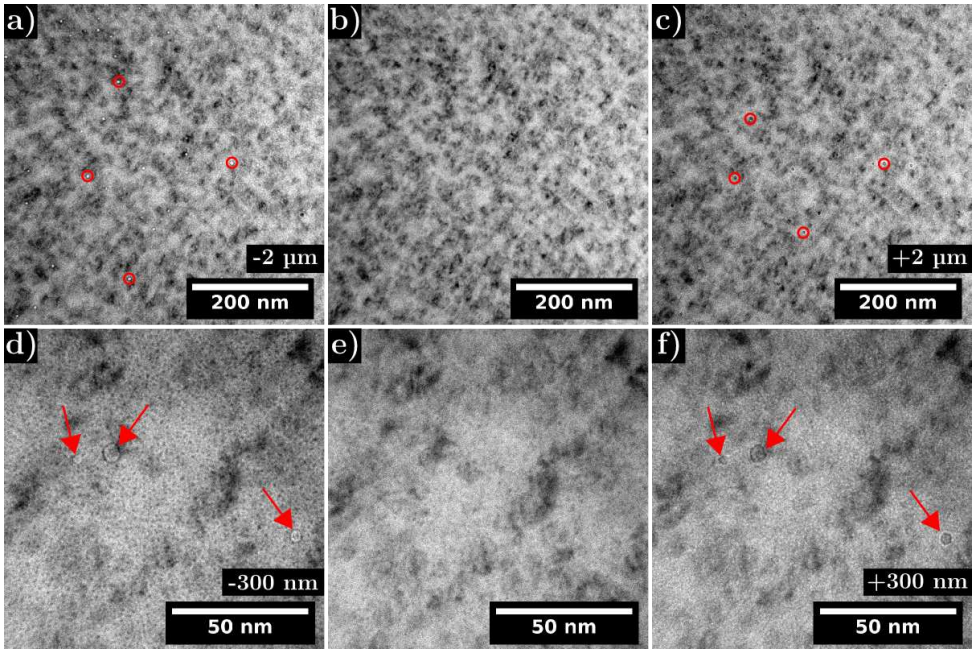

Figure E.8: *TEM BF imaging of the cavities distribution on focus, under-focus and over-focus on the IACIRR area of the Michigan sample a) and d) under-focus, b) and e) focus c) and f) over-focus*

Even fewer voids were observed on the **IACIAC** area of the Michigan sample (Figure E.9). They were looked at on an area 70 ± 10 nm thick. The void ranged from about 1 to 4 nm with a mean size of 2.2 ± 0.9 nm and a density close to $0.3 \pm 0.2 \times 10^{21}$ cavity/m^3.

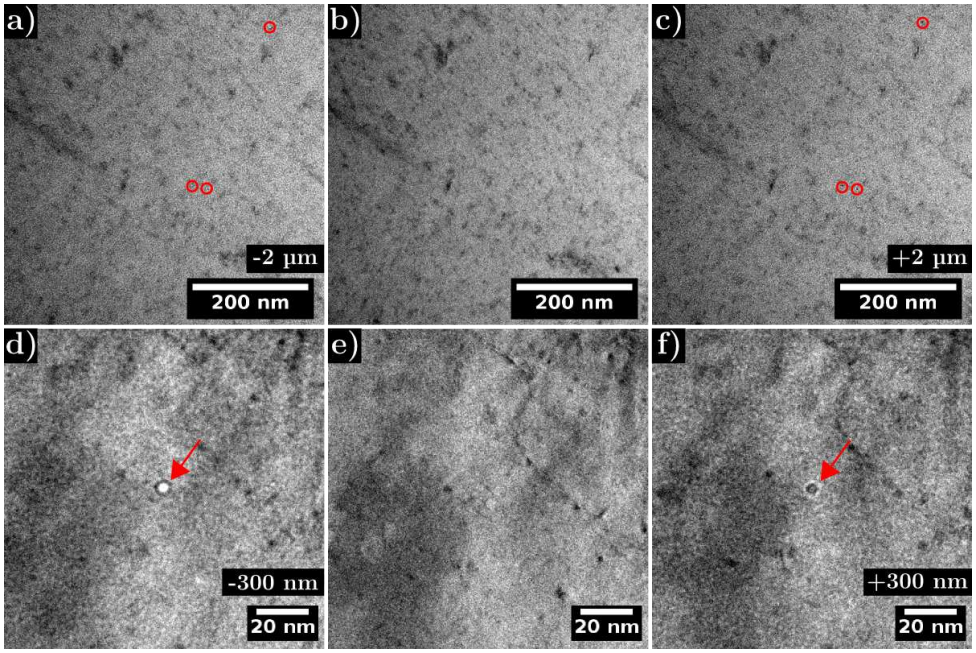

Figure E.9: *TEM BF imaging of the cavities distribution on focus, under-focus and over-focus on the IACIAC area of the Michigan sample a) and d) under-focus, b) and e) focus c) and f) over-focus*

On the decommissioned bolt, the cavity size distribution and density were analysed considering a thickness of about 70 ± 10 nm (Figure E.10). The cavities mean size was found to be 3.8 ± 2.0 nm with cavities ranging from approximately 1 to 11 nm. Their number density is of 30.9×10^{21} void/m^3. Similarly as on the proton irradiated sample the cavities appear faceted with the facet of one void parallel to the facet of the other voids.

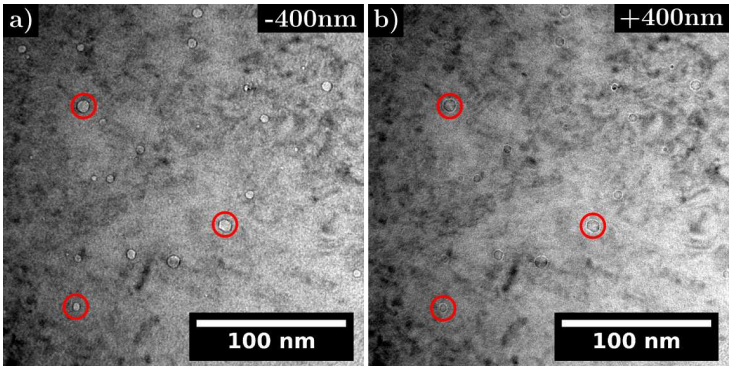

Figure E.10: *TEM BF imaging of the cavities distribution on the decommissioned bolt a) under-focus (-400 nm) b) over-focus (+ 400 nm)*

Intragranular RIS

Other EDXS and EELS maps realised on the Titane 1 dpa **IRR** sample also highlighted segregation on cavities and Frank loops (E.11 and E.12). The area surrounding the cavity appears nickel and silicon enriched while chromium, iron and manganese depleted as visible on Figure E.11. Segregation on another loop edge-on was also observed (Ni/Si enrichment and Cr, Fe and Mn depletion – Figure E.12). The segregation is especially marked at the loop tips.

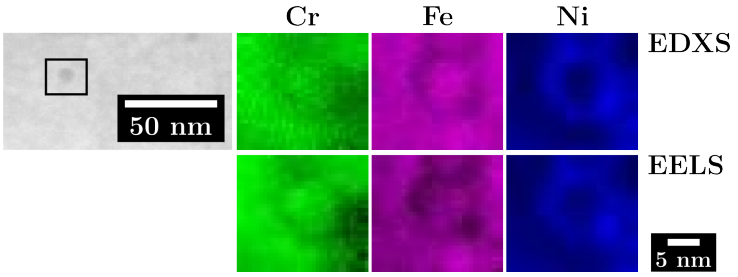

Figure E.11: *HAADF image and associated EDXS/EELS quantitative mapping of Cr, Fe and Ni on a cavity on the Titane 1 dpa IRR sample*

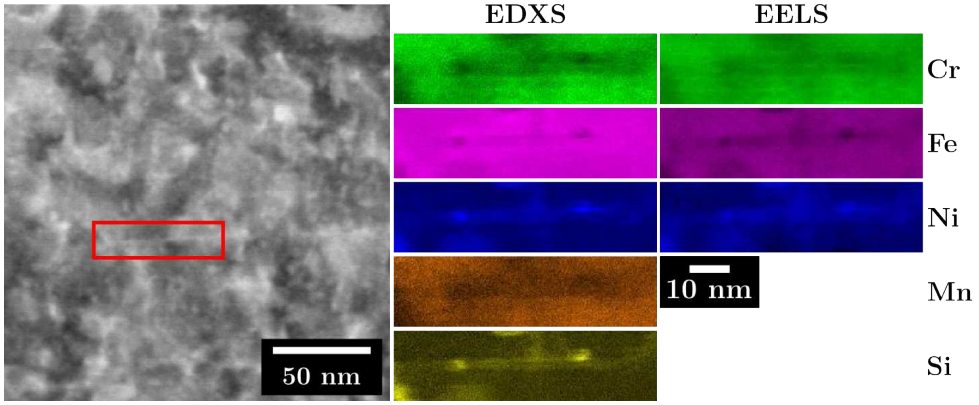

Figure E.12: *HAADF image and EDXS/EELS mapping of Cr, Fe, Ni, Mn and Si on a loop edge-on (close to [101] zone axis) on the Titane 1 dpa IRR sample*

Table E.1 summarise the maximum segregation occurring around cavities and Frank loops on the 1 dpa Titane **IRR** sample. From these quantification the maximum amount of segregation around both defects appear close reaching around $\Delta_{Cr} \approx -4$ at. %, $\Delta_{Ni} \approx +9$ at. % and $\Delta_{Si} \approx +4$ at. % for chromium, nickel and silicon respectively.

Table E.1: *EDXS quantifications on a cavity and a Frank loop on the Titane 1 dpa IRR sample – Results given in the form of Δ = (RIS − matrix) in at. % with regards to the matrix composition (+ and − indicate enrichment and depletion respectively)*

Element	Cavity	Frank loop
Fe	− 6	− 7
Cr	− 4	− 3
Ni	+ 10	+ 8
Mn	≤ − 2	− 1
Si	+ 4	+ 3

No precipitation was clearly evidenced on the 1.5 dpa Titane **IRR** sample from the diffraction patterns (Figure E.13). Another EDXS mapping on a cavity is introduced in Figure E.14. The latter is Ni/Si enriched while Cr/Fe depleted. Table E.2 presents the maximal amount of segregation occurring on both defects on the 1.5 dpa Titane **IRR** sample. From this it seems that the Frank loop tip is slightly more segregated than that on the 1 dpa sample (up to $\Delta_{Cr} \approx -6$ at. %, $\Delta_{Ni} \approx +13$ at. % and $\Delta_{Si} \approx +5$ at. %).

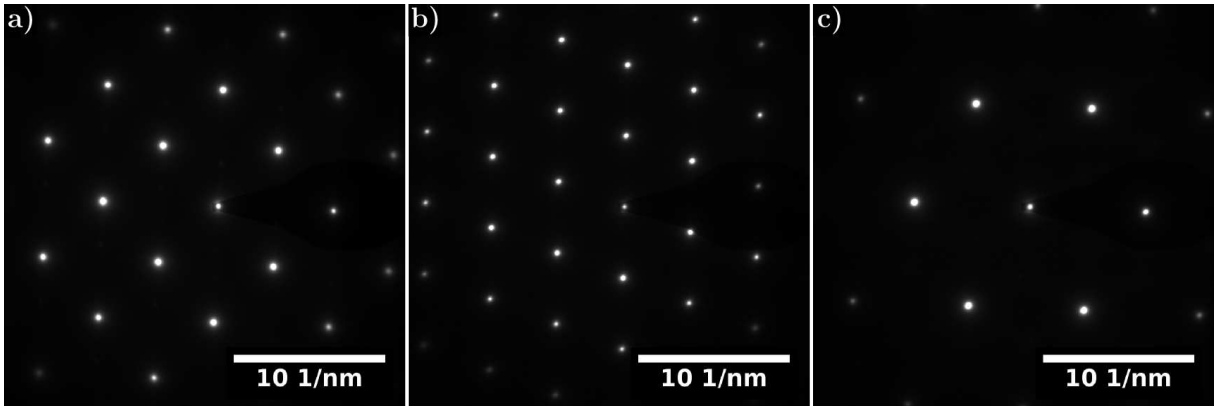

Figure E.13: *Diffraction patterns on the Titane 1.5 dpa IRR sample on a) [100] zone axis b) [101] zone axis and c) [111] zone axis*

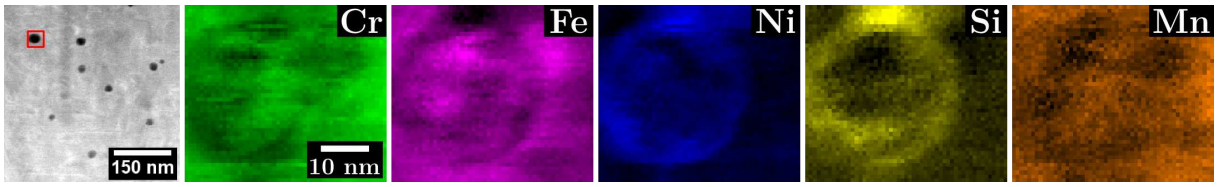

Figure E.14: *HAADF image and EDXS mapping of Cr, Fe, Ni, Si and Mn on a cavity on the Titane 1.5 dpa IRR sample*

Table E.2: *EDXS quantifications on a cavity and a Frank loop on the Titane 1.5 dpa IRR – Results given in the form of* Δ *= (RIS − matrix) in at. % with regards to the matrix composition (+ and − indicate enrichment and depletion respectively)*

Element	Cavity	Frank loop
Fe	− 9	− 10
Cr	− 4	− 6
Ni	+ 11	+ 13
Mn	≤ − 2	≤ − 2
Si	+ 3	+ 5

Results from EDXS and EELS quantifications of a Frank loop edge-on on the **IACIRR** area of the Michigan sample are presented in Table E.3.

Table E.3: *EDXS and EELS quantifications on a Frank loop on the IACIRR area of the Michigan sample – Results given in the form of* Δ *= (RIS − matrix) in at. % with regards to the matrix composition (+ and − indicate enrichment and depletion respectively)*

Element	EDXS analysis	EELS analysis
Fe	− 3	− 2
Cr	− 1	− 1
Ni	+ 4	+ 8
Mn	− 1	≤ − 2
Si	+ 3	≤ + 1

Figure E.15 presents a loop in plane view analysed by EELS mapping on the decommissioned bolt. It clearly points out that the segregation on loops is not homogeneous. The maximal amount of segregation occurring on the loops and cavities is presented in Table E.4.

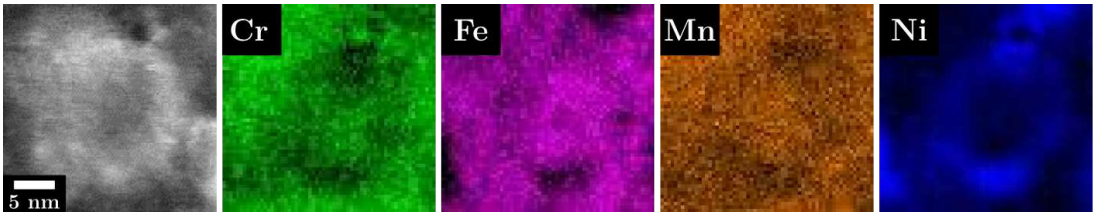

Figure E.15: *HAADF image and EELS quantitative mapping of Cr, Mn, Fe and Ni on a Frank loop in plane view on the decommissioned bolt*

Table E.4: *EELS quantifications on a cavity and a Frank loop on the decommissioned bolt – Results given in the form of* Δ *= (RIS − matrix) in at. % with regards to the matrix composition (+ and − indicate enrichment and depletion respectively)*

Element	Cavity	Frank loop
Fe	− 9	≤ -1
Cr	− 5	− 7
Ni	+ 19	+ 9
Mn	-	≤ -2

Grain boundaries RIS

Figure E.16 image the Radiation Induced Segregation occurring at the grain boundary of the Titane 1 dpa **IRR** sample. The quantification was realised on an area 70 ± 10 nm thick. On both EDXS and EELS maps, the grain boundary appear depleted in chromium, iron and manganese while enriched in nickel and silicon. Moreover, a slight iron enrichment is visible around the grain boundary depletion. Quantitative results of the EDXS and EELS analyses are plotted in Figure E.17. Iron possesses a M-shaped segregation and was depleted to approximately $\Delta_{Fe} \approx -6$ at. %. Chromium was depleted to $\Delta_{Cr} \approx -9$ at. % while Ni was enriched to $\Delta_{Ni} \approx +11$ at. %. In addition, silicium enrichment was highlighted at the grain boundary up to $\Delta_{Si} \approx +7$ at. %. Segregation was found 8.5 ± 1.7 nm wide.

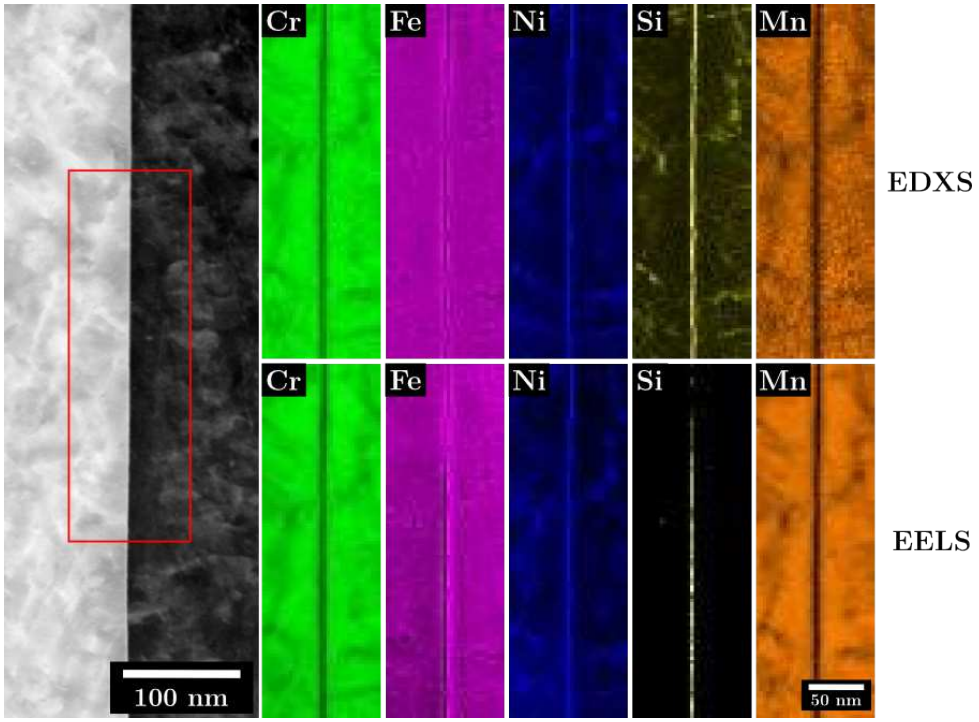

Figure E.16: *HAADF image and associated EDXS and EELS quantitative maps of the grain boundary composition on the Titane 1 dpa IRR sample*

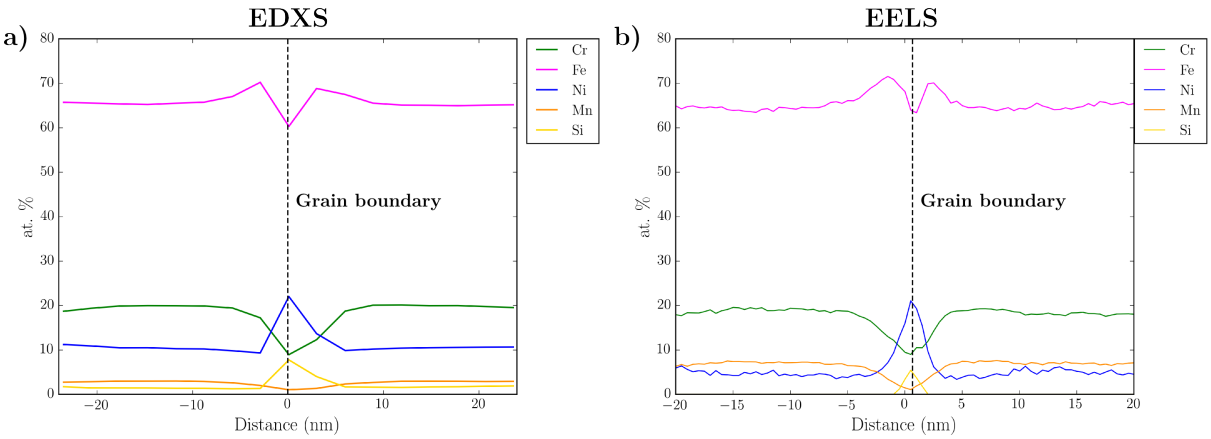

Figure E.17: *Quantitative linescans along the grain boundary on the Titane 1 dpa IRR sample a) EDXS linescans b) EELS linescans*

Figure E.18 images the Radiation Induced Segregation at the grain boundary of the Titane 1.5 dpa **IRR** sample. Quantification was performed on a 60 ± 10 nm thick area. The tortuous appearance of the grain boundary in Figure E.18 is caused by the drift that occurred during the acquisition. The same segregation tendencies can be observed than on the 1 dpa sample. Chromium, iron, manganese and molybdenum are depleted at the grain boundary while nickel, silicon and phosphorus are enriched. Quantitative results of the EDXS and EELS analyses are plotted in Figure E.19. Segregation was found 5.9 ± 1.1 nm wide. As on the 1 dpa sample, iron possesses a M-shaped segregation profile. In addition, Ni has a slight W-shaped profile which can be seen in Figure E.18 but is erased in the plotted profile since a average is made in the length of the grain boundary and due to the dift that occurred during the acquisition. Chromium was even more depleted on this sample ($\Delta_{Cr} \approx -12$ at. %) while the Ni enrichment was even higher, up to $\Delta_{Ni} \approx +18$ at. % as was the Si enrichment ($\Delta_{Si} \approx +10$ at. %). Phosphorus enrichment was noted on this sample as well as molybdenum depletion.

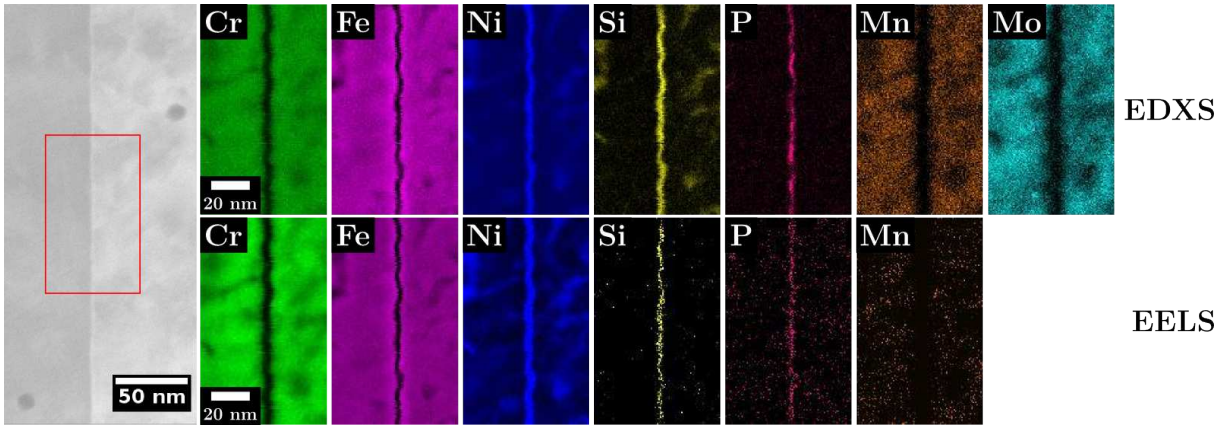

Figure E.18: *HAADF image and associated EDXS and EELS quantitative maps of the grain boundary composition on the Titane 1.5 dpa IRR sample*

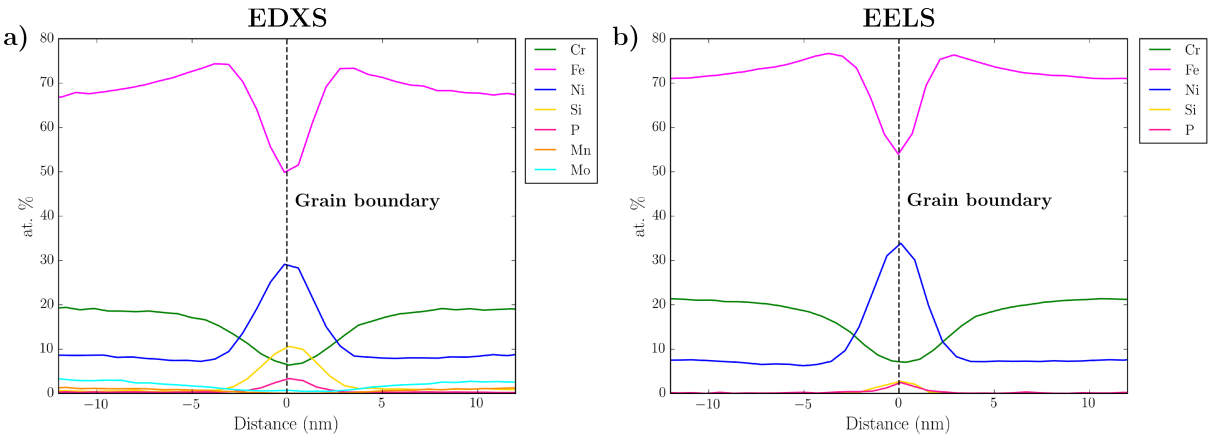

Figure E.19: *Quantitative linescans along the grain boundary on the Titane 1.5 dpa IRR sample a) EDXS profiles b) EELS profiles*

The segregation at grain boundary in the **IACIRR** area of the Michigan sample was also studied using EDXS and EELS and is presented in Figure E.20. The area on which the quantification was made was 70 ± 10 nm thick. As one can see in Figure E.20 c), on the other side of the grain boundary the chemical composition measured by EELS is biased. This is due to ions channelling occurring due to the grain orientation which is close to [101] zone axis after having set the grain boundary edge-on. Segregation was found 7.3 ± 2.0 nm wide with Ni, Si and P enrichment coupled with Cr and Fe depletion. Same segregation tendencies were observed on this sample as observed on the other sample proton pre-irradiated. Ni was enriched up to $\Delta_{Ni} \approx +6$ at. % and Si to $\Delta_{Si} \approx +4$ at. %. A slight phosphorus enrichment was also highlighted. Chromium was depleted to approximately $\Delta_{Cr} \approx -4$ at. %.

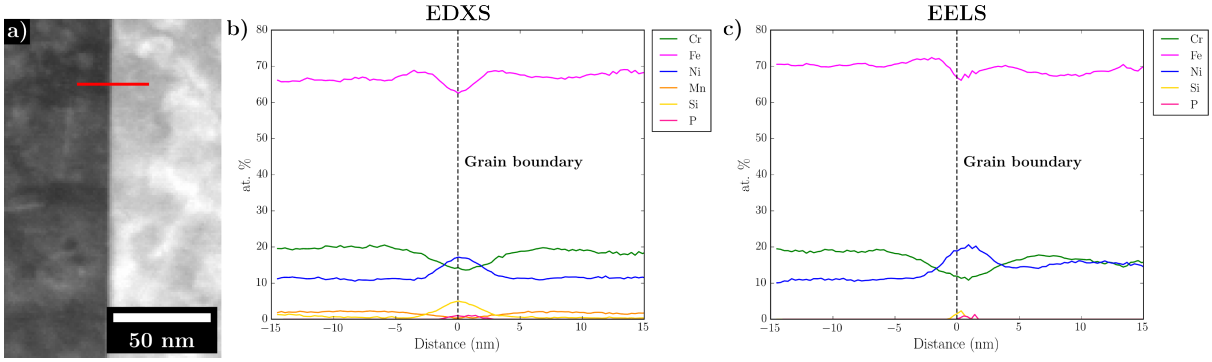

Figure E.20: *STEM image and associated quantitative linescans along the grain boundary on the IACIRR area of the Michigan sample a) STEM HAADF b) EDXS profiles c) EELS profiles*

The grain boundary segregation in the **IACIAC** area of the Michigan sample is presented in Figure E.21. Quantification was performed on an area 70 ± 10 nm thick. Segregation was found 4.0 ± 0.8 nm wide. As previoulsy the grain boundary is depleted in Fe, Cr and Mn while being enriched in Ni, Si and P.

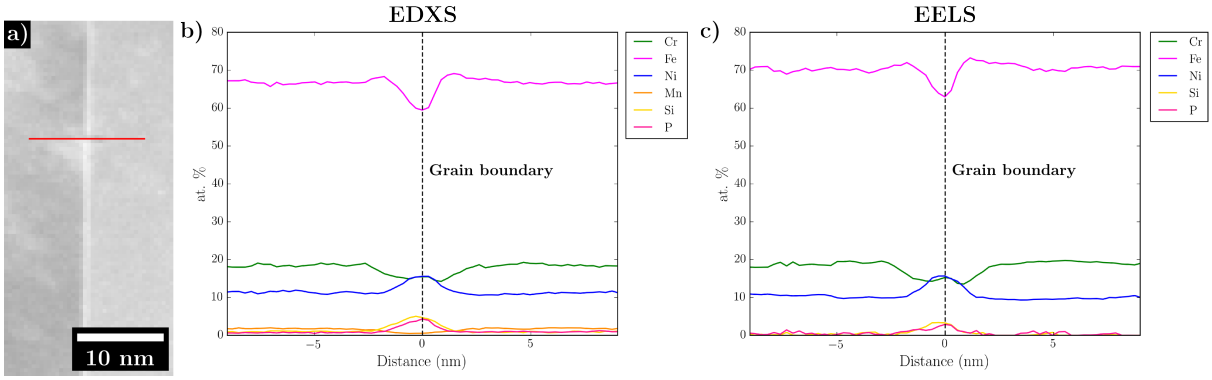

Figure E.21: *Quantitative linescans along the grain boundary on the IACIAC area of the Michigan sample a) EDXS profiles b) EELS profiles*

The studied grain boundary on the decommissioned bolt was set edge-on and can be described as $[101](10\bar{1})(\bar{2}1\bar{3})[4\bar{6}\bar{1}]$. Quantification was performed on a 30 ± 5 nm thick area. Ni/Si segregation was observed coupled with Cr, Fe, Mo and Mn depletion (Figures E.22 and E.23). The amount of segregation is presented in Figure E.23. Iron was depleted up to $\Delta_{\mathrm{Fe}} \approx -21$ at. %. The Ni and Si enrichments reached about $\Delta_{\mathrm{Ni}} \approx +14$ at. % and $\Delta_{\mathrm{Si}} \approx +16$ at. % whereas the depletion value Cr is of $\Delta_{\mathrm{Cr}} \approx -8$ at. %. Moreover, nickel enrichment possessed a W-shaped profile. The segregation was found out to be 7 ± 1.5 nm wide and relatively homogeneous along the grain boundary (Figure E.23).

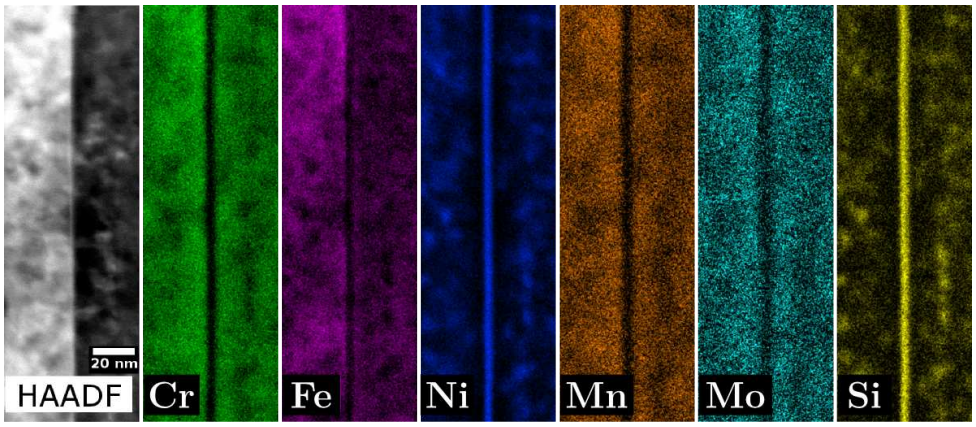

Figure E.22: *HAADF image of the grain boundary and associated EDXS quantitative maps of Cr, Fe, Si, Ni, Mo and Mn on the decommissioned bolt (normalised to 100 %)*

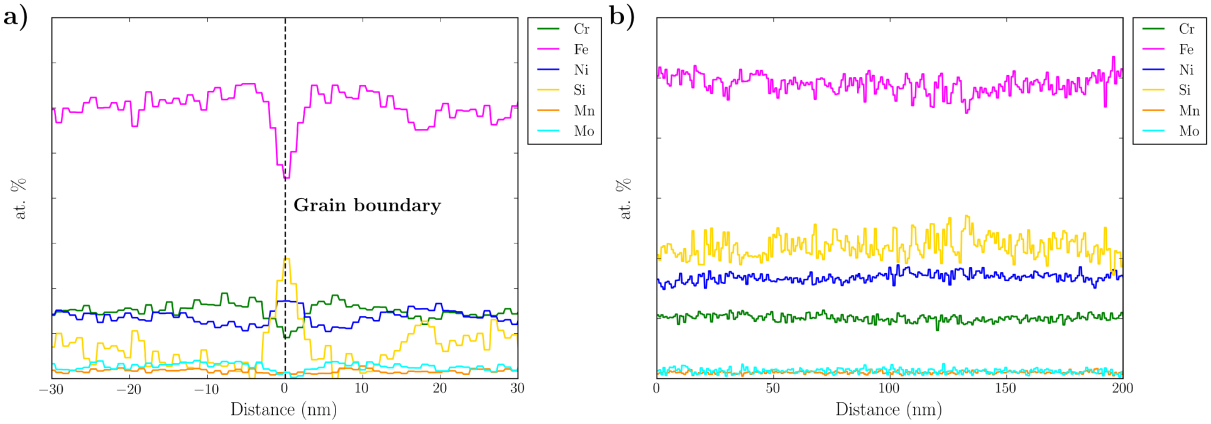

Figure E.23: *EDXS quantitative segregation linescans a) across the grain boundary b) along the grain boundary on the decommissioned bolt*

Appendices

Appendix F

Additional characterisations on the Michigan sample

This appendix reports supplementary characterisations made on the **IACUNIRR** and **IACIRR** areas of the Michigan sample.

IACUNIRR area characterisation

Porosities in the oxide layers were clearly evidenced on the oxide formed on [100] grain orientation and fewer were also observed on [111] grain orientation (Figure F.1). On the thick oxide formed on [100] grain orientation the porosities form a channel from the outer surface to the metal/oxide interface.

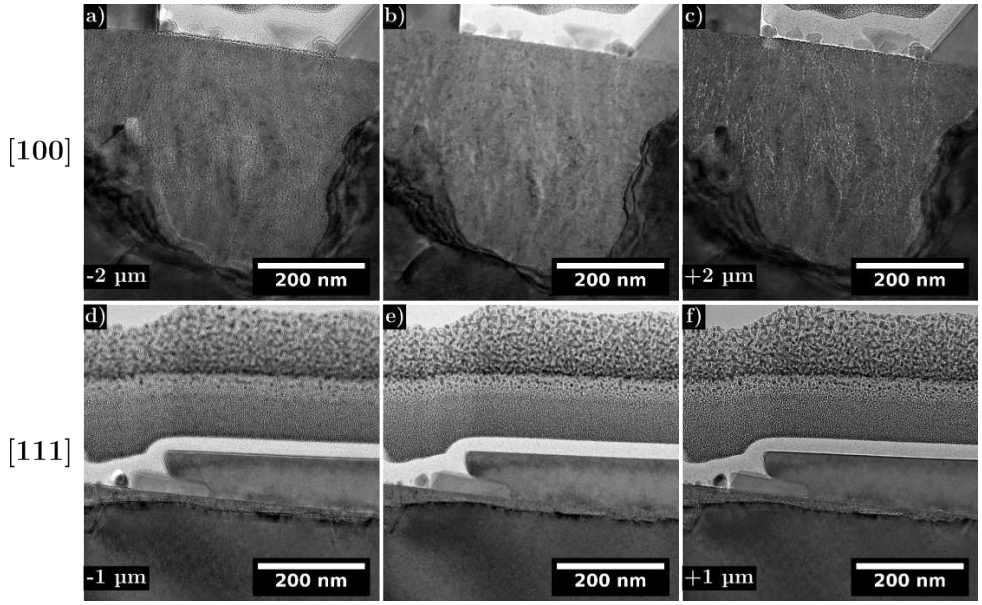

Figure F.1: *TEM BF images on the IACUNIRR area of the Michigan sample on the oxide formed under-focus, focus and over focus on a) b) and c) a [100] grain and d) e) and f) a [111] grain*

Figures F.2 and F.3 introduce DF imaging made on [111] zone axis and obtained on [100] and [111] grain orientations respectively. These show that the inner layer is of spinel structure and epitaxially grown but once again severely strained.

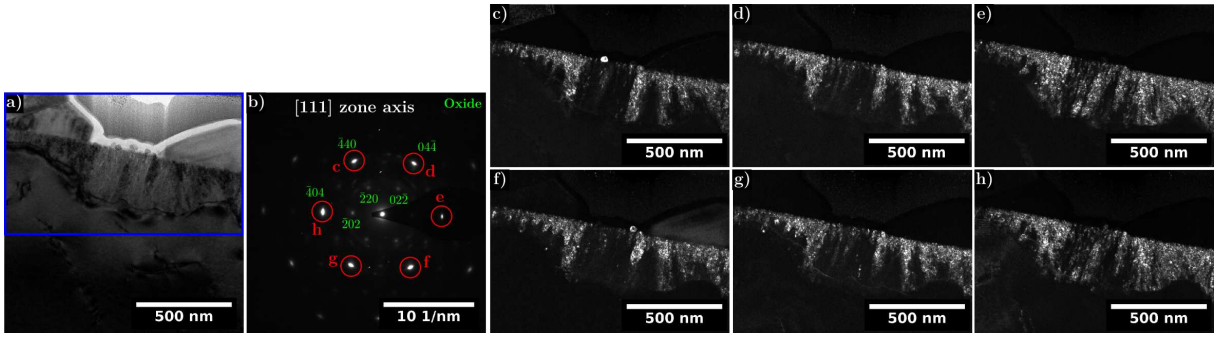

Figure F.2: *IACUNIRR area of the Michigan sample on a [100] grain orientation in [111] zone axis a) BF image b) SAED pattern (red circle: objective aperture) c) to h) DF on the spots circled in b)*

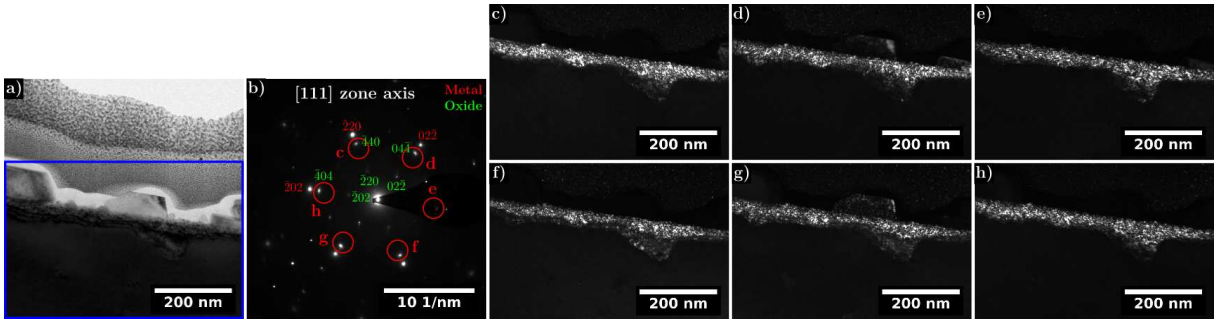

Figure F.3: *IACUNIRR area of the Michigan sample on a [111] grain orientation in [111] zone axis a) BF image b) SAED pattern (red circle: objective aperture) c) to h) DF on the spots circled in b)*

EFTEM maps acquired on both grain orientations are presented in Figure F.4. The outer crystallites are iron-rich while the inner oxide layer is chromium-rich.

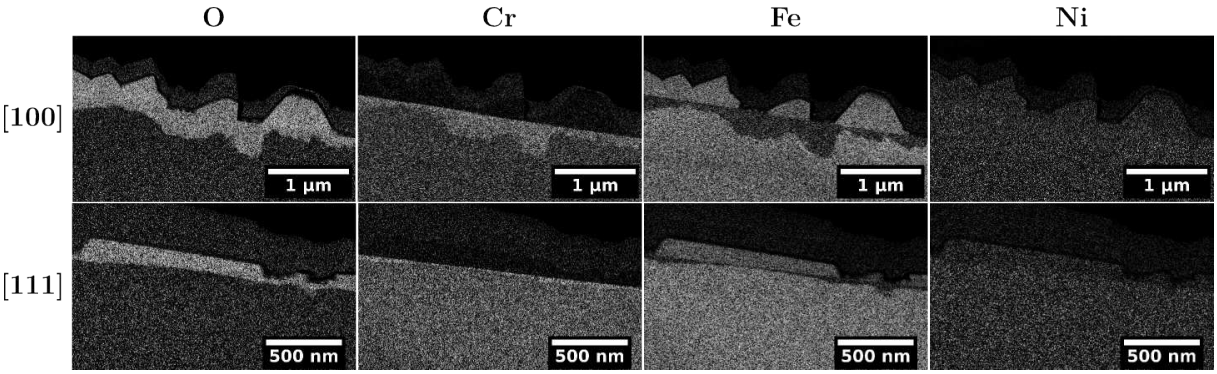

Figure F.4: *EFTEM mapping on the IACUNIRR area of the Michigan sample depending on the crystallographic orientation*

IACIRR area characterisation

STEM and TEM BF images of the duplex oxide layers formed on [100] and [111] grain orientations are introduced in Figure F.5. As on the **IACUNIRR** area the inner oxide layer is much thicker on [100] grain orientation and porosities are evidenced in the latter.

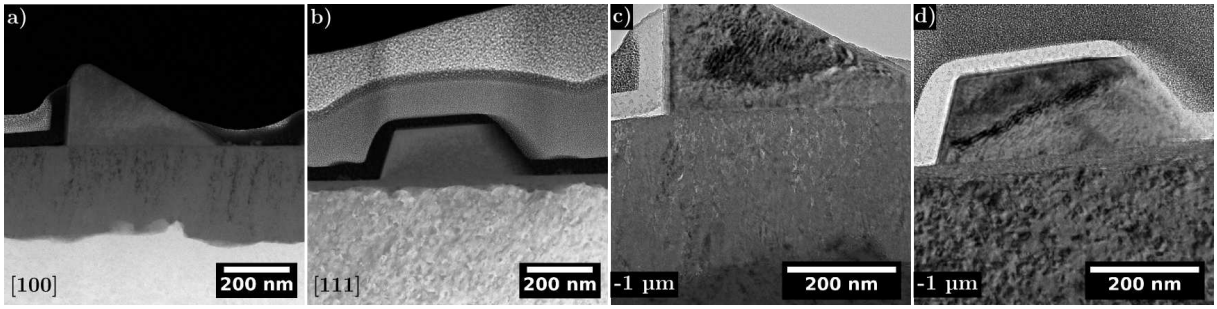

Figure F.5: *TEM images on the IACIRR area of the Michigan sample a) and b) STEM images on respectively a [100] and [111] grain orientations c) and d) BF images on the same grains*

SAED and DF images confirm that the inner oxide layer is of spinel structure and epitaxially grown as previously observed on the **IACUIRR** area.

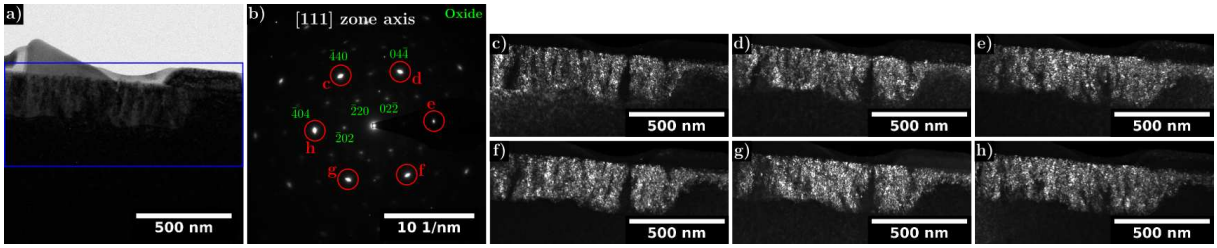

Figure F.6: *IACIRR area of the Michigan sample on a [100] grain orientation in [111] zone axis a) BF image b) SAED pattern (red circle: objective aperture) c) to h) DF on the spots circled in b)*

Raman spectra acquired on the three studied orientations are analogous to that on the **IACUNIRR** area (Figure F.7). More crystallites are contributing to the signal on [100] and [110] grain orientations while the inner oxide layer provides the main response on the [111] grain orientation. More inner oxide response can be detected according to [111]>[100]>[110].

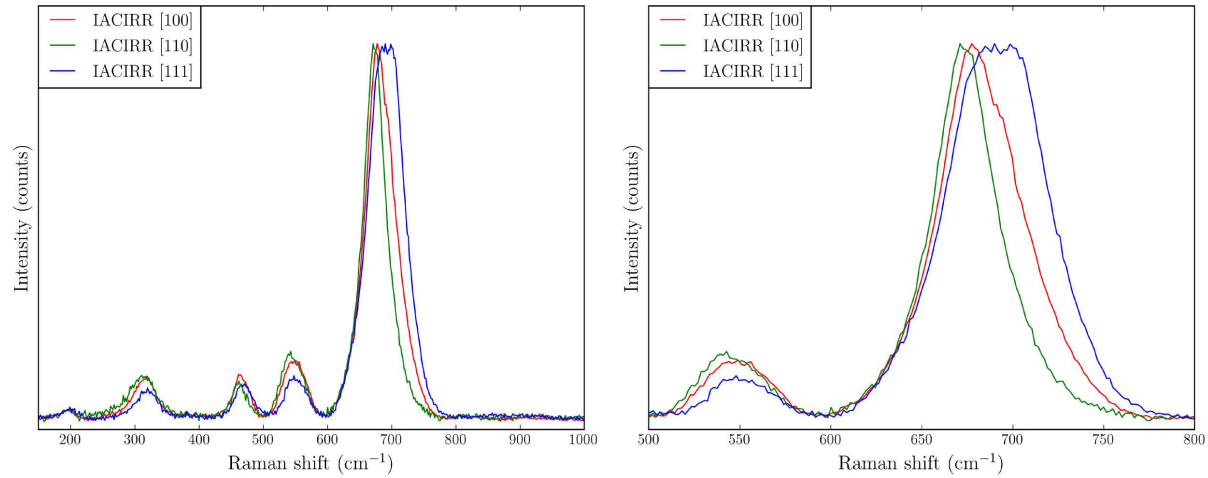

Figure F.7: *Raman spectra on the IACIRR area of the Michigan sample depending on the crystallographic orientation*

As on the **IACUNIRR** areas EFTEM maps evidence iron-rich outer crystallites and chromium-rich inner oxide layers (Figure F.4).

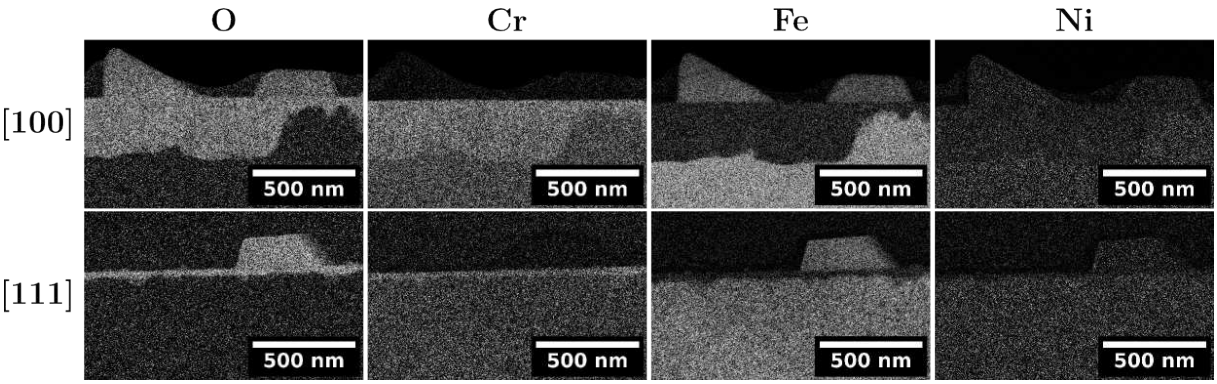

Figure F.8: *EFTEM mapping on the IACIRR area of the Michigan sample depending on the crystallographic orientation*

EDXS and EELS linescans were acquired on both grain orientations but only the latter are reported in Figure F.9. Associated quantifications for the inner oxide layers can be found in Table F.1. These profiles reveal that the outer oxide composition is close to magnetite (Fe_3O_4) while the inner oxide is enriched in chromium and is close to $FeCr_2O_4$. A nickel enrichment at the metal/oxide interface is evidenced on both orientations. Moreover, the inner oxide layer formed on [111] grain orientation is richer in chromium than the one formed on [100] grain orientation.

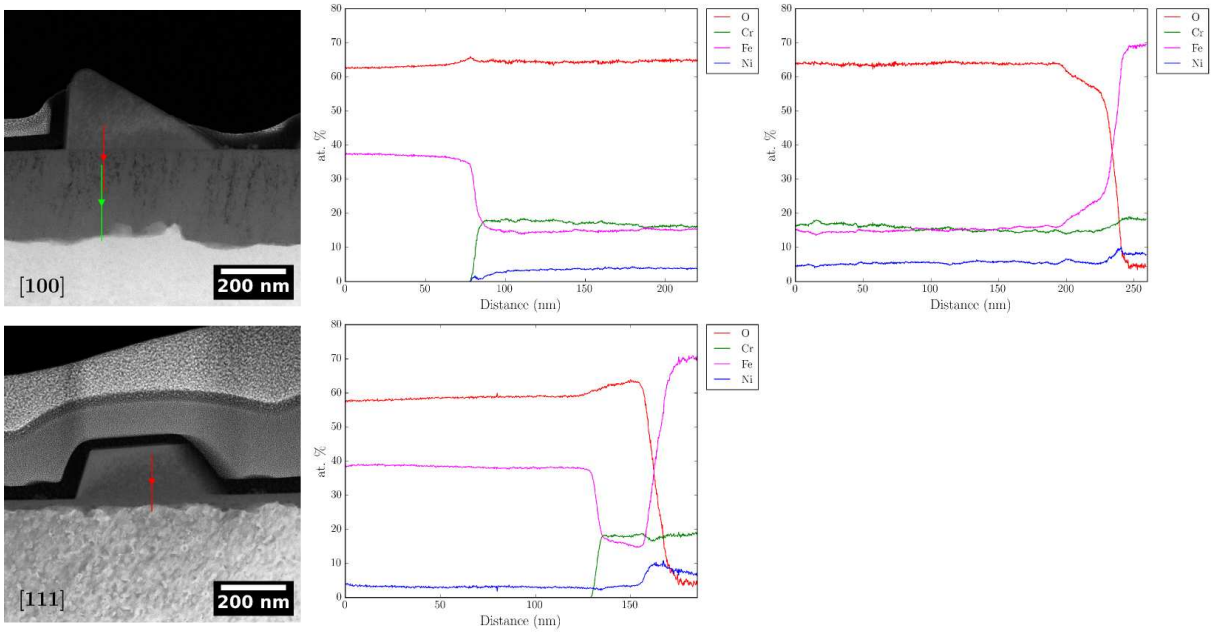

Figure F.9: *STEM images and associated quantitative EELS linescans on the IACIRR area of the Michigan sample on both [100] and [111] grain orientation*

Table F.1: *EELS quantitative analyses of the inner oxides formed on [100] and [111] grain orientations on the Michigan sample in the IACIRR area*

Grain orientation	Method	O (at. %)	Cr (at. %)	Fe (at. %)	Ni (at. %)	$\frac{Cr}{Cr+Fe+Ni}$	AB_2O_4
[100]	EELS	64.0	16.3	14.4	5.3	-	-
	EELS	-	57.8	31.7	10.5	0.58	$Fe_{1.0}Cr_{1.7}Ni_{0.3}O_4$
[111]	EELS	62.7	18.6	14.9	3.8	-	-
	EELS	-	63.8	27.1	9.1	0.64	$Fe_{0.8}Cr_{2.0}Ni_{0.2}O_4$

TEM BF images of the grain boundary oxidation evidence an asymmetric oxide penetration on which one side of the grain boundary is more oxidised than the other (Figure F.10). Porosities are also observed in this oxide as shown by the red arrow.

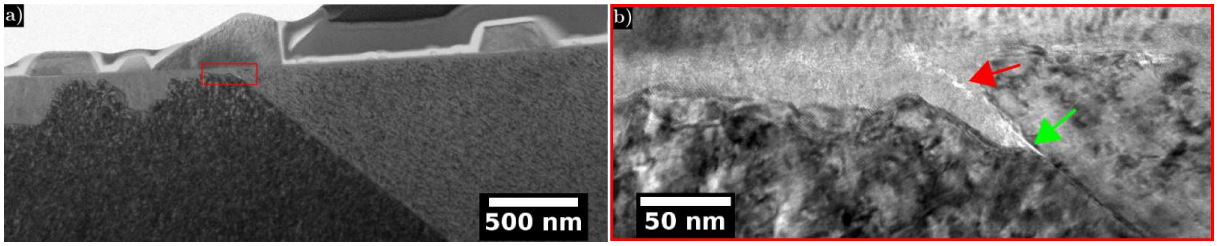

Figure F.10: *TEM BF images a) of the grain boundary oxidation on the IACIRR area of the Michigan sample and b) zoom of the red framed area in a)*

EFTEM maps did not highlighted a clear modification of the chemistry of the oxide penetration at grain boundary minus a slight Ni-enrichment at the tip of the intragranular oxide penetration as shown by the green arrows on Figure F.8. The areas circled in red show the grain boundary RIS already described in Chapter 2 section 2.3.2.2.

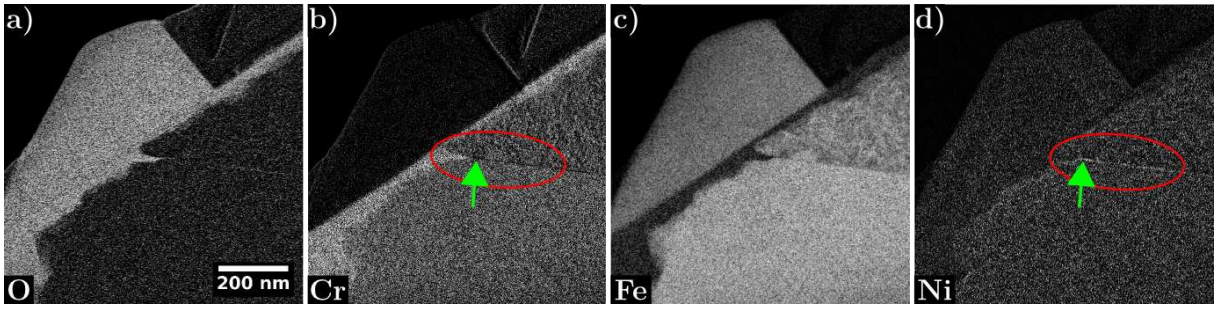

Figure F.11: *EFTEM mapping on the grain boundary on the IACIRR area of the Michigan sample a) oxygen map b) chromium map c) iron map and d) nickel map*

The thin tip of the oxide penetration shown by the green arrows in Figures F.10 and F.11 was mapped using EELS and EDXS and is indeed nickel-rich. Nickel content reaches up to $\sim$ 40 at. % which is way richer than intergranular Ni RIS content on this grain boundary ($\sim$ 20 at. %). This most probably arise from the rejection of nickel from the Cr-rich oxide.

Appendices

Bibliography

[1] C. Pokor, Y. Thebault, C. Pujol, E. Lemaire, and N. Ligneau, "Metallurgical examination update of baffle bolts removed from operating French PWR", in *Proc. of the International Symposium Fontevraud VI*, 2006.

[2] C. Panait, E. Fargeas, S. Miloudi, P. Moulart, M. Tommy-Martin, N. Monteil, and C. Pokor, "Metallurgical examinations update of baffle bolts removed from operating French PWR – Microstructural investigations of a baffle to former bolt located on a high level of the internal structures", in *Proc. of the International Symposium Fontevraud VIII*, 2014.

[3] AFCEN, *Règles de conception et de construction des matériels mécaniques des îlots nucléaires REP RCC-M 3308.*

[4] S. Perrin, L. Marchetti, C. Duhamel, M. Sennour, and F. Jomard, "Influence of irradiation on the oxide film formed on 316L stainless steel in PWR Primary Water", *Oxidation of Metals*, vol. 80, no. 5-6, pp. 623–633, 2013.

[5] M. Dumerval, *Effet des défauts d'implantation sur la corrosion des aciers inoxydables austénitiques en milieu primaire des réacteurs à eau pressurisée.* PhD thesis, Université de Grenoble, Grenoble, France, 2014.

[6] K. Fukuya, H. Nishioka, K. Fujii, and Y. Kitsunai, "Characterization of surface oxides formed on irradiated stainless steels in simulated PWR primary water", in *Proc. of the International Symposium Fontevraud VIII*, 2014.

[7] J. Gupta, *Intergranular stress corrosion cracking of ion irradiated 304L stainless steel in PWR environment.* PhD thesis, Institut National Polytechnique de Toulouse, Toulouse, France, 2016.

[8] P. Deng, Q. Peng, E.-H. Han, W. Ke, C. Sun, and Z. Jiao, "Effect of irradiation on corrosion of 304 nuclear grade stainless steel in simulated PWR primary water", *Corrosion Science*, vol. 127, no. Supplement C, pp. 91 – 100, 2017.

[9] T. Fukumura, K. Fukuya, K. Fujii, T. Miura, and Y. Kitsunai, "Grain boundary oxidation of neutron irradiated stainless steels in simulated PWR water", in *Proceedings of the 18th International Conference on Environmental Degradation of Materials in Nuclear Power Systems – Water Reactors* (J. H. Jackson, D. Paraventi, and M. Wright, eds.), (Cham), pp. 937–947, Springer International Publishing, 2018.

[10] S. Cissé, L. Laffont, B. Tanguy, M.-C. Lafont, and E. Andrieu, "Effect of surface preparation on the corrosion of austenitic stainless steel 304L in high temperature steam and simulated PWR primary water", *Corrosion Science*, vol. 56, pp. 209–216, 2012.

[11] S. Ghosh, M. K. Kumar, and V. Kain, "High temperature oxidation behavior of AISI 304L stainless steel – Effect of surface working operations", *Applied Surface Science*, vol. 264, pp. 312 – 319, 2013.

[12] R. Soulas, *Effet de la cristallographie sur les premiers stades de l'oxydation des aciers austénitiques 316L*. PhD thesis, Institut National Polytechnique de Grenoble, Grenoble, France, 2012.

[13] R. Soulas, M. Cheynet, E. Rauch, T. Neisius, L. Legras, C. Domain, and Y. Brechet, "TEM investigations of the oxide layers formed on a 316L alloy in simulated PWR environment", *Journal of Materials Science*, vol. 48, no. 7, pp. 2861–2871, 2013.

[14] R. Matthews, R. Knusten, J. Westraadt, and T. Couvant, "Intergranular oxidation of 316L stainless steel in the PWR primary water environment", *Corrosion Science*, vol. 125, no. Supplement C, pp. 175 – 183, 2017.

[15] G. S. Was, *Fundamentals of Radiation Materials Science*. Berlin, Heidelberg, Germany: Springer Berlin Heidelberg, 2007.

[16] L. K. Mansur, "Correlation of neutron and heavy-ion damage: II. The predicted temperature shift if swelling with changes in radiation dose rate", *Journal of Nuclear Materials*, vol. 78, no. 1, pp. 156–160, 1978.

[17] L. Mansur, "Theory of transitions in dose dependence of radiation effects in structural alloys", *Journal of Nuclear Materials*, vol. 206, 1993.

[18] P. Scott, "A review of irradiation assisted stress corrosion cracking", *Journal of nuclear Materials*, vol. 211, no. 2, pp. 101–122, 1994.

[19] E. Potter and G. Mann, "Oxidation of mild steel in high-temperature aqueous systems", p. 417, 1961.

[20] R. L. Tapping, R. D. Davidson, E. McAlpine, and D. H. Lister, "The composition and morphology of oxide films formed on type 304 stainless steel in lithiated high temperature water", *Corrosion Science*, vol. 26, no. 8, pp. 563–576, 1986.

[21] D. H. Lister, R. D. Davidson, and E. McAlpine, "The mechanism and kinetics of corrosion product release from stainless steel in lithiated high temperature water", *Corrosion science*, vol. 27, no. 2, pp. 113–140, 1987.

[22] Z. Szklarska-Smialowska, K.-C. Chou, and Z. Xia, "The composition and properties of oxide films on type 304 stainless steel on exposure to lithiated water at 100–350 °C", *Corrosion science*, vol. 32, no. 5, pp. 609–619, 1991.

[23] Y.-J. Kim, "Characterization of the oxide film formed on type 316 stainless steel in 288 °C water in cyclic normal and hydrogen water chemistries", *Corrosion*, vol. 51, no. 11, pp. 849–860, 1995.

[24] M. Da Cunha Belo, M. Walls, N. E. Hakiki, J. Corset, E. Picquenard, G. Sagon, and D. Noël, "Composition, structure and properties of the oxide films formed on the stainless steel 316L in a primary type PWR environment", *Corrosion science*, vol. 40, no. 2, pp. 447–463, 1998.

[25] S. E. Ziemniak and M. Hanson, "Corrosion behavior of 304 stainless steel in high temperature, hydrogenated water", *Corrosion Science*, vol. 44, no. 10, pp. 2209–2230, 2002.

[26] T. Terachi, K. Fujii, and K. Arioka, "Microstructural characterization of SCC crack tip and oxide film for SUS 316 stainless steel in simulated PWR primary water at 320 °C", *Journal of nuclear science and technology*, vol. 42, no. 2, pp. 225–232, 2005.

[27] T. Terachi, T. Yamada, T. Miyamoto, K. Arioka, and K. Fukuya, "Corrosion behavior of stainless steels in simulated PWR primary water effect of chromium content in alloys and dissolved hydrogen", *Journal of Nuclear Science and Technology*, vol. 45, no. 10, pp. 975–984, 2008.

[28] S. Lozano-Perez, T. Yamada, T. Terachi, M. Schröder, C. A. English, G. D. W. Smith, C. R. M. Grovenor, and B. L. Eyre, "Multi-scale characterization of stress corrosion cracking of cold-worked stainless steels and the influence of Cr content", *Acta Materialia*, vol. 57, no. 18, pp. 5361–5381, 2009.

[29] S. Lozano-Perez, D. W. Saxey, T. Yamada, and T. Terachi, "Atom-probe tomography characterization of the oxidation of stainless steel", *Scripta Materialia*, vol. 62, no. 11, pp. 855–858, 2010.

[30] S. Cissé, *Influence de la localisation de la déformation plastique sur la Corrosion sous Contrainte des aciers inoxydables. Application à l'IASCC des internes de cuve*. PhD thesis, Institut National Polytechnique de Toulouse, Toulouse, France, 2012.

[31] K. Kruska, S. Lozano-Perez, D. W. Saxey, T. Terachi, T. Yamada, and G. D. W. Smith, "Nanoscale characterisation of grain boundary oxidation in cold-worked stainless steels", *Corrosion Science*, vol. 63, pp. 225–233, 2012.

[32] J. Chen, Q. Xiao, Z. Lu, X. Ru, H. Peng, Q. Xiong, and H. Li, "Characterization of interfacial reactions and oxide films on 316L stainless steel in various simulated PWR primary water environments", *Journal of Nuclear Materials*, vol. 489, no. Supplement C, pp. 137 – 149, 2017.

[33] X. Cheng, Z. Feng, C. Li, C. Dong, and X. Li, "Investigation of oxide film formation on 316L stainless steel in high-temperature aqueous environments", *Electrochimica Acta*, vol. 56, no. 17, pp. 5860–5865, 2011.

[34] J.-F. Marucco, *La Chimie des solides*. EDP sciences, 2012.

[35] J. Van Vleck, "Theory of the variations in paramagnetic anisotropy among different salts of the iron group", *Physical Review*, vol. 41, no. 2, p. 208, 1932.

[36] M. Robbins, G. Wertheim, R. Sherwood, and D. Buchanan, "Magnetic properties and site distributions in the system $FeCr_2O_4$ – Fe_3O_4 ($Fe^{2+}Cr_{2-x}Fe_x^{3+}O_4$)", *Journal of Physics and Chemistry of Solids*, vol. 32, no. 3, pp. 717–729, 1971.

[37] V. A. Kurepin, "A thermodynamic model of Fe–Cr spinels", *Contributions to Mineralogy and Petrology*, vol. 149, no. 5, pp. 591–599, 2005.

[38] A. Herbelin, T. Couvant, L. Legras, D. Delafosse, and G. Ilbevare, "Oxidation of austenitic stainless steels in PWR primary water", vol. 3, pp. 1592–1608, Curran Associates, Inc. 57 Morehouse Lane Red Hook, NY 12571 USA, 2010.

[39] S. T. S. R. E. Myers, S. M.; Picraux, "Defect trapping of ion-implanted deuterium in Fe", *Journal of Applied Physics*, vol. 50, pp. 5710–5719, 1979.

[40] M. Dumerval, S. Perrin, L. Marchetti, M. Tabarant, F. Jomard, and Y. Wouters, "Hydrogen absorption associated with the corrosion mechanism of 316L stainless steels in primary medium of Pressurized Water Reactor (PWR)", *Corrosion Science*, vol. 85, pp. 251–257, 2014.

[41] B. Stellwag, "The mechanism of oxide film formation on austenitic stainless steels in high temperature water", *Corrosion science*, vol. 40, no. 2, pp. 337–370, 1998.

[42] N. Mott, "A theory of the formation of protective oxide films on metals", *Transactions of the faraday Society*, vol. 35, pp. 1175–1177, 1939.

[43] N. Mott, "The theory of the formation of protective oxide films on metals – II", *Transactions of the faraday society*, vol. 35, pp. 472–483, 1940.

[44] N. Mott, "The theory of the formation of protective oxide films on metals – III", *Transactions of the Faraday Society*, vol. 43, pp. 429–434, 1947.

[45] N. Cabrera and N. F. Mott, "Theory of the oxidation of metals", *Reports on Progress in Physics*, vol. 12, no. 1, p. 163, 1949.

[46] F. P. Fehlner and N. F. Mott, "Low-temperature oxidation", *Oxidation of Metals*, vol. 2, no. 1, pp. 59–99, 1970.

[47] C. Chao, L. Lin, and D. Macdonald, "A point defect model for anodic passive films I. Film growth kinetics", *Journal of the Electrochemical Society*, vol. 128, no. 6, pp. 1187–1194, 1981.

[48] D. D. Macdonald, "The point defect model for the passive state", *Journal of the Electrochemical Society*, vol. 139, no. 12, pp. 3434–3449, 1992.

[49] D. D. Macdonald, "Passivity – the key to our metals-based civilization", *Pure and Applied Chemistry*, vol. 71, no. 6, pp. 951–978, 1999.

[50] D. D. Macdonald, "The history of the point defect model for the passive state: a brief review of film growth aspects", *Electrochimica Acta*, vol. 56, no. 4, pp. 1761–1772, 2011.

[51] D. D. Macdonald, "Some personal adventures in passivity – a review of the point defect model for film growth", *Russian Journal of Electrochemistry*, vol. 48, no. 3, pp. 235–258, 2012.

[52] M. Bojinov, G. Fabricius, P. Kinnunen, T. Laitinen, K. Mäkelä, T. Saario, and G. Sundholm, "Electrochemical study of the passive behaviour of Ni–Cr alloys in a borate solution—a mixed-conduction model approach", *Journal of Electroanalytical Chemistry*, vol. 504, no. 1, pp. 29–44, 2001.

[53] B. Beverskog, M. Bojinov, A. Englund, P. Kinnunen, T. Laitinen, K. Mäkelä, T. Saario, and P. Sirkiä, "A mixed-conduction model for oxide films on Fe, Cr and Fe–Cr alloys in high-temperature aqueous electrolytes –I. Comparison of the electrochemical behaviour at room temperature and at 200°C", *Corrosion science*, vol. 44, no. 9, pp. 1901–1921, 2002.

[54] B. Beverskog, M. Bojinov, P. Kinnunen, T. Laitinen, K. Mäkelä, and T. Saario, "A mixed-conduction model for oxide films on Fe, Cr and Fe–Cr alloys in high-temperature aqueous electrolytes – II. Adaptation and justification of the model", *Corrosion Science*, vol. 44, no. 9, pp. 1923–1940, 2002.

[55] I. Betova, M. Bojinov, P. Kinnunen, K. Lundgren, and T. Saario, "Mixed-conduction model for stainless steel in a high-temperature electrolyte: estimation of kinetic parameters of inner layer constituents", *Journal of the Electrochemical Society*, vol. 155, no. 2, pp. C81–C92, 2008.

[56] A. Seyeux, V. Maurice, and P. Marcus, "Oxide film growth kinetics on metals and alloys – I. Physical model", *Journal of The Electrochemical Society*, vol. 160, no. 6, pp. C189–C196, 2013.

[57] J. Castle and H. Masterson, "The role of diffusion in the oxidation of mild steel in high temperature aqueous solutions", *Corrosion Science*, vol. 6, no. 3, pp. 93–104, 1966.

[58] U. R. Evans, *The corrosion and oxidation of metals: scientific principles and practical applications*. Lond.: Edward Arnold, 1960.

[59] P. Harrison, "Oxidation by transport through blocking pores", *Journal of The Electrochemical Society*, vol. 112, no. 2, pp. 235–237, 1965.

[60] J. Robertson, "The mechanism of high temperature aqueous corrosion of steel", *Corrosion Science*, vol. 29, no. 11, pp. 1275–1291, 1989.

[61] J. Robertson, "The mechanism of high temperature aqueous corrosion of stainless steels", *Corrosion Science*, vol. 32, pp. 443–457, 1991.

[62] A. Machet, *Etude des premiers stades d'oxydation d'alliages inoxydables dans l'eau à haute température*. PhD thesis, Université Pierre et Marie Curie - Paris VI, Paris, France, 2004.

[63] F. Carrette, *Relâchement des produits de corrosion des tubes en alliage 690 de générateur de vapeur du circuit primaire des réacteurs à eau pressurisée*. PhD thesis, Institut National Polytechnique de Toulouse, Toulouse, France, 2002.

[64] A. Mazenc, *Caractérisation par ToF-SIMS des couches de passivation des tubes de générateurs de vapeur en Alliage 690 pour l'industrie nucléaire: apport à la compréhension des mécanismes*. PhD thesis, Université Paris 6, Paris, France, 2013.

[65] M. Dumerval, S. Perrin, L. Marchetti, M. Sennour, F. Jomard, S. Vaubaillon, and Y. Wouters, "Effect of implantation defects on the corrosion of 316L stainless steels in primary medium of pressurized water reactors", *Corrosion Science*, vol. 107, pp. 1 – 8, 2016.

[66] P. Miguet, "Contribution à l'étude de la cinétique de corrosion généralisée de l'alliage 600 en milieu primaire : Etude microstructurale de l'influence de l'écrouissage, de la taille de grains et de l'électropolissage sur la nature et les propriétés du film d'oxyde", Note EDF HT-41/98/038/A, EDF R&D, Moret-sur-Loing, France, 2000.

[67] F. Abe, H. Araki, H. Yoshida, M. Okada, and R. Watanabe, "The effect of grain size on the corrosion behaviour of inconel 600 in high temperature steam", *Corrosion Science*, vol. 21, no. 12, pp. 819–842, 1981.

[68] M. Warzee, J. Hennaut, M. Maurice, C. Sonnen, J. Waty, and P. Berge, "Effect of surface treatment on the corrosion of stainless steels in high temperature water and steam", *Journal of the electrochemical society*, vol. 112, no. 7, pp. 670–674, 1965.

[69] S. E. Ziemniak, M. Hanson, and P. C. Sander, "Electropolishing effects on corrosion behavior of 304 stainless steel in high temperature, hydrogenated water", *Corrosion Science*, vol. 50, no. 9, pp. 2465–2477, 2008.

[70] S. Gardey, *Etude de la corrosion généralisée des alliages 600, 690 et 800 en milieu primaire – Contribution à la compréhension des mécanismes*. PhD thesis, Université Pierre et Marie Curie, Paris, France, 1998.

[71] E.-H. W. J.-Q. Guo, Y.-L.; Han, "Effects of surface states on the oxidation behavior of 316LN stainless steel in high temperature pressurized water", *Materials and Corrosion/Werkstoffe und Korrosion*, vol. 66, pp. 670–680, 07 2015.

[72] F. Delabrouille, *Caractérisation par MET de fissures de corrosion sous contrainte d'alliages à base de nickel: influence de la teneur en chrome et de la chimie du milieu.* PhD thesis, Institut National Polytechnique de Toulouse, Toulouse, France, 2004.

[73] H. Sun, X. Wu, E.-H. Han, and Y. Wei, "Effects of pH and dissolved oxygen on electrochemical behavior and oxide films of 304SS in borated and lithiated high temperature water", *Corrosion Science*, vol. 59, pp. 0–342, 2012.

[74] M. Dupin, P. Gosser, M. Walls, B. Rondot, J.-L. Pastol, S. Faty, M. Ferreira, and M. D. C. Belo, "Influence du pH sur les proprietes chimiques et structurales des films d'oxyde formes sur l'acier 316L et les alliages 600 et 690 dans les milieux aqueux a haute temperature", in *Annales de Chimie Science des Matériaux*, vol. 27, pp. 19–32, Elsevier, 2002.

[75] X. Gao, X. Wu, Z. Zhaoen, H. Guan, and E.-h. Han, "Characterization of oxide films grown on 316L stainless steel exposed to H_2O_2-containing supercritical water", *The Journal of Supercritical Fluids*, vol. 42, pp. 157–163, 2007.

[76] Y.-J. Kim, "Analysis of oxide film formed on type 304 stainless steel in 288 °C water containing oxygen, hydrogen, and hydrogen peroxide", *Corrosion*, vol. 55, no. 1, pp. 81–88, 1999.

[77] W. Kuang, E.-H. Han, X. Wu, and J. Rao, "Microstructural characteristics of the oxide scale formed on 304 stainless steel in oxygenated high temperature water", *Corrosion Science*, vol. 52, no. 11, pp. 3654–3660, 2010.

[78] J. B. Moore and R. L. Jones, "Growth characteristics of iron oxide films generated in dilute lithium hydroxide solution at 300 °C", *Journal of The Electrochemical Society*, vol. 115, no. 6, pp. 576–583, 1968.

[79] Y. Chimi, Y. Kitsunai, S. Kasahara, K. Chatani, M. Koshiishi, and Y. Nishiyama, "Correlation between locally deformed structure and oxide film properties in austenitic stainless steel irradiated with neutrons", *Journal of Nuclear Materials*, vol. 475, pp. 71 – 80, 2016.

[80] L. Marchetti-Sillans, *Corrosion généralisée des alliages à base nickel en milieu aqueux à haute température:apport à la compréhension des mécanismes.* PhD thesis, Ecole Nationale Supérieure des Mines de Saint-Etienne, Saint-Etienne, 2006.

[81] S. S. Raiman, A. Flick, O. Toader, P. Wang, N. A. Samad, Z. Jiao, and G. S. Was, "A facility for studying irradiation accelerated corrosion in high temperature water", *Journal of Nuclear Materials*, vol. 451, no. 1, pp. 40–47, 2014.

[82] S. Raiman, P. Wang, and G. S. Was, "Irradiation accelerated corrosion of stainless steel", 2014.

[83] S. Raiman and G. S. Was, "Composition and morphology of the oxide film formed on 316L stainless steel during in-situ proton irradiation in PWR conditions", in *Proceedings of the 17th International Conference on Environmental Degradation of Materials in Nuclear Power Systems–Water Reactors*, (Ottawa, Ontario, Canada), pp. 567–582, 2015.

[84] S. S. Raiman, D. M. Bartels, and G. S. Was, "Radiolysis driven changes to oxide stability during irradiation-corrosion of 316L stainless steel in high temperature water", *Journal of Nuclear Materials*, vol. 493, 2017.

[85] S. S. Raiman and G. S. Was, "Accelerated corrosion and oxide dissolution in 316L stainless steel irradiated in situ in high temperature water", *Journal of Nuclear Materials*, vol. 493, no. Supplement C, pp. 207 – 218, 2017.

[86] R. D. Hanbury and G. S. Was, "Effect of grain orientation on irradiation assisted corrosion of 316L stainless steel in simulated PWR primary water", in *Proceedings of the 18th International Conference on Environmental Degradation of Materials in Nuclear Power Systems–Water Reactors*, (Portland, Oregon, USA), pp. 1087–1096, Springer, 2018.

[87] Y. Z. Huang and J. M. Titchmarsh, "TEM investigation of intergranular stress corrosion cracking for 316 stainless steel in PWR environment", *Acta Materialia*, vol. 54, no. 3, pp. 635–641, 2006.

[88] G. Han, Z. Lu, X. Ru, J. Chen, J. Zhang, and B. Zou, "Surface oxidation of 316L SS and model alloys in simulated PWR primary water", in *Proceedings of the 17th International Conference on Environmental Degradation of Materials in Nuclear Power Systems–Water Reactors*, 2015.

[89] G. Han, Z. Lu, X. Ru, J. Chen, J. Zhang, and T. Shoji, "Properties of oxide films formed on 316L SS and model alloys with modified Ni, Cr and Si contents in high temperature water", *Corrosion Science*, vol. 106, pp. 157 – 171, 2016.

[90] S. M. Bruemmer, E. P. Simonen, P. M. Scott, P. L. Andresen, G. S. Was, and J. L. Nelson, "Radiation-induced material changes and susceptibility to intergranular failure of light-water-reactor core internals", *Journal of Nuclear Materials*, vol. 274, no. 3, pp. 299–314, 1999.

[91] D. Edwards, E. Simonen, and S. Bruemmer, "Evolution of fine-scale defects in stainless steels neutron-irradiated at 275 °C", *Journal of Nuclear Materials*, vol. 317, no. 1, pp. 13–31, 2003.

[92] S. J. Zinkle, P. J. Maziasz, and R. E. Stoller, "Dose dependence of the microstructural evolution in neutron-irradiated austenitic stainless steel", *Journal of Nuclear materials*, vol. 206, no. 2, pp. 266–286, 1993.

[93] B. H. Sencer, G. S. Was, M. Sagisaka, Y. Isobe, G. M. Bond, and F. A. Garner, "Proton irradiation emulation of PWR neutron damage microstructures in solution annealed 304 and cold-worked 316 stainless steels", *Journal of Nuclear Materials*, vol. 323, no. 1, pp. 18–28, 2003.

[94] G. S. Was, J. Busby, T. Allen, E. Kenik, A. Jenssen, S. Bruemmer, J. Gan, D. Edwards, P. Scott, and P. Andresen, "Emulation of neutron irradiation effects with protons: validation of principle", *Journal of Nuclear Materials*, vol. 300, pp. 198–216, 2002.

[95] C. Pokor, Y. Brechet, P. Dubuisson, J.-P. Massoud, and A. Barbu, "Irradiation damage in 304 and 316 stainless steels: experimental investigation and modeling. Part I: Evolution of the microstructure", *Journal of Nuclear Materials*, vol. 326, no. 1, pp. 19–29, 2004.

[96] P. J. Maziasz, "Overview of microstructural evolution in neutron-irradiated austenitic stainless steels", *Journal of nuclear materials*, vol. 205, pp. 118–145, 1993.

[97] D. Edwards, E. Simonen, F. Garner, L. Greenwood, B. Oliver, and S. Bruemmer, "Influence of irradiation temperature and dose gradients on the microstructural evolution in neutron-irradiated 316SS", *Journal of Nuclear Materials*, vol. 317, no. 1, pp. 32–45, 2003.

[98] K. Fukuya, K. Fujii, H. Nishioka, and Y. Kitsunai, "Evolution of microstructure and microchemistry in cold-worked 316 stainless steels under PWR irradiation", *Journal of Nuclear Science and Technology*, vol. 43, no. 2, pp. 159–173, 2006.

[99] D. Edwards, F. Garner, S. Bruemmer, and P. Efsing, "Nano-cavities observed in a 316SS PWR flux thimble tube irradiated to 33 and 70 dpa", *Journal of Nuclear Materials*, vol. 384, no. 3, pp. 249–255, 2009.

[100] A. Renault, J. Malaplate, C. Pokor, and P. Gavoille, "TEM and EFTEM characterization of solution annealed 304L stainless steel irradiated in PHENIX, up to 36 dpa and at 390°C", *Journal of Nuclear Materials*, vol. 421, no. 1, pp. 124–131, 2012.

[101] G. S. Was, T. R. Allen, J. T. Busby, J. Gan, D. Damcott, D. Carter, M. Atzmon, and E. A. Kenik, "Microchemistry and microstructure of proton-irradiated austenitic alloys: toward an understanding of irradiation effects in LWR core components", *Journal of Nuclear Materials*, vol. 270, no. 1–2, pp. 96–114, 1999.

[102] E. H. Lee, T. S. Byun, J. D. Hunn, K. Farrell, and L. K. Mansur, "Origin of hardening and deformation mechanisms in irradiated 316LN austenitic stainless steel", *Journal of nuclear materials*, vol. 296, no. 1, pp. 183–191, 2001.

[103] J. Gan and G. Was, "Microstructure evolution in austenitic Fe-Cr-Ni alloys irradiated with protons: comparison with neutron-irradiated microstructures", *Journal of Nuclear Materials*, vol. 297, pp. 161–175, 2001.

[104] J. T. Busby, G. S. Was, and E. A. Kenik, "Isolating the effect of radiation-induced segregation in irradiation-assisted stress corrosion cracking of austenitic stainless steels", *Journal of Nuclear Materials*, vol. 302, no. 1, pp. 20–40, 2002.

[105] A. Etienne, M. Hernández-Mayoral, C. Genevois, B. Radiguet, and P. Pareige, "Dislocation loop evolution under ion irradiation in austenitic stainless steels", *Journal of Nuclear Materials*, vol. 400, no. 1, pp. 56–63, 2010.

[106] A. Volgin, *Characterization and understanding of ion irradiation effect on the microstructure of austenitic stainless steels.* PhD thesis, Université de Rouen, Rouen, France, 2012.

[107] M. L. Millier, *Fragilisation des aciers inoxydables austénitiques sous irradiation : évolution de la microstructure et amorçage de la corrosion sous contrainte assistée par l'irradiation en milieu REP.* PhD thesis, Ecole Nationale Supérieure des Mines de Paris, Paris, France, 2014.

[108] K. J. Stephenson and G. S. Was, "Comparison of the microstructure, deformation and crack initiation behavior of austenitic stainless steel irradiated in-reactor or with protons", *Journal of Nuclear Materials*, vol. 456, pp. 85–98, 2015.

[109] J. Gupta, J. Hure, B. Tanguy, L. Laffont, M.-C. Lafont, and E. Andrieu, "Evaluation of stress corrosion cracking of irradiated 304L stainless steel in PWR environment using heavy ion irradiation", *Journal of Nuclear Materials*, vol. 476, pp. 82 – 92, 2016.

[110] L. Legras, A. Volgin, B. Radiguet, P. Pareige, C. Pokor, B. Décamps, T. Couvant, N. Huin, and R. Soulas, "Using microscopy to help with the understanding of degradation mechanisms observed in materials of pressurized water reactors", *Journal of Materials Science and Engineering B*, vol. 7, no. 5, pp. 187–220, 2017.

[111] T. Allen, J. Cole, C. Trybus, D. Porter, H. Tsai, F. Garner, E. Kenik, T. Yoshitake, and J. Ohta, "The effect of dose rate on the response of austenitic stainless steels to neutron radiation", *Journal of Nuclear Materials*, vol. 348, no. 1-2, pp. 148–164, 2006.

[112] T. Shoji, S.-i. Suzuki, and K. S. Raja, "Current status and future of IASCC research", *Journal of nuclear materials*, vol. 258, pp. 241–251, 1998.

[113] J. P. Foster, D. L. Porter, D. Harrod, T. Mager, and M. Burke, "316 stainless steel cavity swelling in a PWR", *Journal of Nuclear Materials*, vol. 224, pp. 207–215, 1995.

[114] P. Maziasz, "Some effects of increased helium content on void formation and solute segregation in neutron irradiated type 316 stainless steel", *Journal of Nuclear Materials*, vol. 108, pp. 359 – 384, 1982.

[115] K. Q. Chen, S. H. Yang, Z. G. Wang, J. G. Sun, J. M. Quan, L. W. Li, and Y. M. Sun, "The analysis of microstructure of helium bubbles in 316L SS induced by 3.02 MeV He ion irradiation", *Journal of Nuclear Materials*, vol. 191–194, Part B, pp. 737–741, 1992.

[116] T. Fukuda, T. Aoki, Y. Isobe, T. Furuya, A. Hasegawa, and K. Abe, "Microchemical and microstructural changes of austenitic steels caused by proton irradiation following helium implantation", *Journal of Nuclear Materials*, vol. 258–263, Part 2, pp. 1694–1699, 1998.

[117] M. Horiki and M. Kiritani, "Microstructural evolution in low-dose neutron-irradiated Fe-16Ni-15Cr alloy", *Journal of nuclear materials*, vol. 212, pp. 246–251, 1994.

[118] P. R. Okamoto and L. E. Rehn, "Radiation-induced segregation in binary and ternary alloys", *Journal of Nuclear Materials*, vol. 83, no. 1, pp. 2–23, 1979.

[119] E. Kenik and K. Hojou, "Radiation-induced segregation in FFTF-irradiated austenitic stainless steels", *Journal of Nuclear Materials*, vol. 191-194, pp. 1331–1335, 1992.

[120] E. Kenik, "Radiation-induced segregation in irradiated type 304 stainless steels", *Journal of nuclear materials*, vol. 187, no. 3, pp. 239–246, 1992.

[121] T. R. Allen, J. T. Busby, G. S. Was, and E. A. Kenik, "On the mechanism of radiation-induced segregation in austenitic Fe–Cr–Ni alloys", *Journal of Nuclear Materials*, vol. 255, no. 1, pp. 44–58, 1998.

[122] T. Fukuda, M. Sagisaka, Y. Isobe, A. Hasegawa, M. Sato, K. Abe, Y. Nishida, T. Kamada, and Y. Kaneshima, "Microstructural changes of austenitic steels caused by proton irradiation under various conditions", *Journal of Nuclear Materials*, vol. 283–287, Part 1, pp. 263–267, 2000.

[123] K. Fukuya, M. Nakano, K. Fujii, and T. Torimaru, "Role of radiation induced grain boundary segregation in irradiation assisted stress corrosion cracking", *Journal of Nuclear Science and Technology*, vol. 41, no. 5, pp. 594–600, 2004.

[124] T. Allen, J. Cole, E. Kenik, and G. Was, "Analyzing the effect of displacement rate on radiation-induced segregation in 304 and 316 stainless steels by examining irradiated EBR-II components and samples irradiated with protons", *Journal of Nuclear Materials*, vol. 376, no. 2, pp. 169–173, 2008.

[125] K. Fukuya, "Current understanding of radiation-induced degradation in light water reactor structural materials", *Journal of Nuclear Science and Technology*, vol. 50, no. 3, pp. 213–254, 2013.

[126] K. G. Field, Y. Yang, T. R. Allen, and J. T. Busby, "Defect sink characteristics of specific grain boundary types in 304 stainless steels under high dose neutron environments", *Acta Materialia*, vol. 89, pp. 438–449, 2015.

[127] Y. Dong, B. H. Sencer, F. A. Garner, and E. A. Marquis, "Microchemical and microstructural evolution of AISI 304 stainless steel irradiated in EBR-II at PWR-relevant dpa rates", *Journal of Nuclear Materials*, vol. 467, Part 2, pp. 692–702, 2015.

[128] R. D. Carter, D. L. Damcott, M. Atzmon, G. S. Was, and E. A. Kenik, "Effects of proton irradiation on the microstructure and microchemistry of type 304L stainless steel", *Journal of Nuclear Materials*, vol. 205, pp. 361–373, 1993.

[129] L. Wen-Jen, K. Ji-Jung, and T. Chuen-Horng, "Proton irradiation induced segregation and phase transformation in AISI 304 and AISI 304L stainless steels", *Journal of Nuclear Materials*, vol. 212–215, Part 1, pp. 476–481, 1994.

[130] T. Duh, J. Kai, and F. Chen, "Effects of grain boundary misorientation on solute segregation in thermally sensitized and proton-irradiated 304 stainless steel", *Journal of Nuclear Materials*, vol. 283–287, Part 1, pp. 198 – 204, 2000. 9th Int. Conf. on Fusion Reactor Materials.

[131] A. Etienne, B. Radiguet, N. Cunningham, G. Odette, and P. Pareige, "Atomic scale investigation of radiation-induced segregation in austenitic stainless steels", *Journal of Nuclear Materials*, vol. 406, no. 2, pp. 244–250, 2010.

[132] A. Etienne, B. Radiguet, N. Cunningham, G. Odette, R. Valiev, and P. Pareige, "Comparison of radiation-induced segregation in ultrafine-grained and conventional 316 austenitic stainless steels", *Ultramicroscopy*, vol. 111, no. 6, pp. 659–663, 2011.

[133] Z. Jiao and G. Was, "Novel features of radiation-induced segregation and radiation-induced precipitation in austenitic stainless steels", *Acta Materialia*, vol. 59, no. 3, pp. 1220–1238, 2011.

[134] N. Sakaguchi, M. Endo, S. Watanabe, H. Kinoshita, S. Yamashita, and H. Kokawa, "Radiation-induced segregation and corrosion behavior on Σ3 coincidence site lattice and random grain boundaries in proton-irradiated type 316L austenitic stainless steel", *Journal of Nuclear Materials*, vol. 434, no. 1–3, pp. 65–71, 2013.

[135] C. M. Barr, G. A. Vetterick, K. A. Unocic, K. Hattar, X.-M. Bai, and M. L. Taheri, "Anisotropic radiation-induced segregation in 316L austenitic stainless steel with grain boundary character", *Acta Materialia*, vol. 67, pp. 145–155, 2014.

[136] A. Etienne, B. Radiguet, P. Pareige, J.-P. Massoud, and C. Pokor, "Tomographic atom probe characterization of the microstructure of a cold worked 316 austenitic stainless steel after neutron irradiation", *Journal of Nuclear Materials*, vol. 382, pp. 64–69, 2008.

[137] A. Etienne, B. Radiguet, and P. Pareige, "Understanding silicon-rich phase precipitation under irradiation in austenitic stainless steels", *Journal of Nuclear Materials*, vol. 406, no. 2, pp. 251–256, 2010.

[138] Z. Jiao and G. S. Was, "Precipitate behavior in self-ion irradiated stainless steels at high doses", *Journal of Nuclear Materials*, vol. 449, no. 1–3, pp. 200–206, 2014.

[139] K. Fujii and K. Fukuya, "Irradiation-induced microchemical changes in highly irradiated 316 stainless steel", *Journal of Nuclear Materials*, 2015.

[140] Y. Isobe, M. Sagisaka, F. Garner, S. Fujita, and T. Okita, "Precipitate evolution in low-nickel austenitic stainless steels during neutron irradiation at very low dose rates", *Journal of Nuclear Materials*, vol. 386-388, pp. 661–665, 2009.

[141] J. Michalička, Z. Jiao, and G. Was, "Radiation-induced precipitates in a self-ion irradiated cold-worked 316 austenitic stainless steel used for PWR baffle-bolts", in *Proceedings of the 18th International Conference on Environmental Degradation of Materials in Nuclear Power Systems – Water Reactors* (J. H. Jackson, D. Paraventi, and M. Wright, eds.), (Cham), pp. 565–580, Springer International Publishing, 2018.

[142] A. Etienne, *Etude des effets d'irradiations et de la nanostructuration dans des aciers austénitiques inoxydables*. PhD thesis, Université de Rouen, Rouen, France, 2009.

[143] L. Priester, *Les joints de grains*. EDP Sciences, 2006.

[144] P. Lejcek, *Grain Boundary Segregation in Metals*. Springer Series in Materials Science 136, Springer-Verlag Berlin Heidelberg, 1 ed., 2010.

[145] A. Morawiec, "Low-Σ twist and tilt grain boundaries in cubic materials", *Journal of Applied Crystallography*, vol. 44, no. 6, pp. 1152–1156, 2011.

[146] D. Brandon, "The structure of high-angle grain boundaries", *Acta Metallurgica*, vol. 14, pp. 1479–1484, 1966.

[147] N. Hashimoto, Y. Eda, and H. Takahashi, "Effect of crystal orientation on grain boundary migration and radiation-induced segregation", *Journal of Nuclear Materials*, vol. 239, pp. 180–184, 1996.

[148] T. Duh, J. Kai, F. Chen, and L. Wang, "Effects of grain boundary misorientation on the solute segregation in austenitic stainless steels", *Journal of Nuclear Materials*, vol. 258–263, Part 2, pp. 2064 – 2068, 1998.

[149] S. Watanabe, Y. Takamatsu, N. Sakaguchi, and H. Takahashi, "Sink effect of grain boundary on radiation-induced segregation in austenitic stainless steel", *Journal of Nuclear Materials*, vol. 283–287, Part 1, pp. 152 – 156, 2000. 9th Int. Conf. on Fusion Reactor Materials.

[150] T. Duh, J. Kai, F. Chen, and L. Wang, "Numerical simulation modeling on the effects of grain boundary misorientation on radiation-induced solute segregation in 304 austenitic stainless steels", *Journal of Nuclear Materials*, vol. 294, no. 3, pp. 267 – 273, 2001.

[151] G.-G. Lee, H.-H. Jin, Y.-B. Lee, and J. Kwon, "Observation and rate theory modeling of grain boundary segregation in Σ3 twin boundaries in ion-irradiated stainless steel 316", *Journal of Nuclear Materials*, vol. 449, no. 1–3, pp. 234 – 241, 2014.

[152] S. Lejček, Pavel; Hofmann, "Thermodynamics and structural aspects of grain boundary segregation", *Critical Reviews in Solid State and Material Sciences*, vol. 20, pp. 1–85, 1995.

[153] G. S. Was and T. R. Allen, "Radiation damage from different particle types", in *Radiation Effects in Solids - NATO Science Series II - Mathematics, Physics and Chemistry*, vol. 235, pp. 65–98, Springer, 2007.

[154] H. Lepp, "Stages in the oxidation of magnetite", 1957.

[155] "Optical constants of Fe_3O_4." `https://refractiveindex.info/?shelf=main&book=Fe3O4&page=Querry`.

[156] C. A. Schneider, W. S. Rasband, and K. W. Eliceiri, "NIH Image to ImageJ: 25 years of image analysis", *Nature methods*, vol. 9, no. 7, p. 671, 2012.

[157] P. Hovington, D. Drouin, and R. Gauvin, "CASINO: A new Monte Carlo code in C language for electron beam interaction — Part I: Description of the program", *Scanning*, vol. 19, no. 1, pp. 1–14, 1997.

[158] D. Drouin, A. R. Couture, D. Joly, X. Tastet, V. Aimez, and R. Gauvin, "CASINO V2.42 — A fast and easy-to-use modeling tool for scanning electron microscopy and microanalysis users", *Scanning*, vol. 29, no. 3, pp. 92–101, 2007.

[159] A. Aitkaliyeva, J. W. Madden, B. D. Miller, J. I. Cole, and J. Gan, "Comparison of preparation techniques for nuclear materials for transmission electron microscopy (TEM)", *Journal of Nuclear Materials*, vol. 459, pp. 241–246, 04 2015.

[160] M.-H. Lee and K.-H. Kim, "Post-thinning using ar ion-milling system for transmission electron microscopy specimens prepared by focused ion beam system",

[161] L. Legras, M. L. Lescoat, S. Jublot-Leclerc, and A. Gentils, "Optimisation of TEM preparation in metallic materials using low voltage ions." Poster presented at the European Microscopy Congress, Lyon, France, 2016.

[162] L. Legras, "Préparation d'échantillons par microscope double faisceau pour observations par MEB équipé d'un détecteur STEM ou par MET", in *Préparation des échantillons pour MEB et Microanalyses*, EDP Sciences, Philippe Jonnard en collaboration avec François Brisset, 2011.

[163] M. Cantoni, "Focused Ion Beam." CIME courses, PDF slides, 2014.

[164] B. Fultz and J. Howe, *Transmission Electron Microscopy and Diffractometry of Materials.* Graduate Texts in Physics, Berlin, Heidelberg, Germany: Springer Berlin Heidelberg, 4th edition ed., 2013.

[165] D. B. Williams and C. B. Carter, *Transmission Electron Microscopy: A Textbook for Materials Science, Second Edition.* Boston, Massachusetts, USA: Springer US, 2nde ed., 2009.

[166] X. Sun, "Study of deformed layer formed during mechnical stages of specimen preparation for EBSD and TEM", internship repport, EDF R&D and PHELMA, Moret Sur Loing, France, 2016.

[167] J. F. Ziegler, M. D. Ziegler, and J. P. Biersack, "SRIM — The Stopping and Range of Ions in Matter", *Nuclear Instruments and Methods in Physics Research Section B: Beam Interactions with Materials and Atoms*, vol. 268, no. 11, pp. 1818–1823, 2010.

[168] R. Stoller, M. Toloczko, G. Was, A. Certain, S. Dwaraknath, and F. Garner, "On the use of SRIM for computing radiation damage exposure", *Nuclear Instruments and Methods in Physics Research Section B: Beam Interactions with Materials and Atoms*, vol. 310, pp. 75–80, 2013.

[169] J. Gan, E. Simonen, S. Bruemmer, L. Fournier, B. Sencer, and G. Was, "The effect of oversized solute additions on the microstructure of 316SS irradiated with 5 MeV Ni^{2+} ions or 3.2 MeV protons", *Journal of Nuclear Materials*, vol. 325, no. 2-3, pp. 94–106, 2004.

[170] P. J. Maziasz and C. J. McHargue, "Microstructural evolution in annealed austenitic steels during neutron irradiation", *International Materials Reviews*, vol. 32, no. 1, pp. 190–219, 1987.

[171] M. Sennour, L. Marchetti, F. Martin, S. Perrin, R. Molins, and M. Pijolat, "A detailed TEM and SEM study of Ni-base alloys oxide scales formed in primary conditions of pressurized water reactor", *Journal of Nuclear Materials*, vol. 402, no. 2-3, pp. 147–156, 2010.

[172] "International Center for Diffraction Data – Powder Diffraction File of chromite ($FeCr_2O_4$) (PDF card 00–034–0140)."

[173] "International Center for Diffraction Data – Powder Diffraction File of magnetite (Fe_3O_4) (PDF card 00–019–0629)."

[174] D. Simeone, G. Baldinozzi, D. Gosset, S. Le Caer, and J.-F. Bérar, "Grazing incidence x-ray diffraction for the study of polycrystalline layers", *Thin Solid Films*, vol. 530, pp. 9–13, 2013.

[175] K. McCarty and D. Boehme, "A Raman study of the systems $Fe_{3-x}Cr_xO_4$ and $Fe_{2-x}Cr_xO_3$", *Journal of Solid State Chemistry*, vol. 79, no. 1, pp. 19–27, 1989.

[176] P. Aaltonen, K. Makela, H. Venz, and H. Meier, "X-ray diffraction characterization of oxide films on primary circuit surfaces at Beznau Unit 1", in *Netherlands Corrosion Centre, EUROCORR'98 Book of Abstracts*, p. 110, 1998.

[177] S. E. Ziemniak and R. A. Castelli, "Immiscibility in the Fe_3O_4–$FeCr_2O_4$ spinel binary", *Journal of Physics and Chemistry of Solids*, vol. 64, no. 11, pp. 2081–2091, 2003.

[178] M. Wang, *Electrochemical behaviour of stainless steel under radiation and exposed to representative chemistry in Pressurised Water Reactor conditions*. PhD thesis, Ecole Polytechnique X, Paris, France, 2013.

[179] H. Ming, Z. Zhang, J. Wang, R. Zhu, J. Ding, J. Wang, E.-H. Han, and W. Ke, "Effect of surface state on the oxidation behavior of welded 308L in simulated nominal primary water of PWR", *Applied Surface Science*, vol. 337, pp. 81–89, 2015.

[180] M. Watanabe, T. Yonezawa, T. Shobu, and T. Shoji, "In situ X-Ray diffraction measurement method for investigating the oxides films on austenitic stainless steel in simulated Pressurized Water Reactor Primary Water", *Corrosion*, vol. 71, no. 10, pp. 1224–1236, 2015.

[181] "International Center for Diffraction Data – Powder Diffraction File of chromium oxide (Cr_2O_3) (PDF card 00–006–0504)."

[182] "Raman spectrum of chromite ($FeCr_2O_4$) obtained with a 532 nm laser." `http://rruff.info/tags=119/R110060`.

[183] A. Wang, K. E. Kuebler, B. L. Jolliff, and L. A. Haskin, "Raman spectroscopy of Fe-Ti-Cr oxides, case study: Martian meteorite EETA79001", *American Mineralogist*, vol. 89, no. 5-6, pp. 665–680, 2004.

[184] B. D. Hosterman, *Raman spectroscopic study of solid solution spinel oxides*. PhD thesis, University of Nevada, Las Vegas, Nevada, USA, 2011.

[185] V. D'Ippolito, G. B. Andreozzi, D. Bersani, and P. P. Lottici, "Raman fingerprint of chromate, aluminate and ferrite spinels", *Journal of Raman Spectroscopy*, vol. 46, no. 12, pp. 1255–1264, 2015.

[186] Y. Behnamian, A. Mostafaei, A. Kohandehghan, B. S. Amirkhiz, J. Li, W. Zheng, D. Guzonas, M. Chmielus, W. Chen, and J. L. Luo, "Characterization of oxide layer and microcrack initiation in alloy 316L stainless steel after 20,000h exposure to supercritical water at 500°c", *Materials Characterization*, vol. 131, pp. 532 – 543, 2017.

[187] D. Tice, N. Platts, A. Panteli, J. Stairmand, and D. Swan, "Influence of steel sulfur content on corrosion fatigue crack growth of types 304 and 316 stainless steels in high temperature water", in *Proceedings of the 17th International Conference on Environmental Degradation of Materials in Nuclear Power Systems–Water Reactors*, (Ottawa, Ontario, Canada), 2015.

[188] E. West, T. Nolan, A. Lucente, D. Morton, N. Lewis, R. Morris, J. Mullen, and G. Newsome, "Effect of sulfur on the SCC and corrosion fatigue performance of stainless steel", in *Proc. of the International Symposium Fontevraud VIII*, 2014.

[189] M. Boisson, "Étude de l'effet de l'irradiation sur l'oxydation de l'acier austénitique inoxydable 316L", Note EDF H-T27-2015-06326-FR, EDF R&D, Moret-sur-Loing, France, 2015.

[190] F.-J. Perosanz, C. Maffiotte, M. Hernández, and S. Merino, "Comparative description of the effect of temperture and pH on oxide growth over time for irradiated 316L versus non-irradiated alloy", Tech. Rep. FP7-232612, Private technical report – PERFORM 60, 2013.

[191] S. Raiman, *Irradiation Accelerated Corrosion of 316L strainless steel in simulated primary water*. PhD thesis, University of Michigan, Ann Harbor, Michigan, USA, 2016.

[192] R. D. Hanbury and G. S. Was, "Effect of irradiation on the corrosion of austenitic stainless steel", tech. rep., Private technical report, 2017.

[193] W. Kuang, X. Wu, and E.-H. Han, "Influence of dissolved oxygen concentration on the oxide film formed on 304 stainless steel in high temperature water", *Corrosion Science*, vol. 63, pp. 259–266, 2012.

[194] W. G. Cook and R. P. Olive, "Pourbaix diagrams for the iron–water system extended to high-subcritical and low-supercritical conditions", *Corrosion Science*, vol. 55, pp. 326 – 331, 2012.

[195] I. Beverskog, B.; Puigdomenech, "Pourbaix diagrams for the ternary system of iron-chromium-nickel", *CORROSION*, vol. 55, pp. 1077–1087, 11 1999.

[196] L. E. Thomas and S. M. Bruemmer, "Analytical transmission electron microscopy characterization of stress corrosion cracks in an irradiated type 316 stainless steel core component", in *Proc. of the International Symposium Fontevraud V*, 2002.

[197] S. Bruemmer and L. Thomas, "High-resolution characterization of stress corrosion crack tips in stainless steel core internals", in *Proc. of the International Symposium Fontevraud VI*, vol. 6, p. 553, 2006.

[198] G. Bertali, M. G. Burke, F. Scenini, and N. Huin, "The effect of temperature on the preferential intergranular oxidation susceptibility of alloy 600", *Metallurgical and Materials Transactions A*, vol. 49, no. 5, pp. 1879–1894, 2018.

[199] M. Meisnar, M. Moody, and S. Lozano-Perez, "Atom probe tomography of stress corrosion crack tips in SUS316 stainless steels", *Corrosion Science*, vol. 98, pp. 661–671, 2015.

[200] H. Chung, J. Sanecki, and F. Garner, "Radiation-induced instability of MnS precipitates and its possible consequences on irradiation-induced stress corrosion cracking of austenitic stainless steels", in *Effects of Radiation on Materials: 18th International Symposium*, ASTM International, 1999.

[201] C. Pokor, *Caractérisation microstructurale et modélisation du durcissement des aciers austénitiques irradiés des structures internes des réacteurs à eau pressurisée*. PhD thesis, Institut National Polytechnique de Grenoble, Grenoble, France, 2002.

[202] F. Jambon, *Mécanismes d'absorption d'hydrogène et intéractions hydrogène-défauts : implications en corrosion sous contrainte des alliages à base nickel en milieu primaire des réacteurs à eau pressurisée*. PhD thesis, Evry-Val d'Essonne, Evry, France, 2012.

[203] A. Chopelas and A. Hofmeister, "Vibrational spectroscopy of aluminate spinels at 1 atm and of $MgAl_2O_4$ to over 200 kbar", *Physics and Chemistry of Minerals*, vol. 18, no. 5, pp. 279–293, 1991.

[204] L. Gasparov, D. Tanner, D. Romero, H. Berger, G. Margaritondo, and L. Forro, "Infrared and Raman studies of the Verwey transition in magnetite", *Physical Review B*, vol. 62, no. 12, p. 7939, 2000.

[205] "Raman spectrum of chromium oxide (Cr_2O_3) obtained with a 532 nm laser." `http://rruff.info/chem=Cr/R060892`.

[206] O. N. Shebanova and P. Lazor, "Raman spectroscopic study of magnetite ($FeFe_2O_4$): a new assignment for the vibrational spectrum", *Journal of Solid State Chemistry*, vol. 174, no. 2, pp. 424–430, 2003.

[207] M. Chen, J. Shu, X. Xie, and H.-k. Mao, "Natural $CaTi_2O_4$-structured $FeCr_2O_4$ polymorph in the Suizhou meteorite and its significance in mantle mineralogy", *Geochimica et Cosmochimica Acta*, vol. 67, no. 20, pp. 3937–3942, 2003.

[208] "Fast STEM spectrum imaging using simultaneous EELS and EDS in Gatan Microscopy Suite software." `http://www.gatan.com/fast-stem-spectrum-imaging-using-simultaneous-eels-and-eds-gatan-microscopy-suite-software`.

[209] E. Casnati, A. Tartari, and C. Baraldi, "An empirical approach to k-shell ionisation cross section by electrons", *Journal of Physics B: Atomic and Molecular Physics*, vol. 15, no. 1, p. 155, 1982.